ESO ASTROPHYSICS SYMPOSIA
European Southern Observatory

Series Editor: Bruno Leibundgut

Published titles include:

Randomized Algorithms for Analysis and Control of Uncertain Systems
Roberto Tempo, Giuseppe Calafiore and Fabrizio Dabbene

Stability and Stabilization of Infinite Dimensional Systems with Applications
Zheng-Hua Luo, Bao-Zhu Guo and Omer Morgul

Nonsmooth Mechanics (Second edition)
Bernard Brogliato

Nonlinear Control Systems II
Alberto Isidori

L_2-Gain and Passivity Techniques in nonlinear Control
Arjan van der Schaft

Control of Linear Systems with Regulation and Input Constraints
Ali Saberi, Anton A. Stoorvogel and Peddapullaiah Sannuti

Robust and H∞ Control
Ben M. Chen

Computer Controlled Systems
Efim N. Rosenwasser and Bernhard P. Lampe

Dissipative Systems Analysis and Control
Rogelio Lozano, Bernard Brogliato, Olav Egeland and Bernhard Maschke

Control of Complex and Uncertain Systems
Stanislav V. Emelyanov and Sergey K. Korovin

Robust Control Design Using H∞ Methods
Ian R. Petersen, Valery A. Ugrinovski and Andrey V. Savkin

Model Reduction for Control System Design
Goro Obinata and Brian D.O. Anderson

Control Theory for Linear Systems
Harry L. Trentelman, Anton Stoorvogel and Malo Hautus

Functional Adaptive Control
Simon G. Fabri and Visakan Kadirkamanathan

Positive 1D and 2D Systems
Tadeusz Kaczorek

Identification and Control Using Volterra Models
F.J. Doyle III, R.K. Pearson and B.A. Ogunnaike

Non-linear Control for Underactuated Mechanical Systems
Isabelle Fantoni and Rogelio Lozano

Robust Control (Second edition)
Jürgen Ackermann

Flow Control by Feedback
Ole Morten Aamo and Miroslav Krstiæ

Learning and Generalization (Second edition)
Mathukumalli Vidyasagar

Constrained Control and Estimation
Graham C. Goodwin, María M. Seron and José A. De Doná

Randomized Algorithms for Analysis and Control of Uncertain Systems
Roberto Tempo, Giuseppe Calafiore and Fabrizio Dabbene

Switched Linear Systems
Zhendong Sun and Shuzhi S. Ge

A. Merloni S. Nayakshin R.A. Sunyaev (Eds.)

Growing Black Holes: Accretion in a Cosmological Context

Proceedings
of the MPA/ESO/MPE/USM Joint Astronomy Conference
Held at Garching, Germany, 21-25 June 2004

Springer

Volume Editors

Dr. Andrea Merloni
Dr. Sergei Nayakshin
Prof. Rashid A. Sunyaev

Max-Planck-Institut for Astrophysics
Karl-Schwarzschild-Str. 1
85741 Garching
Germany

Series Editor

Bruno Leibundgut

European Southern Observatory
Karl-Schwarzschild-Str. 2
85748 Garching

ISBN 10 3-540-25275-4 Springer Berlin Heidelberg New York
ISBN 13 978-3-540-25275-7 Springer Berlin Heidelberg New York

Library of Congress Control Number: 2005922864

Springer is a part of Springer Science+Business Media
springeronline.com

Printed in Germany

Typesetting: Camera-ready by the authors/editors
Final processing by PTP-Berlin Protago-TEX-Production GmbH, Germany
Cover-Design: Erich Kirchner, Heidelberg

Printed on acid-free paper 55/3141/Yu – 5 4 3 2 1 0

Preface

Supermassive black holes (SMBH) are among the most spectacular objects in the Universe, and their study sheds light on fundamental physical phenomena occurring in their immediate vicinity, such as accretion of gas and strong gravity effects. Historically, theories of accretion have been developed and refined based on observational studies of individual objects believed to be powering Quasars, first discovered more than 40 years ago, and X-ray binaries. This research stood somewhat separate from cosmology, dealing primarily with formation and evolution of galaxies. However, in recent years, it has been established that SMBH are not just interesting laboratories of strong gravity and high-energy astrophysics, but have direct impact on the evolution of the large scale structure and have an influence on the appearence of our Universe. For this reason, we thought it was time to bring together scientists from the extra-galactic astronomy, cosmology and accretion physics communities to discuss the implications of the connection between supermassive black hole growth and galaxy formation.

The conference "Growing Black Holes: Accretion in a Cosmological Context" was held in Garching from June 21 to 25, 2004 as a part of the joint MPA/MPE/ESO/USM astronomy conference series. The meeting was attended by about 170 scientists from more than 20 countries all over the world. We are extremely happy with the response of the scientific community, either before, during, and after the conference. Each session featured excellent review and invited talks that summarized the state of the art in the research on the respective topic. These talks were followed and augmented by equally interesting contributed talks, many of which presented original ideas or the latest observational results. Lively discussions and busy poster sessions contributed to the success of the conference. We would like to thank warmly all of the participants for helping us to achieve this. Our hope is that these proceedings will reflect the excellent level of the scientific research discussed at the conference, and that they will become a useful research and reference tool for the entire community.

Many people were involved in the organizational effort; among them, special thanks are due the members of the Scientific Advisory Committee and the Local Organizing Committee. Also, we would like to express our gratitude to all the invited and review speakers for having agreed to participate and bring to the meeting their precious scientific contributions. However, the conference would not have been possible at all without the great support of Maria Depner, Gabriele Kratschmann, Kate O'Shea, Cornelia Rickl, the student helpers and other personnel from the Garching Research Campus. We express our sincere gratitude to all of them.

Garching, January 2005

Andrea Merloni
Sergei Nayakshin
Rashid Sunyaev

Growing Black Holes:

Scientific Advisory Committee:
Ralf Bender, Roger Blandford, Catherine Cesarsky, Reinhard Genzel, Martin Rees, Rashid Sunyaev, Scott Tremaine

Local Organizing Committee:
Jorge Cuadra, Andrea Merloni, Emmi Meyer, Sergei Nayakshin, Thibaut Paumard, Rashid Sunyaev, Gijs Verdoes Kleijn

Invited and Review Speakers:
Marek Abramowicz, Fred Baganoff, Ralf Bender, Roger Blandford, Niel Brandt, Karsten Danzmann, Andy Fabian, Xiaohui Fan, Reinhard Genzel, Zoltan Haiman, Guenther Hasinger, Guineviere Kauffmann, Andrew King, Abraham Loeb, Piero Madau, David Merritt, Sterl Phinney, Martin Rees, Bernard Schutz, Volker Springel

Contents

Part II Observations of Supermassive Black Holes at Higher Redshift

From the Earliest Seeds to Today's Supermassive Black Holes

P. Madau

Department of Astronomy and Astrophysics, University of California, Santa Cruz CA 95064, USA

Abstract. I review scenarios for the assembly of supermassive black holes (MBHs) at the center of galaxies that trace their hierarchical build-up far up in the dark matter halo "merger tree". Monte Carlo realizations of the merger hierarchy in a ΛCDM cosmology, coupled to semi-analytical recipes, are a powerful tool to follow the merger history of halos and the dynamics and growth of the MBHs they host. X-ray photons from miniquasars powered by intermediate-mass "seed" holes may permeate the universe more uniformly than EUV radiation, make the low-density diffuse intergalactic medium warm and weakly ionized prior to the epoch of reionization breakthrough, and set an entropy floor. The spin distribution of MBHs is determined by gas accretion, and is predicted to be heavily skewed towards fast-rotating Kerr holes, already in place at early epochs, and not to change significantly below redshift 5. Decaying MBH binaries may shape the innermost central regions of galaxies and should be detected in significant numbers by *LISA*.

1 Massive black holes and galaxy formation

The strong link observed between the masses of supermassive black holes (MBHs) at the center of most galaxies and the gravitational potential wells that host them suggests a fundamental mechanism for assembling black holes and forming spheroids in galaxy halos. The $m_{\rm BH}$-σ relation [12] [16] implies a rough proportionality between MBH mass and the mass of the baryonic component of the bulge. It is not yet understood whether this relation was set in primordial structures, and consequently how it is maintained throughout cosmic time with such a small dispersion, or indeed which physical processes established such a correlation in the first place [48][13][6].

In cosmologies dominated by cold dark matter (CDM) galaxy halos experience multiple mergers during their lifetime, with those between comparable-mass systems ("major mergers") expected to result in the formation of elliptical galaxies [21]. Simple models in which MBHs are also assumed to grow during major mergers and to be present in every galaxy at any redshift – while only a fraction of them is "active" at any given time – have been shown to explain many aspects of the observed evolution of quasars [7][8][25]. The coevolution of MBHs and their host galaxies in hierarchical structure formation scenarios gives origin to a number of of important questions, most notably:

• *Did the first MBHs form in subgalactic units far up in the merger hierarchy, well before the bulk of the stars observed today?* The seeds of the $z \sim 6$ quasars

ESO Symposia: Growing Black Holes, pp. 3–17, 2005.

discovered in the *Sloan Digital Sky Survey* had to appear at very high redshift, $z \gtrsim 10$, if they are accreting no faster than the Eddington rate. In hierarchical cosmologies, the ubiquity of MBHs in nearby luminous galaxies can arise even if only a small fraction of halos harbor MBHs at very high redshift [32].

• *How massive were the initial seeds, and is there a population of relic pre-galactic MBHs lurking in present-day galaxy halos?* A clue to these questions may lie in the numerous population of ultraluminous off-nuclear ("non-AGN") X-ray sources that have been detected in nearby galaxies [34]. Assuming isotropic emission, the inferred masses of these "ULXs" may suggest intermediate-mass black holes with masses $\gtrsim$ a few hundred $M_\odot$ [9][4].

• *Can coalescing MBH binaries at very high redshift be detected in significant numbers by the planned Laser Interferometer Space Antenna (LISA)?* If MBHs were common in the past (as implied by the notion that many distant galaxies harbor active nuclei for a short period of their life), and if their host galaxies undergo multiple mergers, then MBH binaries will inevitably form in large numbers during cosmic history. MBH pairs that are able to coalesce in less than a Hubble time will give origin to the loudest gravitational wave events in the universe.

• If was first proposed by [10] that the heating of the surrounding stars by a decaying MBH pair would create a low-density core out of a preexisting cuspy (e.g. $\rho_* \propto r^{-2}$) stellar density profile. If stellar dynamical processes can efficiently drive wide MBH binaries to the gravitational wave (GW) emission stage, *what is the cumulative dynamical effect of multiple black hole mergers on galaxy stellar cusps?*

• Active galactic nuclei powered by supermassive holes keep the universe ionized at $z \lesssim 4$, structure the intergalactic medium (IGM), and probably regulate star formation in their host galaxies. Intermediate-mass holes accreting gas from the surrounding medium may shine as "miniquasars" at redshifts as high as $z \sim 20$. *What is the thermodynamic effect of miniquasars on the IGM at early times?*

• Besides their masses, astrophysical black holes are completely characterized by their spins, $S = aGm_{\rm BH}/c$, $0 \leq a/m_{\rm BH} \leq 1$. The spin of a MBH is expected to have a significant effect on its observational manifestation, such as the efficiency of converting accreted mass into radiation and the existence and direction of jets in active nuclei. *What is the expected distribution of MBH spins and how does this evolve with cosmic time?*

In this talk I will review some recent developments in our understanding of the assembly, growth, emission history, and environmental impact of MBHs from early epochs to the present. Unless otherwise stated, all the results shown below refer to the currently favoured (by a variety of observations) ΛCDM world model with $\Omega_M = 0.3$, $\Omega_\Lambda = 0.7$, $h = 0.7$, $\Omega_b = 0.045$, $\sigma_8 = 0.93$, and $n = 1$.

2 MBHs as Population III remnants

The first stars in the universe must have formed out of metal-free gas, in dark matter "minihalos" of total mass $\gtrsim 5 \times 10^5\,\mathrm{M}_\odot$ [14] condensing from the high-σ peaks of the primordial density field at redshift $z = 20 - 30$. Numerical simulations of the fragmentation of primordial clouds in standard CDM theories all show the formation of Jeans unstable clumps with masses exceeding a few hundred solar masses; because of the slow subsonic contraction – a regime set up by the main gas coolant, molecular hydrogen – further fragmentation into sub-components is not seen, and a single very massive star forms from the inside out [5][1][41].

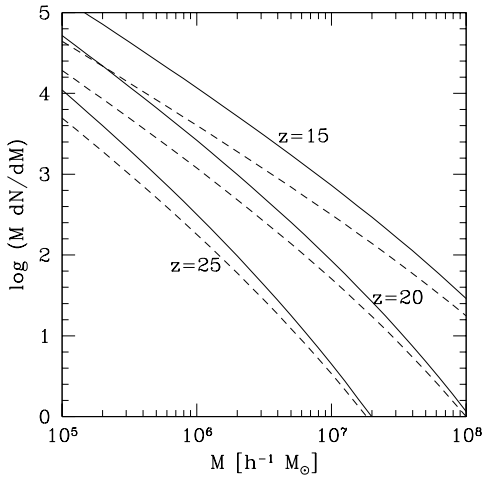

Fig. 1. Mass function of minihalos of mass M formed at $z = 15, 20, 25$ which, by the later time z_0, will have merged into a more massive halo of total mass M_0. *Solid curves:* $z_0 = 0.8$, $M_0 = 10^{12}\,h^{-1}\,\mathrm{M}_\odot$ ("Milky Way" halo). *Dashed curves:* $z_0 = 3.5$, $M_0 = 2 \times 10^{11}\,h^{-1}\,\mathrm{M}_\odot$ (older "bulge"). If only one seed hole formed in each $\sim 10^6\,\mathrm{M}_\odot$ minihalo collapsing at $z \sim 20$ (and triple hole interactions and binary coalescences were neglected), several thousands relic IMBHs and their descendants would be orbiting throughout present-day galaxy halos [29][23].

At zero metallicity mass loss through radiatively-driven stellar winds or nuclear-powered stellar pulsations is expected to be negligible, and Population III stars will likely die losing only a small fraction of their mass (except for $100 < m_* < 140\,\mathrm{M}_\odot$). Nonrotating very massive stars in the mass window $140 \lesssim m_* \lesssim 260\,\mathrm{M}_\odot$ will disappear as pair-instability supernovae [4], leaving no compact remnants and polluting the universe with the first heavy elements [44][39]. Stars with $40 < m_* < 140\,\mathrm{M}_\odot$ and $m_* > 260\,\mathrm{M}_\odot$ are predicted instead to collapse to black holes with masses exceeding half of the initial stellar

mass [20]. Barring any fine tuning of the initial mass function of Pop III stars, intermediate-mass black holes (IMBHs) – with masses above the 4–18 $M_\odot$ range of known "stellar-mass" holes – may then be the inevitable endproduct of the first episodes of pregalactic star formation [29]. Since they form in high-σ rare density peaks, relic IMBHs are expected to cluster in the bulges of present-day galaxies as they become incorporated through a series of mergers into larger and larger systems (see Fig. 1). The presence of a small cluster of IMBHs in galaxy nuclei may have several interesting consequences associated with tidal captures of ordinary stars (likely followed by disruption), capture by the central supermassive hole, and gravitational wave radiation from such coalescences [33]. Accreting pregalactic IMBHs may be detectable as ultra-luminous, off-nuclear X-ray sources [29][26].

3 The first miniquasars

Physical conditions in the central potential wells of young and gas-rich protogalaxies may have been propitious for black hole gas accretion. Perhaps seed black holes grew efficiently in small minihalos just above the cosmological Jeans mass (with shallow potential wells), or maybe gas accretion had to await the buildup of more massive galaxies (with virial temperatures above the threshold for atomic cooling). This issue is important for the detectability of high-z miniquasars: it also determines whether the radiation background at very high redshifts had an X-ray component component able to preheat and partially ionize the IGM.

As mentioned above, gas condensation in the first baryonic objects is possible through the formation of H_2 molecules, which cool via roto-vibrational transitions down to temperatures of a few hundred kelvins. In the absence of a UV photodissociating flux and of ionizing X-ray radiation, three-dimensional simulations of early structure formation show that the fraction of cold, dense gas available for accretion onto seed holes or star formation exceeds 20% for halos more massive than 10^6 $M_\odot$ [28]. On th eother hand, a zero-metallicity progenitor star in the range $40 < m_* < 500$ $M_\odot$ emits about 70,000 photons above 1 ryd per stellar baryon [43]. The ensuing ionization front will completely overrun the host halo, photoevaporating most of the surrounding gas [54]. Black hole remnants of the first stars that created H II regions are then unlikely to accrete significant mass until new cold material will be made available through the hierarchical merging of many gaseous subunits.

Accretion onto IMBHs may be an attractive way to (partially) reionize the low-density IGM [30][42]. A large fraction of the UV radiation from massive stars may not escape the dense sites of star formation, or may be deposited locally in halo gas that recombines almost immediately. The harder radiation emitted from miniquasars is instead more likely to escape from the hosts into intergalactic space, and may then produce more 'durable' (albeit partial) ionization in the diffuse IGM. High-resolution hydrodynamics simulations of early structure formation in ΛCDM cosmologies are a powerful tool to track in de-

tail the thermal and ionization history of a clumpy IGM and guide studies of early reheating. We [27] have used *Enzo*, an adaptive mesh refinement (AMR), grid-based hybrid (hydro+N-body) code developed by Bryan & Norman (see http://cosmos.ucsd.edu/enzo/) to solve the cosmological hydrodynamics equations and simulate the effect of a miniquasar turning on at very high redshift in a volume 1 Mpc on a side (comoving). We first identify in a low-resolution pure N-body simulation the Lagrangian volume of a resolved protogalactic halo with a total mass 7×10^5 $M_\odot$ at $z = 25$, above the cosmological Jeans mass. We then generate new initial conditions with an 128^3 initial static grid that covers a 0.5 Mpc volume centered around the identified high-σ peak. During the evolution, refined grids (for a maximum of 5 additional levels) are introduced with twice the spatial resolution of the parent (coarser) grid to home in, with progressively finer resolution, on the densest parts of the "cosmic web". The simulation follows the non-equilibrium chemistry of the dominant nine species (H, H^+, H^-, e, He, He^+, He^{++}, H_2, and H_2^+) in primordial gas, and includes radiative losses from atomic and molecular line cooling.

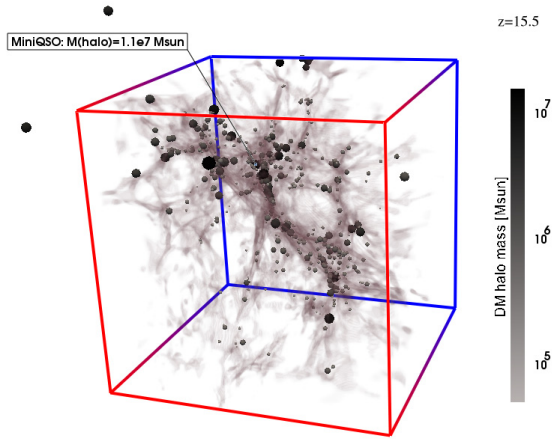

Fig. 2. Gas distribution (at overdensity 2) in the inner 0.5 Mpc of the simulation box at $z = 15.5$. Dark matter halos of different masses (identified with a halo-finder algorithm) are plotted as dark spheres.

At $z = 21$, a miniquasar powered by a 150 $M_\odot$ black hole accreting at the Eddington rate is turned on in the protogalactic halo. The miniquasar shines for a few Salpeter times (i.e. down to $z \sim 15$) and is a copious source of soft X-ray photons, which permeate the IGM more uniformly than possible with extreme ultraviolet (EUV, ≥ 13.6 eV) radiation [38] and make it warm and weakly ionized prior to the epoch of reionization breakthrough [50]. A spectrum with $\nu L_\nu = \text{const}$ (like the nonthermal component observed in ULXs) was assumed for photons with energies in the range 0.2-10 keV, to which the simulation box is

transparent. X-rays alone do not produce a fully ionized medium, but partially photoionize the gas by repeated secondary ionizations. A primary nonthermal photoelectron of energy $E = 1\,\mathrm{keV}$ in a medium with residual ionization (from the recombination epoch) $x = 2 \times 10^{-4}$ will create over two dozens secondary electrons, depositing a fraction $f_{\rm ion} \approx 37\%$ of its initial energy as secondary ionizations of hydrogen, and only $f_{\rm heat} \approx 13\%$ as heat [47]. The timescale for electron-electron encounters resulting in a fractional energy loss $f = \Delta E/E$,

$$t_{\rm ee} \approx 140\,\mathrm{yr}\; Ef\left(1+\frac{z}{20}\right)^{-3}\left(\frac{\ln\Lambda}{20}\right)^{-1} x^{-1} \qquad (1)$$

(where E is measured in keV), is typically much shorter that the electron Compton cooling timescale off cosmic microwave background (CMB) photons, $t_C = (7 \times 10^6\,\mathrm{yr})\,[(1+z)/20]^{-4}$, and thus the primary photoelectron will ionize and heat the surrounding medium before it is cooled by the CMB. Once the IGM ionized fraction increases to $x \approx 0.1$, the number of secondary ionizations per ionizing photon drops to a few, and the bulk of the primary's energy goes into heat ($f_{\rm heat} \approx 0.6$) via elastic Coulomb collisions with thermal electrons.

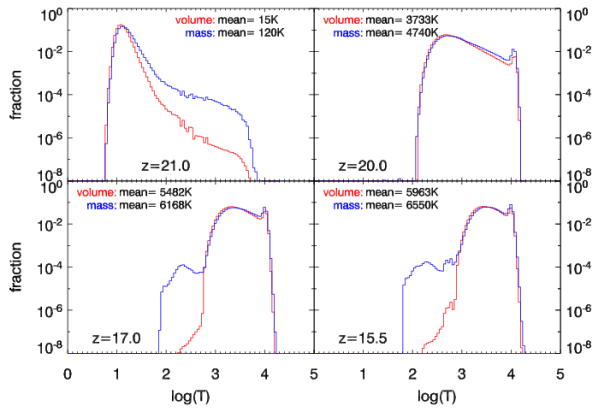

Fig. 3. Mass (upper curves) and volume (lower curves) weighted]gas fraction vs. gas temperature in the simulation box. A miniquasar was turned on at $z = 21$.

Figure 3 shows the mass and volume-weighted gas fraction in the simulation box vs. temperature as four different redshifts. The heating effect of X-rays from the miniquasar is clearly seen, with gas temperatures between 10^3 and 10^4 K at $z < 20$. Strong Jeans mass filtering takes place, and subsequent minihalos will no longer be able to accrete gas due to the smoothing effect of gas pressure. The low-density IGM acquires a uniform "entropy floor" [39] that (a) greatly reduces gas clumping, curtailing the number of photons needed to maintain reionization, and (b) results in significantly lower gas densities in the cores of minihalos that suppress rapid H_2 formation. The latter effect may imply that X-rays inhibit rather than enhance star formation [19][28].

4 MBH binaries and galaxy cores

Frequent galaxy mergers will inevitably lead to the formation of MBH binaries. As dark matter halos assemble, MBHs get incorporated into larger and larger halos, sink to the center owing to dynamical friction, accrete a fraction of the gas in the merger remnant to become supermassive, form a binary system, and eventually coalesce [3]. In a stellar background a "hard" binary shrinks by capturing the stars that pass close to the holes and ejecting them at much higher velocities, a super-elastic scattering process that depletes the nuclear region and turns a stellar "cusp" into a low-density core. Rapid coalescence eventually ensues due to the emission of gravitational radiation. Observationally, there is clear evidence in early-type galaxies for a systematic trend in the distribution of surface brightness profiles, with faint ellipticals showing steep power-law profiles (cusps), while bright ellipticals have much shallower stellar cores [11]. Detailed N-body simulations have confirmed the cusp-disruption effect of a hardening MBH binary [35], but have shed little light on why bright ellipticals have lower central concentrations than faint ellipticals.

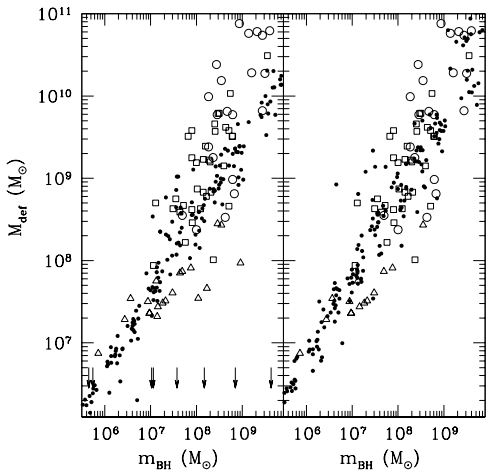

Fig. 4. Mass deficit produced at $z = 0$ by shrinking MBHs in our merger tree as a function of nuclear MBH mass (*filled dots*). *Left panel:* cusp regeneration case. *Right panel:* core preservation case. Galaxies without a core (i.e. those that have never experienced a MBH-MBH merger or with their cusp recently regenerated) are shown as vertical arrows at an arbitrary mass deficit of $10^6\,M_\odot$. *Empty squares*: mass deficit inferred in a sample of galaxies by [36]. *Empty circles*: same for the "core" galaxies of [11]. *Empty triangles*: same for the "cuspy" galaxies of [11], assuming a flat core within the upper limit on the core size. (From [52].)

The role of MBH binaries in shaping the central structure of galaxies is best understood within the framework of a detailed model for the hierarchical assembly of MBHs over cosmic history [51]. Stellar cusps can be efficiently destroyed

over cosmic time by decaying binaries if stellar dynamical processes are able to shrink the binary down to a separation $\lesssim 10\%$ of the separation at which the binary becomes hard. More massive halos have more massive nuclear holes and experience more merging events than less massive galaxies: hence they suffer more from the eroding action of binary MBHs and have larger cores. In [52] we found that a model in which the effect of the hierarchy of MBH interactions is cumulative and cores are preserved during galaxy mergers produces at the present epoch a correlation between the "mass deficit" (the mass needed to bring a flat inner density profile to a r^{-2} cusp) and the mass of the nuclear MBH, with a normalization and slope comparable to the observed relation (see Fig. 4). Models in which the mass displaced by the MBH binary is replenished after every major galaxy merger appear instead to underestimate the mass deficit observed in "core" galaxies. In [52] a simple scheme was applied to hardening pairs, in which the "loss cone" is constantly refilled and a constant density core forms due to the ejection of stellar mass. The effect of loss-cone depletion (the depletion of low-angular momentum stars that get close enough to extract energy from a hard binary) is one of the major uncertainties in computing the decay timescale, and makes it difficult to construct detailed scenarios for coalescing black hole binaries.

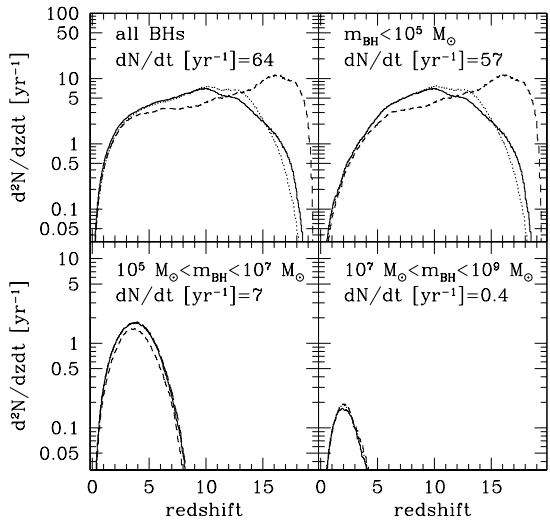

Fig. 5. Number of MBH binary coalescences observed per year at $z = 0$, per unit redshift, in different $m_{\rm BH} = M_1 + M_2$ mass intervals. Each panel also lists the integrated event rate, dN/dt, predicted by [45]. The rates (*solid lines*) are compared to a case in which triple black hole interactions are switched off (*dotted lines*). Triple hole interactions increase the coalescence rate at very high redshifts, while, for $10 < z < 15$, the rate is decreased because of the reduced number of surviving binaries. *Dashed lines*: rates computed assuming binary hardening is instantaneous, i.e. MBHs coalesce after a dynamical friction timescale.

5 Gravitational radiation from inspiraling MBH binaries

MBH binaries, with masses in the range $10^3 - 10^7$ $M_\odot$, are one of the primary target for *LISA* [17][55][45]. Interferometers operate as all-sky monitors, and the data streams collect the contributions from a large number of sources belonging to different cosmic populations. To optimize the subtraction of resolved sources from the data stream, it is important to have a detailed description of the expected rate, duration, amplitude, and waveforms of events. Figure 5 shows the number of MBH binary coalescences per unit redshift per unit *observed* year predicted by [45], using a detailed model of MBH binaries dynamics. The observed event rate is obtained by dividing the rate per unit proper time by the $(1+z)$ cosmological time dilation factor. Each panel shows the rate for different $m_{\rm BH} = M_1 + M_2$ mass intervals, and lists the integrated event rate, dN/dt, across the entire sky. The number of events per observed year per unit redshift peaks at $z = 2$ for $10^7 < m_{\rm BH} < 10^9$ $M_\odot$, at $z = 3-4$ for $10^5 < m_{\rm BH} < 10^7$ $M_\odot$, and at $z = 10$ for $m_{\rm BH} < 10^5$ $M_\odot$, i.e. the lower the black hole mass, the higher the peak redshift. Beyond the peak, the event rate decreases steeply with cosmic time.

In the stationary case, i.e., assuming no orbital decay, the GW emission spectrum of a MBH pair in a circular orbit of radius a is a delta function at rest-frame frequency $f_r = \omega/\pi$, where $\omega = \sqrt{G(M_1+M_2)/a^3}$ is the Keplerian angular frequency of the binary. Orbital decay due to GW emission results in a shift of the emitted frequency to increasingly larger values as the binary evolution proceeds. Typically, the timescale for frequency shift is long compared to the wave period, and short compared to the duration of the observation. Only close to the innermost stable circular orbit (ISCO), the GW frequency changes at a rate comparable to the frequency itself. The rest-frame energy flux (energy per unit area per unit time) associated to the GW is

$$\frac{dE}{dAdt} = \frac{\pi}{4}\frac{c^3}{G} f_r^2 h^2, \tag{2}$$

where the strain amplitude (sky-and-polarisation averaged) at comoving distance $r(z)$ is

$$h = \frac{8\pi^{2/3}}{10^{1/2}} \frac{G^{5/3}\mathcal{M}^{5/3}}{c^4 r(z)} f_r^{2/3}, \tag{3}$$

$\mathcal{M}$ is the "chirp mass" of the binary, and all the other symbols have their standard meaning. The strain is averaged over a wave period. The important quantity to consider is the number of cycles n spent in a frequency interval $\Delta f \simeq f$ around a given frequency f. In general, $n = f^2/\dot{f} \propto f^{-5/3}$. For a periodic signal at frequency f lasting for a time interval longer than the observation time τ, we have simply $n = f\tau$. The characteristic strain in an observation of (observed) duration τ is then

$$h_c = h\sqrt{n} \propto f_r^{-1/6}, \qquad n < f\tau, \tag{4}$$

and

$$h_c = h\sqrt{f\tau} \propto f_r^{7/6}, \qquad n > f\tau, \tag{5}$$

where $f = f_r/(1+z)$ is the observed frequency. In Figure 6 h_c is plotted for different MBH binaries at different redshifts, compared to the *LISA* $h_{\rm rms}$ multiplied by a factor of 5, assuming a 3-year observation.

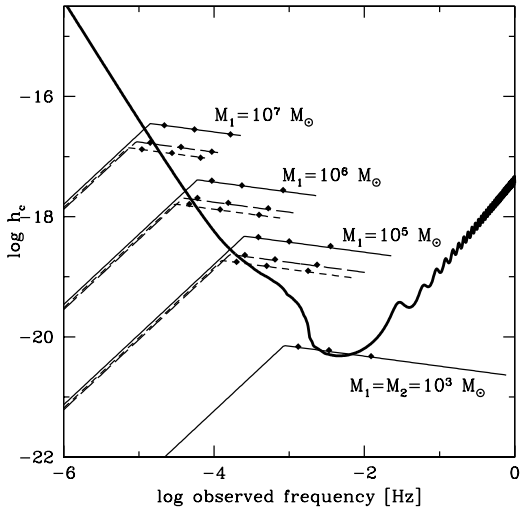

Fig. 6. Characteristic strain h_c for MBH binaries with different masses and redshifts. From top to bottom, the first three curves refer to systems with $\log(M_1/\,{\rm M}_\odot) = 7, 6, 5$, respectively, and $M_2 = 0.1M_1$. The solid, long-dashed, and short-dashed lines assumes the binary at $z = 1, 3, 5$, respectively. A 3-year observation is considered. The lowest solid curve assumes an equal mass binary $M_1 = M_2 = 10^3$ M$_\odot$ at $z = 7$. The small diamonds on each curve mark, from left to right, the observed frequency at 1 year, 1 month and 1 day before coalescence. The thick curve is *LISA* $5h_{\rm rms}$, approximatively the threshold for detection with $S/N \geq 5$. (From [46]).

At frequencies higher than the "knee", the time spent around a given frequency is less than 3 years, and $h_c \propto f^{-1/6}$. The signal shifts toward higher frequency during the observation, and reaches the ISCO and the coalescence phase in most cases. The lowest curve represents a low mass, high redshift equal mass binary. In terms of their detectability by *LISA*, they represent a somewhat different class of events. Contrary to the case of more massive binaries present at lower z, the final coalescence phase of light binaries lies at too high frequecies, well below the *LISA* threshold. For frequencies much below the knee, the characteristic strain is proportional to $f^{7/6}$, as the timescale for frequency shift is longer than 3 years. The signal amplitude is then limited by the observation time, not by the intrinsic properties of the source. The source will be observed as a "stationary source", a quasi-monochromatic wave for the whole duration of the observation. An increase in the observation time will result in a shift of the knee toward lower frequencies. The time needed for the sources to reach the ISCO starting from the knee frequency is, approximatively, the observing time.

As recently shown by [46], the GW signal from MBH binaries will be resolved (assuming a 3-year *LISA* observation) into ~ 100 discrete events, 40 of which will be observed above threshold until coalescence. These "merging events" involve relatively massive binaries, $M \sim 10^5\,\mathrm{M}_\odot$, in the redshift range $2 \lesssim z \lesssim 6$. The remaining ~ 60 events come from higher redshift, less massive binaries ($M \sim 5\times10^3\,\mathrm{M}_\odot$ at $z \gtrsim 6$) and, although their S/N integrated over the duration of the observation can be substantial, the final coalescence phase is at too high frequency to be directly observable by *LISA*. The total number of detected events accounts for a fraction $\gtrsim 90\%$ of all coalescences of massive black hole binaries at $z \lesssim 5$. The residual confusion noise from unresolved massive black hole binaries is expected to be at least an order of magnitude below the estimated stochastic *LISA* noise.

6 MBH spins

The spin of a MBH is determined by the competition between a number of physical processes. Black holes forming from the gravitational collapse of very massive stars endowed with rotation will in general be born with non-zero spin [13]. An initially non-rotating hole that increases its mass by (say) 50% by swallowing material from an accretion disk may be spun up to $a/m_{\rm BH} = 0.84$ [2]. While the coalescence of two non-spinning black holes of comparable mass will immediately drive the spin parameter of the merged hole to $a/m_{\rm BH} \gtrsim 0.8$ [15], the capture of smaller companions in randomly-oriented orbits may spin down a Kerr hole instead [22].

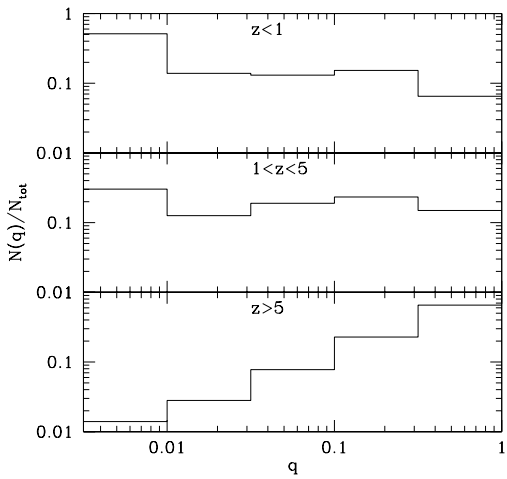

Fig. 7. Normalized distribution of mass ratios, $q = M_2/M_1$, of coalescing MBH binaries at three different epochs. Note that at low redshift MBHs typically capture much smaller companions.

In [53] we have made a first attempt at estimating the distribution of MBH spins and its evolution with cosmic time in the context of hierarchical structure formation theories, following the combined effects of black hole-black hole coalescences and accretion from a gaseous disk on the magnitude and orientation of MBH spins. Here I will briefly summarize our findings. Binary coalescences appear to cause no significant systematic spin-up or spin-down of MBHs: because of the relatively flat distribution of MBH binary mass ratios in hierarchical models (shown in Fig. 7), the holes random-walk around the spin parameter they are endowed with at birth, and the spin distribution retains significant memory of the initial rotation of "seed" holes.

It is accretion, not binary coalescences, that dominates the spin evolution of MBHs (Fig. 8). Accretion can lead to efficient spin-up of MBHs even if the angular momentum of the inflowing material varies in time. This is because, for a thin accretion disk, the hole is aligned with the outer disk on a timescale that is much shorter than the Salpeter time [37], leading to accretion via prograde equatorial orbits. As a result, most of the mass accreted by the hole acts to spin it up, even if the orientation of the spin axis changes in time. For a geometrically thick disk, alignment of the hole with the outer disk is much less efficient, occurring on a timescale comparable to the Salpeter time. Even in this case most holes will be rotating rapidly. This is because, in any model in which MBH growth is triggered by major mergers, every accretion episode must typically increase a hole's mass by about one e-folding to account for the local MBH mass density and the $m_{\rm BH} - \sigma_*$ relation. Most individual accretion episodes thus produce rapidly-rotating holes independent of the initial spin.

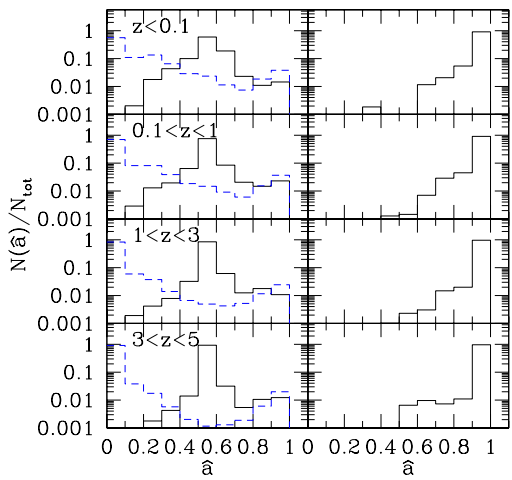

Fig. 8. Distribution of MBH spins in different redshift intervals. *Left panel:* effect of black hole binary coalescences only. *Solid histogram:* seed holes are born with $\hat{a} \equiv a/m_{\rm BH} = 0.6$. *Dashed histogram:* seed holes are born non-spinning. *Right panel:* spin

distribution from binary coalescences and gas accretion. Seed holes are born with $\hat{a} = 0.6$, and are efficiently spun up by accretion via a thin disk.

Under the combined effects of accretion and binary coalescences, we find that the spin distribution is heavily skewed towards fast-rotating Kerr holes, is already in place at early epochs, and does not change significantly below redshift 5. As shown in Figure 9, about 70% of all MBHs are maximally rotating and have mass-to-energy conversion efficiencies approaching 30%. Note that if the equilibrium spin attained by accreting MBHs is lower than the value of $\hat{a} \equiv a/m_{\rm BH} = 0.998$ used here, as in the thick disk MHD simulations of [15], where $\hat{a} \approx 0.93$, then the accretion efficiency will be lower as well, $\approx 17\%$.

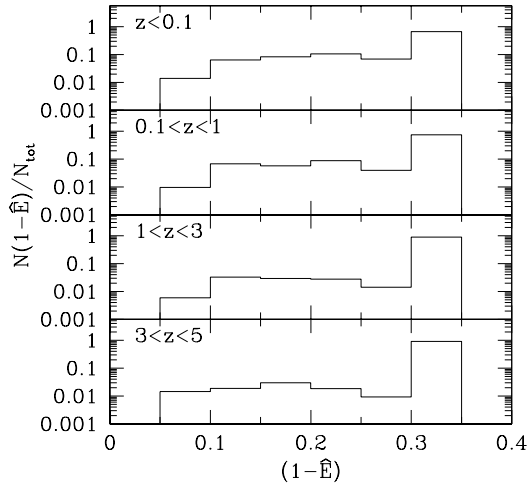

Fig. 9. Distribution of accretion efficiencies, $\epsilon \equiv 1 - \hat{E}$, in different redshift intervals (assuming that the energy radiated is the binding energy at the ISCO). The spin distribution from binary coalescences and gas accretion has been calculated assuming the holes accrete via a thin disk on prograde equatorial orbits.

Even in the conservative case where accretion is via a geometrically thick disk (and hence the spin/disk alignment is relatively inefficient) and the initial orientation between the hole's spin and the disk rotation axis is assumed to be random, we find that most MBHs rotate rapidly with spin parameters $\hat{a} > 0.8$ and accretion efficiencies $\epsilon > 12\%$. As recently shown by [56][5], a direct comparison between the local MBH mass density and the mass density accreted by luminous quasars shows that quasars have a mass-to-energy conversion efficiency $\epsilon \gtrsim 0.1$ (a simple and elegant argument originally provided by [49]). This high average accretion efficiency may suggest rapidly rotating Kerr holes, in agreement with our findings. Since most holes rotate rapidly at all epochs, our results suggest that spin is not a necessary and sufficient condition for producing a radio-loud quasar.

I would like to thank my numerous collaborators on this subject: F. Haardt, M. Kuhlen, P. Oh, E. Quataert, M. Rees, A. Sesana, and M. Volonteri. This manuscript was written while the author was enjoying the hospitality of the Kavli Institute for Theoretical Physics. Support for this work was provided by NASA grant NNG04GK85G, and by NSF grants AST-0205738 and PHY99-07949.

References

1. Abel, T., Bryan, G., & Norman, M. 2000, ApJ, 540, 39
2. Bardeen, J. M. 1970, Nature, 226, 64
3. Begelman, M. C., Blandford, R. D., & Rees, M. J. 1980, Nature, 287, 307
4. Bond, J. R., Arnett, W. D., & Carr, B. J. 1984, ApJ, 280, 825
5. Bromm, V., Coppi, P. S., & Larson, R. B. 1999, ApJ, 527, L5
6. Burkert, A., & Silk, J. 2001, ApJ, 554, L151
7. Cattaneo, A., Haehnelt, M. G., & Rees, M. J. 1999, MNRAS, 308, 77
8. Cavaliere, A., & Vittorini, V. 2000, ApJ, 543, 599
9. Colbert, E. J. M., & Mushotzky, R. F. 1999, ApJ, 519, 89
10. Ebisuzaki, T., Makino J., & Okumura S. K. 1991, Nature, 354, 212
11. Faber, S. M., et al. 1997, AJ, 114, 1771
12. Ferrarese, L., & Merritt, D. 2000, ApJ, 539, L9
13. Fryer, C. L., Woosley, S. E., & Heger, A. 2001, ApJ, 550, 372
14. Fuller, T. M., & Couchman, H. M. P. 2000, ApJ, 544, 6
15. Gammie, C. F., Shapiro, S. L., & McKinney, J. C. 2004, ApJ, 602, 312
16. Gebhardt, K., et al. 2000, ApJ, 543, L5
17. Haehnelt, M.G. 1994, MNRAS, 269, 199
18. Haehnelt, M. G., & Kauffmann, G. 2000, MNRAS, 318, L35
19. Haiman, Z., Abel, T., & Rees, M. J. 2000, ApJ, 534, 11
20. Heger, A., & Woosley, S. E. 2002, ApJ, 567, 532
21. Hernquist, L. 1992, ApJ, 400, 460
22. Hughes, S. A., & Blandford, R. D. 2003, ApJ, 585, L101
23. Islam, R. R., Taylor, J. E., & Silk, J. 2003, MNRAS, 340, 647
24. Kaaret, P., et al. 2001, MNRAS, 321, L29
25. Kauffmann, G., & Haehnelt, M. G. 2000, MNRAS 311, 576
26. Krolik, J. H. 2004, ApJ, in press (astro-ph/0407285)
27. Kuhlen, M., & Madau, P. 2004, in prepration
28. Machacek, M. M., Bryan, G. L., & Abel, T. 2003, MNRAS, 338, 273
29. Madau, P., & Rees, M. J. 2001, ApJ, 551, L27
30. Madau, P., Rees, M. J., Volonteri, M., Haardt, F., & Oh, S. P. 2004, ApJ, 606, 484
31. Marconi, A., Risaliti, G., Gilli, R., Hunt, L. K., Maiolino, R., & Salvati, M. 2004, MNRAS, 351, 169
32. Menou, K., Haiman, Z., & Narayanan, V. K. 2001, ApJ, 558, 535
33. Miller, M. C. 2004, preprint (astro-ph/0409331)
34. Miller, M. C., & Colbert, E. J. M. 2004, Int. J. Mod. Phys. D13, 1
35. Milosavljevic, M., & Merritt, D. 2001, ApJ, 563, 34
36. Milosavljevic, M., Merritt, D., Rest, A., van den Bosch, F. C. 2002, MNRAS, 331, L51
37. Natarajan, P., & Pringle, J. E. 1998, ApJ, 506, L97
38. Oh, P. S. 2001, ApJ, 553, 499
39. Oh, S. P., & Haiman, Z. 2003, MNRAS, 346, 456

40. Oh, S. P., Nollett, K. M., Madau, P., & Wasserburg, G. J. 2001, ApJ, 562, L1
41. Omukai, K., & Palla, F. 2003, ApJ, 589, 677
42. Ricotti, M., & Ostriker, J. P. 2004, MNRAS, 352, 547
43. Schaerer, D. 2002, A&A, 382, 28
44. Schneider, R., Ferrara, A., Natarajan, P., & Omukai, K. 2002, ApJ, 571, 30
45. Sesana, A., Haardt, F., Madau, P., & Volonteri, M. 2004, ApJ, 611, 623
46. Sesana, A., Haardt, F., Madau, P., & Volonteri, M. 2004, ApJ, submitted (astro-ph/0409255)
47. Shull, J. M., & Van Steenberg, M. E. 1985, ApJ, 298, 268
48. Silk, J., & Rees, M. J. 1998, A&A, 331, L1
49. Soltan, A. 1982, MNRAS, 200, 115
50. Venkatesan, A., Giroux, M. L., & Shull, M. J. 2001, ApJ, 563, 1
51. Volonteri, M., Haardt, F., & Madau, P. 2003, ApJ, 582, 559
52. Volonteri, M., Madau, P., & Haardt, F. 2003, ApJ, 593, 661
53. Volonteri, M., Madau, P., Quataert, E., & Rees, M. J. 2004, ApJ, in press (astro-ph/0410342)
54. Whalen, D., Abel, T., & Norman, M. L. 2004, ApJ, 610, 22
55. Wyithe, J.S.B., & Loeb, A. 2003 ApJ, 590, 691
56. Yu, Q., & Tremaine, S. 2002, MNRAS, 335, 965

The Environmental Impact of Supermassive Black Holes

A. Loeb

Astronomy Department, Harvard University, Cambridge MA 02138, USA

Abstract. The supermassive black holes observed at the centers of almost all present-day galaxies had a profound impact on their environment. I highlight the principle of *self-regulation*, by which supermassive black holes grow until they release sufficient energy to unbind the gas that feeds them from their host galaxy. This principle explains several observed facts, including the correlation between the mass of a central black hole and the depth of the gravitational potential well of its host galaxy, and the abundance and clustering properties of bright quasars in the redshift interval of $z \sim 2$–6. At lower redshifts, quasars might have limited the maximum mass of galaxies through the suppression of cooling flows in X-ray clusters. The seeds of supermassive black holes were likely planted in dwarf galaxies at redshifts $z > 10$, through the collapse of massive or supermassive stars. The minimum seed mass can be identified observationally through the detection of gravitational waves from black hole binaries by *Advanced LIGO* or *LISA*. Aside from shaping their host galaxies, quasar outflows filled the intergalactic medium with magnetic fields and heavy elements. Beyond the reach of these outflows, the brightest quasars at $z > 6$ have ionized exceedingly large volumes of gas (tens of comoving Mpc) prior to global reionization, and must have suppressed the faint end of the galaxy luminosity function in these volumes before the same occurred through the rest of the universe.

1 The Principle of Self-Regulation

The fossil record in the present-day universe indicates that every bulged galaxy hosts a supermassive black hole (BH) at its center [1]. These BHs are dormant or faint most of the time, but ocassionally flash in a short burst of radiation that lasts for a small fraction of the Hubble time. The short duty cycle acounts for the fact that bright quasars are much less abundant than their host galaxies, but it begs the more fundamental question: *why is the quasar activity so brief?* A natural explanation is that quasars are suicidal, namely the energy output from the BHs regulates their own growth.

Supermassive BHs make up a small fraction, $< 10^{-3}$, of the total mass in their host galaxies, and so their direct dynamical impact is limited to the central star distribution where their gravitational influence dominates. Dynamical friction on the background stars keeps the BH close to the center. Random fluctuations in the distribution of stars induces a Brownian motion of the BH. This motion can be decribed by the same Langevin equation that captures the motion of a massive dust particle as it responds to random kicks from the much lighter molecules of air around it [2]. The characteristic speed by which the BH wanders around the

ESO Symposia: Growing Black Holes, pp. 18–29, 2005.

center is small, $\sim (m_\star/M_{\rm BH})^{1/2}\sigma_\star$, where $m_\star$ and $M_{\rm BH}$ are the masses of a single star and the BH, respectively, and $\sigma_\star$ is the stellar velocity dispersion. Since the random force fluctuates on a dynamical time, the BH wanders across a region that is smaller by a factor of $\sim (m_\star/M_{\rm BH})^{1/2}$ than the region traversed by the stars inducing the fluctuating force on it.

The dynamical insignificance of the BH on the global galactic scale is misleading. The gravitational binding energy per rest-mass energy of galaxies is of order $\sim (\sigma_\star/c)^2 < 10^{-6}$. Since BH are relativistic objects, the gravitational binding energy of material that feeds them amounts to a substantial fraction its rest mass energy. Even if the BH mass occupies a fraction as small as $\sim 10^{-4}$ of the baryonic mass in a galaxy, and only a percent of the accreted rest-mass energy leaks into the gaseous environment of the BH, this slight leakage can unbind the entire gas reservoir of the host galaxy! This order-of-magnitude estimate explains why quasars are short lived. As soon as the central BH accretes large quantities of gas so as to significantly increase its mass, it releases large amounts of energy that would suppress further accretion onto it. In short, the BH growth is *self-regulated*.

The principle of *self-regulation* naturally leads to a correlation between the final BH mass, $M_{\rm bh}$, and the depth of the gravitational potential well to which the surrounding gas is confined, $\sim \sigma_\star^2$. Indeed such a correlation is observed in the present-day universe [17]. The observed power-law relation between $M_{\rm bh}$ and $\sigma_\star$ can be generalized to a correlation between the BH mass and the circular velocity of the host halo, v_c [4], which in turn can be related to the halo mass, $M_{\rm halo}$, and redshift, z [16]

$$\begin{aligned} M_{\rm bh}(M_{\rm halo},z) &= {\rm const}\times v_c^5 \\ &= \epsilon_{\rm o} M_{\rm halo}\left(\frac{M_{\rm halo}}{10^{12}M_\odot}\right)^{\frac{2}{3}}[\zeta(z)]^{\frac{5}{6}}(1+z)^{\frac{5}{2}}, \end{aligned} \tag{1}$$

where $\epsilon_{\rm o} \approx 10^{-5.7}$ is a constant, $\zeta(z)$ is close to unity and defined as $\zeta \equiv [(\Omega_m/\Omega_m^z)(\Delta_c/18\pi^2)]$, $\Omega_m^z \equiv [1+(\Omega_\Lambda/\Omega_m)(1+z)^{-3}]^{-1}$, $\Delta_c = 18\pi^2+82d-39d^2$, and $d = \Omega_m^z - 1$ (see equations 22–25 in Ref. [1] for the relation between v_c and $M_{\rm halo}$). If quasars shine near their Eddington limit as suggested by observations of low and high-redshift quasars [6,7], then the above value of $\epsilon_{\rm o}$ implies that a fraction of $\sim$ 5–10% of the energy released by the quasar over a galactic dynamical time needs to be captured in the surrounding galactic gas in order for the BH growth to be self-regulated [16].

With this interpretation, the $M_{\rm bh}$–$\sigma_\star$ relation reflects the limit introduced to the BH mass by self-regulation; deviations from this relation are inevitable during episodes of BH growth or as a result of mergers of galaxies that have no cold gas in them. A physical scatter around this upper envelope could also result from variations in the efficiency by which the released BH energy couples to the surrounding gas.

Various prescriptions for self-regulation were sketched by Silk & Rees [12]. These involve either energy or momentum-driven winds, where the latter type is a factor of $\sim v_c/c$ less efficient [13–15]. Wyithe & Loeb [16] demonstrated

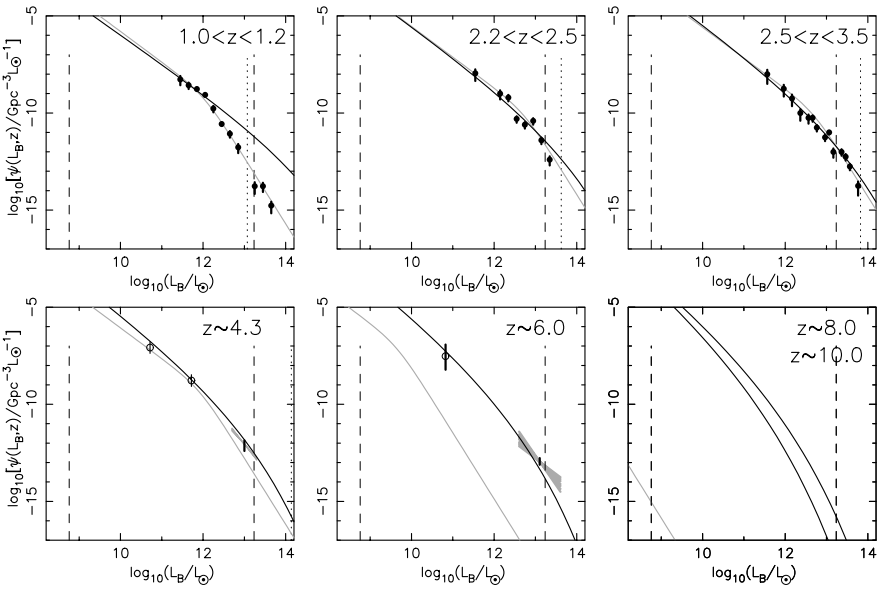

Fig. 1. Comparison of the observed and model luminosity functions (from [16]). The data points at $z < 4$ are summarized in Ref. [8], while the light lines show the double power-law fit to the *2dF* quasar luminosity function [9]. At $z \sim 4.3$ and $z \sim 6.0$ the data is from Refs. [10]. The grey regions show the 1-σ range of logarithmic slope ($[-2.25, -3.75]$ at $z \sim 4.3$ and $[-1.6, -3.1]$ at $z \sim 6$), and the vertical bars show the uncertainty in the normalization. The open circles show data points converted from the X-ray luminosity function [11] of low luminosity quasars using the median quasar spectral energy distribution. In each panel the vertical dashed lines correspond to the Eddington luminosities of BHs bracketing the observed range of the $M_{\rm bh}$–$v_{\rm c}$ relation, and the vertical dotted line corresponds to a BH in a $10^{13.5} M_\odot$ galaxy.

that a particularly simple prescription for an energy-driven wind can reproduce the luminosity function of quasars out to highest measured redshift, $z \sim 6$ (see Figs. 1 and 2), as well as the observed clustering properties of quasars at $z \sim 3$ [17] (see Fig. 3). The prescription postulates that: *(i)* self-regulation leads to the growth of $M_{\rm bh}$ up the redshift-independent limit as a function of v_c in Eq. (1), for all galaxies throughout their evolution; and *(ii)* the growth of $M_{\rm bh}$ to the limiting mass in Eq. (1) occurs through halo merger episodes during which the BH shines at its Eddington luminosity (with the median quasar spectrum) over the dynamical time of its host galaxy, $t_{\rm dyn}$. This model has only one adjustable parameter, namely the fraction of the released quasar energy that couples to the surrounding gas in the host galaxy. This parameter can be fixed based on the $M_{\rm bh}$–$\sigma_\star$ relation in the local universe [4]. It is remarkable that the combination of the above simple prescription and the standard ΛCDM cosmology for the evolution and merger rate of galaxy halos, lead to a satisfactory agreement with the rich data set on quasar evolution over cosmic history.

The cooling time of the heated gas is typically longer than its dynamical time and so the gas should expand into the galactic halo and escape the galaxy if its initial temperature exceeds the virial temperature of the galaxy [16]. The quasar remains active during the dynamical time of the initial gas reservoir, $\sim 10^7$ years, and fades afterwards due to the dilution of this reservoir. Accretion is halted as soon as the quasar supplies the galactic gas with more than its binding energy. The BH growth may resume if the cold gas reservoir is replenished through a new merger.

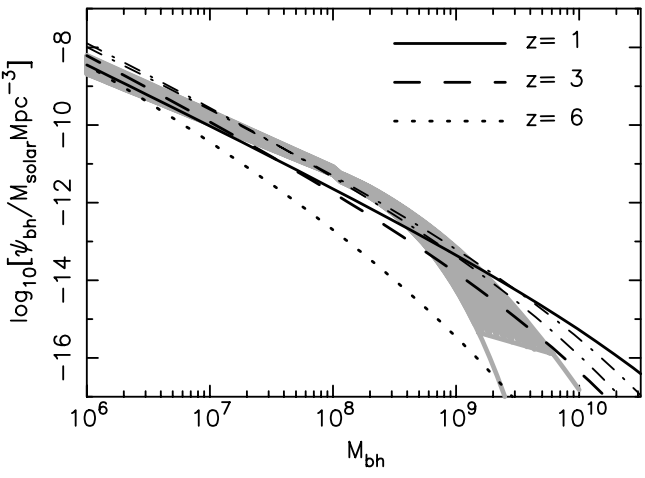

Fig. 2. The comoving density of supermassive BHs per unit BH mass (from [16]). The grey region shows the estimate based on the observed velocity distribution function of galaxies in Ref. [18] and the $M_{\rm bh}$–v_c relation in Eq. (1). The lower bound corresponds to the lower limit in density for the observed velocity function while the grey lines show the extrapolation to lower densities. We also show the mass function computed at $z = 1$, 3 and 6 from the Press-Schechter[19] halo mass function and Eq. (1), as well as the mass function at $z \sim 2.35$ and $z \sim 3$ implied by the observed density of quasars and a quasar lifetime of order the dynamical time of the host galactic disk, $t_{\rm dyn}$ (dot-dashed lines).

Agreement between the predicted and observed correlation function of quasars (Fig. 3) is obtained only if the BH mass scales with redshift as in Eq. (1) and the quasar lifetime is of the order of the dynamical time of the host galactic disk [17],

$$t_{\rm dyn} = 10^7 \ [\xi(z)]^{-1/2} \left(\frac{1+z}{3}\right)^{-3/2} \ {\rm yr}. \qquad (2)$$

The inflow of cold gas towards galaxy centers during the growth phase of the BH would naturally be accompanied by a burst of star formation. The fraction of gas that is not consumed by stars or ejected by supernovae, will continue to feed the BH. It is therefore not surprising that quasar and starburst activities

co-exist in Ultra Luminous Infrared Galaxies [21], and that all quasars show broad metal lines indicating a super-solar metallicity of the surrounding gas [22]. Applying a similar self-regulation principle to the stars, leads to the expectation [16,23] that the ratio between the mass of the BH and the mass in stars is independent of halo mass (as observed locally [24]) but increases with redshift as $\propto \xi(z)^{1/2}(1+z)^{3/2}$. A consistent trend has indeed been inferred in an observed sample of gravitationally-lensed quasars [25].

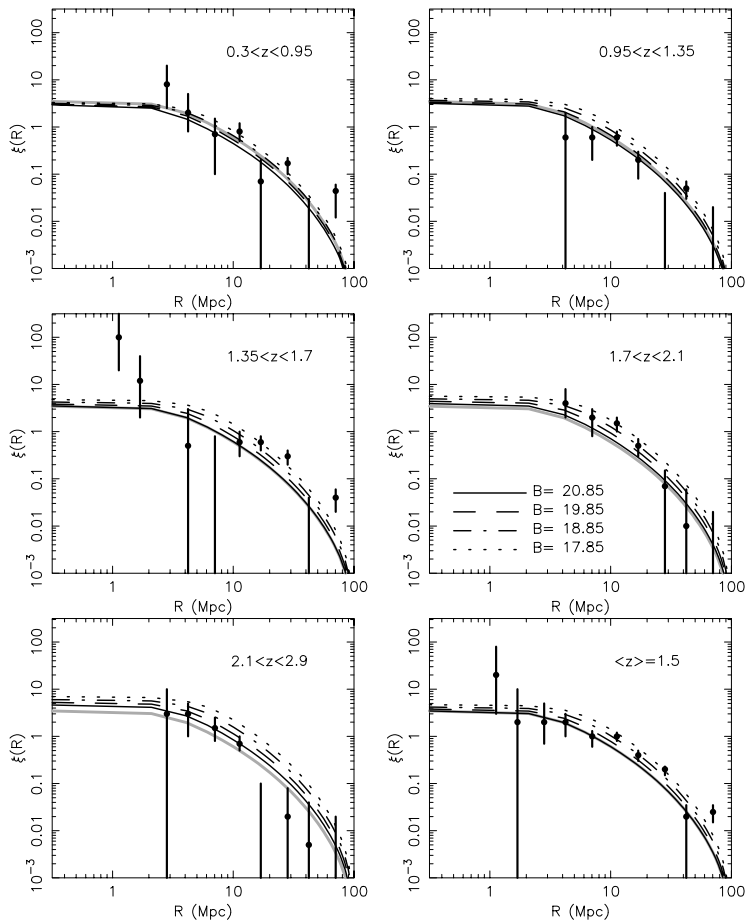

Fig. 3. Predicted correlation function of quasars at various redshifts in comparison to the *2dF* data [20] (from [17]). The dark lines show the correlation function predictions for quasars of various apparent B-band magnitudes. The *2dF* limit is $B \sim 20.85$. The lower right panel shows data from entire *2dF* sample in comparison to the theoretical prediction at the mean quasar redshift of $\langle z \rangle = 1.5$. The $B = 20.85$ prediction at this redshift is also shown by thick gray lines in the other panels to guide the eye. The predictions are based on the scaling $M_{\rm bh} \propto v_c^5$ in Eq. (1).

The upper mass of galaxies may also be regulated by the energy output from quasar activity. This would account for the fact that cooling flows are suppressed in present-day X-ray clusters [26–28], and that massive BHs and stars in galactic bulges were already formed at $z \sim 2$. The quasars discovered by the *Sloan Digital Sky Survey* (*SDSS*) at $z \sim 6$ mark the early growth of the most massive BHs and galactic spheroids. The present-day abundance of galaxies capable of hosting BHs of mass $\sim 10^9 M_\odot$ (based on Eq. 1) already existed at $z \sim 6$ [29]. At some epoch, the quasar energy output may have led to the extinction of cold gas in these galaxies and the suppression of further star formation in them, leading to an apparent "anti-hierarchical" mode of galaxy formation where massive spheroids formed early and did not make new stars at late times. In the course of subsequent merger events, the cores of the most massive spheroids acquired an envelope of collisionless matter in the form of already-formed stars or dark matter [29], without the proportional accretion of cold gas into the central BH. The upper limit on the mass of the central BH and the mass of the spheroid is caused by the lack of cold gas and cooling flows in their X-ray halos. In the cores of cooling X-ray clusters, there is often an active central BH that supplies sufficient energy to compensate for the cooling of the gas [27,26,13]. The primary physical process by which this energy couples to the gas is still unknown.

2 Feedback on Large Intergalactic Scales

Aside from affecting their host galaxy, quasars disturb their large-scale cosmological environment. Powerful quasar outflows are observed in the form of radio jets [30] or broad-absorption-line winds [31]. The amount of energy carried by these outflows is largely unknown, but could be comparable to the radiative output from the same quasars. Furlanetto & Loeb [32] have calculated the intergalactic volume filled by such outflows as a function of cosmic time (see Fig. 4). This volume is likely to contain magnetic fields and metals, providing a natural source for the observed magnetization of the metal-rich gas in X-ray clusters [33] and in galaxies [34]. The injection of energy by quasar outflows may also explain the deficit of Lyα absorption in the vicinity of Lyman-break galaxies [35,36] and the required pre-heating in X-ray clusters [37,27].

Beyond the reach of their outflows, the brightest *SDSS* quasars at $z > 6$ are inferred to have ionized exceedingly large regions of gas (tens of comoving Mpc) around them prior to global reionization (see Fig. 5 and Refs. [38,43]). Thus, quasars must have suppressed the faint-end of the galaxy luminosity function in these regions before the same occurred throughout the universe. The recombination time is comparable to the Hubble time for the mean gas density at $z \sim 7$ and so ionized regions persist [39] on these large scales where inhomogeneities are small. The minimum galaxy mass is increased by at least an order of magnitude to a virial temperature of $\sim 10^5$K in these ionized regions [1]. It would be particularly interesting to examine whether the faint end ($\sigma_\star < 30$km s^{-1}) of

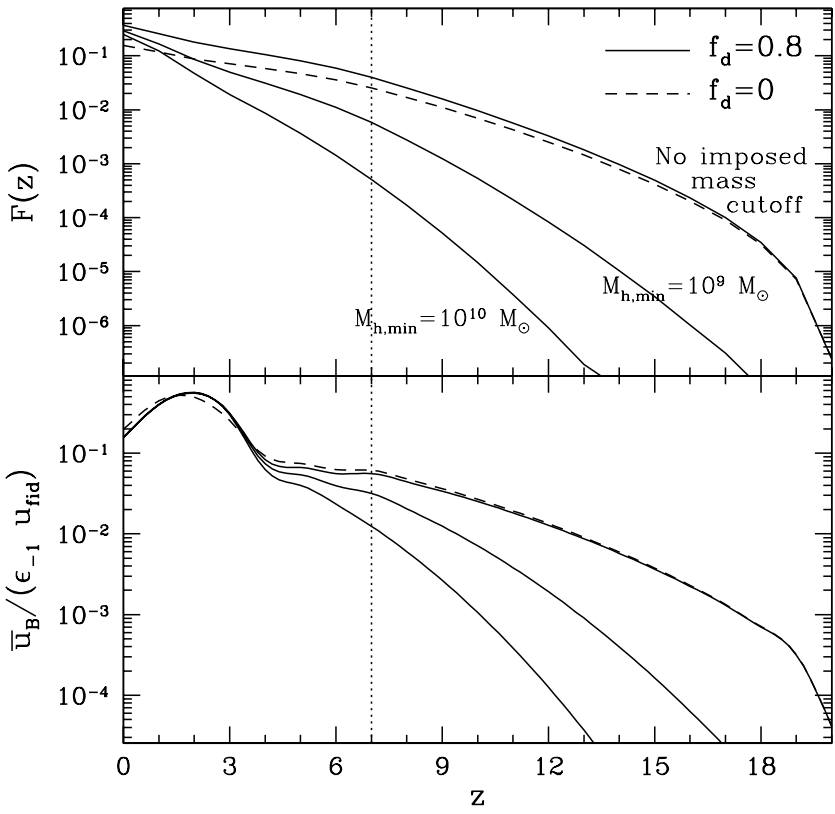

Fig. 4. The global influence of magnetized quasar outflows on the intergalactic medium (from [32]). *Upper Panel:* Predicted volume filling fraction of magnetized quasar bubbles $F(z)$, as a function of redshift. *Lower Panel:* Ratio of normalized magnetic energy density, $\bar{u}_B/\epsilon_{-1}$, to the fiducial thermal energy density of the intergalactic medium $u_{fid} = 3n(z)kT_{IGM}$, where $T_{IGM} = 10^4$ K, as a function of redshift (see [32] for more details). In each panel, the solid curves assume that the blast wave created by quasar ouflows is nearly (80%) adiabatic, and that the minimum halo mass of galaxies, $M_{h,min}$, is determined by atomic cooling before reionization and by suppression due to galactic infall afterwards (top curve), $M_{h,min} = 10^9 M_\odot$ (middle curve), and $M_{h,min} = 10^{10} M_\odot$ (bottom curve). The dashed curve assumes a fully-radiative blast wave and fixes $M_{h,min}$ by the thresholds for atomic cooling and infall suppression. The vertical dotted line indicates the assumed redshift of complete reionization, $z_r = 7$.

the luminosity function of dwarf galaxies shows any moduluation on large-scales around rare massive BHs, such as M87.

To find the volume filling fraction of relic regions from $z \sim 6$, we consider a BH of mass $M_{\rm bh} \sim 3 \times 10^9 M_\odot$. We can estimate the co-moving density of

BHs directly from the observed quasar luminosity function and our estimate of quasar lifetime. At $z \sim 6$, quasars powered by $M_{\rm bh} \sim 3 \times 10^9 M_\odot$ BHs had a comoving density of $\sim 0.5{\rm Gpc}^{-3}$[16]. However, the Hubble time exceeds $t_{\rm dyn}$ by a factor of $\sim 2 \times 10^2$ (reflecting the square root of the overdensity in cores of galaxies), so that the comoving density of the bubbles created by the $z \sim 6$ BHs is $\sim 10^2{\rm Gpc}^{-3}$ (see Fig. 2). The density implies that the volume filling fraction of relic $z \sim 6$ regions is small, $< 10\%$, and that the nearest BH that had $M_{\rm bh} \sim 3 \times 10^9 M_\odot$ at $z \sim 6$ (and could have been detected as an *SDSS* quasar then) should be at a distance $d_{\rm bh} \sim \left(4\pi/3 \times 10^2\right)^{1/3}$ Gpc ~ 140Mpc which is almost an order-of-magnitude larger than the distance of M87, a galaxy known to possess a BH of this mass [44].

What is the most massive BH that can be detected dynamically in a local galaxy redshift survey? SDSS probes a volume of $\sim 1{\rm Gpc}^3$ out to a distance ~ 30 times that of M87. At the peak of quasar activity at $z \sim 3$, the density of the brightest quasars implies that there should be ~ 100 BHs with masses of $3 \times 10^{10} M_\odot$ per ${\rm Gpc}^3$, the nearest of which will be at a distance $d_{\rm bh} \sim 130$Mpc, or ~ 7 times the distance to M87. The radius of gravitational influence of the BH scales as $M_{\rm bh}/v_{\rm c}^2 \propto M_{\rm bh}^{3/5}$. We find that for the nearest $3{\times}10^9 M_\odot$ and $3{\times}10^{10} M_\odot$ BHs, the angular radius of influence should be similar. Thus, the dynamical signature of $\sim 3 \times 10^{10} M_\odot$ BHs on their stellar host should be detectable.

3 What seeded the growth of the supermassive black holes?

The BHs powering the bright *SDSS* quasars possess a mass of a few $\times 10^9 M_\odot$, and reside in galaxies with a velocity dispersion of $\sim 500{\rm km\ s}^{-1}$[45]. A quasar radiating at its Eddington limiting luminosity, $L_E = 1.4 \times 10^{46}$ erg ${\rm s}^{-1} (M_{\rm bh}/10^8 M_\odot)$, with a radiative efficiency, $\epsilon_{\rm rad} = L_E/\dot{M}c^2$ would grow exponentially in mass as a function of time t, $M_{\rm bh} = M_{\rm seed} \exp\{t/t_E\}$ on a time scale, $t_E = 4.1 \times 10^7$ yr$(\epsilon_{\rm rad}/0.1)$. Thus, the required growth time in units of the Hubble time $t_{\rm hubble} = 9 \times 10^8$ yr$[(1+z)/7]^{-3/2}$ is

$$\frac{t_{\rm growth}}{t_{\rm hubble}} = 0.7 \left(\frac{\epsilon_{\rm rad}}{10\%}\right) \left(\frac{1+z}{7}\right)^{3/2} \ln\left(\frac{M_{\rm bh}/10^9 M_\odot}{M_{\rm seed}/100 M_\odot}\right) \ . \qquad (3)$$

The age of the universe at $z \sim 6$ provides just sufficient time to grow an *SDSS* BH with $M_{\rm bh} \sim 10^9 M_\odot$ out of a stellar mass seed with $\epsilon_{\rm rad} = 10\%$ [46]. The growth time is shorter for smaller radiative efficiencies, as expected if the seed originates from the optically-thick collapse of a supermassive star (in which case $M_{\rm seed}$ in the logarithmic factor is also larger).

What was the mass of the initial BH seeds? Were they planted in early dwarf galaxies through the collapse of massive, metal free (Pop-III) stars (leading to $M_{\rm seed}$ of hundreds of solar masses) or through the collapse of even more massive, i.e. supermassive, stars [47]*?* Bromm & Loeb [48] have shown through a hydrodynamical simulation (see Fig. 6) that supermassive stars were likely to

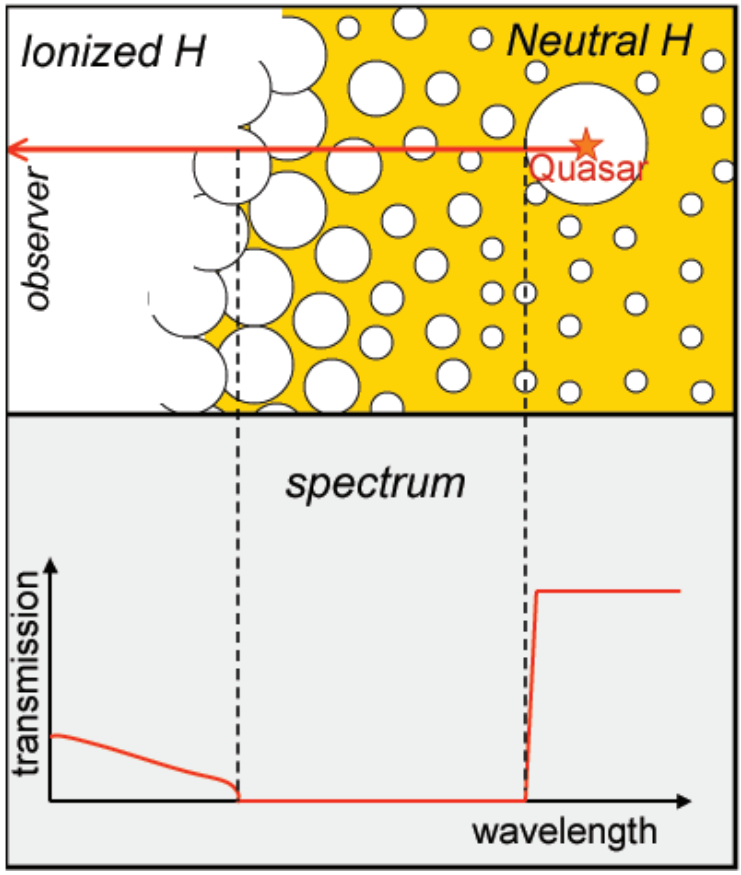

Fig. 5. Quasars serve as probes of the end of reionization. The measured size of the HII regions around *SDSS* quasars can be used [40,41] to demonstrate that a significant fraction of the intergalactic hydrogen was neutral at $z \sim 6.3$ or else the inferred size of the quasar HII regions would have been much larger than observed (assuming typical quasar lifetimes [11]). Also, quasars can be used to measure the redshift at which the intergalactic medium started to transmit Lyα photons[38,43]. The upper panel illustrates how the line-of-sight towards a quasar intersects this transition redshift. The resulting Lyα transmission of the intrinsic quasar spectrum is shown schematically in the lower panel.

form in early galaxies at $z \sim 10$ in which the virial temperature was close to the cooling threshold of atomic hydrogen, $\sim 10^4$K. The gas in these galaxies condensed into massive $\sim 10^6 M_\odot$ clumps (the progenitors of supermassive stars), rather than fragmenting into many small clumps (the progenitors of stars), as it does in environments that are much hotter than the cooling threshold. This formation channel requires that a galaxy be close to its cooling threshold and immersed in a UV background that dissociates molecular hydrogen in it. These

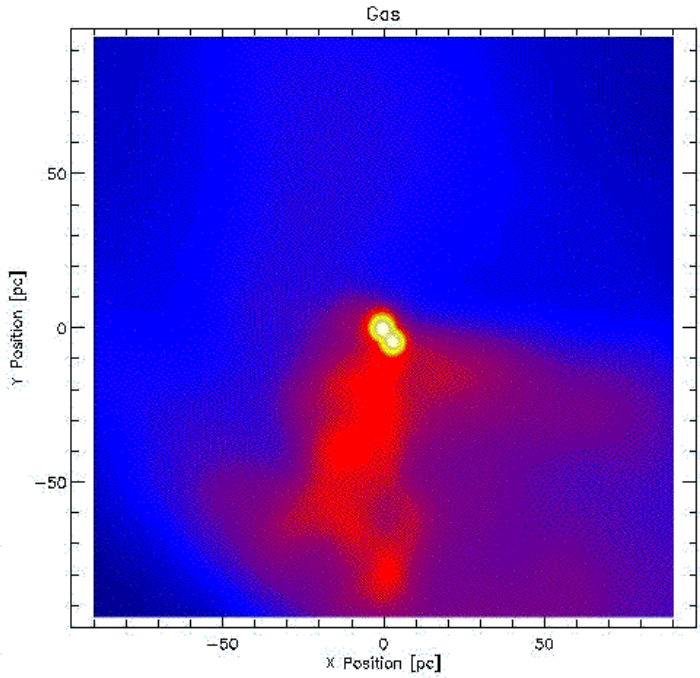

Fig. 6. SPH simulation of the collapse of an early dwarf galaxy with a virial temperature just above the cooling threshold of atomic hydrogen and no H_2 (from [48]). The image shows a snapshot of the gas density distribution at $z \approx 10$, indicating the formation of two compact objects near the center of the galaxy with masses of $2.2 \times 10^6 M_\odot$ and $3.1 \times 10^6 M_\odot$, respectively, and radii < 1 pc. Sub-fragmentation into lower mass clumps is inhibited as long as molecular hydrogen is dissociated by a background UV flux. These circumstances lead to the formation of supermassive stars [47] that inevitably collapse and trigger the birth of supermassive black holes [47,49]. The box size is 200 pc.

requirements should make this channel sufficiently rare, so as not to overproduce the cosmic mass density of supermassive BH.

The minimum seed BH mass can be identified observationally through the detection of gravitational waves from BH binaries with *Advanced LIGO* [51] or with *LISA* [50]. Most of the mHz binary coalescence events originate at $z > 7$ if the earliest galaxies included BHs that obey the $M_{\rm bh}$–v_c relation in Eq. (1). The number of *LISA* sources per unit redshift per year should drop substantially after reionization, when the minimum mass of galaxies increased due to photoionization heating of the intergalactic medium. Studies of the highest redshift sources among the few hundred detectable events per year, will provide unique information about the physics and history of BH growth in galaxies [52].

The early BH progenitors can also be detected as unresolved point sources, using the future *James Webb Space Telescope* (*JWST*). Unfortunately, the spec-

trum of metal-free massive and supermassive stars is the same, since their surface temperature $\sim 10^5$K is independent of mass [53]. Hence, an unresolved cluster of massive early stars would show the same spectrum as a supermassive star of the same total mass.

In closing, it is difficult to ignore the possible environmental impact of quasars on *anthropic* selection. One may wonder whether it is not a coincidence that our Milky-Way Galaxy has a relatively modest BH mass of only a few million solar masses in that the energy output from a much more massive (e.g. $\sim 10^9 M_\odot$) black hole would have disrupted the evolution of life on our planet. A proper calculation remains to be done (as in the context of nearby Gamma-Ray Bursts [54]) in order to demonstrate any such link.

Acknowledgements. I thank the collaborators who inspired my work on this subject: Rennan Barkana, Volker Bromm, Steve Furlanetto, Zoltan Haiman, and Stuart Wyithe. This work was supported in part by NASA grant NAG 5-13292, and by NSF grants AST-0071019, AST-0204514.

References

1. J. Kormendy, preprint astro-ph/0306353 (2003)
2. P. Chatterjee, L. Hernquist, A. Loeb: ApJ **572**, 371 (2002); Phys. Rev. Lett. **88**, 121103 (2002)
3. S. Tremaine, et al.: ApJ **574**, 740 (2002)
4. L. Ferrarese: ApJ **578**, 90 (2002)
5. R. Barkana, A. Loeb: Phys. Rep. **349**, 125 (2001)
6. D. J. E. Floyd: preprint astro-ph/0303037 (2003)
7. C. J., Willott, R. J., McLure, M. J. Jarvis: ApJ Lett. **587**, L15 (2003)
8. Y. C. Pei: ApJ **438**, 623 (1995)
9. B. J. Boyle, et al.: ApJ **317**, 1014 (2000)
10. X. Fan, et al.: AJ **121**, 54 (2001); AJ **122**, 2833 (2001); AJ **125**, 1649 (2003)
11. A. J. Barger, et al.: ApJ **584**, L61 (2003)
12. J. Silk, M. Rees: A& A Lett. **331**, L1 (1998)
13. M. Begelman, M. Ruszkowski: preprint astro-ph/0403128
14. A. King: ApJ **596**, L27 (2003)
15. N. Murray, E. Quataert, T. A. Thompson: ApJ, submitted, astro-ph/0406070 (2004)
16. S. J. B. Wyithe, A. Loeb: ApJ **595**, 614 (2003)
17. S. J. B. Wyithe, A. Loeb: ApJ, in press, astro-ph/0403714 (2004)
18. R. K. Sheth, et al.: ApJ **594**, 225 (2003)
19. W. H. Press, P. Schechter: ApJ **187**, 425 (1974)
20. S. M. Croom, et al.: MNRAS **322**, 29 (2001); **325**, 483 (2001); **335**, 459 (2002)
21. L. J. Tacconi, et al.: ApJ **580**, 73 (2002)
22. M. Dietrich, et al.: ApJ **589**, 722 (2003)
23. G. Kauffmann, M. Haehnelt: MNRAS **311**, 576 (2000)
24. J. Magorrian, et al.: AJ **115**, 2285 (1998)
25. H.-W. Rix, et al.: preprint astro-ph/9910190 (1999)
26. A. Fabian: preprint astro-ph/0407484 (2004)
27. E. Churazov, R. Sunyaev, W. Forman, H. Boehringer: MNRAS, **332**, 729 (2002)

28. S. P. Oh, E. Scannapieco: ApJ **608**, 62 (2004)
29. A. Loeb, P. J. E. Peebles: ApJ **589**, 29 (2003)
30. M. C. Begelman, R. D. Blandford, M. J. Rees: Rev. Mod. Phys. **56**, 255 (1984)
31. P. J. Green et al.: ApJ **558**, 109 (2001); G. Chartas, et al.: ApJ **579**, 169 (2002); S. C. Gallagher, et al.: ApJ, **567**, 37 (2002) A. R. King, K. A. Pounds: MNRAS **345**, 657 (2003); K. A. Pounds, et al.: MNRAS **346**, 1025 (2003)
32. S. R. Furlanetto, A. Loeb: ApJ **556**, 619 (2001)
33. P. P. Kronberg, et al.: ApJ **560**, 178 (2001)
34. R. A. Daly, A. Loeb: ApJ **364**, 451 (1990)
35. K. A. Adelberger, et al.: ApJ **584**, 45 (2003);
36. R. Croft, et al.: ApJ, **580**, 634 (2002)
37. S. Borgani, et al.: MNRAS **336**, 409 (2002)
38. R. L. White, et al.: AJ **126**, 1 (2003)
39. S. P. Oh, Z. Haiman: MNRAS **346**, 456 (2003)
40. S. J. B. Wyithe, A. Loeb: Nature **427**, 815 (2004)
41. A. Mesinger, Z. Haiman: ApJ Letters, in press; astro-ph/0406188 (2003)
42. P. Martini: preprint astro-ph/0304009 (2003)
43. S. J. B. Wyithe, A. Loeb: submitted (2004)
44. H. C. Ford, et al.: ApJ, **435**, L27 (1994)
45. R. Barkana, A. Loeb: Nature **421**, 341 (2003)
46. Z. Haiman, A. Loeb: ApJ **552**, 459 (2001)
47. A. Loeb, F. Rasio: ApJ **432**, 52 (1994)
48. V. Bromm, A. Loeb: ApJ **596**, 34 (2003)
49. M. Saijo, T. W. Baumgarte, S. L. Shapiro, M. Shibata: ApJ **569**, 349 (2002); M. Saijo: ApJ, in press, astro-ph/0407621 (2004)
50. S. J. B. Wyithe, A. Loeb: ApJ **590**, 691 (2003)
51. S. J. B. Wyithe, A. Loeb: ApJ, in press, astro-ph/0312080 (2004)
52. F. Sesana, F. Haardt, P. Madau, M. Volonteri: ApJ, in press, astro-ph/0401543 (2004)
53. V. Bromm, R. Kudritzki, A. Loeb: ApJ **552**, 464 (2001)
54. J. Scalo, J. C. Wheeler: ApJ **566**, 723 (2002)

The Growth of the Earliest Supermassive Black Holes and Their Contribution to Reionization

Z. Haiman, M. Dijkstra, and A. Mesinger

Department of Astronomy, Columbia University, New York, NY 10027, USA

Abstract. We discuss currently available observational constraints on the reionization history of the intergalactic medium (IGM), and the extent to which accreting black holes (BHs) can help explain these observations. We show new evidence, based on the combined statistics of Lyman α and β absorption in quasar spectra, that the IGM contains a significant amount of neutral hydrogen, and is experiencing rapid ionization at redshift $z \sim 6$. However, we argue that quasar BHs, even faint ones that are below the detection thresholds of existing optical surveys, are unlikely to drive the evolution of the neutral fraction around this epoch, because they would over–produce the present–day soft X–ray background. On the other hand, the seeds of the $z \sim 6$ quasar BHs likely appeared at much earlier epochs ($z \sim 20$), and produced hard ionizing radiation by accretion. These early BHs are promising candidates to account for the high redshift ($z \sim 15$) ionization implied by the recent cosmic microwave anisotropy data from WMAP. Using a model for the growth of BHs by accretion and mergers in a hierarchical cosmology, we suggest that the early growth of quasars must include a super-Eddington growth phase, and that, although not yet optically identified, the FIRST radio survey may have already detected several thousand $> 10^8 M_\odot$ BHs at $z > 6$.

1 Black Holes and Reionization

The recent discovery of the Gunn–Peterson (GP) troughs in the spectra of $z > 6$ quasars in the Sloan Digital Sky Survey (SDSS) [5,8,51], has suggested that the end of the reionization process occurs at a redshift near $z \sim 6$. On the other hand, the high electron scattering optical depth, $\tau_e = 0.17 \pm 0.04$, measured recently by the *Wilkinson Microwave Anisotropy Probe (WMAP)* experiment [46] suggests that ionizing sources were abundant at a much higher redshift, $z \sim 15$. These data imply that the reionization process is extended and complex, and is probably driven by more than one population of ionizing sources (see, e.g., [16] for a recent review).

The exact nature of the ionizing sources remains unknown. Natural candidates to account for the onset of reionization at $z \sim 15$ are massive, metal–free stars that form in the shallow potential wells of the first collapsed dark matter halos [13,6,20]. The completion of reionization at $z \sim 6$ could then be accounted for by a normal population of less massive stars that form from the metal–enriched gas in more massive dark matter halos present at $z \sim 6$.

The most natural alternative cause for reionization is the ionizing radiation produced by gas accretion onto an early population of black holes ("mini-quasars"; [21]). The ionizing emissivity of the known population of quasars di-

ESO Symposia: Growing Black Holes, pp. 30–41, 2005.

minishes rapidly beyond $z \gtrsim 3$, and bright quasars are unlikely to contribute significantly to the ionizing background at $z \gtrsim 5$ [44,18]. However, if low–luminosity, yet undetected miniquasars are present in large numbers, they could dominate the total ionizing background at $z \sim 6$ [21]. Recent work, motivated by the *WMAP* results, has emphasized the potential significant contribution to the ionizing background at the earliest epochs ($z \sim 15$) from accretion onto the seeds of would–be supermassive black holes [32,41]. The soft X–rays emitted by these sources can partially ionize the IGM early on [39,48].

In this contribution, we address the following issues: (1) What is the fraction of neutral hydrogen in the IGM at $z \sim 6$? (2) Can quasar black holes contribute to reionization either at $z \sim 6$ or at $z \sim 15$? (3) How did BHs grow, in a cosmological context, starting from early, stellar–mass seeds at $z \sim 20$? (4) Can we detect massive early ($z > 6$) black holes directly? Numerical statements throughout this paper assume a background cosmology with parameters $\Omega_m = 0.27$, $\Omega_\Lambda = 0.73$, $\Omega_b = 0.044$, and $h = 0.71$, consistent with the recent measurements by *WMAP* [46].

2 What is the Neutral Fraction of Hydrogen at $z \sim 6$?

The ionization state of the IGM at redshift $6 \lesssim z \lesssim 7$ has been a subject of intense study over the past few years. While the *WMAP* results imply that the IGM is significantly ionized out to $z \sim 15$, several pieces of evidence suggest that it has a high neutral fraction at $z \sim 6 - 7$.

One argument against a simple model, in which the IGM is ionized at $z \sim 15$, and stays ionized thereafter, comes from the thermal history of the IGM [27,47]. The temperature of the IGM, measured from the Lyα forest, is quite high at $z \sim 4$, with various groups finding values around $T \sim 20,000$K [56,34,43]. As long as the universe is reionized before $z = 10$ *and remains highly ionized thereafter*, the IGM reaches an asymptotic thermal state, determined by a competition between photoionization heating and adiabatic cooling (the latter being due to the expansion of the universe). Under reasonable assumptions about the ionizing spectrum, the IGM then becomes too cold at $z = 4$ compared to observations [27]. Therefore, there must have been significant (order unity) changes in fractions of neutral hydrogen and/or helium at $6 < z < 10$, and/or singly ionized helium at $4 < z < 10$. An important caveat to this argument is the possible existence of an additional heating mechanism that could raise the IGM temperature at $z \sim 4$. Galactic outflows could heat the IGM, in principle, but observations of close pairs of lines of sight in lens systems suggest that the IGM is not turbulent on small-scales, arguing against significant stir–up of the IGM by winds [40]. The known quasar population is likely driving the reionization of helium, HeII→HeIII, at $z \sim 3$ (e.g. [26]). If this process starts sufficiently early, i.e. at $z \gtrsim 4$, then HeII photoionization heating could explain the high IGM temperature. It would be interesting to extend the search for HeII patches that do not correlate with HI absorption to $z \sim 4$ to test this hypothesis.

A second argument for a large neutral fraction comes from the rapid redshift–evolution of the transmission near the redshifted Lyα wavelength in the spectra of distant quasars. The Sloan Digital Sky Survey (SDSS) has detected large regions with no observable flux in the spectra of several z $\sim$ 6 quasars [5,8,51]. The presence of these Gunn-Peterson (GP) troughs by itself only sets a lower limit on the volume weighted hydrogen neutral fraction of $x_{\rm HI} \gtrsim 10^{-3}$ [14]. However, this strong limit implies a rapid evolution in the ionizing background, by nearly an order of magnitude in amplitude, from $z = 5.5$ to $z \sim 6$ [8,14,30] (we note that the Lyman β region of the spectra, which is needed for this conclusion, is dismissed in another recent study [45], which therefore reaches different conclusions). Known ionizing populations (quasars and Lyman break galaxies) do not evolve this rapidly; comparisons with numerical simulations of cosmological reionization (e.g. [15]) suggests that we are, instead, witnessing the end of the reionization epoch, with the IGM becoming close to fully neutral at $z \sim 7$. At this epoch, when discrete HII bubbles percolate, the mean–free–path of ionizing photons can evolve very rapidly (e.g. [22]) and could explain the steep evolution of the background flux.

However, perhaps the strongest argument for a large neutral fraction comes from the presence of the cosmic Strömgren spheres surrounding high–z quasars. If indeed the intergalactic hydrogen is largely neutral at $z \sim 6$, then quasars at this redshift should be surrounded by large ionized (HII) regions, which will strongly modify their absorption spectra [31,7]. Recent work has shown that the damping wing of absorption by neutral hydrogen outside the HII region imprints a feature that is statistically measurable in a sample of $\sim$ 10 bright quasars without any additional assumptions [38]. A single quasar spectrum suffices if the size of the Strömgren sphere is constrained independently [38,37]. In addition, with a modest restriction (lower limit) on the age of the source, the size of the HII region itself can be used to place stringent limits on the neutral fraction of the ambient IGM [54].

To elaborate on these last arguments, based on the quasar's HII region, in Figure 1 we illustrate a model for the optical depth to Lyman α absorption as a function of wavelength towards a $z_Q = 6.28$ quasar, embedded in a neutral medium ($x_{\rm HI} = 1$), but surrounded by a Strömgren sphere with a comoving radius of $R_S = 44$ Mpc. Around bright quasars, such as those recently discovered [20,8] at $z \sim 6$, the proper radius of such Strömgren spheres is expected to be $R_S \approx 7.7\, x_{\rm HI}^{-1/3}\, (\dot{N}_Q/6.5\times10^{57}\ {\rm s}^{-1})^{1/3}\, (t_Q/2\times10^7\ {\rm yr})^{1/3}\, [(1+z_Q)/7.28]^{-1}$ Mpc [31,7]. Here $x_{\rm HI}$ is the volume averaged neutral fraction of hydrogen outside the Strömgren sphere and $\dot{N}_Q$, t_Q, and z_Q are the quasar's production rate of ionizing photons, age, and redshift. The fiducial values are those estimated for the $z = 6.28$ quasar J1030+0524 [19,54]. The mock spectrum shown in Figure 1 was created by computing the Lyman α opacity from a hydrodynamical simulation (kindly provided by R. Cen; the analysis procedure is described in [37]). The optical depth at a given observed wavelength, $\lambda_{\rm obs}$, can be written as the sum of contributions from inside (τ_R) and outside (τ_D) the Strömgren sphere, $\tau_{{\rm Ly}\alpha} = \tau_R + \tau_D$. The residual neutral hydrogen inside the Strömgren sphere at redshift

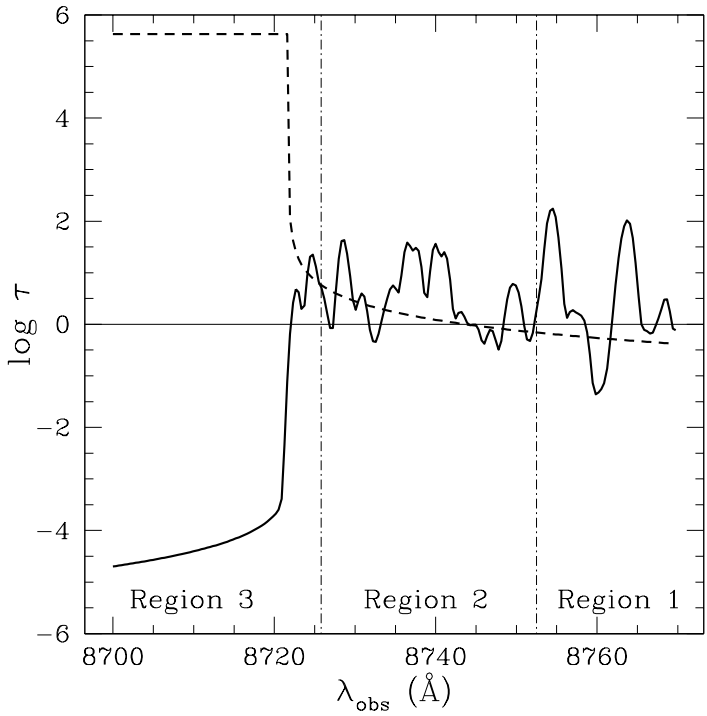

Fig. 1. Model from a hydrodynamical simulation for the optical depth contributions from within (τ_R) and from outside (τ_D) the local ionized region for a typical line of sight towards a $z_Q = 6.28$ quasar embedded in a fully neutral, smooth IGM, but surrounded by a local HII region of (comoving) radius $R_S = 44$ Mpc. The *dashed curve* corresponds to τ_D, and the *solid curve* corresponds to τ_R. The total Lyman α optical depth is the sum of these two contributions, $\tau_{\rm Ly\alpha} = \tau_R + \tau_D$. The *dashed-dotted lines* demarcate the three wavelength regions used for our analysis described in the text. For reference, the redshifted Lyman α wavelength is at 8852 Å, far to the right off the plot.

$z < z_Q$ resonantly attenuates the quasar's flux at wavelengths around $\lambda_\alpha(1+z)$, where $\lambda_\alpha = 1215.67$ Å is the rest-frame wavelength of the Lyman α line center. As a result, τ_R is a fluctuating function of wavelength (solid curve), reflecting the density fluctuations in the surrounding gas. In contrast, the damping wing of the absorption, τ_D, is a smooth function (dashed curve), because its value is averaged over many density fluctuations. As the figure shows, the damping wing of the absorption from the neutral universe extends into wavelengths $\lambda_{\rm obs} \gtrsim 8720$ Å, and can add significantly to the total optical depth in this region.

The sharp rise in τ_D at wavelengths $\lambda_{\rm obs} \lesssim 8720$ Å is a unique feature of the boundary of the HII region, and corresponds to absorption of photons redshifting into resonance outside of the Strömgren sphere. The detection of this feature has been regarded as challenging: since the quasar's flux is attenuated by a factor of $\exp(-\tau_{\rm Ly\alpha})$, an exceedingly large dynamical range is required

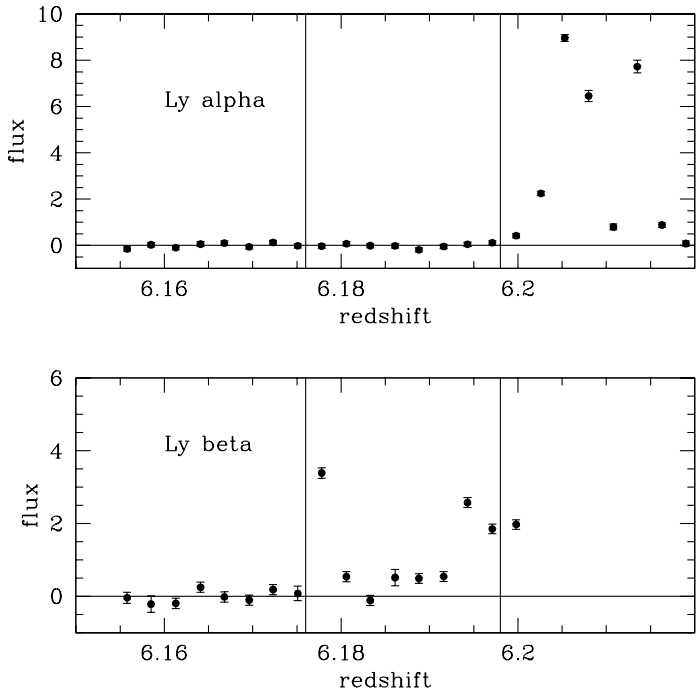

Fig. 2. The Keck ESI spectrum of the $z = 6.28$ quasar SDSS J1030+0524 [51], in units of 10^{-18} erg s^{-1} cm^{-2} Å^{-1}, and including uncorrelated 1σ errors. The upper and lower panels show the regions of the spectrum corresponding to Lyman α and β absorption in the redshift range $6.15 < z < 6.28$. The Lyman β cross section is smaller than Lyman α, and a significantly higher column of neutral hydrogen is required to block the flux in the Lyman β region than in the Lyman α region. This spectrum therefore requires a steep increase in the opacity over the narrow range from $z = 6.20$ to $z = 6.16$, explainable only by a GP damping wing, as shown by the dashed curve in Figure 1.

in the corresponding flux measurements. However, simultaneously considering the measured absorption in two or more hydrogen Lyman lines can provide the dynamical range required to detect this feature [37].

In particular, we modeled broad features of the Lyman α and Lyman β regions of the absorption spectrum of the $z = 6.28$ quasar SDSS J1030+0524. The observational input to our analysis is the deepest available absorption spectrum of SDSS J1030+0524 [51], shown in Figure 2. The spectrum exhibits a strong Lyman α Gunn-Peterson (GP) trough, with no detectable flux between wavelengths corresponding to redshifts $5.97 < z < 6.20$, as well as a somewhat narrower Lyman β trough between $5.97 < z < 6.18$ [51], as shown in Figure 2. The flux detection threshold in the Lyman α and Lyman β regions of this spectrum

correspond to Lyman α optical depths of $\tau_{\rm lim(Ly\alpha)} \approx 6.3$ and $\tau_{\rm lim(Ly\beta)} \approx 22.8$ respectively [1]

To summarize these constraints, we have divided the spectrum into three regions, shown in Figure 1. In Region 1, with $\lambda_{\rm obs} \geq 8752.5$ Å, the detection of flux corresponds to the *upper* limit on the optical depth $\tau_{\rm Ly\alpha} < 6.3$. Region 2, extending from 8725.8 Å $\leq \lambda_{\rm obs} < 8752.5$ Å, is inside the Lyman α trough, but outside the Lyman β trough. Throughout this region, the data requires $6.3 \lesssim \tau_{\rm Ly\alpha} \lesssim 22.8$. Region 3, with $\lambda_{\rm obs} < 8725.8$ Å has a *lower* limit $\tau_{\rm Ly\alpha} \geq 22.8$. As defined, each of these three regions contains approximately eight pixels.

We modeled [37] the absorption spectrum, attempting to match these gross observed features. We utilized a hydrodynamical simulation that describes the density distribution surrounding the source quasar at $z = 6.28$. We extracted density and velocity information from 100 randomly chosen lines of sight (LOSs) through the simulation box. Along each line of sight (LOS), we computed the Lyman α absorption as a function of wavelength. The size of the ionized region (R_S) and the fraction of neutral hydrogen outside it ($x_{\rm HI}$), and the quasar's ionizing luminosity, $L_{\rm ion}$, were free parameters. Note that changing R_S moves the dashed (τ_D) curve in Figure 1 left and right, while changing $x_{\rm HI}$ moves it up and down; changing $L_{\rm ion}$ moves the solid (τ_R) curve up and down. We evaluated τ_R and τ_D for each LOS, and for each point in a three–dimensional parameter space of R_S, $x_{\rm HI}$, and $L_{\rm ion}$, we computed the fraction of the LOSs that were acceptable descriptions of the spectrum of SDSS J1030+0524, based on the criteria defined above.

The procedure outlined above turns out to provide tight constrains on all three of our free parameters *simultaneously*. In particular, we find the allowed range for the radius of the Strömgren sphere to be 42 Mpc $\leq R_S \leq$ 47 Mpc, and a $\sim 1\ \sigma$ lower limit on the neutral fraction of $x_{\rm HI} \gtrsim 0.17$. These results can be interpreted as follows. As mentioned previously, the presence of flux in Region 2 ($\tau_{\rm Ly\alpha} < 22.8$) sets an immediate *lower limit* on R_S. Region 3, however, yields an *upper limit* on R_S, from the requirement that $\tau_{\rm Ly\alpha} > 22.8$ in that region. This high optical depth cannot be maintained by τ_R alone, without violating the constraint in Region 1 of $\tau_{\rm Ly\alpha} < 6.3$. We note that tight constraints on the neutral fraction ($x_{\rm HI} \gtrsim 0.1$) can be obtained from the size of the Strömgren sphere together with an assumed lower limit on its lifetime [54]. Our direct determination of the Strömgren sphere size is only slightly larger than the value assumed in [54], lending further credibility to this conclusion.

Our direct constraint on the neutral hydrogen fraction, $x_{\rm HI}$, on the other hand, comes from the presence of flux in the Lyman β region of the spectrum corresponding to Region 2. Because of fluctuations in the density field (and hence

[1] For our purposes, these optical depths can be taken as rough estimates. Their precise values are difficult to calculate, with $\tau_{\rm lim(Ly\beta)}$ especially uncertain [45,30,8,14]. However, we have verified that our conclusions below remain unchanged when the threshold opacities are varied well in excess of these uncertainties. In particular, considering ranges as wide as $5.5 < \tau_{\rm lim(Ly\alpha)} < 7$ and $10 < \tau_{\rm lim(Ly\beta)} < 30$ would lead to constraints similar to those we derive below.

in τ_R), a strong damping wing is needed to raise $\tau_{\rm Ly\alpha}$ above 6.3 throughout Region 2, *while still preserving* $\tau_{\rm Ly\alpha} < 6.3$ in Region 1. This result is derived from the observed sharpness of the boundary of the HII region alone, and relies only on the gross density fluctuation statistics from the numerical simulation. *In particular, it does not rely on any assumption about the mechanism for the growth of the HII region.*

Using a large sample of quasars (and/or a sample of gamma–ray burst afterglows with near-IR spectra) at $z > 6$, it will be possible to use the method presented here to locate sharp features in the absorption spectrum from intervening HII regions, not associated with the target source itself. The Universe must have gone through a transition epoch when HII regions, driven into the IGM by quasars and galaxies, partially percolated and filled a significant fraction of the volume. The detection of the associated sharp features in future quasar absorption spectra will provide a direct probe of the the 3D topology of ionized regions during this crucial transition epoch (in particular, it should enhance any constraint available from either the Lyman α or β region alone [14]).

3 Did Accreting Black Holes Contribute to Reionization?

The two most natural types of UV sources that could have reionized the IGM are stars or accreting black holes. Deciding which of these two sources dominated the ionization has been studied for over 30 years (e.g. [2]). It has become increasingly clear over the past decade that the ionizing emissivity of the known population of bright quasars diminishes rapidly beyond $z \gtrsim 3$, and they are unlikely to contribute significantly to the ionizing background at $z \gtrsim 5$ [44,18]. This, however, leaves open two possibilities. First, if low–luminosity, yet undetected miniquasars are present in large numbers, they could still dominate the total ionizing background at $z \sim 6$ [21]. Second, the supermassive black holes at $z \sim 6$ must be assembled from lower–mass seeds which accrete and merge during the hierarchical growth of structure. The population of accreting seed BHs can contribute to the ionization of the IGM at $z \sim 20$ [32,41].

The above two possibilities can both involve faint BHs that are not individually detectable. However, a population of acceting BHs at $z \gtrsim 6$ would be accompanied by the presence of an early X-ray background. Since the IGM is optically thick to photons with energies E below $E_{\rm max} = 1.8[(1+z)/15)]^{0.5} x_{\rm HI}^{1/3}$ keV, the soft X-rays with $E \lesssim E_{\rm max}$ would be consumed by neutral hydrogen atoms and contribute to reionization. However, the background of harder X-rays would redshift without absorption and would be observed as a present–day soft X–ray background (SXB). Under the hypothesis that accreting BHs are the main producers of reionizing photons in the high–redshift universe, it is a relatively straightforward exercise to calculate their contribution to the present–day SXB.

We assumed for simplicity [9] that the accreting BHs form in a sudden burst at redshift $z = z_Q$. The total number of BHs was expressed by a normalization constant η, defined as the ratio of the total number of ionizing photons emitted per unit volume produced by the BH population to the number density of hy-

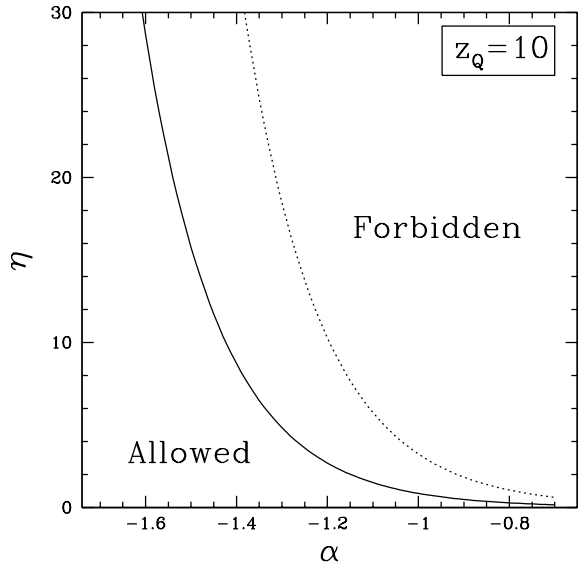

Fig. 3. Constraints on the number of ionizing photons per H atom, η, and the power–law index for the slope of the ionizing background, α, based on the intensity of the present–day SXB. The quasars are assumed to form at $z_Q = 10$ and have a power–law spectrum, $F_E \propto E^{-\alpha}$ for $E > 13.6$ eV. The curves bracket the allowed parameter space for the mean (solid line) or maximum (dotted) unaccounted flux in the SXB at $\sim$1 keV. The curves shift by +0.1 in α if $z_Q = 15$ is assumed.

drogen atoms. Full ionization of the IGM at $z \sim 6$, where recombinations are significant, likely requires $\eta \gtrsim 10$ [18]. We find that in order to account for the electron scattering optical depth $\tau_e \sim 0.17$ by partially (pre–)ionizing the IGM at $z \sim 15$, a somewhat smaller η is sufficient (see below).

The spectrum of the ionizing background is a crucial ingredient of the modeling, and depends on the type of accreting BH that is considered. For luminous quasars powered by supermassive black holes, we adopted a composite spectrum [42], based on the populations of lower redshifts ($0 < z < 5$) QSOs. The spectra of lower–mass miniquasars, with BHs whose masses are in the range $M_{\rm bh} \approx 10^{2-4}$ $M_\odot$, are likely to be harder. For these sources, we followed [32] and adopted a two–component template that includes a multi–temperature accretion disk, and a simple power-law emission to mimic a combination of Bremsstrahlung, synchrotron, and inverse Compton emission by a non-thermal population of electrons.

Finally, we took the unresolved soft X-ray band in the energy range $0.5 - 2.0$ keV to be in the range $(0.35 - 1.23) \times 10^{-12}$ erg s^{-1} cm^{-2} deg^{-2}. This range was obtained [9] from a census of resolved X–ray sources, which we subtracted from the total SXB. We included the uncertainties in both the measurement of the

total SXB (which was dominant) and in the number of resolved point sources. We examined a range of X–ray energies, and found the strongest constraints in the $0.5 - 2$ keV band. We note that a recent study [3] of faint X–ray sources found a significant population of star–forming galaxies among these sources, with a steeply increasing fractional abundance (over AGNs) toward low X–ray luminosities. If this trend continues to a flux limit that is only modestly below the current point–source detection threshold in the deepest Chandra fields, then the SXB would be saturated, strengthening our constraints (leaving less room for any additional, high–z quasars).

We find that models in which $z > 6$ accreting BHs alone fully reionize the universe saturate the unresolved X–ray background at the $\geq 2\sigma$ level. Pre-ionization by miniquasars requires fewer ionizing photons, because only a fraction of the hydrogen atoms need to be ionized, the hard X–rays can produce multiple secondary ionizations, and the clumping factor is expected to be significantly smaller than in the UV–ionization case [18,39]. We find that models in which X–rays are assumed to partially ionize the IGM up to $x_e \sim 0.5$ at $6 \lesssim z \lesssim 20$ are still allowed, but could be constrained by improved future determinations of the unresolved component of the SXB.

As emphasized above, the spectral shape of the putative typical high–z accreting BH is uncertain; the existing templates, motivated by lower–redshift sources, can be considered merely as guides. Figure 3 shows which combinations of α (the logarithmic slope of the ionizing spectrum) and η are allowed by the unaccounted flux in the SXB (the solid and dotted curves cover our inferred range of the unresolved SXB). This figure shows that for $\eta = 10$, a power–law shallower than $\alpha \approx 1.2 - 1.4$ will saturate the unaccounted flux. For comparison, α is in the range $-1.5 \lesssim \alpha \lesssim -0.5$ for $z \lesssim 0.3$, and $-1.2 \lesssim \alpha \lesssim -0.6$ for $1 \lesssim z \lesssim 6$ for optically selected radio quiet quasars [49].

Our constraints derive from the total number of ionizing photons that the population as a whole needs to produce to either fully or partially reionize the universe. Therefore, our conclusions depend mostly on the assumed spectral shape and the required number of ionizing photons per hydrogen atom η. They are independent of the details of the population, such as the luminosity function and its evolution with redshift. Future improvements in resolving the SXB, improving the limits on the unresolved component by a factor of a few, would place stringent constraints on the contribution of $z \sim 15$ accreting BHs to the scattering optical depth measured by WMAP.

4 How Did Black Holes Grow by Accretion and Mergers?

Since the seeds of early BHs may have played a role in reionization, it is all the more interesting to ask how the earliest BH population was formed, and how it evolved. The remnants of metal–free population III stars that form in the first collapsed dark halos can serve as the initial $\sim 100 M_{\odot}$seeds that later accrete and merge together, to give rise to the supermassive BHs making up the quasar population at $0 < z < 6$, and the remnant BHs found at the centers of local

galaxies. Several recent studies [29,35,13,29] have addressed various aspects of the evolution of the BH populations, using the underlying merger trees of dark matter halos.

Recent work on the generation of gravitational waves during the coalescence of a binary black hole [10,36] has suggested that the binary experiences a typical gravitational recoil velocity that may be as large as $\gtrsim$ 100 km s^{-1}. These velocities exceed the escape velocity $v_{\rm esc}$ from typical dark matter halos at high–redshift ($z \gtrsim 6$), and can therefore disrupt the early stages of growth of BHs by ejecting the earliest seeds from their host galaxies. BHs can then start growing effectively only once the typical dark matter potential wells are sufficiently deep to retain the recoiling BHs.

Relatively little time is available for the growth of few$\times 10^9$ M$_\odot$ SMBHs prior to $z \sim 6$, and their seed BHs must be present as early as $z \sim 10$ [26]. A model in which stellar seed BHs appear in small progenitor DM halos is consistent with the presence of a $\sim 4 \times 10^9$ M$_\odot$ SMBH at $z \sim 10$, provided that each seed BH can grow at least at the Eddington–limited exponential rate, and that the progenitor halos can form seed BHs sufficiently early on [26], in halos with velocity dispersions of $\sigma \sim 30$ km/s.

We quantified the effect of gravitational recoil on the growth of a few $\times 10^9$ M$_\odot$ black hole [17], by assuming that progenitor holes are ejected from DM halos with velocity dispersions $\sigma < v_{\rm kick}/2$, and do not contribute to the final BH mass. Each halo more massive than this threshold was assumed to host a seed BH that accretes at the Eddington rate, and the BHs were assumed to coalesce when their parents halos merged. We took, as an example, the SMBH powering the most distant SDSS quasar, SDSS 1054+1024 at redshift $z = 6.43$, with an inferred BH mass of $\sim 4 \times 10^9$ M$_\odot$. We find that recoil velocities with $v_{\rm kick} \gtrsim 65$ km s^{-1} must occur infrequently, or else this SMBH must have had a phase during which it gained mass significantly more rapidly than an Eddington–limited exponential growth rate (with a radiative efficiency of $\sim 10\%$) would imply. The super–Eddington growth phase can be avoided [55] if seed BHs can form and grow by mergers in dark halos with a velocity dispersion as small as $\sigma \approx 5$ km/s, the halos have steep density profiles (increasing the escape velocity [12] from the central regions by a factor of $\gtrsim 5$ relative to the naive formula $v_{\rm esc} = 2\sigma$), and the BHs that are retained during the mergers of their halos can grow uninterrupted at the Eddington rate between their birth and $z \approx 6$.

5 Can We Detect Massive $z > 6$ BHs Directly?

A natural question to ask is whether massive BHs at $z > 6$ can be directly detected. While the SDSS has detected a handful of exceptionally bright, few $\times 10^9$ M$_\odot$ black holes (the BH mass is inferred assuming these sources shine at the Eddington luminosity), they are likely a "tip of the iceberg", corresponding to the rare massive tail of the BH mass function. In X–rays bands, the deepest Chandra fields have reached the sensitivity to detect nearly ~ 100 times smaller holes ([23], provided they radiate the Eddington luminosity, with a few percent

of their emission in the X–ray bands). However, due to the small size of these fields, they have revealed only a handful of plausible candidates [1,2].

Detections however, seem promising in the large radio survey, FIRST. We used a physically motivated semi–analytic model, based on the mass function of dark matter halos, to predict the number of radio–loud quasars as a function of redshift and luminosity [25]. Simple models, in which the central BH mass scales with the velocity dispersion of its host halo as $M_{\rm bh} \propto \sigma^5_{\rm halo}$ have been previously found to be consistent with a number of observations, including the optical and X–ray quasar luminosity functions [21,52]. We find that similar models, when augmented with an empirical prescription for the radio loudness distribution, overpredict the number of faint ($\sim 10\mu$Jy) radio sources by 1–2 orders of magnitude. This translates into a more stringent constraint on the low–mass end of the quasar black hole mass function than is available from the Hubble and Chandra Deep Fields. We interpret this discrepancy as evidence that black holes with masses $\lesssim 10^7$ $M_\odot$ are either rare or are not as radio-loud as their more massive counterparts. Models that exclude BHs with masses below 10^7 $M_\odot$ are in agreement with the deepest existing radio observations, but still produce a significant tail of high–redshift objects. In the 1-10GHz bands, at the sensitivity of $\sim 10\mu$Jy, we find surface densities of ~ 100, ~ 10, and ~ 0.3 deg^{-2} for sources located at $z > 6$, 10, and 15, respectively. The discovery of these sources with instruments such as the *Allen Telescope Array (ATA)*, *Extended Very Large Array (EVLA)*, and the *Square Kilometer Array (SKA)* would open a new window for the study of supermassive BHs at high redshift. We also find surface densities of ~ 0.1 deg^{-2} at $z > 6$ for mJy sources that can be used to study 21 cm absorption from the epoch of reionization. These models suggest that, although not yet optically identified, the FIRST survey may have already detected several thousand such $> 10^8 M_\odot$ BHs at $z > 6$.

ZH thanks the organizers of the conference for their kind invitation. We also thank our recent collaborators, Geoffrey Bower, Renyue Cen, Lam Hui, Avi Loeb and Eliot Quataert for many fruitful discussions, and Rick White for an electronic version of the spectrum of SDSS J1030+0524. ZH acknowledges financial support by NSF through grants AST-0307200 and AST-0307291 and by NASA through grant NAG5-26029.

References

1. D.M. Alexander, et al.: Astron. J. **122**, 2156 (2001)
2. J. Arons, D.W. Wingert: Astroph. J. **177**, 1 (1972)
3. A.J. Barger: Astrophys. J. Lett. **584**, 61 (2003)
4. F.E. Bauer, et al.: Astron. J., in press, astro-ph/0408001 (2004)
5. R.H. Becker et al.: Astron. J. **122**, 2850 (2001)
6. R. Cen: Astroph. J. **591**, 12 (2003)
7. R. Cen, Z. Haiman: Astroph. J. Lett **542**, 75 (2000)
8. R. Cen, P. McDonald: Astroph. J. **570**, 457 (2002)
9. M. Dijkstra, Z. Haiman, A. Loeb: Astroph. J., in press, astro-ph/0403078

10. X. Fan et al.: Astron. J. **122**, 2833 (2001)
11. X. Fan et al.: Astron. J. **123**, 1247 (2002)
12. X. Fan et al.: Astron. J. **125**, 1649 (2003)
13. M. Favata, S.A. Hughes, D.E. Holz: Astroph. J. Lett **607**, 5 (2004)
14. S. Furlanetto, L. Hernquist, M. Zaldarriaga: MNRAS, submitted, astro-ph/0406131 (2004)
15. N. Y. Gnedin: Astroph. J.: **610**, 9 (2004)
16. Z. Haiman: In: *Carnegie Observatories Astrophysics Series, Vol. 1: Coevolution of Black Holes and Galaxies*. ed. by L.C. Ho (Cambridge University Press 2004) pp. 67–84
17. Z. Haiman: Astroph. J. Lett., in press, astro-ph/0404196 (2004)
18. Z. Haiman, T. Abel, P. Madau: Astroph. J. **551**, 599 (2001)
19. Z. Haiman, & R. Cen: Astroph. J. **578**, 702 (2002)
20. Z. Haiman, G.P. Holder: Astroph. J. **595**, 1 (2003)
21. Z. Haiman, A. Loeb: Astroph. J. **503**, 505 (1998)
22. Z. Haiman, A. Loeb: Astroph. J. **519**, 479 (1999)
23. Z. Haiman, A. Loeb: Astroph. J. **521**, 9 (1999)
24. Z. Haiman, A. Loeb: Astroph. J. **552**, 459 (2001)
25. Z. Haiman, E. Quataert, G.C. Bower: Astroph. J., in press, astro-ph/0403104 (2004)
26. S.R. Heap, et al.: Astroph. J. **534**, 69 (2000)
27. L. Hui, Z. Haiman: Astroph. J. **596**, 9 (2003)
28. R.R. Islam, J.E. Taylor, J. Silk: MNRAS **340**, 647 (2003)
29. G. Kauffmann, M. Haehnelt: MNRAS **311**, 576 (2000)
30. A. Lidz, L. Hui, M. Zaldarriaga, R. Scoccimarro: Astroph. J. **579**, 491 (2002)
31. P. Madau, M.J. Rees: Astroph. J. Lett. **542**, 69 (2000)
32. P. Madau, M.J. Rees, M. Volonteri, F. Haardt, S.P. Oh: Astrophys. J. **604**, 484 (2004)
33. P. Madau, E. Quataert: Astroph. J. Lett. **606**, 17 (2004)
34. P. McDonald, et al.: Astroph. J. **562**, 52 (2001)
35. K. Menou, Z. Haiman, V.K. Narayanan: Astroph. J. **558**, 535 (2001)
36. D. Merritt, et al.: Astroph. J. Lett **607**, 9 (2004)
37. A. Mesinger, Z. Haiman: Astroph. J. Lett. **611**, 69 (2004)
38. A. Mesinger, Z. Haiman, R. Cen: Astroph. J. in press, astro-ph/0401130 (2004)
39. S.P. Oh: Astrophys. J. **553**, 25 (2001)
40. M. Rauch, et al.: Astroph. J. **562**, 76 (2001)
41. M. Ricotti, J.P. Ostriker: MNRAS **352** 547 (2004)
42. S.Y. Sazonov, J.P. Ostriker, R.A. Sunyaev, MNRAS **347**, 144 (2004)
43. J. Schaye, et al.: MNRAS **318**, 817 (2000)
44. P.R. Shapiro, M.L. Giroux, A. Babul: Astroph. J. **427**, 25 (1994)
45. A. Songaila: Astron. J. **127** 2598 (2004)
46. D.N. Spergel et al.: Astroph. J. Supp. **148**, 175 (2003)
47. T. Theuns, et al.: Astroph. J. Lett. **567**, 103 (2002)
48. A. Venkatesan, M.L. Giroux, J.M. Shull: Astrophys. J. **563**, 1 (2001)
49. C. Vignali, et al.: Astron. J., **125**, 2876 (2003)
50. M. Volonteri, F. Haardt, P. Madau: Astroph. J. **582**, 559 (2003)
51. R.L. White, R.H. Becker, X. Fan, M.A. Strauss: Astron. J. **126**, 1 (2003)
52. J.S.B. Wyithe, A. Loeb: Astroph. J. **586**, 693 (2003)
53. J.S.B. Wyithe, A. Loeb: Astroph. J. **595**, 614 (2003)
54. J.S.B. Wyithe, A. Loeb: Nature **427**, 815 (2004)
55. J. Yoo, J. Miralda-Escudé: Astroph. J. Lett, in press, astro-ph/0406217 (2004)
56. M. Zaldarriaga, L. Hui, M. Tegmark: Astroph. J. **557**, 519 (2001)

Formation of the First Supermassive Black Holes

V. Bromm

Department of Astronomy, University of Texas, Austin, TX 78712, USA

Abstract. Understanding the emergence of the first supermassive black holes, and hence the first quasars, is a crucial ingredient for models of reionization and galaxy formation. I review recent progress in simulating their formation out of primordial, pure hydrogen-helium gas at redshifts ~ 10. The predicted host systems are early dwarf galaxies with total masses $\sim 10^8 M_\odot$. To be able to form seed black holes, with typical mass $\sim 10^6 M_\odot$, the dwarf galaxy must have avoided previous or concurrent episodes of star formation. The associated feedback effects would otherwise have prevented the effective assembly of gas in the center of the halo potential well. Such a comprehensive suppression of star formation could have been accomplished in rare cosmic environments where a strong UV background had photodissociated any molecular hydrogen which is the only viable coolant in metal-free gas.

1 Introduction

How and when did the first supermassive black holes (SMBHs) form? This question is intricately tied into our recent attempts to elucidate the reionization history of the universe, as the earliest SMBHs have provided the power source of the first quasars via the accretion of surrounding gas [42,54,32,41]. They must have been able to form already early on in cosmic history, as is implied by the recent discovery of quasars at redshifts $z > 6$ (e.g., [8], and references therein). The existence of SMBHs with inferred masses of $\geq 10^9 M_\odot$, less than a billion years after the big bang, provides important constraints on any formation scenario [26].

Here, I describe recent three-dimensional numerical simulations of SMBH formation [12]. The gas physics involved in the formation of SMBHs is still not well understood [41,31,3]. Therefore, it is beneficial to simulate this process under the simplest and best prescribed set of initial conditions; those dictated by the early universe. The earliest galaxies are simple in that they are the first condensations of gas to grow out of the seed inhomogeneities in the early universe (for a recent review, see [10]). The composition of the primordial gas is determined by big bang nucleosynthesis (e.g., [15]), and any primordial magnetic fields are not expected to be dynamically significant.

Previous numerical simulations of early luminous structures [6,7,1,2,36] have focused on the formation of stars inside the very first gaseous objects with a mass, $\sim 10^6 M_\odot$, just above the cosmological Jeans mass. Due to their low virial temperature (~ 1000 K), fragmentation into stars is possible inside these objects through the formation of molecular hydrogen, H_2, which cools efficiently via

ESO Symposia: Growing Black Holes, pp. 42–49, 2005.

rotational-vibrational transitions even at these low temperatures [22]. However, a relatively modest UV flux is sufficient to photodissociate the fragile H_2 molecules and suppress their role in cooling the gas [27,16,25,39]. A destructive flux of UV photons could be produced by a small, early population of stars.

Here, I consider dwarf galaxies with virial temperatures $\geq 10^4$ K inside of which atomic cooling is effective [37]. These galaxies comprise a substantial population at $z \sim 10$ [3] that is expected to dominate the reionization of hydrogen at $z \geq 6$ (e.g., [51]). The simulations use the smoothed particle hydrodynamics (SPH) technique to describe the cooling and dynamics of the gas for different choices of its total angular momentum (or spin parameter), following the suggestion that low-spin systems would be more susceptible to the formation of an SMBH [19]. If H_2 cooling is suppressed inside these galaxies, then their gas will not cool below 10^4 K. When the temperature to which the gas cools is only somewhat lower than the virial temperature of the host galaxy (at which the pressure force balances gravity for the gas), one expects that fragmentation into small clumps will be avoided and the gas will tend to condense isothermally (at its temperature floor of $\sim 10^4$ K) into large clumps. Such large clumps may then collapse to form an SMBH, possibly through an intermediate stage of a supermassive star. The viability of this scenario relies on the suppression of molecular H_2 cooling, which is capable of cooling the gas to a temperature as low as 200 K.

Following a completely different pathway [41], the first massive black holes (BHs) could have also formed out of the gravitational dynamics of clusters of stellar-mass BHs (e.g., [35,30,29,13]).

2 Cosmological context

I first outline the basic physical reason for why small protogalactic systems of virial temperature $\sim 10^4$ K and mass $\sim 10^8 M_\odot$, collapsing before the epoch of reionization at redshifts $z \geq 10$, provide intriguing sites for the formation of the first SMBHs.

The direct collapse of a primordial gas cloud into a central compact object is made difficult by fragmentation and consequent star formation [31]. The ability of the gas to fragment depends on the presence of an efficient cooling mechanism. By a redshift of $z \sim 10$, the intergalactic medium (IGM) is expected to be enriched with heavy elements from the first generation of stars to a level of $Z \geq 10^{-3.5} Z_\odot$ (e.g., [24,34]). Recent numerical investigations have shown that such a metallicity is sufficient to enable the gas to efficiently cool, fragment, and subsequently form stars [38,8,5,44,13]. It is plausible that in some regions of the IGM, the gas that collapses into a dwarf galaxy has not been enriched with metals in excess of $Z_{\rm crit} \sim 10^{-3.5} Z_\odot$ (e.g., [43,21]), and the formation of a SMBH could thus have occurred during the collapse of such a virtually metal-free system.

It is well known that molecular hydrogen can effectively cool metal-free gas, and thus enable the formation of the first stars at $z \simeq 20 - 30$ (e.g., [28,48]). Even in the absence of metals, star formation is therefore expected to occur, and

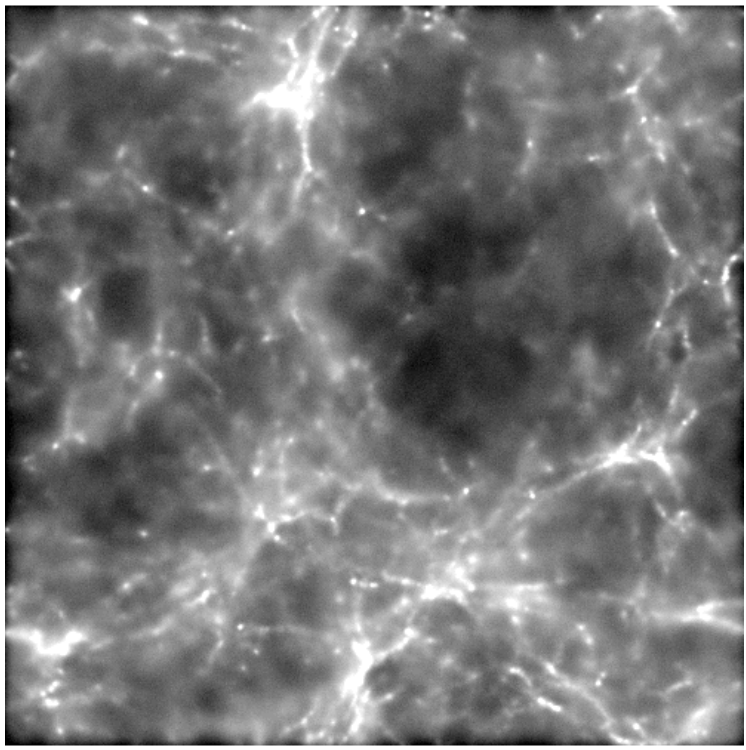

Fig. 1. First dwarf galaxy formation with cosmological initial conditions. Shown is the projected gas density at $z = 10$ in a box of physical (proper) length of 60 kpc. The high-density peaks at the intersection of the filamentary network are possible SMBH formation sites. In the simulation box, three dwarf galaxies have formed at this point.

the subsequent negative feedback due to supernova explosions would prevent the assembly of large quantities of gas in the center of the shallow dark matter (DM) potential well that characterizes the first dwarf galaxies (e.g., [17]). Molecular hydrogen, however, is fragile and can readily be destroyed by photons in the Lyman-Werner (LW) bands, within the energy range $11.2 - 13.6$ eV, via the two-step Solomon process [47]

$$\mathrm{H_2} + \gamma \rightarrow \mathrm{H_2^*} \rightarrow 2\mathrm{H}.$$

The intermediate stage involves an excited electronic state, $\mathrm{H_2^*}$, from which a fraction of the subsequent decays end in the vibrational continuum of the ground state, resulting in the dissociation of the molecule.

The question then arises whether $\mathrm{H_2}$ cooling can indeed be suppressed in the pre-reionization dwarf galaxies considered here. These systems are rather massive compared to the $\sim 10^5 - 10^6 M_\odot$ halos that host the formation of the first stars at $z \geq 20$. The gas might then be able to self-shield against the photodissociating LW background (e.g., [23,33]). Close to the epoch of reionization, however, a

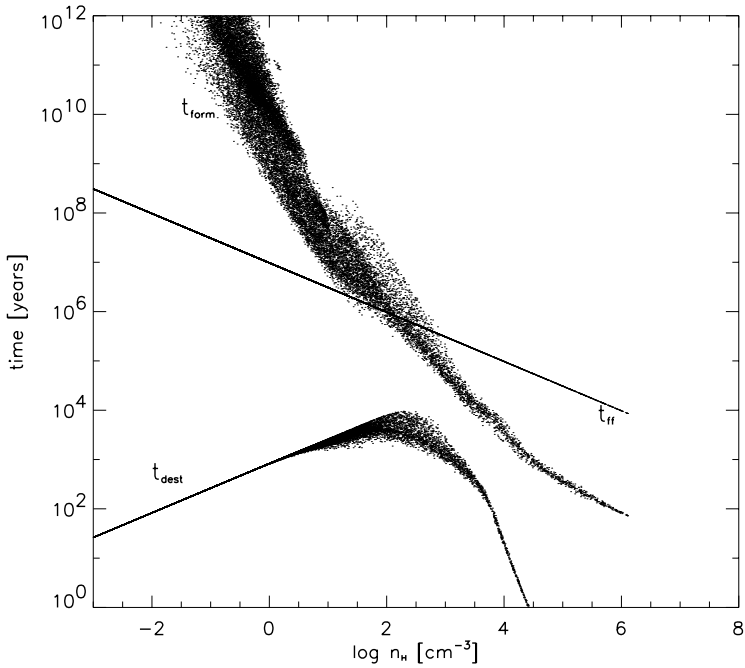

Fig. 2. Important timescales for gas collapsing under the influence of a strong LW background. *Solid line:* Free-fall time vs. hydrogen number density (in cm^{-3}). *Dots:* H_2 formation and destruction times vs. number density for every SPH particle in the simulation. The destruction time increases with density up to $n \sim 10^2$ cm^{-3} because of the effect of self-shielding. H_2 is never formed efficiently, however, as $t_{\rm form} > t_{\rm dest}$ throughout. At $n > 10^3$ cm^{-3}, H_2 is readily destroyed via collisions, and $t_{\rm dest}$ decreases again with density. (Adapted from [12].)

very strong flux in the LW bands ($h\nu < 13.6$ eV) is expected. A significant background of photodissociating photons could also result from star formation in the dwarf galaxy itself (e.g., [40,37]). However, this would also result in the production of metals, probably leading to the rapid enrichment of the galaxy beyond $Z_{\rm crit}$.

The strong UV background flux estimated above makes it possible for H_2 formation to be effectively suppressed close to the redshift of reionization. In the absence of molecular hydrogen, however, cooling can still proceed via atomic transitions in halos of mass (see, e.g., [3])

$$M \geq 10^8 M_\odot \left(\frac{T_{\rm vir}}{10^4 \text{ K}}\right)^{3/2} \left(\frac{1+z}{10}\right)^{-3/2} . \quad (1)$$

The virial temperature, $T_{\rm vir} \sim 10^4$ K, in these more massive halos allows for the very efficient cooling of the gas via lines of atomic hydrogen. Notice that in this case where the gas temperature is close to the virial temperature, the gas cloud

as a whole can undergo collapse but it will not be able to fragment until high enough densities are reached so that the Jeans mass has declined sufficiently. A halo of total mass $\sim 10^8 M_\odot$ and a collapse redshift $z \sim 10$ corresponds to a 2σ peak in the random field of primordial density fluctuations.

How does the cosmological environment for dwarf galaxy formation at redshifts $z \sim 10$ look like? We have studied this process with high-resolution cosmological simulations that are initialized according to a standard ΛCDM model. Fig. 1 shows the resulting gas density field in a box of physical length 60 kpc. At this point in the simulation, three dwarf-sized systems have formed. Not all of them, however, could harbor an SMBH. Otherwise, the locally measured SMBH mass density [4] would be exceeded, already at $z \sim 10$. Within the physical framework suggested here, that seems quite plausible, given the rather special conditions (a *very* strong LW background) required for SMBH formation.

3 Simulations

Can the seeds of SMBHs form through the direct collapse of primordial gas clouds at high redshifts? Previous work [31] has shown that without a pre-existing central point mass, this is rendered difficult by the negative feedback resulting from star formation in the collapsing cloud. The input of kinetic energy due to supernova explosions prevents the gas from assembling in the center of the dark matter potential well, thus precluding the direct formation of an SMBH. If, however, star formation was suppressed in a cloud that could still undergo overall collapse, such an adverse feedback would not occur.

The SMBH formation problem has recently been revisited with SPH simulations of isolated $2\sigma-$peaks with total masses of $10^8 M_\odot$ that collapse at $z_{\rm vir} \sim 10$ [12]. The virial temperature of these dwarf galaxies exceeds $\sim 10^4$ K, so as to allow collapse of their gas through cooling by atomic hydrogen transitions [37]. Since structure formation proceeds in a bottom-up fashion, such a system would encompass lower-mass halos that would have collapsed earlier on. These sub-systems have virial temperatures below 10^4 K, and consequently rely on the presence of H_2 for their cooling. Molecular hydrogen, however, is fragile and readily destroyed by photons in the Lyman-Werner bands with energies ($11.2-13.6$ eV) just below the Lyman limit [27]. These photons are able to penetrate a predominantly neutral IGM. Fig. 2 shows an example of such a successful suppression of H_2 cooling throughout the collapse of a dwarf-sized system.

At first, the limiting case is considered where H_2 destruction is complete. Depending on the initial spin, either one (for zero initial spin) or two compact objects form with masses in excess of $10^6 M_\odot$ and radii < 1 pc (see Fig. 3). In the case of nonzero spin a binary system of clumps has formed with a separation of ~ 10 pc. Such a system of two compact objects is expected to efficiently radiate gravitational waves that could be detectable with the planned *Laser Interferometer Space Antenna*[1] (LISA; [52]).

[1] See http://lisa.jpl.nasa.gov/

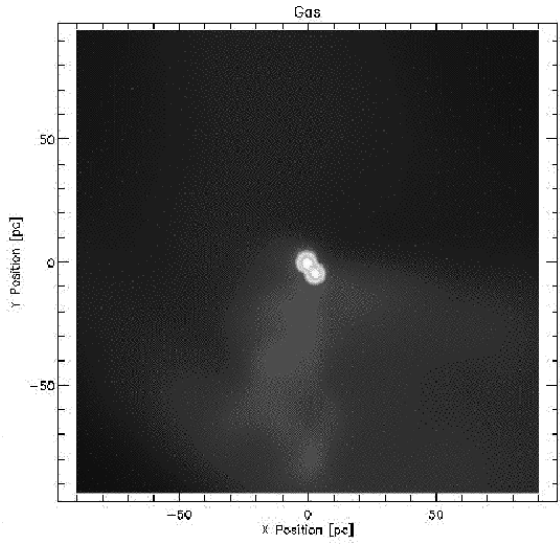

Fig. 3. Central gas density in a dwarf galaxy with virial temperature just above the atomic cooling threshold, but with no H_2 molecules present. Shown is the projection in the $x - y$ plane at $z \sim 10$. The box size is 200 pc on a side. In this case, the initial spin is $\lambda = 0.05$. Two compact objects have formed with masses of $2.2 \times 10^6 M_\odot$ and $3.1 \times 10^6 M_\odot$, respectively, and radii ≤ 1 pc. (Adapted from [12].)

What is the further fate of the central object? Once the gas has collapsed to densities above $\sim 10^{17}$ cm^{-3} and radii $< 10^{16}$ cm, Thomson scattering traps the photons, and the cooling time consequently becomes much larger than both the free-fall and viscous timescales (for details, see [12]). The gas is therefore likely to settle into a radiation-pressure supported configuration resembling a rotating supermassive star. Recent fully-relativistic calculations of the evolution of such stars predict that they would inevitably collapse to a massive black hole [4,45]. Under a wide range of initial conditions, a substantial fraction ($\sim 90\%$) of the mass of the supermassive star is expected to end up in the black hole.

Is such a complete destruction of H_2 possible? When including an external background of soft UV radiation in the simulation, we find that a flux level comparable to what is expected close to the end of the reionization epoch is sufficient to suppress H_2 molecule formation (see Fig. 2). This is the case even when the effect of self-shielding is taken into account [18]. The effective suppression of H_2 formation crucially depends on the presence of a stellar-like radiation background. It is therefore likely that stars existed before the first quasars could have formed.

4 Conclusions

The first quasars, their formation and their cosmological implications, are a fascinating subject at the frontier of modern cosmology. Up to now, most of our efforts have been theoretical, but we are approaching the point where observations can test our ideas. This is very significant, as we are bound to learn important lessons about the physical state of the universe at the end of its dark age. In the decade ahead, we can hope to disentangle the relative contributions to the reionization of the IGM made by stars and quasars, and to understand how this balance may shift over cosmic time. We will learn much more about the growth history of SMBHs, and how we get from the seed black holes at $z \sim 10$ to the observed massive SDSS quasars at $z \sim 6$. Clearly, these will be exciting years of discovery.

References

1. T. Abel, G. L. Bryan, M. L. Norman: ApJ **540** 39 (2000)
2. T. Abel, G. L. Bryan, M. L. Norman: Science **295** 93 (2002)
3. R. Barkana, A. Loeb: Phys. Rep. **349**, 125 (2001)
4. T. W. Baumgarte, S. L. Shapiro: ApJ **526**, 941 (1999)
5. V. Bromm, C. J. Clarke: ApJ **566**, L1 (2002)
6. V. Bromm, P. S. Coppi, R. B. Larson: ApJ **527**, L5 (1999)
7. V. Bromm, P. S. Coppi, R. B. Larson: ApJ **564**, 23 (2002)
8. V. Bromm, A. Ferrara, P. S. Coppi, R. B. Larson: MNRAS **328**, 969 (2001)
9. V. Bromm, R. P. Kudritzki, A. Loeb: ApJ **552**, 464 (2001)
10. V. Bromm, R. B. Larson: ARAA, **42**, 79 (2004)
11. V. Bromm, A. Loeb: ApJ **575**, 111 (2002)
12. V. Bromm, A. Loeb: ApJ **596**, 34 (2003)
13. V. Bromm, A. Loeb: Nature **425**, 812 (2003)
14. V. Bromm, N. Yoshida, L. Hernquist: ApJ **596**, L135 (2003)
15. S. Burles, K. M. Nollett, M. S. Turner: ApJ **552**, L1 (2001)
16. B. Ciardi, A. Ferrara, F. Governato, A. Jenkins: MNRAS **314**, 611 (2000)
17. A. Dekel, J. Silk: ApJ **303**, 39 (1986)
18. B. T. Draine, F. Bertoldi: ApJ **468**, 269 (1996)
19. D. J. Eisenstein, A. Loeb: ApJ **443**, 11 (1995)
20. X. Fan, et al.: AJ **125**, 1649 (2003)
21. S. R. Furlanetto, A. Loeb: ApJ **588**, 18 (2003)
22. D. Galli, F. Palla: A&A **335**, 403 (1998)
23. S. C. O. Glover, P. W. J. L. Brand: MNRAS **321**, 385 (2001)
24. N. Y. Gnedin, J. P. Ostriker: ApJ **486**, 581 (1997)
25. Z. Haiman, T. Abel, M. J. Rees: ApJ **534**, 11 (2000)
26. Z. Haiman, A. Loeb: ApJ **552**, 459 (2001)
27. Z. Haiman, M. J. Rees, A. Loeb: ApJ **476**, 458 (1997)
28. Z. Haiman, A. A. Thoul, A. Loeb: ApJ **464** 523 (1996)
29. R. R. Islam, J. E. Taylor, J. Silk: MNRAS **340**, 647 (2003)
30. R. B. Larson: MNRAS **332**, 155 (2002)
31. A. Loeb, F. A. Rasio: ApJ **432**, 52 (1994)
32. D. Lynden-Bell: Nature **223**, 690 (1969)

33. M. E. Machacek, G. L. Bryan, T. Abel: ApJ **548**, 509 (2001)
34. J. Mackey, V. Bromm, L. Hernquist: ApJ **586**, 1 (2003)
35. P. Madau, M. J. Rees: ApJ **551**, L27 (2001)
36. F. Nakamura, M. Umemura: ApJ **548**, 19 (2001)
37. S. P. Oh, Z. Haiman: 2002, ApJ **569**, 558 (2002)
38. K. Omukai: ApJ **534**, 809 (2000)
39. K. Omukai: ApJ **546**, 635 (2001)
40. K. Omukai, R. Nishi: ApJ **518**, 64 (1999)
41. M. J. Rees: ARAA **22**, 471 (1984)
42. E. E. Salpeter: ApJ **140**, 796 (1964)
43. E. Scannapieco, R. Schneider, A. Ferrara: ApJ **589**, 35 (2003)
44. R. Schneider, A. Ferrara, P. Natarajan, K. Omukai: ApJ **571**, 30 (2002)
45. M. Shibata, S. L. Shapiro: ApJ **572**, L39 (2002)
46. J. Silk, M. J. Rees: A&A **331**, L1 (1998)
47. T. P. Stecher, D. A. Williams: ApJ **149**, L29 (1967)
48. M. Tegmark, J. Silk, M. J. Rees, A. Blanchard, T. Abel, F. Palla: ApJ **474**, 1 (1997)
49. M. Volonteri, F. Haardt, P. Madau: ApJ **582**, 559 (2003)
50. K. Wood, A. Loeb: ApJ **545**, 86 (2000)
51. J. S. B. Wyithe, A. Loeb: ApJ **586**, 693 (2003)
52. J. S. B. Wyithe, A. Loeb: ApJ **590**, 691 (2003)
53. Q. Yu, S. Tremaine: MNRAS **335**, 965 (2002)
54. Y. B. Zeldovich: Dokl. Akad. Nauk SSSR **155**, 67 (1964)

Black Hole Accretion and Starbursts Triggered by Interactions in Hierarchical Galaxy Formation

N. Menci[1], A. Cavaliere[2], E. Giallongo[1], and A. Fontana[1]

[1] INAF, Osservatorio Astronomico di Roma, Via di Frascati 33, I-00040 Montporzio (Roma), Italy
[2] Dip. Fisica, Universitá di Roma Tor Vergata,Via Ricerca Scientifica 1, I-00130 Roma, Italy

Abstract. We include into a semi-analytic model of galaxy formation a physical description of starbursts and of the feeding of supermassive black holes (BHs), powering the Active Galactic Nuclei (AGNs). Both such processes originate from the destabilization of cold galactic gas in galaxy encounters, occuring mainly at redshifts $z \approx 2-4$, preferentially in massive objects, during the phase of galaxy formation characterized by frequent merging events. Our model produces at $z > 3$ a rise, and at $z < 2.5$ a decline of the bright quasar (QSO) population as steep as observed, coupled to an almost passive evolution of the galactic stellar populations in massive galaxies. The high-z star formation rate and B-band luminosity functions, and the luminosity and redshift distribution of galaxies in K-band at $z < 2$ are all in good agreement with the existing observations concerning the bright galaxy population. As for the AGNs, our results closely fit the observed luminosity functions of QSOs, their density from $z \approx 5$ to $z \approx 0$, and the local $m_{BH} - \sigma$ relation.

1 Introduction

The finding of supermassive black holes (BHs) with masses $m_{BH} \sim 10^6 - 5 \times 10^9$ $M_\odot$, at the center of most nearby bright galaxies [22], and the low space density of bright optical quasars (QSOs) compared to galaxies (see [2]), support the view of QSOs as a short ($\Delta t \sim 10^8$ yrs) active phase of supermassive BHs which accrete surrounding gas at rates $\dot{m}_{acc} \sim 1 - 10^2$ $M_\odot$/yr, (see [23]). If the accretion history starts from small primordial seeds [15], the accretion rate sets not only the QSO bolometric luminosities up to $L = \eta\, c^2\, \dot{m}_{acc} \approx 10^{48}$ erg/s (with standard mass-to-energy conversion efficiency $\eta \approx 0.1$; see [29]), but also the relic BH masses. The correlation of m_{BH} with the velocity dispersion σ of the galactic bulge [3,5] indicate that the history of $\dot{m}_{acc}(z)$ is related to the structure and the formation of the host galaxy.

On the other hand, the quantitative predictions of current semi-analytic models (SAMs, [13,26,6,17]) of hierarchical galaxy formation are challanged by several observational results, which indicate that:
a) the star formation rate at high $z > 3$ is larger than the predicted rate: this is indicated by the excess of bright galaxies in the K-band luminosity functions (LFs) at intermediate redshifts ($z \approx 1-2$, see [21]), and by the corresponding execess of $K < 20$ sources in the counts at $z > 1.5$ [12], see Fig. 1. The above observations imply that a significant fraction (~ 0.2) of the present star content

ESO Symposia: Growing Black Holes, pp. 50–55, 2005.

of massive ($m_* \approx 10^{10} - 10^{11}\ M_\odot$) galaxies is already in place at $z \sim 2$, while the gradual star formation typical of SAMs yields a fraction ~ 0.1.
b) the low-z decline of the QSO population is faster than that resulting from the models: indeed, the number density of QSO with $M_B < -24$ drops by almost three orders of magnitude from $z = 2$ to $z = 0$, a behaviour much steeper than that resulting from the SAMs which predict (at $z = 0$) a population of QSO five times larger.

Here we seek for a unique solution of the two problems above, by including in the SAM a description of the starbursts triggered by galaxy encounters (including the fly-by, i.e., grazing encounters not leading to bound merging). The description we adopt for the latter is based on the physical model for the destabilization of cold galactic gas during galactic merging and fly-by developed by [5]. The destabilized gas is assumed to feed in part the accretion onto a central supermassive BH (powering the corresponding QSO) and in part a burst of star formation. The amount of destabilized gas, the duration of the bursts, and their rate (set by the galaxy encounters) are determined by the physical properties of the galaxies and of their host halos (groups or clusters) derived from our SAM, see [17].

2 The SAM Model

The model we adopt is described in detail in [18], [19]. Here we recall the basic points:

We follow the merging histories of DM clumps, adopting the Extended Press & Schechter description [14]. When two haloes merge, the contained galaxies merge on a longer timescale, either with the central dominant galaxy (due to the orbital decay produced by dynamical friction) or with other "satelite" galaxies orbiting the same DM halo ("binary aggregations"). We describe the potential depth of the DM halo associated to a single galaxy through its circular velocity v, while the circular velocity of the halos hosting the galaxies (groups and clusters) is V; the model also computes the tidal radius r_t associated to galaxies with given v.

The properties of the gas and stars contained in the galactic DM clumps are computed following the standard recipes commonly adopted in SAMs. Starting from an initial gas amount $m\,\Omega_b/\Omega$ ($m \propto v^3$ being the DM mass of the galaxies) at the virial temperature of the galactic halos, we compute the mass m_c of cold baryons which are able to radiatively cool in the densest, central regions. This settles into a rotationally supported disk whose radius r_d and rotation velocity v_d is computed after [20]. Stars form with rate $\dot{m}_* \propto (m_c/t_d)$ with the disk dynamical time evaluated as $t_d = r_d/v_d$. Finally, a mass $\Delta m_h = m_*\,(v/v_h)^{\alpha_h}$ is returned from the cool to the hot gas phase due to the energy fed back by canonical type II Supernovae associated to m_*. The values adopted for the free parameters $\alpha_* = -1.5$, $\alpha_h = 2$ and $v_h = 150$ km/s, fit both the local B-band galaxy LF and the Tully-Fisher relation, as illustrated by [17]. The model also matches the bright end of the galaxy B-band LFs up to redshifts $z \approx 3$ (see [17])

and the resulting global star formation history is broadly consistent with that observed up to redshift $z \approx 4$ [19].

At each merging event, the masses of the different baryonic phases are replenished by those in the merging partner; the further increments Δm_c, Δm_*, Δm_h from cooling, star formation and feedback are recomputed on iterating the procedure described above.

The resulting star formation rate (for a given v) is convolved with the spectral energy distribution ϕ_λ obtained from population synthesis models [3] to obtain the integrated galactic stellar emission $S_\lambda(v,t)$ at the wavelength λ.

3 Encounters Triggering Starbursts and BH Accretion

A quantitative model to derive the fraction f of cold gas destabilized by the encounters has been worked out by [5] and has been inserted into a SAM by Menci et al. [18,19].

For a galactic halo with given circular velocity v inside a host halo (group or cluster) with circular velocity V and virial radius R, grazing encounters occur at a rate $\tau_r^{-1} = n_T(V)\,\Sigma(v,V)\,V_r(V)$, where $n_T = 3\,N_T/4\pi R^3$, and the cross section $\Sigma(v,V) \approx \pi\,\langle r_t^2 + r_t^{'2}\rangle$ is averaged over all partners with tidal radius r_t' and circular velocity v' in the same halo V. The membership $N_T(V)$ (i.e., the number of galaxies contained in a group or cluster with circular velocity V), the distributions of v', r_t', and the relative velocity $V_r = \sqrt{2}\,V$ are computed from the SAM. The duration of each encounter is defined as $\tau_e = \langle (r_t + r_t^{'})/V\rangle$ (with an upper limit given by τ_r).

The fraction of cold gas which is destabilized in each interaction event and feeds the starbursts is derived from eq. A3 of [5] in terms of the variation Δj of the specific angular momentum $j \approx Gm/v_d$ of the gas;

$$f(v,V) \approx \frac{1}{2}\left|\frac{\Delta j}{j}\right| = \frac{1}{2}\left\langle \frac{m'}{m}\,\frac{r_d}{b}\,\frac{v_d}{V}\right\rangle . \tag{1}$$

The average runs over the probability of finding a galaxy with mass m' in the same halo V where the galaxy m is located, and the impact parameter b is computed in the SAM. The prefactor accounts for the probability 1/2 of inflow rather than outflow related to the sign of Δj.

We assume that 1/4 of the destabilized fraction f feeds the central BH, while the remaining fraction is assumed to kindle circumnuclear starbursts, see [24]. Thus, the star formation rate in the nuclear region due to interaction-driven bursts is given by

$$\dot{m}_* = (3/4)\,f\,m_c/\tau_d. \tag{2}$$

This adds to the continuous, "quiescent" star formation rate $\dot{m}_* = m_c/\tau_d$.

On the other hand, the average gas accretion rate onto the central black hole is

$$\dot{m}_{acc}(v,z) = \left\langle \frac{f(v,V)\;m_c(v)}{4\,\tau_r(v,V)}\right\rangle , \tag{3}$$

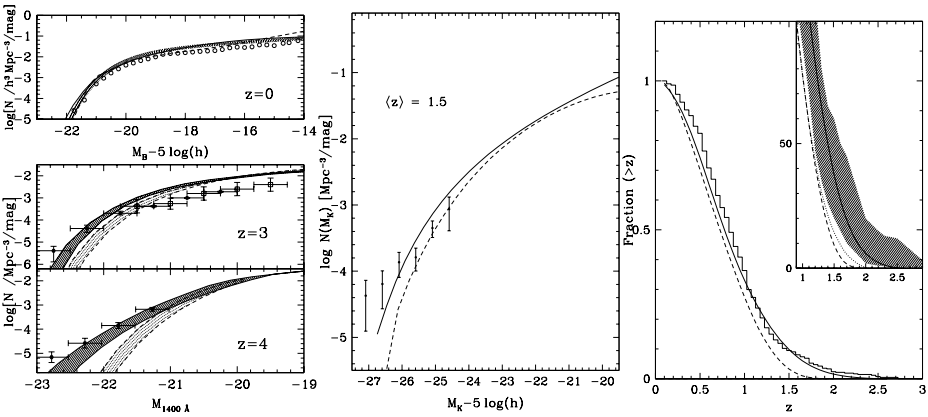

Fig. 1. Left Panels: The predicted LFs of galaxies in the quiescent (dashed lines) and starburst models (solid lines) at $z \approx 0$ (in the B-band, top panel) and at $z = 3 - 4$ (at 1400 Å, bottom panels). In the top panel, the shaded area is the LF measured by the Sloan Digital Sky Survey [4], and the circles are the data from the 2dFGRS survey [16]. In the bottom panel, the two solid lines refer to the burst model and braket the uncertainty due to diferent dust extinction curves; similarly for the dashed curves referring to quiescent models. The spectroscopic data are from [27]. Middle panel: the K-band galaxy LFs at $z = 1.5$ in the quiescent (dashed line) and in the starburst model (solid line) are compared with the data from the K20 survey [21]. Right panel: the corresponding cumulative z-distribution of $m_k < 20$ galaxies is compared with observations from the K20 survey [12]. The inset shows the cumulative distribution in the range $1 < z < 3$ with the 3σ Poissonian confidence region (shaded area); the dotted line reproduces, from [12], the prediction of the SAM by [26].

where the average over all host halos with circular velocity V is computed from the SAM. The bolometric luminosity so produced by the QSO hosted in a given galaxy is then given by

$$L(v,t) = \frac{\eta\, c^2 \Delta m_{acc}}{\tau_e} \ . \tag{4}$$

Δm_{acc} is the gas accreted at the rate given by eq. (3). We take $\eta = 0.1$, and we obtain the blue luminosity L_B by applying a bolometric correction of 13 [3]. The mass of the BH hosted in a galaxy with given v at time t is updated after $m_{BH}(v,t) = (1-\eta)\int_0^t \dot{m}_{acc}(v,t')\,dt'$, assuming in all galaxies small seeds BHs of mass $10^2\, M_\odot$ [15]; our results are insensitive to the specific value as long as it is smaller than $10^5\, M_\odot$.

4 Results

The effect of starbusts on the B, UV, and K-band LFs of galaxies, and on the K-band counts is shown in fig. 1.

The starbursts brighten the B and UV emission (probing mainly the star formation rate) mainly at high $z > 3$, where interactions are more frequent,

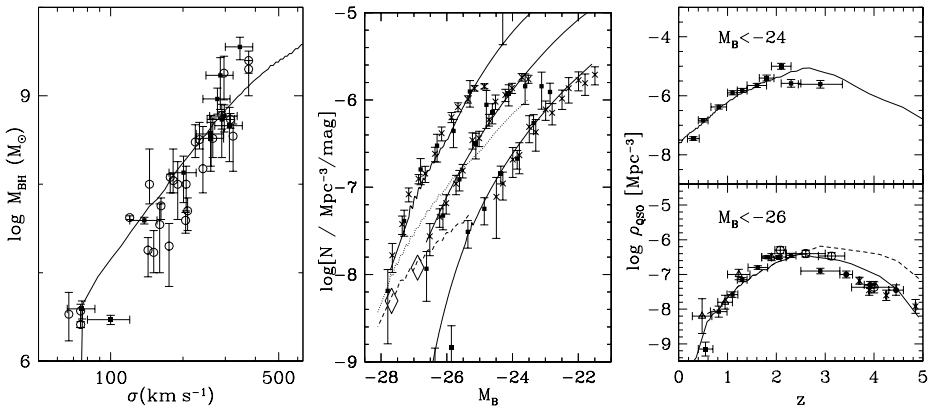

Fig. 2. Left Panel: The predicted $M_{BH}-\sigma$ relation is compared with data from [3, filled squares] and [5, circles]. Middle panel: The LFs from our model (solid lines) are shown for $z = 0.55$ (lower curve), $z = 1.2$ (middle curve) and $z = 2.2$ (uppermost curve), and are compared with the data points. These are taken from [12, solid squares] and [2, crosses], and rescaled to our cosmology. The dashed line is the model LF for $z = 4.2$ compared to the Sloan data from [8, diamonds]. The dotted line is the predicted LF for $z = 3.4$. Right Panel: The predicted cosmic density of bright (upper) and very bright (bottom panel) QSOs, rescaled to a critical cosmology ($h = 0.5$), to compare with the data; these are taken from [12], solid squares; [11], triangles; [28], open circles; [25], filled circles; [8], crosses. The dashed line represents the outcome when no Eddington limit is assumed.

and leave almost unchanged the faint end of the LFs, since the smaller sizes r_d and the slower rotation velocities v_d of less massive galaxies imply lower values of both the interaction rate and the accreted fraction f. The K-band LF is brightened by ~ 0.5 mag at $z \sim 1.5$, causing it to match the observed shape of the LFs (top panel). Correspondingly, the burst model *matches* the observed number of luminous ($m_K < 20$) galaxies at $z \approx 1.5$, while the quiescent model underpredicts the number by a factor $\sim 3-4$.

The results of the model for the QSO population are shown in fig. 2. Note that the model is able to match the observed $M_{BH}-\sigma$ relation whose logarithmic slope ≈ 4 is the combined result of different processes: the merging histories of the galactic DM clumps, which by themselves would imply the mass of cold available gas to scale as $\sigma^{2.5}$; the destabilization of the cold gas by the interactions, which steepens the relation to $\sigma^{3.5}$. The further steepening to σ^4 is provided by the Supernovae feedback which depletes the residual gas content in shallow potential wells. Note also that the evolution of the QSO density resulting from the model shows a decline from $z = 2$ to the present as fast as that observed.

5 Conclusions

The global picture emerging from our model is the following. At $z > 2.5$ the QSOs emit at their full Eddington limit, because the high merging rate in this epoch

of galaxy assemblage insures both a high baryonic content in their hosts and an abundant BH fueling. As shown in fig. 3, in this range the LFs are *flat* and *rise* with time. In this epoch, interactions also trigger strong starbursts which allow to build up a consistent fraction of the stellar content of massive galaxies, so as to match the observed K-band luminisity functions and counts. At $z < 2.5$ the *steep drop* we find for both the starbursts and for the QSO phase of galactic nuclei results from three concurring processes: 1) the declining rate of merging between early galaxies, which halts the acquisition of new gas available for accretion; 2) the progressive exhaustion of the baryon reservoirs in the hosts, consumed by fast conversion into stars and by previous accretion episodes; 3) the eventual decline of the fraction $f \sim \Delta j/j$ of residual cold gas which is destabilized and accreted onto the central BHs by the dwindling interactions between galaxies. The Eddington ratio in AGNs drops to $L/L_E \sim 10^{-2}$ at $z \approx 0$, with a weak dependence on m_{BH} and the massive galaxies enter a phase of almost passive evolution.

References

1. Blanton, M.R. et al.: ApJ, **121**, 2358 (2001)
2. Boyle, B.J. et al.: MNRAS, **317**, 1014 (2000)
3. Bruzual, A.G., & Charlot, S.: ApJ, **105**, 538 (1993)
4. Cimatti, A., et al.: A&A, **391**, 1 (2002)
5. Cavaliere, A., Vittorini, V.: ApJ, **543**, 599 (2000)
6. Cole, S., Lacey, C.G., Baugh, C.M., Frenk, C.S.: MNRAS, **319**, 168 (2000)
7. Elvis M. et al.: ApJS, **95**, 68 (1994)
8. Fan, X. et al.: ApJ, **121**, 54 (2001)
9. Ferrarese, L. Merrit, D.: ApJ, **539**, L9 (2000)
10. Gebhardt, K. et al.: ApJ, **539**, L13 (2000)
11. Goldschmidt, P., Miller, L.: MNRAS, **293**, 107 (1998)
12. Hartwick, F.D.A., Shade, D.: ARA&A, **28**, 437 (1990)
13. Kauffmann, G., White, S.D.M., & Guiderdoni, B.: MNRAS, **264**, 201 (1993)
14. Lacey, C., & Cole, S.: MNRAS, **262**, 627 (1993)
15. Madau, P., & Rees, M.J.: ApJ, **551**, L27 (2000)
16. Madgwick, D.S., et al.: MNRAS, **333**, 133 (2002)
17. Menci, N., Cavaliere, A., Fontana, A., Giallongo, E., Poli, F.: ApJ, **578**, 18 (2002)
18. Menci, N., Cavaliere, A., Fontana, A., Giallongo, E., Poli, F., Vittorini, V.: ApJ, **587**, L63 (2003)
19. Menci, N., Cavaliere, A., Fontana, A., Giallongo, E., Poli, F., Vittorini, V.: ApJ, **604**, 12 (2004)
20. Mo, H.J., Mao, S., & White, S.D.M.: MNRAS, **295**, 319 (1998)
21. Pozzetti, L. et al.: A&A, **402**, 837 (2003)
22. Richstone, D., et al.: Nature, **395**, 14 (1998)
23. Rees, M.J.: ARA&A, **22**, 471 (1984)
24. Sanders, D.B., & Mirabel, I.F.: ARA&A, **34**, 749 (1996)
25. Schmidt, M., Schneider, D.P., Gunn, J.E.: AJ, **110**, 68 (1995)
26. Somerville, R.S., Primack, J.R., & Faber, S.M.: MNRAS, **320**, 504 (2001)
27. Steidel, C.C., Adelberger, K.L., Giavalisco, M., Dickinson, M., & Pettini, M.: ApJ, **519**, 1 (1999)
28. Warren, S.J., Hewett, P.C., Osmer, P.S.: ApJ, **421**, 412 (1994)
29. Yu, Q., & Tremaine, S.: MNRAS, **335**, 965 (2002)

Calibrating the Galaxy Halo – Black Hole Relation Based on the Clustering of Quasars

S. Wyithe

University of Melbourne, Parkville Vic 3010, Australia

Abstract. The relationship between the mass of a black-hole and the circular velocity of its host dark-matter halo is fundamental to the clustering length of quasars. The slow evolution of the clustering length with redshift inferred in the 2dF quasar redshift survey strongly favors a scenario where the central black-holes comprise a larger fraction of the host galaxy mass at higher redshifts. In a scenario where quasars are triggered by halo mergers, this scaling, in combination with observed number counts imply that quasars have an episodic lifetime that is set by the dynamical time of a galactic disk rather than by the Salpeter time.

1 Introduction

The Sloan Digital Sky Survey [33] and the 2dF quasar redshift survey [4] have measured redshifts for large samples of quasars, and determined their luminosity function over a wide range of redshifts [4,12,13,8]. The 2dF survey has also been used to constrain the clustering properties of quasars [5]. Quasars appear more clustered at high redshift, although with a relatively mild trend. There is also evidence that more luminous quasars may be more highly clustered [6]. In this work we argue that the correlation length of quasars is fundamentally determined by the relation between the masses of SMBHs and their host galactic halo. We show that the evolution of the correlation length is sensitive to how the SMBH – halo relation evolves with redshift, and therefore to the physics of SMBH formation and quasar evolution.

2 The Correlation Function of Quasars

The dark-matter halo correlation function for halos of mass M is obtained from the product of the mass correlation function $\xi_{\rm m}(M, M, R)$ and the square of the ratio between the variances of the halo and mass distributions. We constrain the relationship between SMBH mass, $M_{\rm bh}$, and galactic halo mass, $M_{\rm halo}$, by constructing a theoretical quasar correlation function $\xi_{\rm q}(L, L, R)$ for comparison with observational data. We therefore need to associate the B-band luminosity $L_{\rm B}$ of a quasar with the halo mass of its host galaxy $M_{\rm halo}$. We begin by assuming quasars to have a spectral energy distribution corresponding to the median of their population [7]. We then allow the SMBH to shine at its Eddington luminosity, so that in solar units, the B-band luminosity of the quasar is

ESO Symposia: Growing Black Holes, pp. 56–59, 2005.

$\frac{L_{\rm B}}{L_{\rm B,\odot}} = 5.73 \times 10^{12} \left(\frac{M_{\rm bh}}{10^9 M_\odot}\right)$. We also need to specify a relation between SMBH and halo mass.

Dormant SMBHs are ubiquitous in local galaxies [29]. The masses of these SMBHs scale with physical properties of their hosts (e.g. [29,18,11]), for example the central velocity dispersion, the circular velocity $v_{\rm c}$ or the halo mass $M_{\rm halo}$. Measurement of the $M_{\rm bh}$–$M_{\rm halo}$ relation for local galaxies requires a choice for the relationship between the circular velocity at the radius probed by observations of galaxies, and the circular velocity at the virial radius. Here we show results for the simplifying assumption that the circular velocity of a galaxy represents the virial velocity of its halo as is the case for a singular isothermal sphere. We consider two different forms for the redshift dependence of the observed local $M_{\rm bh}$–$M_{\rm halo}$ relation:

- **Case A**: we assume that SMBH mass is correlated with the halo circular velocity. This is expected if the SMBH growth is regulated by feedback from quasar outflows (e.g. [15,71])

$$M_{\rm bh}(M_{\rm halo}, z) = {\rm const} \times v_c^5 = \epsilon M_{\rm halo} \left(\frac{M_{\rm halo}}{10^{12} M_\odot}\right)^{\frac{2}{3}} [\zeta(z)]^{\frac{5}{6}} (1+z)^{\frac{5}{2}}, \quad (1)$$

  where ϵ is a normalizing constant, and $\zeta(z)$ is close to unity (see equations 22–25 in [2] for more details).
- **Case B**: we consider the scenario in which the SMBH mass maintains the same dependence on its host halo mass at all redshifts, namely

$$M_{\rm bh}(M_{\rm halo}, z) = {\rm const} \times M_{\rm halo}^{5/3} = \epsilon M_{\rm halo} \left(\frac{M_{\rm halo}}{10^{12} M_\odot}\right)^{\frac{2}{3}} [\zeta(0)]^{\frac{5}{6}}.$$

The normalizing constant in these relations has an observed value of $\epsilon \approx 10^{-5.1}$ at $z = 0$ [7].

3 Comparison to Observations

We compare model correlation functions to observations from the 2dF quasar redshift survey [5,6] as a function of apparent Johnson B-magnitude. The magnitude limit of the 2dF quasar redshift survey is $B \sim 20.85$, and so the data should be compared with the model correlation function corresponding to $B \sim 20 - 21$. The upper panels of Figure 1 show the dependences of the clustering length, R_0 [defined through the condition $\xi_{\rm q}(R_0) = 1$] for the case where the SMBH mass scales with halo circular velocity. We find the predictions for R_0 to be consistent with observations. The lower panels of Figure 1 plot the correlation length in the alternative case where SMBH mass has a redshift independent scaling with the halo mass rather than halo circular velocity. This case results in a correlation length that varies significantly more with redshift than the data requires. Thus the evolution of the correlation length of quasars implies that the mass of a SMBH depends on the depth of the host halos potential well, and therefore comprises a larger fraction of the host halos mass at earlier times.

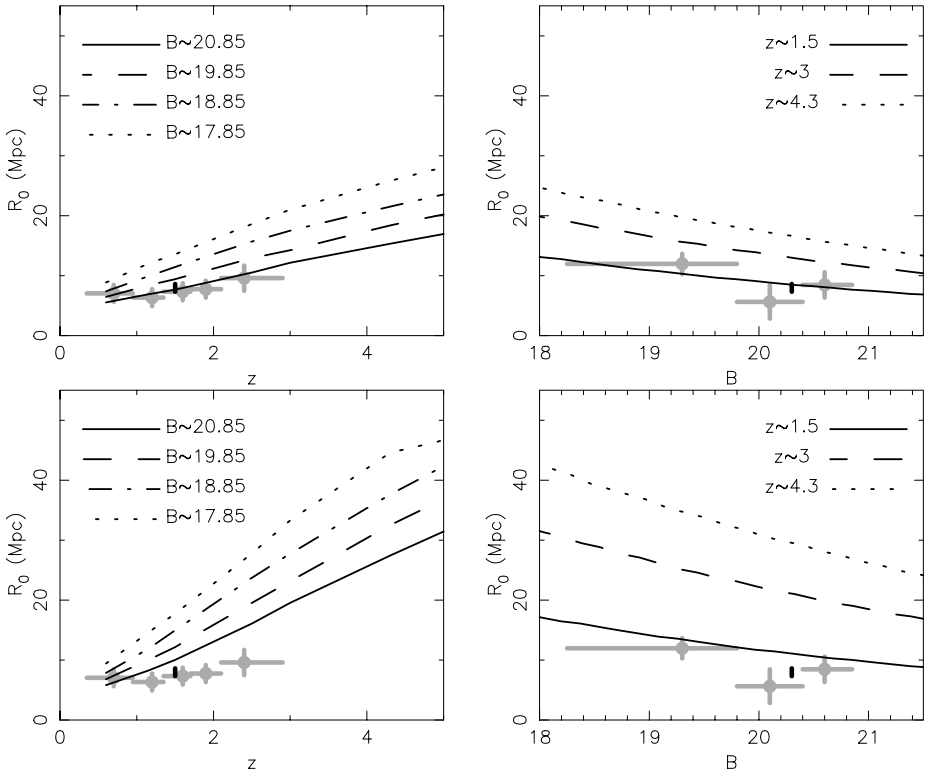

Fig. 1. The correlation length, R_0 [defined through $\xi_{\rm q}(R_0) = 1$] plotted as a function of redshift (left hand panel) and apparent magnitude (right hand panel). The data is from the 2dF quasar redshift survey [5,6]. The theoretical models assume $M_{\rm bh} \propto v_c^5$ (upper panels) and $M_{\rm bh} \propto M_{\rm halo}$ (lower panels).

4 The Luminosity Function and Quasar Lifetime

A simple model that attributes quasar activity to major mergers, assumes a $M_{\rm bh}$–$M_{\rm halo}$ relation that is described by equation (1), and sets the quasar lifetime equal to the dynamical time of a galactic disk, accurately reproduces the entire optical and X-ray luminosity functions of quasars at redshifts between 2 and 6 [71]. At lower redshifts ($z < 2$), this prescription correctly predicts the luminosity function at luminosities below the characteristic break [4]. Figure 5 shows the comparison of this model with observations. We reinforce the important qualitative result that since the evolution of quasar correlations require SMBHs to take a larger fraction of the halo mass at high redshift (case **A**, see equation 1), the observed evolution in the number counts requires a quasar lifetime that is shorter at higher redshifts, scaling approximately as the dynamical time of a dark matter halo [$\propto (1+z)^{-3/2}$].

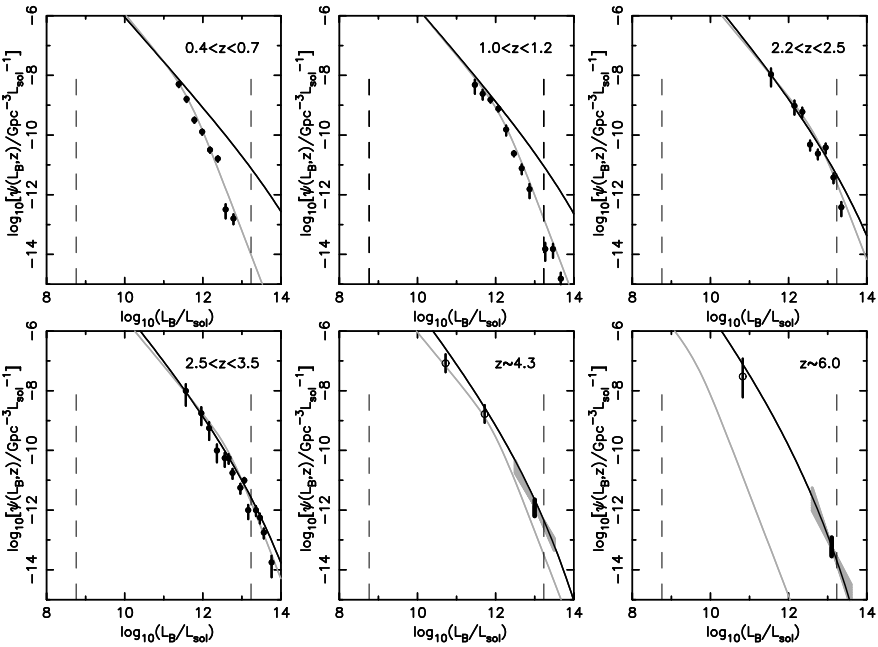

Fig. 2. Comparison of the model and observed quasar luminosity functions [14,12,13,8,4]. The light lines show the double power-law fit to the 2dF quasar luminosity function [4]. The gray regions show the 1-σ range of logarithmic slope ($[-2.25, -2.75]$ at $z \sim 4.3$ and $[-1.6, -3.1]$ at $z \sim 6$). The dashed pairs of vertical lines show the luminosities corresponding to the range of locally observed SMBHs accreting at their Eddington rate.

References

1. Barger, A. J., et al.: astro-ph/0301232 (2003)
2. Barkana, R., & Loeb, A.: Phys. Rep., 349, 125 (2001)
3. Boyle, B. J., et al.: MNRAS, 317, 1014 (2000)
4. Croom, S. M., et al.: MNRAS, 322, L29 (2001a)
5. Croom, S. M., et al.: MNRAS, 325, 483 (2001b)
6. Croom, S. M., et al.: MNRAS, 335, 459 (2002)
7. Elvis, M. et al.: Ap. J. S., 95, 1 (1994)
8. Fan, X., et al.: AJ, 121, 54 (2001a)
9. Fan, X., et al.: AJ, 122, 2833 (2001b)
10. Fan, X., et al.: astro-ph/0301135 (2003)
11. Ferrarese, L.: Ap. J., 578, 90 (2002)
12. Magorrian, J. et al.: Astron. J., 115, 2285 (1998)
13. Merritt, D., & Ferrarese, L.: ApJ., 547, 140 (2001)
14. Pei, Y. C.: ApJ, 438, 623 (1995)
15. Silk, J. & Rees, M. J.: Astron. Astrophys., 331, L1 (1998)
16. Tremaine, S. et al.: Ap. J., 574, 740 (2002)
17. Wyithe, J. S. B. & Loeb, A.: Ap. J., 595, 614 (2003)
18. York, D. G. et al.: Astron. J., 120, 1579 (2000)

From First Galaxies to QSOs – Feeding the Baby Monsters

L. Danese[1], F. Shankar[1], G.L. Granato[2,1], L. Silva[3,1], A. Bressan[2,1], G. De Zotti[2,1], P. Salucci[1], and M. Cirasuolo[1]

[1] SISSA/ISAS, via Beirut 2, I-34014 Trieste, Italy
[2] INAF - Osservatorio Astronomico di Padova, I-35122 Padova, Italy
[3] INAF - Osservatorio Astronomico di Trieste, I-34131 Trieste, Italy

Abstract. We present a physical model for the coevolution of massive spheroidal galaxies and active nuclei at their centers. Supernova heating is increasingly effective in slowing down the star formation and in driving gas outflows in smaller and smaller dark matter halos. Thus the more massive protogalaxies virializing at early times are the sites of faster star formation. The correspondingly higher radiation drag causes a faster angular momentum loss by the gas and induces a larger accretion rate onto the central black hole. In turn, the kinetic energy of the outflows powered by the active nuclei can unbind the residual gas in a time shorter for larger halos. The model accounts for a broad variety of dynamical, photometric and metallicity properties of early-type galaxies, for the $M_{\rm BH}$–σ relation and for the local supermassive black-hole mass function.

1 Introduction

There is growing evidence that massive galaxies at high redshifts are far more numerous than predicted by standard semi-analytic models [4,26,8,32,15,34]. Also, the $[\alpha/Fe]$-magnitude relation points towards a higher abundance of α-elements for more luminous/massive galaxies, indicating that the time for type Ia SNe to enrich the ISM must have been shorter for the more massive systems [22]. Extremely massive black holes (BH), with $\log\,(M_{\rm BH}/M_\odot) > 8$–9, must also have formed very quickly at early cosmic times to power highly luminous quasars at redshift of up to > 6 [11].

As stressed by [17,18,32], in the framework of the hierarchical clustering paradigm there are enough massive dark halos to accommodate the observed high redshift galaxies. The problem is to find a mechanism explaining the faster and more efficient star-formation in more massive galactic halos.

The tight relationship between dynamic and photometric properties of galactic bulges and the masses of BHs at their centers [12,16,1,5,21] indicates that a key ingredient in this context is likely to be the mutual feedback from star formation and the growing active nucleus. Indeed the close interplay of the two components has a crucial role in the *Anti-hierarchical Baryon Collapse* (ABC) model by Granato et al. [17,18], that appears to overcome the main shortcomings of current semi-analytic models. In the following we briefly describe this model and summarize some of its predictions.

ESO Symposia: Growing Black Holes, pp. 60–65, 2005.

2 The Model

The ABC model applies to massive spheroidal galaxies and galactic bulges (halo mass $\log(M_{\rm halo}/M_\odot) > 11.4$), virializing at $z \geq 1.5$. In practice, it is assumed that massive halos virializing in this redshift range end up as spheroidal galaxies, while those virializing at later times host disks or irregular galaxies. The virialization rate of these objects is given by the positive term of the derivative of the Press & Schechter [25] mass function, while the negative part (corresponding to their disappearance due to merging) is negligible. Numerical simulations [35,36] have shown that the build-up of DM halos consists of an early phase of fast accretion, during which there is a rapid increase of the specific binding energy and of the central potential well, and of a late phase of slow accretion with no significant change of the binding energy and of the circular velocity.

The diffuse gas within the DM well, shock heated to the virial temperature of the halo, falls into the star forming regions at a rate ruled by the cooling and dynamic timescales. The cooled gas feels the feedback from SNe and from the central AGN which heat and possibly expel the gas from the potential well. In small halos a few SNe are sufficient to quench the star formation, while in the big ones nothing prevents a huge starburst (1000 $M_\odot$/yr over 0.5 Gyr). Furthermore, the radiation drag damps down the angular momentum of the cool gas [20], letting it inflow into a reservoir around the central super-massive BH (SMBH). Viscous drag then causes the gas to flow from the reservoir into the SMBH, increasing its mass and powering the nuclear activity until its feedback is strong enough to unbind the residual ISM, thus stopping the star formation and letting the active nucleus shine unobscured. The time required to sweep out the ISM decreases with increasing halo mass, thus accounting for the $[\alpha/Fe]$-magnitude relation. An almost passive evolution of the stellar population, with a dormant SMBH, follows.

3 Results

As shown by [18], the ABC model, coupled with the spectro-photometric code GRASIL by Silva et al. [29], accounts for a broad variety of data, including the SCUBA counts at 850 μm (which are strongly under-predicted by the other semi-analytic models), the corresponding preliminary redshift distribution, and the local K-band luminosity function of massive spheroidal galaxies. In Fig. 1 we compare the model predictions with the distribution of stellar masses in galaxies up to $z \simeq 2$ determined by [14]. At $z \sim 3$ the model predicts a comoving number density of galaxies with masses $M_{star} \geq 10^{11} M_\odot$ of $n \sim 10^{-4}$/Mpc^3 in excellent agreement with the estimate by [32] (Fig. 2).

For a given cosmology, a halo of mass $M_{\rm halo}$ virializing at $z_{\rm vir}$ can be characterized by its circular velocity, $V_{\rm halo}$. Thus, the velocity functions of halos virializing at any given redshift, predicted by the standard hierarchical clustering model for galaxy formation, can be straightforwardly computed from their mass function. Integrating over redshift, for $z_{\rm vir} \geq 1.5$, the local velocity function of spheroids can be obtained. Adopting a constant ratio of the velocity

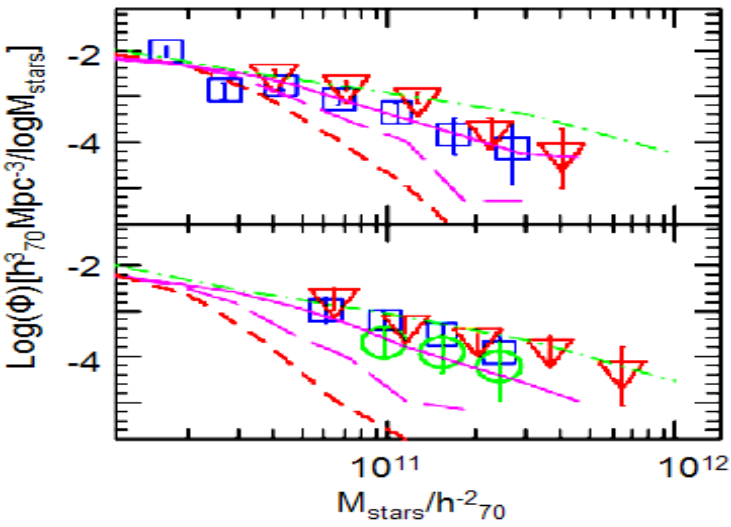

Fig. 1. Stellar mass functions of galaxies in the ranges $1. \leq z < 1.5$ (upper panel) and $1.5 \leq z < 2$ (lower panel) derived by [14] (different symbols correspond to different methods to estimate the stellar mass), compared with theoretical predictions (dot-dashed line: ABC model; dashed and thick solid lines: [30,31]; short dashed line: [6])

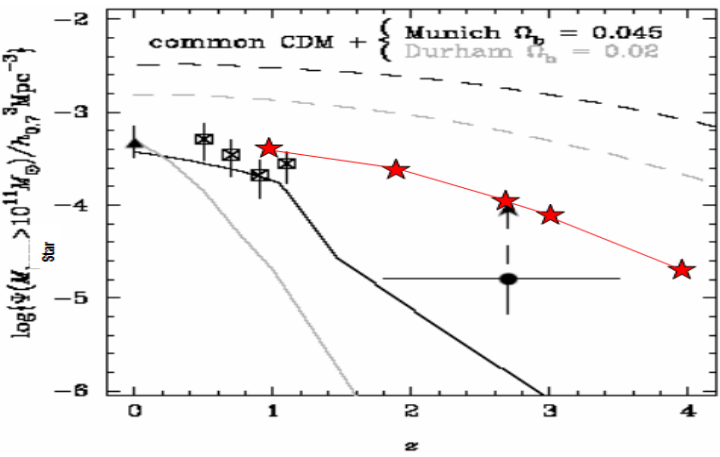

Fig. 2. Comoving number densities of galaxies with baryonic masses $\geq 10^{11} M_\odot$ as a function of redshift. The triangle and open rectangles show densities of massive stellar systems at z=0 [7] and $z \sim 1$ [10]. The circle with upward arrow is the lower limit by [32]. The solid curves show the predictions of [19] (upper) and [2]; the dashed curves show the number densities of halos with available baryonic masses $\geq 10^{11} M_\odot$ for the values of Ω_b adopted by [19] (upper) and [2]. The line with stars is the ABC model prediction. Adapted from [32]

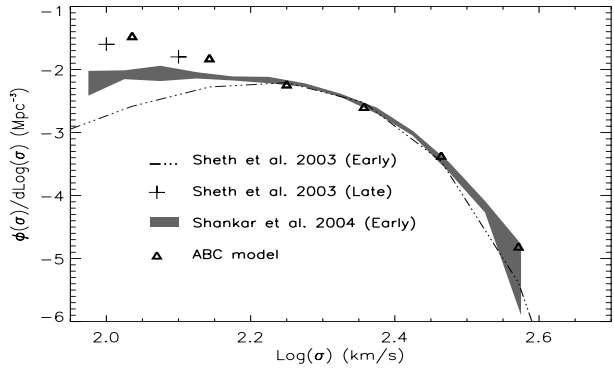

Fig. 3. Local velocity dispersion function derived from the SDSS data [28,4] compared with that predicted by the ABC model

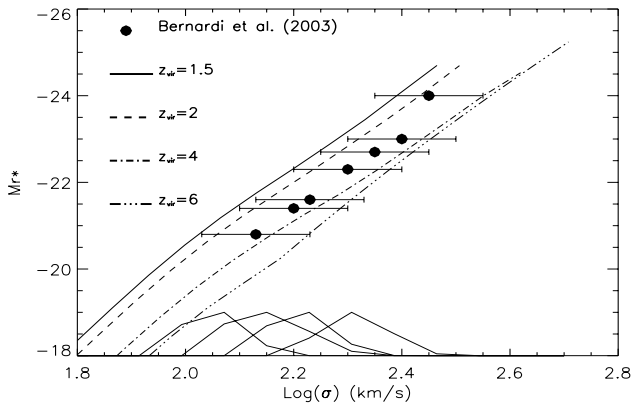

Fig. 4. Faber-Jackson relation predicted by the ABC model for various virialization redshifts compared with data by [3]. Just above the x-axis are the normalized distributions of velocity dispersions of galaxies in 4 absolute magnitude bins 0.5 mag wide, centered at $Mr* = -20.2$, -21, -22, and -23 (from left to right), as predicted by the ABC model. The FWHMs of the distributions are remarkably close to the observed values (FWHM ~ 0.09, see [3])

dispersion at $r_e/8$, σ, to $V_{\rm halo}$, $\sigma/V_{\rm halo} = 0.55$, consistent with the results by [13], Cirasuolo et al. [5] have found a very good match to the velocity dispersion function (Fig. 3) of early-type galaxies and bulges derived by [28,4] using SDSS data [3]. Furthermore, [5] have shown that the relationship between the luminosity of spheroids and their velocity dispersion, predicted by the ABC model, fits the Faber-Jackson relation for NVSS galaxies [3] (Fig. 4); the observed distribution of velocity dispersions at given luminosity is accounted for by the range of virialization redshifts.

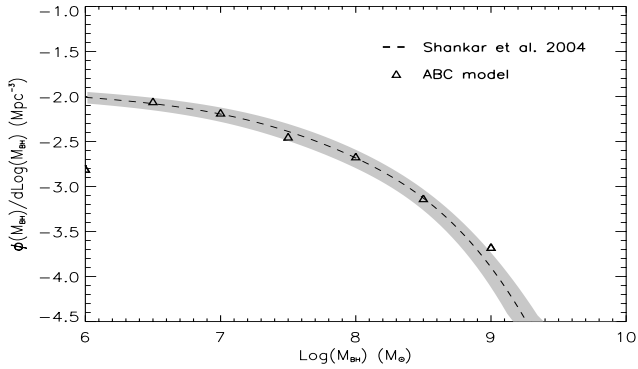

Fig. 5. Predicted local supermassive black hole mass function compared with the one obtained by [4] from kinematic and photometric data on spheroidal galaxies

In the ABC model, the final (i.e. present day) mass of SMBHs in galaxy centers is also a function of $M_{\rm halo}$ and $z_{\rm vir}$ only. In Fig. 1 the predicted local supermassive BH mass function is compared with the recent estimate by [4]. As shown by [18,5] the model also gives a good fit of the $M_{BH} - \sigma$ relation.

4 Summary and conclusions

The spheroid-SMBH coevolution model described here is based on the idea of *Anti-hierarchical growth* of the baryonic component in DM halos. The heating from SNe is increasingly effective in slowing down the star formation and driving gas outflows in shallower potential wells. As a consequence, the star formation is faster within the most massive halos. A higher star formation implies a higher radiation drag, a faster SMBH fuelling and growth, and therefore a stronger AGN kinetic output ($\propto M_{BH}^{3/2}$, see [24]) causing an earlier sweeping out of the ISM. Thus the duration of the starburst and of the SMBH growth is shorter for more massive halos ($\leq 1\,$Gyr for $M_{\rm halo} \geq 10^{12} M_\odot$ and $3 \leq z_{\rm vir} \leq 6$).

During the intense starburst and SMBH growth phase the spheroid is heavily dust obscured (SCUBA phase); the model indeed fits the SCUBA counts and the (albeit limited) data on the redshift distribution. We attribute the relatively high hard X-ray emission recently detected from SCUBA galaxies by [1] ($L_X \sim 10^{43}$–10^{44} erg/s) as associated to the growing phase of the central SMBH.

When the AGN reaches its maximum power, the ISM is blown away and the AGN shines unobscured (QSO phase). The gas surrounding powerful high-z QSOs is therefore expected to exhibit at least solar abundances and α-enhancement, as indeed found by [9].

Afterwards the spheroids evolve passively (ERO phase). The model reproduces the mass and redshift distributions of sources detected by deep K-band surveys, which proved to be extremely challenging for all the other semi-analytical

models, as well as the dynamical/photometric properties of spheroidal galaxies in the SDSS survey [3].

Finally, the model accounts for the local SMBH mass function for $M_{\rm BH} > 10^7\,M_\odot$, and for the the $M_{\rm BH}$–σ relation. It predicts a steepening at $\sigma \leq 150\,{\rm km/s}$ as the SMBH growth is hindered by the combined effect of SNe heating and decreased radiation drag.

References

1. D.M. Alexander et al.: AJ **125**, 383 (1988)
2. C.M. Baugh, A.J. Benson, S. Cole, C.S. Frenk, C. Lacey in: *The Masses of Galaxies at Low and High Redshift* R. Bender, A. Renzini, (eds. Berlin: Springer), **91** (2003)
3. M. Bernardi et al.: AJ **125**, 1849 (2003)
4. A.W. Blain et al.: Phys Rep. **369**, 111 (2002)
5. M. Cirasuolo et al.: in preparation
6. S. Cole et al.: MNRAS **319**, 168 (2000)
7. S. Cole et al.: MNRAS **326**, 255 (2001)
8. E. Daddi et al.: ApJ **588**, 50 (2003)
9. V. D'Odorico et al.: MNRAS **351**, 976 (2004)
10. N. Drory et al.: ApJ, in press, astro-ph/0403041 (2004)
11. X. Fan et al.: AJ **122**, 2833 (2001)
12. L. Ferrarese, D. Merritt: ApJ **539**, L9 (2000)
13. L. Ferrarese: ApJ **578**, 90 (2002)
14. A. Fontana et al.: A&A accepted, astro-ph/0405055 (2004)
15. M. Franx et al.: ApJ **587**, L79 (2003)
16. K. Gebhardt et al.: ApJ **539**, L13 (2000)
17. G.L. Granato et al.: MNRAS **324**, 757 (2001)
18. G.L. Granato, G. De Zotti, L. Silva, A. Bressan, L. Danese: ApJ **600**, 580 (2004)
19. G. Kauffmann et al.: MNRAS **303**, 188 (1999)
20. N. Kawakatu, M. Umemura, M. Mori: ApJ **583**, 85 (2003)
21. A. Marconi, L.K. Hunt: ApJ **589**, L21 (2003)
22. F. Matteucci: A&A **288**, 37 (1994)
23. R.J. McLure, J.S. Dunlop: MNRAS accepted, astro-ph/0310267
24. N. Murray, J. Chiang, S.A. Grossman, G.M. Voit: ApJ **451**, 498 (1995)
25. W.H. Press, P. Schechter: ApJ **187**, 425 (1974)
26. S.E. Scott et al.: MNRAS **331**, 817 (2002)
27. F. Shankar et al.: MNRAS accepted, astro-ph/0405585 (2004)
28. R.K. Sheth et al.: ApJ **594**, 225 (2003)
29. L. Silva, G.L. Granato, A. Bressan, L. Danese: ApJ **509**, 103 (1998)
30. R.S. Somerville et al.: 'Modeling the Multi-wavelenght Universe: the assembly of massive galaxies'.In: *Multiwavelength Mapping of galaxy Formation and Evolution* R. Bender, A. Renzini (eds.), in press, astro-ph/0401570 (2004)
31. R.S. Somerville et al.: ApJ **135**, 600L (2004)
32. M. Tecza et al.: ApJ **605**, L109
33. S. Tremaine et al.: ApJ **574**, 740 (2002)
34. P.G. van Dokkum et al.: ApJ **587**, L83 (2003)
35. R.H. Wechsler et al.: ApJ **568**, 52 (2002)
36. D.H. Zhao, H.J. Mo, Y.P. Jing, G. Børner: MNRAS **339**, 12 (2003)

Evolution of the ISM in Elliptical Galaxies and Black Hole Growth

V. Gaibler[1], M. Camenzind[1], and M. Krause[1]

Landessternwarte Königstuhl, D-69117 Heidelberg, Germany

Mass and Energy Injection into Spheroidal Bulges: The hot phase of the ISM in nearby elliptical galaxies is observed to have temperatures in the range of 10 Mio degrees. While stellar wind and mass–loss by planetary nebulae are widely seen as the sources for the interstellar gas, there is no generally established model to explain the heating of the ISM (supernovae, AGN heating and collisions).

The evolution of the ISM is simulated in one or two spatial dimensions under the influence of the gravitational field of a stellar distribution $\rho_*(r)$ (Plummer or some Zhao profile) and of the central Black Hole [1]

$$\frac{\partial \rho}{\partial t} + \nabla \cdot (\rho \boldsymbol{u}) = \alpha\, \rho_* \tag{1}$$

$$\frac{\partial (\rho \boldsymbol{u})}{\partial t} + \nabla \cdot (\rho \boldsymbol{u} \otimes \boldsymbol{u}) = -\nabla P - \rho\, \nabla \Phi \tag{2}$$

$$\frac{\partial e}{\partial t} + \nabla \cdot (e \boldsymbol{u}) = -P\, \nabla \cdot \boldsymbol{u} + \alpha \rho_* c_V T_0 - \rho^2 \Lambda\,. \tag{3}$$

Here, ρ, $\boldsymbol{u}$, T, P and e are the state variables of the gas, α the mass injection rate, $\rho^2\Lambda$ is the cooling rate, and $c_V T_0$ the energy supplied by supernova heating relative to mass injection. Heating is controlled by the effective temperature T_0. Mass injection and heating are assumed to be proportional to the stellar density. The computations were performed with the NIRVANA_CP code, including cooling and parallelization, added by Krause [2] and Thiele [3].

In– and Outflow States: For constant mass–injection and heating we generally find steady state solutions which are either inflow or outflow, but not hydrostatic equilibrium (Fig. 1). Inflow solutions show temperatures near the virial temperature and subsonic gas flows towards the center (cooling flows). Outflows are generally supersonic, of high temperature and low density. Velocity and temperature profiles are found to be largely independent on the mass injection rate, while they scale with powers of the heating rate. The ISM evolution with time–dependent mass injection and heating can be understood by examining the evolution of the model in (α, T_0) parameter space (Fig. 1, bottom). The time–dependence of the mass injection is determined by the initial mass function, with the scaling $\alpha(t) \propto t^{-1.3}$.

References

1. V. Gaibler: *Evolution of the Interstellar Medium in Elliptical Galaxies*, Diploma Thesis, LSW Heidelberg (2004)

ESO Symposia: Growing Black Holes, pp. 66–67, 2005.

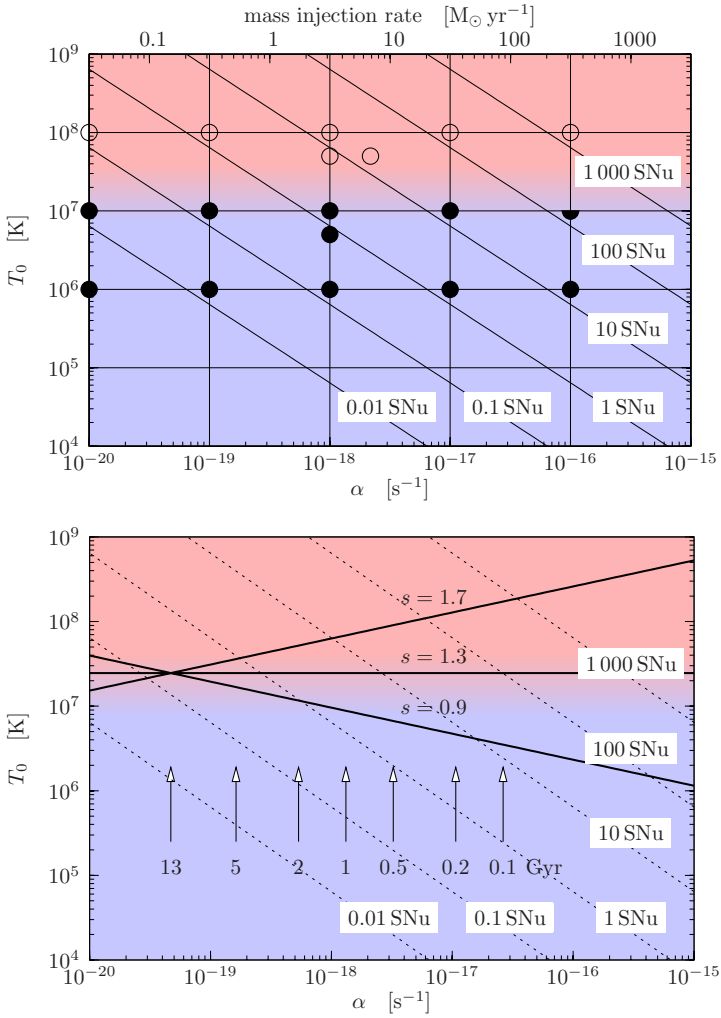

Fig. 1. Top: Inflow (filled symbols) and outflow (open symbols) solutions in the parameter space spanned by mass injection and SN heating. 1 SNu corresponds to 1 SN per 100 years and per $10^{10}\,L_{\odot}$. Bottom: Evolution of SN Ia heating in the (α, T_0) parameter space for a time–dependent SN rate, $SN(t) \propto t^{-s}$, and $\alpha(t) \propto t^{-1.3}$. The arrows show the position of the galaxy at the corresponding age in units of Gyears

2. M. Krause, M. Camenzind: In: *High Performance Computing in Science and Engineering '03*, ed. by E. Krause, W. Jäger (Springer, Heidelberg 2003) pp. 95–106
3. M. Thiele: *Numerical Simulations of Protostellar Jets*, PhD Thesis, University Heidelberg, Heidelberg (2000)

A Physically Motivated Toy Model for the BH-Spheroid Coevolution

L. Ciotti[1], J.P. Ostriker[2,3], and S. Yu. Sazonov[4,5]

[1] Dept. of Astronomy, Bologna University, Italy
[2] Institute of Astronomy, Cambridge, UK
[3] Dept. of Astrophysical Sciences, Princeton University, USA
[4] Max-Planck-Institut für Astrophysik, Garching bei München, Germany
[5] Space Research Institute, Russian Academy of Sciences, Moscow, Russia

Abstract. We present a summary of the results obtained with a time-dependent, one-zone toy model aimed at exploring the importance of radiative feedback on the co-evolution of massive black holes (MBHs) at the center of stellar spheroids and their stellar and gaseous components. We consider cosmological infall of gas as well as the mass and energy return for the evolving stellar population. The AGN *radiative* heating and cooling are described by assuming photoionization equilibrium of a plasma interacting with the average quasar SED. Our results nicely support a new scenario in which the AGN accretion phase characterized by a very short duty-cycle (and now common in the Universe) is due to radiative feedback. The establishment of this phase is recorded as a fossil in the Magorrian and $M_{\rm BH}-\sigma$ relations.

1 A simple scenario

In [1,2,3] we discuss the importance of radiative feedback on the co-evolution of MBHs at the center of spheroidal galaxies and that of their stellar and gaseous components. After assessing the energetics of the radiative feedback by using the results in [4], in [1,3] we demonstrate that the observed relation between the MBH mass and the stellar velocity dispersion can be the natural consequence of the MBHs growth at early times in the galaxy history and the gas depletion of the galaxy gaseous content due to star formation. In particular, in [1] we show that *radiative feedback from the central AGN is effective in halting accretion* when the gas temperature is $> 3\times10^4$ K, and the mass of the MBH has grown to a critical value:

$$\frac{M_{\rm BH}^{\rm crit}}{10^{11}M_\odot}\simeq\left(\frac{\sigma_*}{200{\rm km/s}}\right)^4\frac{L_{\rm Edd}}{L_{\rm BH}}\frac{M_{\rm gas}}{M_{\rm gal}} \tag{1}$$

where σ_* is the stellar velocity dispersion in the spheroid, $M_{\rm gal}$ is its mass, $L_{\rm BH}$ is the accretion luminosity. Under the assumption that $L_{\rm BH}\simeq L_{\rm Edd}$ during the phases of significant growth of the central MBH (e.g., [5,6,7]), one can derive a condition on $M_{\rm gas}/M_{\rm gal}$ in order to satisfy the $M_{\rm BH}-\sigma$ relation observed today (e.g., see [8,9,10]):

$$\frac{M_{\rm gas}}{M_{\rm gal}}\simeq 10^{-3}\frac{L_{\rm BH}}{L_{\rm Edd}}. \tag{2}$$

ESO Symposia: Growing Black Holes, pp. 68–69, 2005.

In [1,3], with the aid of a simple yet physically motivated toy model, we show that such low-density, hot-temperature phases for the ISM are established early in the lifetime of stellar spheroids as a natural consequence of galaxy formation.

In our simulations we always find that at the epoch of the transition between cold and hot solutions $10^{-3} < M_{\rm gas}/M_{\rm gal} < 10^{-2}$, in very good agreement with the request of Eq. (2). Remarkably, if in our toy model we adopt duty-cycles of the order of those obtained in numerical hydrodynamical simulations and also derived from observations ($\sim 10^{-3}$, see [5,6,7]), we obtain present-day MBHs that follow the observed scaling relations. Substantially longer duty-cycles with (very) low accretion efficiencies are not a viable alternative, because in this case accretion would be dominated by Bondi accretion, resulting in too massive MBHs. Gas heating due to the evolving galaxy stellar component in its various forms (stellar winds thermalization, SNII and SNIa explosions), is confirmed to be an important ingredient in galaxy evolution. Due to their shallower potential well, low mass galaxies host stronger galactic winds than more massive galaxies. In the toy model AGN heating is not sufficient "per se" to produce galaxy degassing, even though is able to maintain the ISM temperature near to the galaxy virial temperature.

Thus, a plausible (and observationally supported) scenario for the coevolution of MBHs and stellar spheroids, is the following: at early times in the galaxy life, when the protogalactic gas was dense and cold, star formation and MBH growth were approximately parallel [7]. Later on, due to the MBH growth on one side and the gas depletion (due to star formation and reduced cosmological infall) on the other, $M_{\rm BH}$ reaches the value $M_{\rm BH}^{\rm crit}$. After this, accretion is characterized by a short duty cycle, of the order of 10^{-3}, with only a marginal growth of the central BH, even in presence of the non negligible stellar mass losses of the passively evolving stellar population [11].

References

1. S.Yu. Sazonov, J.P. Ostriker, L. Ciotti, & R.A. Sunyaev: MNRAS **submitted**, (2004)
2. S.Yu. Sazonov, J.P. Ostriker, & L. Ciotti: this Conference
3. J.P. Ostriker, L. Ciotti: Phil.Trans. of Roy.Soc. part A **in press** (2004)
4. S.Yu. Sazonov, J.P. Ostriker, & R.A. Sunyaev: MNRAS **347**, 144 (2004)
5. L. Ciotti, J.P. Ostriker: ApJL **487**, L105 (1997)
6. L. Ciotti, J.P. Ostriker: ApJ **551**, 131 (2001)
7. Z. Haiman, L. Ciotti, & J.P. Ostriker: ApJ **606**, 763 (2004)
8. J. Magorrian, et al.: AJ **115**, 2285 (1998)
9. L. Ferrarese, D. Merritt: ApJ **539**, L9 (2000)
10. S. Tremaine, et al.: ApJ **574**, 740 (2002)
11. L. Ciotti, A. D'Ercole, S. Pellegrini, & A. Renzini: ApJ **376**, 380 (1991)

Highest Redshift Quasars and the Early Growth of Supermassive Black Holes in the Universe

X. Fan

University of Arizona, Tucson, AZ 85721, USA

Abstract. The discovery of luminous quasars at $z > 6$ indicates the existence of billion-solar-mass black holes at the end of cosmic dark ages. They provide the best probes of the early growth of supermassive black holes in the universe, the relation between the formation of early galaxies and black holes, and put constraints on the role of quasars and AGNs to the cosmic reionization. About 1000 quasars have been discovered at $z > 4$, including 50 at $z > 5$ and eight at $z > 6$. In this proceeding, I review the recent observational results on surveys and detailed follow-up observations of the highest redshift quasars, including the evolution of luminosity function, the evolution of spectral properties and chemical enrichment history, distribution of black hole masses and the host galaxy properties.

1 Introduction

Discoveries of luminous quasars at $z > 6$ [12,8,16] indicate the existence of billion solar mass black holes in a few hundred million years after the big bang, at the end of cosmic dark ages. How does the black hole population grow with cosmic time? How does the evolution of quasar density traces the accretion history of first BHs?

Locally, the tight correlation between the mass of central BHs and the velocity dispersion of host galaxies indicates that black hole activities and galaxy formation are strongly coupled (e.g. [10]). How are the formation of the earliest galaxies and black holes related?

Finally, the detection of complete Gunn-Peterson [19] troughs in the highest redshift quasars [2,11,14,30] indicates that the reionization process ended at $z \sim 6$. What is the role black hole accretion power played in the reionization of the Universe? Detailed observations of the highest-redshift quasars known provide crucial answers to these important questions about quasar formation, galaxy evolution and the evolution of intergalactic medium (IGM).

2 Discovery of High-z Quasars

In the past decade, because of wide-field CCD technology and a number of new and very powerful surveys, such as the Sloan Digital Sky Survey (SDSS, [33]), the studies of highest redshift quasars entered a new era: not only can we probe the $z > 5$ universe, nearing the end of the cosmic dark ages, but also begin to collect large samples of high redshift quasars to ask detailed statistical questions

ESO Symposia: Growing Black Holes, pp. 75–89, 2005.

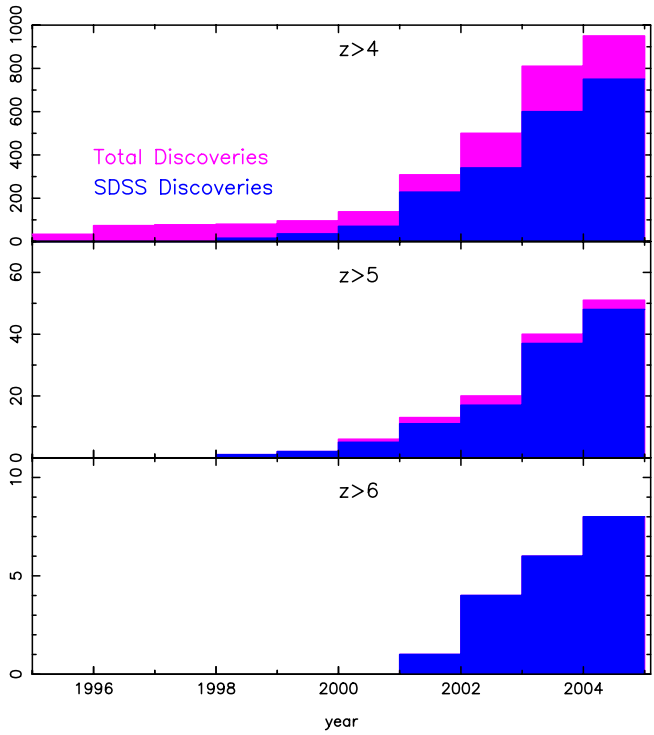

Fig. 1. History of discovery of $z > 4$ quasars. More than 1000 quasars at $z > 4$ have been discovered; most are from the Sloan Digital Sky Survey, forming a large, complete sample for statistical studies of high-redshift quasar evolution.

about their properties and their evolution. These surveys revolutionized quasar research, and gave us some first glimpse of the questions posted above.

Figure 1 shows the number of quasars at high-redshift discovered at the time of this proceeding [16]. There are almost 1000 quasars discovered at $z > 4$, comparing to less than 100 merely five years ago. The majority of them are from the SDSS, forming a uniformly selected statistical sample. There are more than 50 quasars at $z > 5$, and currently eight quasars have been found at $z > 6$, with the highest-redshift at $z = 6.42$ [8].

In the past five years, the SDSS team have been carrying out a i-dropout survey for $z \sim 6$ quasar quasars using SDSS data. By now, we have surveyed more than 6000 deg^2, and resulted in the discovery of 16 luminous quasars at $z > 5.7$, the most distant quasars known to date, including five new ones in the past year. In addition, we are trying to push to fainter magnitude, and should be able to double this number by the time we finish the survey. Figure 2 shows the spectra of these sixteen quasars. Note the strong and complete Gunn-Peterson troughs in the highest redshift objects, and the existence of strong metal emission lines in all quasars.

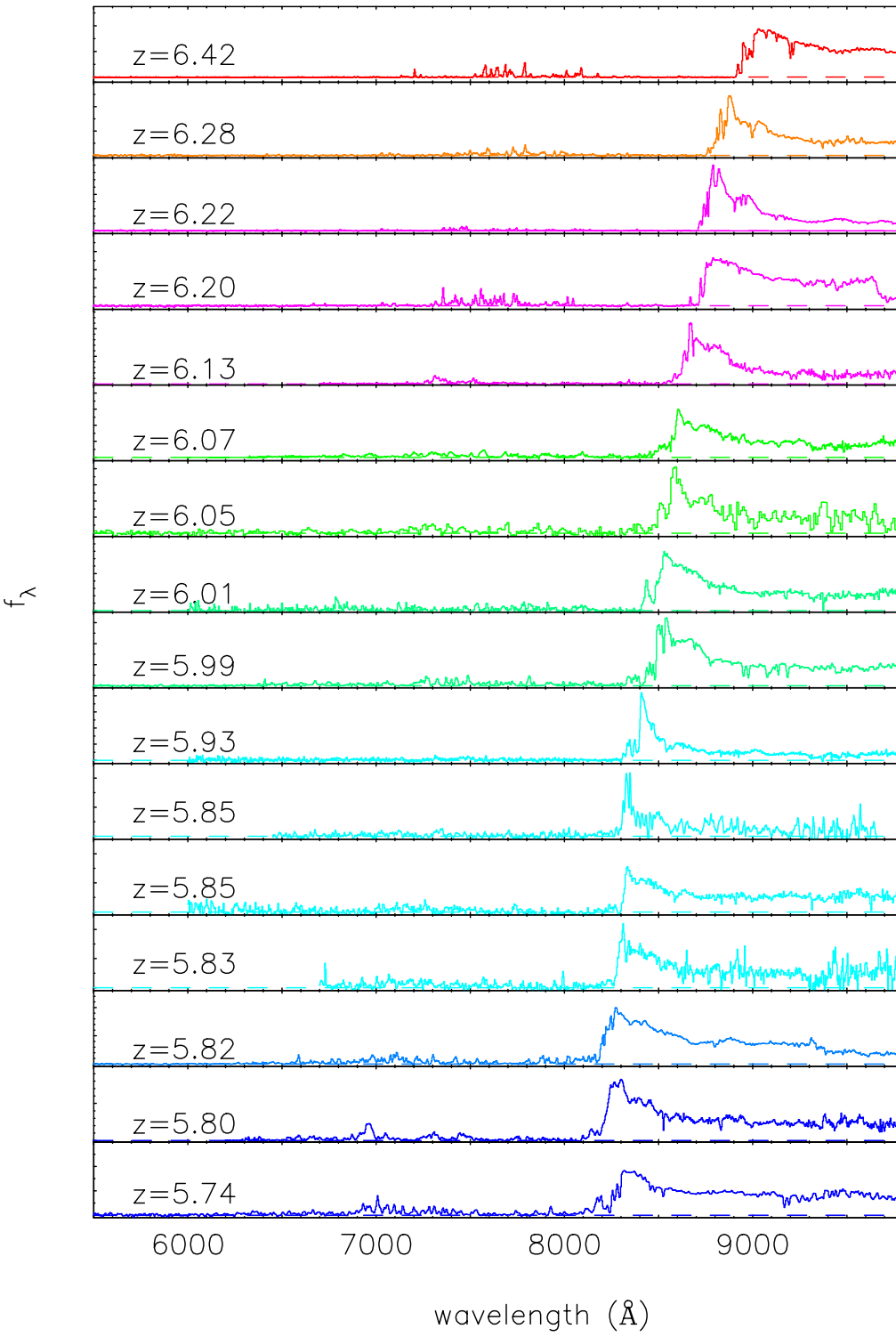

Fig. 2. Low dispersion spectra of the sixteen quasars known (as of Fall 2004) at $z > 5.7$. Note the strong Lyα absorption blueward of Lyα emission and the existence of strong metal emission lines in the spectra.

3 Evolution of Quasar Density at High-redshift

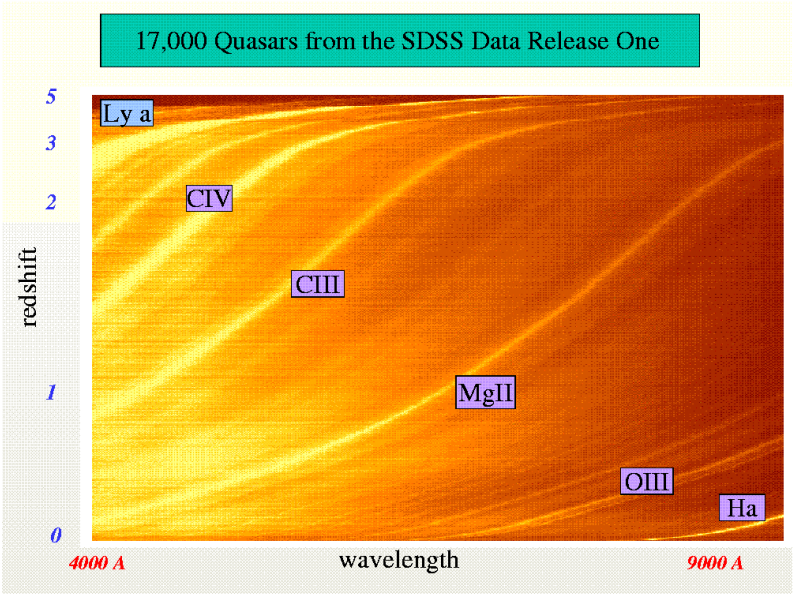

Fig. 3. A two-dimensional composite of the 17,000 quasars from the SDSS DR1 quasar catalog.

Figure 3 is a composite 2-dimensional spectra (as a function of both wavelength and redshift) of the 17,000 quasars in the SDSS public data release 1 sample [45]. We take all the 1-dimensional spectra, order them by redshift to construct this 2-dimensional image. This figure also illustrates two fundamental properties about quasar evolution:

- The strong evolution of quasar number density. The distribution along y-axis in Figure 3 is a number count of quasars as a function of redhsift of this flux-limited sample: luminous quasars are very rare in the early universe and we are seeing the initial rise of quasar population in the early times.
- In sharp contrast to that is the lack of strong evolution of quasar spectral properties. The strength of emission lines remains roughly constant through cosmic history. The immediate environment of quasars matures very early on, and is somewhat decoupled from the cosmic evolution. In other words, quasar emission looks the same even up to the highest redshift, which implies that the knowledge about quasar emission we learned from local universe can be applied to the highest redshift. We will discuss both points in more detail.

The density of luminous quasars is a strong function of redshift: it peaks at $z \sim 2-3$ and declines exponentially towards lower and higher redshift (e.g. [25,4]). Compared to the evolution of star-formation rate in the Universe, the quasar density peaks at higher redshift, and evolves much faster. This exponential decline continues to the highest redshifts. In Figure 4, we show the density of quasars at $M_{1450} < -26.7$ found in 6000 deg^2 of SDSS data at $z \sim 6$, along with the results from lower redshift [25,4,13]. The quasar density at $z \sim 6$ found here is consistent with extrapolating the best-fit quasar luminosity functions in the range $3 < z < 5$. The comoving density of luminous quasars at $z \sim 6$ is 30 times smaller than that at $z \sim 3$. The highest-redshift quasars are tracing the initial rise of the earliest supermassive black hole population.

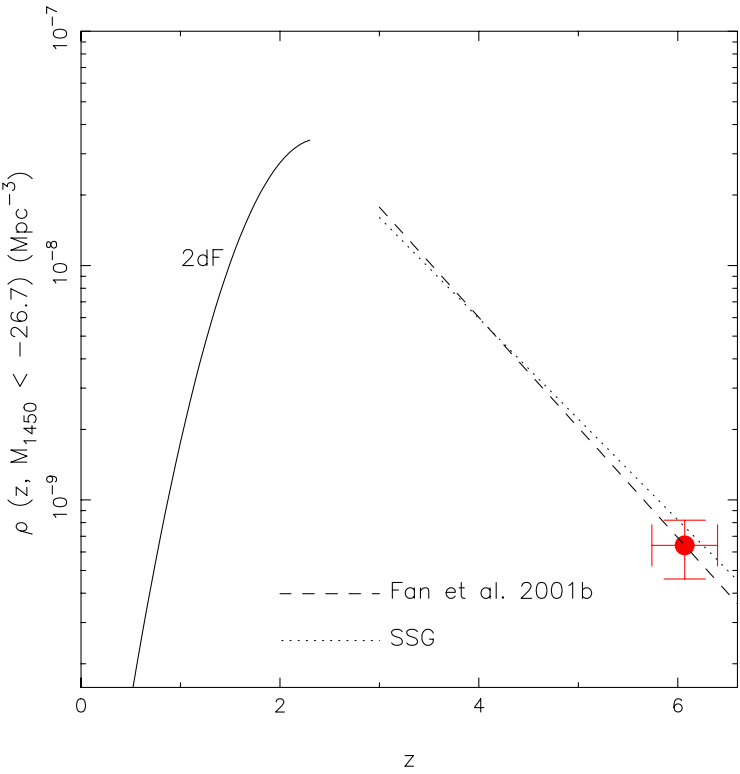

Fig. 4. The evolution of the quasar comoving spatial density at $M_{1450} < -26.7$. The filled circle represents the result from this survey. The error-bar in redshift indicates the redshift range covered by the i-dropout survey. The dashed and dotted lines are the best-fit models from [13] and [25] (SSG), respectively. The solid line is the best-fit model from the 2dF survey [14] at $z < 2.3$

The mere existence of these objects is amazing feat of galaxy formation process. The SDSS $z \sim 6$ quasars are among the most luminous quasars at any

redshift; their apparent magnitudes are ~ 19 even at $z > 6$! They are likely powered by supermassive black holes with several billion solar masses, and reside in dark matter halo of $10^{13} M_{\odot}$. They are among the most massive black holes and galaxies at any redshifts. It is a serious challenge as how the universe could have formed with such massive galaxies, and in particular, have assembled such massive black holes in the first Gyr of the cosmic evolution. They are clearly the rarest and most biased systems in the early universe, and probably have started the initial assemble at redshift much higher than 10, well into the dark ages, providing important clues to the co-formation and co-evolution of the earliest supermassive black holes and galaxies.

4 Evolution of Faint Quasars

Surveys such as SDSS only sample the brightest end of the quasar luminosity function. Does fainter quasars and AGNs evolve differently at high-redshift? We know from the 2dF quasar survey that at low-redshift, quasar luminosity function is well fit by a double power law with pure luminosity evolution, in the sense that the characteristic luminosity of quasars decreases at lower redshift. This can be understood in the sense that the black hole activities powering the quasars is downsizing towards current epoch, not dissimilar to what people found in X-ray selected samples (e.g. [7]).

But at high redshift, we currently have very little constraints on the LF shape. The SDSS main surveys are limited to $M_B < -26$ at $z > 4$. Is the difference between X-ray and optically selected samples a true reflection of the different evolution of the obscured population? Or is it simple a luminosity effect? Are we seriously biased by only looking at the luminous sources?

To answer this question, wide, shallow surveys such as the SDSS does not go deep enough. We are currently using the repeated imaging in the SDSS deep stripe in the Southern Galactic Cap to select faint, high-redshift quasar candidates and carry out a deep quasar survey with the 300 fiber HECTOSPEC spectrograph on the MMT. This deep survey will reach 2 to 3 mag fainter than the SDSS main survey. We will be able to find several thousand new faint quasars, including few hundred at $z > 3$, and a reasonable number at $z \sim 6$ (depending on the unknown slope of quasar luminosity function at high-redshift). This new survey will enable us to reach AGN luminosity at $z \sim 3$ in wide area, and bridge the current SDSS wide area sample with deep pencil beam surveys such as the CDFS.

As a pilot program for the SDSS deep stripe survey, we have followed up a sample of faint quasar candidates in the $z = 4 - 5$ range with single slit spectrographs, and extended the measurements of quasar luminosity function 1.5 magnitude deeper than our previous studies. Figure 5 shows a summary of quasar luminosity function measurements at $z \sim 4.5$, from the SDSS main survey, from our deep survey, as well as from the photometrically selected COMBO-17 sample [31] and AGN candidates in GOODS [8]. It is evident from the figure that the high-redshift quasar luminosity function is much flatter than that at

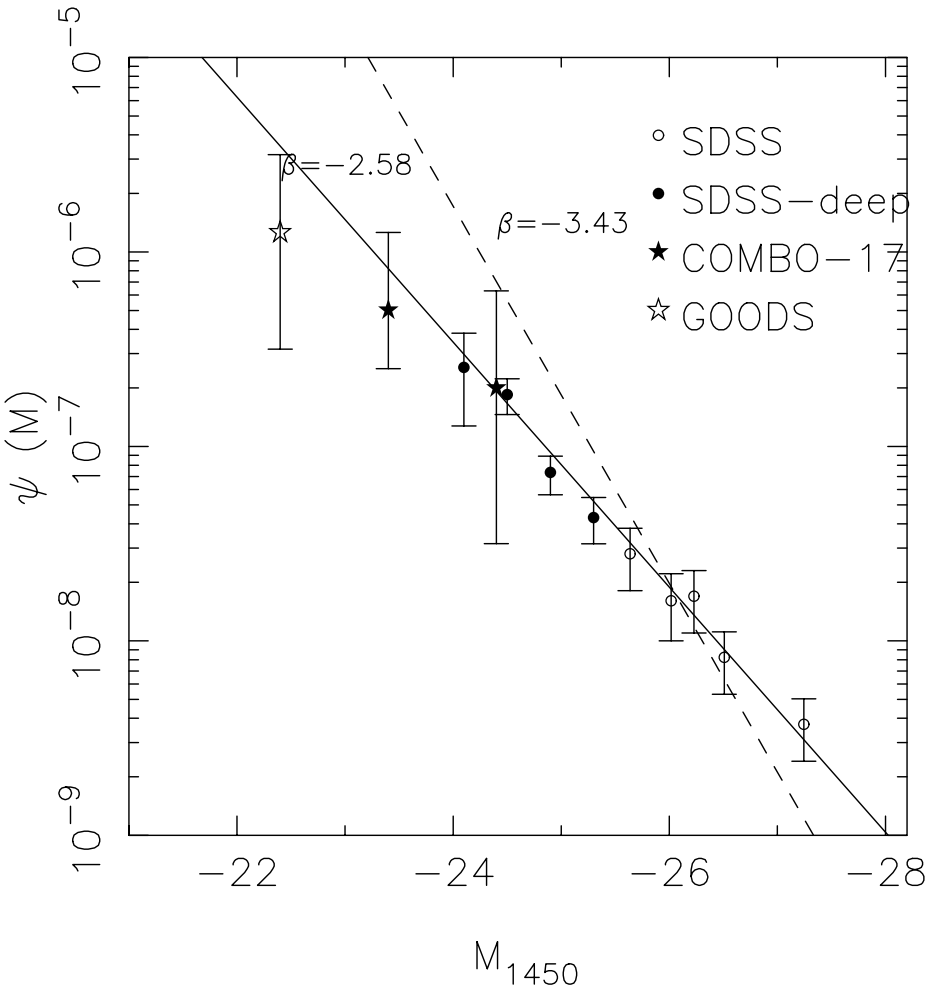

Fig. 5. The luminosity function of quasars at $z \sim 4.5$, comparing the data from the SDSS main survey, the SDSS deep survey, COMBO-17 survey and quasar candidates in the GOODS field. It is evident that quasar luminosity function at $z \sim 4$ is shallower than that at $z < 2$.

low-redshift. Assuming a power law luminosity function $\Psi(L) \propto L^{-\beta}$, the power law index changed from $\beta \sim 3.4$, found in the 2dF and SDSS at $z < 2$, to $\beta \sim 2.6$ at $z \sim 4$. It shows that the pure luminosity evolution does not continue pass the quasar density peak at $z = 2 - 3$.

The implication of the different behaviors of QLF at low and high redshift, or at the falling and rising part of quasar evolution, might be important to the model of quasar formation, in particular in term of what triggered the BH

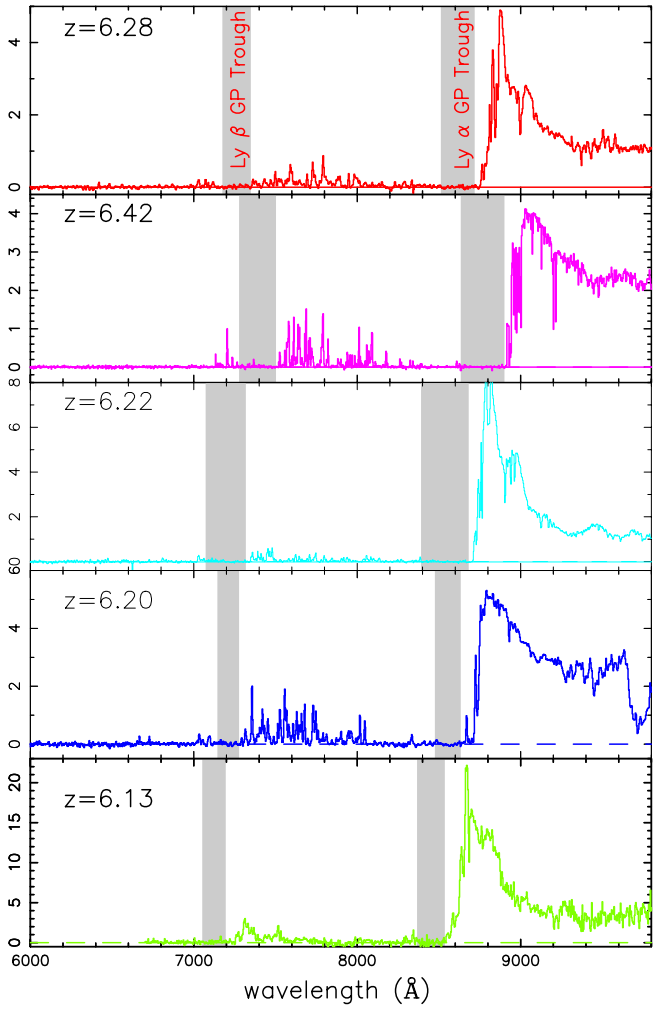

Fig. 6. Gunn-Peterson troughs in the five highest-redshift quasars known to date.

activity, and what is the quasar accretion or radiation efficiency as a function of luminosity or redshift.

5 Quasar Contributions to the Reionization

Recent observations of the Cosmic Microwave Background and of the intergalactic medium at high redshift begin to reveal the history of reionization and its relation to the first generation galaxy formation. The CMB polarization results from WAMP indicate the reionization process starts early, with substantial activity by $z \sim 17$ [21]; the detection of Gunn-Peterson troughs in the spectra of $z > 6$

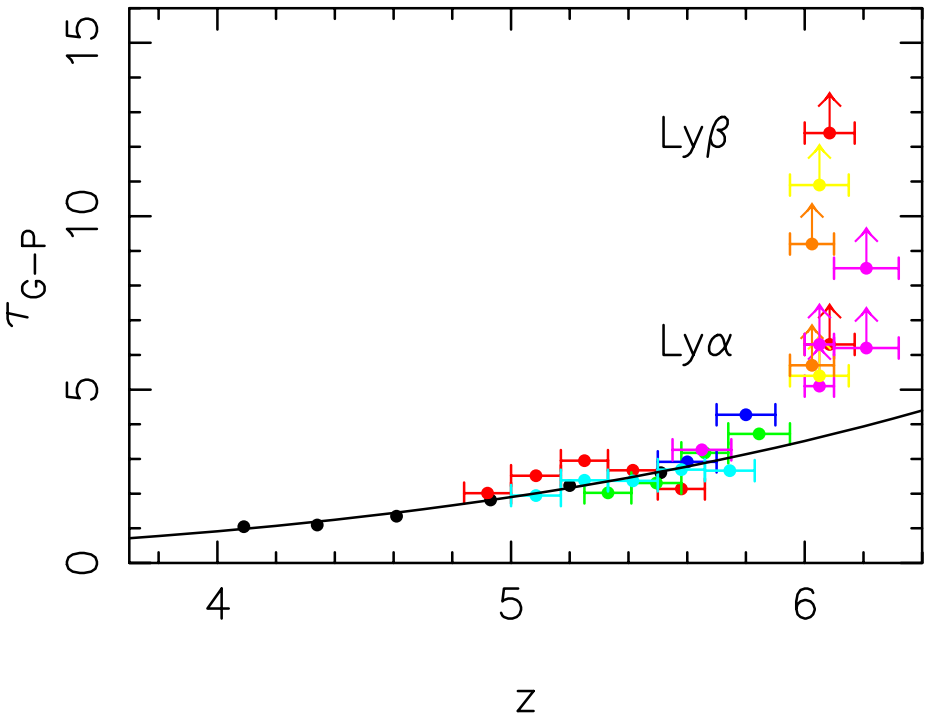

Fig. 7. The evolution of Gunn-Peterson optical depths as a function of redshift. The emergence of Gunn-Peterson troughs at $z > 6$ marks a rapid transition in the neutral fraction of the IGM, especially when using the optical depth inferred from the Lyβ measurements.

quasars from the Sloan Digital Sky Survey [2] marks the trailing end of the reionization at that epoch. We now have discovered five quasars at $z > 6.1$. Figure 6 shows the absorption spectra of these five objects: all of them show evidences of strong, complete Gunn-Peterson troughs in both Lyα and Lyβ transitions. The redshifts where the trough started seem to differ from line of sight to light of sight, which is almost certainly a reflection of difference in the propagation of the ionization front. However, as shown in Figure 7, the rapid transition in the neutral fraction of the IGM at $z \sim 6$ is now well established. This trend is consistent with the overlapping of HII regions happened at somewhere $z > 6$, with the all reionization process ended at $z \sim 6$.

What ionized the Universe, or at least kept the universe ionized at $z \sim 6$? Is it UV photons from early star formation or UV photons from accretion onto black holes? The quasar luminosity function presented in §3 puts constraint on the total ionizing photons generated by the quasar/AGN population. Figure 8 shows the number of ionizing photons generated by quasars and AGNs at $z \sim 6$, as a function of the slope and the characteristic luminosity of quasar luminosity function. Clearly, with the current constraint, especially the relatively

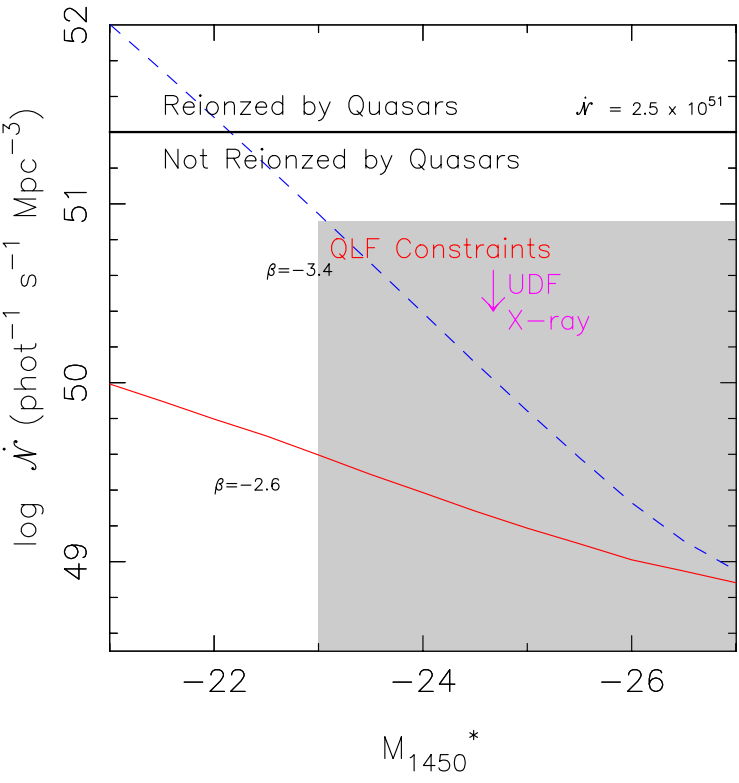

Fig. 8. Comoving emission density rate of hydrogen Lyman continuum photons from quasars integrated over the full luminosity function, compared with the minimum rate (heavy solid line) that is needed to fully ionize a universe at $z = 6$, with a clumping factor of 30. The current constraints on the quasar luminosity function at high-redshift suggest that the Universe was not ionized by quasars/AGNs.

flat luminosity function at high luminosity, the quasar population comes up short from generating enough photons. An independent constraint came from recent work by Moustakas & Immler [8], based on stacking of X-ray images of Lyman break galaxies in the UDF. Therefore, the Universe would either have to be ionized by star formation, or some other source, such as soft X-rays from mini-quasars at higher redshift.

6 Spectral Evolution and Black Hole Mass at High-Redshift

The spectral energy distributions of luminous quasars show little evolution out to high redshift. There is growing evidence from emission line ratio measurements that quasar broad emission line regions have roughly solar or even higher

metallicities at $z > 4$ (e.g., [4]), similar to that in low redshift quasars. [10] found the FeII/MgII ratio to have roughly the same value in a sample of $z \sim 5$ quasars as at lower redshift, suggesting that the metallicity of quasar emission line region remains high to even earlier epochs.

The sample of quasars at $z > 5.7$ from the SDSS provides the first opportunity to study the evolution of quasar spectral properties at $z \sim 6$, less than 1 Gyr after the Big Bang and only 700 million years from the first star formation in the Universe. Optical and infrared spectroscopy of some $z \sim 6$ quasars already indicates *a lack of evolution* in the spectral properties of these luminous quasars: [14] show that the CIV/NV ratio in two $z \sim 6$ quasars are indicative of supersolar metallicity in these systems. [17] and [4] detected strong FeII emission in the spectra of four $z \sim 6$ SDSS quasars. In addition, the optical-to-X-ray flux ratios and X-ray continuum shapes show at most mild evolution from low redshift [5,69]. Figure 9 shows the composite of our $z \sim 6$ quasar spectra. It demonstrates the lack of evolution in the quasar intrinsic spectral properties more clearly: the spectral composite of the 12 known $z \sim 6$ quasars is almost identical to the low-z composite, both in term of the spectral slope, and emission line strength. The only differences are that the Lyα forest is much stronger at $z \sim 6$ and the blue wing of Lyα is also affected.

Using chemical evolution models, especially with diagnostic lines such as N, Fe or C, we find that the strength of these emission lines indicates that the metallicity of quasar emission line region is supersolar. This is a direct evidence of rapid chemical enrichment processes through multiple generations of star formation in the immediate environment of these luminous quasars. These results, if confirmed with a larger sample, suggest that the accretion disk and the photoionization structure of quasars reached maturity very early on and are probably insensitive to the host galaxy environment.

The continuum and emission line scaling relations provide currently the only viable way to estimate black holes mass of quasars at high-redshift. This method is very appealing, because the emission line measurement is relatively easy, and can be applied to the highest redshift, when no other BH mass estimate can be applied with any accuracy. As discussed above, quasars do not show strong spectral evolution, indicating that their emission line region structure is not a function of redshift, and is not affect by cosmic environment. This implies that the measurement calibrated locally can be reliably applied to high-redshift.

The black hole mass estimates of the $z \sim 6$ SDSS quasars range from several times $10^8 M_\odot$ to several times $10^9 M_\odot$. Assuming continuous Eddington accretion from a seed black hole of 100 $M_\odot$, the formation redshift for seed black holes must be at $z > 10$. Even with continuous accretion, black holes in the most luminous quasars barely had enough time growing. While there are various ways of accreting faster than Eddington, the fact that the highest redshift quasars sit right at the threshold of the reionization epoch simply indicates that the initial growth of those BHs have to be very efficient and very early on.

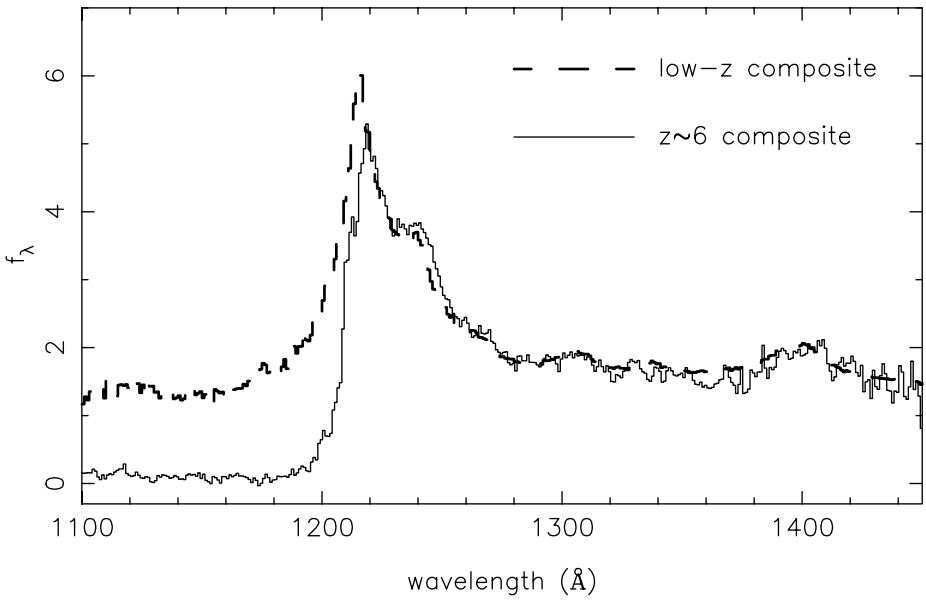

Fig. 9. The composite spectrum of eleven $z \sim 6$ quasars (solid line). For comparison, we also plot the low-redshift quasar spectral composite from Vanden Berk et al. [32]. The effective redshift in the 1000 – 1500Å range in the Vanden Berk et al. composite is about 2. The quasar intrinsic spectrum redward of Lyα emission shows no detectable evolution up to $z \sim 6$, in terms of both the continuum shape and emission line strengths. On the blue side of Lyα emission, the strong IGM absorption at $z \sim 6$ removes most of the quasar flux.

7 Probing the Host Galaxy Evolution

Direct imaging of the stellar light of host galaxies is extremely difficult with current technology, because of the enormous luminosity of the central quasar and the $(1+z)^4$ dimming in surface brightness. The best way to probe the host galaxy is to look at longer wavelength where the contribution from the central AGN is not dominating. At observed far-IR to mm wavelength, the radiation of radio quiet quasars is dominated by reprocessed radiation of cool dust in the host galaxy. Combining with IR measurement such as those coming from Spitzer, which probes the hot dust heated by the AGN itself, one can then have a reliable estimate of the star formation rate in the host galaxy. ALMA, which not only has high resolution imaging in these wavelength, but also provides a wealth of information on various line diagnostics, will revolutionize the study of quasar host galaxies in the sub-millimeter wavelengths.

A large number of high-z quasars have been observed with either IRAM 30m or SCUBA on JCMT. Roughly 40% of the radio-quiet quasars are detected at 1mm at 1mJy level (e.g., [6,15]). The submm radiation almost certainly comes from warm dust in the quasar host galaxy. The FIR luminosity, of the order

$10^{13} L_{\odot}$, is as bright as the brightest nearby ULIRGs such as Arp 220, implying a dust mass of the order $10^{8} M_{\odot}$. If the dust heating came from star burst activity, that would suggest an enormous star formation rate of several hundred, sometimes several thousand solar masses per year. The most massive black holes in the early universe likely live in the most intensive star formation sites in the early universe.

The most striking example of the possible connection between star formation and black hole activity at early epoch is the observation of the highest redshift quasar SDSS J1148+5251 at $z = 6.42$. This object is detected as a strong mm source using IRAM 30 m [2], indicating a dust mass of several times $10^{8} M_{\odot}$. Subsequent observations show strong CO emission in several transitions [19], signaling a large molecular gas reservoir of the order $10^{10} M_{\odot}$. The submm and radio observations suggest an on-going SFR of 1000 $M_{\odot}$ per year.

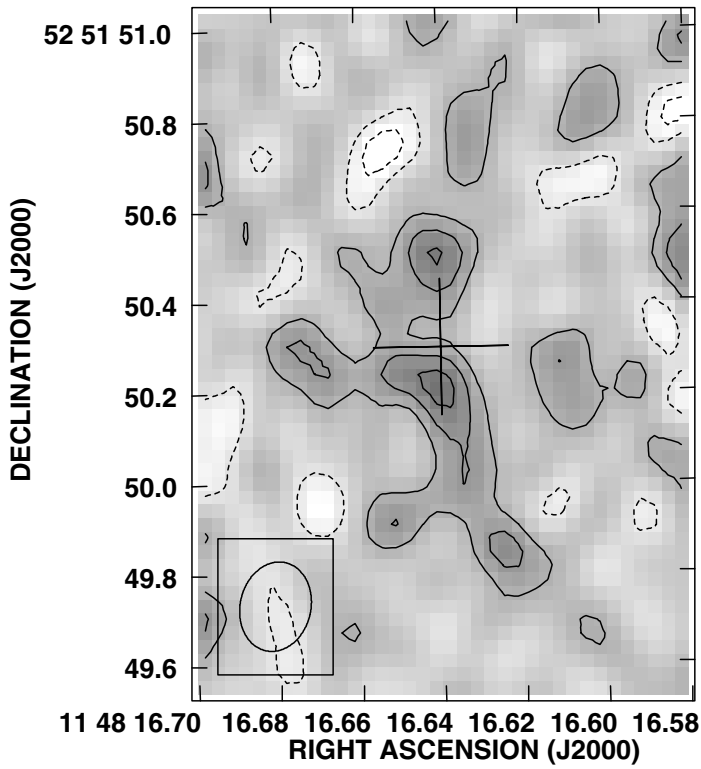

Fig. 10. VLT CO (3-2) map at 1kpc resolution in the central region of the host galaxy of SDSS J1148+5251 ($z = 6.42$, adapted from [29]). The host galaxy is clearly resolved.

More recently, Walter et al. ([29], Figure 10) obtained high-resolution VLA observations of the CO in this z=6.42 quasar. The VLA CO 3–2 data have a resolution of 0.15", or about 1kpc at $z = 6.4$, and enable us to resolve the molecular gas both spatially and in velocity space. Spatially, CO is extended to a radius of 2 kpc, with the central region showing two peaks separated by 0.3", and the quasar roughly at the center of the two peaks. Does this suggest a disk like structure? The VLA channel map shows the velocity structure of the various components, with a velocity resolution of 60 km/s. The total gas has a line-width of 280 km/s, and the centroid of the emission shifts by 1.5 kpc over 120 km/s. This is the first time a high-z host is resolved both spatially and kinematically. Assuming the gas is bound, the estimated dynamically mass is about $10^{10} M_{\odot}$ within a radius of 2 kpc. In other words, there just isn't a lot of mass there. If the system is living in some kind of bulge, the mass even within 20 kpc is still only $10^{11} M_{\odot}$, much smaller than the $10^{12} M_{\odot}$ one would expect from the local M-σ relation. While it is only one system, and the dynamical situation there is far from clear, it is highly suggestive that this luminous quasars at high-redshift does not live in a fully developed galaxy with a massive central bulge. Does this suggest that black hole formed before galaxy assembly? More such observations would be extremely valuable to answer this question.

Acknowledgements. Funding for the creation and distribution of the SDSS Archive has been provided by the Alfred P. Sloan Foundation, the Participating Institutions, the National Aeronautics and Space Administration, the National Science Foundation, the U.S. Department of Energy, the Japanese Monbukagakusho, and the Max Planck Society. The SDSS Web site is http://www.sdss.org/. The SDSS is managed by the Astrophysical Research Consortium (ARC) for the Participating Institutions. The Participating Institutions are The University of Chicago, Fermilab, the Institute for Advanced Study, the Japan Participation Group, The Johns Hopkins University, the Korean Scientist Group, Los Alamos National Laboratory, the Max-Planck-Institute for Astronomy (MPIA), the Max-Planck-Institute for Astrophysics (MPA), New Mexico State University, University of Pittsburgh, Princeton University, the United States Naval Observatory, and the University of Washington. I thank the support from NSF grant AST 03-07384, a Sloan Research Fellowshipand the University of Arizona.

References

1. Barth, A. J., Martini, P., Nelson, C. H., & Ho, L. C. 2003, ApJ, 594, L95
2. Becker, R. H. et al. 2001, AJ, 122, 2850
3. Bertoldi, F. et al. 2003, A&A, 409, 47
4. Boyle, B.J., Shanks, T., Croom, S. M., Smith, R . J., Miller, L., Loaring, B., & Heymans, C. 2000, MNRAS, 317, 1014
5. Brandt, W.N., et al. 2002, ApJ, 569, L5
6. Carilli, C. et al. 2001, ApJ, 555, 625
7. Cowie, L. L., Barger, A. J., Bautz, M. W., Brandt, W. N., & Garmire, G. P. 2003, ApJ, 584, L57

8. Cristiani, S. et al. 2004, astro-ph/0403494
9. Croom, S. M., Smith, R. J., Boyle, B. J., Shanks, T., Miller, L., Outram, P. J., & Loaring, N. S., 2004, MNRAS, 349, 1397
10. Dietrich, M., Hamann, F. Shields, J. C., Constantin, A., Heidt, J., Jaeger, M., Vestergaard, M., & Wagner, S. J., 2003, ApJ, 722, 732
11. Djorgovski, S. G., Castro, S., Stern, D., & Mahabal, A. A. 2001, ApJ, 560, L5
12. Fan, X. et al. 2001a, AJ, 122, 2833
13. Fan, X. et al. 2001b, AJ, 121, 54
14. Fan, X. et al. 2002, AJ, 121, 123, 1247
15. Fan, X. et al. 2003, AJ, 121, 125, 1649
16. Fan, X. et al. 2004, AJ, 121, 128, 515
17. Freudling, W., Corbin, M. R., & Korista, K. T. 2003, ApJ, 587, L67
18. Gebhardt, K. et al. 2001, ApJ, 539, L13
19. Gunn, J. E., & Peterson, B. A. 1965, ApJ, 142, 1633
20. Hamann, F., & Ferland, G., 1993, ApJ, 418, 11
21. Kogut, A. et al. 2003, ApJS, 148, 161
22. Moustakas, L. A., & Immler, S. 2004, astro-ph/0405270
23. Pentericci, L., et al.: AJ, **123**, 2151 (2002)
24. Priddey, R. et al. 2003, MNRAS, 339, 1183
25. Schmidt, M., Schneider, D. P., & Gunn, J.E., 1995, AJ, 110, 68
26. Schneider, D. P. et al. 2003, AJ, 126, 2579
27. Vignali, C., Brandt, W.N., Schneider, D.P., Garmire, G.P., & Kaspi, S. 2003, ApJ, 125, 2876
28. Walter, F. et al. 2003, Nature, 426, 406
29. Walter, F. et al. 2004, ApJ, 615, L17
30. White, R. L., Becker, R. H., Fan, X., & Strauss, M. A., 2003, AJ, 126, 1
31. Wisotzki, L. et al. 2004, astro-ph/0404331
32. Vanden Berk, D. E., et al. 2001, AJ, 122, 549
33. York, D. G., et al. 2000, AJ, 120, 1579

X-rays from the First Massive Black Holes

W.N. Brandt[1], C. Vignali[2], B.D. Lehmer[1], L.A. Lopez[1], D.P. Schneider[1], and I.V. Strateva[1]

[1] Department of Astronomy & Astrophysics, The Pennsylvania State University, 525 Davey Lab, University Park, PA 16802, USA
[2] Dipartimento di Astronomia, Università degli Studi di Bologna, Via Ranzani 1, 40127 Bologna, Italy

Abstract. We briefly review some recent results from *Chandra* and *XMM-Newton* studies of the highest redshift ($z > 4$) active galactic nuclei (AGNs). Specific topics covered include radio-quiet quasars, radio-loud quasars, moderate-luminosity AGNs in X-ray surveys, and future prospects. No significant changes in AGN X-ray emission properties have yet been found at high redshift, indicating that the small-scale X-ray emission regions of AGNs are insensitive to the dramatic changes on larger scales that occur from $z \approx 0$–6. X-ray observations are also constraining the environments of high-redshift AGNs, relevant emission processes, and high-redshift AGN demography.

1 Introduction

Understanding of the X-ray emission from the highest redshift ($z > 4$) active galactic nuclei (AGNs) has advanced rapidly over the past five years, due to the superb capabilities of *Chandra* and *XMM-Newton* combined with plentiful high-redshift discoveries by wide-field optical surveys. The number of X-ray detections at $z > 4$ has increased from 6 in 2000 to ≈ 100 today.

Are the first massive black holes feeding and growing in the same way as local ones? X-ray observations can address this question effectively, as they probe the immediate vicinity of the black hole where changes in the accretion mode should be most apparent. For example, high-redshift AGNs might typically have different values of $\dot{M}/\dot{M}_{\rm Edd}$, given that they reside in young, forming galaxies that differ greatly from the majority of those in the local universe. Galactic black holes and local AGNs both show strong X-ray spectral changes with $\dot{M}/\dot{M}_{\rm Edd}$ that should be detectable at high redshift (e.g., Brandt 1999; McClintock & Remillard 2004). X-ray observations can also constrain the environments of high-redshift AGNs (e.g., via X-ray absorption studies), relevant emission processes (e.g., in AGN jets), and high-redshift AGN demography.

We have been addressing the issues above using a combination of snapshot *Chandra* observations, spectroscopic *XMM-Newton* observations, X-ray survey data, and archival X-ray data. Below we will briefly review some of our results and will discuss some future prospects. We adopt $H_0 = 70$ km s^{-1} Mpc^{-1}, $\Omega_{\rm M} = 0.3$, and $\Omega_\Lambda = 0.7$ throughout.

ESO Symposia: Growing Black Holes, pp. 90–101, 2005.

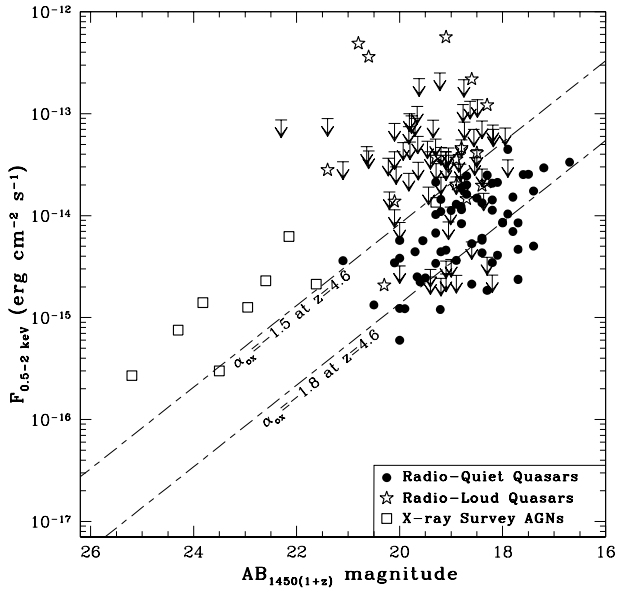

Fig. 1. Observed-frame, Galactic absorption-corrected 0.5–2 keV flux versus $AB_{1450(1+z)}$ magnitude for $z > 4$ AGNs. Object types are as shown in the legend; downward-pointing arrows indicate X-ray upper limits. The slanted lines show $\alpha_{ox} = -1.5$ and $\alpha_{ox} = -1.8$ loci at a fiducial redshift of $z = 4.6$. Adapted from Vignali et al. (2005).

2 High-Redshift Radio-Quiet Quasars

Most of the $z > 4$ AGNs with X-ray detections are luminous ($M_B < -26$) radio-quiet quasars (RQQs) that have been discovered in wide-field optical surveys and targeted with snapshot (4–12 ks) *Chandra* observations. For example, we have been targeting the most luminous RQQs ($M_B \approx -27$ to -29.5) from the Palomar Digital Sky Survey (DPOSS) and the Automatic Plate Measuring facility survey (APM) as well as some of the highest redshift RQQs ($z > 4.8$) from the Sloan Digital Sky Survey (SDSS).

Figure 1 shows the X-ray and optical fluxes for $z > 4$ AGNs with sensitive X-ray observations. As expected, the X-ray and optical fluxes for the RQQs are generally correlated, but there is significant scatter in this relation (see Vignali et al. 2003ac, 2005 for details). Even the optically brightest RQQs at $z > 4$ have relatively low 0.5–2 keV fluxes of a few $\times 10^{-14}$ erg cm^{-2} s^{-1}, so X-ray spectroscopy of these objects is challenging. Nevertheless, there has been respectable progress constraining the basic X-ray spectral properties of $z > 4$ RQQs using joint X-ray spectral fitting (Vignali et al. 2003ac, 2005) and single-object spectroscopy (Ferrero & Brinkmann 2003; Farrah et al. 2004; Grupe et al. 2004;

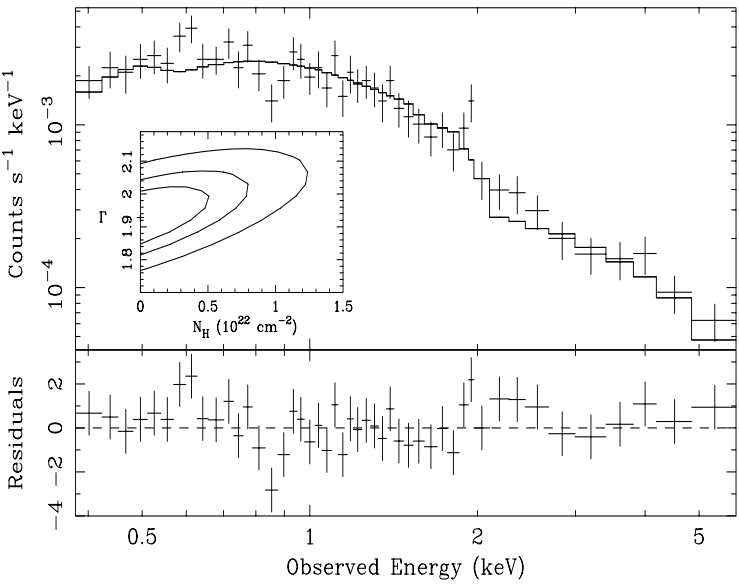

Fig. 2. Stacked *Chandra* spectrum constructed from 48 RQQs at $z = 3.99$–6.28. The spectrum has $\approx$ 870 source counts and an effective exposure time of 244 ks. The spectrum has been fit with a power-law model including Galactic absorption, and data-to-model residuals (in units of σ) are shown in the lower panel. The fit is statistically acceptable. The inset shows the 68, 90, and 99% confidence regions for the power-law photon index and intrinsic column density derived from joint spectral fitting with the Cash (1979) statistic. Adapted from Vignali et al. (2005).

Schwartz & Virani 2004). Figure 2, for example, shows the results from joint X-ray spectral fitting of 48 RQQs from $z = 3.99$–6.28 (with a median redshift of 4.43) using the Cash (1979) statistic (Vignali et al. 2005). This joint-fitting approach provides a stable estimate of average 2–40 keV rest-frame spectral properties. The spectrum is well fit by a power-law model with $\Gamma = 1.93^{+0.10}_{-0.09}$ and Galactic absorption; any widespread intrinsic absorption by neutral material has $N_{\rm H} \lesssim 5 \times 10^{21}$ cm^{-2}. No iron K line emission or Compton reflection is detected, although the statistical constraints on such spectral components are not yet particularly meaningful.

Figure 3 summarizes the current X-ray spectral results on high-redshift RQQs, comparing their power-law photon indices to those of RQQs at lower redshift. There is significant intrinsic scatter in the photon indices at all redshifts. This scatter is believed to be due to object-to-object variations in the temperature and optical depth of the accretion-disk corona, likely arising from variations in $\dot{M}/\dot{M}_{\rm Edd}$ (see Section 1). However, there is no detectable systematic change in the photon-index distribution at high redshift. On average, the accretion-disk coronae of high-redshift and low-redshift RQQs appear to have similar properties.

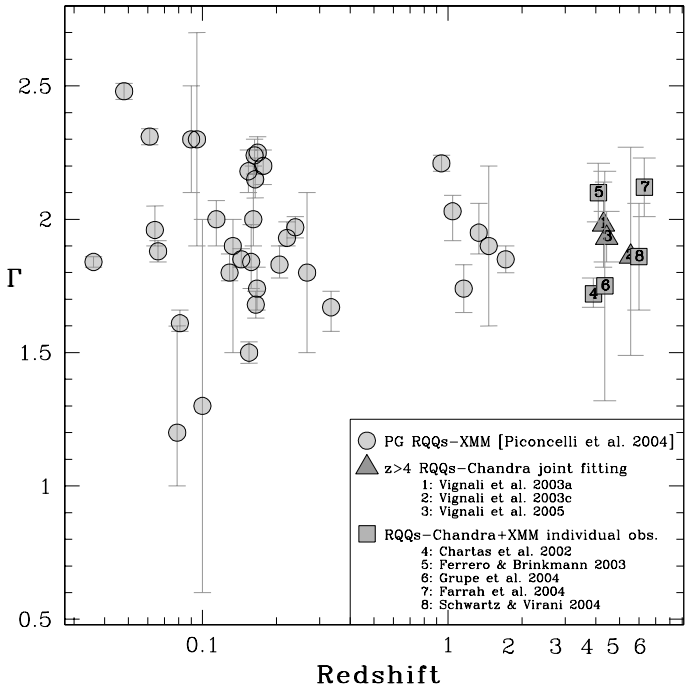

Fig. 3. Hard X-ray photon index versus redshift. The circles at $z < 2$ indicate RQQs from the Bright Quasar Survey (PG) analyzed by Piconcelli et al. (2004). At higher redshift, the data points have been derived from both joint spectral fitting (triangles) and single-object spectroscopy (squares); the data points are numbered with corresponding citations given in the figure legend.

In addition to measuring X-ray spectral properties, it is also informative to investigate relations between X-ray and longer wavelength emission. Any changes in accretion mode over cosmic time might lead to changes in the fraction of total power emitted as X-rays. Investigations of this type have been performed since the 1980's (e.g., Avni & Tananbaum 1986), often utilizing $\alpha_{\rm ox}$, which is defined as the point-to-point spectral slope between 2500 Å and 2 keV in the rest frame. Studies of the dependence of $\alpha_{\rm ox}$ upon redshift and luminosity are challenging for several reasons: (1) broad ranges of sample redshift and luminosity are required to break statistical degeneracies between these two quantities, since they are correlated in flux-limited AGN samples, (2) a high fraction of X-ray detections is required to minimize statistical problems inherent in AGN samples with censoring, (3) absorbed AGNs, such as broad absorption line (BAL) quasars, need to be excluded when possible and controlled for when not, (4) radio-loud AGNs, which have an additional jet-linked X-ray emission component, need to be excluded, and (5) high-quality photometry/spectroscopy in the optical/UV,

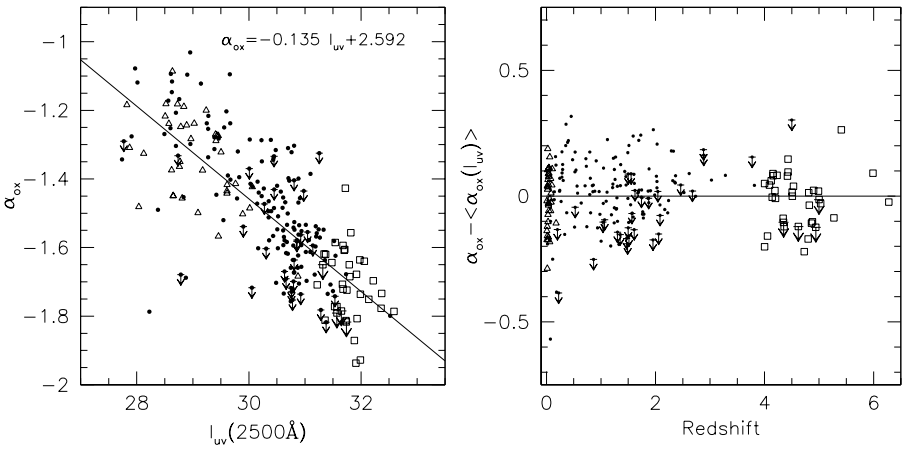

Fig. 4. The left panel shows α_{ox} versus 2500 Å luminosity density for optically selected, radio-quiet AGNs: Seyfert 1 galaxies from Walter & Fink (1993; open triangles), SDSS AGNs in medium-depth *ROSAT* observations (filled circles), and $z > 4$ RQQs from Vignali et al. (2003c; open squares). Large negative values of α_{ox} correspond to relatively weak X-ray emission, and downward-pointing arrows indicate X-ray upper limits. The best fit to the data is also shown. The right panel shows α_{ox} residuals versus redshift after removing the best-fit luminosity dependence of α_{ox}. Note that no systematic trends remain. Adapted from Strateva et al. (2005).

allowing mitigation of host-galaxy contamination, is required. We are currently completing the most detailed study to date of the dependence of α_{ox} upon redshift and luminosity, taking into account the issues above (Strateva et al. 2005; also see Vignali, Brandt, & Schneider 2003b). We are predominantly utilizing a sample of 156 SDSS RQQs lying serendipitously in medium-depth *ROSAT* observations. Our partial correlation analyses find a highly significant (up to 10.7σ) anti-correlation between α_{ox} and 2500 Å luminosity density when controlling for any redshift dependence (see Figure 4). In contrast, no significant correlation between α_{ox} and redshift is found when controlling for the 2500 Å luminosity-density dependence. Qualitatively, our results are consistent with much, but not all, of the earlier work on this topic. Quantitatively, our results are more robust and have much better control of statistical and systematic errors than previous studies.

In summary, the typical RQQ (of a given luminosity) does not change its basic X-ray spectral shape or optical/UV-to-X-ray flux ratio over most of cosmic history. It appears that the small-scale X-ray emitting regions of RQQs are insensitive to the dramatic changes on larger scales that occur from $z \approx 0$–6. The data are consistent with the idea that high-redshift RQQs are feeding and growing in basically the same way as local ones.

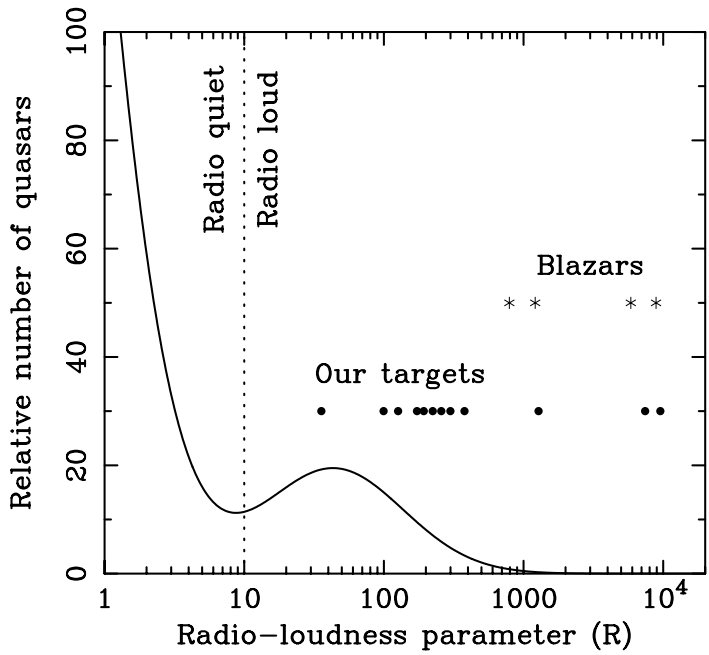

Fig. 5. The solid curve shows the relative number of quasars versus radio-loudness parameter (R) from Ivezić et al. (2002), and the dotted vertical line shows the standard R separation between RQQs and RLQs. Circles denote the R values for the RLQs we have been studying, and stars denote those for the four $z > 4$ blazars with X-ray spectra (the y-axis locations for these data points are arbitrary).

3 High-Redshift Radio-Loud Quasars

Until recently there were only a few $z > 4$ radio-loud quasars (RLQs) with sensitive X-ray observations. Most of these were highly radio-loud "blazars" with $R \approx 1000$–$10{,}000$; here R is the standard radio-loudness parameter, defined as $R{=}f_{5\ \mathrm{GHz}}/f_{4400\ \text{Å}}$ (in the rest frame). While these blazars are not representative of the quasar population, or even the RLQ population, as a whole (see Figure 5), they have been intensively targeted for X-ray observations due to their relatively high X-ray fluxes (note the data points in Figure 1 with 0.5–2 keV fluxes of a few $\times 10^{-13}$ erg cm^{-2} s^{-1}). Two of the four $z > 4$ blazars with X-ray spectra show evidence for substantial X-ray absorption (e.g., Worsley et al. 2004ab), a result that is broadly consistent with earlier findings that the fraction of RLQs with X-ray absorption rises with redshift (e.g., Cappi et al. 1997; Elvis et al. 1998; Fiore et al. 1998; Reeves & Turner 2000). The observed X-ray absorbing gas is thought to be associated with the RLQs' environments, but its precise nature is unclear: it may be circumnuclear, located in the host galaxy, or entrained by the radio jets.

We have recently performed 4–8 ks *Chandra* snapshots to determine the basic X-ray properties of nine flat-spectrum RLQs with $R \approx 30$–400 and $z = 4.0$–4.8 (Bassett et al. 2004; Lopez et al. 2005). These lie much closer than the blazars to the peak of the R distribution for RLQs, and they are thus more representative of the high-redshift RLQ population (see Figure 5). We have also observed three recently discovered blazars with $R \approx 1300$–9600 and $z = 3.5$–4.6 to enlarge the sample of these objects with X-ray data. All 12 of our targets are clearly detected, and we have performed joint X-ray spectral fitting and $\alpha_{\rm ox}$ analyses analogous to those described for RQQs in §2. As expected from similar RLQs at low redshift, the X-ray emission from our targets usually appears to have a large contribution from a jet-linked spectral component, probably synchrotron self-Compton emission arising on sub-parsec scales. The degree of X-ray enhancement provided by this component (relative to RQQs), as well as its X-ray spectral shape, appear consistent at high and low redshift. Our analyses of X-ray absorption via joint spectral fitting are ongoing, but they are challenging due to instrumental issues and limited photon statistics. Some X-ray absorption may be present with typical column densities of a few $\times 10^{22}$ cm^{-2}. *XMM-Newton* spectroscopy of several of these objects is needed to establish if X-ray absorption is common among typical flat-spectrum RLQs at high redshift, or if it is instead confined to the minority of RLQs with $R \gtrsim 1000$.

Our *Chandra* observations also provide useful constraints on kpc-scale X-ray jet emission from these RLQs; the on-axis angular resolution of *Chandra* at $z = 4$ corresponds to ≈ 4 kpc. One leading model for X-ray jet emission invokes highly relativistic bulk motions on kpc scales, thereby allowing electrons/positrons in the jet to Compton upscatter photons from the Cosmic Microwave Background (CMB) into the X-ray band (e.g., Tavecchio et al. 2000; Celotti, Ghisellini, & Chiaberge 2001). In this model, jets should remain X-ray bright at high redshift owing to the $(1+z)^4$ increase in CMB energy density which compensates for the usual $(1+z)^{-4}$ decrease of surface brightness (Schwartz 2002; also see, e.g., Rees & Setti 1968). In fact, if this model is correct, $z \gtrsim 4$ X-ray jets are often expected to outshine their X-ray cores (which dim with luminosity distance squared). We have looked for such X-ray luminous jets in our RLQ *Chandra* observations, and they are not detected. Any spatially resolvable X-ray jets must be ≈ 5–10 times fainter than their X-ray cores.[1] In some cases jets might be unresolvable due to an almost perfectly "pole-on" orientation, but such an orientation is unlikely for all our RLQs ($\alpha_{\rm ox}$ analyses also constrain this possibility). One plausible explanation for our nondetections is that most of the X-rays from RLQ jets are made via a process other than CMB Compton upscattering, such as synchrotron radiation by multiple electron populations (e.g., Atoyan & Dermer

[1] An X-ray jet has been detected from the $z = 4.30$ blazar GB 1508+5714 (Siemiginowska et al. 2003; Yuan et al. 2003). In this case, however, the jet-to-core X-ray flux ratio is $\approx 3\%$, substantially less than the $\approx 100\%$ discussed by Schwartz (2002). Additionally, the putative X-ray jet from the $z = 4.01$ blazar GB 1713+2148 (Schwartz 2004) is not confirmed in a pointed *Chandra* observation (D.A. Schwartz 2004, pers. comm.).

Table 1. Moderate-luminosity $z > 4$ AGNs found in X-ray surveys

AGN name	Redshift	Rest-frame $\log(L_{2-10})$	Representative reference
CXOCY J033716.7 − 050153	4.61	44.54	Treister et al. (2004)
CLASXS J103414.33+572227	5.40	44.44	Steffen et al. (2004)
RX J1052 + 5719	4.45	44.72	Schneider et al. (1998)
CXOMP J105655.1 − 034322	4.05	44.92	Silverman et al. (2005)
CXOHDFN J123647.9 + 620941	5.19	44.00	Vignali et al. (2002)
CXOHDFN J123719.0 + 621025	4.14	43.72	Vignali et al. (2002)
CXOCY J125304.0 − 090737	4.18	44.39	Castander et al. (2003)
CXOMP J213945.0 − 234655	4.93	44.79	Silverman et al. (2002)

The third column above is the rest-frame 2–10 keV luminosity (in erg s^{-1}), computed using a power-law photon index of $\Gamma = 2$. We have only included AGNs in this table with $\log(L_{2-10}) < 45$. A few higher luminosity AGNs have also been found in X-ray surveys, such as RX J1028.6−0844 (Zickgraf et al. 1997) and RX J1759.4+6638 (Henry et al. 1994).

2004; Stawarz et al. 2004). Alternatively, RLQ jets may often be "frustrated" at high redshift by their environments and thus only rarely achieve large angular sizes; this possibility can be tested with improved high-resolution radio imaging of $z > 4$ RLQs.

4 X-ray Survey Constraints on Moderate-Luminosity Active Galactic Nuclei at High Redshift

The analyses above engender confidence that X-ray selection should remain effective at finding AGNs at the highest redshifts, and the deepest current surveys with *Chandra* and *XMM-Newton* (e.g., Brandt & Hasinger 2005) have sufficient sensitivity to detect $z > 4$ AGNs that are $\approx$ 10–30 times less luminous than the quasars found in wide-field optical surveys (see Figure 1). For example, AGNs similar to Seyfert galaxies in the local universe, with X-ray luminosities of $\gtrsim 5 \times 10^{43}$ erg s^{-1}, should be detectable to $z \approx 10$ in the 2 Ms *Chandra* Deep Field-North (CDF-N; Alexander et al. 2003) observation. Such moderate-luminosity AGNs are much more numerous and thus more representative of the AGN population than the luminous quasars from wide-field optical surveys. Furthermore, X-ray surveys suffer from progressively less absorption bias as higher redshifts are surveyed (penetrating $\approx$ 2–40 keV rest-frame X-rays are sampled at $z > 4$), whereas optical surveys sample rest-frame ultraviolet light which can be absorbed by dust.

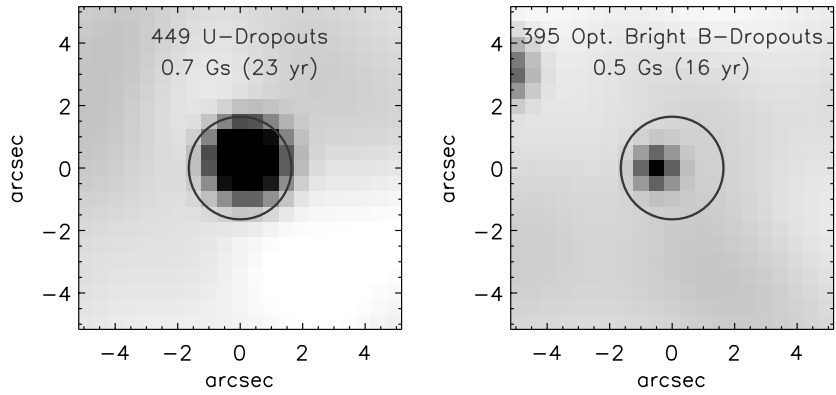

Fig. 6. Stacked images of Lyman break galaxies from the Great Observatories Origins Deep Survey (GOODS) in the 0.5–2 keV band. The left panel shows the stacking results for 449 U-dropouts with a typical redshift of $z = 3.0$ (7.1σ detection), and the right panel shows those for 395 optically bright B-dropouts with a typical redshift of $z = 3.8$ (3.2σ detection). The effective exposure times for the left and right panels are 23 and 16 yr, respectively. Adapted from Lehmer et al. (2005).

Moderate-luminosity X-ray detected AGNs at $z = 4$–6.5 are expected to have I-band magnitudes of ≈ 23–27; optical spectroscopy of these objects is thus challenging. Nevertheless, significant constraints on sky density have been set via intensive follow-up studies with large optical telescopes and color selection (e.g., Alexander et al. 2001; Barger et al. 2003; Cristiani et al. 2004; Koekemoer et al. 2004; Wang et al. 2004b). The sky density of $z > 4$ AGNs is ≈ 30–150 deg^{-2} at a 0.5–2 keV flux limit of $\approx 10^{-16}$ erg cm^{-2} s^{-1}; for comparison, the sky density of $z = 4$–5.4 SDSS quasars is ≈ 0.12 deg^{-2} at an i-magnitude limit of ≈ 20.2 (e.g., Schneider et al. 2003). While the constraints on the faint end of the AGN X-ray luminosity function at $z > 4$ have large statistical errors, the data are already sufficient to argue convincingly that the AGN contribution to reionization at $z \approx 6$ is small.

Table 1 lists the moderate-luminosity $z > 4$ AGNs found in X-ray surveys. The number of objects is small but is increasing fairly rapidly, as can be seen from the publication dates of the associated papers. With appropriate effort it should be possible to generate ≈ 50 moderate-luminosity $z > 4$ AGNs over the next ≈ 5 years, thereby defining in respectable detail the faint end of the luminosity function. Current X-ray spectral and $\alpha_{\rm ox}$ analyses, albeit limited, suggest that the moderate-luminosity $z > 4$ AGNs found in X-ray surveys have similar basic emission properties to comparably luminous objects at low redshift (e.g., Vignali et al. 2002).

High-redshift AGN populations with even lower luminosities can be constrained with X-ray source-stacking analyses. These search for an average signal from a set of high-redshift sources whose individual members lie below the single-source X-ray detection limit. The most sensitive X-ray source-stacking analyses at $z \approx 4$ or higher have employed samples of $\approx$ 250–1700 Lyman break galaxies (e.g., Lehmer et al. 2005; B, V, and i dropouts) and $\approx$ 100 Lyα emitters (e.g., Wang et al. 2004a; at $z \approx 4.5$). Average X-ray detections have presently been obtained up to $z \approx 4$ (see Figure 6), while physically interesting upper limits are obtained at higher redshifts. The data are plausibly consistent with any X-ray emission from these objects arising from stellar processes (e.g., X-ray binaries and supernova remnants); X-ray emission from numerous, low-luminosity AGNs is not required. These average constraints at luminosities below those that can be probed by single-source analyses further limit the contribution that AGNs could have made to reionization at $z \approx 6$. A complementary average constraint, derived by considering the unresolved component of the 0.5–2 keV background, provides additional evidence that AGNs and lower mass black holes did not dominate reionization (Dijkstra, Haiman, & Loeb 2004).

5 Some Future Prospects

The work described above can be extended in several ways with *Chandra* and *XMM-Newton* observations:

1. The number of X-ray detections at $z > 5$ is still relatively small at present, and this can be increased substantially with appropriate *Chandra* snapshots of the highest redshift quasars.
2. Only the most basic X-ray properties of typical RLQs at $z > 4$ are now known. *XMM-Newton* spectroscopy should allow their X-ray continuum and absorption properties to be determined much better, and deeper *Chandra* imaging of some objects is needed to search for X-ray jets more sensitively (in conjunction with improved radio imaging). Steep-spectrum RLQs at $z > 4$ also need to be studied in the X-ray band.
3. Additional X-ray investigations of minority AGN populations at $z > 4$, such as weak emission-line quasars and BAL quasars, can provide insight into their nature.
4. X-ray studies of $z > 4$ AGNs selected at infrared, submillimeter, and millimeter wavelengths (or with remarkable properties at these wavelengths) can establish the relative importance of AGN vs. stellar processes in these objects and allow assessment of extinction biases.
5. The number of known moderate-luminosity AGNs at $z > 4$ should increase significantly over the next few years, as follow-up studies of the many ongoing X-ray surveys progress. Uniform searches for such AGNs are particularly important for setting reliable demographic constraints.
6. Deeper X-ray surveys than those to date (e.g., 5–10 Ms *Chandra* observations) would allow improved searches for highly obscured AGNs at $z > 4$.

7. X-ray stacking analyses can be improved as high-redshift source samples are enlarged and refined.

In the more distant future, *Constellation-X* and *XEUS* should allow X-ray spectroscopy down to 0.5–2 keV flux levels of $\approx 5 \times 10^{-16}$ and $\approx 5 \times 10^{-17}$ erg cm^{-2} s^{-1}, respectively (see Figure 1). Precise X-ray measurements of continuum shape, absorption, iron K line emission, and Compton reflection should be possible for many $z > 4$ AGNs. Ultimately, a mission such as *Generation-X* should be able to survey the $z \approx 10$–15 X-ray universe, searching for X-rays from proto-quasars and the ≈ 100–300 $M_\odot$ black holes made by the deaths of the first stars.

Acknowledgments

We thank all of our collaborators on this work. We thank D.M. Alexander, L.C. Bassett, F.E. Bauer, C.C. Cheung, S. Heinz, D.A. Schwartz, and A.T. Steffen for helpful discussions. We acknowledge funding from NASA LTSA grant NAG5-13035 (WNB, DPS, IVS), NSF CAREER award AST-9983783 (WNB, BDL), *Chandra* and *XMM-Newton* grants (WNB, DPS), and MIUR COFIN grant 03-02-23 (CV).

References

1. D.M. Alexander, W.N. Brandt, A.E. Hornschemeier, et al.: AJ **122**, 2156 (2001)
2. D.M. Alexander, F.E. Bauer, W.N. Brandt, et al.: AJ **126**, 539 (2003)
3. A. Atoyan, C.D. Dermer: ApJ **613**, 151 (2004)
4. Y. Avni, H. Tananbaum: ApJ **305**, 83 (1986)
5. A.J. Barger, L.L. Cowie, P. Capak, et al.: ApJ **584** L61 (2003)
6. L.C. Bassett, W.N. Brandt, D.P. Schneider, C. Vignali, G. Chartas, G.P. Garmire: AJ **128**, 523 (2004)
7. W.N. Brandt: 'Ultrasoft Narrow-Line Seyfert 1 Galaxies: An Extreme of the Seyfert Phenomenon'. In: *High Energy Processes in Accreting Black Holes*, ed. by J. Poutanen, R. Svensson (ASP, San Francisco 1999), pp. 166–177
8. W.N. Brandt, G. Hasinger: ARA&A, submitted (2005)
9. M. Cappi, M. Matsuoka, A. Comastri, et al.: ApJ **478**, 492 (1997)
10. W. Cash: ApJ **228**, 939 (1979)
11. F.J. Castander, E. Treister, T.J. Maccarone, et al.: AJ **125**, 1689 (2003)
12. A. Celotti, G. Ghisellini, M. Chiaberge: MNRAS **321**, L1 (2001)
13. G. Chartas, W.N. Brandt, S.C. Gallagher, G.P. Garmire: ApJ **579**, 169 (2002)
14. S. Cristiani, D.M. Alexander, F.E. Bauer, et al.: ApJ **600**, L119 (2004)
15. M. Dijkstra, Z. Haiman, A. Loeb: ApJ **613**, 646 (2004)
16. M. Elvis, F. Fiore, P. Giommi, P. Padovani: ApJ **492**, 91 (1998)
17. D. Farrah, R. Priddey, R. Wilman, M. Haehnelt, R. McMahon: ApJ **611**, L13 (2004)
18. E. Ferrero, W. Brinkmann: A&A **402**, 465 (2003)
19. F. Fiore, M. Elvis, P. Giommi, P. Padovani: ApJ **492**, 79 (1998)
20. D. Grupe, S. Mathur, B.J. Wilkes, M. Elvis: AJ **127**, 1 (2004)
21. J.P. Henry, I.M. Gioia, H. Boehringer, et al.: AJ **107**, 1270 (1994)

22. Z. Ivezić, G.T. Richards, P.B. Hall, et al.: 'Quasar Radio Dichotomy: Two Peaks, or not Two Peaks, that is the Question'. In: *AGN Physics with the Sloan Digital Sky Survey*, ed. by G.T. Richards, P.B. Hall (ASP, San Francisco 2004) pp. 347–350
23. A.M. Koekemoer, D.M. Alexander, F.E. Bauer, et al.: ApJ **600**, L123 (2004)
24. B.D. Lehmer, W.N. Brandt, D.M. Alexander, et al.: AJ, in press (2005; astro-ph/0409600)
25. L.A. Lopez, W.N. Brandt, D.P. Schneider, C. Vignali, G. Chartas, G.P. Garmire: AJ, in preparation (2005)
26. J.E. McClintock, R.A. Remillard: 'Black Hole Binaries'. In: *Compact Stellar X-ray Sources*, ed. by W.H.G. Lewin, M. van der Klis (Cambridge University Press, Cambridge 2004), in press (astro-ph/0306213)
27. E. Piconcelli, E. Jimenez-Bailón, M. Guainazzi, N. Schartel, P.M. Rodriguez-Pascual, M. Santos-Lleó: A&A, in press (2004; astro-ph/0411051)
28. M.J. Rees, G. Setti: Nature **219**, 127 (1968)
29. J.N. Reeves, M.J.L. Turner: MNRAS **316**, 234 (2000)
30. D.P. Schneider, M. Schmidt, G. Hasinger, et al.: AJ **115**, 1230 (1998)
31. D.P. Schneider, X. Fan, P.B. Hall, et al.: AJ **126**, 2579 (2003)
32. D.A. Schwartz: ApJ **569**, L23 (2002)
33. D.A. Schwartz, S.N. Virani: ApJ **615**, L21 (2004)
34. D.A. Schwartz: 'An X-ray View of Radio Sources'. In: *Radio Astronomy at 70: From Karl Jansky to Microjansky*, ed. by L. Gurvits, S. Frey, S. Rawlings (EDP Sciences, Les Ulis 2004), in press (astro-ph/0402303)
35. A. Siemiginowska, R.K. Smith, T.L. Aldcroft, D.A. Schwartz, F. Paerels, A.O. Petric: ApJ **598**, L15 (2003)
36. J.D. Silverman, P.J. Green, D.W. Kim, et al.: ApJ **569**, L1 (2002)
37. J.D. Silverman, P.J. Green, W.A. Barkhouse, et al.: ApJ, in press (2005; astro-ph/0409337)
38. L. Stawarz, M. Sikora, M. Ostrowski, M.C. Begelman: ApJ **608**, 95 (2004)
39. I.V. Strateva, W.N. Brandt, D.P. Schneider, D.G. Vanden Berk, C. Vignali: AJ, in preparation (2005)
40. A.T. Steffen, A.J. Barger, P. Capak, L.L. Cowie, R.F. Mushotzky, Y. Yang: AJ **128**, 1483 (2004)
41. F. Tavecchio, L. Maraschi, R.M. Sambruna, C.M. Urry: ApJ **544**, L23 (2000)
42. E. Treister, F.J. Castander, T.J. Maccarone, et al.: ApJ **603**, 36 (2004)
43. C. Vignali, F.E. Bauer, D.M. Alexander, et al.: ApJ **580**, L105 (2002)
44. C. Vignali, W.N. Brandt, D.P. Schneider, G.P. Garmire, S. Kaspi: AJ **124**, 418 (2003a)
45. C. Vignali, W.N. Brandt, D.P. Schneider: AJ **125**, 433 (2003b)
46. C. Vignali, W.N. Brandt, D.P. Schneider, et al.: AJ **125**, 2876 (2003c)
47. C. Vignali, W.N. Brandt, D.P. Schneider, S. Kaspi: AJ, submitted (2005)
48. J.X. Wang, J.E. Rhoads, S. Malhotra, et al.: ApJ **608**, L21 (2004a)
49. J.X. Wang, S. Malhotra, J.E. Rhoads, C.A. Norman: ApJ **612**, L109 (2004b)
50. M.A. Worsley, A.C. Fabian, A. Celotti, K. Iwasawa: MNRAS **350**, L67 (2004a)
51. M.A. Worsley, A.C. Fabian, A.K. Turner, A. Celotti, K. Iwasawa: MNRAS **350**, 207 (2004b)
52. W. Yuan, A.C. Fabian, A. Celotti, P.G. Jonker: MNRAS **346**, L7 (2003)
53. F.J. Zickgraf, W. Voges, J. Krautter, et al.: A&A **323**, L21 (1997)

A Search for the First Massive Galaxy Clusters

C.J. Willott[1], D. Crampton[1], J.B. Hutchings[1], M. Sawicki[1], L. Simard[1], M.J. Jarvis[2], R.J. McLure[3], and W.J. Percival[3]

[1] Herzberg Institute of Astrophysics, National Research Council, 5071 West Saanich Rd, Victoria, B.C. V9E 2E7, Canada
[2] Astrophysics, Department of Physics, Keble Road, Oxford, OX1 3RH, U.K.
[3] Institute for Astronomy, University of Edinburgh, Royal Observatory, Blackford Hill, Edinburgh, EH9 3HJ, U.K.

Abstract. We have obtained deep, multi-band imaging observations around three of the most distant known quasars at redshifts $z > 6$. Standard accretion theory predicts that the supermassive black holes present in these quasars were formed at a very early epoch. If a correlation between black hole mass and dark matter halo mass is present at these early times, then these rare supermassive black holes will be located inside the most massive dark matter halos. These are therefore ideal locations to search for the first clusters of galaxies. We use the Lyman-break technique to identify star-forming galaxies at high redshifts. Our observations show no overdensity of star-forming galaxies in the fields of these quasars. The lack of (dust-free) luminous starburst companions indicates that the quasars may be the only massive galaxies in their vicinity undergoing a period of intense activity.

1 Introduction

The existence of inactive supermassive black holes in the nuclei of massive nearby galaxies [29] is a sure sign that most galaxies underwent substantial active phases. Furthermore, the correlation between the amount of material accreted (black hole mass) and the galaxy mass indicates important links between galaxy formation and AGN activity. One implication is that the most massive black holes live in the most massive galaxies which reside in the most massive dark matter halos.

The $z > 6$ quasars being discovered in the Sloan Digital Sky Survey (see Fan, this volume) have exceptionally high luminosities ($M_{1450} < -27$). The available evidence suggests that these luminosities are not amplified by gravitational lensing [8] or beaming [14,20]. Assuming that these quasars are radiating at the Eddington limit gives a lower limit on their black hole masses of several billion solar masses. These are comparable to the black holes inside the largest dominant cluster ellipticals at the present time. Applying local calibrations from this black hole mass to galaxy and halo masses suggests that these quasars reside in halos with mass $\sim 10^{13}\,\mathrm{M}_{\odot}$ (e.g. [20]). LCDM simulations show that structure grows 'bottom-up' with the largest halos typically collapsing at the latest epochs. Halos with mass $> 10^{13}\,\mathrm{M}_{\odot}$ at $z = 6$ are therefore extremely rare (the fraction of mass in such halos is of order 10^{-8}; [16])

ESO Symposia: Growing Black Holes, pp. 102–107, 2005.

There is evidence that at least some of these quasars are located in massive galaxies. Sub-millimetre photometry of several of them show very high far-infrared luminosities, implying extreme starbursts of $> 1000\,\mathrm{M}_\odot\,\mathrm{yr}^{-1}$ [2,15]. The most distant quasar, SDSS J1148+5251 at $z = 6.42$, contains $\gtrsim 10^{10}\,\mathrm{M}_\odot$ of molecular gas, again indicative of a massive, primeval galaxy [19]. These distant quasars, which are thought to be residing in massive galaxies, are therefore ideal places to search for the first clusters of galaxies. The most straightforward method for identifying galaxies at such high redshifts is the Lyman-break technique – a large discontinuity in the spectral slope due to absorption by neutral hydrogen (e.g. [18]). The increase in the optical depth of hydrogen absorption at such high redshifts (e.g. [17]) makes the Lyman-break technique even more effective at $z \sim 6$ than at lower redshifts. To search for galaxies in these putative mass overdensities, we carried out a search for Lyman-break galaxies in fields of three $z > 6.2$ SDSS quasars.

2 Observations

We have imaged three quasar fields with the GMOS-North imaging spectrograph on the Gemini-North Telescope: SDSS J1030+0524 at $z = 6.28$, SDSS J1048+4637 at $z = 6.23$ and SDSS J1148+5251 at $z = 6.42$. The imaging field-of-view is 5.5 arcmin on a side, equivalent to a co-moving size of 13 Mpc at $z = 6.3$. Observations were carried out in queue mode during November and December 2003. The typical seeing FWHM of the observations is in the range 0.5 to 0.7″. Typical exposure times are ≈ 2 hours in the z'-band and ≈ 3 hours in the i'-band. The relative exposure times were designed to give similar sensitivity in the two bands for very red objects with colours of $i' - z' \approx 1.5$. Full details of these observations and their reduction will be published elsewhere.

Detection of objects in the reduced images was performed using the Sextractor software [1]. The z'-band was selected as the primary detection waveband since $z > 6$ galaxies are expected to have $i' - z' > 2$ and may therefore be undetected at i'. Sextractor was run in "double-image" mode to determine i'-band measurements for objects detected in z'. Magnitudes on the AB system were measured in circular apertures of diameter 1.5″. Aperture corrections were applied statistically to the z'-band magnitudes by fitting a linear function to the difference between the total magnitude and aperture magnitude as a function of aperture magnitude. Typical magnitude limits (3σ limits in 1.5″ apertures) are $z' \approx 26.2$ and $i' \approx 27.6$.

To assess the completeness of the z'-band catalogues we consider both the observed number counts and the recovery of simulated objects. The number counts in the three fields do not differ significantly from each other. They agree well with the z'-band counts determined from a much larger area survey (0.2 square degrees or thirty times the GMOS-North field-of-view) by Capak et al. [5]. The number counts in the quasar fields begin to change slope at $z' > 25.5$ and turn over at $z' = 26$, indicating this is where the sample becomes incomplete.

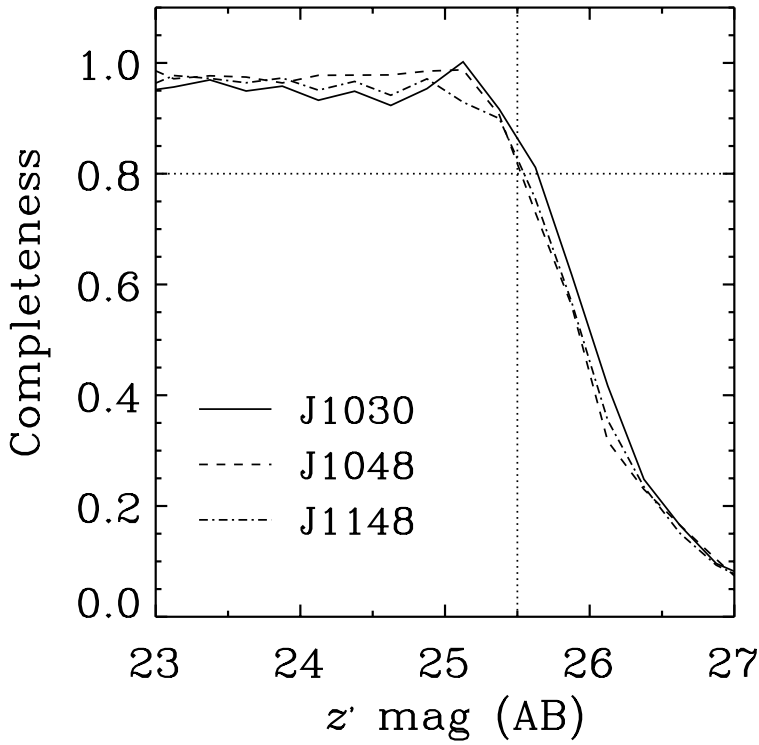

Fig. 1. Completeness ratio against aperture-corrected z'-band magnitude derived from recovery of simulated galaxies. The curves are quite similar for the three different quasar fields. Dotted lines indicate the location of a completeness ratio of 0.8 and the adopted complete magnitude limit of $z' = 25.5$.

The source recovery as a function of magnitude was determined by populating the images with artificial galaxies and then using Sextractor to attempt to detect these objects. About 10 000 artificial galaxies with magnitudes in the range $23 < z' < 27$ were placed into copies of the z' images of each quasar. Regions of the images already occupied by objects were masked out of the process to eliminate incompleteness due to blending. The resulting completeness ratio is plotted as a function of magnitude for the three quasar fields in Fig. 1. The completeness in all the fields is fairly flat at close to 1 up to $z' = 25.2$ and then begins to decline. The rapid decline occurs at $z' > 25.5$ and the completeness drops to 0.5 by $z = 26.0$. All the fields have completeness > 0.8 at $z' = 25.5$ and we adopt this as the magnitude at which completeness begins to become an issue. This analysis with simulated objects agrees well with the results for the number counts discussed previously.

3 High-redshift galaxies in the quasar fields

The $z > 6$ SDSS quasars have $z' \approx 20$ and colours of $i' - z' = 3.25, 2.98, 3.25$ respectively for J1030, J1048 and J1148. Quasars and star-forming galaxies have broadly similar spectra over the rest-frame wavelength range $90 - 140$ nm probed by the i' and z' filters. Their spectra are dominated by a large break due to absorption by neutral hydrogen. Therefore one would expect companion galaxies to have comparable colours to the quasars.

A colour-magnitude diagram for objects in the field of SDSS J1030+0524 is shown in Fig. 2. Most objects have colours in the range $0 < i' - z' < 1$ as is well known from previous surveys [6,5]. Also plotted are curves showing the colour-magnitude relation for two different types of galaxy. Model galaxy spectra were generated from the [4] spectral synthesis code with Lyman forest absorption evolution matching the observations of [17]. The upper curve is a present-day L* elliptical which formed all of its stars in a starburst starting at $z = 10$ with a characteristic timescale of 1 Gyr and evolved since without merging. Note that there is no dust extinction assumed for this model, but in reality the dust extinction would increase with redshift (due to evolution and k-correction) making the galaxy fainter than plotted at higher redshifts. The lower curve is a L* Lyman-break galaxy model where the galaxy is observed 0.5 Gyr into a constant star formation rate starburst.

A search was made for objects which could plausibly be high-redshift galaxies. The i'-band dropout selection criteria adopted were snr in the z'-band ≥ 4 and a colour of $i' - z' \geq 1.5$. Possible candidates were inspected and magnitudes checked to ensure their unusual colours are not spurious. A total of four objects satisfying these criteria were found; two in the field of SDSS J1030+0524, shown in Fig. 2 with filled symbols, and one in each of the other two fields. Only one of these four galaxies has a magnitude brighter than the completeness limit of $z' = 25.5$. This object has $i' - z' = 1.56 \pm 0.31$ which is quite close to the colour selection value and the size of the uncertainty means it is quite plausible that photometric errors have scattered the colour into the dropout range. The measured colour is about 5σ away from the colours of the SDSS quasars, which suggests that if it is a high-redshift galaxy, then it is most likely foreground to the quasars with a redshift in the range $5.7 < z < 6$. The other three objects have $z' \approx 25.6$ and only lower limits on their $i' - z'$ colours which lie in the range $1.7 - 1.9$.

Our z'-band images are complete at the greater than 80% level to $z' = 25.5$. At $z' \leq 25.5$, every single z'-band object detected on our images has a counterpart at the $> 3\sigma$ level in the i'-band image. At fainter magnitudes, this is no longer true and our constraints on the $i' - z'$ colours of objects at these magnitudes becomes very weak due to uncertainty in both the z' and i' magnitudes. We now consider the number of i'-band dropouts we could have expected to find under the assumption that the quasar fields are "random" and show no enhancement due to the existence of the quasars. The best comparison dataset which goes deep enough over a wide area is the *Hubble Space Telescope* ACS imaging of the GOODS regions [15]. These observations give a surface

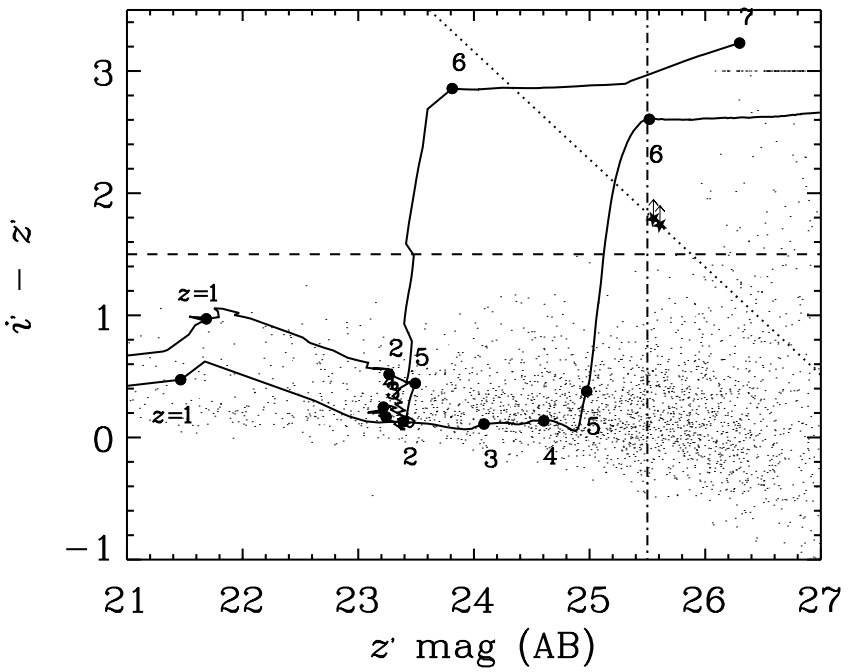

Fig. 2. Colour-magnitude diagram for objects detected at z'-band in the field of the $z = 6.28$ quasar SDSS J1030+0524. The completeness limit of $z' = 25.5$ is shown with a dot-dashed line. The high-redshift galaxy selection criterion of $i' - z' > 1.5$ is marked with the dashed line. The dotted line represents the colour of an object which is just detected at the 3σ level in the i'-band as a function of the z'-band magnitude. Most objects with measured zero or negative flux in the i'-band are plotted at $i' - z' = 3$. The exceptions to this are objects which pass the i'-band dropout selection criteria discussed in the text. These are shown with star symbols and lower limits on the i'-band 3σ line. The dots at $i' - z' > 1.5$ indicate sources which are detected at less than 4σ at z'-band and hence have very large uncertainties on their magnitudes and colours and in some cases may be spurious. The labelled curves show the colour and magnitude as a function of redshift for an evolving L* elliptical (upper curve) and a non-evolving L* Lyman-break galaxy (lower curve) – see text for more details.

density of objects with $z' < 25.5$ and $i' - z' > 1.5$ of 0.02 arcmin^{-2} [6,3]. The total sky area we have surveyed with GMOS-North is 82 arcmin^2. Therefore on the basis of the GOODS observations we would expect 1.6 i'-band dropouts in our total area. Our finding of one dropout is entirely consistent with the expectations for blank fields.

Our observations show that these quasar fields do not exhibit an excess of luminous companion galaxies. The magnitude limit of $z' = 25.5$ corresponds to a UV luminosity of $L_{1500} = 2.5 \times 10^{29}$ergs^{-1}Hz^{-1} at a redshift of $z = 6.3$. This is equivalent to an unobscured star formation rate of $SFR = 30\ \mathrm{M}_\odot\ \mathrm{yr}^{-1}$, assuming the conversion given in [41]. The few known galaxies at redshifts

$z \approx 6.6$ discovered in narrow-band surveys have star formation rates derived from their UV luminosities comparable to this limit [10,11]. For comparison, the millimeter detections of dust in J1048 and J1148 imply total star formation rates $> 1000\ M_{\odot} yr^{-1}$ in the host galaxies of the quasars [2].

How do we explain the lack of companion galaxies with high star formation rates? One possibility is that galaxies undergoing intense star formation do exist but they are heavily extinguished by dust. Such galaxies may be detectable via their far-infrared emission and we are conducting a program of sub-mm imaging around these quasars to identify such galaxies. Deep observations with the IRAC camera on the *Spitzer Space Telescope* would also be able to reveal these obscured galaxies. Another possibility is that massive companion galaxies exist but they are not observed during a period of intense star formation. This possibility seems unlikely since the youth of the universe at this redshift means galaxies would likely be gas-rich and forming stars, especially if located in a dense environment which is not yet virialized. Finally, we raise a question mark over the notion that these rare massive black holes actually reside in the rarest, densest peaks in the dark matter distribution. Perhaps the correlation between black hole mass and dark matter halo mass (or halo circular velocity – see [21]) does not apply to these quasars and they are actually located inside less massive dark matter halos.

References

1. Bertin, E., Arnouts, S.: A&AS, 117, 393 (1996)
2. Bertoldi, F., et al. 2003, A&A, 406, L55 (2003)
3. Bouwens, R. J., et al. 2004, ApJ, 606L, 25 (2004)
4. Bruzual, G., Charlot, S. 2003, MNRAS, 344, 1000 (2003)
5. Capak, P., et al. 2004, AJ, 127, 180 (2004)
6. Dickinson, M., et al. 2004, ApJ, 600, L99 (2004)
7. Fan, X., et al. 2001, AJ, 122, 2833 (2001)
8. Fan, X., et al. 2003, AJ, 125, 1649 (2003)
9. Giavalisco, M., et al. 2004, ApJ, 600, L93 (2004)
10. Hu, E. M., et al. 2002, ApJ, 568, L75 (2002)
11. Kodaira, K., et al. 2003, PASJ, 55L, 17 (2003)
12. Madau, P., Pozzetti, L., Dickinson, M. 1998, ApJ, 498, 106 (1998)
13. Magorrian J., et al. 1998, AJ, 115, 2285 (1998)
14. Pentericci, L., et al. 2002, AJ, 123, 2151 (2002)
15. Priddey, R. S., et al. 2003, MNRAS, 344L, 74 (2003)
16. Sheth, R. K., Tormen, G. 1999, MNRAS, 308, 119 (1999)
17. Songaila, A., Cowie, L. L., 2002, AJ, 123, 2183 (2002)
18. Steidel, C. C., et al. 1996, ApJ, 462L, 17 (1996)
19. Walter, F., et al. 2003, Nature, 424, 406 (2003)
20. Willott, C. J., McLure, R. J., Jarvis, M. J. 2003, ApJ, 587, L15 (2003)
21. Wyithe, J. S. B., Loeb, A. 2004, ApJ, submitted, astro-ph/0403714 (2004)

The Spatial Clustering of X-ray Selected AGN in the Chandra Msec Fields

R. Gilli

INAF - Osservatorio Astrofisico di Arcetri, Largo E. Fermi 5, 50125 Firenze, Italy

Abstract. I present here the first estimates of the spatial correlation function of X-ray selected AGN in the 2Msec Chandra Deep Field North (CDFN) and 1Msec Chandra Deep Field South (CDFS). The AGN clustering amplitude, measured for sources with median luminosity $L_{0.5-10} \sim 10^{43}$ erg s^{-1} and at a median redshift of ~ 0.9, is found to be a factor of ~ 2 higher in the CDFS than in the CDFN, revealing large cosmic variance in these 0.1 deg^2 fields. The extra correlation signal in the CDFS is produced by two prominent redshift structures at $z = 0.67$ and $z = 0.73$. Within each field, no significant differences are found between the clustering properties of soft and hard X-ray selected sources, or, similarly, between those of type 1 and type 2 AGN. The high ($5 - 10\,h^{-1}$ Mpc) correlation length measured for AGN at $z \sim 0.9$ in the two *Chandra* Msec fields is comparable to that of early type galaxies at the same redshift.

1 Introduction

Active Galactic Nuclei (AGN) represent an excellent tool to trace the large scale structure of the Universe at intermediate-high redshifts, $z \sim 1 - 2$, i.e. at an epoch where matter was transiting from the initially smooth state observed at the recombination to the clumpy distribution observed at present time [18]. The spatial clustering of AGN has been directly measured by means of optical surveys encompassing an increasing number of blue, unobscured QSOs [24,16,8], while it is still poorly constrained in the X-ray band, where the bulk of the obscured AGN population should emerge [7,39,23]. The standard statistics used to carachterize the clustering properties of galaxies and AGN is the two-point correlation function, which essentially measures the probability over random of finding a source pair at a given separation [10]. Significant clustering signal in the X-rays has been detected from angular correlations [27,11,2,28,4], which have been often converted into spatial correlations by assuming an *a priori* redshift distribution. Unfortunately, this method suffers from several uncertainties and did not provide stringent results. To date, the only direct measurement of the spatial correlation function of X-ray selected AGN, usually approximated by a powerlaw $\xi(r) = (r/r_0)^{-\gamma}$, has been obtained by [22], who found $r_0 = 7.4 \pm 1.8\,h^{-1}$ Mpc for the AGN in the ROSAT NEP survey (the slope was fixed to $\gamma = 1.8$). Because of the short exposure times and ROSAT limited sensitivity, only bright sources, with a surface density of ~ 3 deg^{-2}, were detected in the NEP survey. Since the spatial correlation function is a power law increasing at lower pair separations, deep pencil beam surveys like the 1Msec *Chandra* Deep Field South (CDFS [23,12]) and the 2Msec *Chandra* Deep Field North (CDFN

ESO Symposia: Growing Black Holes, pp. 108–113, 2005.

[1,2]), where the X-ray source surface density is about $3000 - 4000$ deg^{-2}, are expected to provide the highest signal significance with the minimum number of identified objects. The drawbacks are that, on small areas, these strong signals may be subject to substantial variance, so that the "real" correlation amplitude would need a large set of measurements in independent fields to be reliably estimated.

2 The *Chandra* Msec Fields

In the 1Msec ACIS-I observation of the CDFS a total of 346 X-ray sources have been detected over the whole 0.1 deg^2 field [23,12]. In the center of the field limiting fluxes of 5.5 10^{-17} erg cm^{-2} s^{-1} and 4.5 10^{-16} erg cm^{-2} s^{-1} have been achieved in the 0.5-2 keV (soft) and 2-10 keV (hard) band, respectively. So far 127 high quality redshifts with two or more identified lines ($\sim$ 35% of the total sample) have been obtained by means of VLT spectroscopy [25]. The spectroscopic completeness increases to 78% when considering X-ray sources with optical counterparts brighter than R=24. As shown in the left panel of Fig. 1, the redshift distribution is dominated by two large concentrations of sources at $z = 0.67$ and $z = 0.73$, while other smaller peaks are also visible [14].

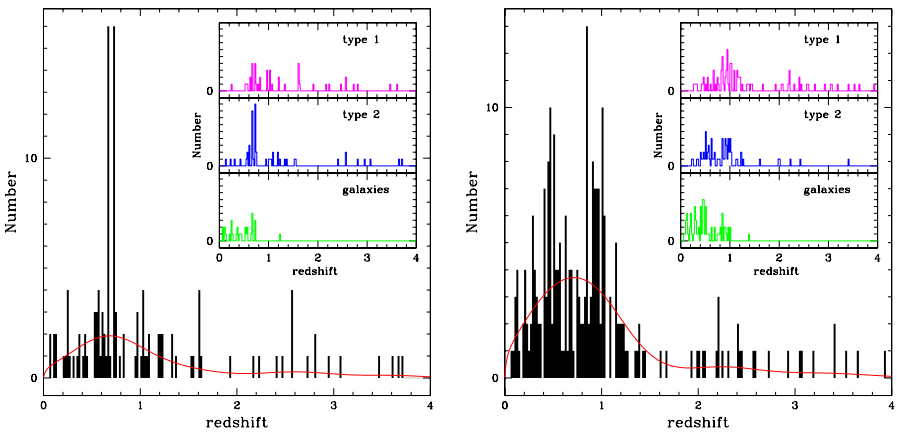

Fig. 1. Left: Redshift distribution for CDFS sources in bins of $\Delta z = 0.02$. Only sources with robust spectroscopic redshift are considered. The solid curve shows the smoothed distribution used to calculate $w(r_p)$ (see text). The inset shows the redshift distribution for different source classes. Right: same as in the left panel but for CDFN sources.

The CDFN [1,2] has been observed with ACIS-I for a total 2 Msec exposure. Limiting fluxes of ~ 2.5 10^{-17} erg cm^{-2} s^{-1} and ~ 1.4 10^{-16} erg cm^{-2} s^{-1} have been reached in the soft and hard band, respectively. A total sample of 503 X-ray sources has been collected over an area of 0.13 deg^2 [1]. The LRIS and DEIMOS

instruments at the Keck telescope were primarily used for the optical follow-up of the X-ray sources [2]. The final catalog includes 252 sources with robust spectroscopic redshift, corresponding to a spectroscopic completeness of $\sim 50\%$. The redshift distribution for the considered spectroscopic sample is shown in the right panel of Fig. 1. As in the case of the CDFS redshift distribution, several spikes, although less prominent, can be immediately identified, e.g. at $z \sim 0.85$ and $z \sim 1.02$ [2]. When comparing the redshift distributions of the two fields, it is evident that in the CDFN the fraction of low redshift sources is higher than in the CDFS. As an example, 28% of CDFN sources lay at $z < 0.5$, while the corresponding fraction in the CDFS is 17%. This difference is explained by the deeper CDFN exposure, which is able to pick up the faint X-ray emission of nearby normal and starburst galaxies (see [15] and the insets of Fig. 1). The R-band magnitude distributions are instead more similar, with most of the spectroscopically confirmed sources in the range $19 < \mathrm{R} < 24$ in both samples, confirming that the spectroscopic observations have been equally deep in both fields.

3 Clustering analysis

The full clustering analysis for the sources in the *Chandra* Msec Fields is presented in [15]. Its main features are briefly summarized below. To measure the clustering properties of different source populations, the X-ray hardness ratio vs. X-ray luminosity diagram presented by [25] was used to classify the X-rays sources as type-1 AGN, type-2 AGN and galaxies. Indeed, most of the X-ray sources in the *Chandra* Msec Field have faint optical counterparts, for which detailed line diagnostics is impossible. The two-point correlation function has been expressed in terms of the separations perpendicular (r_p) and parallel to the line of sight, and then integrated along the line of sight to get the so-called projected correlation function $w(r_p) \propto r_0^{\gamma} r_p^{1-\gamma}$ [10]. This procedure corrects for the distortions produced by peculiar velocities. The minimum variance estimator proposed by [19] was used to measure the correlation function, and special care was taken in creating the random control sample. In particular the objects in the random sample were placed at the coordinates of the real sources, and their redshifts were extracted from a smoothed distribution of the observed one (see Fig. 1). This procedure was extensively tested and found to be appropriate for the CDFS and CDFN samples [15]. The projected correlation function $w(r_p)$ was measured at different scales r_p and the best fit parameters γ and r_0 were determined via χ^2 minimization. It is noted here that, while Poisson errorbars underestimate the true uncertainties on the r_0 and γ values when the source pairs are not independent, bootstrap resampling techniques [21], which are often used to circumvent this problem, may substantially overestimate the real uncertainties. In the considered samples bootstrap errors are found to be a factor of ~ 2 larger than Poisson errors [15]. In the following the r_0 and γ values will be quoted together with their 1σ Poisson errors, bearing in mind that the most likely uncertainty lay between the quoted number and its double. A flat

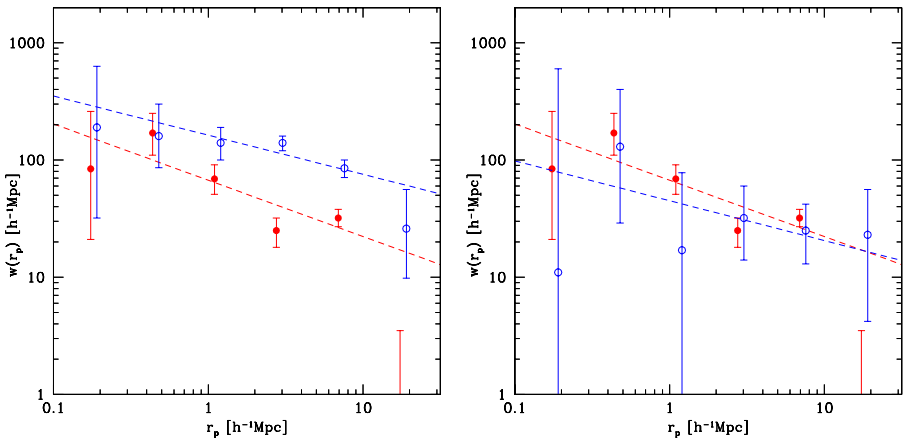

Fig. 2. Left: AGN projected correlation functions in the CDFN (filled circles) and CDFS (open circles). Right: AGN projected correlation function for the CDFN sample (filled circles) and for the CDFS sample obtained by excluding the sources in the two redshift spikes at z=0.67 and z=0.73 (open circles). In both panels errors are 1σ Poisson confidence intervals; the best fit power laws are also shown as dashed lines.

cosmology with $\Omega_m = 0.3$ and $\Omega_\Lambda = 0.7$ was assumed; comoving distances in units of h^{-1} Mpc are quoted, where $H_0 = 100\ h$ km s^{-1} Mpc^{-1}.

4 Results

The clustering level of the total samples in the CDFS and CDFN is dominated by that of AGN, which indeed represent the majority of the identified sources. In both fields the correlation function is measured on scales $r_p = 0.16 - 20\ h^{-1}$ Mpc for AGN at a median redshift of $z \sim 0.9$ and with median X-ray luminosity of $L_{0.5-10} \sim 10^{43}$ erg s^{-1}, i.e. in the luminosity regime of Seyfert galaxies. The best fit parameters of the AGN correlation function were found to be $r_0 = 10.3 \pm 1.7 h^{-1}$ Mpc, $\gamma = 1.33 \pm 0.14$ in the CDFS and $r_0 = 5.5 \pm 0.6 h^{-1}$ Mpc, $\gamma = 1.50 \pm 0.12$ in the CDFN (see Fig. 2, left panel). As verified by [15], the difference in the r_0 values between the two fields is not due to observational biases affecting in different ways the two samples (i.e. different X-ray sensitivity or spectroscopic incompleteness), but is rather due to genuine cosmic variance. Indeed, while in the CDFS about 1/3 of the identified sources lay within the two redshift spikes at $z = 0.67$ and $z = 0.73$, no such prominent features are observed in the CDFN (for comparison, the two most populated spikes of the CDFN contain only 1/8 of the identified sources). As shown in the right panel of Fig. 2, when excluding the sources in the two spikes at $z = 0.67$ and $z = 0.73$, the AGN correlation length in the CDFS is found to be similar to that measured in the CDFN. The slope of the correlation, $\gamma = 1.3 - 1.5$, is flatter than that commonly observed for galaxies ($\gamma \sim 1.7 - 2.0$ [20,17]), but consistent within the errors with the value

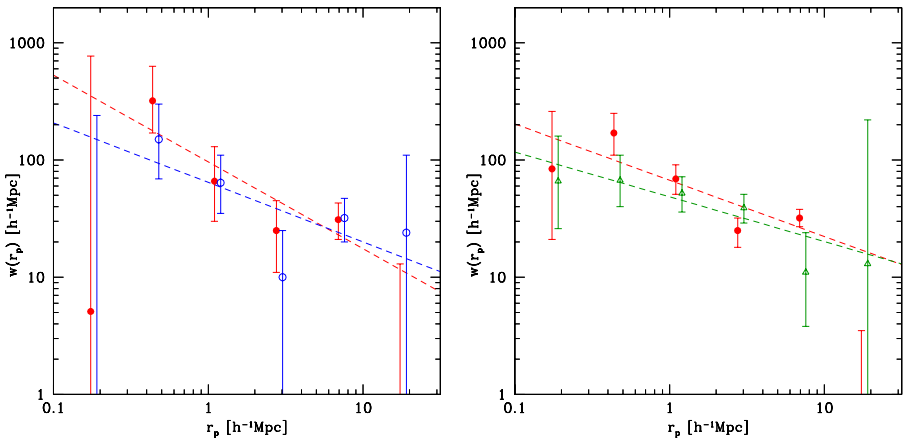

Fig. 3. Left: Projected correlation functions for type 1 AGN (filled circles) and type 2 AGN (open circles) in the CDFN. Right: Projected correlation functions for AGN (circles) and galaxies (triangles) in the CDFN. In both panels errors are 1σ Poisson confidence intervals; the best fit power laws are also shown as dashed lines.

of $\gamma = 1.56 \pm 0.10$ measured for the sample of $> 10^4$ optically selected QSOs in the 2QZ survey [8]. It is noted that, when fixing the slope of the correlation to $\gamma = 1.8$, the best fit r_0 values measured in the two *Chandra* Msec Fields increase by only 15%. Within each field no significant differences are found between the clustering properties of soft and hard X-ray selected sources, or, similarly, between those of type-1 and type-2 AGN. The comparison between the clustering properties of type-1 and type-2 AGN in the CDFN (where the statistics is higher) is shown in the left panel of Fig. 3: although the two correlations seem to have different slopes and amplitudes, they are in agreement within the errors. In the CDFN the clustering of X-ray selected galaxies was also measured and compared with that of the AGN in the same field (see Fig. 3, right panel). Again, due to the relatively large errors, no significant differences can be claimed.

5 Final notes

The high correlation length measured for the AGN in the CDFS is similar to that of Extremely Red Objects at the same redshift ($z \sim 1$), which are thought to be the progenitors of early type galaxies [9]. When considering the lower amplitude observed in the CDFN, we can estimate the correlation length of the AGN in the *Chandra* Msec fields to be in the range $5 - 10\ h^{-1}$ Mpc. Recently, [6] have measured with a good accuracy the correlation length of both early-type and late-type galaxies in the DEEP2 survey at $z = 0.7 - 1.25$, finding $r_0 = 6.61 \pm 1.12\ h^{-1}$ Mpc for early type galaxies and $r_0 = 3.17 \pm 0.54\ h^{-1}$ Mpc for late type galaxies. These measurements are then consistent with the idea

that Seyfert-like AGN at $z \sim 1$ are generally hosted by early type galaxies.

This work has been done in collaboration with many people of the CDFS and K20 team who are gratefully acknowledged: E. Daddi, G. Zamorani, P. Tozzi, S. Borgani, J. Bergeron, R. Giacconi, G. Hasinger, V. Mainieri, C. Norman, P. Rosati, G. Szokoly, W. Zheng, A. Cimatti, L. Kewley, M. Nonino, J.X. Wang, M. Mignoli, A. Zirm.

References

1. D.M. Alexander, F.E. Bauer, W.N. Brandt et al.: Astron. J. **126**, 539 (2003)
2. A. Akylas, I. Georgantopoulos, M. Plionis: Mon. Not. Roy. Ast. Soc. **318**, 1036 (2000)
3. A.J. Barger, L.L. Cowie, P. Capak et al.: Astron. J. **126**, 632 (2003)
4. S. Basilakos et al.: Astrophys. J. **607**, L79 (2004)
5. A. Cimatti, M. Mignoli, E. Daddi et al.: Astron. Astrophys. **392**, 395 (2002)
6. A.L. Coil et al.: Astrophys. J. **609**, 525 (2003)
7. A. Comastri, G. Setti, G. Zamorani, G. Hasinger: Astron. Astrophys. **296**, 1 (1995)
8. S.M. Croom et al.: Mon. Not. Roy. Ast. Soc. **325**, 483 (2001)
9. E. Daddi et al.: Astron. Astrophys. **376**, 825 (2001)
10. M. Davis, P.J.E. Peebles: Astrophys. J. **267**, 465 (1983)
11. R. Giacconi, P. Rosati, P. Tozzi et al.: Astrophys. J. **551**, 624 (2001)
12. R. Giacconi, A. Zirm, J. Wang et al.: Astrophys. J. Suppl. **139**, 369 (2002)
13. R. Gilli, M. Salvati, G. Hasinger: Astron. Astrophys. **366**, 407 (2001)
14. R. Gilli, A. Cimatti, E. Daddi et al.: Astrophys. J. **592**, 721 (2003)
15. R. Gilli, E. Daddi, G. Zamorani et al.: Astron. Astrophys. **submitted** (2004)
16. A. Grazian, M. Negrello, L. Moscardini et al.: Astron. J. **127**, 592 (2004)
17. L. Guzzo, M.A. Strauss, K.B. Fisher et al.: Astrophys. J. **489**, 37 (1997)
18. F.D.A. Hartwick, D. Schade: Ann. Rev. Astron. Astrophys. **28**, 437 (1990)
19. S.D. Landy, A.S. Szalay: Astrophys. J. **412**, 64 (1993)
20. O. Le Fevre, D. Hudon, S.J. Lilly et al.: Astrophys. J. **461**, 534 (1996)
21. H.J. Mo, Y.P. Jing, G. Börner: Astrophys. J. **392**, 452 (1992)
22. C.R. Mullis, J.P. Henry, I.M. Gioia et al.: Astrophys. J. **in press** (2004) [astro-ph/0408304]
23. P. Rosati, P. Tozzi, R. Giacconi et al.: Astrophys. J. **566**, 667 (2002)
24. T. Shanks, R. Fong, B.J. Boyle, B.A. Peterson: Mon. Not. Roy. Ast. Soc. **277**, 739 (1987)
25. G. Szokoly, J. Bergeron, G. Hasinger et al.: Astrophys. J. Suppl. **in press** (2004) [astro-ph/0312324]
26. Y. Ueda, M. Akiyama, K. Ohta, T. Miyaji: Astrophys. J. **598**, 886 (2003)
27. A. Vikhlinin, W. Forman: Astrophys. J. **455**, L109 (1995)
28. Y. Yang, R.F. Mushotzky, A.J. Barger et al.: Astrophys. J. **585**, L85 (2003)

What Powers High-Redshift SCUBA Galaxies?

D.M. Alexander

Institute of Astronomy, Madingley Road, Cambridge CB3 0HA, UK

Abstract. We investigate the origin of the huge luminosities produced by high-redshift SCUBA galaxies using the combination of ultra-deep X-ray observations (the 2 Ms *Chandra* Deep Field-North) and deep optical spectroscopic data. Even though a large fraction of high-redshift SCUBA galaxies host AGN activity (upward of 38%), we argue that in almost all cases the AGNs are not bolometrically important (i.e., contribute $< 20\%$ of the energetics). Thus, most high-redshift SCUBA galaxies appear to be star-formation dominated. A substantial fraction of high-redshift SCUBA galaxies show evidence for binary AGN activity. Since these systems appear to be interacting and merging at optical/near-IR wavelengths, their super-massive black holes are likely to eventually coalesce.

1 Introduction

Blank-field SCUBA surveys have uncovered a large population of submillimetre (submm; $\lambda = 300$–1000 μm) emitting galaxies (≈ 1000–10000 sources deg^{-2} at $f_{850\mu\mathrm{m}} \approx 1$–$5$ mJy; e.g. [5,9,10,17,20,28]). The majority of these sources are faint at all other wavelengths, hindering source identification studies. However, due to a considerable amount of intensive multi-wavelength follow-up effort, it is becoming clear that almost all are dust-enshrouded galaxies at $z > 1$ (e.g. [12,23,30,33]). With estimated bolometric luminosities of $\approx 10^{12}$–10^{13} L$_\odot$, these galaxies outnumber comparably luminous local galaxies by several orders of magnitude.

Central to the study of SCUBA galaxies is the physical origin of their extreme luminosities [i.e., starburst or Active Galactic Nucleus (AGN) activity]. If these sources are shown to be ultra-luminous starburst galaxies then their derived star-formation rates suggest a substantial increase in star-formation activity at $z > 1$ (e.g. [9]). For example, their luminosity derived star-formation rates (of order 1000 M$_\odot$ yr^{-1}) are potentially large enough to produce the stellar population of an $\approx L_*$ galaxy in ≈ 0.1 Gyrs. Conversely, if these sources are shown to be ultra-luminous AGNs then they outnumber comparably luminous optical quasars by ≈ 1–2 orders of magnitude. Both of these scenarios provide challenges to models of galaxy formation and evolution.

2 Searching for AGN activity in SCUBA galaxies

It was initially expected that deep SCUBA surveys would identify large numbers of high-redshift ultra-luminous starburst galaxies. However, the first SCUBA

ESO Symposia: Growing Black Holes, pp. 114–119, 2005.

source to be unambiguously identified via optical/near-IR spectroscopy was actually found to contain an obscured AGN, probably a BALQSO (i.e., the $z = 2.81$ source SMMJ02399–0136; [21,32]); subsequent moderately deep *Chandra* observations showed that this AGN is luminous at X-ray energies ($L_X \approx 10^{45}$ erg s^{-1}; [8]). Although clearly containing a powerful AGN, sensitive CO (3–2) observations of SMMJ02399–0136 suggested that star formation contributes $\approx 50\%$ of the total bolometric luminosity [19]. The lesson learnt from SMMJ02399–0136 is that the identification of an AGN at optical/near-IR wavelengths does not necessarily imply that the AGN is bolometrically dominant.

Extensive optical follow-up observations of other SCUBA sources have revealed further AGNs, a few starburst galaxies, and many sources with uncertain classifications (e.g., [12,22,30]). Although clearly successful in identifying the presence of an AGN in some SCUBA galaxies, optical spectroscopy has a number of limitations for AGN identification in all SCUBA galaxies:

- The large positional uncertainty of SCUBA sources often makes it challenging to identify an optical counterpart securely.
- A large fraction of the SCUBA sources with secure optical counterparts are optically faint ($I \geq 24$), making optical source classification challenging despite success in redshift identification (e.g., [12]).
- AGNs do not always show clear AGN signatures at optical wavelengths due to dust absorption and dilution by host-galaxy light (e.g., [15]).

Arguably the best discriminator of AGN activity is the detection of luminous hard X-ray emission (i.e., > 2 keV).[1] Hard X-ray emission is relatively insensitive to obscuration (at least for sources that are Compton thin; i.e., $N_{\rm H} < 1.5 \times 10^{24}$ cm^{-2}), and any hard X-ray emission from star formation in the host galaxy is often insignificant when compared to that produced by the AGN. Hard X-ray observations can even provide a secure AGN identification in sources where the optical signatures and counterparts are weak or even non existent (e.g., [1]). Due to their high-energy X-ray coverage, high X-ray sensitivity, and excellent positional accuracy, the *Chandra* and *XMM-Newton* observatories offer the best opportunities for the X-ray investigation of SCUBA galaxies.

3 AGN activity in SCUBA Galaxies

The ultra-deep *Chandra* Deep Field-North (CDF-N; [2]) studies have shown that a significant fraction of submm galaxies host AGN activity [3,6]. Indeed, using the 2 Ms CDF-N survey, [3,4] estimated that upwards of 38% of bright submm galaxies ($f_{850\mu{\rm m}} \geq 5$ mJy; S/N>4) harbour an AGN. The predominantly flat or inverted X-ray spectral slopes of these sources indicated that most are heavily obscured. Since a (possibly large) fraction of the intrinsic power of the AGN

[1] Radio observations can also be useful in identifying AGNs in SCUBA galaxies; however, not all AGNs are bright at radio wavelengths, and radio emission from strong star formation can easily mask the radio emission from a radio-quiet AGN.

is being absorbed, an accurate calculation of the contribution it makes to the bolometric luminosity requires a good measurement of the amount of obscuration. The most critical determination of the amount of obscuration towards the AGN is whether or not it is Compton thick (e.g., [18]). In Compton-thick AGNs (the most heavily obscured objects), the observed X-ray emission may account for <1% of the intrinsic power of the AGN at X-ray energies. The most direct determination of a Compton-thick AGN is made from X-ray spectral analyses. For example, a flat or inverted ($\Gamma < 0$) X-ray spectral slope and a large equivalent width Iron Kα emission line ($EW \geq 1$ keV) provides almost unambiguous evidence of Compton-thick absorption (e.g., [25,26]).

The first X-ray spectral analyses of submm galaxies was performed using the 2 Ms CDF-N [3]. They suggested that most of the X-ray detected AGNs in submm galaxies were Compton thin and estimated that they only contribute to a small fraction of the total bolometric output. However, although providing the tightest X-ray constraints on submm galaxies to date, only one source had a spectroscopic redshift (the rest of the sources had redshifts determined with the considerably less certain radio-submm photometric redshift technique; e.g., [11]), restricting more accurate and quantitative conclusions. Considerable progress in the optical identification of SCUBA galaxies has since been made due to the pioneering deep optical spectroscopic work of [12,14]. By targeting radio and/or X-ray detected SCUBA galaxies, source redshifts for a sizable fraction of the submm galaxy population have now been obtained. CO emission line observations have confirmed that both the redshift and counterpart are correct in many cases (e.g., [27]). Here we present preliminary results from X-ray analyses of the spectroscopically identified submm galaxies in the CDF-N.

4 What Powers High-Redshift SCUBA Galaxies?

Fifteen of the 20 $z > 1$ spectroscopically identified submm galaxies in the CDF-N are X-ray detected. We have directly performed X-ray spectral analyses for the X-ray detected submm galaxies; however, due to the limited space available here we simply note that the results are consistent with those of [3]. Based on our preliminary analyses of these data, the full range of absorption-corrected X-ray luminosities is $L_X \approx 10^{42}$–10^{45} erg s^{-1}; see Figure 1. While a number of the sources have X-ray luminosities consistent with those of X-ray luminous starburst galaxies (i.e., no AGNs), the majority clearly host AGN activity. The AGNs generally have X-ray luminosities consistent with those of Seyfert galaxies; however, three could be considered obscured QSOs (i.e., $L_X > 3 \times 10^{44}$ erg s^{-1}).

We calculated rest-frame far-IR luminosities for all of the sources from their radio luminosities, using the local radio-far-IR correlation found for starburst galaxies. The comparison of rest-frame far-IR luminosity with unabsorbed X-ray luminosity is shown in Figure 1. This figure provides an indicator of the AGN

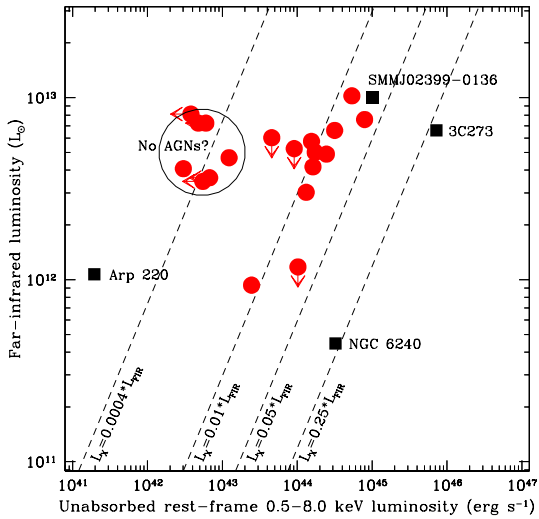

Fig. 1. Rest-frame far-IR versus absorption-corrected 0.5–8.0 keV X-ray luminosities for the X-ray detected submm galaxies with spectroscopic redshifts. The far-IR luminosities have been calculated from the 1.4 GHz radio luminosity (assuming the far-IR-radio correlation) and the X-ray luminosities have been corrected for the effect of absorption. The submm galaxy SMMJ02399–0136, and three luminous nearby galaxies (Arp 220, NGC 6240, and 3C273) are shown for comparison. The line indicating the smallest L_X/L_{FIR} ratio corresponds to the average found for starburst galaxies (e.g., [7]).

contribution to the bolometric luminosity.[2] Assuming that the far-IR emission from NGC 6240 and 3C273 is dominated by AGN activity, the AGNs in these submm galaxies contribute at most 20% of the bolometric luminosity and more typically a few percent. If instead we determine the AGN bolometric contributions based on the spectral energy distribution of SMMJ02399–0136 (i.e., $\approx 50\%$, [8,19]) then the AGN contributions increase by a factor of ≈ 2.5. Clearly, there is a range of X-ray to bolometric luminosity conversions for AGNs; however, on average the AGNs are unlikely to contribute more than $\approx$ 10–20% of the bolometric luminosity. Hence, although a large fraction of bright SCUBA galaxies host an AGN (i.e., at least $\approx 38\%$), in general, star formation is likely to dominate their bolometric output.

[2] When the radio emission has a large AGN component the far-IR luminosity will be overestimated and the AGN bolometric contribution will be underestimated; however, in general the radio emission appears to be star-formation dominated.

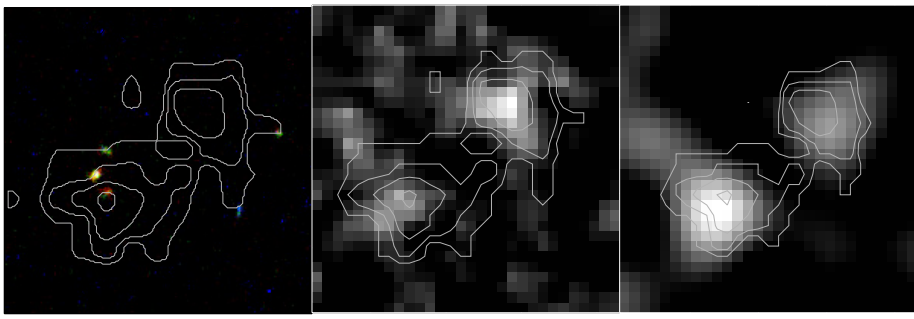

Fig. 2. *HST*-ACS (left), HK′-band (middle), and 1.4 GHz radio (right) images with overlaid X-ray contours for a SCUBA galaxy with a candidate binary AGN. Each panel is 6″ on a side.

5 Evidence for binary AGN activity

An unexpected result in the 2 Ms study of [3] was that two ($\approx 30\%$) of the seven X-ray detected submm galaxies were individually associated with X-ray pairs (see Figure 2). The small angular separations of these pairs ($\approx$ 2–3″) correspond to just ≈ 20 kpc at $z = 2$ (approximately one galactic diameter); the probability of a projected chance association is $<1\%$. From *HST* imaging, it has been shown that the majority of SCUBA sources appear to be galaxies involved in major mergers (e.g., [13,16,22,29]). At X-ray energies we are presumably witnessing binary AGN activity fuelled by galaxy mergers that will ultimately lead to the coalescence of the super-massive black holes. Recent X-ray studies are only just beginning to show the late stages of binary AGN activity in AGNs at much lower redshifts (e.g., NGC 6240; [24]); however, in this ultra-deep X-ray observation we have good evidence that this is occurring at $z \approx 2$! Since the smallest linear separation we can resolve with *Chandra* at $z \approx 2$ is ≈ 10 kpc, many of the other X-ray detected submm galaxies could be binary AGNs with smaller separations (e.g., the linear separation of the two AGNs in NGC 6240 is ≈ 1 kpc). Five ($\approx 3\%$) of the 193 X-ray sources in this region are close X-ray pairs, showing that binary AGN behaviour appears to be closely associated with submm galaxies (see also [31]). Qualitatively, this picture is consistent with that expected for major merger activity.

Acknowledgments

It is a pleasure to acknowledge my collaborators on this latest study (F. E. Bauer, S. C. Chapman, I. Smail, A. W. Blain, W. N. Brandt, and R. J. Ivison). I thank the organisers for putting together an interesting and stimulating conference program. Generous support was provided by the Royal Society via a University Research Fellowship.

References

1. Alexander, D. M., Brandt, W. N., Hornschemeier, A. E., et al.:AJ, **122**, 2156 (2001)
2. Alexander, D. M., Bauer, F. E., Brandt, W. N., et al.: AJ, **126**, 539 (2003a)
3. Alexander, D. M., Bauer, F. E., Brandt, W. N., et al.: AJ, **125**, 383 (2003b)
4. Alexander, D. M., Bauer, F. E., Chapman, S. C., et al: Multiwavelength Mapping of Galaxy Formation and Evolution, astro-ph/0401129 (2004)
5. Barger, A. J., Cowie, L. L., Sanders, D. B.: ApJ, **518**, L5 (1999)
6. Barger, A. J., Cowie, L. L., Steffen, A. T., et al.: ApJ, **560**, L23 (2001)
7. Bauer, F. E., Alexander, D. M., Brandt, W. N., et al.: AJ, **124**, 2351 (2002)
8. Bautz, M. W., Malm, M. R., Baganoff, F. K., et al.: ApJ, **543**, L119 (2000)
9. Blain, A. W., Smail, I., Ivison, R. J., et al.: MNRAS, **302**, 632 (1999)
10. Blain, A. W., Smail, I., Ivison, R. J., et al.: Physics Reports, **369**, 111 (2002)
11. Carilli, C. L., Yun, M. S.: ApJ, **513**, L13 (1999)
12. Chapman, S. C., Blain, A. W., Ivison, R. J., Smail, I. R.: Nature, **422**, 695 (2003a)
13. Chapman, S. C., Windhorst, R., Odewahn, S., et al.: ApJ, **599**, 92 (2003b)
14. Chapman, S. C., et al.: ApJ, submitted (2004)
15. Comastri, A., Mignoli, M., Ciliegi, P., et al.: ApJ, **571**, 771 (2002)
16. Conselice, C. J., Chapman, S. C., Windhorst, R. A.: ApJ, **596**, L5 (2003)
17. Cowie, L. L., Barger, A. J., Kneib, J.-P.: AJ, **123**, 2197 (2002)
18. Fabian, A. C., Smail, I., Iwasawa, K., et al.: MNRAS, **315**, L8 (2000)
19. Frayer, D. T., Ivison, R. J., Scoville, N. Z., et al.: ApJ, **506**, L7 (1998)
20. Hughes, D. H., Serjeant, S., Dunlop, J., et al.: Nature, **394**, 241 (1998)
21. Ivison, R. J., Smail, I., Le Borgne, J.-F., et al.: MNRAS, **298**, 583 (1998)
22. Ivison, R. J., Smail, I., Barger, A. J., et al.: MNRAS, **315**, 209 (2000)
23. Ivison, R. J., Greve, T. R., Smail, I., et al.: MNRAS, **337**, 1 (2002)
24. Komossa, S., Burwitz, V., Hasinger, G., et al.: ApJ, **582**, L15 (2003)
25. Maiolino, R., Salvati, M., Bassani, L., et al.: A&A, **338**, 781 (1998)
26. Matt, G., Brandt, W. N., Fabian, A. C.: MNRAS, **280**, 823 (1996)
27. Neri, R. et al.: ApJ, **597**, L113 (2003)
28. Smail, I., Ivison, R. J., Blain, A. W.: ApJ, **490**, L5 (1997)
29. Smail, I., Ivison, R. J., Blain, A. W., Kneib, J.-P.: ApJ, **507**, L21 (1998)
30. Smail, I., Ivison, R. J., Blain, A. W., et al.: MNRAS, **331**, 495 (2002)
31. Smail, I., Scharf, C. A., Ivison, R. J., et al.: ApJ, **599**, 86 (2003)
32. Vernet, J., Cimatti, A.: A&A, **380**, 409 (2001)
33. Webb, T. M. A., Lilly, S. J., Clements, D. L., et al.: ApJ, **597**, 680 (2003)

Early Spitzer Detections of Extreme X-ray/Optical Sources (EXOs)

A.M. Koekemoer[1], D.M. Alexander[2], F.E. Bauer[2], J. Bergeron[3], W. N. Brandt[4], S. Cristiani[5], M. Dickinson[6], N.A. Grogin[7], V. Mainieri[8], L. Moustakas[1], and C. M. Urry[9]

[1] Space Telescope Science Institute, 3700 San Martin Drive, Baltimore, MD 21218, USA
[2] Institute of Astronomy, Madingley Road, Cambridge, CB3 0HA, UK
[3] Institut d'Astrophysique de Paris, 98bis Bd Arago, F-75014 Paris, France
[4] Penn State University, 525 Davey Lab, University Park, PA 16802 USA
[5] INAF-Osservatorio Astronomico, via Tiepolo 11, I-34131 Trieste, Italy
[6] National Optical Astronomy Observatory, 950 N. Cherry Ave, Tucson, AZ 85719, USA
[7] Department of Physics and Astronomy, Johns Hopkins University, Baltimore, MD 21218, USA
[8] Max-Planck-Institut für extraterrestrische Physik, Giessenbachstrasse Postfach 1312, Garching 85748, Germany
[9] Yale Center for Astronomy & Astrophysics, Department of Physics (JWG 460), Yale University, P.O. Box 208121, New Haven CT 06520-8121, USA

Abstract. The first Spitzer images from the GOODS survey have revealed detections of all the Extreme X-ray / Optical sources ('EXO's) in the CDF-South. These X-ray sources are completely undetected in our deep optical GOODS HST/ACS imaging, to limits that place them at the extreme end of the $F_{\rm X}/F_{\rm opt}$ parameter space, with values about 100 to 1000 times higher than generally found for Active Galactic Nuclei (AGN). We use their Spitzer detections to investigate two possible scenarios for their nature: (1) their hosts could be extremely faint, obscured high-redshift Extremely Red Objects (EROs), at redshifts about 2 - 5, thus higher redshift than previously studied EROs; (2) some of them could lie at redshifts above about 6 - 7, such that their Lyman-alpha emission is completely redshifted into the IR. In either case, these objects serve as a valuable probe of black hole growth and accretion activity in the early universe.

1 Introduction

A key question in astrophysics concerns the evolution of active galactic nuclei (AGN) during the "quasar epoch" and earlier ($z \sim 2-6$), where their space density evolves rapidly [9,10,3]. Their evolution appears to track the star formation rate [17] thereby suggesting an empirical link between galaxy growth and AGN fuelling. A connection between galaxies and AGN is also suggested by the black hole / bulge mass relationship [11,12].

X-ray emission provides a powerful tool to investigate such relationships since it directly tracks AGN accretion luminosity. Ultra-deep *Chandra* X-ray surveys on the Hubble Deep Field North (HDFN [4]), and Chandra Deep Field South

ESO Symposia: Growing Black Holes, pp. 120–125, 2005.

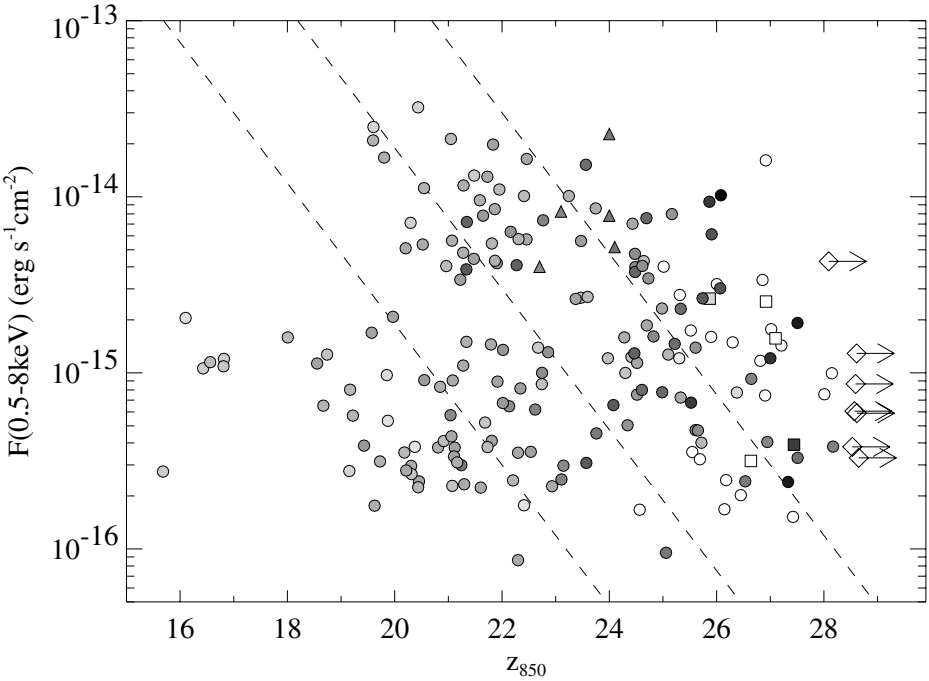

Fig. 1. Total X-ray flux ($0.5-8\,\mathrm{keV}$) against z_{850} magnitude for all the CDFS X-ray sources [16], including those unidentified in z_{850} (indicated by diamonds with arrows). Lines indicate $F_{\mathrm{X}}/F_{\mathrm{opt}} = 0.1, 1, 10$. Symbol shading shows the $z_{850} - K$ colour of each source, ranging from light to dark for $z_{850}-K \sim 0-5$. White symbols (no shading) were undetected in K. Squares show our measured ACS magnitudes for sources reported as undetected in ground-based data [19], and triangles indicate X-ray selected EROs in the Lockman Hole [18].

(CDFS [13]) are sufficiently sensitive to reveal AGN up to cosmological distances. The GOODS survey [14,8] obtained multi-band coverage on these fields with *Hubble*, *Spitzer*, and large ground-based telescopes, providing deep images across a wide wavelength range.

In particular, an interesting class of sources discovered from these surveys are sources with extreme X-ray / Optical flux ratios (*"EXO"*s [16]), that are detected in X-rays and the near-IR, but completely undetected in the optical to $m(AB) \sim 28$. They are all detected in the mid-IR by *Spitzer*, and here we discuss possible interpretations for them and their relationship to AGN evolution. Throughout this paper we adopt a standard ΛCDM cosmology.

2 Selection of EXO's

The EXO's in the CDFS were identified by matching the X-ray catalogs [2] to the ACS z_{850} catalogs [14], and are shown in Figure 2. Most of the 225 X-ray sources

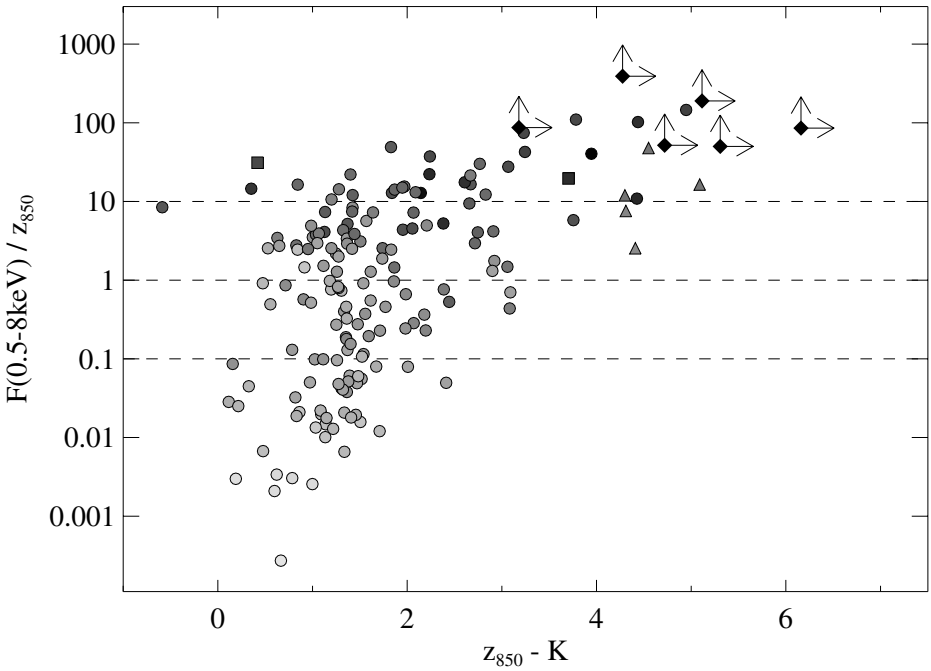

Fig. 2. Ratio of $F_{0.5-8\,\mathrm{keV}}$ to z_{850} flux for all the CDFS X-ray sources, plotted against $z_{850} - K$ [16]. Shading represents z_{850} magnitude, fainter sources being darker. Normal galaxies and starbursts ($F_{\mathrm{X}}/F_{\mathrm{opt}} \lesssim 0.1 - 1$) are relatively blue, and the only redder objects are those with higher $F_{\mathrm{X}}/F_{\mathrm{opt}}$.

in the ACS field have optical counterparts, and consist either of moderate-luminosity AGN or star-forming galaxies. However, 7 of the X-ray sources have no ACS counterparts; furthermore, when their X-ray fluxes are compared with their optical limits, they are found to have a ratio of $F_{0.5-8\,\mathrm{keV}}/F_{\mathrm{z850}}$ 100, at least an order of magnitude above most AGN. In Figure 2 we also plot our measured ACS magnitudes for CDFS sources reported as undetected in ground-based data by [19], and show Extremely Red Objects (EROs) from previous studies [1,15,18].

Our recent *Spitzer* observations of the CDFS were obtained using the IRAC instrument in all four channels: 3.6, 4.5, 5.8, 8 μm. In the first epoch, most of the field was covered by only two bands (either 3.6 and 5.8 μm, or 4.5 and 8 μm), with only one EXO covered by all 4 channels. However, it is clear that all the EXO's are readily detected by *Spitzer*, as shown in Figure 3.

Six of the EXO's are detected in K-band with $AB(K) \sim 22 - 24$, thus their $z - K$ colours are redder than almost all the other X-ray sources, with $z_{850} - K \gtrsim 4.2 - 6.2$. Both their high X-ray/optical ratios and their red colours are interesting, since it is not expected *a priori* that optically undetected objects should have strong X-ray flux, nor that they should be particularly red (see also [5,6]).

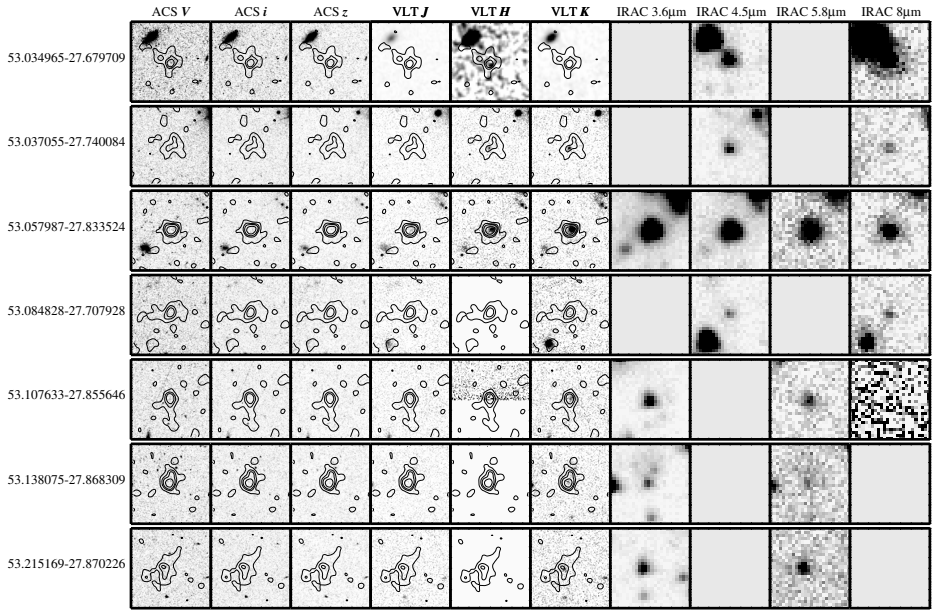

Fig. 3. The 7 EXO's in the CDFS [16], showing the ACS non-detections as well as the VLT JHK images. Each panel is $15''$ on a side, with contours showing the $0.5-8$ keV *Chandra* detections. We also show the *Spitzer* IRAC images, which readily detect all the EXO's.

3 Possible Constituents of the "EXO" Population

Using our optical, near-IR and *Spitzer* data, we have carried out some preliminary SED modelling of the EXO's in order to investigate their nature. The fundamental observational features that need to be explained are: (1) their extremely red optical/near-IR colours; (2) their red near-IR/mid-IR colours; and (3) their colours as measured within IRAC, most of which are red although one or two of the sources have flat or blue spectra within IRAC. Since we observe no optical flux at all, it is highly unlikely that any of these objects are Type 1 unobscured AGN, since their X-ray flux is relatively bright and some optical flux would have been expected. Therefore, we consider a scenario where the light from the AGN itself is obscured and the emission is dominated by the host galaxy, thus we aim to understand these objects by modelling their host galaxy stellar populations.

We examined both single-burst and continuous star-forming populations [7], exploring a parameter space defined by age, reddening, metallicity, and redshift. For each source, we computed SEDs covering a range of values for each parameter, then determined the best-fitting SED based on a chi-squared minimization of the SED compared with the multi-band photometry of the source, taking into account the optical non-detections as well as the measured fluxes in the near-IR and Spitzer bands.

We find that in general, the EXO's are well fit by sources with either an evolved single-burst population or a younger reddened star-forming population, at $z \sim 2-5$. A common feature of the best-fitting models is that the stellar mass is relatively low when compared with the host galaxies of most other AGN of similar X-ray luminosity: their stellar masses tend to lie in the range $\sim 10^9-10^{10} M_\odot$. Their X-ray luminosities are in the range $L_X \sim 10^{44} - 10^{45}$ erg s^{-1}, and locally AGN of this luminosity tend to be found in galaxies with a mass $\sim 10^{11} M_\odot$, thus the EXO host galaxies appear to be about a factor of 10 intrinsically underluminous, or under-massive, compared to what would be expected based on their X-ray luminosity.

The EXO's are also at higher redshifts ($z \sim 2-5$) than ERO's or other lower-z populations, thereby making the EXO's a valuable tracer of galaxies that are undergoing relatively intense star formation activity at high redshifts. We note that one of the objects is not well fitted by any stellar models with redshifts below $z \sim 6-7$; if fit with a $z \sim 7$ dusty starburst, its mass is $\sim 10^{10} M_\odot$. This source has much redder IRAC colours than any of the other EXO's, which is what drives the SED constraints. However, our near-IR data on this source are not as deep as some of the other EXO's, and we aim to obtain further data on this source in order to investigate it further.

4 Conclusions

We have presented new *Spitzer* data on Extreme X-ray / Optical sources (EXOs) that were detected in the GOODS survey of the CDF-South. These sources have $F_{\rm X}/F_{\rm opt}$ at least an order of magnitude above those typically found for AGN. They are generally undetected in the optical, some are detected in our near-IR VLT imaging data, and all of them are detected in the first *Spitzer* IRAC imaging of CDFS in the $3.6-8\,\mu$m bands. We have used the resulting photometry to perform SED fitting of the sources, and find that some of them are well fit by evolved SEDs, while the remainder are better fit by dusty, reddened star forming populations. The best-fitting redshifts lie between about $\sim 2-5$, thereby placing these sources at higher redshifts than most other samples of ERO's or star-forming galaxies. One of the EXO's is not well fit by any SEDs below $z \sim 7$, thereby making it a potential tracer of very high redshift AGN activity.

We also find that the majority of the EXO's appear to be explained by relatively under-luminous, or under-massive, host galaxies compared with their X-ray emission, or conversely, their X-ray emission appears enhanced over what would normally be expected. A possible explanation for this may be a period of increased AGN luminosity, for example related to the dusty starforming activity that is indicated by the SEDs. The extinction form the dust would also account for the fact that their nuclei appear to be completely obscured at optical wavelengths. If this is the case, then these objects are likely a valuable tracer of enhanced AGN accretion associated with galaxy interaction events at high redshift.

References

1. Alexander, D., Vignali, C., Bauer, F., Brandt, W. N., Hornschemeier, A., Garmire, G., & Schneider, D. 2002, AJ 123, 1149
2. Alexander, D., Bauer, F., Brandt, W. N., Schneider, D., Hornschemeier, A., Vignali, C., Barger, A., Broos, P., Cowie, L., Garmire, G., Townsley, L., Bautz, M., Chartas, G., & Sargent, W. 2003, AJ 126, 539
3. Barger, A., Cowie, L., Capak, P., Alexander, D., Bauer, F., Brandt, W. N., Garmire, G., & Hornschemeier, A. 2003, ApJ 584, L61
4. Brandt, W. N., Hornschemeier, A., Alexander, D., Garmire, G., Schneider, D., Broos, P., Townsley, L., Bautz, M., Feigelson, E., & Griffiths, R. 2001, AJ 122, 1
5. Brusa, M., Comastri, A., Daddi, E., Cimatti, A., Mignoli, M., & Pozzetti, L. 2002, ApJ 581, L89
6. Cagnoni, I., Elvis, M., Kim, D. W., Nicastro, F., & Celotti, A. 2002, ApJ 579, 148
7. Charlot, S. & Bruzual, G. 2003, MNRAS 344, 1000
8. Dickinson, M. et al. 2004, in preparation
9. Fan, X. et al. 2001, AJ 121, 54
10. Fan, X. et al. 2003, AJ 125, 1649
11. Ferrarese, L. & Merritt, D. 2000, ApJ, 539, 9
12. Gebhardt, K., Kormendy, J., Ho, L., Bender, R., Bower, G. Dressler, A., Faber, S., Filippenko, A., Green, R., Grillmair, C., Lauer, T., Magorrian, J., Pinkney, J., Richstone, D., & Tremaine, S. 2000, ApJ, 539, 13
13. Giacconi, R., Zirm, A., Wang, J. X., Rosati, P., Nonino, M., Tozzi, P., Gilli, R., Mainieri, V., Hasinger, G., Kewley, L., Bergeron, J., Borgani, S., Gilmozzi, R., Grogin, N., Koekemoer, A., Schreier, E., Zheng, W. & Norman, C. 2002, ApJS 139, 369
14. Giavalisco, M. et al. 2004, ApJL, 600, L93
15. Koekemoer, A. M., Grogin, N. A., Schreier, E. J., Giacconi, R., Gilli, R., Kewley, L., Norman, C., Zirm, A., Bergeron, J., Rosati, P., Hasinger, G., Tozzi, P., & Marconi, A. 2002, ApJ, 567, 657
16. Koekemoer, A. M., Alexander, D. M., Bauer, F. E., Bergeron, J., Brandt, W. N., Chatzichristou, E., Cristiani, S., Fall, S. M., Grogin, N. A., Livio, M., Mainieri, V., Moustakas, L. A., Padovani, P., Rosati, P., Schreier, E. J., & Urry, C. M., 2004, ApJL 600, L123
17. Steidel, C., Adelberger, K., Giavalisco, M., Dickinson, M., & Pettini, M. 1999, ApJ 519, 1
18. Stevens, J., Page, M., Ivison, R., Smail, I., Lehmann, I., Hasinger, G. & Szokoly, G. 2003, MNRAS 342, 249
19. Yan, H., Windhorst, R., Röttgering, H., Cohen, S., Odewahn, S., Chapman, S., & Keel, W. 2003, ApJ 585, 67

The Masses of X-ray Emitting EROs

M. Brusa[1], A. Comastri[2], E. Daddi[3], L. Pozzetti[2], G. Zamorani[2], C. Vignali[4], A. Cimatti[5], F. Fiore[6], M. Mignoli[2], P. Ciliegi[2], H.J.A. Röttgering[7]

[1] MPE - 85740 Garching, Germany
[2] INAF – Osservatorio Astronomico di Bologna, Bologna, Italy
[3] ESO, Garching bei Muenchen, Germany
[4] Dipartimento di Astronomia Universita' di Bologna, Bologna, Italy
[5] INAF – Osservatorio Astrofisico di Arcetri, 50125 Firenze, Italy
[6] INAF – Osservatorio Astronomico di Roma, 00040 Monteporzio, Italy
[7] Sterrewacht Leiden, PO Box 9513, 2300 RA, Leiden, The Netherlands

Hard X–ray surveys efficiently sample the obscured AGN population and in particular those with redder colors which would not be selected by UVX surveys. The discovery that a sizable fraction ($\sim$ 20%) of hard X–ray sources are also associated to extremely red objects (EROs) with optical to near–infrared colour R-K>5 is even more intriguing [1,2,1].

We will briefly discuss how it is possible, combining near–infrared and X–ray data, to constrain the masses of the black holes powering the X–ray emission in AGN EROs. We have considered a sample of 128 X–ray detected EROs, both from our XMM-*Newton* survey of optically selected EROs in the "Daddi Field" [4] and from published deep and medium deep hard X–ray surveys [2,5,2,7–10]. A linear correlation characterized by a relatively small scatter appears to be present between the X–ray and K–band fluxes of X–ray emitting EROs (see left panel of Figure 1). and it is similar to that observed for Broad Line AGN. This relation is present despite the large redshift range of our sources and may reflect a proportionality also between the luminosities, $L_X \propto L_K$. Such a correlation is reminiscent of the ones observed locally between the BH mass and the global galaxy properties [5,3,13] and may be related to them.

In order to test such a possibility we have considered those EROs with a secure spectroscopic identification (21) and the 9 EROs in our XMM–*Newton* observation for which the redshifts have been estimated via the Fiore et al. (2003) relation. Although EROs and bluer AGN have similar X/K ratio, we limited our analysis to EROs since there are several indications that the near–infrared emission of these X–ray selected *obscured* AGN is dominated by their host galaxy starlight [2,10]. The rest–frame K–band luminosities have been thus computed using an evolving *elliptical* galaxy template to properly account for the K–corrections. The results are shown in the right panel of Fig. 1. The correlation between the near–infrared and X–ray luminosities observed for these high–redshift EROs (i.e. $L_X \propto L_K$) closely resembles that between the BH mass and the K band luminosity for a sample of local galaxies [13]. Assuming that the X–ray luminosity of our AGN EROs is proportional to the BH mass (i.e. the Eddington ratio $L/L_{\rm Edd}$ and the bolometric correction $k_{\rm bol}$ are not a strong function of the BH mass) the observed correlation implies $L_{\rm K} \propto M_{\rm BH}$. It is thus possible to tentatively constrain the BH masses that would follow if also the nor-

ESO Symposia: Growing Black Holes, pp. 126–127, 2005.

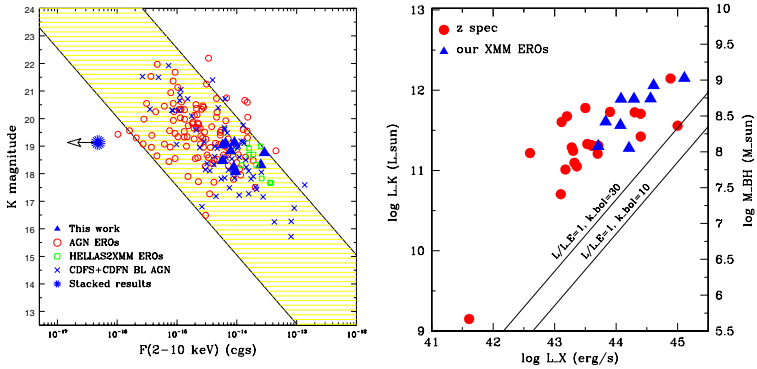

Fig. 1. *Left panel*: K band magnitudes vs. 2-10 keV flux for AGN EROs and BL AGN. *Right panel*: K–band luminosities versus the 2–10 keV X–ray luminosities. The two continuous lines represent the expected correlation computed for Eddington limited accretion ($L_{\rm bol}/L_{\rm Edd} = 1$) and for two different values ($k_{\rm bol}$=30 and $k_{\rm bol}$=10) of the bolometric correction. Symbols as labeled. See [4] for details.

malization of such relation does not significantly evolve with redshift, if not for the expected change of stellar mass to light ratio of the host galaxies due to the evolution of the stellar populations (our AGN EROs sample being at $z = 1$–2). The resulting M_{BH} are reported in the the right axis of the Figure. Although the discussion above has been conducted only in a qualitative way and neglecting the uncertainties and scatter associated to the observed relations, it appears fully reasonable that the close correlation that we have detected between the X–ray flux and the K–band magnitude of AGN EROs is the high redshift analogous of the correlations observed locally, implying a close connection between the black hole and AGN host galaxies also at earlier epochs ($z = 1 - 2$).

References

1. I. Lehmann, et al.: in *X-rays at Sharp Focus* ASP Conf. Proc. 262, p. 105 (2001)
2. V. Mainieri, et al.: A&A **393**, 425 (2002)
3. D.M. Alexander, et al.: AJ **123**, 1149 (2002)
4. M. Brusa, et al.: A&A, in press (2004)
5. C. Willott, et al.: MNRAS **339**, 397 (2003)
6. A.J. Barger, et al.: AJ **126**, 632 (2003)
7. G.P. Szokoly, et al.: ApJS, in press (2004) 2004)
8. C.S. Crawford, et al.: MNRAS **324**, 427 (2001)
9. M. Brusa, et al.: A&A **409**, 65 (2003)
10. M. Mignoli, et al.: A&A **418**, 827 (2004)
11. K. Gebhardt, et al.: ApJ **539**, L13 (2000)
12. L. Ferrarese, D. Merritt: ApJ **539**, L9 (2000)
13. A. Marconi, L. Hunt: ApJ **589**, L21 (2003)
14. F. Fiore, et al.: A&A **409**, 79 (2003)

Why Are Only High-Redshift Obscured AGN Bright Submillimeter Sources?

F.J. Carrera[1], M.J. Page[2], J.A. Stevens[3], and J.P.D. Mittaz[4]

[1] Instituto de Física de Cantabria (CSIC-UC), Santander, Spain
[2] Mullard Space Science Laboratory-UCL, Dorking, United Kingdom
[3] ATC, Royal Observatory, Blackford Hill, Edinburgh, United Kingdom,
[4] Dept. of Physics, University of Alabama, Huntsville, United States

1 Submillimetre photometry of obscured and unobscured AGN

The bulk of the QSO luminosity density was produced at $1 < z < 3$, and with 0.5-2 keV luminosities close to the break of the X-ray luminosity function [6,5]. We have used sensitive submillimetre (submm) observations [8,9,12] (using SCUBA at the JCMT) to show that the submm luminosities of unabsorbed and absorbed broad line QSO in those intervals are radically different ($> 3\sigma$): only 1 out of 20 unabsorbed QSO has been detected, while 8 out of 19 absorbed QSOs have been detected, all of them are ULIRGs at $z > 1.5$ (see Fig. 1). Furthermore, there is a significant correlation between the far infrared luminosity L_{FIR} and the redshift of the absorbed QSOs. The FIR emission of these objects is due to dust heated by starbursts, rather than reprocessed QSO emission [8,12]. The implied star formation rates (SFR) are > 1000 $M_\odot$/y, sufficient to build a substantial fraction of a galaxy spheroid in only a few 100 Myr.

We have argued [9,12] that: (1) the relative space densities of absorbed and unabsorbed QSOs indicate that the duration of absorbed phase is ∼15% that

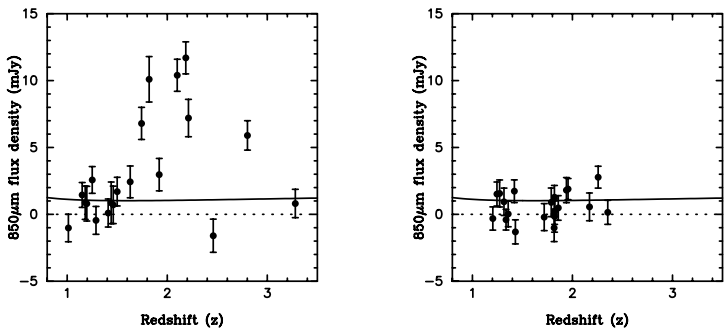

Fig. 1. 850 μm flux densities of the sample of 19 X-ray absorbed QSOs (left panel) and 20 X-ray unabsorbed QSOs(right panel). The solid line on both panels shows the predicted 850 μm flux density of the nearby submillimetre luminous, X-ray absorbed QSO Mrk 231 if it were viewed at redshift z

ESO Symposia: Growing Black Holes, pp. 128–129, 2005.

of the unabsorbed phase (2) unabsorbed QSOs have already built most of their stellar mass implying that the absorbed phase precedes the epoch of luminous unobscured QSO activity (3) the X-ray luminosities of the absorbed sources imply that they contain BH of mass $> 10^8$ $M_\odot$.

This, together with the strong correlation between L_{FIR} and z, lead us to conclude that absorbed QSOs are observed during a transition phase between their highly-obscured growth and a period of unabsorbed QSO activity. The population of high redhsift submillimetre luminous galaxies selected in blank field surveys and the CDFN by SCUBA (e.g. [10,2,3]) and MAMBO [4] have Seyfert-like X-ray luminosities and might be in an earlier growth stage than our absorbed QSOs. This is in agreement with the predictions of models with joint spheroid/QSO evolution within a hierarchical clustering scenario [10].

2 Large scale structure around RXJ094144.51+385434.8

SCUBA submm imaging of a region around RXJ094144 (one of our submm-bright obscured QSOs at $z = 1.819$) reveals a remarkable ∼400 kpc long filament of galaxies, each with an obscured star formation rate enough to build a massive spheroid in less than 1Gyr [11]. This order-of-magnitude overdensity of galaxies [10] implies that they are probably associated with the QSO. We suggest that their star formation is triggered by galaxy mergers or encounters within the filament, as predicted by hierarchical models of galaxy formation. We argue that these systems are the precursors of elliptical galaxies found today in the core regions of all rich galaxy clusters.

Our observations suggest that strong absorption in the X-ray spectra of high-redshift QSOs may result from gas brought about by mergers, rather than by orientation effects.

References

1. D.M. Alexader, et al.: AJ **125**, 383 (2003)
2. S.C. Chapman, A.W. Blain, R.J. Ivison, I. Smail: Nature **422**, 695 (2003)
3. G.L. Granato, G. DeZotti, L. Silva, A. Bressan, L. Danese: ApJ **600**, 580
4. T.R. Greve, R.J. Ivison, F. Bertoldi, J.A. Stevens, J.S. Dunlop, D. Lutz, C.L. Carilli: MNRAS, submitted (2004)
5. T. Miyaji, G. Hasinger, M. Schmidt: A&A, **369**, 49
6. M.J. Page, K.O. Mason, I.M. McHardy, L.R. Jones, F.J. Carrera: MNRAS **291**, 324 (1997)
7. M.J. Page, J.P.D. Mittaz, F.J. Carrera: MNRAS **325**, 575 (2001)
8. M.J. Page, J.A. Stevens, J.P.D. Mittaz, F.J. Carrera: Science **294**, 2516 (2001)
9. M.J. Page, J.A. Stevens, R.J. Ivison, F.J. Carrera: ApJL **611**, 85 (2004)
10. I. Smail, R.J. Ivison, A.W. Blain, J.-P. Kneib: MNRAS **331**, 495
11. J.A. Stevens, M.J. Page, R.J. Ivison, I. Smail, F.J. Carrera: ApJL **604**, 17 (2004)
12. J.A. Stevens, M.J. Page, R.J. Ivison, F.J. Carrera, J.P.D. Mittaz, I. Smail: MNRAS, submitted (2004)

VLT Adaptive Optics Imaging of QSO at z ∼ 2.5

R. Falomo[1], J. Kotilainen[2], R. Scarpa[3], and A. Treves[4]

[1] INAF, Osservatorio Astronomico di Padova, Vicolo dell'Osservatorio 5 I-35122 Padova, Italy
[2] Tuorla Observatory, University of Turku Väisäläntie 20 FIN-21500 Piikkiö, Finland
[3] European Southern Observatory, 3107 Alonso de Cordova Santiago, Chile
[4] Università dell'Insubria, Dip. di Fisica, Via Valleggio 11 I-22100 Como, Italy

Abstract. We report on ESO–VLT near-IR adaptive optics imaging of one radio-loud and two radio quiet quasars at z > 2. In the first case we are able to resolve the QSO and find that it is hosted by an elliptical of $M_K = -27.6$. This result, though restricted to a single object, extends up to z=2.5 the finding that cosmic evolution of radio-loud hosts follows the trend expected for luminous and massive spheroids undergoing passive evolution.

1 The Program

Ground–based imaging together with higher resolution HST data clearly show that in the local universe (z<0.5) powerful quasars are found in massive galaxies dominated by the spheroidal component. At higher redshift (up to z ∼ 2) the few available data seem to confirm this scenario in particular indicating that the luminosity of quasar host galaxies is consistent with that of massive spheroids undergoing passive evolution. In this context it is therefore very important to push as far as possible in redshift the direct detection and characterization of QSO host galaxies. However, the properties of quasar hosts at high redshift are very difficult to characterize because of the severe difficulties of getting direct information on these galaxies. This information is difficult to attain with HST because of its modest aperture that translates into a limited capability to detect faint extended nebulosity. One has thus to resort to 10 meter class telescopes equipped with adaptive optics (AO) systems.

In order to investigate the properties of quasar hosts near the peak of QSO activity we have carried out a pilot program to secure K band images of quasars in the redshift range $2 < z < 3$ using the AO system at the VLT. We have selected quasars in this redshift range and $\delta < 0$, having a star brighter than V=14 within 30 arcsec. In these conditions the AO system at the VLT is expected to deliver images of Strehl ratio better than ∼ 0.2 when the external seeing is <0.6 arcsec. Here we present preliminary results for one radio-loud (PKS 0113–283) and two radio-quiet (Q 0045-3337 and Q0101-337) quasars. $H_0 = 70$ km s^{-1} Mpc^{-1}, $\Omega_m = 0.3$, and $\Omega_\Lambda = 0.7$ are used.

ESO Symposia: Growing Black Holes, pp. 130–131, 2005.

2 Results

K-band images were secured in service mode using NAOS - CONICA at VLT under good seeing conditions. The image of Q 0045-3337 shows the presence of a likely foreground disc galaxy at 1.2 arcsec from the QSO to the QSO which is acting as a gravitational lens on the QSO since the angular distance is likely smaller than the Einstein ring. However no multiple images are detected. In the case of Q0101-337 no host galaxy was clearly detected but a number of faint galaxies are detected in the immediate environment suggesting this high z QSO belongs to a group of distant galaxies.

Extended nebulosity surrounding the nucleus was clearly detected for the radio loud quasar. The host galaxy is a luminous giant elliptical: K=19.1 ± 0.3 corresponding to M_K = -27.6 (including K-correction) and an effective radius Re = 7.5 ± 3 kpc. The luminosity of this z∼2.6 quasar host taken, together with the available data on quasar hosts for lower redshift objects (see Figure 1), indicate that up to quite high redshift, radio loud quasars are hosted by massive fully formed galaxies. This result contrasts with the expectation of the hierarchical merging scenario for the formation and evolution of spheroidal galaxies which predicts they should be smaller and less massive in the past.

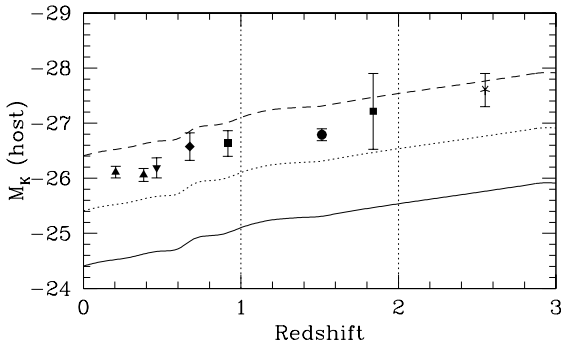

Fig. 1. The evolution of radio loud quasar host luminosity compared with that expected for massive ellipticals (at M^*, M^*-1 and M^*-2; *solid, dotted and dashed* line) undergoing passive stellar evolution. The new detected host galaxy at z ∼ 2.5 (asterisk) is compared with the data for samples of lower redshift RLQ presented in [1]. Each point is plotted at the mean redshift of the considered sample while the error bar represents the 1σ dispersion of the mean except for the new detection where the uncertainty of the measurement is given.

References

1. R. Falomo et al.: ApJ, **604**, 495 (2004)

XMM-Newton Observations of Four High-z Quasars

E. Ferrero[1] and W. Brinkmann[2]

[1] Max-Planck-Institut für Extraterrestrische Physik, Garching, Germany
[2] Center for Interdisciplinary Plasma Science, Max-Planck-Institut für Extraterrestrische Physik, Garching, Germany

1 Introduction

High-z quasars are key objects for understanding galaxy formation and evolution, and the physical conditions in the early Universe, since they are the most luminous and distant sources of electromagnetic radiation known. The X-ray emission gives insight into the accretion mechanisms onto super-massive black holes. Current questions are whether quasars exhibit spectral evolution or not and whether absorption in excess of the galactic $N_{\rm H}$ is a general feature of high-z quasars. The X-ray spectral analysis is essential to address these questions. We have performed a spectral analysis of two radio-loud (PKS 2126-158 and PKS 2149-306) and two radio-quiet (Q 0000-263 and Q 1442+2931) $z > 2$ quasars with XMM. For more details see [1].

2 Data Analysis

The results of the spectral analysis are presented in Table 1. We give the power law slopes for the PN fits with free absorption in the 0.2–10 keV energy band. The quoted errors are at the 90% level and the error on $\alpha_{\rm ox}$ is estimated to be less than about 5%. Figure 1 shows the power law fit with galactic absorption to the PN data of PKS 2126-158 over the restricted energy band 2–10 keV, extrapolated to lower energies. This figure clearly demonstrates the necessity for more absorption at low energies.

Table 1. Results of the spectral analysis.

Source	type	z	$m_{\rm V}$	$\alpha_{\rm ox}$ **(1)**	Γ **(2)**	$L_{2-10\ \rm keV}$ [$\times 10^{47}$ erg/s]	$N_{\rm H}$ ($\times 10^{21}$ **cm**$^{-2}$)	$\chi^2_{\rm red}$/dof
PKS 2149−306	RL	2.34	18.5	0.95	1.53±0.02	1.03	0.294	1.08/528
PKS 2126−158	RL	3.27	17.0	1.11	1.51±0.02	1.97	1.1	0.98/492
Q 1442+2931	RQ	2.64	17.0	1.70	1.92±0.07	0.06	galactic	0.87/105
Q 0000−263	RQ	4.10	18.0	1.78	2.19±0.12	0.05	galactic	0.91/64

ESO Symposia: Growing Black Holes, pp. 132–133, 2005.

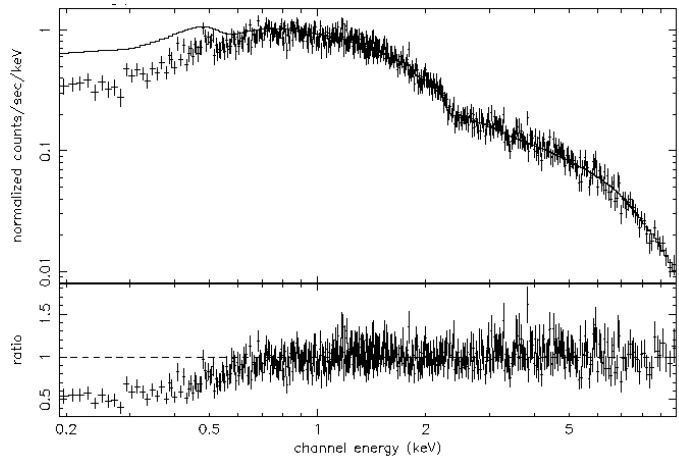

Fig. 1. Power law fit with galactic absorption for PKS 2126-158 over the restricted energy band 2–10 keV, extrapolated to lower energies.

3 Results

For the radio-loud quasars a simple power law with photoelectric absorption is a viable model with photon indices $\Gamma \sim 1.5$, slightly flatter than values commonly found for low redshift objects. We confirm absorption in excess of the galactic value in PKS 2126-158, but not in PKS 2149-306. The data are consistent with both a cold and a warm absorber. The redshift of the absorber is not constrained, but is compatible with being at the source's position. With X-ray luminosities of $\sim 10^{47}$ erg s^{-1} and optical-X-ray broadband spectral index $\alpha_{\rm ox} \sim 1$ they are considerably X-ray brighter than their low redshift counterparts.
For the radio-quiet quasars, we determined reliable spectral parameters for the first time. A simple power law with galactic absorption describes the spectra well, with slopes $\Gamma \sim 2$ similar to the typical low redshift values. The radio-quiet objects have much smaller X-ray luminosities ($L_{\rm X} \sim 10^{45}$ erg s^{-1}) than the two radio-loud quasars and with $\alpha_{\rm ox} \sim 1.7$ they are more X-ray quiet than their low redshift counterparts.

References

1. E. Ferrero & W. Brinkmann, A&A 402, 465 (2003)

Black Hole Mases of the SDSS QSO Sample

E. Ovcharov[1], V. D. Ivanov[2], and P. Nedialkov[1]

[1] Department of Astronomy, Sofia University, 5 James Bourchier, 1164 Sofia, Bulgaria; *evgeni, japet@phys.uni-sofia.bg*
[2] European Southern Observatory, Ave. Alonso de Cordova 3107, Vitacura, Casilla 19001, Santiago 19, Chile; *vivanov@eso.org*

Abstract. This is a progress report on a project to measure the black hole masses of the SDSS quasar sample from their broad emission lines and the continuum luminosity. We have developed an automated procedure to fit the continuum, and to deconvolve the broad and narrow line components. We find good agreement of the derived line parameters for quasars in common with other samples. Next, we plan to investigate the connection of the black hole mass and other quasar parameters, taking advantage of the unprecedented size of the SDSS QSO sample.

1 Introduction

Upon completion, the Sloan Digital Sky Survey [4] will offer a sample of nearly 100,000 QSOs. The goal of this project is to create a database of emission line measurements for them, deconvolving the broad and narrow components, when possible. Next, we will use this catalog to measure the masses of super-massive black holes M_{BH} from the virial theorem: $M_{BH} \sim r \times v^2 / G$, where v is the velocity dispersion at radius of the broad line region r, and G is the gravitational constant. It is assumed that the emitting gas is gravitationally bound to the BH. Here v is equal to the FWHM of the broad lines [5]. The radius r can be determined from the empirical correlation between the size of the BLR and the continuum luminosity [5]. Calibrations for MgII $\lambda\,2799$ Å, and Hβ are available from [4], and for C IV $\lambda\,1549$ Å from [6].

2 Results and Discussion

We have developed an automatic tool that: **(i)** fits a power-law to the continuum and subtracts it, using the continuum pass bands defined by [2], and **(ii)** deconvolves the emission lines into broad and narrow components via χ^2 minimization. The uncertainties are estimated via Monte-Carlo simulation. Examples of some fitted spectra (after the continuum removal) are shown in Figure 1. We compared our measurements with the literature (Figure 2) and obtained reasonable agreement, given the limited number of objects.

The quality of the data is crucial for the analysis: S/N$\geq$20 is needed to obtain well-constrained line decomposition. The typical accuracy of FWHM is usually 100-500 km s^{-1} for the narrow lines width and 500-1000 km s^{-1} for the broad ones. The intervening absorption is a major problem: the strong cases are easy

ESO Symposia: Growing Black Holes, pp. 134–135, 2005.

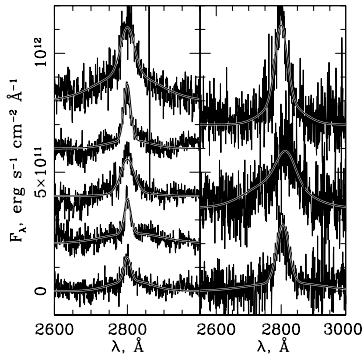

Fig. 1. Example of fits to the MgII λ 2799 Å line for a subset of the SDSS QSOs. The middle QSO on the right panel shows intervening absorption.

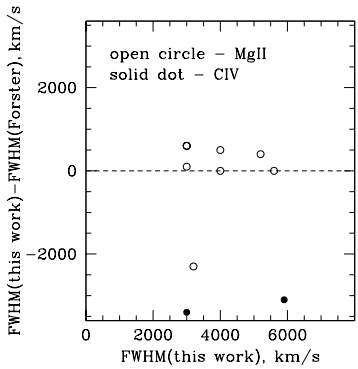

Fig. 2. Comparison of our FWHMs with those from [2]. Single component fits were used for compatibility. The differences may partially be due to variability.

to detect automatically and we skip them but the weaker ones are hard to detect and they can affect the measured line parameters significantly. These constraints are likely to limit our automatic processing to $\sim 20\%$ of the SDSS QSO sample.

Acknowledgments: This research was partially supported by the grant F-1302/2003 with the National Science Foundation, Bulgaria.

References

1. G. R. Richards, X. Fan, H. Newberg, et al.: AJ, **123**, 2945 (2002)
2. K. Forster et al.: ApJ, **134**, 35 (2001)
3. S. Kaspi et al.: ApJ, **533**, 631 (2000)
4. R. J. McLure & M. J. Jarvis: MNRAS, **337**, 109 (2002)
5. B. M. Peterson & A. Wandel: ApJ, **521**, L95 (1999)
6. M. Vestergaard: ApJ, **571**, 733 (2002)

Beyond the Spectroscopic Limit in the GOODS/CDFS Survey

V. Mainieri[1] and the GOODS/CDFS team

[1]Max-Planck-Institut fuer extraterrestrische Physik, Giessenbachstrasse, D-85748 Garching bei Munchen, Germany

1 Optically Faint Sources in GOODS/CDFS

A quarter of the X-ray sources from recent *Chandra* and XMM-*Newton* deep surveys has optical counterparts too faint (R$\geq$25) for spectroscopy, even with the 8-10 m class telescopes. In this work we focus on this subsample of X-ray sources with R$\geq$ 25 and will refer to them as *Optically Faint Sources (OFS)*. This criterium reflects an observational limit beyond which we need to rely on accurate photometric measurements over a large baseline and X-ray spectral information to estimate their redshift and to establish their nature. Since the OFS represent a significant fraction of the entire X-ray sample, they have an important impact on statistical studies, such as the X-ray luminosity function, the evolution of the TypeI/TypeII ratio and the overall N_H distribution. A first study on the nature of the OFS (I$\geq$ 24) in the Chandra Deep Field North was done by [1].

We take advantage of the unique multi-wavelength coverage of the GOODS survey in the Chandra Deep Field South to constrain the redshift distribution of OFS. An area of $\approx$ 160 arcmin^2 of GOODS/CDF-S has been imaged with ACS/HST in the F435W, F606W, F775W and F850LP bands [3]. A large program with the VLT is under way to image the GOODS area in the J, H, K_s bands, using some 32 ISAAC fields to mosaic a 150 arcmin^2 region (Vandame et al. in preparation)[1]

2 The redshift distribution

We have used the public available code BPZ [2][2] to compute photometric redshifts for the OFS and tested their reliability by comparing them with secure spectroscopic redshifts [5].

We compare in Fig. 1 the redshift distribution of optically bright (R$<$ 25) and OFS. We use the spectroscopic redshift if known or the derived photometric redshift if the source is still unidentified. We find that a larger fraction of the OFS (76%) sources are at redshift z $>$ 1 compared to the optically bright sample (49%). This finding attenuates the disagreement between the observed redshift distribution in *Chandra* deep fields and the one predicted by XRB models, as

[1] see:http://www.eso.org/science/goods/
[2] BPZ is available from http://acs.pha.jhu.edu/~txitxo/

ESO Symposia: Growing Black Holes, pp. 136–137, 2005.

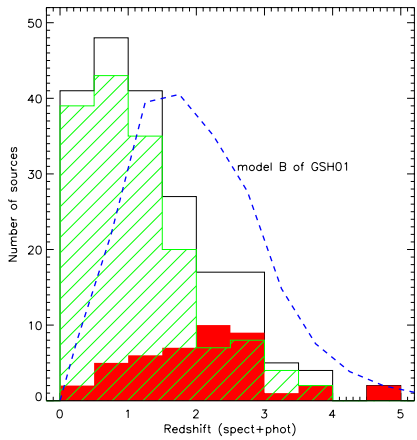

Fig. 1. Distribution of redshifts (spectroscopic and photometric) for the Optically faint (shaded histogram), Optically bright (hatched histogram) and the total X-ray sample (empty histogram). Sources belonging to the large scale structures in the CDF-S have been excluded. The dashed line is the redshift distribution predicted by the model B of Gilli, Salvati and Hasinger [4] normalized to the total number of sources in the "GOODS area" for which we have either a spectroscopic or a photometric redshift.

the majority of the still unidentified X-ray sources in these deep fields are OFS. However, a significant disagreement still remains. One solution would involve implementing a new X-ray luminosity function for AGN in the XRB synthesis models, by combining Deep *Chandra* and XMM-*Newton* fields with shallower surveys.

3 X-ray absorption

Several dignostics clearly indicate that the majority of the OFS are X-ray absorbed. Their hardness ratio distribution is biased toward hard values, indicating a large fraction of the OFS with a flat X-ray spectrum probably due to intrinsic absorption. Their optical/near-IR photometry is dominated by the emission of the host galaxies and their colours are in average red (65% are EROs, R-K$\geq$ 5). We have performed an X-ray spectral analysis and the distribution of N_H values shows that $\sim$ 83% of OFS have column densities larger than 10^{22} cm^{-2}.

References

1. Alexander, D.M., Brandt, W.N., Hornschemeier, A.E.,et al., AJ, **122**, 2156 (2001)
2. Benitez, N. 2000, ApJ, **536**, 2000 (2000)
3. Giavalisco, M., Ferguson, H.C., Koekemoer, A.M., et al., ApJL, **600**, 93
4. Gilli, R., Salvati, M., & Hasinger, G. , A&A, **366**, 407 (2001)
5. Szokoly, G.P., Bergeron, J., Hasinger, G., et al., AJS in press, [astro-ph/0312324]

AGN and Starbursts Already Massive at z > 3

B. Rocca-Volmerange and M. Remazeilles

Institut d'Astrophysique de Paris, 98 bis Bd Arago F-75014 Paris, France

Abstract. The most massive galaxies are powerful radio emitters with maximum masses of $\simeq 10^{12}$ $M_\odot$ [6] and massive black holes of $\simeq 10^9$ $M_\odot$, even at $z = 4$. These results impose short time-scales of mass accumulation and star formation. Moreover from continuous X to radio observations, we show that the powerful 3CR radio galaxies are highly dissipative at $\simeq$ 8microns (Rocca-Volmerange & Remazeilles, in press). By following the evolution of stellar dissipation sources with our evolutionary code, we check that galaxies hosting active nuclei have cooling time-scales of the same order than their self-gravitation time-scales, satisfying to the critic value of the Rees & Ostriker [5] model.

1 The most massive galaxies host massive black holes

In a recent article [6], we showed that the distribution of galaxies in the K-band Hubble diagram is fully covered by the predictions of elliptical galaxy masses of 10^{9-12} $M_\odot$. The maximum limit 10^{12} $M_\odot$ fits the well delimitated relation K-z populated by the most powerful radio sources, even at z=4. Because no brighter galaxies are observed, this line defines the fragmentation limit of the dissipative gravitational model of Rees & Ostriker [5]. Fig. 1 compares the predictions of ellipticals formed at the redshift z_{for}=30. It confirms the results

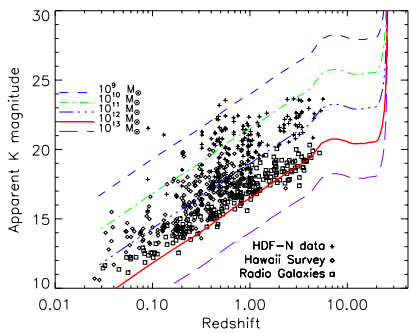

Fig. 1. Five mass sequences of elliptical galaxies reproducing the K-band Hubble diagram: the K-z relation traced by radio galaxies formed at z_{for}=30 traces the maximum mass limit (see [6].

ESO Symposia: Growing Black Holes, pp. 138–139, 2005.

on the fragmentation limit derived at z_{for}=10 in [6]. We use the evolution code PÉGASE (*www.iap.fr/pegase*, [1]) and its recent extensions on ionized gas (NEBPEG by [4]) based on CLOUDY [2], and on the high spectral resolution with the code PÉGASE-HR [3] allowing spectral synthesis at the resolution power R=10000, also offered to the scientific community.

2 Preliminary estimates of energy dissipation sources

In most computations of dissipation processes used in galaxy formation models, the cooling time-scale is derived from the factor $t_{cool} = T/n\Lambda(\mathrm{T})$ where $\Lambda(\mathrm{T})$ is the cooling function of an ionized "primordial" mixture of H and He gas initial cloud, see [5] for references. With the evolutionary code for galaxy synthesis, we are able to follow the evolution of the most dissipative processes due to the stellar population (ionized gas, dust, continua and supernovae). Moreover in Rocca-Volmerange and Remazeilles, in press, we find that the powerful active galaxies 3CR are intense sources of dissipation by dust at $\simeq$ 8 microns. Table 1 summarizes the main sources of dissipation by assuming the nucleus is active at 90 Myr when the stellar emission of the elliptical scenario is maximum. The dissipation processes by stars and AGN (evolution of the stellar continuum, evolution of the gas ionized by stars, energy released by gas ionized by AGN, synchrotron, grains) are followed in more details by Rocca-Volmerange and Remazeilles, in press. They confirm that when massive galaxies are active, the corresponding cooling time-scale is of the same order than the gravitational time-scale ($n^{-1/2}$) bringing strong constraints for galaxy formation models. The Spitzer data will rapidly confirm our results.

Table 1. Dissipative energy estimates in 10^{46} ergs. s^{-1}

	Ion. Gas(*)	Ion. Gas(AGN)	Star cont.	Dust	Synchrotron
Age: 90 Myr	0.29	0.050	4.6	7.3	0.3
energy fraction	0.04	0.007	0.63	1.	0.041

References

1. Fioc. M., Rocca-Volmerange, B., A. & A. **326**, 950 (1997)
2. Ferland, G: HAZY, Univ. of Kentucky, Intern. Rep. (1996)
3. Le Borgne, D.,et al.: astro-ph/0408419 (2004)
4. Moy, E., Rocca-Volmerange, B., Fioc, M.: A & A, **365**, 347 (2001)
5. Rees, M., Ostriker, J.: MNRAS, **179**, 541 (1977)
6. Rocca-Volmerange, B., et al.: A & A, **415**, 931 (2004)

VLT Optical Spectroscopy of BL Lac Objects

B. Sbarufatti[1], A. Treves[1], R. Falomo[2], J. Heidt[3], J. Kotilainen[4], and R. Scarpa[5]

[1] Università dell'Insubria, Dip. di Fisica, Via Valleggio 11 I-22100 Como, Italy
[2] INAF, Osservatorio Astronomico di Padova, Vicolo dell'Osservatorio 5 I-35122 Padova, Italy
[3] Lanenssterwarte Heidelberg, Königstuhl D-69117 Heidelberg, Germany
[4] Tuorla Observatory, University of Turku Väisäläntie 20 FIN-21500 Piikkiö, Finland
[5] European Southern Observatory, 3107 Alonso de Cordova Santiago, Chile

Abstract. We report here the first results of a program aimed at obtaining high signal to noise (up to ~ 500) optical spectroscopy of a large sample of BL Lac objects using ESO VLT+FORS1. New spectroscopic observations have been obtained for 31 objects, which allows us to obtain new redshift for 13 targets and provide better classification for others. In a number of cases no lines are detected and lower limits to the redshift can be estimated.

1 The Program

BL Lac objects are AGN which are characterized by strong non-thermal emission, high flux and polarization variability, and quasi-featureless optical spectra. The latter property hinders in many cases the determination of the redshift and thus hampers a proper evaluation the physical parameters of the objects.

The weak emission lines are likely generated by fluorescence in clouds as in the other AGN, but their equivalent width could be reduced by the beaming of the continuum emission. On the other hand absorption lines can be produced either from spectral features of the stellar population of the host galaxy or from intervening halos as in the case of quasars (mainly for high redshift sources). The possibility of detecting such lines depends on the ratio between the nucleus and the galaxy luminosity, on the redshift of the source and on the the S/N of the spectra. Previous spectroscopic programs to derive the redshift of BL Lacs used mainly 4m class telescopes and failed to determine the redshift with very weak lines. In order to further explore these sources of unknown redshift we are undertaking a program to obtain high S/N spectra of selected targets using VLT + FORS1 during non optimal sky conditions at Paranal

2 Results

So far we secured spectra for 31 targets. The analysis of these data shows that 24 objects have optical spectra consistent with the BL Lac classification (see table 1), 3 turned out to be high z type 1 QSO, 2 are early type galaxies and 2 are stars. We are able to derive new redshifts for 13 of the 24 confirmed BL Lacs.

ESO Symposia: Growing Black Holes, pp. 140–141, 2005.

For the remaining 11 BL Lacs, in spite of the high S/N spectra, no emission or absorption features are found up to EW limits of a fraction of 1 Å (see table 1). These extremely lineless objects are likely characterized by a high Nucleus to Host Galaxy luminosity ratio. This could be due either to an underluminous host galaxy or to a strongly beamed non-thermal continuum.

Table 1. Spectroscopy of BL Lacs

Object name	z	V	line type	S/N	EW limit (Å)
PKS 0047+02	...	18.0	...	80	0.3
PKS 0048−09	...	17.4	...	250	0.1
02272+0201	0.457	18.8	g	100	0.4
0306+102	0.862	18.0	e	20	2.8
RXJ03162−2607	0.443	17.5	e, g	130	0.4
PKS 0338−214	0.223	16.9	e	200	0.2
PKS 0422+004	...	16.5	...	230	0.4
PKS0426−380	1.105*	18.0	e, a	100	0.5
EXO0556.4−3838	0.302	17.1	g	280	0.2
PKS 0627−19	...	18.7	...	50	1.0
PKS 0723−00	...	18.0	...	250	0.5
0808+019	1.148	17.5	e	140	1.0
1012.2+0631	0.727	16.8	e	200	0.2
1222+102	...	17.6	a	160	1.5
PKS 1250−33	0.856	20.9	e	30	1.0
PKS 1256−229	0.481	18.0	e	40	0.3
PKS 1349−439	...	18.0	...	240	0.2
PKS 1519−273	1.297*	18.5	e	170	0.2
PG1553+113	...	15.0	...	250	0.1
PKS 1722+119	...	15.7	...	350	0.1
PKS2012−01	...	17.4	...	130	0.2
MH 2136−428	0.497	17.1	g	490	0.1
PKS 2254−204	...	17.5	...	220	0.1
S5 2354−02	0.816	21.2	e	30	1.6

*: see also Heidt et al.,2004, A&A, 418, 813.

**: observed spectral features type: e: emission lines; g: host galaxy lines; a: intervening absorptions.

Red Optical Quasars are X-ray Blue Quasars

T. Urrutia[1,2], M. Lacy[1,2,3], R. Becker[1,2], and M. Gregg[1,2]

[1] UC Davis, Department of Physics, 1 Shields Ave., Davis, CA 95616; urrutia@physics.ucdavis.edu
[2] IGPP, L413, Lawrence Livermore National Laboratory, Livermore, CA 94550
[3] Spitzer Science Center, MS 314-6, California Institute of Technology, 1200 E. California Boulevard, Pasadena, CA 91125

Abstract. We have selected a sample of 12 dust-reddened quasars with extremely red colors, reddenigs and redshifts in the range of $0.4 < z < 2.21$ using a combination of various surveys in the radio, infrared and optical. We obtained Chandra observations of these quasars, estimated the column densities towards them, and hence obtained the gas:dust ratios in the material obscuring the quasar. The reddenings do not correlate with the column densities or the hardness ratios in the X-rays. All of the sources show absorbed X-ray spectra, although none of them present Seyfert 2 typical column densities. When we correct the luminosity for absorption, they can be placed among high luminosity quasars, therefore our objects seem to be the high luminosity analogues of the sources contributing to the X-ray background seen in deep X-ray observations.

1 The Sample

To find the bright analogues of the obscured quasars that should make up the X-ray background, we have been selecting red quasars by matching the 2MASS near-infrared survey, the FIRST radio survey and the APM scans of the POSS plates. To find broad lined red quasars we employ two different effective color selection techniques: J - K $>$ 1.7 and R - K $>$ 4, or R - K $>$ 5. The details of this survey can be found in Glikman et al. 2004 [1]. We followed up on 12 of the red quasars with *Chandra*. For the observations the ACIS-S was used in faint mode. We detect all but one of the red quasars in the X-rays.

We constructed spectra for the X-ray sources with more than 40 counts detected. An absorbed power-law model at the quasar redshift was applied to the spectra. For the quasars, where we could extract a spectrum we corrected the luminosity for the absorption given by our deduced column density, which places the quasars among high luminosity quasars. At lower X-ray luminosities we should find higher numbers of them, in agreement with the results from the X-ray deep fields and optical studies [5]. Our quasars represent the high luminosity analogues of the deep Chandra fields, therefore the hard X-ray background cannot be purely made up of Type 2 AGN.

2 Comparison to Optical Data

One of the remarkable results we find, is that all of our red quasars are absorbed to some degree in the X-rays. Most of our sources have a low S/N, so we cannot

ESO Symposia: Growing Black Holes, pp. 142–143, 2005.

get accurate spectral slopes (Γ) and column densities. Yet, from the HRs alone, we can already reach some conclusions. Our sample has a mean HR of 0.08 ± 0.11. This value already is higher than expected in non-biased X-ray surveys, where the median HR of typical quasar lies around -0.5 [2]. We find no obvious correlation between reddening and absorption or hardness ratio. Nevertheless, our values all lie around the area where the column density tends to be around $1.0 - 6.0 \times 10^{22} cm^{-2}$, a sign for obscuration in the quasars, but not the high column density seen in Seyfert 2 galaxies. These values are also in agreement with the column densities of the objects, where we had enough counts to construct an X-ray spectrum. Figure 1 shows a plot of redshift corrected hardness ratio versus reddening of our sources compared to some models with various gas:dust ratios.

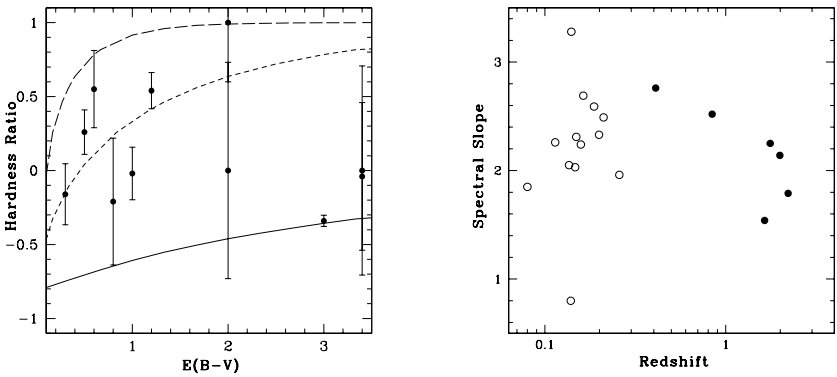

Fig. 1. Left: Distribution of redshift corrected hardness ratios versus reddening. The solid line is a model with galactic gas:dust ratio, for the small dotted line the gas:dust ratio is 20 times and for the long dashed line 100 times galactic value. **Right**: Spectral slopes vs. redshift. Filled dots are from our sample, open dots are from Wilkes' low redshift red AGN sample [6], where we had redshift information to fit to the spectra.

The unweighted mean Γ for our radio-selected sample is 2.20 ± 0.37. Usually quasars tend to have $< \Gamma > \approx$ 1.8-1.9 for energies between 0.2-10.0 keV [4], so our mean is slightly above the expected spectral index. There is a weak correlation between spectral slope and redshift (Figure 1). The fact that Γ decreases with redshift is again consistent with results from Seyfert 1 galaxies [3], as we are probing different regimes of the SED.

References

1. Glikman E. et al.: ApJ, 607, 60 (2004)
2. Rosati, P. et al.: ApJ, 556, 667 (2002)
3. Schartel, N.,et al.: MNRAS, 283, 1015 (1996)
4. Walter, R., Fink, H. H.: A&A, 274, 105 (1993)
5. White, R. L. et al.: AJ, 126, 706 (2003)
6. Wilkes, B. J. et al.: ApJL, 564, L65 (2002)

Supermassive Black Holes in Nearby Galaxy Centers

R. Bender

University Observatory of the LMU, Scheinerstr. 1, D-81679 Munich, Germany, and
MPI for Extraterrestrial Physics, Giessenbachstr., D-85748 Garching, Germany

1 Introduction

Almost exactly 40 years ago, quasars were discovered by M. Schmidt [43] and others. Soon thereafter, Zel'dovich [50] and Salpeter [42] suspected that accretion onto compact objects, like black holes, provided the only efficient and plausible way to generate the required luminosities. Little later, Lynden-Bell [28] refined the picture which became to be known as the black hole paradigm for active galactic nuclei.

The evidence for supermassive black holes in AGN has been strong for a long time but crucial questions remained unanswered until about 10 years ago. E.g., it was unclear, whether the black hole density in local galaxies matched the energy requirements set by the total integrated AGN luminosities. Moreover, it was not known, whether all galaxies contained black holes and how their masses correlated with galaxy properties. Last but not least, even for the most nearby galaxies, it had not been shown that the dynamically discovered central dark objects were indeed black holes (or just dark clusters of neutron stars, white dwarfs or stellar mass black holes). Especially concerning these questions, tremendous progress has been made in the last decade, mostly thanks to the Hubble Space Telescope.

In the past three years, many extensive reviews (e. g., [38]) and whole conferences (e. g., [17]) have been devoted to the subject of supermassive black holes (SMBHs) in nearby galaxy centers. Therefore, this paper is restricted to a brief summary of key results and references.

2 Searching black holes and estimating their masses

Inactive SMBHs can only be found if they noticeably influence the motion of stars or gas at radii that can be resolved observationally. The radius of influence R_i of a SMBH of mass $M_\bullet$ can be defined as:

$$R_i = \frac{GM_\bullet}{V_G^2}$$

where V_G is a rotation velocity or velocity dispersion characteristic for the inner parts of the galaxy. At a distance D of the object, this translates into an angular

ESO Symposia: Growing Black Holes, pp. 147–153, 2005.

radius of influence α_i of:

$$\alpha_i \sim 1'' \left(\frac{M_\bullet}{10^8\,M_\odot}\right) \left(\frac{V_G}{100\,\mathrm{km\,s^{-1}}}\right)^{-2} \left(\frac{D}{10\,\mathrm{Mpc}}\right)^{-1}$$

While the radius of influence of the SMBH in the Milky Way is large ($40''$), it already shrinks to $2''$ for the SMBH in M31, or $0.5''$ for a giant elliptical in the Virgo cluster (assuming a $10^9 M_\odot$ black hole for the latter). SMBHs at a few Mpc distance with masses below $10^8 M_\odot$ require HST resolution or adaptive optics on ground-based telescopes for the resolution of their sphere of influence.

If the spatial resolution is much too low, SMBH masses can be biased towards higher masses, see the discussion in [24] on [29]. However, once spatial resolution is getting close to adequate, lower spatial resolution does in general not bias SMBH mass estimates [13,24] but just makes it less reliable and increases the error bars.

Different techniques have been used to detect and measure SMBHs: stellar dynamics, ionized gas dynamics, maser gas dynamics, and reverberation mapping. All these methods have strengths and weaknesses. Stellar dynamical measurements generally suffer from anisotropy ambiguities which need to be cured with assumptions about the phase space distribution (e.g. via entropy maximization). Gas dynamical measurements are often hampered by non-circularity or non-gravitational forces. Maser emission from molecular gas in Keplerian rotation around a SMBH is only available for very few objects, and reverberation mapping requires assumptions about the structure and geometry of the emission line regions near the SMBH.

Still, careful analysis seems to have kept systematic effects largely under control for these methods, as they yield virtually indistinguishable $M_\bullet - M_{B,\mathrm{bulge}}$ and $M_\bullet - \sigma$ correlations (e. g., [26,5]), see Figure 2 below. In addition, for some galaxies SMBH masses have been derived with independent methods producing largely consistent results (Milky Way: [45,15]; NGC 4258: [46]; M31: [2]).

Beyond these four methods, SMBH masses have also been estimated using emission line widths of active nuclei. Here, systematic effects are even more difficult to control and could indeed be the origin of discrepancies between the $M_\bullet - \sigma$ relations of broad- and narrow-line Seyfert 1 galaxies (e.g. [4]).

3 Have we really discovered black holes?

In the Milky Way and in NGC 4258, astrophysically plausible alternatives to SMBHs can almost certainly be ruled out [36,31,4]. On time scales much shorter than the Hubble time, dark clusters made of brown dwarf stars become luminous as the stars collide, merge, and become massive enough for nuclear energy generation. Clusters of stellar remnants (white dwarf stars, neutron stars, or stellar-mass black holes) evaporate as a result of two-body relaxation. HST STIS observations now make M 31 the third galaxy in which SMBH alternatives are very unlikely [2,24].

In $\sim$ 40 other galaxies, evidence for central dark objects has been reported (for references, see [38]). In these, the constraints on the sizes and densities of the central dark objects are not strong enough to exclude dark clusters on the grounds of short relaxation times. However, in some cases, the clusters would be too tiny to have contained the remnants' progenitor stars without an embarrassingly large number of stellar collisions. In any case, viable alternatives to SMBHs seem to be short-lived compared to the ages of galaxies and are likely to either dissolve or to form an SMBH [39].

Of course, the combination of dynamical results and indirect evidence from active galactic nuclei makes a strong case for SMBHs. Particularly compelling are X-ray observations of Fe Kα emission with line widths of $\sim 1/3$ of the speed of light (see [40] for a review).

4 Correlations between black hole masses and galaxy properties

If we assume that the dynamically detected dark objects are SMBHs, then we find that their masses correlate well with the bulge luminosities or bulge masses of their host galaxies [21,22,29]. The most reliable observations ([38], see Figure 1) yield:

$$M_\bullet \sim 0.0013 \cdot M_{\rm bulge} \quad .$$

It is important to note that SMBH mass does not correlate with galaxy disks. Figure 1 shows how the correlation of $M_\bullet$ with bulge luminosity (left) is destroyed for disk galaxies (right: open symbols and crosses) when the disk luminosity is included. Especially evident is the case of the bulgeless spiral M 33 [10,18] On the other hand, some pure disks seem to have Seyfert nuclei and so presumably do contain SMBHs [9]. However, their masses appear to be *much* smaller than the canonical 0.13 % of the bulge mass implied by the left panel of Figure 1. It will be crucial to improve the statistics on small SMBHs in disk galaxies.

There also is a tight correlation (Figure 2) between SMBH mass and the velocity dispersion σ of the bulge (measured at radii much larger than the radius of influence of the SMBH, [4,21] The scatter is almost as small as the measurement errors (typically a factor of ~ 2 in $M_\bullet$). Figure 2 gives:

$$\frac{M_\bullet}{M_\odot} \sim 0.1 \left(\frac{\sigma}{\rm km\ s^{-1}}\right)^4$$

[11]. Based on these data, $M_\bullet$ seems to correlate better with velocity dispersion than with bulge luminosity. This would imply that, at a given bulge luminosity, more massive black holes live in more compact bulges. Other analyses (e.g. [44]) have found equally good correlations between SMBH mass and velocity dispersion on the one hand and between SMBH mass and bulge luminosity on the other hand. Clearly, more and better data are needed to make progress on this issue. In any case, the tight connection between $M_\bullet$ and the bulge parameters is part of the growing evidence that SMBHs and bulges formed together.

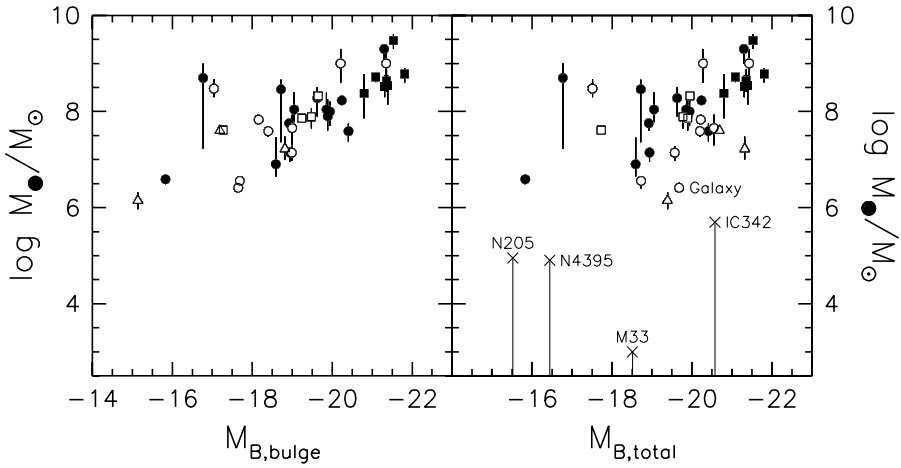

Fig. 1. Black hole mass *versus* (left) bulge and (right) total galaxy luminosity. Note: luminosities are measured in "absolute magnitudes", $M_{B,\mathrm{bulge}} = -2.5 \log L_{B,\mathrm{bulge}} +$ constant; these are not to be confused with masses M_{bulge} in the equations below. Filled symbols are for elliptical galaxies, open symbols are for bulges, and crosses are for bulgeless disks. Circles indicate masses derived from stellar dynamics, squares are based on ionized gas dynamics, and triangles are based on maser gas dynamics. This figure is from [38].

Interestingly, pseudobulges [20], which likely formed secularly from disk material, follow the same $M_\bullet - M_{B,\mathrm{bulge}}$ and $M_\bullet - \sigma$ relations as classical bulges and ellipticals [38]. Again, the formation of bulges and the growth of SMBHs apprears to have proceeded in lockstep.

Supermassive black holes have become critical to our understanding of why galaxies have cores, i. e., central regions in which the stellar density gradient is shallow compared to the rest of the galaxy. Galaxy mergers should destroy cores: smaller galaxies have higher densities and, in the absence of supermassive black holes, these high densities are preserved in a merger (e. g., [5,18,19]). If the merger progenitors contain gas, then this gas is expected to fall to the center and further build up the stellar density [34]. How, then, can the highest-luminosity galaxies – which surely are merger remnants – have the fluffiest centers? Many papers have explored the attractive idea that SMBH binaries formed in galaxy mergers decay by flinging stars away, thereby excavating a low-density region near the galaxy center (e. g., [1,4,30,37,38,5,35,27]). It will be important to check whether its predictions – e. g., high tangential velocity dispersions near galaxy centers – can be confirmed by observations.

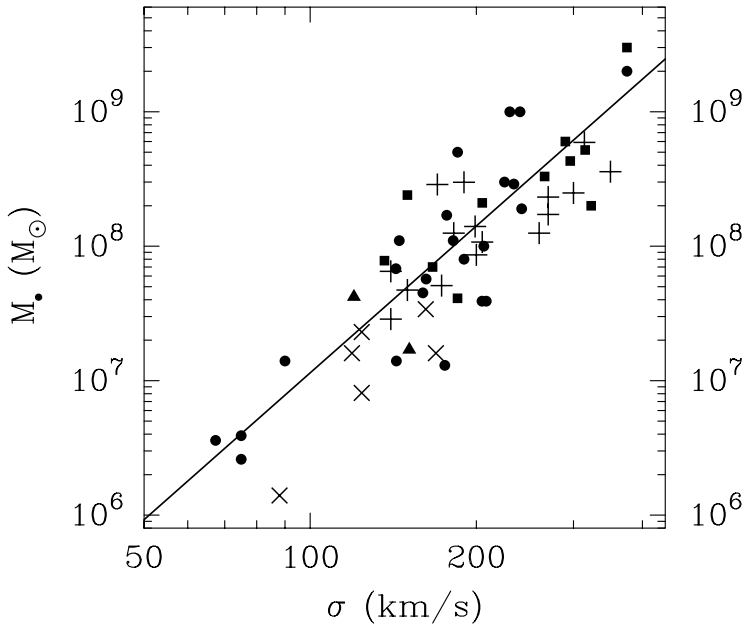

Fig. 2. The relation between black hole mass and bulge velocity dispersion [38]. Different symbols indicate different methods of estimating the black hole mass and galaxy velocity dispersion. Filled symbols represent dynamical analyses of stars (circles), gas (squares), or masers (triangles). Crosses are based on reverberation mapping, and plus signs are based on ionization models.

5 Is the local black hole density sufficient to explain the total luminosity of all AGN?

The $M_\bullet$ – $M_{\rm bulge}$ relation implies a volume mass density of SMBHs in the local universe of ([22], [7] and references therein):

$$\rho_\bullet({\rm local}) \;=\; (2-6)\cdot 10^5 {\rm M}_\odot\,{\rm Mpc}^{-3}.$$

A probably more reliable estimate is provided by the $M_\bullet$ – σ relation yields [22]:

$$\rho_\bullet({\rm local}) \;=\; (2.5\pm 0.4)\cdot 10^5 {\rm M}_\odot\,{\rm Mpc}^{-3}.$$

Both estimates are consistent with the [63] number, i.e. the expected mass density of quasar remnants:

$$\rho_\bullet({\rm AGN}) \;\sim\; (2-4)\cdot 10^5 \frac{{\rm M}_\odot}{{\rm Mpc}^3}\frac{{\rm C_B}}{11.8}\frac{0.1(1-\epsilon)}{\epsilon}$$

with C_B being the bolometric correction for the B-band and ϵ the accretion efficiency ([22], see also e. g. [41,6]). Evidently, the local SMBH density approximately matches the integrated luminosity of AGNs. This is very reassuring and

a big success for the black hole paradigm. Nevertheless, we could still be a factor 2 off from the true numbers. If the density of AGN of Type II (heavily obscured AGNs) is as large as the density of the classical Type I AGN, then the Soltan number may be as high as $5 \cdot 10^5 M_\odot\,\mathrm{Mpc}^{-3}$ (e. g., [6]) which could imply that we either still miss a fraction of SMBHs, or, SMBHs are accreting at efficiencies $\epsilon > 0.1$. The latter would be possible if SMBHs are generally rotating rapidly. This is not implausible and, indeed, evidence for a high spin may have been found for the Galactic SMBH already [5].

Acknowledgements. It is a pleasure to thank the Nuker team, and especially John Kormendy, for many years of productive collaboration. The Nuker team members are D. Richstone (PI), R. Bender, G. Bower, A. Dressler, S. M. Faber, A. Filippenko, K. Gebhardt, R. Green, C. Grillmair, L. C. Ho, J. Kormendy, T. R. Lauer, J. Magorrian, J. Pinkney, C. Siopis, and S. Tremaine.

References

1. Begelman, M. C., Blandford, R. D., and Rees, M. J,: Nature, **287**, 307 (1980)
2. Bender et al.: ApJ submitted (2004)
3. Bridle, A. H., Perley, R. A.: ARA&A, **22**, 319 (1984)
4. Ebisuzaki, T., Makino, J., Okamura, S. K.: Nature, **354**, 212 (1991)
5. Faber et nuk.: AJ, **114**, 1771 (1997)
6. Fabian, A.: in *Carnegie Observatories Centennial Symposium on Coevolution of Black Holes and Galaxies*, ed. L. Ho, Cambridge: Cambridge University Press (2004)
7. Ferrarese, L.: astro-ph/0203047 (2002)
8. Ferrarese, L., Merritt, D.: ApJ, **539**, L9 (2000)
9. Filippenko, A. V., Ho, L.: preprint (2002)
10. Gebhardt, K. et nuk.: ApJ, **539**, L13 (2000a)
11. Gebhardt, K. et nuk.: ApJ, **543**, L5 (2000b)
12. Gebhardt, K. et nuk.: AJ, **122**, 2469 (2001)
13. Gebhardt, K. et nuk.: ApJ, **583**, 92 (2003)
14. Genzel, R. et al.: Nature, **425**, 934 (2003)
15. Genzel, R.: this conference (2004)
16. Grupe, D., Mathur, S.: ApJ, **606**, L41 (2004)
17. Ho, L. C.: *Carnegie Observatories Centennial Symposium on Coevolution of Black Holes and Galaxies*, Cambridge: Cambridge University Press (2004)
18. Holley-Bockelmann, K., Richstone, D.: ApJ, **517**, 92 (1999)
19. Holley-Bockelmann, K., Richstone, D.: ApJ, **531**, 232 (2000)
20. Kormendy, J.: in *IAU Symposium 153, Galactic Bulges*, eds. H. Dejonghe, H. Habing, Dordrecht: Kluwer (1993a)
21. Kormendy, J.: in *The Nearest Active Galaxies*, eds. J. Beckman, L. Colina, H. Netzer, Madrid: Consejo Superior de Investigaciones Científicas, 197 (1993b)
22. Kormendy, J., Richstone, D.: ARA&A, **33**, 581 (1995)
23. Kormendy, J., Gebhardt, K.,: in *20th Texas Symposium on Relativistic Astrophysics*, eds. H. Martel, J. C. Wheeler, New York: AIP, 363 (2001)
24. Kormendy, J.: in *Carnegie Observatories Centennial Symposium on Coevolution of Black Holes and Galaxies*, ed. L. Ho, Cambridge: Cambridge University Press (2004)
25. Kormendy et al.: in preparation (2004)

26. Laor, A.: ApJ, **505**, L83 (1998)
27. Lauer, T. R. et nuk..: AJ, **124**, 1975 (2002)
28. Lynden-Bell, D.: Nature, **223**, 690 (1969)
29. Magorrian, J. et nuk.: AJ **115**, 2285 (1998)
30. Makino, J., Ebisuzaki, T.: ApJ, **465**, 527 (1996)
31. Maoz, E.: ApJ, **494**, L181 (1998)
32. Marconi, A., Hunt, L. K.: ApJ, **589**, L21 (2003)
33. Merritt, D., Ferrarese, L., Joseph, C. L.: Science, **293**, 1116 (2001)
34. Mihos, J. C., Hernquist, L.: ApJ, **437**, L47 (1994)
35. Milosavljević, M., Merrit, D.: ApJ **563**, 34 (2001)
36. Miyoshi, M. et al.: Nature, **373**, 127 (1995)
37. Quinlan, G. D.: NewA, **1**, 35 (1996)
38. Quinlan, G. D., Hernquist, L.: NewA, **2**, 533 (1997)
39. Rees, M. 1984: ARAA, **22**, 471 (1984)
40. Reynolds, C. S., Nowak, M. A.: Physics Reports, in press, astro-ph/0212065 (2002)
41. Richstone, D. et nuk.: Nature, **395A**, 14 (1998)
42. Salpeter, E. E.: ApJ, **140**, 796 (1964)
43. Schmidt, M.: Nature, **197**, 104 (1963)
44. Schödel et al.: Nature, **419**, 694 (2002)
45. Schödel et al.: ApJ, **596**, 1015 (2003)
46. Siopis et nuk., ApJ submitted (2004)
47. Soltan, A., MNRAS, **200** (1982)
48. Tremaine, S. et nuk.: ApJ, **574**, 740 (2002)
49. Yu, Q., Tremaine, S.: MNRAS, **335**, 965 (2002)
50. Zel'dovich, Ya. B.: Soviet Physics – Doklady, **9**, 195 (1964)

Intermediate-Mass Black Holes in Active Galactic Nuclei

A.J. Barth[1], J.E. Greene[2], and L.C. Ho[3]

[1] Department of Physics and Astronomy, 4129 Frederick Reines Hall, University of California, Irvine, CA 92697-4575, USA
[2] Harvard-Smithsonian Center for Astrophysics, 60 Garden Street, Cambridge, MA 02138, USA
[3] Observatories of the Carnegie Institution of Washington, 813 Santa Barbara Street, Pasadena, CA 91101-1292, USA

Abstract. Little is currently known about the demographics of black holes in the intermediate-mass range $10^3 - 10^6$ $M_\odot$, but a small fraction of dwarf galaxies and late-type spirals contain active nuclei that can be used to study black holes in this mass range. We review the properties of the best-known cases and describe a new project that uses AGNs from the Sloan Digital Sky Survey to extend the $M - \sigma$ relation to masses below 10^6 $M_\odot$.

1 Introduction

Over the past decade, tremendous progress has been made in surveying the demographics of supermassive black holes in nearby galaxies over a mass range of about 3 orders of magnitude ($10^{6.5} - 10^{9.5}$ $M_\odot$). Black holes of lower mass might exist in the centers of very late-type spiral galaxies or dwarf ellipticals, but very little is known about how common or how rare such objects might be. Searches for "intermediate-mass" black holes in the range $10^3 - 10^6$ $M_\odot$ are potentially worthwhile as they may help to answer important questions about the formation and evolution of massive black holes and their connection with their host galaxies. Does the correlation between black hole mass and host galaxy velocity dispersion (the $M - \sigma$ relation; [21,25]) continue with the same slope all the way from giant elliptical galaxies down to dwarf galaxies and globular clusters? Do *all* galaxies with bulges contain central black holes, or is there some limiting galaxy mass or dark halo mass below which massive black holes will not form? Do black holes form only in bulges, or can they form in pure disk galaxies? If black holes form in dwarf galaxies, are they ejected by gravitational radiation recoil following mergers [5,7]?

Gravitational-wave emission from mergers of intermediate-mass black holes will be detectable by *LISA*, and this gives an additional motivation to try to extend the black hole census to masses below 10^6 $M_\odot$. Any observational constraints on the mass function of intermediate-mass black holes would be useful for prediction of the expected *LISA* event rates.

For Sc and later Hubble types, there are no galaxies for which central black holes have been detected dynamically, but upper limits to $M_{\rm BH}$ can still be

ESO Symposia: Growing Black Holes, pp. 154–158, 2005.

determined. The most important case is M33, for which *HST* observations have shown that there is no black hole down to astonishingly tight limits (either 1500 or 3000 $M_\odot$, according to [10] or [18]). Outside the Local Group, measured upper limits to black hole masses in late-type spirals and dwarf ellipticals are less restrictive [3,20,11].

Even if dynamical detection of black holes below 10^6 $M_\odot$ is currently impossible for galaxies more distant than a few Mpc, the presence of a black hole in some cases can be established if the black hole is in an active accretion state. By searching for AGNs in dwarf galaxies and late-type spirals, it is possible to identify at least a small fraction of the population of intermediate-mass black holes and extend our understanding of the relationship between black hole mass and host galaxy properties to low masses.

2 AGNs in dwarf galaxies: the two best cases

Two examples of AGNs in dwarf galaxies were discovered fortuitously in surveys in the 1980s. The best-studied object is the nearby, late-type, bulgeless Sdm spiral galaxy NGC 4395. It contains the least-luminous known Seyfert 1 nucleus, discovered in the Palomar spectroscopic survey of nearby galaxies [8]. The stellar velocity dispersion of the central star cluster surrounding the AGN is $\sigma < 30$ km s^{-1} [7] and its black hole has a likely mass in the range of $10^4 - 10^5$ $M_\odot$, based on estimates of the broad-line region size derived from photoionization modeling [3] or from extrapolating the BLR size-luminosity relation of Seyfert 1 galaxies [7]. The X-ray variability power density spectrum gives a mass estimate in this range as well [23].

The second example is POX 52, discovered in the POX objective-prism survey [17]. As a Seyfert in a dwarf galaxy host, it was identified as an unusual object [16], but was subsequently nearly forgotten. Recent observations [2] reveal that it is a Seyfert 1 with an emission-line spectrum nearly identical to that of NGC 4395, and that its host galaxy appears to be a dwarf elliptical. An estimate of the black hole mass, based on extrapolating the BLR size-luminosity relationship, is $\sim 1.6 \times 10^5$ $M_\odot$, and its stellar velocity dispersion is $\sigma = 36 \pm 5$ km s^{-1}. If this black hole mass estimate is correct, then POX 52 lies nearly exactly on the same $M - \sigma$ relation as massive galaxies [11].

Until very recently, only a few other examples of AGNs had been identified having $M_{\rm BH} < 10^6$ $M_\odot$ or in host galaxies having $\sigma < 60$ km s^{-1}. Other cases include NGC 4051, which may have a black hole mass as low as $5^{+6}_{-3} \times 10^5$ $M_\odot$ based on recent reverberation data [21], and NGC 1058, an Sc galaxy hosting very weak Seyfert 2 activity, which has $\sigma = 31 \pm 6$ km s^{-1} [1]. Surveys of narrow-line Seyfert 1 galaxies have identified a handful of objects having estimated black hole masses below 10^6 $M_\odot$ based on the Hβ linewidths and AGN continuum luminosity [4,4].

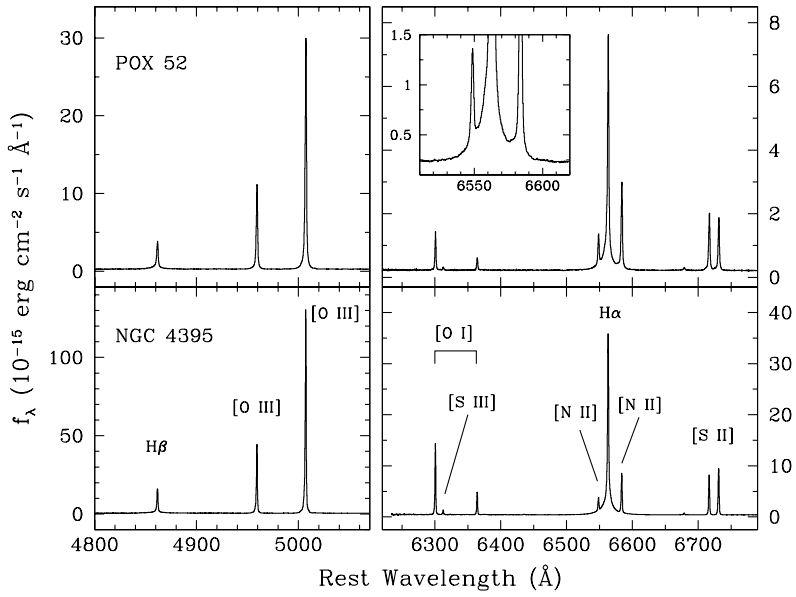

Fig. 1. Optical spectra of the dwarf Seyfert 1 galaxies POX 52 and NGC 4395, taken with the ESI spectrograph at Keck [2].

3 Tracing the $M - \sigma$ relation below 10^6 $M_\odot$

Understanding the demographics of AGNs with low-mass black holes requires a statistically meaningful sample. The first systematic search for AGNs with low-mass black holes was recently carried out by Greene & Ho [17], using the Sloan Digital Sky Survey Data Release 1 (DR1) archives. Starting with the sample of $\sim 150,000$ galaxy and AGN spectra in DR1 at $z < 0.35$, they performed starlight subtraction and identified objects with broad Hα emission. Black hole mass estimates were derived using the broad-line widths (Hα in this case because of the weakness of Hβ in low-luminosity AGNs) and the AGN continuum luminosity, following the correlations from Kaspi et al. [5]. This search identified 19 Seyfert 1 galaxies having black hole mass estimates in the range $4.9 < \log(M_{\rm BH}/M_\odot) < 6.0$. The nuclear luminosities are in the range $M_g = -15$ to -18, and assuming a standard bolometric correction for Seyfert 1 galaxies, the ratio $L_{\rm bol}/L_{\rm Edd}$ is typically ~ 1. In some cases the host galaxy morphology is clearly a late-type spiral, but most of the objects are compact and nearly unresolved in the SDSS images due to their distance and the presence of the AGN point source.

This is the first sample of galaxies selected to have black hole masses below 10^6 $M_\odot$, allowing us to examine the $M - \sigma$ relation in this low mass range. The Sloan spectra themselves cannot be used to measure the stellar velocity dispersions for two reasons: the spectral resolution of the Sloan data only permits measurement of σ for galaxies having $\sigma > 70$ km s^{-1}, and in most cases the

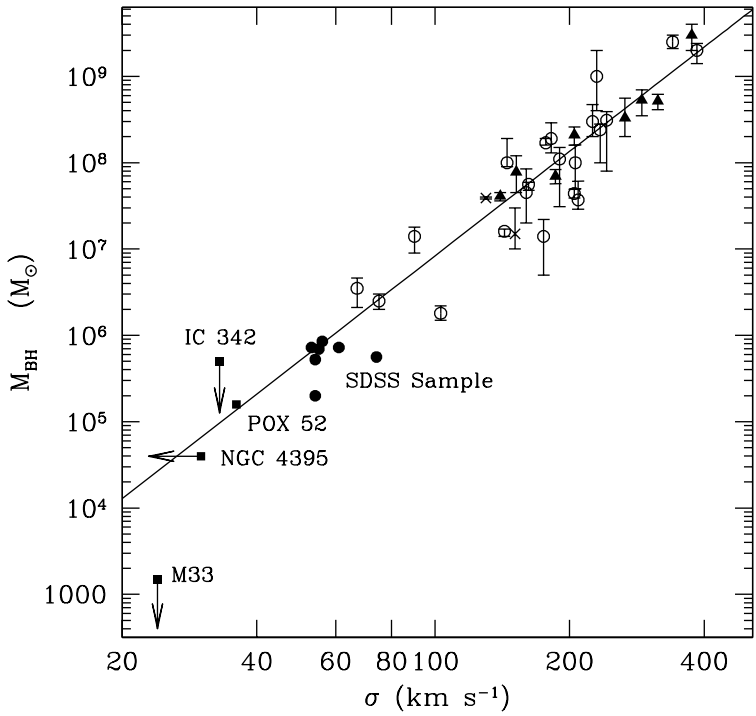

Fig. 2. The $M - \sigma$ relation for massive black holes, including preliminary results for intermediate-mass black holes selected from SDSS. Points in the upper half of the diagram represent black holes with dynamical detections from the sample compiled by Tremaine et al. 2002. Open circles are stellar-dynamical detections and filled triangles are gas-dynamical detections. Upper limits to $M_{\rm BH}$ in M33 and IC 342 are from [10] and [3], respectively. The solid line is the best-fitting $M - \sigma$ slope from Tremaine et al. (2002). Objects from the SDSS sample of Greene & Ho (2004) are shown as filled circles.

AGN continuum dominates the optical spectrum so the stellar features are not detected with high S/N. We are currently carrying out a project to measure the stellar velocity dispersions of these galaxies using the ESI spectrograph at the Keck Observatory. Preliminary results from our first observing run, including 7 objects from the Greene & Ho sample, are shown in Figure 2. The Sloan AGNs cluster very close to an extrapolation of the Tremaine et al. [11] $M - \sigma$ relation, and the scatter is remarkably small given the expected factor of ~ 3 uncertainty in the black hole mass estimates. In upcoming observing runs we will attempt to complete the velocity dispersion measurements for the entire Greene & Ho sample.

Combining these results with previous measurements for POX 52 and NGC 4395, it appears that the $M - \sigma$ relationship may continue with the same slope over a mass range of 5 orders of magnitude. An important caveat, however, is that the Sloan selection based on AGN properties may bias this sample toward objects with the highest-mass black holes for a given velocity dispersion, since these black holes will support more luminous AGNs that are more easily identified in the Sloan spectra. Thus, this low-mass AGN sample may not be representative of the general population of black holes in galaxies with low σ. Another caveat for the Sloan sample is that in most cases we do not know whether the velocity dispersion measurement is dominated by disk or bulge light because the optical morphology of most of the host galaxies is unknown. Future high-resolution imaging data from *HST* and/or from ground-based telescopes equipped with adaptive optics will allow us to determine whether these galaxies have bulges and examine the relation between bulge mass and black hole mass for $M_{\rm BH} < 10^6$ $M_\odot$.

References

1. Barth, A. J., Ho, L. C., & Sargent, W. L. W.: AJ, **124**, 2607 (2002)
2. Barth, A. J., Ho, L. C., Rutledge, R. E., & Sargent, W. L. W.: ApJ, **607**, 90 (2004)
3. Böker, T., van der Marel, R. P., & Vacca, W. D.: AJ, **118**, 831 (1999)
4. Botte, V., Ciroi, S., Rafanelli, P., & Di Mille, F.: AJ, **127**, 3168 (2004)
5. Favata, M., Hughes, S. A., & Holz, D. E.: ApJ, **607**, L5 (2004)
6. Ferrarese, L. & Merritt, D.: ApJ, **539**, L9 (2000)
7. Filippenko, A. V. & Ho, L. C.: ApJ, **588**, L13 (2003)
8. Filippenko, A. V. & Sargent, W. L. W.: ApJ, **342**, L11 (1989)
9. Gebhardt, K., et al.: ApJ, **539**, L13 (2000)
10. Gebhardt, K., et al.: AJ, **122**, 2469 (2001)
11. Geha, M., Guhathakurta, P., & van der Marel, R. P.: 2002, AJ, **124**, 3073 (2002)
12. Greene, J. E., & Ho, L. C.: ApJ, **610**, 722 (2004)
13. Grupe, D., & Mathur, S.: ApJ, **606**, L41 (2004)
14. Kaspi, S., Smith, P. S., Netzer, H., Maoz, D., Jannuzi, B. T., & Giveon, U.: ApJ, **533**, 631 (2000)
15. Kraemer, S. B., Ho, L. C., Crenshaw, D. M., Shields, J. C., & Filippenko, A. V.: ApJ, **520**, 564 (1999)
16. Kunth, D., Sargent, W. L. W., & Bothun, G. D.: AJ, **93**, 29 (1987)
17. Kunth, D., Sargent, W. L. W., & Kowal, C.: A&AS, **44**, 229 (1981)
18. Merritt, D., Ferrarese, L., & Joseph, C. L.: Science, **293**, 1116 (2001)
19. Merritt, D., Milosavljevic, M., Favata, M., Hughes, S. A., & Holz, D. E.: ApJ, **607**, 9 (2004)
20. Salucci, P., Ratnam, C., Monaco, P., & Danese, L.: MNRAS, **317**, 488 (2000)
21. Shemmer, O., Uttley, P., Netzer, H., & McHardy, I. M.: MNRAS, **343**, 1341 (2003)
22. Sheth, R. K., et al.: , ApJ, **594**, 225 (2003)
23. Shih, D. C., Iwasawa, K., & Fabian, A. C.: MNRAS, **341**, 973 (2003)
24. Tremaine, S., et al.: ApJ, **574**, 740 (2002)

Growing Black Holes: Observational Evidence for Stellar Tidal Disruption Events

S. Komossa

Max-Planck-Institut für extraterrestrische Physik, Giessenbachstr. 1, 85748 Garching, Germany; skomossa@mpe.mpg.de

Abstract. Three major feeding mechanisms have been studied in the context of black hole growth: accretion, black hole - black hole mergers, and tidal capture/disruption of stars. While there is ample evidence that accretion is ongoing in active galaxies, observational evidence for the two other processes remained elusive for many years. Given the intense theoretical work on these latter two processes, it is of great interest to see whether such events do occur in nature, how frequent they are, and which properties they show. In this contribution, I will give a review of observational evidence for stellar tidal disruption events concentrating on X-ray flares of giant amplitude detected from the centers of several galaxies. These represent the most dramatic variability events, in terms of amplitude, ever recorded among galaxies.

1 Introduction

The capture and disruption of stars by supermassive black holes is one of the three major processes studied in the context of black hole growth, together with accretion of interstellar matter and black hole - black hole merging. The relative importance of these three processes in feeding black holes is still under investigation. Different processes may dominate in different stages of the evolution of galaxies. In particular, it was recently suggested that tidal capture may play a role in explaining the $M_\bullet - \sigma$ relation of galaxies (e.g., [20,7,6]).

Occasional tidal disruptions of stars by supermassive black holes (SMBHs) and the subsequent accretion of their debris is an unavoidable consequence of the existence of SMBHs at the centers of galaxies. The events would appear as luminous flares of radiation emitted when the stellar debris is accreted by the black hole.

Various aspects of tidal disruption were studied intensely theoretically (e.g., [5,2,1,14,16,21]; see Sect. 3 of [7] for further references). It is therefore of great interest to see whether these events occur in nature and how frequent they are. This paper concentrates on observations of giant-amplitude X-ray flares from the centers of several (optically non-active) galaxies, and their interpretation in terms of stellar tidal disruption events.

Several luminous flares of X-ray radiation were first detected with *ROSAT* (review by Komossa [7]) from three optically non-active galaxies and from the HII galaxy NGC 5905 [8] which shows a low-luminosity high-excitation core detected with *HST* [3], either excited by the flare emission or (favored by Gezari et al. [3]) sign of the presence of a permanent very low-luminosity AGN. Some key

ESO Symposia: Growing Black Holes, pp. 159–163, 2005.

properties of the X-ray flares are summarized in Table 1. Here, I review recent *Chandra* and *XMM* follow-up observations which allowed some key tests of the previous suggestion [8] that we have observed flares from stars tidally disrupted by supermassive black holes (see [4,10,11] for further information).

Table 1. Summary of the X-ray and optical properties of the flaring galaxies where z is redshift, A is the total amplitude of variability measured so far, and $L_{\rm x,bb}$ gives the intrinsic luminosity in the (0.1–2.4) keV band, based on a black body spectral fit. This is a lower limit to the actual peak luminosity, since we most likely have not caught the sources exactly at maximum light, since the spectrum may extend into the EUV, and since it was conservatively assumed that no additional X-ray absorption occurs intrinsic to the galaxies. 'Opt. type' corresponds to the galaxy type based on optical spectroscopic classification where 'no em' means, no optical emission lines were detected at all. RA and DEC give the coordinates (J 2000) of the optical centers of the galaxies identified as counterparts to the X-ray flares (NGC 5905, RXJ1242−1119A, RXJ1624+7554; positional uncertainty is about 1″) or the X-ray position (RXJ1420+5334).

galaxy name	RA	DEC	z	opt. type	$L_{\rm x,bb}$ [erg/s]	A
NGC 5905	$15^{\rm h}15^{\rm m}23.4^{\rm s}$	$+55°31'02''$	0.011	HII/Sy2*	$3\ 10^{42}$**	1000
RXJ1242−1119	$12^{\rm h}42^{\rm m}38.5^{\rm s}$	$-11°19'21''$	0.050	no em	$9\ 10^{43}$	1000
RXJ1624+7554	$16^{\rm h}24^{\rm m}56.5^{\rm s}$	$+75°54'56''$	0.064	no em	$\sim 10^{44}$	6000
RXJ1420+5334	$14^{\rm h}20^{\rm m}24.2^{\rm s}$	$+53°34'11''$	0.147	no em	$8\ 10^{43}$	150

*The ground-based optical classification of NGC 5905 is that of an HII galaxy, while in an HST spectrum taken several years after outburst, weak AGN-like emission-lines show up. These either indicate permanent very low-level Seyfert activity, or possibly these lines were still excited by the flare itself. **Mean luminosity during the outburst; since the flux varied by a factor ∼3 during the observation, the peak luminosity is higher.

2 *Chandra* imaging and *XMM* spectroscopy of the late flare phase of RXJ1242-1119

A flare from the direction of the galaxy RX J1242–1119 was detected by *ROSAT* in 1992 with an X-ray luminosity of $L_{\rm x} \simeq 9\times10^{43}$ ergs s^{-1} [9], which is exceptionally large given the absence of any optical signs of Seyfert activity of RX J1242–1119. We re-observed RX J1242–1119 with *Chandra* and *XMM-Newton* in order to confirm the optical counterpart, follow the long-term temporal behavior, study the spectral evolution and measure the post-flare spectrum, and to use these results to test the favored outburst model, tidal disruption of a star by a supermassive black hole. Among the few known X-ray flaring galaxies, RX J1242–1119 was our target of choice for follow-up X-ray observations because it flared most

recently, so the probability of catching the source in the declining phase - before it had faded away completely - was highest.

The *Chandra* data allowed to locate precisely the counterpart of the X-ray source which coincides with the center of the galaxy RXJ1242-1119A. The X-ray emission is pointlike, and the X-ray flux dropped dramatically by a factor ∼200.

With *XMM*, for the first time a good-quality X-ray spectrum of one of the few flaring galaxies was obtained. The spectrum is well fit by a power law (photon index $\Gamma_{\rm x} = -2.5$). There is no evidence for excess absorption, and the post-flare spectrum is harder than the flare maximum.

Compared with the blue luminosity of RX J1242–1119A, inferred from the extinction-corrected blue magnitude $m_{B,0} = 17.43$ mag measured with the Optical Monitor aboard *XMM* [10], the X-ray emission of this galaxy is still very high, even in its low state in 2001. A further decline of the X-ray emission is expected as more and more of the stellar debris is accreted by the black hole. Indeed, re-observation of RX J1242–1119 with *Chandra* in 2004 showed a further fading of the X-ray source by a factor of several (Komossa et al. [11], in prep.).

3 Joint X-ray lightcurve of the flare events

Two more *ROSAT* flares were followed up with *Chandra* and data for a third one are expected soon. Only few, if any, photons from the galaxies' centers were detected, making their total amplitude of variability extremely large, a factor >1000 (NGC 5905; [4]) and >6000 (RXJ1624+75; [4,19]).

Fig. 1 shows the collective X-ray lightcurve of the flare events, shifted in time to the same high-state time as NGC 5905. The lightcurves of all events are relatively similar, and consistent with a faster rise, and a slower decline on the timescale of months - years. Most of the data points are consistent with a $t^{-5/3}$ decline law which is expected for the 'fall-back' phase of tidal disruption (e.g., [15,12]) *if* the bolometric correction is constant.

In the late phases of the tidal debris evolution, a steeper decline of the lightcurve is expected, once the accretion rate becomes so low that the accretion switches to a radiatively more inefficient mode. Indeed, the latest *Chandra* data points suggest such a trend, but further monitoring is required for confirmation.

In summary, the observed events match basic predictions from models of the tidal disruption of stars by supermassive black holes at the centers of the flaring galaxies (see [8,4,10,11] for a more detailed discussion). The observed X-ray flares represent the highest amplitudes of variability - up to a factor > 6000! – ever recorded among galaxies, including active galaxies.

4 Future applications of tidal disruption flares

The search for more tidal disruption flares is presently ongoing using *XMM* [23] and *Chandra* data. In particular, future X-ray surveys should be efficient in finding more events, like the surveys planned with *DUO*, the *LOBSTER* ISS X-ray

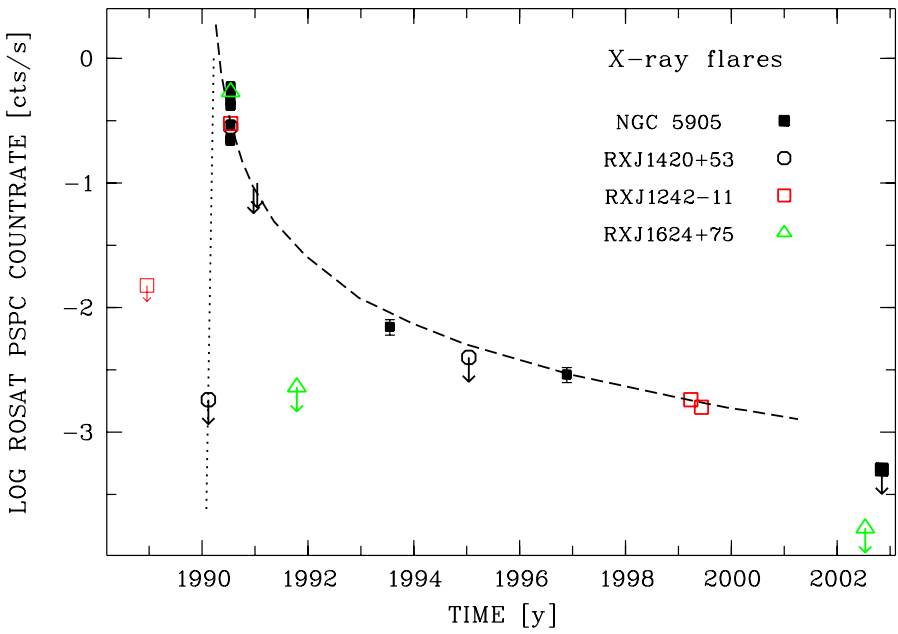

Fig. 1. Collective X-ray lightcurves of the four flaring galaxies, all shifted to the same peak time. The dashed line follows a $t^{-5/3}$ law matched to the high- and first low-state data point of of RXJ 1242-1119. The dotted line corresponds to the least fastest rise to high-state consistent with the upper limit of RXJ1420+53. Conversion of countrates to *ROSAT* PSPC was done using Galactic $N_{\rm H}$ values, and spectral shapes as measured when available (see [11] for details). The last data point of NGC 5905 corresponds to the central point source only, while previous X-ray measurements of NGC 5905 plotted in this figure include both extended and core emission not spatially resolved prior to *Chandra*.

all-sky monitor, *ROSITA* and *MAXI*. Dedicated X-ray follow-up observations with high spectral and temporal resolution might then allow to follow the complex stellar debris evolution in detail, and, e.g., search for signs of relativistic precession.

After the discovery of new X-ray flares from *non-active* galaxies, *rapid follow-up multi-wavelength* observations will be essential. If the soft X-ray flare emission has an extension into the EUV, which is highly likely, then optical observations will be important in order to detect potential emission lines that were excited by the outburst emission. Any gaseous material close to the nucleus is expected to show an emission-line response. The temporal variability of these lines will allow a reverberation mapping of the circumnuclear gas; line profiles, and line-ratios will allow to estimate the velocity structure and physical conditions (density, abundances) of this gas. Results would also allow us to address important ques-

tions related to the link between active and non-active galaxies: e.g, do these (in quiescence non-active) galaxies permanently harbor a broad-line region (BLR) which is usually invisible, because the black hole is not accreting, or is the BLR absent?

If a long-lasting, relatively stable accretion disk forms from the stellar debris, the outer parts of that disk itself may radiate emission lines as suggested to be the case in some LINERs (e.g., NGC 1097; [18]).

Finally, it is interesting to note that tidal capture of compact sources (NS, BH) at the centers of galaxies or capture of main sequence stars at the center of our galaxy might produce gravitational wave radiation strong enough for detection with *LISA* (e.g., [17]).

References

1. Carter B., Luminet J.P.: Nature **296**, 211 (1982)
2. Gurzadyan V.G., Ozernoi, L.M.: Nature **280**, 214 (1979)
3. Gezari S., Halpern J., Komossa S., Grupe D., Leighly K.: ApJ **592**, 42 (2003)
4. Halpern J., Gezari S., Komossa S.: ApJ **604**, 572 (2004)
5. J. G. Hills: Nature, **254**, 295 (1975)
6. Miralda-Escude J., Kollmeier J.A.: ApJ, submitted (astro-ph/0310717)
7. Komossa S.: In: Reviews in Modern Astronomy (ed. R.E. Schielicke) **15**, 27, Wiley (2002)
8. Komossa S., Bade N.: A&A **343**, 775 (1999)
9. Komossa S., Greiner J.: A&A **349**, L45 (1999)
10. Komossa S., Halpern J., Schartel S., Hasinger G., Santos-Lleo M., Predehl P.: ApJ **603**, L17 (2004a)
11. Komossa S., et al.: in prep. (2004b)
12. Li, L.-X., Narayan, R., Menou, K.: ApJ **576**, 753 (2002)
13. Merritt D., Poon M.Y.: ApJ, **606**, 788 (2004)
14. Rees M.: Nature **333**, 523 (1988)
15. Rees M.: Science **247**, 817 (1990)
16. Simkin M.V., Roychowdhury V.P.,: Complex Syst. **14**, 269 (2003)
17. Sirgudsson S.: In: The Astrophysics of Gravitational Wave Sources (ed. J. Centrella), AIP **686**, 99 (2004)
18. Storchi-Bergmann T., da Silva R.N., Eracleous M., et al.: ApJ **598**, 956 (2003)
19. Vaughan S., Edelson R., Warwick R.S.: MNRAS, in press (2004)
20. Zhao H.S., Haehnelt M.G., Rees M.: New Ast. **7**, 385 (2002)
21. Wang J., Merritt, D.: ApJ **600**, 147 (2004)
22. Yuan W., et al.: In: *Proceedings of the 35th COSPAR Scientific Assembly*, eds: T. Courvoisier et al., in press (2004)

Narrow Line Seyfert 1 Galaxies and the "Anti-hierarchical" Black Hole Growth

S. Mathur and D. Grupe

The Ohio State University, Columbus, OH 43210, USA

Abstract. Using a complete sample of soft X-ray selected AGNs, we show that highly accreting AGNs do not follow the $M_{\rm BH}$–σ relation of normal galaxies. This statistical result is robust, with important consequences towards our understanding of black hole formation and growth at present epoch: black holes grow by accretion in well formed bulges, possibly after a major merger. As they grow, they get closer to the $M_{\rm BH}$–σ relation for normal galaxies. The relationship between a BH and its bulge appears to be a function of redshift. Our finding of BHs which are still growing at present epoch is consistent with the scenario of downsizing of AGN activity with time or the "anti-hierarchical" BH growth.

1 NLS1s and the $M_{\rm BH}$–σ relation

The observation of a tight correlation between the velocity dispersion σ of the the bulge in a galaxy and the mass of its nuclear black hole $M_{\rm BH}$ was a surprising discovery over the last few years [4], [2]. Even more surprisingly, the above relation for normal galaxies was also found to extend to active galaxies [5], [3]. A lot of theoretical models attempt to provide explanation for the $M_{\rm BH}$–σ relation in the framework of models of galaxy formation, black hole growth and the accretion history of active galactic nuclei (e.g. [7], [8]). To understand the origin of the $M_{\rm BH}$–σ relation, and to discriminate among the models, it is of interest to follow the tracks of AGNs on the $M_{\rm BH}$– σ plane.

Mathur et al. [10] suggested that the narrow line Seyfert 1 galaxies (NLS1s), a subclass of Seyfert galaxies believed to be accreting at a high Eddington rate, do not follow the $M_{\rm BH}$–σ relation. [NLS1s are defined as Seyfert galaxies with full width at half maximum of Hβ lines less than 2000 km/s]. Figure 1 shows our new result using a complete sample of soft X-ray selected AGNs [6]. We determined black hole mass–bulge velocity dispersion relation for 43 broad line Seyfert 1s and 32 narrow line Seyfert 1s using luminosity and FWHM(Hβ) as surrogates for black hole mass and FWHM([OIII]) as a surrogate for the bulge velocity dispersion. We find that NLS1s lie below the $M_{\rm BH}$–σ relation of BLS1s, confirming the Mathur et al. [10] result. The statistical result is robust and not due to any systematic measurement error. This result has important consequences towards our understanding of black hole formation and growth: black holes grow by accretion in well formed bulges, possibly after a major merger. As they grow, they get closer to the $M_{\rm BH}$–σ relation for normal galaxies. The accretion is highest in the beginning and dwindles as the time goes by. While a theoretical model to explain all the observations has yet to come, the above

ESO Symposia: Growing Black Holes, pp. 164–169, 2005.

result allows to rule out a class of models: e.g. the above result does not support theories of $M_{\rm BH}$–σ relation in which the black hole mass is a constant fraction of the bulge mass/velocity dispersion *at all times* in the life of a black hole or those in which bulge growth is controlled by AGN feedback. A broad consistency is found with the model of Miralda-Escudé& Kollmeier [12].

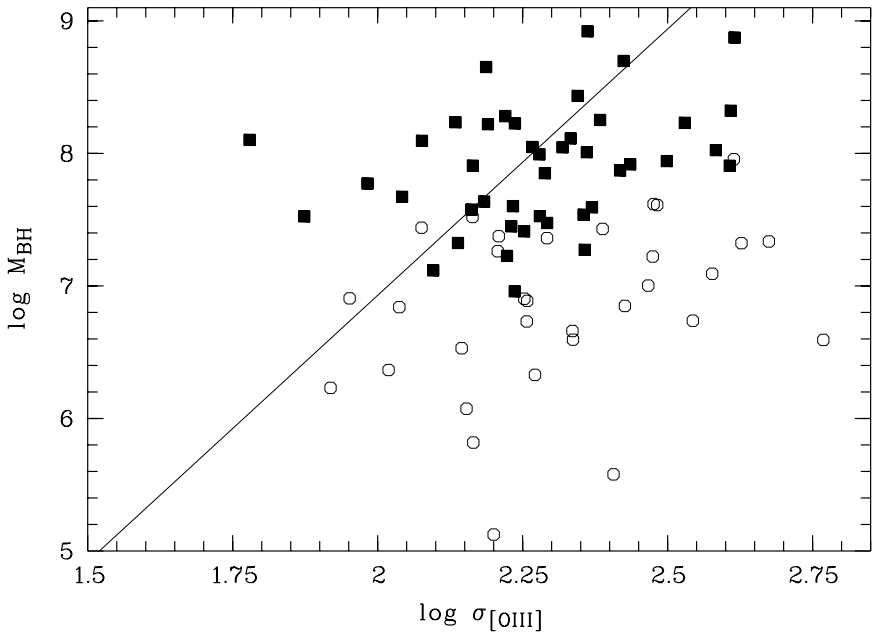

Fig. 1. Velocity dispersion $\sigma_{\rm [OIII]}$ vs. log $M_{\rm BH}(\rm H\beta)$. NLS1s are marked as open circles and BLS1s as filled squares. Black hole masses are given in units of solar masses. The solid line marks the relation of [11]

Given the obvious importance of the result, we have to make sure that the result is not spurious. A spurious result may be obtained if the black hole masses of NLS1s are systematically underestimated or if their velocity dispersions are systematically overestimated relative to BLS1s. We will check these two cases below.

Are the black hole masses of NLS1s wrong? The cumulative fraction of the distributions of the inferred black hole masses shows that NLS1 and BLS1s have different distributions of the black hole masses (see fig. 2 in [6]). In general, more luminous AGNs have higher black hole masses, but for a given luminosity NLS1s have black hole masses about an order of magnitude lower than BLS1s (note that the BLS1s and NLS1s in our sample have similar luminosities; see details in [6]). This result confirms earlier findings of, e.g. [15] and [13] and is unlikely to be spurious. In fact, NLS1s have narrower broad emission lines because of the

smaller black hole masses. If they had masses similar to the BLS1s, their BLRs would have to be relatively farther away from the black hole. This, however, is not the case; NLS1s and BLS1s follow the same relation between the BLR size and luminosity [13]. We thus conclude that there is a real difference in the black hole mass distribution of BLS1s and NLS1s.

Note also that the original Mathur et al [10] result was based on estimating black hole masses by fitting X-ray power-law slopes to the accretion disk models. Czerny et al. [1] confirmed the above result using power-spectrum analysis of X-ray variability data to estimate the black hole masses. Since three completely different methods of black hole mass estimates led to the same result, it is highly unlikely that the result is spurious on account of faulty mass estimates.

Are the estimates of velocity dispersion wrong? If FWHM([OIII]) is not a good surrogate, our estimates of σ may well be wrong. This could produce dichotomy between NLS1s and BLS1s if $\sigma_{[OIII]} - \sigma_*$ is systematically different for the two classes. The first indication that this is not the case comes from the similarity of distribution of their σ (see fig. 2 in [6]). A KS test shows that the two classes do not show any significant difference.

We also test whether poor instrumental resolution, under-subtraction of FeII contribution or asymmetry in [OIII] lines led to overestimation of σ and found it to be not the case [6].

We find that BLS1s and NLS1s occupy two distinct regions in the $M_{\rm BH}$–σ plane. This does not appear to be a result of systematically underestimating black hole masses or systematically overestimating the [OIII] line widths of NLS1s. The errors on the values of $M_{\rm BH}$ and σ for individual objects are large, and we emphasize that this is a statistical result. The BH mass to σ ratios of BLS1s and NLS1s are significantly different, with formal K-S test probability of being drawn from the same population < 0.001 (Figure 2).

Notice in Figure 1, however, that some NLS1s, at the low end of the observed range of velocity dispersion, lie on/close to the $M_{\rm BH}$–σ relation. Even though our statistical result is robust, in that NLS1s *as a class* do lie below the $M_{\rm BH}$–σ relation of normal galaxies, the observation of some NLS1s on/close to the relation affects the interpretation of the result. If we are to interpret the observations in terms of black hole growth by the highly accreting NLS1s, why have some NLS1s already reached their "final" mass?

The first hint towards the resolution of the above conflict came from the observation of Williams, Mathur & Pogge [16]. With *Chandra* observations we found that a significant fraction of NLS1s have flat X-ray spectra and those with flatter spectra are preferentially lower luminosity objects likely to be accreting at a substantially lower, sub-Eddington rate, compared to the NLS1s with steep X-ray spectra. In the framework of our black hole growth scenario these objects with low accretion rate may then be the ones close to the $M_{\rm BH}$–σ relation, as they would have already gone through their high $\dot{m}$ state and their black holes would have accumulated most their mass.

To test the above hypothesis we divided our NLS1 sample in two parts, with low and high values of σ such that NLS1s with low σ are close to the

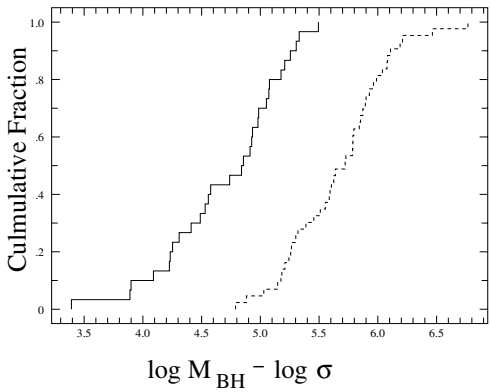

Fig. 2. Cumulative fraction of a KS test of the distributions of the black hole mass $M_{\rm BH}$ divided by the stellar velocity dispersion σ. The distribution of NLS1s is shown as a solid line and BLS1s are shown as a dashed line. The two populations are clearly different

$M_{\rm BH}$–σ relation. Figure 3 compares the distribution of $\rm L/L_{Eddington}$ for the two samples. The K-S cumulative distribution for the two samples is significantly different with the formal K-S test probability of being drawn from the same population P=0.1. This result is also statistical in nature. The error on values of $\rm L/L_{Eddington}$ for each object, assuming a bolometric correction factor, may be a factor of several. The point to note here is the *difference* in the two populations with low and high σ which correspond to objects close to and away from the $M_{\rm BH}$–σ relation respectively. Figure 3 thus shows that the objects closer to the $M_{\rm BH}$–σ relation have lower $\rm L/L_{Eddington}$ and those lying below the relation have statistically higher $\rm L/L_{Eddington}$.

One has to be cautious interpreting the above result, because one may obtain high values of $\rm L/L_{Eddington}$ if black holes masses are underestimated. As discussed above, this is not the case; the BH masses in our sample are unlikely to be systematically underestimated. Moreover, the value of σ plays no role in BH mass estimates, so even if the BH masses were underestimated, they would be so for all NLS1s, irrespective of σ and not for high σ objects only. Nonetheless, another test of the above hypothesis may be a comparison of the X-ray power-law slopes of the two populations of high and low σ. If our hypothesis is correct, and if steep and flat X-ray spectra result in NLS1s with high and low $\rm L/L_{Eddington}$ respectively, then we should find that the NLS1s with low values

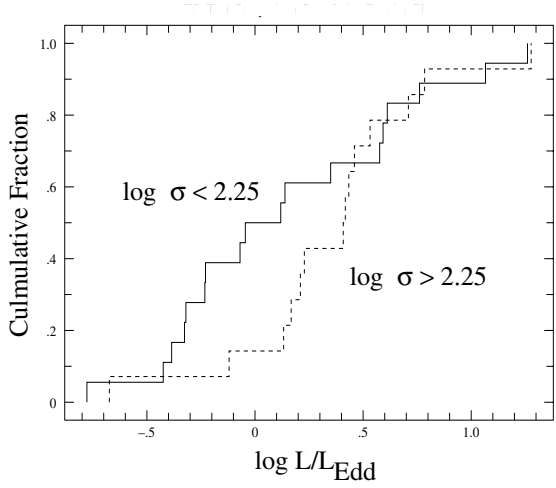

Fig. 3. Cumulative fraction for a K-S test of $L/L_{Eddington}$ for NLS1 with $\log\sigma_{[OIII]} < 2.25$ (solid line) and $\log\sigma_{[OIII]} > 2.25$ (dashed line). The two distributions are clearly different. The NLS1s with high $L/L_{Eddington}$ occupy a distinct region on the M_{BH}–σ plane.

of σ i.e. those close to the M_{BH}–σ relation to have flatter α (and lower $\dot{m}$) compared to NLS1s with high values of σ. We find again that the two populations are very different with the low σ population having flatter spectra. The K-S test probability of being drawn from the same population is P=0.2 [11].

2 Conclusion

We thus re-affirm the scenario first presented in Mathur et al. [10] and confirmed by Grupe & Mathur [6]: at present epoch, black holes grow in mass substantially in their high accretion phase. As they grow, they may approach the M_{BH}–σ relation for normal galaxies. The mass growth in the low accretion phase, as in BLS1s and also in some NLS1s, appears to be insignificant. his scenario is also consistent with the proposal that NLS1s are younger members of the Seyfert population [9].

The relationship between BH mass and the bulge mass appears to be a function of redshift. At high redshift, Rix et al. (this meeting) have found that some quasars lie above the M_{BH}–σ relation, implying that the BH growth precedes the bulge growth. At low redshift, we find the opposite. These results are consistent with the downsizing of AGN activity or the "anti-hierarchical" BH growth found by many authors (e.g. Merloni, these proceedings). In this scenario, high

mass BHs were in place at high redshift and BHs with lower mass became active and go through substantial growth phase at progressively lower redshifts. It makes sense then that the BH of mass $10^6 - 10^7$ $M_\odot$ are still growing today. Since the galaxies have mostly formed at high redshift, the growing BHs have to "catch-up" to be on the $M_{\rm BH}$–σ relation, while at high redshift, evolution toward the $M_{\rm BH}$–σ relation could be driven by the growth of the host galaxies. In the scenario of downsizing of AGN activity, the AGN lifetimes also depend upon mass. Marconi and collaborators (these proceedings) found that the average total lifetime of active phases ranges from 4.5×10^8 yr for $M_{\rm BH} < 10^7$ $M_\odot$ to $\sim 1.5 \times 10^8$ yr for $M_{\rm BH} > 10^9$ $M_\odot$. This, again, is consistent with our observations of NLS1s. Assuming that the highly accreting NLS1s will eventually reach the $M_{\rm BH}$–σ relation, we found that the lifetime of these BHs of $\sim 10^7$ $M_\odot$ to be $> 3 \times 10^8$ years [10]. It is thus encouraging that observations of a wide range of phenomena, including the X-ray background, BHs in local galaxies, NLS1s, and high-redshift quasars, are still able to suggest a consistent picture of black hole growth.

References

1. Czerny, B., Nikolajuk, M., Piasecki, M., Kuraszkiewicz, J.: MNRAS, **325**, 865 (2001)
2. Ferrarese, L., & Merritt, D.: ApJ, **539**, L9 (2000)
3. Ferrarese, L., Pogge, R.W., Peterson, B.M., Merritt, D., Wandel, A., & Joseph, C.L.: ApJ, **555**, L55 (2001)
4. Gebhardt, K., Bender, R., Bower, G., Dressler, A., Faber, S.M., et al.: A&A, **539**, L13 (2000)
5. Gebhardt, K., Kormendy, J., Ho, L.C., Bender, R., Bower, G., et al.: ApJ, **543**, L5 (2000)
6. Grupe, D. & Mathur, S.: ApJL, **606**, L41 (2004)
7. Haehnelt, M.: Classical and Quantum Gravity, **20**, S31 (2003)
8. King, A.: ApJL, **596**, L27 (2003)
9. Mathur, S.: MNRAS, **314**, L17 (2000)
10. Mathur, S., Kuraszkiewicz, J., & Czerny, B.: New Astronomy, **6**, 321 (2001)
11. Mathur, S. & Grupe, D.: A&A, submitted (2004).
12. Miralda-Escudé, J. & Kollmeier, J.A.: ApJ, submitted (astro-ph/0310717) (2004).
13. Peterson, B.M., McHardy, I.M., Wilkes, B.J., Berlind, P., Bertram, R., et al.: ApJ, **542**, 161 (2000)
14. Tremaine, S., Gebhardt, K., Bender, R., et al.: ApJ, **574**, 740 (2002)
15. Wandel, A., & Boller, T.: A&A, **331**, 884 (1998)
16. Williams, R. J., Mathur, S., Pogge, R. W.: ApJ, **610**, 737 (2004)

Measuring the Masses and Accretion Rates in Rapidly Growing Young NLS1s

T. Boller

Max-Planck-Institut für extraterrestrische Physik, Garching, Postfach 1312, 85741 Garching

Abstract. We find that Narrow-Line Seyfert 1 Galaxies accrete at moderately super-Eddington rates. This was already suggested with the discovery of extreme soft X-ray excesses with ROSAT, and now can be quantitatively measured with XMM-Newton. NLS1s are, in this context, reminiscent of Galactic Black Hole Binary systems in the soft state. Here we report on the XMM-Newton observation of IRAS 13224–3809 and 1H 0707–495, the latter was observed once in 2000, and again in 2002. Both objects show a common characteristic spectral shape: a strong soft X-ray excess; and a steep hard power-law component, which gradually flattens with increasing energies and abruptly drops at energies above 7 keV. The slim-disc model can explain the strong soft X-ray excesses and high disc temperatures, which exceed the standard Shakura-Sunyaev optically thick and geometrically thin accretion disc expectation. We find that both objects accrete close to, or even above the Eddington rate, and that the accretion rate is on the order of 10 to 20 Eddington units. As a results, NLS1s become normal broad-line Seyfert objects on time scales of only a few 10 Million years, assuming that the high accretion rate ceases. In addition the ionizing continuum is also a function of time as the black hole mass increases. The increasing black hole mass in NLS1s can also account for the evolutionary sequences of: steep to flat ROSAT spectra, the flattening of the 2-10 keV power-law slope, and most probably the decreasing optical Fe II multiplet emission.

1 NLS1s accrete at moderately super-Eddington rates

The slim-disc model was first worked out by Abramowicz et al. (1988). The model contains a solution for high accretion rate systems based on additional advection of heat and relativistic Roche-Lobe overflow, and introduces a new branch to the Shakura-Sunyaev surface density-accretion rate plane. The disc now becomes optically- and geometrically-thick. Mineshige et al. (2000) found that all NLS1s observed with ASCA fall into the slim-disc regime with accretion rates (dM/dt) / (L_E/c^2) between 10 and 20. Tanaka et al. (2004) have estimated the black hole masses of IRAS 13224–3809 and 1H 0707-495 to be $(1-2)\cdot 10^6$ solar masses. Extrapolating Fig. 1 of Watarai gives an estimated accretion rate of (10 - 20) ·(L_E/c^2), corresponding to about $6\cdot 10^{24}$ gs^{-1}.

ESO Symposia: Growing Black Holes, pp. 170–174, 2005.

2 Expected parameter changes due to the black hole mass growth

2.1 FWHM of optical emission lines

Under the simple assumption that the accretion luminosity equals the luminosity derived from a simple Planck emission law one gets: $\mathrm{FWHM(t)} = (\xi \cdot {n_e}^{1/4}) \cdot 2\eta \cdot (M^2/(dM/dt))^{3/16}$. Assuming that the high accretion rate ceases for some time, the increasing black hole mass results in increasing optical emission line widths. In the case of 1H 0707–495, the FWHM of the Hβ at present is 1000 kms^{-1}. In Fig. 1 we demonstrate the increase of the optical line widths as a function of time for linear and exponential growth of the black hole mass. A comparison with the SDSS early data release, Williams et al. (2002) found 135 NLS1s out of 934 Seyfert 1 galaxies with optical Hβ line widths above 2000 kms^{-1} (the arbitrary line width used to discriminate NLS1s from broad-line Seyfert 1 galaxies). Assuming a mean AGN life time of 10^8 years, results in a mean NLS1 phase of about 15 million years, in good agreement with the NLS1 phase of 25 million years predicted for 1H 0707–495. In Figure 2 we show the predicted black hole mass growth for 1H 0707–495 assuming the black hole mass and accretion rate estimated from the XMM-Newton observations as given above. For the exponential growth rate the black hole mass doubling time is only 12 million years, and after 90 million years the black hole mass of 1H 0707–495 has increased by two orders of magnitude.

2.2 Other parameter changes

In addition to the increasing line widths due to the increasing black hole mass, other parameters are expected to change with time. One of these parameters is the ionizing continuum. As the temperature of the accretion disc is inversely related to the black hole mass, the temperature of the disc will decrease with time. This explains the decreasing ROSAT photon index slope in dependence of the optical line widths (Fig. 8 of Boller et al. 1996). In addition, the cooling of the accretion disc corona becomes more inefficient due to the decreasing ionizing photons and therefore the corona is expected to become hotter. This is indicated by the decreasing 2-10 keV photon index as a function of optical line widths as shown by Brandt et al. (1997). Finally, let's speculate on the physical reason for the extreme optical Fe II multiplet emission as observed in NLS1s and the weak Fe II emission seen in broad-line Seyfert 1 galaxies. Fe II multiplet emission requires densities above 10^9 particles per cm^3. Therefore X-rays are required to ionize Fe I to Fe II. As the ionizing continuum is decreasing with time the efficiency to ionize Fe is also decreasing, which might explain the significant difference in the optical Fe II multiplet emission as observed in NLS1s and broad-line Seyfert 1 galaxies.

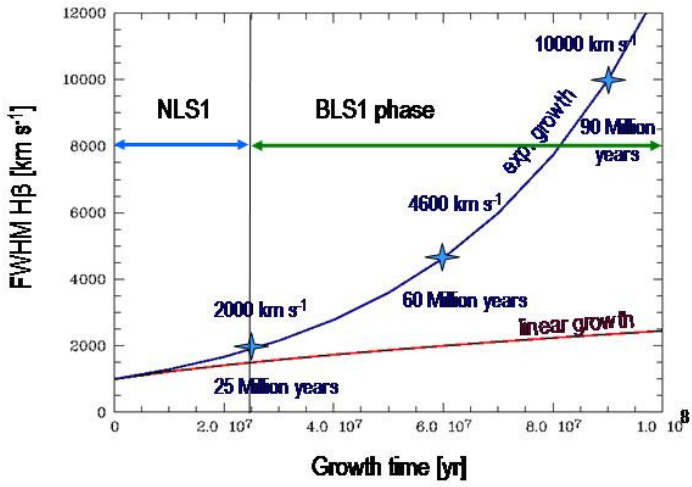

Fig. 1. Evolution of the Hβ emission line width as a function of black hole growth rate for the NLS1 1H 0707–495. The presently measured FWHM of 1000 km s^{-1} increases by a factor of 2 within only 25 million years assuming an exponential growth of the black hole mass. Assuming that the high accretion rate is ceased for some time, the optical line widths reaches 10000 km s^{-1} after 90 million years.

3 Implications of super-Eddington accretion

Super-Eddington luminosities might cause the observed high-velocity outflows observed in IRAS 13224–3809 (Fe K edge energy shifted to 8.2 keV, implies an outflow of neutral Fe of about 0.15 c) and 1H 0707-495 (Fe K edge observed at 7.5 keV, implies 0.05 c). The sharpness of the edge, which is about 200 eV (within the energy resolution of the EPIC instruments on-board XMM-Newton) and the missing Kβ UTA absorption feature (Palmeri et al. 2003) suggest that the Fe is neutral and hence in approaching matter (see also Boller et al. 2003, Gallo et al. 2004). The high accretion rates indicate a gas rich environment surrounding the black hole. The observed Fe overabundance ($>$ 3 x solar) represent significant contribution from type Ia supernovae. These facts imply a recent star formation episode. The low black hole masses of NLS1s are rapidly growing due to high accretion rates, implying that NLS1s become normal Seyfert 1s on time scales of less than 10^8 years. These results are consistent with the cosmological evolution of AGN: the lower the mass, the more recent is the peak activity, putting forward Smitha Mathur's view of NLS1s as AGN in the making (Mathur 2000).

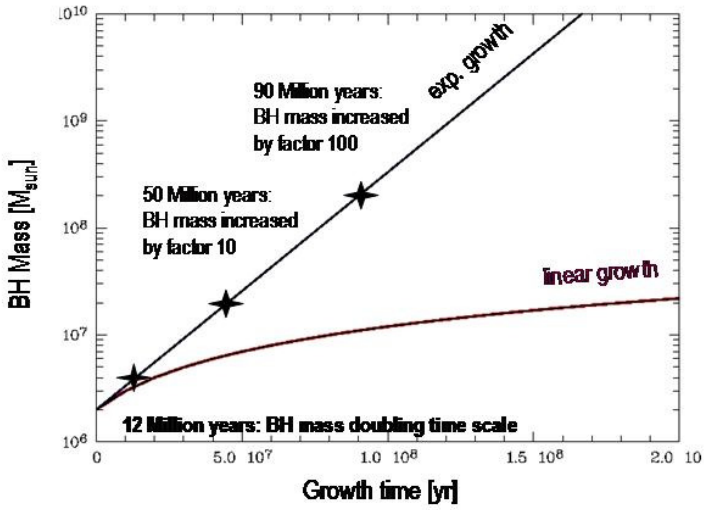

Fig. 2. Predicted black hole mass of 1H 0707–495 as a function of time. The mass and accretion rate has been estimated from the XMM-Newton observations (see text for details). After 90 Million years the presently measured mass has increased by two orders of magnitude.

4 Summary

XMM-Newton observations allow us to measure black hole masses and black hole growth rates . The NLS1s 1H 0707–495 (GT and AO2) and IRAS 13224–3809 are accreting at luminosities close to, or above the Eddington luminosity: $L_{min}/L_{edd} \sim 1-2$. The blackbody temperature is high: 90-120 eV, and exceeds the limit from standard geometrically thin accretion discs. The objects have relatively low black hole masses of about 10^6 solar masses and are rapidly growing with $dM/dt \sim (10-20)(L_{edd}/c^2)$. Assuming that at some point the high accretion rates are ceased, NLS1s become normal Seyfert 1s within a few tens million years. These results are consistent with the cosmological evolution of AGN: the lower the mass, the more recent is the peak of activity.

References

1. M.A. Abramowicz, A. Marek A.R. Prasanna: ApJ **332**, 646, (1988)
2. Th. Boller, W.N. Brandt, H. Fink: AA **305**, 53, (1996)
3. Th. Boller, Y. Tanaka, A. Fabian et al: MNRAS **343**, 89, (2003)

4. W.N. Brandt, S. Mathur, M. Elvis: MNRAS **285**, 25, (1997)
5. L. C. Gallo, Y. Tanaka, Th. Boller et al: MNRAS in press (astro-ph/0405159)
6. S. Mathur, New Astronomy Reviews **44**, 469, (2000)
7. S. Mineshige, T. Kawaguchi, M. Takeuchi et al.: PASJ **52**, 499, (2000)
8. P. Palmeri, C. Mendoza, C. Kallman et al: AA **403**, 1175, (2003)
9. Y. Tanaka, Th. Boller, L. Gallo et al.: PASJ **56**, L9, (2004)
10. K. Watarai, T. Mizuno, S. Mineshige: ApJ **549**, 77, (2001)
11. R. Williams, R. Pogge, S. Mathur, AJ **124**, 3042, (2002)

X-ray/UV Correlation in MCG–6-30-15

P. Arévalo[1], I. Papadakis[2],
B. Kuhlbrodt[3,4], and W. Brinkmann[1]

[1] MPE, Postfach 1312, 85748 Garching, Germany
[2] Department of Physics, University of Crete, Heraklion, Greece
[3] Astrophysikalisches Institut Potsdam, Potsdam, Germany
[4] Hamburger Sternwarte, Hamburg, Germany

1 Introduction

The connection between the UV and X-ray emission in AGN depends mainly on two processes: Comptonisation of UV photons into the X-ray range and thermal reprocessing of X-rays into the UV band. Both processes introduce correlations between the light curves of these energy bands but predict opposite time lags. The study of the correlated variability in these bands can in principle determine which of the emission processes dominates in a given object. In this paper we study the variability of the narrow line Seyfert 1 galaxy MCG–6-30-15 using simultaneous X-ray and UV data obtained with *XMM-Newton*. A complete account on this work is given in [1].

2 Light Curves

MCG–6-30-15 was observed by XXM-Newton during three revolutions producing ∼300 ks of scientifically useful data. The X-ray light curve was constructed using all single and double events on the PN detector within a radius of 50" from the centre of the source, with QUALITY FLAG=0 and energies in the 0.2–10.0 keV range. The resulting light curve has an average luminosity $\sim 10^{43}$ erg/s and the minimum to maximum flux ratio is ~ 5. The U band (3000−4000 Å) data from the OM instrument consisted of a series of 274 snapshots, each 800 s long. To obtain the AGN flux accurately we decomposed the images into nuclear point source plus disc galaxy components [3]. The fitted nuclear fluxes were then used to build the light curve and binned to reduce the scatter. The binned U band light curve variability amplitude is $\sim 15\%$ and its average luminosity is $\sim 10^{41}$ erg/s.

3 Cross Correlation Analysis

The cross correlation between the UV and X-ray light curves was computed using the discrete correlation function (DCF) [2]. The most significant feature found was a positive correlation peak at $\tau_{\max} = 160^{+45}_{-65}$ ks with amplitude $DCF_{\max} = 0.82^{+0.17}_{-0.25}$ where the UV leads the X-rays. No significant peaks were evident in negative lags i.e. there is no indication of UV variations being driven by changes in the X-ray flux.

ESO Symposia: Growing Black Holes, pp. 175–176, 2005.

4 Discussion and Conclusions

4.1 Reprocessing Scenario

There is observational evidence that the X-ray source in this object illuminates cooler nearby material [7]. It is therefore also expected that part of the X-ray flux will be thermally reprocessed and re-emitted in the U band. However, the DCF between the light curves shows no significant features with X-rays leading the UV and so give no indication of reprocessing.

We estimated the expected amount of reprocessed U flux using a simple model: a standard thin disc and a compact X-ray source located on the disc axis at a height $h = 3 - 10\,R_{\rm S}$. The U flux was then integrated from all radii in the disc assuming that the total X-ray flux adds to the viscous dissipation flux producing local black body spectra. A change by a factor of 4 in the X-ray flux induced 4%−11% U flux variations, where smaller effects result from smaller values of h. Therefore, the reprocessed component might be present but too small to be detected in this data, especially if h is small.

4.2 Comptonisation Scenario

The positive peak found in the DCF with UV variations leading the X-ray's suggests that variations in the thermal component drive the changes in the emission of the scatterer and give evidence for the Comptonisation scenario. To investigate the origin of the time lag we estimated the physical separation of the emitting regions. The X-rays are probably emitted by a compact source close to the central black hole [7]. The U band emission is probably produced thermally through viscous dissipation in the accretion disc. Again using the thin disc approximation we calculated the radii of the disc that produce most of the U band flux. The light travel time between this region and the centre resulted to be a few ks, too short to explain the measured lag. However, as the disc probably extends down to the last stable orbit, most of the seed photons for Comptonisation should come from this inner region and with higher energies than the observed U band. Therefore it is probable that the U band flux is mainly emitted in a different region of the accretion disc than the seed photons. The length of the measured time lag favours models where these regions are connected by variations in the accretion flow which affect first the flux in outer radii, responsible for the U emission, and then in the centre, where the seed photons are mainly produced.

References

1. P. Arévalo, I. Papadakis, B. Kuhlbrodt, W. Brinkmann: submitted to A&A
2. R.A. Edelson, J.H. Krolik: ApJ **333**, 646 (1988)
3. B. Kuhlbrodt, L. Wisotzki, K. Jahnke: MNRAS **349**, 1027 (2004)
4. B.M. Peterson, I. Wanders, K. Horne, et al.: PASP **110**, 660 (1998)
5. J. Timmer, M. König: A&A **300**, 707 (1995)
6. S. Vaughan, A.C. Fabian, K. Nandra: MNRAS **339**, 1237 (2003)
7. S. Vaughan, A.C. Fabian: MNRAS **348**, 1415 (2004)

Dynamical Models Linking BH Masses and DM Content

P. Buyle, H. Dejonghe, and M. Baes

Ghent University, Krijgslaan 281 S9, Ghent B-9000, Belgium

Abstract. We investigate the relation between the dark matter distribution of galaxies and their central supermassive black holes which is suggested by the $v_c - \sigma$ relation. Since early-type galaxies appear to have larger black holes than late-type ones, we look for an equivalent pattern in the dark matter distribution as a function of Hubble type. To achieve our goal we use a state-of-the-art modelling code that allows a variety of geometries to be fitted to a combination of radio and optical observations of galaxies with different morphology.

1 Introduction

Current models for galaxy formation and evolution all incorporate the role of a supermassive black hole. More in particular, they are usually calibrated against known observational relations, such as the Tully-Fisher, $M_{BH} - \sigma$ [4,6] and the $v_c - \sigma$ [2,5] correlations. Since it becomes clear that the $v_c - \sigma$ relation is gaining importance due to its putative redshift independence, a firm observational basis for it seems to be called for. However, at the moment the relation is based on only 28 galaxies making it impossible to measure the intrinsic scatter. Moreover, its precise meaning is not established at all, let alone the combination of it with the $M_{BH} - \sigma$ relation. This in turn points to a poorly understood connection between the dark matter distribution and the SBH (Fig. 1a):

$$\log\left(\frac{M_{BH}}{M_\odot}\right) = (4.21 \pm 0.60)\log\left(\frac{v_c}{u_0}\right) + (7.24 \pm 0.17), \quad u_0 = 200\ km\ s^{-1}. \quad (1)$$

2 Intrinsic scatter of the v_c-σ relation

We started a project to measure the central velocity dispersions of 20 spiral galaxies with the 3.5m telescope at Calar Alto and we recently observed 12 Low Surface Brightness (LSB) galaxies with the VLT [3]. The majority of the LSB galaxies of our sample have asymptotic circular velocities below 100 km s^{-1}, while the velocities of the 20 spiral galaxies of our second sample are all between 100 km s^{-1} and 150 km s^{-1}. In combination with our already obtained data with velocities above 150 km s^{-1} [2], this will allow us to obtain the real intrinsic scatter of the $v_c - \sigma$ relation and to investigate this relation in the low mass regime, where it is hinted by small-number statistics to deviate from the known relation. The sample has also a nice spread along the Hubble sequence and therefore it allows us to investigate any morphological dependence as well.

ESO Symposia: Growing Black Holes, pp. 177–178, 2005.

3 Dark matter distribution

Almost all information that we have about the dark matter distribution within galaxies is based on rotation curves only and models that assume a spherical dark matter distribution. We plan to improve on the modelling part with a code which allows for both spherical and axisymmetric geometries to be fitted to a combination of radio and optical observations. The aim is to fit a model directly to the radio observations including the full emission distribution along the line-of-sight at each point without making preliminary assumptions of the circular velocity. Models will be fitted to a sample of 12 Low Surface Brightness galaxies of which HI observations are being made at the ATCA and of which we will propose photometry at the AAT to be able to derive the contribution of the luminous and dark matter. Instead of measuring rotation curves, we will derive distribution functions which contain all kinematical information of the system. In particular, we plan to investigate the link between the distribution function and morphology in our Low Surface Brightness sample, with the aid of diagrams in turning point space, such as Fig.1b.

References

1. M. Baes, P. Buyle, G. Hau & H. Dejonghe: MNRAS, **341**, L44-L48 (2003)
2. P. Buyle, L. Ferrarese, M. Baes & H. Dejonghe: *in preparation*
3. S. De Rijcke et al.: accepted for A&A (2004)
4. L. Ferrarese & D. Merritt: ApJ, **539**, L9 (2000)
5. L. Ferrarese: ApJ, **578**, 90 (2002)
6. K. Gebhardt et al.: ApJ, **539**, L13 (2000)
7. A. Kronawitter et al.: A&AS, **144**, 53 (2000)

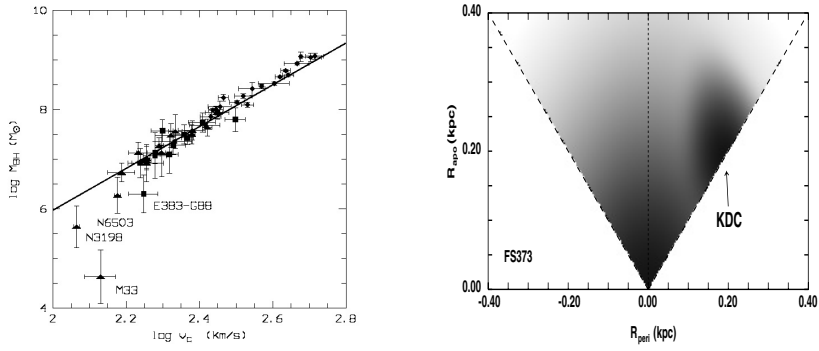

Fig. 1. (a) The $v_c - M_{BH}$ relation (1). Ferrarese's data [5] are represented by triangles, Kronawitter's [7] by circles and Baes et al.'s by squares. **(b)** Optical based distribution function of FS373 [3]

Super Massive Black Holes in Disk Galaxies: HST/STIS Observations for 3 new Objects

L. Coccato[1], M. Sarzi[2], E. Maria Corsini[1], A. Pizzella[1], and F. Bertola[1]

[1] Dipartimento di Astronomia, Università di Padova, 35122, Padova, Italy
[2] Physics Department, University of Oxford, OX1 3RH, UK

1 Sample selection, ionized-gas kinematics and model

As demonstrated in [1], it is possible to detect from ground-based observations the presence of a circumnuclear Keplerian disk (CNKD) around a super massive black hole (SMBH) with a large mass ($M_\bullet$). Its identification is possible from the study of the position-velocity (PV) diagram as done by [2]. From their work and literature data we select three disk galaxies, namely NGC 2179, NGC 4343 and NGC 4435, which have (i) a PV diagram consistent with the presence of a CNKD and (ii) a central stellar velocity dispersion (σ_c) which falls in a poorly sampled region of the $M_\bullet - \sigma_c$ relation [21,25].

For each target galaxy we obtained with HST/STIS the Hα and [NII] 6583 Å kinematics along the major axis and two 0.″25 parallel offset positions on either sides of the nucleus. We used the G750M grating with 0.″2 slit. For NGC 4435 an HST/STIS spectrum obtained along the disk minor axis was available in HST Archive with the same set-up. For NGC 2179 and NGC 4343 the spectrum reveals a disturbed gas kinematics. These two objects show an irregular dust-lane morphology, too. On the contrary, NGC 4435 shows a regular kinematics as well as a CNKD with a regular dust-lane morphology. This galaxy is a good candidate to model the ionized-gas velocity field in order to determine $M_\bullet$.

In the model we assumed an exponential radial profile both for the velocity dispersion and emission-line flux. We build the model velocity field by considering the contribution of the stellar potential and the Keplerian potential of a SMBH. The stellar potential was measured from the surface-brightness radial profile using a constant mass-to-light ratio and spherical symmetry, by means of the Multi-Gaussian Method [5] as done in [6]. Effects of the STIS PSF, of the slit width and the bleeding of charge between adjacent pixels in the CCD were also taken into account. The analysis of the dust-lane morphology provided the initial guesses for the position angle and inclination of the CNKD. The rotation curves obtained from the best-fit model and adopting a $M_\bullet$ as predicted by the $M_\bullet - \sigma_c$ relation are compared to the observed gas kinematics in Fig. 1.

2 Results and conclusions

Ground-based observations evidence that about 20% of galaxies show a PV diagram which is consistent with the presence of a CNKD [2]. This criterion should

ESO Symposia: Growing Black Holes, pp. 179–180, 2005.

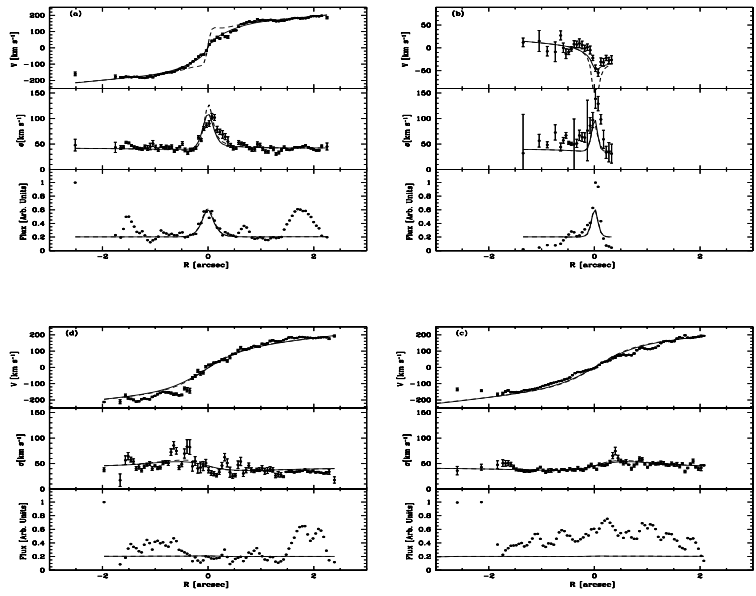

Fig. 1. Observed ionized-gas kinematics (*filled circles*) and model predictions for NGC 4435. Rotation curve (*upper panel*), velocity dispersion profile (*central panel*), and emission-line flux profile (*lower panel*) are shown for the major axis *(a)*, minor axis *(b)*, $+0\farcs25$ offset axis *(c)*, and $-0\farcs25$ offset axis *(d)*. The *continuous line* and *dashed line* represent the best-fit model prediction with $M_\bullet \simeq 1 \times 10^7 M_\odot$ and the model with $M_\bullet \simeq 8 \times 10^7 M_\odot$ as predicted by $M_\bullet - \sigma_c$ relation, respectively.

be combined with the presence of a regular dust-lane morphology, according to the results later found by [7]. Indeed in our sample NGC 4435 is the only galaxy that shows a regular dust-lane morphology as well as a regular rotation curve. The modeling work is still in progress, but preliminary results give a $M_\bullet \simeq 10^7 M_\odot$. On the contrary, the $M_\bullet - \sigma_c$ relation predicts for NGC 4435 $M_\bullet \simeq 8 \times 10^7 M_\odot$ for the observed $\sigma_c = 174$ km s^{-1} [8]. However, as shown in Fig. 1, the central velocity gradient obtained for $M_\bullet \simeq 8 \times 10^7 M_\odot$ is not consistent with the observed one.

References

1. F. Bertola et al.: ApJ **509**, L93 (1998)
2. J. G. Funes et al.: A&A, **388**, 50 (2002)
3. L. Ferrarese, D. Merritt: ApJ, **539**, L9 (2000)
4. K. Gebahrdt et al.: ApJ, **539**, L13 (2000)
5. G. Monnet, R. Bacon, E. Emsellem: A&A, **253**, 336 (1992)
6. M. Sarzi et al.: ApJ, **555**, 685 (2001)
7. L. C. Ho et al.: PASP, **114**, 137 (2002)
8. M. Bernardi et al.: AJ, **123**, 2990 (2002)

X-ray Variability of the Milky Way

H.-J. Grimm[1], M. Gilfanov[2], and R. Sunyaev[2]

[1] Harvard-Smithsonian Center for Astrophysics, Cambridge MA 02138, USA
[2] Max-Planck-Institut für Astrophysik, Karl-Schwarzschild-Str. 1, 85741 Garching, Germany

Abstract. By constructing the power density spectrum of the Milky Way due to Galactic X-ray binaries (XRB) we investigate the prospect of disentangling the X-ray emission of galaxies due to SMBHs and X-ray binary populations for future X-ray missions.

XRBs are known to exhibit variability on a very broad range of timescales, from very long ($\sim$ years) to very short (few tens to thousands of Hertz). Our goal in this paper is to study the X-ray variability of the Milky Way due to its XRB population. For this purpose we combine the power density spectra (PDS) of X-ray binaries for all available timescales of variability from $\sim 10^{-8}$ Hz up to $\sim 10^{2}$ Hz. Accounting for the different contributions from sources the PDS is combined according to

$$PDS_{combined} = \frac{\sum_{all\ sources} PDS_s L_s^2}{(\sum_{all\ sources} L_s)^2}, \quad (1)$$

At low frequencies ($\sim 10^{-8} - 10^{-4}$ Hz) the combined (PDS) of XRBs can be described by a simple power law. At high frequencies ($\sim 10^{-2} - 10^{2}$ Hz) it exhibits an excess of power compared to the power law at low frequencies. The shape of the power spectrum is dominated by the PDS of GRS 1915+105. The total fractional *rms* of the Milky Way is 20–40%. Up to ∼30% of this *rms* is generated at high frequencies ($\sim 10^{-2} - 10^{2}$ Hz).

We investigate the possibility to use this excess power to distinguish the X-ray luminosity contribution of a population of XRBs from an AGN. Assuming an observation time of 100 ks, a frequency range of 1 Hz at 1 Hz and a detection significance of 3 σ, the distance out to which XEUS will be able to detect Milky Way variability (fractional *rms* ∼0.01–0.2, depending on GRS 1915+105) is plotted in Fig. 2. The Milky Way would be detectable for XEUS1 out to 7–24 Mpc, depending on the strength of variability. A galaxy with a luminosity of 10^{41} erg/s and a fractional *rms* of 10% will be observable out to 40 Mpc.

References

1. Markowitz A., Edelson R., Vaughan S., Uttley P., George I. M., Griffiths R. E., Kaspi S., Lawrence A., McHardy I., Nandra K., Pounds K., Reeves J., Schurch N., Warwick R.:ApJ, **593**, 96 (2003)
2. McHardy I. M., Papadakis I. E., Uttley P., Page M. J., Mason K. O.: MNRAS, **348**, 783 (2004)

ESO Symposia: Growing Black Holes, pp. 181–182, 2005.

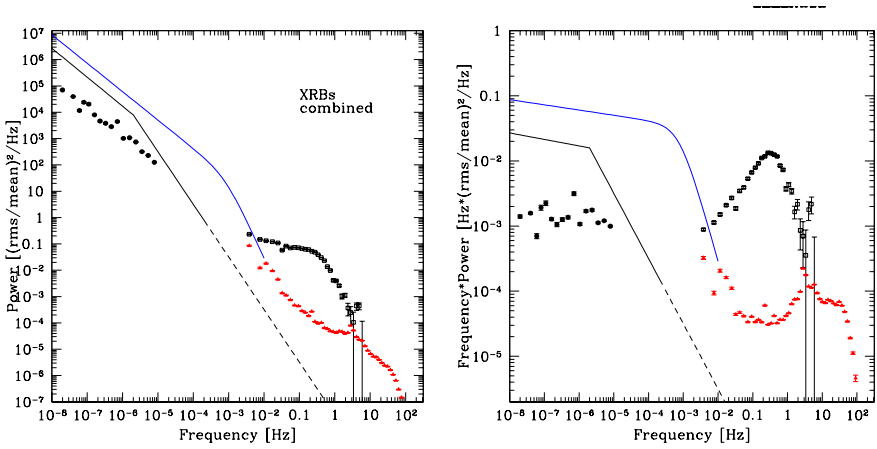

Fig. 1. Combined PDS of Galactic X-ray binaries. Filled circles show ASM data, open squares and filled triangles PCA data for different observations. The best fits to the PDS' of the AGN NGC 3516 [1] and NGC 4051 [2] is plotted (solid lines). The dashed line is a continuation to guide the eye. The left panel shows the PDS in units of fractional rms^2/Hz, the right panel in νP_ν. The strongest variability is observed at frequencies below ∼1 Hz in the high *rms* state (open squares). In the low *rms* state most power is emitted in the ASM energy range where νP_ν is flat. At PCA frequencies most of the power is emitted between $10^{-3}-10^{-2}$ Hz, and around 3 Hz. These frequency ranges are the most promising to be studied with XEUS.

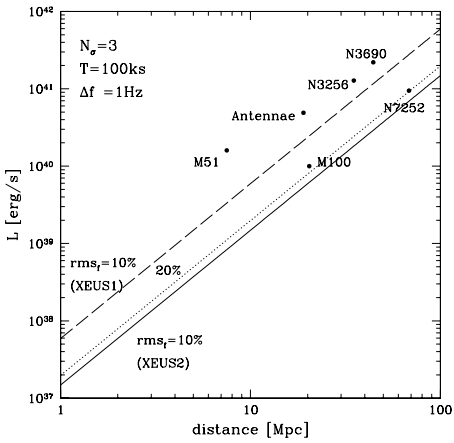

Fig. 2. Sensitivity estimate for XEUS assuming values of *rms* of 10% and 20%, an observation time of 100 ks, a frequency range of 1 Hz and a detection significance of 3 σ. The plot shows the dependence of the minimum luminosity of a galaxy on the distance for given parameters for the first and second configuration of XEUS. For comparison, the locations of some nearby galaxies are plotted.

Growing Black Holes in Narrow-Line Seyfert 1 Galaxies

D. Grupe and S. Mathur

The Ohio State University, 140W. 18th Av., Columbus, OH 43210, USA

Abstract. One of the most fundamental relations found among nearby galaxies and AGN is the M-σ relation between the black hole mass and the bulge stellar velocity dispersion (e.g. [11]). However, Narrow-Line Seyfert 1 galaxies (NLS1s) seem to deviate from this relation. We studied a sample of 75 soft X-ray selected AGN, 43 Broad Line Seyfert 1s and 32 NLS1s. We find that NLS1s lie below the M-σ relation as suggested by Mathur et al. [9]. Our result does not support theories of the M-σ relation in which the black hole mass is a constant fraction of the bulge mass (see also Mathur & Grupe in these proceedings). Black holes grow by accretion in well-formed bulges. As they grow they get closer to the M-σ relation of normal galaxies. Our results also support the hypothesis that NLS1s are AGN in a young state of their development [2,8].

1 Estimates of $M_{\rm BH}$ and σ

Our original sample of 110 AGN was selected from the ROSAT All-Sky Survey [33] by the selection criteria given in Grupe et al. [5]. About half of these sources are NLS1s (51 objects) and 59 are broad line Seyfert 1s (BLS1s). NLS1s and BLS1s show similar distribution in their redshifts, luminosities and equivalent widths of Hβ [5]. We removed all the objects in which [OIII] lines were severely unresolved leading to errors in the FWHM measurements, with S/N$<$ 3. This left us with a sample of 75 AGNs, 32 NLS1s and 43 BLS1s [6].

The black hole masses were estimated by the FWHM(Hβ) and the luminosity at 5100Å as described by Kaspi et al [5]. For the stellar velocity dispersion σ we used the FWHM([OIII]λ5007) as a surrogate, as suggested by [10].

2 Results

As shown in Fig. 1 in [6] (see also Mathur & Grupe in these proceedings), NLS1s and BLS1s occupy two distinct regions in the $M_{\rm BH} - \sigma$ plane. For a given velocity dispersion NLS1s tend to have smaller black hole masses than BLS1s. In [6] we discuss possible errors in the mass and velocity dispersion estimates. We concluded that there is a real mass difference between NLS1s and BLS1s. If FWHM([OIII]) were not a good surrogate for σ, we could expect to see a dichotomy between NLS1s and BLS1s. However, as shown in Figure 3 in [6] this is not the case: NLS1s and BLS1s have similar distributions in their σ.

ESO Symposia: Growing Black Holes, pp. 183–184, 2005.

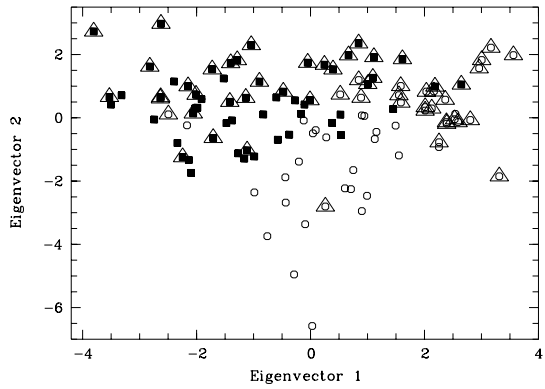

Fig. 1. Eigenvector 1 vs. 2 with NLS1s displayed as open circles, BLS1s as filled squares, and high luminosity sources with log L_X >37.0 [W] as triangles.

3 Discussion

We found that BLS1s do follow the M-σ relation of normal galaxies, while NLS1s do not. NLS1s are AGN which accrete at their Eddington limit [1,4] with black hole masses still growing through accretion. This result is supported by the findings from a Principal Component Analysis (PCA) of the original sample of 110 AGN: NLS1s are objects with a large Eigenvector 1 (EV1) and small Eigenvector 2 (Fig. 1). The interpretation of EV1 is that it represents the Eddington ratio and EV2 is the mass of the black hole. NLS1s are therefore AGN with relatively small black hole masses but high Eddington ratio [4]. Our result suggests that the black hole mass is *not a constant fraction* of the bulge mass or the stellar velocity dispersion at all times. Accretion (and therefore black hole growth) is highest at the beginning and decreases as time goes by. Black holes is NLS1s are still growing towards the Tremaine et al. [11] M-σ relation. This scenario is also consistent with the proposal of [2], [3] and [8] that NLS1s are AGN in an early state of their development.

References

1. Boroson: ApJ, **565**, 78 (2002)
2. Grupe: PhD Thesis, Göttingen (1996)
3. Grupe et al.: A&A, **350**, 805 (1999)
4. Grupe: AJ, **127**, 1799 (2004)
5. Grupe et al.: AJ, **126**, 156 (2004)
6. Grupe, Mathur: ApJ, **606**, L41 (2004)
7. Kaspi et al.: ApJ, **533**, 631 (2000)
8. Mathur: MNRAS, **317**, L17 (2000)
9. Mathur et al.: New Astr., **6**, 321 (2001)
10. Nelson: ApJ, **544**, L91 (2000)
11. Tremaine et al.: ApJ, **574**, 740 (2002)
12. Voges et al.: A&A, **349**, 389 (1999)

SMBH Mass Derived from Reverberation Mapping and Gravitational Redshift

W. Kollatschny

Universitäts-Sternwarte, D-37083 Göttingen, Germany

1 Introduction

We carried out a spectroscopic variability campaign of the narrow-line Seyfert 1 galaxy Mrk 110 with the 10m Hobby-Eberly Telescope at McDonald Observatory. High signal-to-noise spectra with exactly the same instrumentation were taken over a period of more than six months.

2 Reverberation Mapping

We observed variations in the integrated Balmer and Helium lines. They are delayed by 3 to 33 light days with respect to the continuum variations respectively. The line widths of the individual Balmer and Helium rms profiles are different. The widths of these emission lines are correlated with their delayed response (see Fig.1). We derived a central black hole mass of $M_{\rm virial} = 1.8 \pm 0.4 \times 10^7 M_\odot$ from

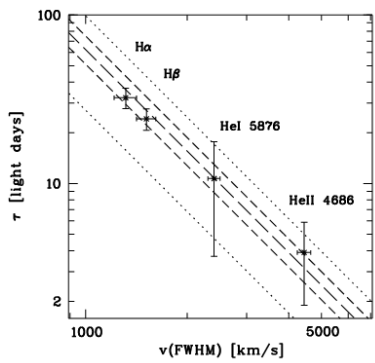

Fig. 1. Results of the HET variability campaign of Mrk 110: time lag of Balmer and Helium lines as a function of FWHM of the rms profiles. Dotted and dashed lines indicate calculated virial masses of $0.8, 1.5, 1.8, 2.2, 2.9 \times 10^7 M_\odot$ (from bottom to top).

the variable lines [4] making the assumption that the line widths are caused by gas dynamics in the broad-line region surrounding the central massive black hole. We could show from our 2-D velocity maps of the broad emission line profiles

ESO Symposia: Growing Black Holes, pp. 185–186, 2005.

that only Keplerian accretion disk BLR models match the observed velocity-delay pattern [3,1]. Therefore the calculated black hole mass is affected by the unknown orientation of the accretion disk.

3 Gravitational Redshift

We determined mean and rms emission line profiles of the most intense lines Hα, Hβ, HeIλ5876, and HeIIλ4686 from our variability campaign. The rms profiles are a measure of the variable component of the line profile. We detected a shift in all rms emission line profiles with respect to their mean profiles. The variable rms line components originate more closely to the central black hole. We took the shifts $\Delta v = \Delta z\ c$ in the variable line components as gravitational redshift and calculated a central black hole mass of $M_{\rm grav} = 14.0 \pm 3.0 \times 10^7 M_\odot$ [2]. This

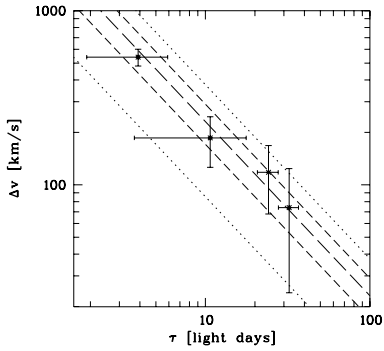

Fig. 2. Redshift of the rms profiles of the HeIIλ4686, HeIλ5876, Hβ and Hα lines as a function of the distance of the rms line emitting region. The dotted and dashed curves show computed lines of gravitational redshifts for central masses of $5.0, 10.0, 13.5, 17.0, 22.0 \times 10^7 M_\odot$ (from bottom to top).

derived black hole mass $M_{\rm grav}$ is not affected by the orientation of the central accretion disk in contrast to the mass $M_{\rm orbital}$ derived from the emission line widths.

Acknowledgment: Part of this work has been supported by DFG grant Ko857/24.

References

1. W. Kollatschny: A&A **407**, 461 (2003a)
2. W. Kollatschny: A&A **412**, L61 (2003b)
3. W. Kollatschny, K. Bischoff: A&A **386**, L19 (2002)
4. W. Kollatschny, et al.: A&A **379**, 125 (2001)

At the Beer and brezen' party on Tuesday

At the Beer and brezen' party on Tuesday

First Simultaneous NIR/X-ray Flare Detection from SgrA*

A. Eckart[1], F. K. Baganoff[2], M. Morris[3], M.W. Bautz[2], W.N. Brandt[4], G.P. Garmire[4], R. Genzel[5,6], T. Ott[5], G.R. Ricker[2], C. Straubmeier[1], T. Viehmann[1], R. Schödel[1], G.C. Bower[6], and J.E. Goldston[6]

[1] I.Physikalisches Institut, Universität zu Köln, Zülpicher Str.77, 50937 Köln, Germany, email: eckart@ph1.uni-koeln.de
[2] Center for Space Research, Massachusetts Institute of Technology, Cambridge, MA 02139-4307, USA, email: fkb@space.mit.edu
[3] Department of Physics and Astrometry, University of California Los Angeles, Los Angeles, CA 90095-1562, USA
[4] Department of Astronomy and Astrophysics, Pennsylvania State University, University Park, PA 16802-6305, USA
[5] Max Planck Institut für extraterrestrische Physik, Giessenbachstraße, 85748 Garching, Germany
[6] Department of Astronomy and Radio Astronomy Laboratory, University of California at Berkeley, 601 Campbell Hall, Berkeley, CA 94720, USA

Abstract. We summarize some of the results on the first simultaneous near-infrared/X-ray detection of the SgrA* counterpart which can be associated with the massive 3–$4\times10^6 M_\odot$ black hole at the center of the Milky Way. We report on observations with the NACO adaptive optics (AO) instrument at the European Southern Observatory's Very Large Telescope[1] and the ACIS-I instrument aboard the *Chandra X-ray Observatory*. Quasi-simultaneous observations have also been carried out at a wavelength of 3.4 mm using the Berkeley-Illinois-Maryland Association (BIMA) array. In the 2 - 8 keV X-domain we detected a flare with an excess luminosity of about 6×10^{33} erg/s. Coincidently with the peak of the X-ray flare a fading flare of Sgr A* with >2 times the interim-quiescent flux was detected at the beginning of the NIR observations. The event overlapped with the fading part of the X-ray flare. The NIR/X-ray flare was also accompanied by increased mm-activity measured about 8 hours afterwards. The event implies that the NIR/X-ray flare emission was coupled without a time lag larger than 15 min and probably originated from the same ensemble of electrons.

1 Introduction

Over the last decade, the investigation of the dynamics of stars has provided compelling evidence for the existence of a massive black hole (MBH) at the center of the Milky Way [4,9,10,12–15,5,31,32]. Located at a distance of only 8 kpc from the solar system [30,8] it allows detailed observations of stars at distances much less than 1 pc from the central black hole candidate, the compact radio source Sgr A*. Additional strong evidence for a massive black hole at the position of

[1] Based on observations at the Very Large Telescope (VLT) of the European Southern Observatory (ESO) on Paranal in Chile; Program: 271.B-5019(A).

ESO Symposia: Growing Black Holes, pp. 191–196, 2005.

Sgr A* came from the observation of interim-quiescent (or IQ) and flare activity from that position both in the X-ray and recently in the near-infrared wavelength domain [2,3,6,7,27,17,3,16].

The first observations of SgrA* covering an X-ray flare simultaneously in the near-infrared using seeing limited exposures revealed only upper limits to the NIR flux density [6]. Eckart et al. [7] now report on the first successful simultaneous NIR/X-ray campaign using adaptive optics. Details of the observations in the NIR, X-ray and mm-wavelength range are given in [7].

1.1 First Simultaneous X-Ray/NIR Detection of Sgr A*

Simultaneous monitoring programs from the radio to the X-ray regime will allow us to investigate the physical processes that are associated with the variable emission from Sgr A* at the position of the massive black hole at the center of the Milky Way. Eckart et al. [7] reported on the first simultaneous near-infrared/X-ray detection of Sgr A* (Fig. 1 and Fig. 2).

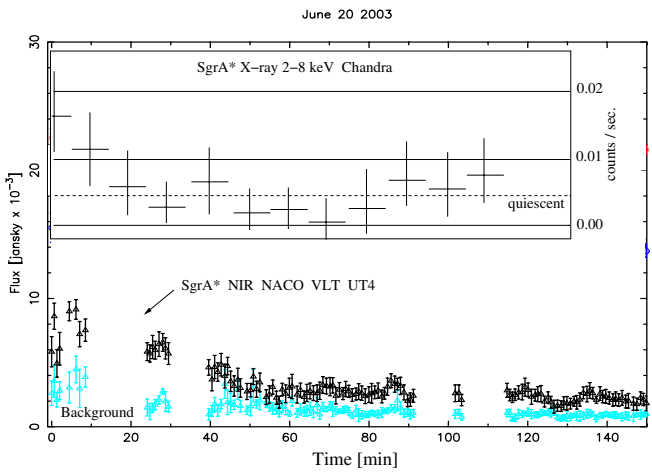

Fig. 1. Overlapping parts of the Chandra X-ray and VLT K-band light curves of the first simultaneously detected flare from Sgr A* as shown by [7]. The X-ray and NIR light curves are plotted with a common time axis. Straight solid lines in the inserted box represent the 0.00, 0.01, and 0.02 counts per second levels. The straight dashed line represents the X-ray IQ-state flux density level. The NIR observations started on 20 June 2003 at 23:51:15 (UT). The NIR data started 0.38 minutes before the midpoint of the highest X-ray data point.

These measurements are based on observations in June 2003 with the NACO/ VLT adaptive optics instrument and the ACIS-I instrument aboard the Chandra X-ray observatory. A fading flare of Sgr A* with more than 2 times the interim-quiescent flux was detected at the beginning of the NIR observations. The same

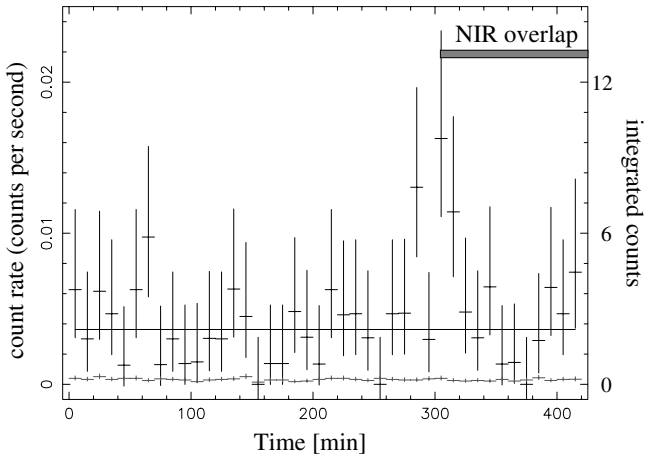

Fig. 2. X-ray light curve as observed by Chandra in the 1.0 arcsecond aperture and shown by [7]. The bin interval is 10 minutes. The solid straight line represents the X-ray IQ-state count rate. The background (lower points) was steady throughout the observations which started on 19 June 2003 at 18:46:38 (UT). The overlap with the NIR observations is indicated.

flare was also seen in the X-domain with an excess $2-10$ keV luminosity of about 6×10^{33} erg/s.

The simultaneous data allow to estimate a conservative upper limit of the time lag between the end of the NIR and X-ray flare of the order 15 minutes. These observations strongly support the assumption that X-ray and NIR flares are closely related processes. An important advantage of the simultaneous NIR/X-ray measurements is that the orders of magnitude higher resolution in the NIR clearly shows that the X-ray flares are associated with Sgr A* and no other object within the $\sim 1''$ beam of the Chandra telescope. A convenient explanation of the flaring state can be given by a synchrotron self-Compton model involving up-scattered sub-millimeter photons from a compact source component allowing for modest bulk relativistic motion.

Quasi-simultaneous observations of the same flare event have also been carried out at a wavelength of 3.4 mm using the Berkeley-Illinois-Maryland Association (BIMA) array. Compared to 8-9 hours before the NIR/X-ray flare, [7] report a significant 3-4σ increase (11 ± 3 %) in the millimeter flux density of Sgr A* during measurements about 7-9 hours afterwards. The slightly higher mm-flux density after the flare may be related to the flare activity observed in the X-ray and NIR domains. In three cases now there seems to be some evidence for a correlation between increased flare activity in the mm/sub-mm and the X-ray domain (see [7]). Future observations will reveal whether and how the individual mm-flare events or a general flare activity are related to events in the NIR or X-ray regime.

1.2 Sgr A* Flare Models

The overall emission from SgrA* is sub-luminous compared to purely radial Bondi-Hoyle accretion models (e.g. [23]). The overall emission is currently described in the framework of RIAF models (e.g. [21,34,28,24,25]). The models by [21] that describe the flare emission of SgrA* are based on synchrotron or on synchrotron self-Compton emission (SSC). They may be regarded as exemplary and applicable to other RIAF models (e.g. [34,28]). Such flare models raise the idea that the flares from Sgr A* may involve the conversion of magnetic energy into particle energy in the accretion flow. Such events could be similar to solar flares, where magnetic reconnection accelerates the coronal plasma.

The flare may also arise from a short-term overall increase in mass accretion onto Sgr A*, or an increase of the electron temperature or magnetic field strength. However, Markoff et al. [21] argue that these models are unlikely because the existing observations at radio and infrared wavelengths have never detected a sufficiently large increase in energy output as expected from the strength of the X-ray emission in these models (see also [19,6,32,33]).

Another model by Markoff et al. [21] is the so-called 'shock flare' or 'acceleration flare'. It involves processes (e.g., Fermi acceleration or magnetic reconnection) that accelerate a small fraction of the thermal electron population into a power-law tail of the electron distribution function. This model does not cause a large change of emission at infrared and radio/mm wavelengths, but can account for significant changes of the X-ray luminosity. Since the cooling time of synchrotron losses is much shorter than the observed length of the flares, this model requires repeated or continuous acceleration of the electrons. Other flare models as suggested by [20,3,26] are discussed in [7] as well.

Eckart et al. [7] fit a simple SSC spectrum to the first simultaneous NIR/X-ray measurement of a flare from Sgr A*. Here the X-ray flux is produced by up-scattering of a power-law distribution of sub-mm-wavelength photons into the NIR and X-ray domain. They have used the formalism given by [22] and [18]. Such a single SSC component model (although possibly too simplistic for the Galactic Center) explains the major flare characteristics and results in values for the electron Lorentz factor of a few 10^2 to a few 10^3 as well as magnetic field strengths of the order of a few Gauss to about 20 Gauss, which is well within the parameter range expected in the framework of RIAF models.

1.3 Flare Statistics

While the flare substructure is very likely linked with the dynamics of the accreted material [3,1], the overall flare rate is probably coupled to the tenuous material provided by the strong winds of the He-star within the central parsec [28,29,35]. These winds can be assumed to be clumpy. A first and simple attempt to describe the NIR flare activity of SgrA* would be to assume that the emission consists of successive flares with a characteristic duration but of varying intensity and that the flare intensity follows a power-law. In Fig. 2 we show a

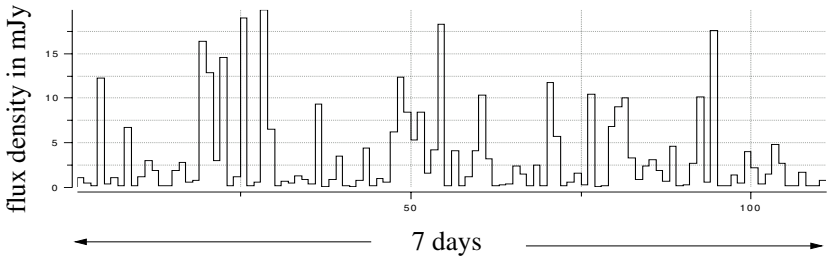

Fig. 3. Simulation of the SgrA* flare activity assuming a power spectrum relation between flare amplitude and the number of flares.

simulation of a seven day period during which the flare amplitudes A follow an expression $ln(N) = \xi\ ln(A) + C$.

Here N is the number of flares with a given amplitude, ξ the power spectral index, and C a constant. For a suitable value of ξ and a lower and upper amplitude limit (1.5 and 25 mJy and $\xi \sim -1.0$ in the case of Fig. 2) it is possible to statistically describe some of the observed NIR flare characteristics [3,6,16]. In the framework of such a power-law description the quasi continuous flux density between flares would correspond to the median flux density of low amplitude flare events. As for the relation between the NIR flares and variability at other wavelengths, the durations, rise and decay times, and spectral luminosities of X-ray flares are similar (e.g. [2,27,17]).

The NIR flare rate, however, appears to be almost twice as high as that in the X-ray flare rate during the Chandra monitoring in 2002 (1.2 ± 0.4 flares per day; [3,6]). The most recent AO data from the VLT and the Keck telescope taken in 2004 show that the NIR flare emission found in 2003 is likely to be a persistent phenomenon. Yet NIR flares stronger than the emission from the nearby high velocity stars S1 and S2 have not been detected so far.

References

1. Aschenbach, B., Grosso, N., Porquet, D., & Predehl, P.: A&A, **417**, 71 (2004)
2. Baganoff, F.K., Bautz, M.W., Brandt, W.N., et al.: Nature, **413**, 45 (2001)
3. Baganoff, F. K., Maeda, Y., Morris, M., et al.: ApJ, **591**, 891 (2003)
4. Eckart, A. & Genzel, R.: Nature **383**, 415 (1996)
5. Eckart, A., Genzel, R., Ott, T. and Schödel, R.: MNRAS, **331**, 917 (2002)
6. Eckart, A., Moultaka, J., Viehmann, T. et al.: In *Proceedings of the Galactic Center Workshop 2002 - The central 300 parsecs of the Milky Way*, Eds. A. Cotera, T. Geballe, S. Markoff, H. Falcke, Astron. Nachr. **324**, 557 (2003)
7. Eckart, A., Baganoff, F.K., Morris, M., Bautz, M.W., Brandt, W.N., Garmire, G.P., Genzel, R., Ott, T., Ricker, G.R., Straubmeier, C., Viehmann, T., Schödel, R., Bower, G.C., Goldston, J.E.: A&A in press, astro-ph/0403577 (2004)
8. Eisenhauer, F., Schödel, R., Genzel, R., et al.: ApJ, **597**, L121 (2003)
9. Genzel, T., Eckart, A., Ott, T. & Eisenhauer, MNRAS, **291**, 219 (1997)

10. Genzel, R., Pichon, C., Eckart, A., Gerhard, O.E., Ott, T.: MNRAS, **317**, 348 (2000)
11. Genzel, R., Schödel, R., Ott, T., Eckart, A., Alexander, T., Lacombe, F., Rouan, D., Aschenbach, B.: Nature, **425**, 934 (2003)
12. Ghez, A., Klein, B.L., Morris, M. & Becklin, E.E.: ApJ, **509**, 678 (1998)
13. Ghez, A., Morris, M., Becklin, E.E., Tanner, A. & Kremenek, T.: Nature, **407**, 349 (2000)
14. Ghez, A. M., Duchéne, G., Matthews, K., et al.: ApJ, **586**, L127 (2003a)
15. Ghez, A.M., Salim, S., Hornstein, S.D., et al.: ApJ, submitted, astro-ph/0306130 (2003b)
16. Ghez, A.M., Wright, S.A., Matthews, K., et al.: ApJ, **601**, 159 (2004)
17. Goldwurm, A., Brion, E., Goldoni, P. et al.: ApJ, **584**, 751 (2003)
18. Gould, R.J.: A&A, **76**, 306 (1979)
19. Hornstein, S.D., Ghez, A.M., Tanner, A., Morris, M., Becklin, E.E., and Wizinowich, P.: ApJ, **577**, L9 (2002)
20. Liu, S. and Melia, F.: ApJ, **566**, L77 (2002)
21. Markoff, S., Falcke, H., Yuan, F. & Biermann, P.L.: A&A, **379**, L13 (2001)
22. Marscher, A.P.: ApJ, **264**, 296 (1983)
23. Melia, F. & Falcke, H.: ARA&A, **39**, 309 (2001a)
24. Narayan, R., Quataert, E., Igumenshchev, I.V., & Abramowicz, M.A.: ApJ, **577**, 295 (2002)
25. Narayan, R., Igumenshchev, I.V. and Abramowicz, M.A.: Publications of the Astronomical Society of Japan, **55**, pp. L69 (2003)
26. Nayakshin, S., Cuadra, J., Sunyaev, R.: A&A, **413**, 173 (2004)
27. Porquet, D., Predehl, P., Aschenbach, et al.: A&A, **407**, L17 (2003)
28. Quataert, E.: In *Proceedings of the Galactic Center Workshop 2002 - The central 300 parsecs of the Milky Way*, Eds. A. Cotera, T. Geballe, S. Markoff, H. Falcke, Astron. Nachr. **324** p. 435 (astro-ph/0304099) (2002)
29. Quataert, E., submitted to ApJ Letters astro-ph/0310446 (2004)
30. Reid, M. J., Readhead, A. C. S., Vermeulen, R. C., & Treuhaft, R. N. 1999, ApJ, 524, 816
31. Schödel, R., Ott, T., Genzel, R. et al.: Nature, **419**, 694 (2002)
32. Schoödel, R., Genzel, R., Ott, et al.: ApJ,**596**, 1015 (2003)
33. Viehmann, T. Eckart, A. Moultaka, J. Straubmeier, C.: In*Proceedings of the 4th Cologne-Bonn-Zermatt-Symposium*, ed. S. Pfalzner, C. Kramer, C. Straubmeier, and A. Heithausen (Springer Verlag), p.303 (2004)
34. Yuan, F., Quataert, E. & Narayan, R.: ApJ, **598**, 301 (2003)
35. Yuan, F., Quataert, E. & Narayan, R.: ApJ, **606**, 894 (2004)

Sgr A West: A Parsec Scale Reservoir for Accretion onto Sgr A*?

T. Paumard[1], J.-P. Maillard[2], and M. Morris[3]

[1] Max-Planck-Institut für extraterrestrische Physik,
Postfach 1312, 85741 Garching, Germany
[2] Institut d'astrophysique de Paris, 98 bis boulevard Arago, 75014 Paris, France
[3] University of California, Los Angeles, Div. of Astronomy,
Dept of Physics and Astronomy, Los Angeles, CA 90095-1562, USA

Abstract. Sgr A*, the super-massive black hole at the centre of the Milky Way, is surrounded by the H II region Sgr A West, which appears in projection like a mini-spiral with three "arms". We have used high spectral resolution spectro-imaging data to analyse the velocity field of this ionised gas in a one-parsec wide field, and have come to the conclusion that the spiral pattern is only a projection effect. The mini-spiral is indeed composed of at least eight distinguishable clouds of material containing dust and ionised gas, and tidally stretched by the super-massive black hole. We have been able to derive an estimate of the mass of these clouds, as well as of their dynamical time-scale, through a kinematic model of the main "arm". The origin and fate of this material will be discussed, in the perspective of accretion onto Sgr A*.

1 Introduction

At the very centre of the Galaxy lies the super-massive black hole candidate Sgr A* [1,2], surrounded by a parsec-scale star cluster consisting of an old spheroidal stellar population intermixed with another population of early type stars of unknown origin, possibly confined within two disks [3], and containing several dozen Wolf-Rayet stars as well as a cluster (GCIRS16) of half a dozen luminous blue supergiants in a transitional phase; and by a complex of ionised gas clouds (Sgr A West or the "Minispiral"), itself contained within the Central Cavity of a Cirumnuclear Disk (CND). Study of these interstellar elements should lead to a better understanding of the star formation and accretion processes in this extreme environment. It would be very interesting to determine the fate of the material contained in the Minispiral: most likely accretion onto the central black hole, condensation into stars, or ejection from the region. The determination of the mass of material contained in this reservoir is also a crucial question with regard to accretion onto the black hole, and that of its three-dimensional structure is essential for inferring its origin, understanding the shadowing and extinction effects and evaluating the influence of cloud–cloud collisions and cloud–star interactions. In order to address these questions, we have obtained spectro-imaging data using BEAR on the Canada–France–Hawaii Telescope, in the Brγ ($\lambda = 2.166\,\mu$m) and He I ($\lambda = 2.058\,\mu$m) lines. In Sect. 2, we briefly describe these data as well as their reduction and analysis, and in

ESO Symposia: Growing Black Holes, pp. 197–202, 2005.

particular a decomposition of Sgr A West into individual gas clouds and the establishment of a three-dimensional model of the main cloud, the *Northern Arm*. We will try in Sect. 3 to summarise the constraints that these observational results put on the origin and fate of this reservoir.

2 Observational results

BEAR [4,5] is a prototype, made of the CFHT Fourier Transform Spectrometer (FTS), coupled with a NICMOS 3 camera. As such, it is an Imaging Fourier Transform Spectrometer. The FTS provides a very high spectral resolution, which can indeed be chosen at observation time, depending on the target. In practice, resolutions up to 30,000 have been obtained in this mode. The field of view is set by the original design of the FTS, which was not built with spectro-imaging in mind, and is thus limited to $24''$. This prototype does not make use of an adaptive optics system and its spatial resolution is therefore seeing-limited. This instrument has now been decommissioned with the closure of the CFHT infrared focus; however, a specifically designed instrument following the basic concept of BEAR with adaptive optics would provide a very useful observing mode for the new telescopes, allowing for large field, high spectral and spatial resolution spectro-imaging.

2.1 Observations and data processing

We have obtained several datasets concerning the Galactic Centre: in He I at a spectral resolution of $52.9\,\mathrm{km\,s^{-1}}$, as a mosaic of three subfields; and in Brγ, at a spectral resolution of $21.3\,\mathrm{km\,s^{-1}}$, as a mosaic of two subfields. These data, covering most of a $40'' \times 40''$ field at a resolution of $\simeq 0.5''$, as well as the results summarised here, are presented in depth in [6].

A coarse examination of the data-cubes shows that the line emission at each point of the field (Fig. 1) is a sum of several velocity components. A multi-component line fitting routine has therefore been specifically developed to decompose each spectrum in the data-cube into a sum of individual Gaussian lines, convolved with the instrumental line shape (a sine cardinal "sinc" function), taking into account as much as possible the two-dimensional information contained in the cube. From this decomposition, the radial velocity and intensity maps of individual layers of coherently moving gas can be reconstructed using only a continuity criterion on the radial velocity. This led to the identification of nine distinct components of various size and shape in Brγ, the names of which are reported in Fig. 2, all of them except one being also detected in He I. The line ratio varies between the components and within each of them (Fig. 1), but these variations are compatible with a well mixed material of uniform composition in a non-uniform UV field due to the specific location of the individual early type stars (Fig. 2).

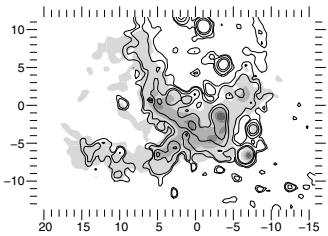

Fig. 1. The brightest parts of the Minispiral emission in Brγ (*grey scale*) and He I (*contours*). Some emission line stars are also visible. On all figures, axes are offsets from Sgr A* in arcsec

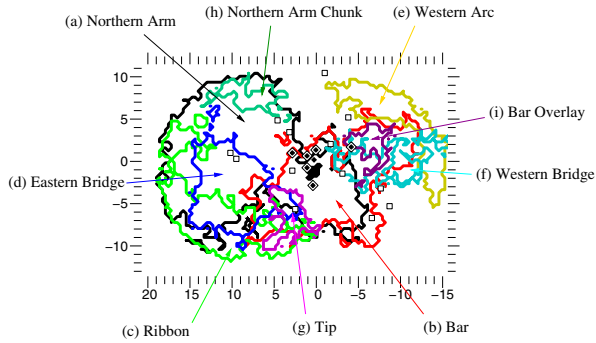

Fig. 2. Outline of the nine ISM features. The GCIRS 16 cluster of luminous blue supergiants (*filled diamonds*) and a few Wolf-Rayet stars (*empty squares*) are shown. Available in colour in [6]

2.2 3D structure of the Minispiral

In order to better understand the nature and dynamics of the Northern Arm, we have developed software that allows for fitting a bundle of Keplerian orbits on a radial velocity map, and thus gives rise to a three-dimensional, dynamical model of the Northern Arm. This work allows us to demonstrate that the shape of the ionised structure associated with the Northern Arm (Fig. 3) is compatible with that of the ionised surface of a tidally stretched, otherwise neutral cloud, the source of ionising photons being the central cluster of hot stars. The Northern Arm is much more extended eastwards than usually thought and is almost in the same plane as the CND. As the orbits are very eccentric, they extend far northwards of the BEAR field of view – still following the shape of the Northern Arm as observed on wide field, high resolution imaging data – and some of them come back in the western part of the field, were they fit remarkably well the few data points available for the Western Arc, which is known to be the photo-ionised inner edge of the CND, thus supporting the hypotheses that the Northern Arm and the Western Arc are a single entity, and that the Northern Arm is one of the clouds forming the CND, that happens to be diving into the Central Cavity. It is also interesting to note that some of the orbits have best-fit eccentricities above 1, denoting unbound material. This three-dimensional model of the Northern Arm ionised layer provides a reference for placing the other elements in the central parsec along the line-of-sight.

The Tip of the Eastern Arm is a very straight feature, aligned with Sgr A* (in projection), and having a very high velocity gradient, reaching high radial velocities ($\simeq 300\,\mathrm{km\,s^{-1}}$ redshift). The most likely explanation is that this feature is in free fall towards Sgr A*. In this case, the sign of the velocity is indicative that the Tip is closer to the observer than Sgr A*. The end of the Tip furthest away from Sgr A* seems to be connected with the Ribbon of the Eastern Arm through a Microcavity (Fig. 4). The interpretation favoured in [6] is that the Ribbon is a gently flowing cloud, that forms the Microcavity as it collides with

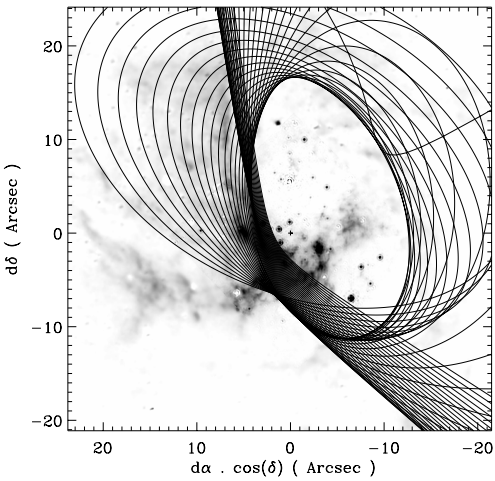

Fig. 3. Northern Arm orbits from our model over a high resolution HST/NICMOS Paα map of the Minispiral on a large field [7]

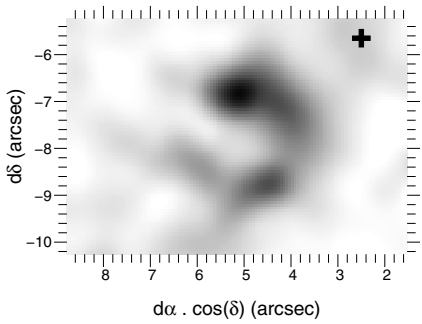

Fig. 4. Microcavity between the Ribbon and the Tip of the Eastern Arm (integrated Brγ line flux 220–240 km s^{-1}). The position of the Helium star GCIRS 9W is given (*cross*)

another flow, maybe a stellar wind or a jet – from a star or perhaps Sgr A* – at which point the material in the Ribbon loses all its orthoradial velocity and dives onto the black hole, forming the Tip.

A comparison of the He I and Brγ maps shows that the projected limit between the Ribbon and the Eastern Bridge coincides with a region of high excitation in the latter. That may indicate that the two structures are indeed colliding. Furthermore, the intensity map of the Northern Arm exhibits a discontinuity line (Fig. 5), where the line flux drops by about 50%, that closely coincides with the outline of the Eastern Bridge. We interpret this in terms of extinction of the Northern Arm emission by the foreground Eastern Bridge. From this A_K value and the areal size of the Eastern Arm (within our field of view), we give in [6] a rough estimate for the mass of this structure: about 15 $M_\odot$.

A similar effect is seen on the intensity map of the Bar, which exhibits the outline of the Minicavity, a cavity surrounded at its periphery by material attributed to the Northern Arm. This time, we must conclude that the Bar is behind the Northern Arm, in the Background. This is consistent with the model for the Bar proposed in [8] of a portion of an highly inclined ($i = 76°$) planar ring, almost perpendicular to the galactic plane, extending from 0.3 to 0.8 pc from Sgr A*, and containing about 27 $M_\odot$ of ionised material.

The GCIRS 13E cluster [9] coincides with a bright spot in the Minispiral, located in projection at the northern end of the western edge of the Minicavity (Fig. 5). However, the Minicavity itself is contained within the western end of the Northern Arm, but the bright spot coinciding with GCIRS 13E itself shows up only in the intensity map of the Bar. One must therefore conclude that the alignment between this spot and the edge of the Minicavity is only fortuitous and that the GCIRS 13E cluster is most likely responsible for an enhanced

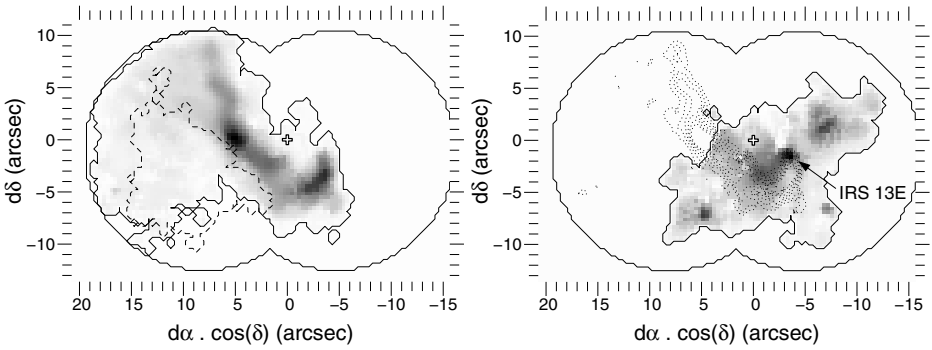

Fig. 5. Flux maps of the Northern Arm (*left*) and of the Bar (*right*), on which the enhanced extinction traces respectively the outline of the Eastern Bridge (*dashed line*) and the density gradient in the Minicavity (*dotted contours*). A bright spot on the Bar, coincident with the GCIRS 13E compact star cluster, is also shown. Axes are offsets from Sgr A* (*cross*), in arcsec

excitation of the Bar at the location of the bright spot, and must therefore be either within or very close to the Bar along the line-of-sight. Furthermore, if the compact cluster of hot stars were located inside the Bar, its wind would most likely be responsible for a cavity similar to the Minicavity or a bow shock as seen around GCIRS 21 [10]. As no such feature is observed in the Bar, we argue that GCIRS 13E is not inside the Bar but hovering close to its surface.

3 Discussion

The Eastern Arm (Ribbon and Tip) does not appear to reside in the same plane as the CND and the Northern Arm and seems to be counter-rotating with respect to these structures. The Bar, as shown in [8], is almost perpendicular to the galactic disk and the CND. On the other hand, the plane of the Northern Arm is close to that of the CND within $\simeq 10°$, rotates in the same direction, and may connect continuously with the Western Arc, which is the ionised inner edge of the CND. This means that not all of the Minispiral structures can directly come from the CND, some of them must be run-in clouds from the outside or have been formed in-situ. However, the Northern Arm itself shows kinematic properties that relate it with the CND. Furthermore, the two-dimensional size that we can infer from our decomposition of the Minispiral into structures is of the same order as that of the 10–20 clouds of $\simeq 10^3\,\mathrm{M}_\odot$ each that compose the CND according to [11]. It seems reasonable to suggest it may have been kicked out of the CND by a passing cloud on a fairly eccentric orbit.

It is argued in [6] that the winds of the $\simeq 20$ high mass loss stars present in the centre region that supply about $10^{-4}\,\mathrm{M}_\odot\,\mathrm{yr}^{-1}$ each [12] sum up to a steady-state stellar-origin gas mass of a few $10\,\mathrm{M}_\odot$ after a dynamical timescale ($10^4\,\mathrm{yr}$). This order compares well with the mass estimates for both the part of the Eastern Bridge contained within the BEAR field ($\simeq 15\,\mathrm{M}_\odot$, see above) and

the Bar ($27\,M_\odot$, [8]). One of them or a large fraction of both could therefore in principle be made of material of stellar origin. If that were the case, the stellar-origin ISM would most likely take the form of a ring, residing in the same plane as one of the two stellar disk patterns mentioned in [3], a possibility that our data do not seem to support. The suggested proximity between the Bar and the GCIRS 13E cluster raises the question of a link between them, but it can be discarded as the GCIRS 13E cluster proper motion is mostly East–West [9], not within the plane of the Bar.

Our data illustrate three kinds of momentum loss processes. First of all, a number of ISM-star interactions are listed in [6]. Although most of them seem to only affect the ISM dynamics at a local level (e.g. the bow-shock star, [10]), there are also a few cases where the impact of the interaction upon the dynamics of the material seems much more important, the most striking case being that of the Microcavity at the elbow between the Ribbon and the Tip of the Eastern Arm, where the eccentricity of the material seems to change dramatically as it dives onto the black hole. Second, given the various inclinations of the structures' orbital planes, cloud–cloud collisions between them seem fairly likely; indeed, the enhanced He I/Brγ line ratio in the Eastern Bridge at its projected interface with the Ribbon may be a signature of such a collision. Finally, our kinematic model of the Northern Arm illustrates that this feature should form a complete ring within $\simeq 10^4$ yr, at which stage it may undergo self-collision. The two latter effects should make all the ISM (maybe $\simeq 10^3\,M_\odot$ as discussed above) settle into a single disk-like feature within a few dynamical timescales, although some of it must be able to escape, as shown by the fact that some of the Northern Arm material seems to be on unbound orbits.

References

1. R. Genzel: these proceedings
2. M. Morris et al.: these proceedings
3. M. Horrobin, F. Eisenhauer, et al.: Astronomische Nachrichten, **325**, 88 (2004)
4. J.P. Maillard: '3D-Spectroscopy with a Fourier Transform Spectrometer'. In *Tridimensional Optical Spectroscopic Methods in Astrophysics*, ed. by G. Comte, M. Marcellin, ASP Conf. Ser., **71**, 316 (1995)
5. J.P. Maillard: 'BEAR Imaging FTS: High Resolution Spectroscopy in Infrared Emission Lines'. In *Imaging the Universe in Three Dimensions*, ed. by W. van Breugel, J. Bland-Hawthorn, ASP Conf. Ser., **195**, 185 (2000)
6. T. Paumard, J.P. Maillard, M. Morris: A&A, in press `[astro-ph/0405197]` (2004)
7. N.Z. Scoville, S.R. Stolovy et al.: ApJ, **594**, 294 (2003)
8. H.S. Liszt: A&A, **408**, 1009 (2003)
9. J.P. Maillard, T. Paumard, S.R. Stolovy, F. Rigaut: A&A, **423**, 155 (2004)
10. A. Tanner, A. Ghez, M. Morris: ApJ, submitted (2004)
11. M.H. Christopher, N.Z. Scoville: 'OVRO High Resolution Imaging of Dense Molecular Clouds in the Central Three Parsecs of the Galaxy'. In: *Active Galactic Nuclei: from Central Engine to Host Galaxy*, ed. by S. Collin, F. Combes, I. Shlosman, ASP Conf. Ser., **290**, 389 (2003)
12. F. Najarro, D.J. Hillier, R.P. Kudritzki et al.: A&A, **285**, 573 (1994)

Star Formation in the Accretion Disk of Sgr A* a Million Years Ago

S. Nayakshin

Max-Planck-Institut für Astrophysik, Karl-Schwarzschild-Str. 1, 85740 Garching, Germany

Abstract. When the accretion disk mass exceeds about 1 % of the supermassive black hole (SMBH) mass, local gravitational instabilities develop and expected to lead to star formation inside the disk. Here we attempt to put constraints on the properties of a putative accretion disk that could have resulted in the formation of the two observed circum-nuclear young stellar rings in Sgr A*[3]. We find the minimum disk mass to be around $10^4\,M_\odot$. The observed relatively small velocity dispersion of the young stars rules out disks more massive than around $10^5\,M_\odot$: heavier stellar or gas disks would warp each other by orbital precession in an axisymmetric potential too strongly. Since the present day total mass of each of the two stellar rings is estimated to be $\lesssim 10^3\,M_\odot$, most of the gaseous disk mass should have been accreted by Sgr A* or used up in formation of young massive stars. The latter possibility appears to be more likely.

1 Introduction

At a radial distance of a fraction of a parsec from Sgr A*, two rings populated by young massive stars require a recent burst of star formation [3,4]. This is usually considered surprising, given that the tidal force of the SMBH would easily tear apart gas clouds even with densities orders of magnitude higher than the highest density cores of GMCs observed in the Galaxy. However, we argue that such a "shearing demise" of a massive molecular cloud near a SMBH will only lead to a re-arrangement of the gaseous mass distribution. Shearing in the radial and *contracting* in the perpendicular direction, the cloud will settle to an accretion disk configuration if radiative cooling is efficient. AGN disks are known to be as dense as $10^{10} - 10^{15}$ particles cm^{-3}. If the disk mass is large enough, it becomes self-gravitating and *may* form stars [9]. Therefore, [6] and [8] suggested that the origin of the young stars is a massive self-gravitating accretion disk existing in Sgr A* in the past.

Here we attempt to put some flesh on this idea. We estimate the minimum mass of such accretion disks to be around $10^4\,M_\odot$, for each of the two stellar rings. In addition, we rule out the possibility that a less massive accretion disk could capture enough low mass stars from the pre-existing "relaxed" Sgr A* cusp and then grow them by accretion into massive stars. We find that stellar orbits in both rings should remain close to circular Keplerian orbits up to this day (if stars were indeed born in a disk). The velocity dispersion of the outer ring may result from the stellar disk warping in the gravitational potential of the inner ring. Such warping sets the upper limit on the disk mass of about $10^5\,M_\odot$.

ESO Symposia: Growing Black Holes, pp. 203–208, 2005.

It is found that young massive stars would not migrate much radially in the disk, meaning that they are probably located at the radius where they were originally formed. Small scale proto-stellar disks around the embedded stars may be gravitationally unstable as well and may create further generations of stars. Hierarchical growth and merging of such objects may result in the creation of "mini star clusters" with the central object collapsing to an intermediate mass black hole. This could be relevant to the observations of IRS13 cluster [10].

2 A self-gravitating disk in Sgr A* $\gtrsim 10^6$ years ago

For large radii ($r \gg 1$) the standard accretion disk equations yield

$$\frac{H}{R} = 2.7 \times 10^{-3} \, (\alpha M_8)^{-1/10} \, r^{1/20} \dot{m}^{1/5} \, , \tag{1}$$

$$T = 6.3 \times 10^2 \text{ K} \, (\alpha M_8)^{-1/5} \dot{m}^{2/5} \left[\frac{R}{10^5 R_S} \right]^{-9/10} \, . \tag{2}$$

Where H is the disk vertical height scale, R is the distance from the SMBH, T is the midplane gas temperature, α is the dimensionless viscosity parameter, $M_8 = M_{\rm BH}/10^8 \, M_\odot$, $r = R/R_{\rm S}$, $R_S = 2GM_{\rm BH}/c^2$ is the Schwarzschild radius of the SMBH and Σ is the surface density of the accretion disk. The dimensionless accretion rate $\dot{m}$ is defined as $\dot{m} = \dot{M}/\dot{M}_{\rm Edd}$, where $\dot{M}_{\rm Edd} = L_{\rm Edd}/\varepsilon c^2$ is the accretion rate corresponding to the Eddington luminosity and $\varepsilon \approx 0.06$ is the radiative efficiency of the standard accretion flow.

Figure 1 shows some of the disk parameters plotted for $M_{\rm BH} = 3 \times 10^6 \, M_\odot$, $\alpha = 1$, and two values of the dimensionless accretion rate, $\dot{m} = 0.03$ (thick lines) and $\dot{m} = 1$ (thin lines). The mass of the disk as a function of radius is approximated as $M_{\rm d} \approx \pi R^2 \Sigma$. It is well known that the standard accretion disk becomes self-gravitating at large enough radii, when the Toomre parameter Q becomes less than unity,

$$Q = \frac{c_{\rm s} \Omega}{\pi G \Sigma} \approx \frac{H}{R} \frac{M_{\rm BH}}{M_{\rm d}} < 1 \tag{3}$$

($c_{\rm s}$ is the sound speed inside the disk and Ω its angular velocity). The radius where $Q = 1$ yields the minimum mass of the disk needed for the latter to become self-gravitating. From Fig. 1, this mass is at least $10^4 \, M_\odot$.

[1] noted that stars on orbits relatively close to the local circular rotation of the accretion disk will be captured by the disk. The stars can then rapidly grow by gas accretion. We however estimate that the required disk mass is at least $M_d \sim (1-3) \times 10^5 \, M_\odot$ to capture enough stars in the time available. With this, the disk would already be self-gravitating and may produce many more young stars inside the disk. Nevertheless, the disk capture of stars may bring in some *late* type stars into the plane of the young massive stars, and may thus be still important observationally.

3 Constraints from stellar velocity dispersion

The velocity dispersion σ of stars grows due to N-body interactions at the rate

$$\frac{d\sigma}{dt} \sim \frac{4\pi G^2 M_* \rho_*}{\sigma^2} \ln \Lambda_* \tag{4}$$

where $\Lambda_* \sim H_* \sigma^2 / G M_*$ is the Coulomb logarithm for stellar collisions; H_* is the stellar disk height scale, $H_* \sim R\sigma / v_{\rm K}$. The relaxation time, defined as the time needed for the stellar disk to thicken to height H_* can be found from equation 4:

$$\frac{t_{\rm rel}}{t_{\rm dyn}} \sim \left[\frac{H_*}{R}\right]^4 \frac{M_{\rm BH}^2}{4 M_{\rm d*} M_* \ln \Lambda_*} \,, \tag{5}$$

where $M_{\rm d*}$ is $\pi R^2 H_* \rho_*$, the mass of the stellar disk. Equation 5 yields

$$\frac{t_{\rm rel}}{t_{\rm dyn}} \sim \; 2500 \, \frac{10^4 \, M_\odot}{M_{\rm d*}} \, \frac{10 \, M_\odot}{M_*} \, \left[\frac{H_*/R}{0.1}\right]^4 \ln \Lambda_*^{-1} \,. \tag{6}$$

With $t_{\rm dyn} \sim 300$ years, we have $t_{\rm rel} \sim 10^6$ years. Hence the geometrical thickness of the rings, and the ratio of velocity dispersion to the local Keplerian velocity, $\sigma / v_{\rm K}$, are expected to be of order 0.1 for the two young stellar rings in the GC. The individual stellar velocities should thus be still close to the local *circular* Keplerian values if the origin of the stars is in the gaseous disk.

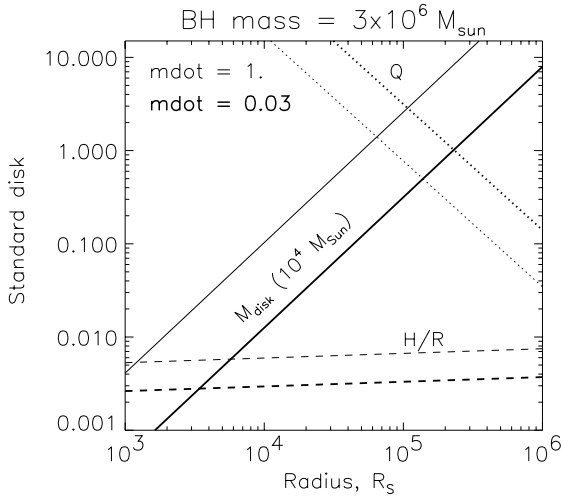

Fig. 1. The disk mass in units of $10^4 \, M_\odot$, the Toomre instability parameter Q, and the ratio of the disk height scale H to radius R as a function of radius for the standard accretion disk model. The thick curves are plotted for $\dot{m} = 0.03$, whereas thin ones are for $\dot{m} = 1$. In both cases the disk is unstable to self-gravity at $R \gtrsim 10^5 R_{\rm S}$, where its mass is $M_{\rm d} \gtrsim 10^4 \, M_\odot$.

[6] estimate the geometrical thickness of the inner stellar disk in Sgr A* to be of order $H_*/R = 0.1$. This ratio appears to be $H_*/R \sim 0.3$ for the outer, counter-rotating, disk (e.g. Fig. 15 in [3]). One may try to invert equation 6 to constrain the initial stellar mass of the disks. Unfortunately the limits are not very stringent. A disk mass as high as $M_{\rm d} \sim 3 \times 10^5\, M_\odot$ could still be consistent with the observations for the inner stellar ring. For the outer stellar ring, the velocity dispersion is too high to be explained by the N-body scattering effects.

A disk of stars or gas around the SMBH introduces a quadrupole moment in the gravitational potential. Stellar orbits then precess around the axis of symmetry in an axisymmetric potential. We approximated the star-gas disk potential by the Kuzmin one and numerically integrated stellar orbits, starting from nearly circular Keplerian orbits. The orbits remain approximately circular, and conserve the inclination angle i between the orbital plane and the disk plane. The stellar orbital plane precesses with respect to the disk at a rate

$$\dot{\phi} = C_{\rm p} q P^{-1} \cos i \ , \tag{7}$$

where $C_{\rm p}$ is a constant (for a given orbit and given geometry) of order unity. Angle ϕ is the azimuthal angle of the lines of the nodes for the orbit in cylindrical coordinates used to define the Kuzmin potential. Setting $i = 74^\circ$ ([3]), we obtain

$$\Delta\phi \simeq \ C_{\rm p}\ \frac{q}{0.003}\frac{t}{10^3 P} \ . \tag{8}$$

The value of $C_{\rm p}$ depends on the disk radius-parameter a with respect to the radius of the stellar orbit; for a of order the radius, $C_{\rm p} \sim 1$.

The important point to note is that nearly circular orbits of stars at different radii from the SMBH will precess by different amounts $\Delta\phi$. Therefore such a precession leads to a warping of the stellar disk. After a time long enough to yield $\Delta\phi \gtrsim 1$ somewhere in the disk, the initially flat stellar disk will be disfigured and will not be recognizable as a disk at all by an observer. A rather robust value for the upper mass of the disks appears to be

$$\max M_{\rm d} \approx 10^5\, M_\odot \ . \tag{9}$$

4 Accretion onto embedded stars, their migration and escape from the disk plane

The accretion of gas onto a star is determined by the rate at which differential rotation brings the matter into the Hill's sphere, $\dot{M}_*$. The accretion time scale for a star embedded into a disk is $t_{\rm acc} \equiv M_*/\dot{M}_*$. Figure 2 shows $t_{\rm acc}$ (dashed line) for a 10 $M_\odot$ star. For the considered parameters, the accretion rate onto the star is close to the Eddington value. Stellar mass doubles every few thousand years. Growing stars as massive as 100 $M_\odot$ in a million years in a disk with gas mass $M_d \gtrsim 10^4\, M_\odot$ appears to be no problem at all.

We also estimate the radial migration time scale, $t_{\rm migr}$, using the prescription for the radial migration velocity based on the numerical calculations of Bate et

al. (2003). For the parameters chosen, $t_{\rm migr} = t_{\rm visc}$, the disk viscous time scale (two solid curves in Figure 2). The migration time scale is very long, indicating that stars will remain pretty much where they were born in the accretion disk.

The two dozens embedded stars would thus rapidly devour the accretion disk of Sgr A* before most of it could have been accreted onto the SMBH. One last hope to save the gaseous food for the SMBH is to have the embedded stars dislodged from the disk midplane by a possible disk rotation occurring over a time $t_{\rm rot}$. We define a critical rotation time scale, $t_{\rm rc}$, such that for disk plane changes occurring on time scales shorter than $t_{\rm rc}$, the stars are dislodged from the gas disk. For $t_{\rm rot} > t_{\rm rc}$, on the contrary, the stars remain bound to the disk. Figure 2 shows the critical rotation time scales (dotted curves) along with other important time scales for the standard accretion disk model with same parameters as used for Fig. 1 and for a 10 Solar mass star.

Note that $t_{\rm rc}$ is longer than $t_{\rm dyn}$ but is much shorter than $t_{\rm visc}$. This implies that if accretion disk plane changes occurs on a viscous time scale, which is the most likely case, the stars would remain bound to the disk. Only very fast plane changes could dislodge the stars from the disk midplane, thus most likely the stars did accrete most of the Sgr A* disk gaseous fuel.

5 Growth of "mini star clusters" and IMBHs

[5] have recently suggested that it is possible to grow supermassive stars in AGN accretion disks. The maximum mass of a star is the disk mass in a ring with width of order the Hill's radius of the star, $R_H = (M_*/3M_{\rm BH})^{1/3}$. This is the "isolation" mass, $M_i \simeq M_d^{3/2} M_{\rm BH}^{-1/2}$,

$$M_i \approx 550\, M_\odot \left[\frac{M_d}{10^4\, M_\odot}\right]^{3/2} \left[\frac{3\times 10^6\, M_\odot}{M_{\rm BH}}\right]^{1/2} . \qquad (10)$$

However, is all of the disk mass delivered by the differential rotation into the Hill's radius around the star is accreted onto the star? This is not obviously so because the gas still has to loose most of its angular momentum. The fringes of the small scale disk around the embedded stars themselves become self-gravitating and may therefore also form stars or planets [7]. It is thus possible to grow star clusters in situ around a massive locally dominant gravitating center. The supermassive star could collapse directly into a black hole if the star is more massive than 300 $M_\odot$ [2]. The maximum total mass of such a cluster should be close to the isolation mass. This may be relevant to the observations of the IRS13 cluster near Sgr A*[10].

6 Conclusions

We have attempted to put constraints on the properties and fate of an accretion disk that could have given birth to the young massive stars in the two nuclear rings in Sgr A*some few million years ago. Our main results are:

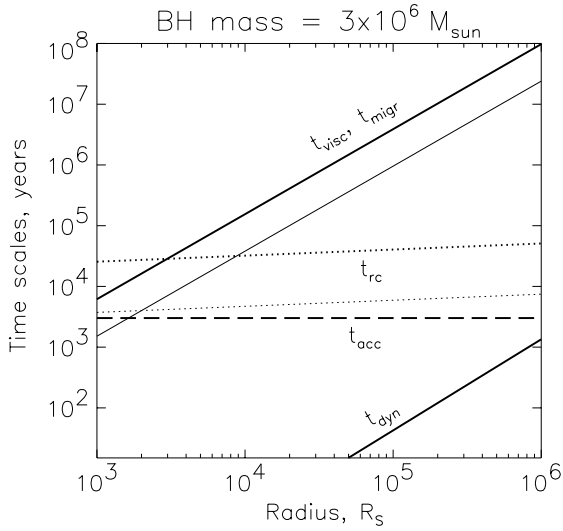

Fig. 2. Time scales for a 10 Solar mass star embedded in the standard accretion disk with parameters as in Fig. 1. As before, thick curves correspond to $\dot{m} = 0.03$, whereas thin ones are for $\dot{m} = 1$. The solid lines show the viscous and the dynamical time scales for the disk, as labelled in the figure. The star is massive enough to open up a gap and hence migrates inward on the viscous timescale ($t_{\rm migr} = t_{\rm visc}$). The dashed and dotted lines are the accretion and the critical rotation time scales, respectively.

- The minimum disk mass is $10^4\,M_\odot$. The maximum disk mass that would avoid too strong orbital precession and ring warping is around $10^5\,M_\odot$.
- It is most likely that young stars quickly devoured the disk of its mass. The fraction of gas that made it into Sgr A* is uncertain but is likely small.
- Hierarchical growth and formation of self-gravitating structures in the disk may create "mini star clusters" with an IMBH at the center, possibly similar to the IRS 13 cluster.

Acknowledgement. Jorge Cuadra has significantly contributed to this work.

References

1. Artymowicz, P. et al. 1993, ApJ, 409, 592
2. Fryer, C.L., Woosley, S. E., & Heger, A., ApJ, 550, 372
3. Genzel, R., et al. 2003, ApJ, 594, 812
4. Ghez, A.M., Duchene, G., et al. 2003, ApJ, 596, L127
5. Goodman, J., & Tan, J.C. 2004, ApJ, 608, 108
6. Levin, Y., & Beloborodov, A.M. 2003, ApJL, 590, L33
7. Milosavljevic, M., & Loeb, A., 2004, ApJL, 604, L45
8. Nayakshin, S, Cuadra, J., & Sunyaev, R. 2004, A&A, 413, 173
9. Paczyński, B. 1978, Acta Astron., 28, 91
10. Maillard, J.P., et al. 2004, to appear in A&A (astro-ph/0404450)

Accretion in the Galactic Center: Via a Cool Disk?

B.F. Liu, F. Meyer, and E. Meyer-Hofmeister

Max-Planck-Institut für Astrophysik, Karl-Schwarzschild Str.1, 85740, Garching

Abstract. We study the interactions between a presumed cool disk and its hot corona in the Galactic Center. If the interactions are dominated by mass evaporation, the resultant evaporation rate is larger than the Bondi accretion rate of $10^{-5}M_{\odot}$/yr, thus, the disk should have been depleted since the last star had formed. If the interactions result in hot gas steadily condensing into the disk, a very high mass flow rate is required, which is inconsistent with observations. We conclude that, for standard viscosity, there is no thin disk in the Galactic Center now. For very small viscosity, see [4] for an alternative model.

1 The physics of interaction between disk and corona

Interaction between the disk and the corona occurs via energy and mass exchange [2,3,1]. The hot corona conducts heat downward by electrons. At the bottom the heat is radiated away. If the density in the corona is too low, Bremsstrahlung is inefficient and the thermal conductive flux heats up some of the disk gas leading to mass evaporation. If the coronal density is too high, radiative cooling is too strong and gas condenses into the disk. At the final equilibrium density, cold gas steadily evaporates from the disk into the corona if mass is drained continuously from the corona inward by diffuse flow, or hot gas steadily condenses to the disk if the corona continuously gains mass by mass flow.

2 Condensation or evaporation in our Galactic Center?

At the Galactic Center, hot gas accretes at a Bondi accretion rate of $\sim 10^{-4}\dot{M}_{\rm Edd}$ from the capture radius $R \sim 10^5 R_{\rm S}$ and circularizes at $R \sim 10^4 R_{\rm S}$. We thus investigate the coronal features in a region from $10^4 R_{\rm S}$ to $10^5 R_{\rm S}$ for the Galactic Center with a mass of black hole $3.3 \times 10^6 M_{\odot}$ (e.g. [5]) and viscosity $\alpha = 0.3$.

2.1 Evaporation solutions

Fig.1 shows the radial mass flow rate in the corona for distances $10^4 R_{\rm S}$ to $10^5 R_{\rm S}$. We see that the mass flow rates are around $10^{-3}\dot{M}_{\rm Edd}$, about 10 times higher than the incoming mass flow estimated from Bondi accretion and Chandra observations as $\dot{M} \sim 10^{-4}\dot{M}_{\rm Edd}$. This indicates that the disk could have been eventually depleted by the evaporation owing to lower mass supply, if there had been a disk in early phase.

ESO Symposia: Growing Black Holes, pp. 209–210, 2005.

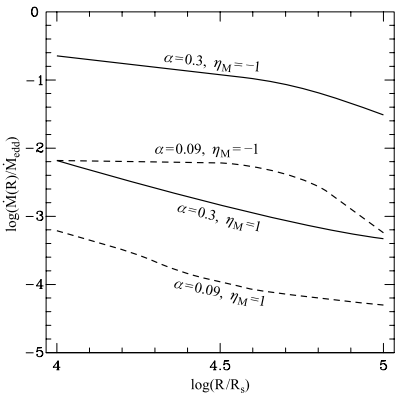

Fig. 1. Mass flow rate in the corona for evaporation ($\eta_M = 1$) and condensation ($\eta_M = -1$) solutions. Solid lines for standard viscosity; dashed lines for small viscosity.

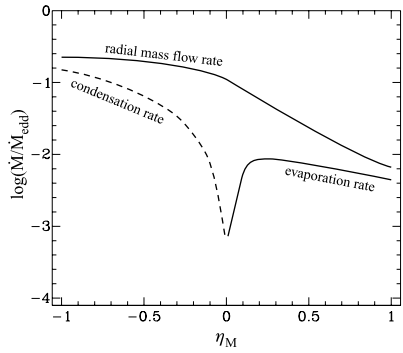

Fig. 2. Mass flow rate in the corona changing with mass exchange rate, from complete condensation ($\eta_M = -1$) to strong evaporation ($\eta_M = 1$). The figure shows that no matter condensation or evaporation, the resultant mass flow rates are much higher that the Bondi accretion rate observed in the Galactic Center.

2.2 Condensation solutions

To let coronal gas condense to the disk, we need high pressure in the corona. This requires more gas feeding into the corona from outside than gas flowing out of the corona at the inner boundary (see Fig.2). Fig.1 shows the condensation rate is far too high compared to the Bondi accretion rate in the Galactic Center. The density in such a corona is also much higher than the value inferred from the observations. Therefore, we cannot expect that, if there is a cool disk in the Galactic Center, hot gas captured by the black hole at the Bondi radius mainly condenses into the disk and is deposited there. Instead, the disk gas will evaporate into the corona, increasing the coronal flow inward significantly. This process can finally deplete the cool disk. From then on no cool disk exists anymore in the Galactic Center.

References

1. Liu, B.F., Mineshige, S., Meyer, F. et al.: ApJ, **575**, 117 (2002)
2. Meyer, F., & Meyer-Hofmeister, E.: A&A, **288**, 175 (1994)
3. Meyer, F., Liu, B. F., & Meyer-Hofmeister, E.: A&A, **361**, 175 (2000)
4. Nayakshin, S.: these proceedings (2004)
5. Schödel, R., Ott, T., Genzel, R. et al.: ApJ, **596**, 1015 (2003)

A Disk in the Galactic Center in the Past?

E. Meyer-Hofmeister, F. Meyer, and B. Liu

Max-Planck-Institut für Astrophysik, Garching, Germany

Abstract. We raise the question whether in the past a disk could have existed in our Galactic Center which has disappeared now. Our model for the interaction of a cool disk and a hot corona above (Liu et al. 2004) allows to estimate an upper limit for the mass that might have been present in a putative accretion disk after a last star forming event, but would now have evaporated by coronal action.

1 The evaporation process

We study the possibility of a cool disk existing in the Galactic Center in the framework of the disk-corona evaporation. Interaction between the hot corona and the cool disk underneath occurs via energy and mass exchange. The hot corona conducts heat downward by electrons. At the bottom the heat is radiated away. An equilibrium is established: If the density in the corona is too low, Bremsstrahlung is inefficient and the thermal conductive flux heats up some of the disk gas leading to mass evaporation from the disk into the corona. The resulting density increase in the corona raises the radiation loss and thereby counteracts further evaporation. If the coronal density is too high, radiative cooling is too strong and gas condenses into the disk. At the final equilibrium density one of the processes works, either evaporation of disk mass to the corona or condensation of mass from the corona into the cool disk. The outcome depends on the mass flow in the corona from outside.

2 The mass flow in the inner disk

Assuming the applicability of our model for the evaporation/condensation process we can estimate how much mass would have evaporated by coronal action during a given time interval. We get an upper limit for the mass that might have been left over in a putative accretion disk after a last star forming event, assuming that no thin disk exists now.

We consider the region at the distance $10^4 - 10^5$ Schwarzschild radii from the black hole which corresponds to $\frac{1}{400}$ to $\frac{1}{40}$ pc. For an assumed standard value of the viscosity parameter α =0.3 and no wind escape from the corona we found a rate of about 10^{-3} times the Eddington accretion rate corresponding to 10^{-4} solar masses per year.

Chandra observations directly image the hot X-ray-emitting thermal gas in the vicinity of the Bondi accretion radius where the surrounding gas is captured

ESO Symposia: Growing Black Holes, pp. 211–212, 2005.

by the gravitational pull of the central black hole, and determine temperatures and densities that allow to estimate a mass accretion rate of Sgr A* of $\dot{M}_{\rm Bondi} \sim (0.3-1) \times 10^{-5} M_{\odot}$/yr (e.g. Baganoff et al. 2003). If we assume that inflow rate during the time since the last star forming event, always disk evaporation would have been present.

3 The history

We consider the history of our Galactic Center during the lifetime of the stars observed close to the Galactic Center. After the last star forming event in a then gravitationally unstable disk a certain amount of gas might have remained. This mass left over then should no longer have been gravitationally unstable. We here ask how much of this mass would have evaporated.

The observations, especially spectroscopy of one star, S0-2, observed in the vicinity of Sgr A* suggest that these stars are main sequence O/B stars (Eisenhauer et al. 2003, Ghez et al. 2003). The main sequence lifetime of these stars is of order of $10^{6.5} - 10^{7}$ years (Maeder & Meynet 1989). We consider the disk evolution during this time interval. From the evaporation rate we find an upper limit of 300 to 1000 solar masses for the amount of gas that remained in a disk after these stars had been formed and was then evaporated until now. This value is in the range of mass of the presently observed bright O/B stars close to the Galactic Center. This means about the same amount of mass as used up in star formation could have remained in a thin disk.

Such an estimate would also be of interest in the framework of star formation in the Galactic Center as recently discussed by Milosavljević and Loeb (2004). They suggest star formation in a warm molecular disk where newly formed self-gravitating objects can have protostellar disks where fragmentation leads to multiple clumps resembling the IRS 13 complex in the neighborhood of Sgr A*.

Interestingly this amount of gas is also close to that of the stability limit of a disk against self-gravitation. This suggests as a possible picture for the evolutionary history that a disk could have become unstable by self-gravitation and formed the presently observed young massive stars around the Galactic Center until the gravitational instability had ceased. Even if such a disk could have been too cool to allow magnetic dynamo action and would then have negligible internal viscosity and mass flow, it would have disappeared by now by evaporation.

References

1. B.F. Liu, F. Meyer, E. Meyer-Hofmeister: A&A **421**, 659 (2004)
2. F. K. Baganoff, Y. Maeda, M. Morris et al.: ApJ **591**, 891 (2003)
3. F. Eisenhauer, R. Schödel, R. Genzel et al: ApJL **597**, 121 (2003)
4. A.M. Ghez, G. Duchene, K. Matthews et al.: ApJ **586**, L127 (2003)
5. A. Maeder, G. Meynet: A&A **210**, 155 (1989)
6. M. Milosavljević, A. Loeb: ApJ **604**, 45 (2004)

Accretion onto a Dupermassive Black Hole in Sgr A*

M. Moscibrodzka[1], B. Czerny[1], and V. Beskin[1,2]

[1] N.Copernicus Astronomical Centre, Bartycka 18, 00-716 Warsaw, Poland
[2] Lebedev Physical Institute, Moscow, Russia

Abstract. We propose a model of accretion onto a black hole at the center of our Galaxy. This model describes a situation in which Sgr A* is accreting a hot stellar wind predominantly from star complex IRS13E. We further assume an existence of a cold, optically thick, geometrically thin disk that surrounds a black hole. A fraction of matter inflowing into area described by our model settles onto a disk. The rest of it is falling under horizon.
We estimate a fraction of matter that settles onto a disk. We assume that all kinetic energy is lost during the impact, and then re-radiated from the disk surface. Our main goal was to compare the modeled flux emitted by the disk with flux obtained from observations. Our calculations show that existence of such disk is rather excluded.

1 Model

Our model assumes the presence of a cold, inactive disk that surrounds the black hole existing in the center of the Milky Way. The existence of such disk was discussed by [3], [5] & [4]. The inner radius of the disk is at $3R_{schw}$, bellow the matter is free falling under horizon. The outer radius of the disk is a parameter of the model. Inclination angle of the disk plane with respect to the flow is 90 degrees. Because of observational aspects [4] we chose rather large inclination angles of the disk relatively to the observer (close to edge-on view).

Sgr A* is surrounded by a cluster of young, luminous stars [3]. One of these stars, a Wolf-Rayet star IRS13 E3, is a particulary effective source of stellar wind. We assume that a fraction of this material moves toward the Galactic center with zero angular momentum and slightly subsonic velocity. To describe a flow of matter that is moving relatively to the black hole (Bondi-Hoyle accretion) we use solution obtained by Beskin [1]. Trajectories of matter are determined by constant flow lines: $\Phi/\Phi_0 = const$, where

$$\Phi = \Phi_0(1 - cos\Theta + \varepsilon g_1(r,\Theta)sin^2(\Theta)) \quad (1)$$

Here: Θ is angle in cylindrical coordinates, r is distance from a black hole, g_1 is a radial function and ε is small parameter defined as $\frac{v_\infty}{c_\infty}$, where v_∞ is the velocity of matter and c_∞ is the sound speed at infinity. Expression (1) was obtained from linearized version of Grad-Sharfranov equation [1]. In our model equation (1) is describing the flow far from a black hole. Closer, at distances smaller than the outer radius of the cold disk, the flow is described by standard ballistic equations.

ESO Symposia: Growing Black Holes, pp. 213–214, 2005.

As the boundary conditions, we assume that the mass flux density of the material flowing toward the black hole from IRS 13E complex $\sim 10^{-15}$g/s/cm^2. In calculations we used typical quantities characteristic for vicinity of Sgr A*. Thus $n = 26$ cm^{-2}, $T_\infty = 1.5{\cdot}10^7$K (Chandra observations of Sgr A*). Parameter of the model $\frac{v_\infty}{c_\infty} = 0.84$.

2 Results and conclusions

The main results of the simulation are:

- Calculations shows that part of the material coming form IRS13E is accreting directly onto a black hole. Accretion rate at distances larger than the outer radius of the disk is $\dot{\mathrm{M}}_{\mathrm{accreting}} = 4.8 \cdot 10^{-7}\mathrm{M}_\odot\mathrm{yr}^{-1}$. For all model parameters about 99% of accreting matter settles onto a cold disk. Rest of it is falling under horizon.
- The material settling onto a disk is losing its kinetical energy. The energy is re-emitted mainly in the near infrared band. We obtained radial profiles of temperature of the disk. The temperature is in general decreasing function of the disk radius.
- We tested our model for different disk outer radii and we obtained spectra emitted by the disk. We compared these modeled spectra with data obtained by [3] and [6]. General conclusion is that only large disks with very high inclinations angles relative to the observer (close to edge-on view) do not contradict the data.
- As a result of oversimplifications we obtained that tracks of matter are colliding. Because the structure of the wind matter is unknown we can propose two approaches. The material can avoid collisions if it is in a form of clumps; otherwise, a continuous stationary shock can be formed.

References

1. V.S. Beskin, Yu.N. Pidoprygpra, "Hydrodynamic accretion onto black holes", Zh. Eksp. Fiz. 107, 1025-1046, (April 1995)
2. R. Genzel, R. Schodel, T. Ott, Einsenhauer F., Hofman R., Lehnert M. ApJ, 594:812-832, (2003)
3. F. Melia & H. Falcke, Annual Reviews, 309 (2001)
4. S. Naykshin, J. Cuadra, R. Sunayev, A&A, 413, 173-188 (2004)
5. B.F. Liu, F. Meyer, & E. Meyer-Hofmeister 2004, A&A, v.421 p.659-666.
6. S. Markoff, H. Falcke, F. Yuan & P.L. Biermann 2001, A&A, 379, L13

Non-Keplerian Potential at the Galactic Centre?

N. Mouawad[1], S. Pfalzner[1], R. Schödel[1], R. Spurzem[2], J. Moultaka[1], and A. Eckart[1]

[1] I. Physikalisches Insitut, University of Cologne, 50937 Cologne, Germany
[2] Astronomisches Recheninstitut, Mönchhofstr. 12-14, 69120 Heidelberg, Germany

1 Introduction

High resolution observations (NTT, VLT and KECK) showed that the supermassive black hole (SBH) at the Galactic Centre is located at the centre of a compact stellar cluster [2,5]. However, the observed stellar sources may represent only a fraction of the total mass implying high M/L(2μm). Stars like S2, with orbital periods as short as 15 yrs [4,7] play a key role in determining the potential in the vicinity of the SBH. We show that it is possible, by fitting the available data on S2, to estimate an upper limit on the amount of the extended dark mass and thus on the M/L(2μm) that could be present at the very centre of the Galaxy.

2 Method

Fig. 1 (left) is a potential fit of the stellar number density counts (for M/L(2μm) constant at all radii). This density profile is consistent with dynamical mass estimates at larger radii (see [8]). We use a fourth order Hermite integrator and

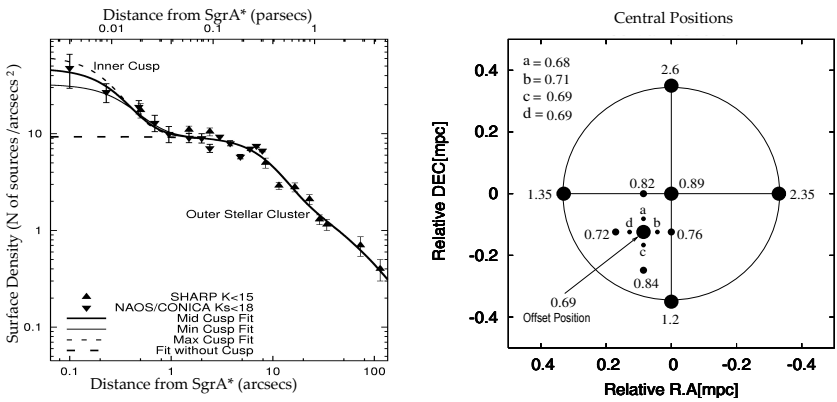

Fig. 1. Left: Plummer models fit to the number density counts (M/L(2μm)=$2M_\odot/L_\odot$), the region inside $\sim$ 15mpc is indicated by the 'inner cusp', and the outer region showing much lower densities by the 'outer stellar cluster'. Right: Probed different locations of the central mass position, *P*. For each position is given the lowest obtained reduced $\tilde{\chi}^2$.

ESO Symposia: Growing Black Holes, pp. 215–216, 2005.

the potential derived above to fit the path of S2 to the radial and positional data [6,7]. The initial parameters are ten: the six initial coordinates, the total central mass, M_{tot} (mass of SBH + mass of the 'inner cusp', M_{cusp}), the cusp fraction, f (M_{cusp}/M_{tot}), and the central mass position, P. These are varied on a grid at different discrete values representing ∼360 orbits. The different P locations are plotted in Fig. 1 (right).

3 Results and Analysis

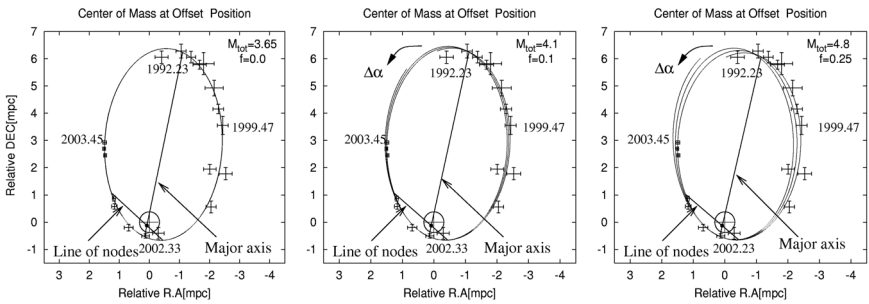

Fig. 2. Three exemplary Keplerian and non-Keplerian 1σ limit orbits for f equal to 0, 0.1 and 0.25 respectively, and M_{tot} (in $10^6 M_\odot$) equal to 3.65, 4.1 and 4.8 respectively.

Non-Keplerian orbits show the same 1σ limit fit as Keplerian (Fig. 2). Thus implying that there could exist an amount of extended dark mass in addition to the $\sim 3\times10^6$ SBH and the observed stellar content. At a 1σ level, the derived upper limit corresponds to 5% in terms of M_{S2cusp}/M_{tot}, where M_{S2cusp} is the cusp mass inside the sphere of radius the apo-centre of S2 (∼9mpc). A large number of massive dark objects ($1m_\odot$-$25m_\odot$ stellar remnants) could have segregated into, and may dominate the mass density inside the sphere of influence of the SBH [1,3]. Under certain assumptions, we find that such a cluster of stellar remnants could show stability over significant fractions of the age of the Milky Way (for further details, see [8]).

References

1. M. Morris: ApJ **408**, 2 (1993)
2. A. Eckart and R. Genzel: MNRAS **284**, 3 (1997)
3. J. Miralda-Escudé and A. Gould: ApJ **545**, 2 (2000)
4. R. Schödel, T. Ott, R. Genzel et al.: Nature **419**, 6908 (2002)
5. R. Genzel, R. Schödel, T. Ott et al.: ApJ **594**, 2 (2003)
6. F. Eisenhauer, R. Schödel, R. Genzel et al.: ApJ **597**, 2 (2003)
7. A. M. Ghez, G. Duchêne, K. Matthews et al.: ApJ **586**, 2 (2003)
8. N. Mouawad, A. Eckart, S. Pfalzner et al.: A&A, submitted. astro-ph/0402338 (2004)

The Compact Stellar Cluster Around Sgr A* and the Nature of Sgr A*

R. Schödel[1], R. Genzel[2,3], A. Eckart[1], and T. Ott[2]

[1] I.Physikalisches Institut, Universität zu Köln, 50937 Köln, Germany
[2] Max-Planck-Institut für extraterrestrische Physik, 85741 Garching, Germany
[3] Department of Physics, University of California, Berkeley, CA 94720, USA

The velocity dispersion of stars in the Milky Way's central stellar cluster traces the gravitational potential of a point mass of $3-4\times10^6\,M_\odot$ from distances of a light year down to a few light days from the compact, non-thermal radio source Sgr A* (e.g., [3,7,4]).

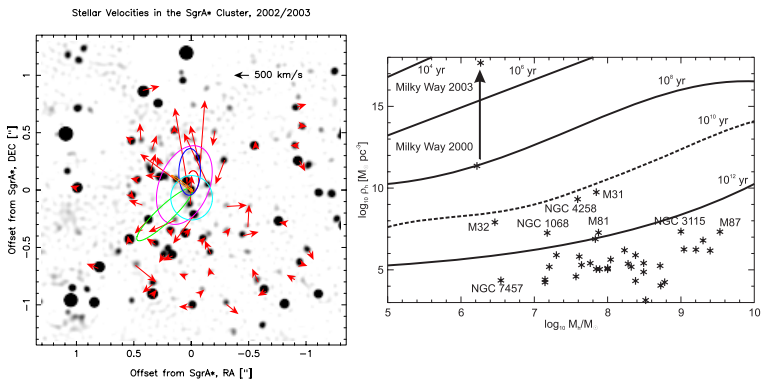

Fig. 1. Left: Proper motion velocities and orbits of stars within ∼50 mpc of Sgr A* [13]. Right: Theoretical life time of clusters (Plummer models, characterized by half mass and half density) against evaporation and collisional destruction (see [11]). The proper motions of stars observed at the center of the Milky Way constrain the life time of such hypothetical dark clusters to $\leq 10^8$ yr (Milky Way 2000). Orbits of individual stars give a limit of $\leq 10^5$ yr (Milky Way 2003). Data on extragalactic compact, central masses from [10].

Orbits of individual stars (Fig. 1) allow to constrain the extent of the dark mass down to a few light hours from Sgr A*. They exclude non-black hole models such as neutrino balls or clusters of dark objects (Fig. 1). The GC is now the strongest case for the existence of supermassive black holes (e.g., [12,8]). Observations of the intrinsic size of Sgr A* with mm-interferometry (e.g., [2]), or the timescales of bursts of emission in the X-ray [1] and NIR domains [6,9] provide further strict upper limits on the size of Sgr A* (see Fig. 2).

Stellar surface number density counts based on deep AO imaging with the NAOS/CONICA AO system/NIR camera allow to confirm the existence of a

ESO Symposia: Growing Black Holes, pp. 217–218, 2005.

density cusp of the stellar cluster centered on Sgr A* as predicted by theoretical considerations. The stellar density within a few mpc of Sgr A* appears to exceed 10^8 pc^{-3} [5].

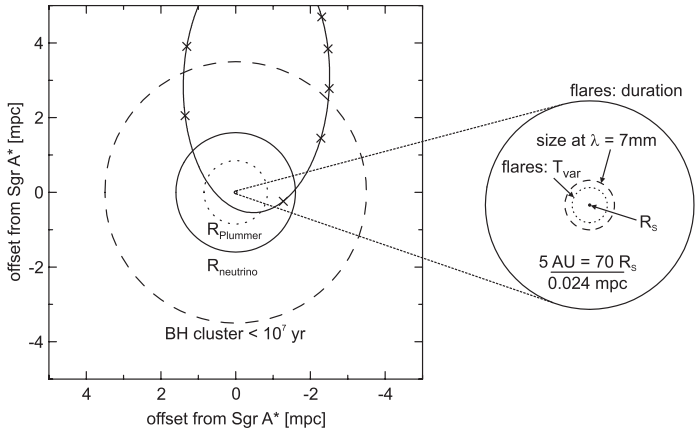

Fig. 2. Left: Illustrations of spatial scales related to Sgr A*. $R_{plummer}$ is the core radius of a hypothetical dense Plummer model cluster of $\sim 3 \times 10^6$ M$_\odot$ marginally compatible with the orbit of S2. $R_{neutrino}$ is the radius of a 3.6×10^6 M$_\odot$ neutrino ball made of 17 keV neutrinos (e.g. [14]). Also indicated is the size of a cluster of 3 M$_\odot$ black holes with a life time of 10^7 yr. Right: Magnification of the small central circle in the left-hand figure. Illustrated are the size scales derived from the duration of Sgr A* flares ($\sim$60 min; [1,6,13]), 7 mm VLBI [2], and from the variability time scales of the Sgr A* NIR flares (5-10 min; [6,13]). The central tiny circle is defined by the event horizon of a 3.6×10^6 M$_\odot$ black hole.

References

1. F. K. Baganoff, M. W. Bautz, W. N. Brandt et al.: Nature **413**, 349 (2001)
2. G. C. Bower, H. Falcke, R. M. Herrnstein et al.: Science **304**, 704 (2004)
3. A. Eckart & R. Genzel: Nature **383**, 415 (1996)
4. R. Genzel, C. Pichon, A. Eckart, O. E. Gerhard, & T. Ott: MNRAS **317**, 348 (2000)
5. R. Genzel, R. Schödel, T. Ott, et al.: Ap.J. **594**, 812 (2003)
6. R. Genzel, R. Schödel, T. Ott, et al.: Nature **425**, 934 (2003)
7. A. Ghez, B. L. Klein, M. Morris, & E. E. Becklin: Ap.J. **509**, 678 (1998)
8. A. M. Ghez, G. Duchêne, K. Matthews, et al.: Ap.J. **586**, L127 (2003)
9. A. M. Ghez, S. A. Wright, K. Matthews, et al.: Ap.J. **601**, L15 (2004)
10. J. Kormendy: In: *Coevolution of Black Holes and Galaxies.* ed. by L. C. Ho (Cambridge University Press, Cambridge 2004) pp. 1
11. E. Maoz: Ap.J. **494**, L181 (1998)
12. R. Schödel, T. Ott, R. Genzel, et al.: Nature **419**, 694 (2002)
13. R. Schödel: PhD Thesis, Ludwig-Maximilians-Universität, München (2004)
14. D. Tsiklauri, & R.D. Viollier: Ap.J. **500**, 591 (1998)

Interaction of Supermassive Black Holes with Their Stellar and Dark Matter Environments

D. Merritt

Rochester Institute of Technology, Rochester, NY, USA

1 Introduction

While supermassive black holes probably gained most of their mass via accretion of gas, the galactic nuclei in which they are currently situated are dominated by stars. This article reviews recent theoretical work on the interaction between black holes and their stellar environment, and highlights ways in which the observed structure of galactic nuclei can be used to constrain the formation history of black holes. Nuclei may also contain dark matter, and the possibility of detecting supersymmetric particles via annihilation radiation from the Galactic center has generated some interest[26]. The evolution of the dark matter distribution in the presence of a black hole in a stellar nucleus is also discussed.

2 Matter Distribution around Black Holes

Figure 1 shows two natural models for the evolution of the stellar density around a black hole. If the star-star relaxation time is long, the form of $\rho(r)$ will still reflect the way the nucleus formed. The simplest possible picture is growth of a black hole at a fixed location in space due to some spherically-symmetric accretion process. As the black hole grows it pulls in stars. If the growth time is long ("adiabatic") compared with orbital periods, the change in $\rho(r)$ is unique and straightforward to compute [51,64]. Figure 1a shows the result if the initial density is a power law, $\rho \propto r^{-\gamma_0}$. The final profile is well described as two power laws joined at a radius $r_{\rm cusp}$ where

$$r_{\rm cusp} = \alpha r_h, \quad 0.19 \lesssim \alpha \lesssim 0.22, \quad 0.5 \le \gamma_0 \le 1.5 \tag{1}$$

and r_h is the radius containing a mass in stars equal to twice the final black hole mass. The final density within $r_{\rm cusp}$ is

$$\rho \propto r^{-\gamma}, \quad 2.29 \le \gamma \le 2.5. \tag{2}$$

This result is insensitive to the geometry (flattened, triaxial, etc.) and degree of rotation of the nucleus.

If the nucleus is older than roughly one relaxation time, a different sort of mass distribution is set up around the black hole, corresponding to a steady-state solution of the Fokker-Planck equation. This steady state has a nearly zero net flux of stars with respect to energy and the density profile is given

ESO Symposia: Growing Black Holes, pp. 221–235, 2005.

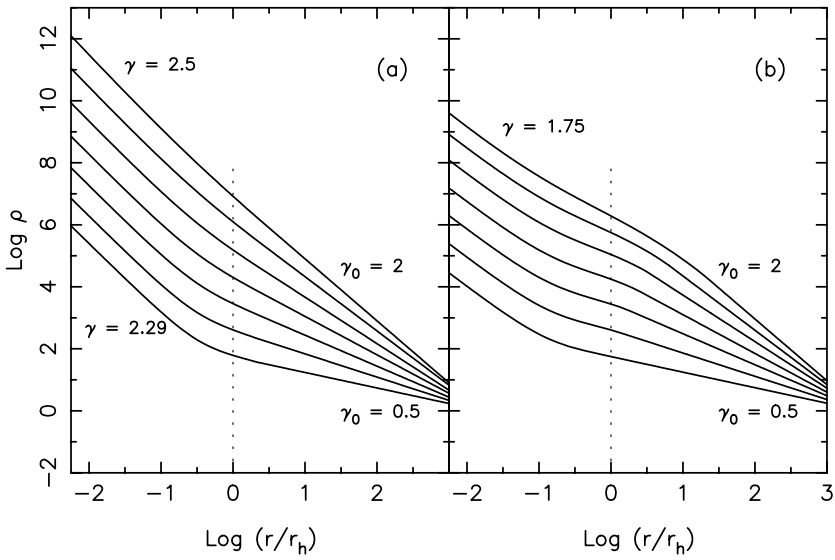

Fig. 1. (a) "Collisionless" density profiles, resulting from growth of a black hole at a fixed location. Initial profiles were power laws, $\rho \propto r^{-\gamma_0}$, with γ_0 increasing upwards in steps of 0.25. The radial scale is normalized to r_h as defined in the initial (pre-black-hole) galaxy. (b) "Collisional" density profiles, computed as steady-state solutions to the Fokker-Planck equation. The density inside $\sim 0.1 r_h$ satisfies $\rho \propto r^{-7/4}$.

uniquely as $\rho \propto r^{-7/4}$ near the black hole [57,3]. Figure 1b shows the result, again assuming various power-law slopes for the initial $\rho(r)$. The $r^{-7/4}$ dependence is only reached at $r \lesssim r_{\rm cusp} \approx 0.1 r_h$.

The condition for the appearance of a collisional, $\gamma = 7/4$ cusp is that the relaxation time,

$$T_r(r) = \frac{\sqrt{2}\sigma(r)^3}{\pi G^2 m \rho(r) \log \Lambda}, \tag{3}$$

measured at $\sim r_h$ be less than the age of the nucleus [3,52]. Figure 4 shows $T_r(r_h)$ for a sample of elliptical galaxies drawn from Faber et al. [11]. Only a few galaxies, all low luminosity ellipticals, have $T_r < 10^{10}$ yr. Two examples are well known: the Milky Way bulge, which has $T_r \approx 2 \times 10^9$ yr (assuming $m = M_\odot$), and M32, for which $T_r \approx 3 \times 10^9$ yr. Both galaxies should have collisionally relaxed nuclei. In the Milky Way, $r_h \approx 1.7$ pc $\approx 40''$ [15] and $r_{\rm cusp} \approx 4''$. The stellar density profile has been determined into $\sim 0.1''$; it is a broken power law with $\gamma \approx 1.4$ inside of $\sim 10''$ and $\gamma \approx 2.0$ outside [15]. The break radius is reasonably close to the predicted value of $r_{\rm cusp}$ but the interior slope is significantly flatter than 7/4. In the case of M32, $r_h \approx 2.9$ pc $\approx 0.9''$ and $r_{\rm cusp} \approx 0.1''$ [28]. The stellar luminosity density has been determined into only $\sim 0.15''$, not quite far enough to test for the existence of a collisional cusp. The situation is worse for more distant galaxies that might harbor collisionally relaxed nuclei, making the

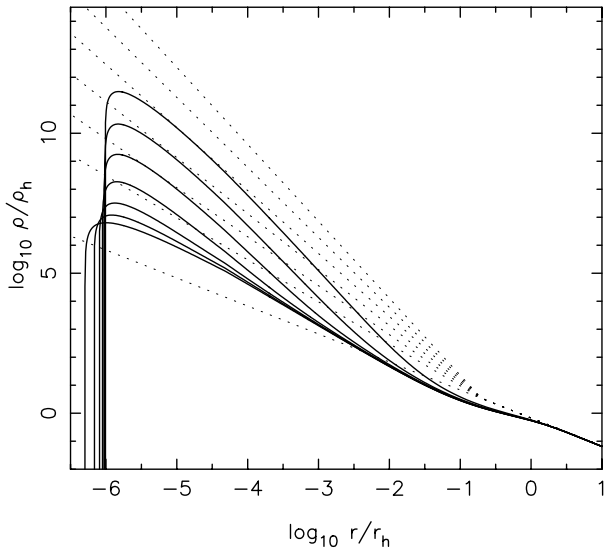

Fig. 2. Dark matter density at $t = 0$ (dotted lines) and 10^{10} yr (solid lines) after heating by stars in the Galactic bulge [38].

Milky Way nucleus the only system in which the theory can currently be tested. The fact that $\gamma < 7/4$ in the Milky Way nucleus may be due to mass segregation which produces a flatter density profile for the less-massive stars [4,50].

Galaxies fainter than M32 or the Milky Way bulge may contain nuclear black holes. If the black holes in dwarf elliptical galaxies obey the $M_\bullet - \sigma$ relation, then $r_h \approx GM_\bullet/\sigma^2$ implies $r_h \propto M_\bullet^{0.6}$ and $r_{\rm cusp}$ would be below resolution limits. This may be the origin of the unresolved nuclei in many dE galaxies.

Particle dark matter, if present in galactic nuclei, would respond to the growth of the black hole according to the "collisionless" model. Its density near the black hole could therefore be very high, resulting in a substantial rate of self-annihilations if the particles are supersymmetric neutralinos [17]. The dark matter distribution would also evolve due to scattering off of stars, on a time scale close to T_r, the star-star relaxation time [27,38,16]. In effect, the stars act as a heat source for the dark matter. Figure 2 illustrates this via time-dependent solutions to the Fokker-Planck equation. Given the appropriate normalization with respect to the dark matter density near the solar circle, this nuclear profile implies a potentially observable flux of annihilation products [38].

3 Feeding Rates

In a spherical galaxy, stars or dark matter particles with angular momenta less than $J_{lc} \approx \sqrt{2GM_\bullet r_t}$ will pass within a distance r_t of the center of the black hole. The "loss cone" is that set of orbits satisfying $J \leq J_{lc}(E)$. If we imagine

that the black hole is embedded in a steady-state galaxy populated by stars with $J \leq J_{lc}$, stars on loss cone orbits will be consumed in one orbital period or less, giving a transitory feeding rate of $\sim 4\pi^2 f(E,0) J_{lc}^2(E)$ stars per unit energy per unit time. This is sometimes called the "full loss cone" consumption rate and it is an effective upper limit to how quickly stars can be supplied to the black hole. For instance, in a $\rho \sim r^{-2}$ nucleus, the full loss cone feeding rate due to all stars with $E > \Phi(r_h)$ is $\sim \sigma^5 r_t / G^2 M_\bullet$ or $\sim \sigma^5 / G c^2$ when $r_t \approx r_s \equiv 2GM_\bullet/c^2$. This is a high enough rate to grow black holes of the correct size after 10^{10} yr, i.e. $\sim 10^{-2} M_\odot$ yr^{-1} for $\sigma \approx 200$ km s^{-1}.

Full loss cones have been postulated from time to time, perhaps first by Hills [22], later by P. Young and co-authors (for the "black-tide" model of quasar fueling) [63,65], and most recently by Zhao, Haehnelt & Rees [68], who noted that the σ^5 scaling is consistent with the $M_\bullet - \sigma$ relation. But while transient loss cone refilling during, say, galaxy mergers is imaginable, it is hard to see how a galaxy could arrange for the 10^5 or more refilling events that would be needed to keep a loss cone continuously filled.

Instead, the loss cone is probably usually empty at radii $r < r_{crit}$, where r_{crit} is the radius at which the scattering time into the loss cone equals the orbital period. Below r_{crit}, stars are lost the moment they enter the loss cone, while above r_{crit}, stars may scatter in and out of the loss cone in a single orbit. For $M_\bullet \approx 10^7 M_\odot$, $r_{crit} \approx r_h$, and $r_{crit} < r_h$ at larger $M_\bullet$ [13]. The feeding rate due to stars inside r_{crit} is $\sim M(r_{crit})/T_r(r_{crit})$ since in one relaxation time a star's angular momentum can change by of order itself. Outside r_{crit}, the loss cone is effectively full but the feeding rate drops off rapidly with radius since the capture sphere subtends such a small angle (the "pinhole" regime). One finds in a careful calculation that the flux into the black hole is strongly peaked at energies near $\Phi(r_{crit})$ [30,7].

Figure 3 shows tidal disruption rates computed in a sample of elliptical galaxies, with r_t set to the tidal radius for solar-mass stars [60]. (For $M_\bullet \gtrsim 10^8 M_\odot$, $r_t < r_s$ and stars would be swallowed whole.) The numbers in this plot supersede the estimates in [32] which were based on the now-discredited Magorrian et al. [31] black hole masses. Disruption rates reach $\sim 10^{-3}$ yr^{-1} in the faintest galaxies with verified black holes like M32. The dashed lines in that figure are the predicted rates in a singular isothermal sphere nucleus:

$$\dot{N} \approx 2.5 \times 10^{-3} \mathrm{yr}^{-1} \left(\frac{\sigma}{100 \text{ km s}^{-1}} \right)^{7/2} \left(\frac{M_\bullet}{10^6 M_\odot} \right)^{-1} \propto M_\bullet^{-0.25} \qquad (4)$$

and in a nucleus with $\rho \propto r^{-3/2}$:

$$\dot{N} \approx 1.0 \times 10^{-3} \mathrm{yr}^{-1} \left(\frac{\sigma}{100 \text{ km s}^{-1}} \right)^{21/5} \left(\frac{M_\bullet}{10^6 M_\odot} \right)^{-4/5} \propto M_\bullet^{0.10} \qquad (5)$$

where the latter expressions in each case use the $M_\bullet - \sigma$ relation [41]. The tidal flaring rate is probably nearly independent of $M_\bullet$ for $M_\bullet \lesssim 10^6 M_\odot$, and if dE galaxies contain black holes, they would dominate the total flaring rate [60].

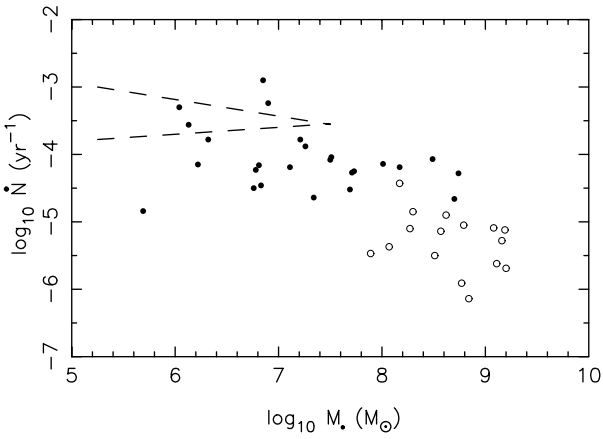

Fig. 3. Stellar tidal disruption rates in a sample of elliptical galaxies computed using the Cohn-Kulsrud [7] loss cone boundary conditions [60]. Open circles are "core" galaxies and filled circles are "power-law" galaxies. Upper and lower dashed lines are disruption rates in power-law nuclei with $\rho \propto r^{-2}$ and $r^{-1.5}$ respectively.

A fraction $25\% - 50\%$ of a tidally disrupted star is expected to remain gravitationally bound to the black hole [2]. If this is the case, and if disruption rates have remained nearly constant over 10^{10} yr, Figure 3 suggests that stellar consumption could be a major contributor to the growth of black holes with $M_\bullet \lesssim 10^7 M_\odot$.

The feeding rates estimated above were based on a theory derived in the late 1970's to describe consumption rates of stars by massive black holes at the centers of globular clusters [3,30,7]. Globular clusters are many relaxation times old, and the assumption of a collisionally-relaxed steady state is built into the theory. For instance, the Cohn-Kulsrud [7] loss cone boundary conditions, used in Figure 3, are only valid in a collisionally relaxed system. But relaxation times in galactic nuclei can be very long and this fact requires a re-thinking of loss cone theory. Figure 4 shows histograms of three time scales relevant to feeding rates. The bottom panel is the relaxation time T_r (eq. 3) evaluated at the black hole's influence radius r_h. T_r exceeds 10^{10} yr in most galaxies. The middle and upper panels show two time scales more directly related to the establishment of a steady-state loss cone. The time scale for scattering of low angular momentum stars into the loss cone is

$$T_\theta(r) \approx \theta(r)^2 T_r(r) \tag{6}$$

where $\theta(r)$ is the scattering angle as seen from a star at radius r; the square-root dependence of θ on T_θ reflects the fact that entry into the loss cone is a diffusive process. If the stellar phase space is initially well-populated by stars whose angular momenta are close to the critical value for capture J_{lc}, encounters will set up a steady state near the loss cone in the scattering time corresponding

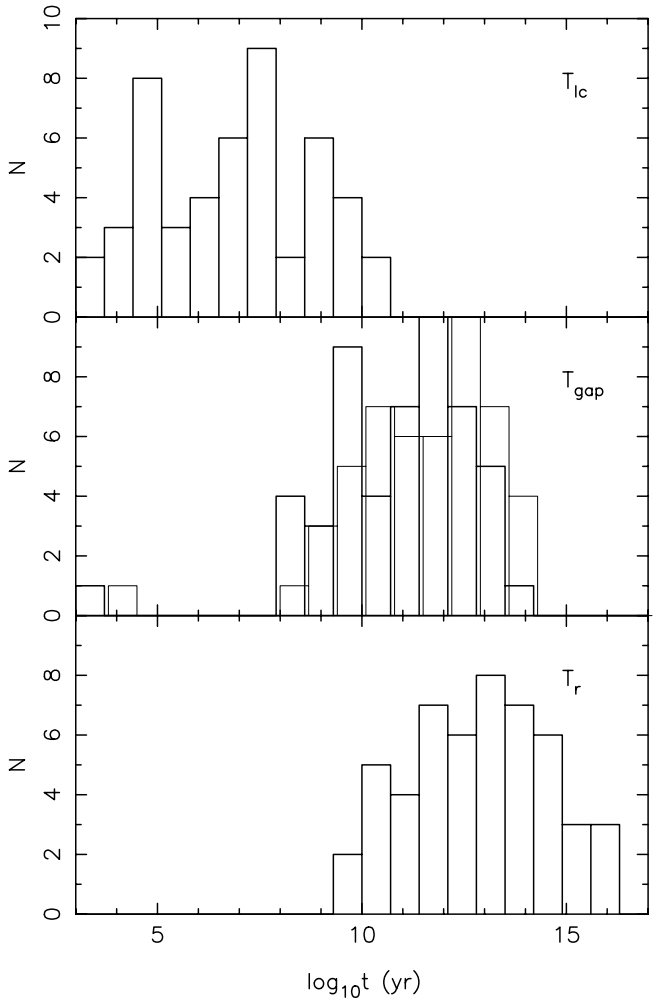

Fig. 4. Time scales T_r, T_{lc} and T_{gap} defined in the text, for the sample of elliptical galaxies in Fig. 3. Thick/thin histograms of T_{gap} are for $m_2/m_1 = (0.1, 1)$, where m_2/m_1 is the mass ratio of the binary black hole that preceded the current, single black hole.

to $\theta = \theta_{lc} \approx (r_t/r)^{1/2}$, or

$$T_{lc} \approx \frac{r_t}{r} T_r. \tag{7}$$

Figure 4 shows that T_{lc} is shorter than 10^{10} yr in most galaxies.

But suppose that the loss cone was initially emptied of all stars with pericenters below some radius $r_0 \gg r_t$; for instance, a binary black hole might have ejected such stars via the gravitational slingshot (§4). Once the two black holes

had coalesced, the time to diffusively fill this angular momentum gap would be

$$T_{gap} \approx \frac{r_0}{r} T_r \gg T_{lc}. \tag{8}$$

In the binary black hole model, most stars with pericenters

$$r_p \lesssim K a_h = K \frac{G\mu}{4\sigma^2} \tag{9}$$

will have been ejected prior to the coalescence. Here $a_h \gg r_t$ is the semimajor axis of the binary when it first becomes "hard," μ is the reduced mass of the binary, and $K \approx 2$. The middle histogram in Figure 4 shows T_{gap} for two values of the binary mass ratio, $m_2/m_1 = (0.1, 1)$. In every galaxy,

$$T_{lc} \ll T_{gap} < T_r. \tag{10}$$

Whereas T_{lc} is generally shorter than 10^{10} yr, T_{gap} exceeds 10^{10} yr in most galaxies and this is true for all "core" galaxies which show evidence of cusp destruction.

A more careful calculation [61], applying the time-dependent Fokker-Planck equation to the galaxies in Figure 3, shows that the time $t_{1/2}$ for the feeding rate to reach 1/2 of its steady-state value after loss cone depletion by a binary black hole is approximately

$$\frac{t_{1/2}}{10^{11}\mathrm{yr}} \approx \frac{\mu}{10^7 M_\bullet} \approx 10 \frac{q}{(1+q)^2} \frac{M_\bullet}{10^8 M_\odot} \tag{11}$$

with $q = m_2/m_1$ the binary mass ratio. While this is a highly idealized model, it gives an indication of the time required for loss cone feeding to reach a steady state in galactic nuclei, and suggests that the tidal flaring rates in luminous "core" galaxies might be much lower than suggested by Figure 3.

4 Interaction of Binary Black Holes with Stars

Binary supermassive black holes are inevitable consequences of galaxy mergers. Unless one of the black holes is very small, the two quickly form a bound pair at a separation $a \approx a_h \equiv G\mu/4\sigma^2 \approx [\mu/4(m_1+m_2)]r_h$ with μ the reduced mass. Subsequently the binary separation can decrease, but only if the binary is able to exchange angular momentum with stars or gas. (See [42] for a review of binary-gas interactions.) Stars that pass within a distance $\sim 3a$ of the binary undergo a complex 3-body interaction followed by ejection of the star at a velocity of order μ/m_{12} times the binary orbital velocity (the "gravitational slingshot" [56]). Each ejected star carries away energy and angular momentum, causing the semi-major axis, eccentricity, orientation, and center-of-mass velocity of the binary to change and the local density of stars to drop [25,23,24,46,53,36,37].

In principle, N-body studies can reveal both the long-term evolution of the binary as it interacts with stars, and the back-reaction of the binary on its stellar

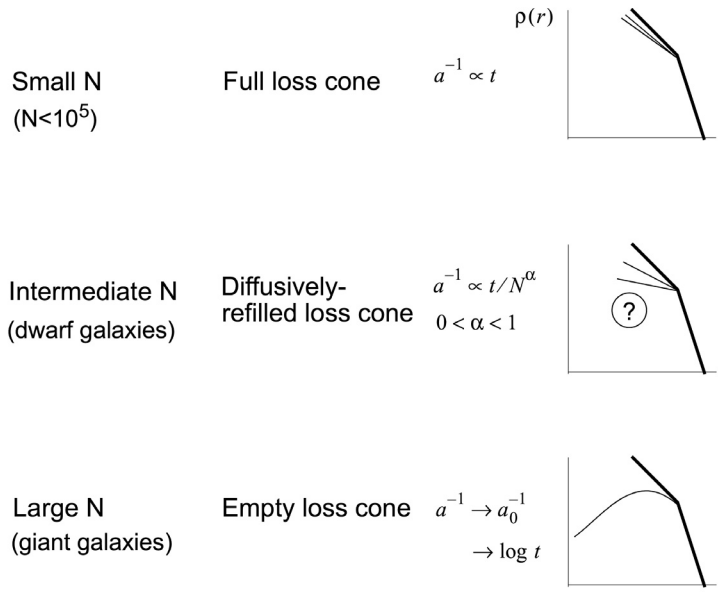

Fig. 5. Physical regimes for the decay of massive black hole binaries [48].

surroundings. But unless great care is taken, N-body simulations are likely to give misleading results. The reason is that time scales for two-body scattering of stars into the binary's loss cone are shorter by factors of $\sim N/10^{11}$ in the simulations than in real galaxies, and the long-term evolution of the binary is likely to be dominated by spurious loss cone refilling, wandering of the binary, and other noise-driven effects. Values of N that are easily accessible to direct-summation N-body simulation, $N \lesssim 10^5$, are so small that stars tend to be scattered into the binary's loss cone at a faster rate than they are kicked out by the gravitational slingshot [48]. This is analogous to the "full loss cone" around a single black hole and it guarantees that the binary will never run out of stars.

N-body studies are most reliable when characterizing the early stages of binary formation and decay. Due to algorithmic limitations, most such studies [9,34,33,21,6,35] have been based on galaxy models with unphysically large cores. The first simulations with realistically dense initial conditions [39,47,43] showed that the stellar density around the binary drops very quickly after the binary first becomes hard, converting a $\rho \propto r^{-2}$ cusp to a shallower $\sim r^{-1}$ cusp.

But the long-term evolution of massive binaries in real galaxies, and the effect of binary evolution on nuclear structure, are not well understood. Figure 5 summarizes the likely regimes. For small N, of the order easily accessible to N-body simulations, collisionality is so high that the binary's loss cone remains full. The binary's binding energy increases linearly with time, $a^{-1} \propto t$, and the stellar density profile becomes gradually flatter. The same sort of evolution would occur in a triaxial nucleus where centrophilic orbits can continuously repopulate

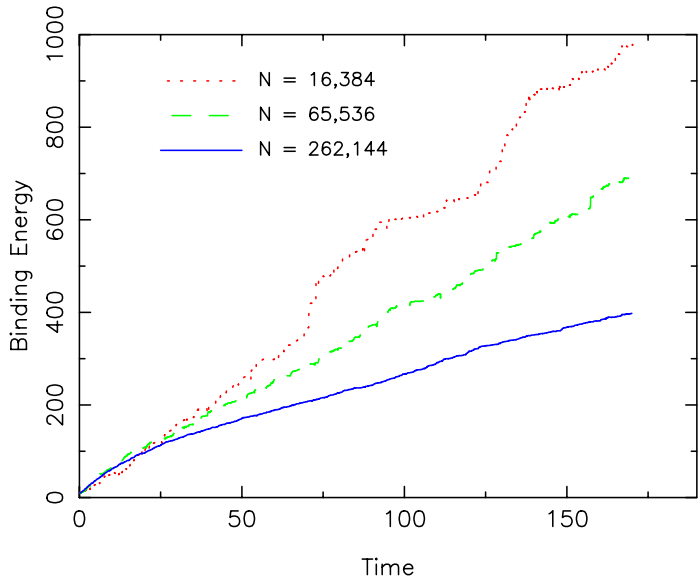

Fig. 6. N-dependence of the decay rate of a massive binary in N-body simulations [58]. Each of the three runs started from the same initial state, an equal-mass binary with a binding energy of 10. For small N, the long-term decay satisfies $a^{-1} \sim t$, the expected behavior in the full-loss-cone regime (Fig. 5). As N increases, the lower degree of collisionality allows the loss cone around the binary to remain partially unfilled and decay slows.

the loss cone [45]. At the other extreme, in giant galaxies, relaxation times are very long and almost no stars would be scattered into the binary's loss cone. The decay stalls, leaving a "hole" in the stellar density [67]. A mechanism that might contribute to continued decay in this regime is re-ejection: stars ejected with less than galactic escape velocity can continue to interact with the binary [48]. The most interesting, and least-understood, regime is the intermediate one, corresponding to galaxies in which two-body scattering contributes substantially to the binary's decay without completely re-filling its loss cone [66]. Reproducing this regime requires either N-body simulations with $N \gtrsim 10^7$, or a hybrid scheme that combines a Fokker-Planck integrator with a central binary. Figure 6 shows a step in this direction: N-body integrations for N up to 0.25×10^6 using a GRAPE-6 special-purpose computer, coupled with a chain regularization algorithm to follow close interactions of star and black hole particles [58]. The N-dependence of the decay rate is clearly visible. Similar results were obtained [35] using a lower-accuracy N-body code. Increasing N by an order of magnitude will soon be feasible and this will allow simulations in which the binary's evolution is dominated by slow diffusion into the loss cone, as in real galaxies.

5 Brownian Motion

Both single and binary black holes undergo a random walk in momentum space as their motion is perturbed by gravitational encounters with nearby stars. Simple encounter theory predicts that a massive black hole reaches a state of kinetic energy equipartition with the stars, giving it a mean square velocity of $\langle V^2\rangle \approx 3(m/M_\bullet)\sigma^2$. This "gravitational Brownian motion" has been suggested as a mechanism for enhancing the supply of stars to a massive binary; indeed it has been asserted [54,6] that wandering of the binary's center of mass can itself guarantee a continued supply of stars.

While Brownian motion probably does affect the decay rate of binaries in the N-body simulations [48], it is doubtful that the effect is significant in real galaxies. The Brownian velocity of *single* black holes is found in N-body simulations to be [29]

$$\frac{1}{2}M_\bullet\langle V^2\rangle \approx \frac{3}{2}m\tilde{\sigma}^2 \tag{12}$$

where $\tilde{\sigma}^2$ is the 1D, mean square stellar velocity within a region $r \lesssim 0.5r_h$ around the black hole and m is the stellar mass. Equation (12) holds in galaxy models with a wide range of nuclear density slopes, black hole masses and particle numbers up to 10^6, the largest values so far used in direct-summation N-body simulations [8]. In the case of the Milky Way black hole, equation (12) implies $V_{\rm rms} \approx 0.17$ km s^{-1} (assuming $m = M_\odot$), a little larger than the "equipartition" value. The reason is that the black hole responds to perturbations from stars whose velocities have themselves been increased by the presence of the black hole [29].

Brownian motion of a massive *binary* is larger than that of a single black hole, for two reasons [36]. (1) Stars are ejected superelastically from the binary, imparting a greater momentum to the binary than they would to a single black hole. (2) The dynamical friction force acting on the binary is less than that acting on a single particle due to the randomization of the ejection angles. The first factor dominates and produces an extra fractional contribution to $\langle V^2\rangle$ that is approximately $H/(32\sqrt{2}\pi\ln\Lambda)$, with $H \approx 16$ the dimensionless hardening rate of the binary [53]. Thus the Brownian motion of a binary is only slightly larger than that of a single black hole of the same mass. This prediction has been verified in N-body simulations [47,35]. The rms displacement of a binary from its otherwise central location would be very small in a real galaxy, probably even less than the separation between the two black holes.

The claim that wandering can guarantee a continued supply of stars to a binary is based on the following conceptual model [54,6]. As N increases, the wandering first drops as expected from equation (12), but at sufficiently large $M_\bullet/m$ the binary empties its loss cone, producing a low-density core in which the binary is easily displaced. The amplitude of the binary's center-of-mass motion increases, allowing it to interact with a larger number of stars.

The motivation for this model was the complex N-dependence observed in a set of binary decay simulations [54,6]: the decay rate first dropped with increasing N until $N \approx 2\times 10^5$, then remained constant when N was doubled.

But the postulated N-dependence of the *wandering* was never verified. Even if the interpretation in terms of wandering is correct, extrapolating the N-body results from $N \lesssim 10^6$ to $N \approx 10^{11}$ is problematic. Furthermore the galaxy models were Plummer spheres which have a much lower degree of concentration than real galaxies. and the wandering amplitudes inferred by these authors would be enormous if scaled to real galaxies, $\gtrsim 10^2$ pc, Extended simulations of binary hardening in realistic galaxy models with $N > 10^6$ should soon settle this matter.

6 Evidence for Cusp Destruction

The structural parameters of elliptical galaxies display a smooth dependence on galaxy luminosity from dE galaxies up to the brighter ellipticals, $M_V \approx -20$ [18]. Above this luminosity, galaxies generally have cores, regions near the center where the density falls below the inward extrapolation of the outer profiles (although the density almost always continues to rise inward). It is natural to attribute the cores to stellar ejection by a binary black hole and to use the "mass deficit" as a quantitative test of the binary black hole model (Fig. 7). In two studies [49,55], pre-merger profiles for a sample of galaxies were constructed by extrapolating power laws, $\rho \propto r^{-\gamma_0}$, inward of the core radius. Milosavljevic et al. [49] found mean mass deficits of $\sim 1 M_\bullet$ for $\gamma_0 = 1.5$. More recently, Graham [19] fit the outer luminosity data to Sersic profiles and defined the mass deficit with respect to this template; mass deficits were found to be slightly larger, about twice $M_\bullet$.[1] These numbers are reasonable but it is difficult to say more given the difficulties cited above in interpreting N-body simulations of binary evolution.

An interesting unsolved problem is the effect of multiple mergers on the central density profiles of galaxies containing black holes. A simple argument suggests that the net effect, e.g. the core size, should increase both with the final black hole mass *and* with the number of merger events. Consider the merger of two galaxies with steep central cusps and black holes of mass m_1 and m_2; the result will be a galaxy with a shallower central profile and black hole of mass $m_{12} = m_1 + m_2$. Now imagine that that same galaxy is produced by the merger of two galaxies whose central density cusps had already been destroyed by previous merger events. The final merger would lower the central density still more, producing a larger core for the same m_{12}. Testing this prediction via N-body simulations will be difficult for all the reasons discussed above, but it should be possible at least to test how the early evolution of binaries affects the central profiles of galaxies in multiple mergers.

The idea that cores grow cumulatively in mergers was used by Volonteri et al. [59] to predict the evolution of luminous and dark matter cores in galaxies. In their most extreme ("core preservation") model, the binaries were assumed to

[1] Graham (2004) presents his mass deficits as significantly *smaller* than in the earlier study, but he bases his comparison exclusively on values of $M_{\rm def}$ computed by Milosavljevic et al. using $\gamma_0 = 2$; the latter authors computed $M_{\rm def}$ for a range of values $1.5 \le \gamma_0 \le 2.0$.

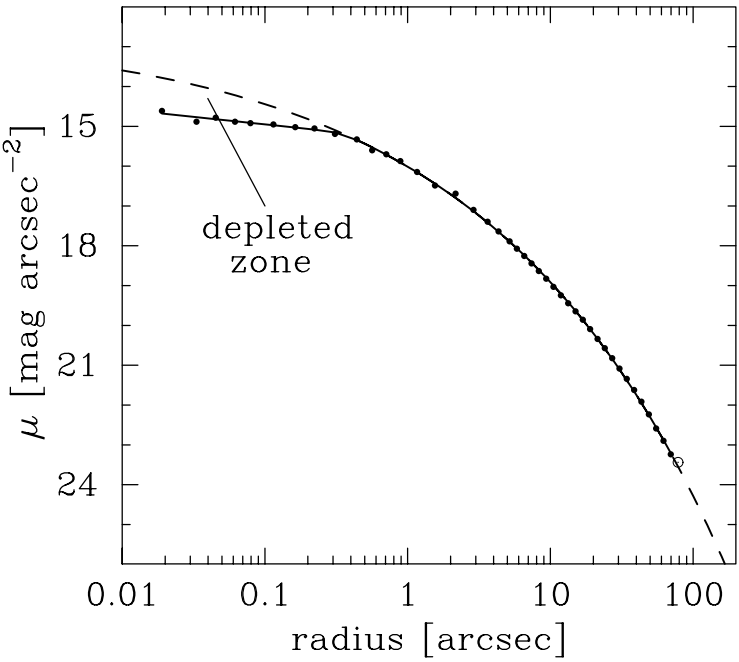

Fig. 7. Observed surface brightness profile of NGC 3348. The dashed line is a Sersic model fit to the large-radius data. The mass deficit is illustrated by the area designated "depleted zone" and the corresponding mass is roughly $3 \times 10^8 M_\odot$ [19].

eject as much stellar mass as needed to shrink to a separation where gravitational radiation losses induce coalescence. The result, after 10^{10} yr, was cores with sizes of order $3r_h$. While intriguing, this model lacks a firm foundation in the N-body simulations.

In small dense galaxies, a destroyed cusp would be expected to re-form via the collisional mechanism discussed above, *if* the relaxation time at the core radius is less than the elapsed time since the merger. Alternatively, steep cusps may be due to star formation that occurred after the most recent merger.

There is one context in which formation of cores by black holes has been tested and shown to work. Globular clusters in the Large and Small Magellanic Clouds exhibit a range of ages and core sizes, and the mean core radius increases as the logarithm of the age [10]. The observed age dependence is reproduced very well by a model in which the first population of stars leave behind $\sim 10 M_\odot$ remnants which sink to the center and displace the less massive stars before ejecting themselves via three-body interactions [40]. This model may have some relevance to galactic nuclei if supermassive binaries stall long enough for third or fourth black holes to fall in.

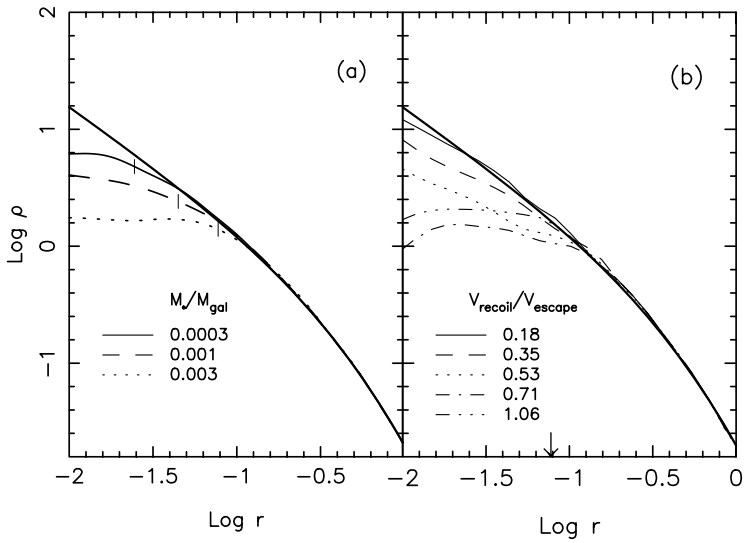

Fig. 8. Effect on the nuclear density profile of black hole ejection. The initial galaxy model (black line) has a $\rho \sim r^{-1}$ density cusp. (a) Impulsive removal of the black hole. Tick marks show the radius of the black hole's sphere of influence r_h before ejection. A core forms with radius $\sim 2r_h$. (b) Ejection at velocities less than escape velocity. The black hole has mass $0.003M_{\rm gal}$; the galaxy is initially spherical and the black hole's orbit remains nearly radial as it decays via dynamical friction. The arrow marks r_h.

7 Black Hole Ejections

If two black holes do manage to coalesce due to emission of gravitational radiation, linear momentum carried by the waves will impart a kick to the coalesced hole of amplitude $\sim 10^{-3}c$ [14]. The recoil velocity depends in a complicated way on the mass ratio and spins of the two black holes and on the spin orientations [12]. At present only the mass ratio dependence is well understood: the recoil velocity peaks at $m_2/m_1 \approx 0.38$ and falls to zero at $m_2/m_1 = 0$ or 1. As discussed by Hughes, Favata & Holz in these proceedings, uncertainty about the strong-field behavior of the effect allows only plausible upper and lower limits to be placed on the magnitude of the kicks. However for moderately large spins and prograde capture, even the lower limits exceed 100 km s^{-1} for $0.2 \lesssim m_2/m_1 \lesssim 0.6$, and the upper limit estimates reach $\sim$ 500 km s^{-1} for favorable mass ratios [44].

An important possible consequence of the kicks is ejection of black holes from galaxies, particularly in the early universe when potential wells were shallow [44,20,62]. Whether or not a black hole is completely ejected, displacement of the black hole transfers energy to the nucleus and lowers its density within a region of size $\sim r_h$ (Fig. 8). Impulsive removal at $V_{\rm kick} \gg V_{\rm escape}$ produces a core of roughly constant density within a radius $\sim 2r_h$ if the initial density profile is $\rho \propto r^{-1}$. The net effect is greater if $V_{\rm kick} \lesssim V_{\rm escape}$ since the black hole can return

to the nucleus several times before settling down. For $V_{\rm kick} \lesssim 0.25 V_{\rm escape}$ the change in the density is negligible. Cores formed in this way have a similar size to those produced in the binary black hole model and complicate the interpretation of mass deficits.

References

1. S. Aarseth: Pub. Astron. Soc. Pac. **111**, 1333 (1999)
2. S. Ayal, M. Livio, T. Piran: Astrophys. J. **545**, 772 (2000)
3. J. N. Bahcall, R. A. Wolf: Astrophys. J. **209**, 214 (1976)
4. J. N. Bahcall, R. A. Wolf: Astrophys. J. **216**, 883 (1977)
5. P. Chatterjee, L. Hernquist, A. Loeb: Astrophys. J. **572**, 371 (2002)
6. P. Chatterjee, L. Hernquist, A. Loeb: Astrophys. J. **592**, 32 (2003)
7. H. Cohn, R. Kulsrud: Astrophys. J. **226**, 1087 (1978)
8. E. N. Dorband, M. Hemsendorf, D. Merritt: J. Comp. Phys. **185**, 484 (2003)
9. T. Ebisuzaki, J. Makino, S. K. Okumura: Nature **354**, 212 (1991)
10. R. Elson: Astrophys. J. Suppl. **76**, 185 (1991)
11. S. M. Faber et al.: Astron. J. **114**, 1771 (1997)
12. M. Favata, S. Hughes, D. Holz: Astrophys. J. Lett. **607**, L5 (2004)
13. J. Frank, M. J. Rees: Mon. Not. R. Astron. Soc. **176**, 633 (1976)
14. M. Fitchett: Mon. Not. R. Astron. Soc. **203**, 1049 (1983)
15. R. Genzel et al.: Astrophys. J. **594**, 812 (2003)
16. O. Gnedin, J. Primack: Phys. Rev. Lett. **93**, 061302 (2004)
17. P. Gondolo, J. Silk: Phys. Rev. Lett. **83**, 1719 (1999)
18. A. W. Graham, R. Guzman: Astron. J. **125**, 2936 (2002)
19. A. W. Graham: Astrophys. J. **613**, L33 (2004)
20. Z. Haiman: astro-ph/0404196 (2004)
21. M. Hemsendorf, S. Sigurdsson, R. Spurzem: Astrophys. J. **581**, 1256 (2002)
22. J. G. Hills: Nature **254**, 295 (1975)
23. J. G. Hills: Astron. J. **88**, 1269 (1983)
24. J. G. Hills: Astron. J. **103**, 1955 (1992)
25. J. G. Hills, L. W. Fullerton: Astron. J. **85**, 1281 (1980)
26. D. Hooper, I. Perez, J. Silk, F. Ferrer, S. Sarkar: J. Cosmol. Astropart. Phys. **9**, 2 (2004)
27. A. S. Ilyin, K. P. Zybin, A. V. Gurevich: astro-ph/0306490 (2003)
28. T. R. Lauer et al.: Astron. J. **116**, 2263 (1998)
29. F. Laun, D. Merritt: astro-ph/0408029 (2004)
30. A. P. Lightman, S. L. Shapiro: Astrophys. J. **211**, 244 (1977)
31. J. Magorrian et al.: Astron. J. **115**, 2285 (1998)
32. J. Magorrian, S. Tremaine: Mon. Not. R. Astron. Soc. **309**, 447 (1999)
33. J. Makino: Astrophys. J. **478**, 58 (1997)
34. J. Makino, T. Fukushige, S. K. Okumura, T. Ebisuzaki: Pub. Astron. Soc. J. **45**, 303 (1993)
35. J. Makino, Y. Funato:Astrophys. J. **602**, 93 (2004)
36. D. Merritt: Astrophys. J. **556**, 245 (2001)
37. D. Merritt: Astrophys. J. **568**, 998 (2002)
38. D. Merritt: Phys. Rev. Lett. **92**, 201304 (2004)
39. D. Merritt, F. Cruz: Astrophys. J. Lett. **551**, L41 (2001)

40. D. Merritt, S. Piatek, S. Portegies Zsart, M. Hemsendorf: Astrophys. J. Lett. **608**, L25 (2004)
41. D. Merritt, L. Ferrarese: 'Relation of Black Holes to Bulges'. In: *The Central Kiloparsec of Starbursts and AGN*, ASP Conf. Ser. Vol. 249, ed. by J. H. Knapen et al. (ASP, San Francisco 2001) pp. 335–362
42. D. Merritt, M. Milosavljevic: Massive Binary Black Hole Evolution, *Living Reviews in Relativity* (2004)
43. D. Merritt, M. Milosavljevic, L. Verde, R. Jimenez: Phys. Rev. Letts. **88**, 191301 (2002)
44. D. Merritt, M. Milosavljevic, M. Favata, S. Hughes, D. Holz: Astrophys. J. Lett. **607**, L9 (2004)
45. D. Merritt, M. Y. Poon: Astrophys. J. **606**, 788 (2004)
46. S. Mikkola, M. J. Valtonen: Mon. Not. R. Astron. Soc. **259**, 115 (1992)
47. M. Milosavljevic, D. Merritt: Astrophys. J. **563**, 34 (2001)
48. M. Milosavljevic, D. Merritt: Astrophys. J. **596**, 860 (2003)
49. M. Milosavljevic, D. Merritt, A. Rest, F. C. van den Bosch: Mon. Not. R. Astron. Soc. **331**, L51 (2002)
50. B. W. Murphy, H. N. Cohn, R. H. Durisen: Astrophys. J. **370**, 60 (1991)
51. P. J. E. Peebles: Gen. Rel. Grav. **3**, 61 (1972)
52. M. Preto, D. Merritt, R. Spurzem: Astrophys. J. **613**, 000 (2004)
53. G. D. Quinlan: New Astron. **1**, 35 (1996)
54. G. D. Quinlan, L, Hernquist: New Astron. **2**, 533 (1997)
55. S. Ravindranath, L. C. Ho, A. V. Filippenko: Astrophys. J. **566** 801 (2002)
56. W. C. Saslaw, M. J. Valtonen, S. J. Aarseth: Astrophys. J. **190**, 253 (1974)
57. S. L. Shapiro, A. P. Lightman: Nature **262**, 743 (1976)
58. A. Szell, D. Merritt: in preparation (2004)
59. M. Volonteri, P. Madau, F. Haardt: Astrophys. J. **593**, 661 (2003)
60. J. Wang, D. Merritt: Astrophys. J. **600**, 149 (2004)
61. J. Wang, D. Merritt: in preparation
62. J. Yoo, J. Miralda-Escude: astro-ph/0406217 (2004)
63. P. J. Young: Astrophys. J. **215**, 36 (1977)
64. P. J. Young: Astron. J. **242**, 1232 (1980)
65. P. J. Young, G. R. Shields, J. C. Wheeler: Astrophys. J. **212**, 367 (1977)
66. Q. Yu: Mon. Not. R. Astron. Soc. **331**, 935 (2002)
67. C. Zier, P. L. Biermann: Astron. Astrophys. **377**, 23 (2001)
68. H. Zhao, M. G. Haehnelt, M. J. Rees: New Astron. **7**, 385 (2002)

ISM Dynamics Around Black Holes in Nearby (Radio) Early-Type Galaxies with HST

G. Verdoes Kleijn[1], R. van der Marel[2], and J. Noel-Storr[2]

[1] ESO, Karl-Schwarzschild-Strasse-2, D-85748, Garching, Germany
[2] STScI, 3700 San Martin Drive, Baltimore, MD 21218, USA

Abstract. The black holes (BHs) at the centers of present-day bright early-type galaxies might represent the most massive endpoints for BH growth in the Universe. The majority of these galaxies contains detectable amounts of emission-line gas at their centers which indicate that their black holes are still growing, but typically at very modest rates. The gas kinematics potentially form a valuable diagnostic of both this growth process and the gravitational potential well of the BH. Here we focus on the nuclear gas velocity dispersion which often exceeds the stellar velocity dispersion. This could be due to either the gravitational potential of the black hole or turbulence associated with the accretion process. We try to discriminate between these two scenarios.

1 Introduction

The mass of the central black hole (BH) in tens of nearby ($D < 100h^{-1}$Mpc) spiral and elliptical galaxies has been directly weighed using stars, optical emission-line gas or maser clouds as 'test particles' moving in the nuclear gravitational potential (see e.g., [8,9] for reviews). The inferred BH masses $M_\bullet$ are in the range $M_\bullet \sim 10^6 - 5 \times 10^9$ M$_\odot$ and correlate with host spheroid luminosity L_B, global stellar velocity dispersion σ_s and spheroid mass [8,7,6,11]. These correlations summarize our current knowledge of the local BH demography. The modeling of BH growth in a cosmological context relies on accurate determination of these correlations (e.g., [16,13]). Here we explore a potential caveat of $M_\bullet$ determinations which use the central emission-line gas disks. The measurement of the most massive black holes (i.e., $M_\bullet \geq 10^9$M$_\odot$), relies almost solely on this method. (The central stellar surface brightness of the hosts, giant ellipticals, is typically too low to obtain accurate stellar kinematics.) A similar analysis for spiral galaxies has been performed by Sarzi et al. [15].

The extended gas velocities in galactic nuclei have been modeled as a thin disk of gas clouds in circular rotation. While successful in explaining gas velocities, it is often found that the nuclear velocity dispersion exceeds the prediction for a thin disk [1,18,4,20]). The origin of this 'excess' velocity dispersion is unknown.

A purely gravitational origin for the excess would imply that the gas clouds rotate at sub-circular speeds and do not form thin disks. This in turn would imply that the inferred BH masses are lower limits. If the excess dispersion has a non-gravitational origin, it might also violate the thin circular disk approximation. We would like to search for relations between excess dispersion and both nuclear activity and host galaxy properties. This might point to galaxies without excess

ESO Symposia: Growing Black Holes, pp. 236–241, 2005.

dispersion for which the nuclear gas dispersion allows the detection of BH masses well below those measurable from its extended gas rotation. This would firm our constraints on the scatter towards low BH masses in the aforementioned correlations. Claims of unusually low $M_\bullet$ exist for narrow-line Seyfert 1 galaxies using other methods to estimate $M_\bullet$ (e.g., [12]).

2 Sample and Data Analysis

The sample of 27 galaxies (Table 1) consists of galaxies which meet the following requirements: (a) distance below 110 Mpc; (b) HST optical emission line spectroscopy around Hα+[NII] with a $\sim 0.1'' - 0.2''$ aperture size for which gas velocity dispersions and emission-line profiles are either published (20 galaxies) or were derived by us using HST archival observations (7 galaxies); (c) published large-scale stellar velocity dispersions; (d) early-type host morphology; (e) an identifiable (i.e., relatively unobscured) nucleus in HST imaging. We determine the sub-pixel location of the nucleus from the continuum and emission-line flux profile. At the central aperture, we obtain the gas dispersion from single Gaussian fits to each of the lines of the Hα+[NII] composite and to the weaker [SII]6716, 6731 lines where possible. We fit one additional Gaussian for NGC 3245, NGC 3998, NGC 4278 and NGC 6251 which clearly contain a broad Hα component. We parameterize the emission-line surface brightness by fitting a double exponential function, taking into account the PSF. In our models we use black hole masses estimated from the $M_\bullet - \sigma_{\rm s}$ relation as determined by Tremaine et al. [17]. We estimate a $\sim 7\%$ difference between $\sigma_{\rm s}$ in Table 1 and the definition of $\sigma_{\rm s}$ by Tremaine et al. due to aperture differences. We use gas disk inclinations i inferred for the extended gas and dust distributions under the assumption of thin disks. We assume $i = 60^\circ$ if we cannot obtain a reliable fit.

3 Excess gas dispersion under the assumption of disks

Well-defined extended dust and gas disks are present in 67% of the sample galaxies. Thus the gas might be settled into a thin circular disk all the way to the nucleus in general. However, in the case of NGC 7052 [18], IC 1459 [4,19] and NGC 4335 [20], an excess in dispersion by a factor ~ 2 or more is observed for a thin disk model. For NGC 3245 [1], a smaller excess of $\sim 35\%$ was observed, while in M 87 [10], no dispersion excess was observed.

To determine the presence of excess dispersion for the complete sample, we construct simplified thin disk models (using the method described in [18]) which only take to into account the BH potential and neglect the stellar potential. We estimate (from direct comparison to the four detailed models and additional modeling) that this causes the predicted velocity dispersion to be underestimated by $\sim 10\%$ or less. A fraction of 21/27 galaxies have observed gas dispersions $\sigma_{\rm g}$ in excess of that predicted by a disk model (Fig. 1). For 10/27 galaxies the gas dispersion falls above the 1σ scatter region expected from the intrinsic 0.3dex scatter in the $M_\bullet - \sigma_{\rm s}$ relation [17]. Only one galaxy has a predicted dispersion

Table 1. Early-Type Galaxy Sample Col.(1): radio galaxies are indicated by a *. Col.(3): galaxy distances. Col.(4): stellar velocity dispersions integrated over a kpc-scale central region.

Galaxy	Type	D(Mpc)	σ_s($\mathrm{km\,s^{-1}}$)	Galaxy	Type	D(Mpc)	σ_s($\mathrm{km\,s^{-1}}$)
IC 989	E	101	185	NGC 4459	SO	17	186
IC 1459	E	29	340	NGC 4486*	E	15	375
NGC 315*	E	68	296	NGC 4526	SO	36	264
NGC 383*	E/SO	65	277	NGC 5077	E	36	258
NGC 541*	E/SO	73	212	NGC 5127*	E	64	193
NGC 741*	E	70	290	NGC 5490*	E	69	292
NGC 2329	E/SO	77	242	NGC 6251*	E	99	290
NGC 3078	E	35	251	NGC 6861	E/SO	28	382
NGC 3245	SO	21	205	NGC 7052*	E	55	266
NGC 3862*	E	84	272	NGC 7626*	E	47	272
NGC 3998	SO	14	302	UGC 1841*	E	85	348
NGC 4278	E	16	239	UGC 7115*	E	91	194
NGC 4335*	E	62	282	UGC 12064*	E/SO	68	254
NGC 4374*	E	15	281				

below this region. Intriguingly, there is a trend of increasing ratio of predicted over observed dispersion with decreasing disk inclination (Fig. 1). In fact, the four largest ratios are all in galaxies with gas disk inclinations $i < 40°$, i.e., close to face-on disks. This trend between disk inclination and excess dispersion suggests that a solution to account for the excess gas dispersion must be sought in having a significant vertical velocity dispersion component. We explore this scenario in the next two sections. We discuss in Section 6 caveats of our modeling. and alternative explanations for the excess in gas dispersion.

4 Can a spheroidal gas distribution explain the excess velocity dispersion?

Can the gas dispersions still be explained gravitationally by invoking a more spheroidal gas distribution instead of a thin disk? The answer to this question is not simple. First, gas in a vertically extended distribution (e.g., a spherical one) tends to collapse quickly to a disk due to hydrodynamical forces. Thus, to maintain a spheroidal structure, one would have to assume that the gas is located in individual clouds that move collisionless. The plausibility of this is unclear. Second, one needs to know the phase-space distribution of the clouds to compute the observed velocity dispersion along the line of sight. The phase-space distribution involves a spatial component such as a radial number density profile. We do not know this profile. We only know the flux distribution, which could be quite different. The phase-space distribution also requires knowledge about the nature of the cloud kinematics, for example anisotropies in the velocity dispersion. Also these are unknown.

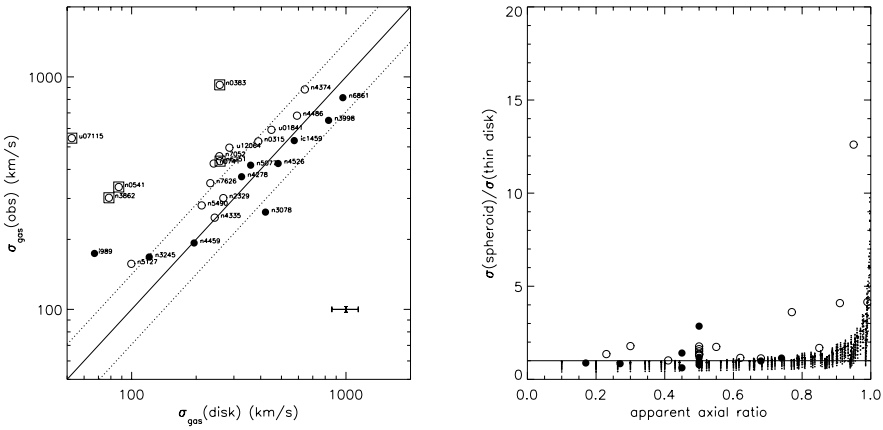

Fig. 1. The observed versus predicted gas velocity dispersion for radio galaxies (open circles) and galaxies without large-scale radio jets (filled circles) assuming thin gas disks. Galaxies with a disk inclination $i < 40^\circ$ are indicated by squares. Radio galaxies, especially those with close to face-on disks, have an excess in observed gas dispersion while the observed dispersions in normal early-type galaxies scatter around the model.

Fig. 2. The ratio R_{σ_g} of the velocity dispersion for a spheroid divided and a thin disk as a function of apparent axis ratio of the gas distribution for models (small dots). Gas disk and spheroid have identical surface density distributions. A range of spheroid axis ratios, densities and dispersion anisotropies are explored at each axis ratio. The ratios R_{σ_g} of the observed velocity dispersions and predicted velocity dispersion for a thin disk are overplotted for non-radio galaxies (filled circles) and radio galaxies (open circles). The former lie systematically above the predictions for all spheroid models. Thus, it seems unlikely that a spheroidal distribution of collisionless gas clouds can account for the observed excess velocity dispersions.

Therefore we explore the line-of-sight velocity dispersion for a plausible range of phase-space distributions. We use axisymmetric dynamical models presented in [3]. We explore gas clouds with an axisymmetric power-law number density distribution ρ with axis ratio q (i.e., $\rho(R,z) = \rho_0[R^2 + z^2/q^2]^{-\gamma/2}$) in the Kepler potential of the BH. The gas clouds are assumed to have a constant dispersion anisotropy $\beta = 1 - (v_\theta^2 + v_\phi^2)/(2v_r^2)$ (i.e., the 'case II' models in [3]; cf. [2]). Thus we have four free parameters: the number density scaling constant ρ_0, axis ratio q, the power-law slope γ of particle density profile and dispersion anisotropy β.

We determine the ratio R_σ of the velocity dispersion of the spheroid and that of a thin disk, which produces the same surface density distribution and apparent axial ratio. This fixes the scaling constant ρ_0 for both spheroid and disk. We calculate R_σ as the line-of-sight dispersion weighted by the number density and integrated over an aperture which is typical for the observations. The following parameter ranges are explored: $\gamma = [-1.5, -10]$, $q = [0.1, 0.9]$, $\beta = [-\inf, 1]$.

Only spheroidal distributions at $q > 0.5$ have an increase in velocity dispersion compared to a thin disk, regardless of the choice of the other model parameters (Fig. 2). This increase is not enough to account for the observed excesses for radio galaxies. Moreoever, various radio galaxies with $q < 0.5$ also show an excess dispersion. The conclusion is that it seems unlikely (but not impossible given the limitations of the modeling), that a spheroidal distribution of collisionless gas clouds at the center of gas disks can account for the excess velocity dispersions.

5 The non-gravitational gas dispersion component

Intriguingly, nine of the ten galaxies with excess dispersion more than 0.3dex from the prediction are radio galaxies while the only galaxy with a dispersion more than 0.3dex below the prediction is not a radio galaxy cf. Fig 1. This trend between excess dispersion and active nucleus together with the trend between excess dispersion and disk inclination suggest the presence of a non-gravitational dispersion component in active nuclei, which is either rather isotropic or perpendicular to the extended disk. Some additional support for a non-gravitational origin is given by the absence of a relation between excess dispersion and BH mass or circular velocity at half-light radius for the radio galaxies. Unfortunately, we do not have a good diagnostic of the kinetic energy output by the active nucleus to more directly test if it can cause the excess gas dispersion. Three indicators of the radiative power of the active nucleus, the extended and core radio luminosity and core emission-line luminosity do not correlate with the excess dispersion.

6 Caveats

Various (potential) caveats may lead to overestimates of the excess dispersion. *Underestimate of BH mass by the $M_\bullet - \sigma_s$ relation.* This would not explain the correlation between excess dispersion and disk inclination. Furthermore, the gas velocity gradients measured near the BH, but outside the region with excess dispersion, would in some cases be inconsistent with larger BH masses. For seven galaxies a $M_\bullet$ estimate is available from detailed analysis of the gas rotation curves. Using these masses instead of the $M_\bullet - \sigma$ relation does not alter our results; there is no systematic difference between the two estimates.

Systematic overestimate of the width of the emission-line flux profiles. The width of the flux profile is sometimes close to the spatial scale of the PSF. Then the unresolved part of the flux is significant and could be arbitrarily close to the BH driving up the dispersion. The flux profiles fore NGC 2329, NGC 3862 and NGC 6251 are very compact and we could consider their excess dispersions as upper-limits. However, the absence of any relation between profile width and distance to the galaxies argues against an overestimate of the profile width.

Difference between disk inclination at nucleus and larger radii. This would cause a trend between extended disk inclination and inferred excess dispersion. However, the ratio between observed and predicted dispersion is above 1 in about 30% of the galaxies even if we would assume that all disks are edge-on.

Weak broad lines. There is tentative indications for a weak broad Hα line in seven of the radio galaxies in our sample [14]. These seven galaxies do not change the overall result obtained together with the 13 other radio galaxies, for which the excess dispersion remains.

7 Discussion

A main conclusion is that an excess in nuclear gas dispersion of non-gravitational origin is present in mainly radio galaxies and absent in other early-type galaxies. This conclusion holds if the nuclear gas resides in a thin disk and likely also if the gas has a more spheroidal distribution. It is especially the dispersions from closer to face-on disks that reveal the excess dispersion. It implies the presence of gas motions out of the plane of the surrounding disk. The correlation of excess dispersion with nuclear activity then suggests that the active BH provides a continuous input of energy. For radio galaxies, there is a good correlation between nuclear emission-line flux and core optical and radio flux (e.g., [5,20]). This might indicate that the emission-lines are powered by photo-ionization, but could indicate that kinetic output of the AGN with jets is deposited into the gas, i.e., outflows and shocks. Finally, we assumed here that the BH masses inferred from the $M_\bullet - \sigma_s$ relation are correct. As pointed out in Section 6 it is unlikely that the $M_\bullet$ are underestimates. Nevertheless, if this would be the case, the ratio of observed over predicted dispersion has a typical value of ~ 2 (Fig. 2). To first approximation this corresponds to a factor ~ 4 higher BH mass.

References

1. Barth, A. J., et al. : ApJ, 555, 685 (2001)
2. Binney, J.: MNRAS, 190, 873 (1980)
3. de Bruijne, J. H. J., van der Marel, R. P., de Zeeuw, P. T.: MNRAS, 282, 909 (1996)
4. Cappellari, M., et al. : ApJ, 578, 787 (2002)
5. Chiaberge, M., Capetti, A., Celotti, A.: A&A, 349, 77 (1999)
6. Ferrarese L.C., Merritt D.: ApJ, 539, L9 (2000)
7. Gebhardt K., et al.: ApJ, 539, L13 (2000)
8. Kormendy, J. & Richstone, D.: ARA&A, 33, 581 (1995)
9. Kormendy J., Gebhardt K.: in The 20th Texas Symposium on Relativistic Astrophysics, eds. H. Martel, J.C. Wheeler: AIP, 363 (2001)
10. Macchetto F.D., Marconi A., et al.: ApJ 489, 579 (1997)
11. Marconi A., Hunt L. K.: ApJ, 589, L21 (2003)
12. Mathur, S., et al. , these proceedings (2004)
13. Merloni, A., these proceedings (2004)
14. Noel-Storr, J., et al. :ApJS, 148, 419 (2003)
15. Sarzi, M., et al.: ApJ, 567, 237 (2002)
16. Soltan, A.: MNRAS, 200, 115 (1982)
17. Tremaine, S., et al.: ApJ, 574, 740 (2002)
18. van der Marel R.P., van den Bosch F.C.: AJ, 116, 2220 (1998)
19. Verdoes Kleijn, G. A., et al. : AJ, 120, 1221 (2000)
20. Verdoes Kleijn G.A., van der Marel R.P., et al.: AJ, 124, 2524 (2002)

Torus Models for Obscuration in Type 2 AGN

T. Beckert[1], W.J. Duschl[2], and B. Vollmer[3]

[1] Max-Planck-Institut für Radioastronomie, Auf dem Hügel 69, 53121 Bonn, Germany
[2] Institut für Theoretische Astrophysik der Universität Heidelberg, Tiergartenstraße 15, 69121 Heidelberg, Germany
[3] CDS, Observatoire astronomique de Strasbourg, UMR 7550, 11 rue de l'université, 67000 Strasbourg, France

Abstract. We discuss a clumpy model of obscuring dusty tori around AGN. Cloud-cloud collisions lead to an effective viscosity and a geometrically thick accretion disk, which has the required properties of a torus. Accretion in the combined gravitational potential of central black hole and stellar cluster generates free energy, which is dissipated in collisions, and maintains the thickness of the torus. A quantitative treatment for the torus in the prototypical Seyfert 2 nucleus of NGC 1068 together with a radiative transfer calculation for NIR re-emission from the torus is presented.

1 Introduction: Dusty tori in the unified model of AGN

Starting with the interpretation of spectropolarimetry of NGC 1068 by Antonucci & Miller [1,2], the difference between type 1 and type 2 AGN is attributed to aspect-angle-dependent obscuration. The central continuum source is thought to be surrounded by a dusty molecular gas distribution, which is flattened by rotation into a torus or thick disk. The simplest unification scheme assumes that all Seyfert 2 nuclei harbor a Seyfert 1 core, so that the ratio of type 1s to 2s measures the thickness of the torus. Present estimates range form 1:4 [3] to 1:1 [4] when selected in the mid–infrared. The torus should therefore have a thickness $H/R \sim 1$.

For more than a decade, clumpy models for the circumnuclear torus have been discussed [5]. It was recognized early on that dust will only survive in distinct clouds, which are embedded in the inter-cloud medium of the geometrically thick torus. This idea was nonetheless not included in the following radiative transfer calculations [6–9] of dust emission from these tori. Only recently, Nenkova et al. [10] developed a scheme which uses the clumpiness of the torus for an approximative and statistical calculation of the thermal IR-emission from clouds, which are individually optically thick $\tau_V > 40$. This approach resolved some of the problems with earlier radiative transfer calculations. The toroidal distribution of atomic and molecular material is also inferred from observed HI absorption and H_2 emission, for example in the nucleus of NGC 4151 [11].

In two papers [12,13] we studied the consequences of the proposed clumpiness. It turns out that a scenario with distinct, quasi-stable clouds, which experience frequent cloud-cloud collisions, is unavoidable for geometrically thick torus. In

ESO Symposia: Growing Black Holes, pp. 242–247, 2005.

this paper we emphasize the importance of cloud collisions and present the results of radiative transfer calculations for the torus in NGC 1068.

2 Dusty clouds in the torus

Cold, molecular and dusty clouds are the basic constituents of an accretion scenario of the torus. In spite of the complexity of their internal physics, we regard them as spherical clouds, which are sufficiently described by their radius $r_{\rm Cl}$ and internal sound speed c_s. The clouds must be self-gravitating to prevent dissolving in the inter cloud medium, which implies that the clouds free-fall time and the sound crossing time are approximately equal. This determines the volume filling factor

$$\phi_V = \frac{32 G \rho_0 r_{\rm Cl}^2}{3\pi c_s^2} \tag{1}$$

of clouds, where $\rho_0 = \phi_V \rho_{\rm Cl}$ is the mean mass density in the torus and $\rho_{\rm Cl}$ the density of individual clouds. The most important parameter of the torus in radiative transfer calculations is the vertical optical depth for intercepting a cloud

$$\tau = \int {\rm d}z \; \tilde{l}_{\rm coll}^{-1} = \xi \frac{H}{l_{\rm coll}} \; , \tag{2}$$

where $l_{\rm coll}$ is the mean free path in the torus midplane ($\tilde{l}_{\rm coll}$ is the local value) and ξ is the coefficient of the linear relation between ρ_0, pressure scale height H, and surface density $\Sigma = \xi \rho_0 H$, which follows from the vertical integration of the density. The radius $r_{\rm Cl}$ of clouds can then be expressed as a function of τ, c_s, and Σ.

The mean free path is likely to be dominated by the largest clouds present. These clouds are more affected by tidal shear than smaller ones, which sets an upper limit to the possible cloud sizes. We expect that clouds accumulate at the shear limit when they experience increasing tidal forces while being accreted to the center. The upper limit is

$$r_{\rm Cl} \leq \frac{\pi}{\sqrt{8}} \frac{c_s}{\Omega} \; . \tag{3}$$

This is also a lower limit to the surface density

$$\Sigma \geq \frac{\tau}{\sqrt{8}} \frac{M(R)}{R^2} \frac{c_s}{v_\phi} \; . \tag{4}$$

Here $M(R)$ is the total enclosed mass in stars and black hole at radius R and v_ϕ is the Keplerian circular velocity at that position. Both mass and optical depth will be dominated by the largest clouds and the right side of (4) will be a good measure of the true surface density. This implies a one to one correspondence between Σ and τ. For the mass of individual clouds

$$M_{\rm Cl} \leq M(R) \frac{\pi^3}{16\sqrt{2}} \frac{c_s^3}{v_\phi^3} \tag{5}$$

we find an upper limit, which is much smaller than the typical mass of molecular clouds in the ISM of normal galaxies. At a radius of 2 pc with an enclosed mass of $10^7\,\mathrm{M}_\odot$ and an internal sound speed against gravitational cloud collapse of $c_s = 2\,\mathrm{km/s}$ gives a largest possible mass of $35\,\mathrm{M}_\odot$. Contrary to the cloud mass we find a lower limit for the hydrogen column density through an individual cloud

$$N_H \geq \frac{M(R)}{\mu m_H} \frac{c_s}{\sqrt{8} R^2 v_\phi} \tag{6}$$

which is about $10^{24}\,\mathrm{cm}^{-2}$ in the environment close to the sublimation radius parameterized above.

For the distribution of clouds in the torus we assume hydrostatic equilibrium for the vertical stratification. In [13] we used a modified isothermal distribution function of cloud velocities in an external potential, which includes a cut-off scale height x_H at which the density drops to zero. This leaves room for a wide polar funnel or an outflow cavity. We consider only cases, where the cut-off height is larger than the pressure scale height H. An example for the case of NGC 1068 is shown in Fig. 1. The radial structure is derived from the stationary accretion scenario described below.

3 Cloud collisions and accretion

The unified model of AGN requires at least $\tau \sim 1$ for obscuration of the AGN for line of sights through the torus. As τ is also a dimensionless collision frequency $\tau \sim \omega_c/\Omega$, this implies that cloud-cloud collisions are frequent in a torus. For anisotropic velocity dispersions of clouds Goldreich & Tremaine [14] derived an effective viscosity

$$\nu = \frac{\tau}{1+\tau^2} \frac{\sigma^2}{\Omega} \tag{7}$$

for angular momentum redistribution[1]. The required anisotropy can be determined self-consistently for thin accretion disks and we use this limit also for the torus.

Because in our scenario clouds in a torus are quasi-stable and only created or destroyed in cloud collisions, the momentum transfer from supernovae and stellar winds is inefficient for maintaining a large velocity dispersion of clouds. Accretion in the gravitational potential due to cloud collisions generate the free energy to balance collisional dissipation.

Like in ordinary accretion disks, the effective viscosity from (7) allows mass to be accreted towards the black hole. The conservation law of angular momentum for the torus clouds with a viscous torque can be integrated once for stationary accretion

$$\nu \Sigma R^3 \frac{\partial \Omega}{\partial r} - \nu_i \Sigma_i R_i^3 \left(\frac{\partial \Omega}{\partial r} \right) \Bigg|_{r=R_i} = -\frac{\dot{M}}{2\pi} R^2 \Omega \left(1 - \frac{\Omega_i}{\Omega} \left(\frac{R_i}{R} \right)^2 \right) . \tag{8}$$

[1] The enhanced viscosity due to collective effects described by Wisdom & Tremaine [15] is unimportant for geometrically thick disks or tori with $\Phi_V \ll 1$.

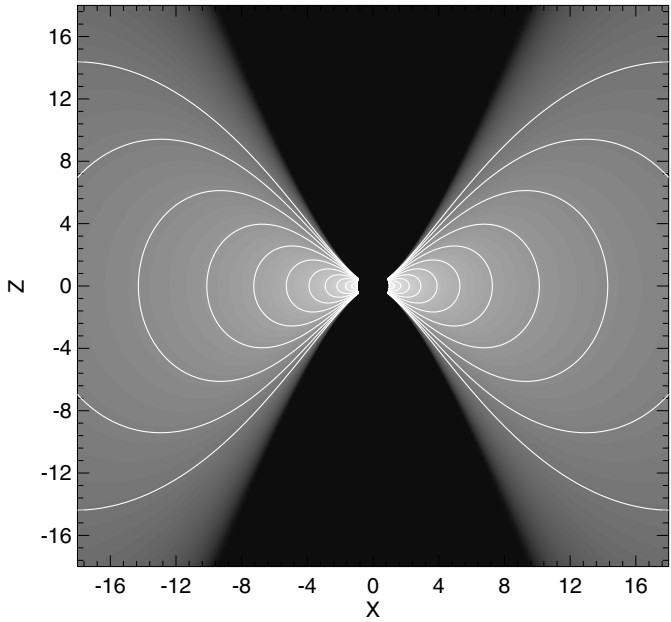

Fig. 1. Meridional cut through the probability density distribution of finding a dusty cloud in the torus. The distribution leaves room for an outflow along the polar axis and is derived from the model of Beckert & Duschl [13]. The spatial scale is in units of the dust sublimation radius. The mean number of clouds along a line of sight to the center drops below 1 for angels larger that 40° from the midplane ($Z = 0$).

Special attention must be paid to the inner boundary at R_i (index i). This boundary will be at the sublimation radius for dust ($R \sim 1\,\mathrm{pc}$), where neither torque nor shear will vanish. In addition the torque at the inner boundary is most likely not well described by the viscosity (7). Here $\dot{M}$ is the total mass accretion rate, which we assume to be constant at all radii throughout the torus. The outer boundary of our model is determined by the feeding process. The mass supply can be either a steady inflow driven by circumnuclear star formation, discrete interactions with GMCs coming from large radii, or an inflow created by bars in the galactic potential.

In cloud-cloud collisions a fraction $\frac{1}{2}(1 - \epsilon^2)$ of the average relative kinetic energy of clouds is dissipated, where ϵ is the coefficient of restitution, which approaches 1 for elastic collisions. We use ϵ to parameterize cloud collisions and ignore the possibly more complex momentum redistribution in actual collisions. The energy dissipation appears as a sink term in the energy balance. For thin accretion disks with $\tau \sim 1$ we find $\epsilon > 0.8$, which is uncomfortably large. Smaller values of ϵ are possible in geometrically thick tori, because energy advection can balance the increased dissipation in collisions. For a given set of parameters

$(\epsilon, \dot{M}, M(R))$ the surprising result is that tori with high accretion rates are geometrically thick $H/R \sim \sqrt{2R\dot{M}/(c_s\, M(R))}$ in spite of the smaller ϵ of collisions. The elasticity, which leads to reasonably thick tori have ϵ in the range 0.2–0.6, which might be provided by magnetic fields in the clouds.

4 The Torus in NGC 1068

For a detailed model of the torus one needs to know the mass distribution in the center. For the case of NGC 1068 we collected the data in [13]. Some of the observed H_2O-maser spots [16] around the radio core component S1 [17] trace a rotating disk or ring. The maser velocities appear inconsistent with Keplerian rotation around a central point mass. The rotation profile can be due to a massive disk [18], but we follow [19] and find a model with a black hole mass of $1.2\,10^7 M_\odot$ and a strongly concentrated stellar cluster with $\rho_\star \propto R^{-\alpha}$ at large radii, a core radius of 0.32 pc and a core density of $\rho_{\star,c} = 5.25\,10^6 M_\odot\,\mathrm{pc}^{-3}$. Core radius and density are comparable to the nuclear stellar cluster in the center of our Galaxy [20]. The observational data from $0.3''$ to $4''$ from the nucleus are consistent with

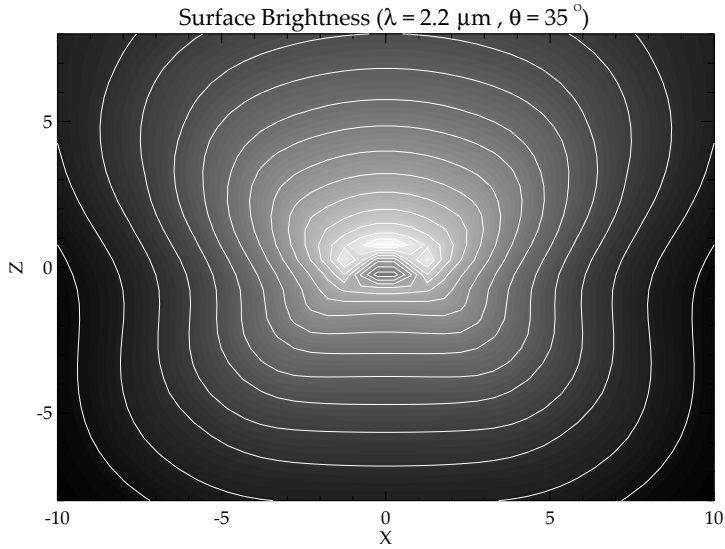

Fig. 2. K-band brightness distribution of our radiative transfer calculations based on the method of Nenkova et al. [10] and the scenario of Beckert & Duschl [13] for an inclination of 35° from the midplane. The spatial scale is in units of the dust sublimation radius. The contour scale of the surface brightness is logarithmic with a dynamic range of 2^{14}.

this mass distribution. The central cluster extends out to 250 pc and the dusty torus lives in the gravitational potential of this cluster.

With the mass distribution, the model for individual clouds, and the cloud density distribution from Fig. 1 we performed radiative transfer calculations based on the method of Nenkova et al. [10]. An example of the surface brightness distribution is shown in Fig. 2. The simulation demonstrate that the observed core component in Speckle images [21] in the NIR indeed measures the size of the sublimation radius to $R = 1 \pm 0.4\,\mathrm{pc}$.

5 Conclusions

We described a dynamical approach to the radial and vertical structure of a clumpy torus around an AGN following the ideas of Krolik & Begelman [5] and Vollmer et al. [12]. The vertical thickness is derived from an accretion scenario for a geometrically thick torus, which is based on cloud-cloud collisions. The inferred mass accretion rates for scale heights $H > 0.5R$ in the torus are larger than the Eddington rate for the central black hole and the model requires massive outflows from within the sublimation radius for dust. It is found that along typical lines of sight to the center (for angles $< 45°$ w.r.t. the torus midplane) between one and ten clouds on average obscure the AGN. Only a small fraction of the mass accreted through the torus eventually reaches the black hole but is sufficient to generate the ionizing luminosity. An in depth analysis of cloud collisions in the environment of an AGN is required to test our model assumptions for ϵ and the structure of individual clouds.

References

1. J. S. Miller, R. R. J. Antonucci: ApJ, **271**, L7 (1983)
2. R. R. J. Antonucci, J. S. Miller: ApJ, **297**, 621 (1985)
3. R. Maiolino, G. H. Rieke: ApJ, **454**, 95 (1995)
4. M. Lacy, L. J. Storrie-Lombardi, A. Sajina et al.: ApJS, **154**, 166 (2004)
5. J. H. Krolik M. C. Begelman: ApJ **329**, 702 (1988)
6. E. A. Pier, J. H. Krolik: ApJ, **401**, 99 (1992)
7. E. A. Pier, J. H. Krolik: ApJ, **418**, 673 (1993)
8. G. L. Granato, L. Danese: MNRAS, **268**, 235 (1994)
9. A. Efstathiou, M. Rowan-Robinson: MNRAS, **273**, 649 (1995)
10. M. Nenkova, Ž. Ivezić, M. Elitzur: ApJ **570**, L9 (2002)
11. C. G. Mundell, J. M. Wrobel, A. Pedlar, J. F. Gallimore: ApJ, **583**, 192 (2003)
12. B. Vollmer, T. Beckert, W. J. Duschl: A&A **413**, 949 (2004)
13. T. Beckert, W. J. Duschl: A&A **426**, 445 (2004)
14. P. Goldreich, S. Tremaine: Icarus, **34**, 227 (1978)
15. J. Wisdom, S. Tremaine: AJ, **95**, 925 (1988)
16. L. J. Greenhill, C. R. Gwinn: Astrophysics and Space Science, **248**, 261 (1997)
17. J. F. Gallimore, S. A. Baum, C. P. O'Dea: ApJ, **613**, 794 (2004)
18. J.-M. Huré: A&A, **395**, L21 (2002)
19. P. Kumar: ApJ, **519**, 599 (1999)
20. R. Schödel, T. Ott, R. Genzel et al.: ApJ, **596**, 1015 (2003)
21. G. Weigelt, M. Wittkowski, Y. Y. Balega et al.: A&A, **425**, 77 (2004)

Growing Stars in AGN Disks

J. Cuadra and S. Nayakshin

MPI für Astrophysik, Karl-Schwarzschild-Str.1, D-85741 Garching, Germany

1 Introduction: Stars in AGN Disks

The outer parts ($> 1000\,R_{\rm S}$) of Active Galactic Nuclei (AGN) disks are expected to become self-gravitating and form stars [6]. Indeed, in our own Galactic Centre a few dozens of young hot stars are confined to two well defined rings of truly nuclear scale ($\sim 0.1\,$pc) [3]. This lends support to theoretical predictions of star formation in accretion disks, but also creates a problem: how do luminous quasars transfer the gas to the super-massive black hole (SMBH) avoiding turning all of this gas into stars [4]? Here we attempt to answer whether the newly born stars can leave the disk midplane, cutting off their further growth by accretion.

2 Mechanisms for Stars–Gas Decoupling

Material falling into the inner regions of galaxies can have fluctuating angular momentum, changing the accretion disk orientation on the viscous time scale. However, we find that the gas forces acting on the stars, friction [1] and gravity, bind the stars and the gas disk together effectively [5]. Baring "catastrophic" events changing abruptly the gas disk orientation, the stars will follow the gas disk turning.

On the other hand, interactions between stars tend to thicken the stellar disk, eventually "relaxing" the system to spherical symmetry. So there is a competition between the scattering and the gas forces. To solve this problem, we performed N-body simulations (using `NEMO` [7]'s `gyrfalcON` [2]) of a disk-like stellar system where we added the gas forces. We find that, only when the surface density of the stellar system is comparable to or larger than the gas disk surface density, do most stars increase their velocity dispersion (Fig. 1a), making the stellar disk thicker with time. In that case, the rate at which stars accrete from the gas disk decreases (Fig. 1b).

3 Conclusions: Growing Stars

Disk plane changes are not fast enough to let stars leave the disk midplane, unless these changes take effect on time scales comparable to the dynamical time. N-body scattering is efficient in making the stellar disk much thicker, but only once most of the gas has already been transformed into stars. Without stellar feedback effects (e.g., supernovae, stellar winds), which were not included here, we find that it is hard to avoid rapid gas accretion onto embedded stars.

ESO Symposia: Growing Black Holes, pp. 248–249, 2005.

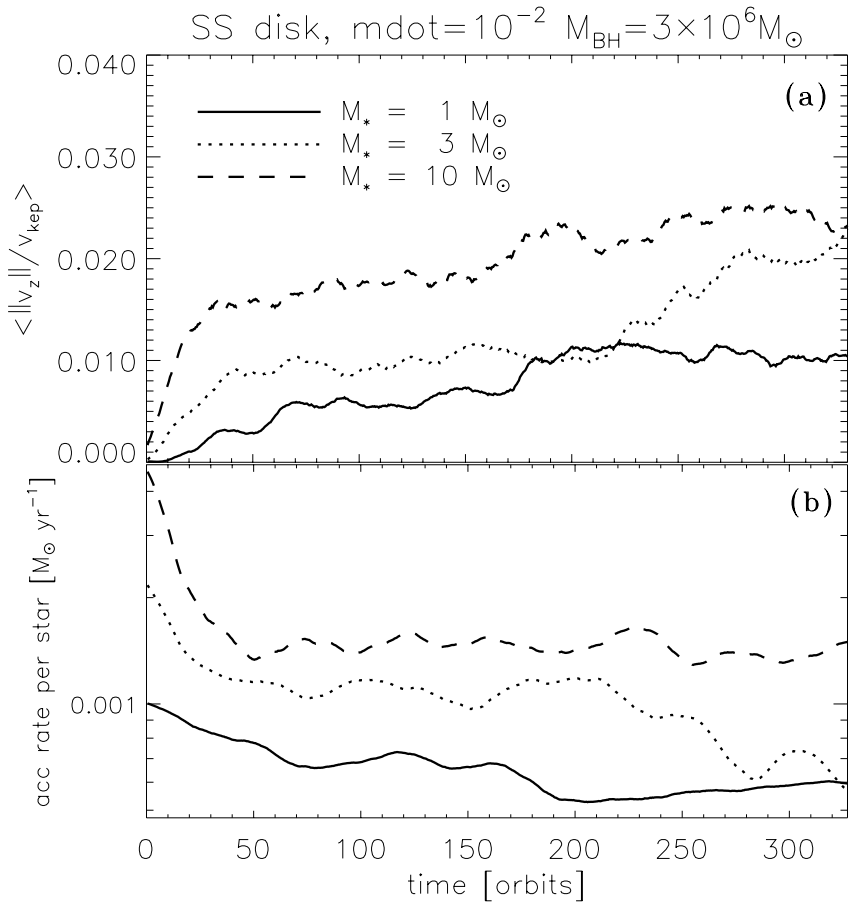

Fig. 1. (**a**) Vertical velocity dispersion as a function of time for stellar systems of different star masses and surface density comparable to the gas disk. Compare with the standard accretion disk $H/R = 0.0025$. (**b**) Average accretion rate per star. Note that while it does decrease as the stars leave the disk, it is still very large

References

1. P. Artymowicz: ApJ **423**, 581 (1994)
2. W. Dehnen: Journal of Computational Physics **179**, 27 (2002)
3. R. Genzel, R. Schödel, T. Ott et al.: ApJ **594**, 812 (2003)
4. S. Nayakshin: MNRAS **352**, 1028 (2004)
5. S. Nayakshin, J. Cuadra: submitted to A&A. (astro-ph/0409541)
6. I. Shlosman, M. C. Begelman, J. Frank: Nature **345**, 679 (1990)
7. P. Teuben: 'The Stellar Dynamics Toolbox NEMO'. In *ASP Conf. Ser. 77: Astronomical Data Analysis Software and Systems IV*, ed. by R. Shaw, H.E. Payne, J.J.E. Hayes (ASP, San Francisco 1995) pp. 398–401

Modelling a Nuclear Star Cluster – Interaction with an Embedded Accretion Disc

L. Šubr[1] and V. Karas[2,1]

[1] Astronomical Institute, Charles University, Prague, Czech Republic
[2] Astronomical Institute, Academy of Sciences, Prague, Czech Republic

Abstract. We explore the structure of a stellar cluster dominated by gravitation of a central mass (a supermassive black hole, BH) and by a dissipative interaction of orbiting stars with an accretion disc. We show that the cluster properties are determined predominantly by the radial profile of the disc characteristics (i.e. surface density, geometrical thickness, viscosity, etc). We develop a simple steady-state model of the cluster structure and we estimate the rate at which stars migrate to the centre.

1 Individual Orbits

Stars are loosing their orbital energy by means of successive dissipative passages through the accretion disc. The overall trend is to circularize orbits and decline them into the plane of the disc. The following combinations of orbital parameters stay roughly constant: $C_1 = a(1-e^2)(1+\cos^2 i)$ and $C_2 = e^2(1+\cos i)^3(1-\cos i)^{-1}$. These can be conveniently employed in the numerical integration of the orbital decay in the phase when collisions are negligible [2].

Different modes of radial migration to the centre are considered for stars that have been dragged into the disc: either a star succeeds to open a gap in the disc medium (then it sinks towards the centre with roughly the same radial velocity as an unperturbed disc), or the star is entirely embedded in the disc medium and the orbital decay proceeds by density waves excitation. The latter mode is typically faster than the former one.

2 The Cluster

We aim to examine the structure of a stellar system in the region of the BH gravitational dominance $R_{\rm h}$, including effects due to gaseous disc. In order to simplify the computations, we distinguish two regions of the cluster which are treated in different ways, according to dominating time-scales. The *outer cluster* is assumed to reach a relaxed form of distribution $f_0(a) \propto a^{1/4}$ derived in [1] and it acts as a reservoir of fresh satellites that are being continuously injected inwards at a rate inversely proportional to the relaxation time $t_{\rm r}$. Stars on orbits with grinding time shorter than $t_{\rm r}$ contribute to the *inner cluster*. Our computational scheme allows us to further distinguish between two subsamples of the inner cluster — the *dragged inner cluster* consists of stars on orbits intersecting periodically the disc, while the *embedded inner cluster* is formed by stars entirely aligned with the disc. Details of the model setup have been described in [5].

ESO Symposia: Growing Black Holes, pp. 250–251, 2005.

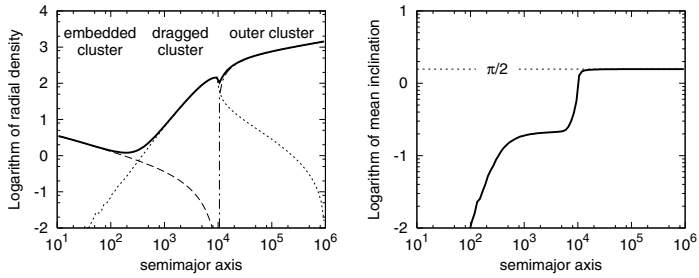

Fig. 1. Left: Semi-major axes distribution; thin lines represent the embedded (*dashed*), dragged (*dotted*) and outer (*dash-dotted*) subsamples. Right: Mean inclination as a function of semi-major axis; indicated value of $\pi/2$ corresponds to isotropic system.

Semi-major axes distribution in the cluster can be approximated by a broken power-law. Its exponent is determined by the dominating mode of the star–disc interaction in the relevant region. Isotropy of the outer cluster is violated in the inner regions where the mean inclination saturates at ≈ 0.2 in the dragged cluster. It drops down to zero in the region where the embedded orbits dominate.

3 Feeding a Black Hole

Another prediction which emerges from our model is related to the forthcoming gravitational waves experiments. The orbits are aligned and circularized at radii of $10^2 \div 10^3 R_\mathrm{g}$, spiraling further on nearly circular orbits towards the centre. This poses certain limits on the expected waveforms from the cluster. The rate of the capture events can be estimated analytically. We find [5]:

$$\dot{M}_\mathrm{s} \approx 10^{-2} M_8^{5/4} \left(\frac{n_0}{10^6\,\mathrm{pc}^{-3}}\right)^2 \left(\frac{M_*}{M_\odot}\right)^2 \left(\frac{R_\mathrm{d}}{10^4 R_\mathrm{g}}\right) M_\odot\,\mathrm{yr}^{-1}\,.$$

The total accretion rate onto the black hole is a sum of $\dot{M}_\mathrm{s}$, which involves stars from the cluster, and the accretion rate $\dot{M}$ of gas in the disc. A more detailed study of relationship of these two rates could lead to a picture of a balanced accretion flow fed by outer stellar cluster, similar to Miralda-Escudé & Kollmeier [3]. Although the above-described model is intended mainly for active galactic nuclei with a relatively dense accretion disc or a dusty torus, the problem of stars crashing on a gaseous disc may be relevant also for the centre of our Galaxy [4].

References

1. J. N. Bahcall, R. A. Wolf: ApJ **209**, 214 (1976)
2. V. Karas, L. Šubr: A&A **376**, 687 (2001)
3. J. Miralda-Escudé, J. A. Kollmeier: astro-ph/0310717 (2003)
4. S. Nayakshin, J. Cuadra, R. Sunyaev: A&A **413**, 173 (2004)
5. L. Šubr, V.Karas, J. M. Huré: MNRAS, accepted; astro-ph/0408053 (2004)

At the Conference Dinner on Thursday

At the Conference Dinner on Thursday

Super-Eddington Black Hole Accretion:
Polish Doughnuts and Slim Disks

M.A. Abramowicz

Nordita, Copenhagen, Denmark

On leave from: Faculty of Natural Sciences, Theoretical Physics, Göteborg University
Address: Chalmers University, S-412-96 Göteborg, Sweden, *marek@fy.chalmers.se*

Abstract. The theory of highly super-Eddington black hole accretion, $\dot{M} \gg \dot{M}_{\rm Edd}$, was developed in the 1980s in Warsaw by Paczyński and his collaborators [1]–[9] in terms of *Polish doughnuts*[1], i.e. low viscosity, rotating accretion flows that are optically thick, radiation pressure supported, cooled by advection, and radiatively very inefficient. Polish doughnuts resemble fat tori with two narrow funnels along rotation axis. The funnels collimate radiation into beams with highly super-Eddington luminosities. *Slim disks*[1] introduced later by Abramowicz, Lasota and collaborators first in [10], and more fully in [11] have only moderately super-Eddington accretion rates, $\dot{M} \geq \dot{M}_{\rm Edd}$, rather disk-like shapes, and almost thermal spectra [12]-[14].

1 Introduction

Is there an upper limit to the accretion rate $\dot{M}$, preventing astrophysical black holes to swallow all the matter infalling into them? Many astrophysicists are convinced that the answer to this fundamental question should be: *yes, the limit exist and it is given by the standard Eddington accretion rate*,

$$\dot{M}_{\rm Edd} = \frac{L_{\rm Edd}}{c^2} = 1.5 \times 10^{17} \left(\frac{M}{M_\odot}\right) [\,{\rm g\ sec}^{-1}]. \tag{1}$$

However, because there is a clear observational evidence for super-Eddington luminosities, e.g. from X-ray binaries (SS433, GRS 1915+105), and because super-Eddington luminosities powered by accretion imply highly super-Eddington accretion rates, this almost unanimous consensus[2] is to me rather befuddling.

I review here fundamental theoretical predictions about super-Eddington accretion: (1) super-Eddington luminosities are typical for rotating, radiation pressure supported black hole accretion flows, (2) these flows have very small efficiency and therefore they must have highly super-Eddington accretion rates, (3) super-Eddington accretion does not necessarily imply strong outflows.

These predictions are solidly based on standard physics, and it should not be surprising that recent 3D hydro and MHD supercomputer simulations provide many beautiful illustrations for them [15]-[18].

[1] The name *Polish doughnuts* was coined by M.Rees, and *slim disks* by A.Kołakowska.

[2] All works on cosmic structure formation reported at this Conference, used $\dot{M}_{\rm Edd}$ as the upper limit for the black hole growth rate.

ESO Symposia: Growing Black Holes, pp. 257–273, 2005.

1.1 Sub-Eddington accretion: standard thin disks and adafs

The sub-Eddington accretion is far more familiar to astrophysicists. Well known theory predicts for $\dot{M} \ll \dot{M}_{\rm Edd}$ two types of stable accretion, depending on the optical depth, τ.

When $\tau \gg 1$, accretion is described in terms of the famous *standard thin disk* model by Shakura & Sunyaev [19]. Standard thin disks are supported by gas pressure, cooled by radiation, and very efficient. They are geometrically thin in the vertical direction, $H/R \ll 1$.

When $\tau \ll 1$, accretion is described by the *adaf*[3] model, propheted in 1977 by Ichimaru in a paper [20] that was ignored by everybody for twenty years[4]. Only after their rediscovery in the mid 1990 by Narayan[5] & Yi [22], [23], and by Abramowicz, Chen, Kato, Lasota & Regev [24], adafs started to be intensely studied by many authors (see reviews in [25], [26]). Adafs are cooled by advection. They are very inefficient, geometrically thick, $H/R \sim 1$, and very hot (close to the virial temperature). Because of their very low efficiency, they are much less luminous than the standard thin disks.

2 Fundamental limits for power: Planck and Eddington

The Planck power (i.e. power expressed in Planck's units) equals

$$L_{\rm Planck} = \frac{c^5}{G} \approx 10^{58}\ [{\rm erg\,sec}^{-1}] = 10^{52}\ [{\rm Watts}]. \tag{2}$$

Rather surprisingly, it does not depend on the Planck constant h. The maximal energy available from an object with the mass M (and gravitational radius $R_{\rm G} = GM/c^2$) is $E_{\rm max} = Mc^2$. The minimal time in which this energy may be liberated is $t_{\rm min} = R_{\rm G}/c$. Thus, the maximal power $L_{\rm max} = E_{\rm max}/t_{\rm min} = c^5/G = L_{\rm Planck}$. This is the absolute upper limit for power of anything in the Universe: all objects, phenomena, explosions, and evil empires[6].

For example, a sphere with radius R containing blackbody radiation at temperature T radiates power $L \sim (caT^4)R^2$. The gravitational mass of the radiation inside the sphere is $M \sim (aT^4/c^2)R^3$, where $a = 8\pi^5 k^4/15c^3h^3$ is the radiation constant. Thus $R_{\rm G} \sim (aT^4G/c^4)R^3$, and from $R_{\rm G} < R$ one gets $L < c^5/G$.

Consider a stationary object with mass M in which gravity and radiation are in equilibrium. Sikora [27] noticed that the upper limit for the object radiative power may be expressed by $L_{\rm Edd} = L_{\rm Planck}\Sigma_{\rm grav}/\Sigma_{\rm rad}$. Here $\Sigma_{\rm grav}$ is the object

[3] The name *adaf* was coined by J.-P.Lasota.

[4] However, many elements of the adafs theory were present in the influential "ion tori" paper by Rees, Phinney, Begelman & Blandford [21].

[5] R.Narayan did more than anybody else to develop the adaf idea into a useful and mature astrophysical theory.

[6] A power needed for the Creation was the rate at which the Big Bang transferred energy from a pre-Planck to the post-Planck state. For the reason outlined here, no more than 10^{52} Watts was needed to create the Universe.

total effective gravity cross section, and $\Sigma_{\rm rad}$ is its total radiative cross section. Sikora's expression is the most general version of the Eddington limit. Eddington himself, first in [28], and then in [29]-[32], considered a much more specific case of a radiation pressure supported star[7], assuming that radiation interacts with matter by electron scattering (thus $\Sigma_{\rm rad} = N\sigma_T$ in Sikora's expression), and that effective gravity is provided by the Newton gravity alone (thus $\Sigma_{\rm grav} = 4\pi R_G^2$). Here N is the number of electrons in the object ($N = M/m_{\rm P}$ for pure hydrogen, $m_{\rm P}$ is the proton mass), $\sigma_T = 8\pi e^4/3m_{\rm e}^2c^2$ is the Thomson cross section (e is the electron charge and $m_{\rm e}$ its mass). In this specific case, Sikora's elegant argument immediately gives the standard formula for the Eddington limit,

$$L_{\rm Edd} = L_{\rm Planck}\frac{\Sigma_{\rm grav}}{\Sigma_{\rm rad}} = \frac{4\pi GMm_{\rm P}c}{\sigma_{\rm T}} = 1.4\times 10^{38}\left(\frac{M}{M_\odot}\right)[\,{\rm erg\ sec^{-1}}]\,. \qquad (3)$$

The Eddington limit for a spherical, non-rotating, homogenous object was discussed from a modern perspective by Joss, Salpeter & Ostriker [42]. In addition to the discussion given there, let us note that, obviously, the limit for radiative power may increase above the standard Eddington limit, in objects with a gravitational cross section greater than the standard one, or with a radiative cross section smaller than the standard one[8],

$$\Sigma^*_{\rm grav} > \Sigma_{\rm grav} \equiv 4\pi R_G^2, \quad \Sigma^*_{\rm rad} < \Sigma_{\rm rad} \equiv \frac{M}{m_{\rm P}}\,\sigma_T\,. \qquad (4)$$

[7] In 1913, shortly before the war, Białobrzeski [33] pointed out that radiation pressure may be important in stellar equilibria (see also [34]-[36]). Eddington independently discovered the same three years later [28], already during the war. Eddington, as a Quaker, avoided an active war service and was able to continue his research during the war years 1914-1918 at Cambridge, as the Director of the Observatory there. Only after the war ended, the two scientists could communicate, and Eddington wrote to Białobrzeski: *I congratulate you on having been apparently the first to point out the large share of radiation pressure in internal equilibrium of stars* (quotation after [37]). Białobrzeski's contribution (and priority) was remembered by astronomers still in the 1930s, (see the 1936 monograph by Tiercy [38] and the 1939 book by Chandrasekhar [39]), but today is almost totally forgotten — Chandrasekhar [40] makes no mention of it in his 1983 book on Eddington. (A.K. Wróblewski [41] provided most of historical information for this footnote.)

[8] In no circumstances $L_{\rm Edd}$ can grow above $L_{\rm Planck}$. I noticed [43] that the two limits are equal when $M \approx N_0 m_{\rm P}$, with $N_0 = N^2_{\rm Dirac}/3$, where the Dirac number $N_{\rm Dirac} = e^2/Gm_{\rm e}m_{\rm P}$ equals the ratio of Coulomb's to Newton's force between electron and proton. Then $N_0 \approx N_{\rm Edd} \equiv 136\times 2^{256} \approx 1.6\times 10^{79}$, where $N_{\rm Edd}$ is the Eddington number that played an important role in Eddington's *Fundamental Theory* [44]. The number was introduced by Eddington's immortal statement, *I believe there are 15 747 724 136 275 002 577 605 653 961 181 555 468 044 717 914 527 116 709 366 231 425 076 185 631 031 296 protons in the universe and the same number of electrons.* One thus may write, $L_{\rm Edd} = (N/N_{\rm Edd})\,L_{\rm Planck}$. A very Eddingtonish connection indeed, embracing his luminosity and his number, of which he was not aware.

Several types of astrophysical sources give a clear observational evidence for super-Eddington luminosities. I will mention here only two specific types that provide examples for the two possibilities listed in (4).

Novae outbursts. They are due not to accretion but to thermonuclear power [45]. Luminosity increases within a few hours by factors of 10^4, and stay for a very long duration at a clearly super-Eddington level, $L > 10\,L_{\rm Edd}$. Shaviv [45], [46] shows that the observed increase of the radiative power over the Eddington limit, may be attributed to $\Sigma^*_{\rm rad} < \Sigma_{\rm rad}$, because in a locally inhomogeneous medium, the ratio of averaged radiation force to emitted flux, $F_{\rm rad}/f_{\rm rad} \equiv \sigma^*_{\rm rad}/c < \sigma_T/c$.

X-ray binaries. Some of them show super-Eddington luminosities, powered, most likely, by super-Eddington accretion: in high-mass binaries undergoing a thermal-time-scale mass transfer, e.g. in SS433, [47], and in the low-mass binaries during long-lasting transient outbursts, e.g. in GRS 1915+105, [48].

The rest of my review is devoted to the discussion of a possibility that the reason for super-Eddington luminosities in the X-ray binaries and similar objects may be the fast differential rotation of accretion disks present in these sources. It strengthens the effective gravity, so that $\Sigma^*_{\rm grav} > 4\pi R_G^2$.

3 Eddington limit for rotating bodies

I now consider the Eddington limit for a perfect-fluid rotating body in equilibrium, following the line of arguments first presented by Abramowicz, Calvani & Nobili [6]. Having in mind most general astrophysical applications, I will consider two topologically different cases:

Rotating stars. The surface of the star has a topology of the sphere. The whole mass M is included in the sphere.

Accretion disks. The surface of the disk has a topology of the torus. The mass of the disk $M_{\rm disk}$ is contained in the torus, but the mass $M_{\rm centr}$ of the central black hole is outside. The total mass $M = M_{\rm centr} + M_{\rm disk} \approx M_{\rm centr}$, because $M_{\rm centr} \gg M_{\rm disk}$. In accretion disk theory it is customary to neglect the mass of the disk, so formally $M = M_{\rm centr}$, and $M_{\rm disk} = 0$. The Eddington limit always refers to the total mass M.

Let $\mathbf{f}_{\rm rad}$ be the local flux of radiation somewhere at the surface of the body, S. The corresponding radiative force is $\mathbf{F}_{\rm rad} = (\sigma_{\rm rad}/c)\mathbf{f}_{\rm rad}$. Let $\mathbf{F}_{\rm eff} = \mathbf{F}_{\rm grav} + \mathbf{F}_{\rm rot}$, be the effective gravity force, with $\mathbf{F}_{\rm grav} = m\boldsymbol{\nabla}\Phi$ being the gravitational force (Φ is the gravitational potential), and with $\mathbf{F}_{\rm rot} = m(\Omega^2 r)\,\mathbf{e}_{\rm r}$ being the centrifugal force (Ω is the angular velocity, r is the distance from the axis of rotation, and $\mathbf{e}_{\rm r} = \boldsymbol{\nabla} r$ a unit vector showing the off-axis direction).

The necessary condition for equilibrium is $\mathbf{F}_{\rm rad} < \mathbf{F}_{\rm eff}$. From this one deduces the Eddington limit for rotating perfect-fluid bodies,

$$L = \int_{\rm S} \mathbf{f}_{\rm rad} \cdot d\mathbf{S} = \frac{c}{\sigma_{\rm rad}} \int_{\rm S} \mathbf{F}_{\rm rad} \cdot d\mathbf{S} \; < \; \frac{c}{\sigma_{\rm rad}} \int_{\rm S} \mathbf{F}_{\rm eff} \cdot d\mathbf{S} \equiv L^{\rm rot}_{\rm Edd} \qquad (5)$$

Using the Gauss theorem to transform the surface integral of $\mathbf{F}_{\rm eff}$ into a volume integral of $\boldsymbol{\nabla} \cdot \mathbf{F}_{\rm eff}$, Poisson equation $\boldsymbol{\nabla}^2\Phi = 4\pi G\rho$, and introducing the specific angular momentum $\ell = \Omega r^2$, one gets after twenty or so lines of simple algebra,

$$L_{\rm Edd}^{\rm rot} = L_{\rm Edd}\left[\, X^2_{\rm mass} + X^2_{\rm shear} - X^2_{\rm vorticity}\,\right], \tag{6}$$

where the dimensionless number $X^2_{\rm mass}$ depends on whether the body is a star, or an accretion disk,

$$X^2_{\rm mass} = \frac{1}{M}\int_{\rm V} \rho dV = \begin{cases} 1 & \text{for stars,} \\ \\ 0 & \text{for accretion disks,} \end{cases} \tag{7}$$

and where $X^2_{\rm shear}$, $X^2_{\rm vorticity}$ are dimensionless, necessarily positive quantities, representing shear and vorticity integrated over the whole volume of the body,

$$X^2_{\rm shear} = \frac{1}{16\pi GM}\int_{\rm V} r^2(\boldsymbol{\nabla}\Omega\cdot\boldsymbol{\nabla}\Omega)\,dV, \tag{8}$$

$$X^2_{\rm vorticity} = \frac{1}{16\pi GM}\int_{\rm V} r^{-2}(\boldsymbol{\nabla}\ell\cdot\boldsymbol{\nabla}\ell)\,dV. \tag{9}$$

Shear increases the Eddington limit, and vorticity decreases it.

The rotation of astrophysical objects is far from simple, but an insight could be gained by considering a simple power law for the angular momentum distribution, $\ell(r,z) = \ell_0 r^a$, with ℓ_0 and a constant. Rigid rotation has $a = 2$, Keplerian rotation $a = 1/2$, and constant angular momentum rotation $a = 0$. It is $X^2_{\rm shear}/X^2_{\rm vorticity} = (a-3)^2/a^2$. This means that $X^2_{\rm shear} > X^2_{\rm vorticity}$ when $a < 3/2$.

Rotating stars have $X^2_{\rm shear} < X^2_{\rm vorticity}$, because they rotate almost rigidly. Thus, for rotating, radiation pressure supported stars, $L \approx L^{\rm rot}_{\rm Edd} < L_{\rm Edd}$ *always*. Contrary to this, constant angular momentum tori are dominated by shear, $X^2_{\rm shear} \gg 1 \gg X^2_{\rm vorticity}$ and consequently, when they are radiation pressure supported, $L \approx L^{\rm rot}_{\rm Edd} \gg L_{\rm Edd}$.

4 Polish doughnuts

For a simplicity of presentation, let me assume that $\ell = \ell_0 = {\rm const}$, i.e. that the angular momentum is constant in the whole body. One does not know a priori what is the actual distribution of the angular momentum inside the body, as this depends on the nature of viscosity. Paczyński explained why a physically realistic distribution of angular momentum must indeed be close to $\ell = {\rm const}$ in the inner part of the flow, and why most likely it approaches the Keplerian distribution, $\ell(r,z) = \ell_K(r) \equiv (GMr)^{1/2}$ far away from the center.

Adopting Paczyński's argument, one may assume that the local physical properties of the innermost part of black hole accretion flows are rather well described by the model with $\ell = {\rm const}$, but one must be careful with the physical interpretation of the $\ell = {\rm const}$ assumption at large radii. I will return to this point later in this section.

Assuming constant angular momentum, and using Newton's expression for gravitational potential $\Phi = -GM/(r^2+z^2)^{1/2}$ in cylindrical coordinates $[\,r,z,\phi\,]$,

I deduce the shape of equipressure surfaces $P = \text{const}$ from the Bernoulli equation,

$$-\frac{GM}{(r^2+z^2)^{\frac{1}{2}}} + \frac{1}{2}\frac{\ell^2}{r^2} + W(P) = \text{const.} \tag{10}$$

Here $W(P) = -\int dP/\rho$. This equation cannot be obeyed at the rotation axis (where $z \neq 0$, $r = 0$), which has an obvious, but important, consequence: no equipressure surface cross the axis. For a constant angular momentum fluid, equipressure surfaces must be toroidal, or open. The marginally open surface has just one point ($r = \infty, z = 0$) at infinity. This particular surface encloses the *largest possible* torus. From (10) it is obvious, that in this case $W(P) = W(0) = 0$.

Maximal pressure locates at a circle $z = 0, r = r_0 = GM/\ell_0^2$. Using the radius r_0 as a scale, $\xi = r/r_0$, $\eta = z/r_0$, $w = W/(GM/r_0)$, one may write equation (10) in the dimensionless form, and solve for $\eta = \eta(\xi; w)$ to obtain the explicit form of all equipressure surfaces,

$$\eta^2 = Q^2(\xi) \equiv 4\xi^4 \left(1 - 2\xi^2 w\right)^{-2} - \xi^2, \quad -1/2 \leq w \leq w_S. \tag{11}$$

The value $w = -1/2$ gives the location of the center, and $w = w_S \leq 0$ the location of the surface. For the *slender torus* $w_S \approx -1/2$, and the *fat torus* $w_S \approx 0$.

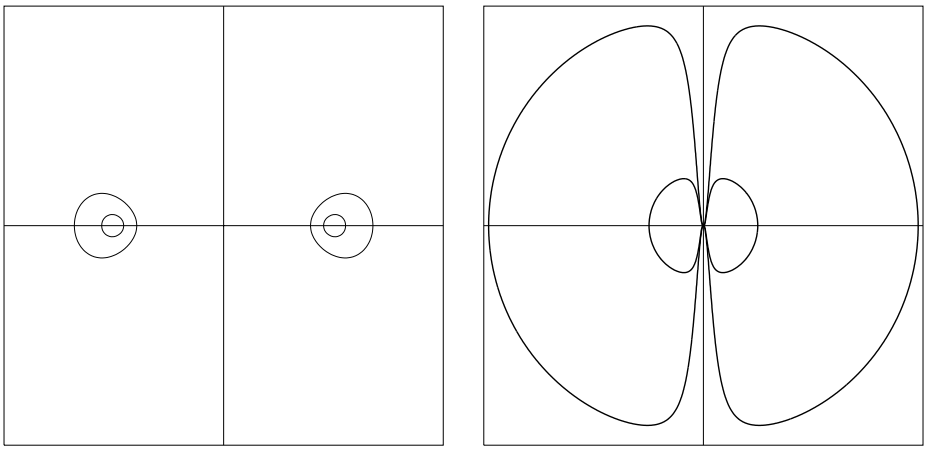

Fig. 1. Contours of equipotential surfaces on the meridional cross section of a constant angular momentum torus. *Left*: a slender torus, $w_S \approx -1/2$. The contours approach circles around the locus of the maximum pressure, at $\xi = 1$. *Right*: a fat torus $w_s \approx 0$. The contours tend to concentric circles with the center at $\xi = 0$. Close to axis they change into a pair of conical funnels.

4.1 The slender torus

One may introduce toroidal coordinates centered at the circle of the maximal pressure by a coordinate transformation, $x = [\eta^2 + \xi_*^2]^{1/2}$, $\alpha = \tan^{-1}(\eta/\xi_*)$. Here $\xi_* \equiv 1 - \xi$. It is then not difficult to show that in the slender torus limit, i.e. when $w + 1/2 = \epsilon \ll 1$, it is $w = w(x) + \mathcal{O}^2(\epsilon)$. This means that at the meridional section of the torus, equipressure surfaces are concentric circles, as first noticed by Paczyński [49]. This additional symmetry was used by Blaes [50] to obtain a general analytic solution for all possible slender torus oscillation modes. In particular, Blaes demonstrated that there exists a set of non-axisymmetric (i.e. with $m \neq 0$) global modes $\delta X_{mn} = F_{mn}(x, \alpha) \exp(-i\omega_{mn} t + m\phi)$ of the slender torus oscillations, with the eigenfrequencies,

$$\omega_{mn} = -m\Omega_K \left[1 + i\epsilon \left(\frac{3}{2n+2} \right)^{\frac{1}{2}} \right] + \mathcal{O}^2(\epsilon), \quad n = 1, 2, 3, ... \tag{12}$$

Because $\Im(\omega_{mn}) < 0$ these oscillations are unstable. The growth rate of the instability is $\sim m\Omega_K$. Here Ω_K is the Keplerian frequency at the torus center, and thus the instability is a *dynamical* one. Indeed, this is the famous instability, discovered in the seminal papers by Papaloizou and Pringle [51], [52].

4.2 The fat torus

It is easy to understand shapes of equipotential surfaces in a fat torus (shown in Figure 1). Very far from the axis of rotation one has $|2w\xi| \gg 1$. Inserting this into (11) one gets $\eta^2 + \xi^2 = 1/w^2$ which means that far from the rotation axis the equipotential surfaces are spheres with radius $1/|w|$, and that the outer radius of the torus is at $r_{\rm out} = r_0/|w_S|$. Spherical equipotentials are in accord with the fact that very far from the axis, $\xi \gg 1$, the centrifugal force $\sim \ell_0/\xi^3$ is negligible with respect to the gravitational force $\sim GM/\xi^2$. Therefore, the effective gravity is determined by Newton's attraction alone, as for spherical stars. For the same reason, the radiation power from this part of the surface of a fat, radiation pressure supported torus (i.e. Polish doughnut) is *one Eddington luminosity*, the same as from a spherical non-rotating, radiation pressure supported star[9].

Note, however, that the asymptotically spherical shape of a fat torus is a direct consequence of the assumption $\ell(r, z) = \text{const}$, which was made ad hoc. If

[9] M. Rees [53] told me in 1980 that this implied that Polish doughnuts, with at least one Eddington luminosity from whatever direction, were obviously too luminous to describe very "dim" active galactic nuclei, such as radio galaxies: "while apparently supplying tremendous power to their extended radio-emitting regions, the nuclei of most radio galaxies emit little detectable radiation." He and his collaborators at Cambridge found later a possible solution to this puzzle in terms of the *ion pressure supported tori* [21]. The ion tori have the same shapes as the Polish doughnuts, in particular funnels, but much lower, indeed very sub-Eddington, luminosities. The power in jets comes from tapping rotational energy of the central black hole by the Blandford-Znajek mechanism [54].

one adopts a more physically realistic assumption that asymptotically $\ell(r,z) = \ell_K$, one may use the standard Shakura-Sunyaev model in its radiation pressure version, to get the asymptotic shape of the fat torus,

$$z_\infty = \frac{3\sigma_T}{8\pi c m_p}\dot{M}. \tag{13}$$

Closer to the axis, $|2w\xi| \sim 1$, which means that $\xi^2 \sim -1/2w$ and this together with (11) gives $\eta^2/\xi^2 = (1/|w|) - 1 = (1/\sin^2\theta) - 1$, i.e. that closer to the axis, equipotential surfaces corresponding to $w \sim w_S \sim 0$ have conical shapes with the half opening $\theta \sim \sqrt{w}$. The surfaces are highly non spherical because centrifugal force dominates. Integrating effective gravity along the conical funnel is elementary, and one gets [3] that $L^{\rm rot}_{\rm Edd}/L_{\rm Edd} = (1/2)\ln(1/|w_S|)$. This estimate may be used to find the total luminosity for the radiation pressure supported fat torus. i.e. a Polish doughnut,

$$\frac{L_{\rm total}}{L_{\rm Edd}} \approx \frac{L^{\rm rot}_{\rm Edd}}{L_{\rm Edd}} \approx \frac{1}{2}\ln\left(\frac{r_{\rm out}}{r_0}\right) = 1.15\,\log\left(\frac{r_{\rm out}}{r_0}\right). \tag{14}$$

It should be clear from our derivation, that the logarithmic scaling of the luminosity with the torus size is a genuine property of the Polish doughnuts, including those that have a non-constant angular momentum distribution. The logarithm in (14) is of a crucial importance, as it prevents astrophysically realistic doughnuts (i.e. with $r_{\rm out}/r_0 < 10^6$, say) to have highly super-Eddington luminosities. Thus, the theory predicts that for such "realistic" fat tori, only a slightly super-Eddington total (isotropic) luminosities, $L_{\rm total} \geq 7\,L_{\rm Edd}$, may be expected.

However, because the funnels have solid angles $\theta^2 \sim r_0/r_{\rm out}$, radiation in the funnels may be, in principle, collimated to highly super-Eddington values $L_{\rm coll}/L_{\rm Edd} = \Theta \sim r_{\rm out}/r_0 \gg 1$. This simple estimate agrees with a more detailed modelling of the Polish doughnuts radiation field by Sikora [55] and Madau [56] who obtained $\Theta \leq 10^2$ for disks with $r_{\rm out}/r_0 \sim 10^2$. A typical value that follows from observational estimates for non-blazar active galactic nuclei, e.g. by Czerny and Elvis [57] and Malkan [58], is $\Theta \sim 10$, but of course for blazars and other similar sources (e.g. for ULXs, if they are powered by stellar mass black holes, as argued by King [59]), it must be $\Theta \gg 10$.

Such high values of Θ are also consistent with the idea, suggested by Paczyński [60] and independently by Lynden-Bell [61], that relativistic electron-positron e^-e^+ jets may be very effectively accelerated by the radiation pressure in the fat tori funnels[10]. Note, that if the flux in the funnel is Θ times the Eddington flux, the e^-e^+ plasma feels the "effective" radiative force corresponding to the Eddington ratio $m_p/m_e \approx 10^3$ times greater[11]. Detailed calculations (e.g. [62], [55], [63]) demonstrated that indeed the e^-e^+ jets may be accelerated in funnels

[10] Lynden-Bell called this an "entropy fountain".

[11] Note that in Shaviv's explanation of the situation during nova outburst, the luminosity is *physically* very close to the Eddington one (in the sense of Sikora's definition), although its value is greater than the standard Eddington limit. For the e^-e^+ jets

up to the Lorentz factor $\gamma \leq 5$. However, if jets are initially pre-accelerated by some black-hole electrodynamical processes (such as the Blandford-Znajek mechanism [54]) to highly relativistic velocities $\gamma > 10^6$, they will be decelerated in the funnels by the Compton drag, reaching the asymptotic Lorentz factor [64],

$$\gamma_\infty = \left(\Theta \frac{m_p}{m_e} \right)^{\frac{1}{3}} = 10\, \Theta^{\frac{1}{3}}. \tag{15}$$

Observations tell that $\gamma_\infty < 10^2$, and thus equation (15) suggests that $\Theta < 10^3$.

4.3 Rise and Fall of the Polish Doughnuts

In the time of their début, Polish doughnuts could theoretically confirm the observed super-Eddington luminosities, highly collimated beams of radiation, and perhaps even the relativistic speeds of jets, fulfilling another principle attributed to Eddington [65]: *one should never believe any experiment until it has been confirmed by theory.* These virtues attracted initially some interest of the astrophysical community, but the interest has quickly drained with the discovery of the Papaloizou-Pringle instability. It was thought that Polish doughnuts must necessarily suffer from the instability and thus, in reality, they cannot exist. The important discovery by Blaes [66] that the Roche lobe overflow stabilizes Polish doughnuts against the Papaloizou-Pringle instability, came too late — in the advent of numerical simulations of black hole accretion flows. Too late, because numerical simulations rediscovered and absorbed many of the Polish doughnuts results. Today, these results exist in the consciousness of many astrophysicists as a set of several numerically established, important but unrelated facts. They do not form a consistent scheme that the Polish doughnuts once offered: clear, simple, following directly from the black hole physics[12].

In the rest of my review, I recall the most fundamental of these results, almost totally forgotten today: the relativistic Roche lobe overflow mechanism. The mechanism not only stabilizes Polish doughnuts against the Papaloizou-Pringle and other instabilities. It also assures that highly super-Eddington accretion rates always imply a very low efficiency of accretion[13].

---

the situation is very much different (opposite): the luminosity is *physically* very super-Eddington, although it may be just slightly above the standard limit.

[12] There are at least three brilliant and very pedagogical expositions of the Polish doughnuts scheme: two by Paczyński himself, [67], [68], and one in the text book by Frank, King and Raine [69].

[13] Sołtan's well known argument [70] shows that *on average* the AGN efficiency cannot be small. The argument does not exclude a possibility of a flip-flop sequence of periods of low and high efficiency, rather like in [71] for thin disks. Although the possibility of a flip-flop behavior with timescale $\sim 10^4$ yrs (for AGN) has some observational back-up [72], it was never studied sufficiently deeply.

5 Efficiency of black hole accretion

I like to illustrate the physical meaning of accretion disk efficiency in terms of the Bekenstein engine[14]. Bekenstein [74] discussed a black hole engine that converts mass to energy with a perfect efficiency, following an earlier unpublished remark by Geroch [75]. The engine works by slowly lowering on a strong wire a mass m into a black hole with the Schwarzschild radius $R_S = 2\,R_G = 2GM/c^2$ and mass M.

As the mass is lowered to a radius R, the energy $E(R)$ measured at infinity is gravitationally redshifted and thus goes down relative to the initial energy $E_0 = mc^2$. The change in energy equals to the mechanical work done by the wire back at the engine. The efficiency $e \equiv [E_0 - E(R)]/E_0$ may be calculated from the gravitational redshift formula, $e = 1-(1-R_S/R)^{1/2}$. If the mass could be lowered to the horizon $R \to R_S$, the efficiency would go to 1. Of course, the mass cannot touch the horizon, because the tension in the wire would be then infinite, and even the strongest wire would break. Real wires, that may sustain only a finite tension (see e.g. Gibbons [76]), would break a finite distance $R = R_{in}$ from the horizon. In a region below the breaking radius, $R < R_{\rm in}$, the mass falls down freely, keeping its energy measured at infinity unchanged. Therefore, the efficiency is determined by the radius $R = R_{\rm in}$ at which the wire breaks, $e \equiv [E_0 - E(R_{\rm in})]/E_0$.

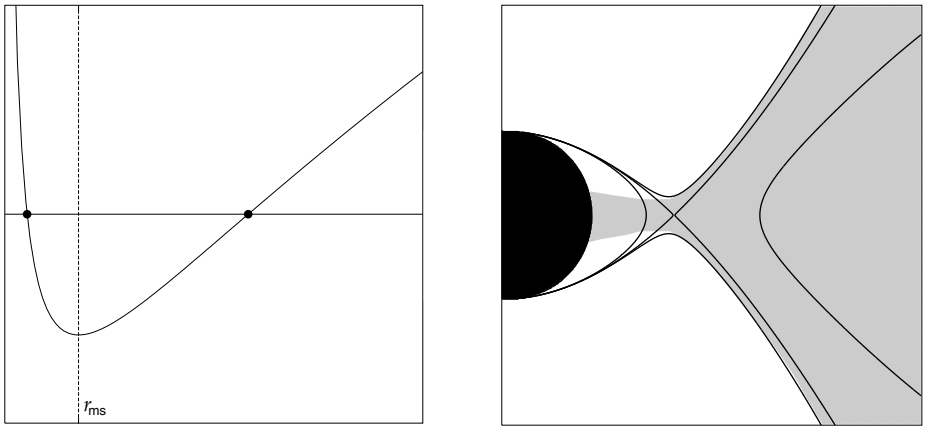

Fig. 2. Left Figure shows that angular momentum in the fat torus crosses twice the Keplerian angular momentum. Right Figure, shows schematically that if the the doughnut slightly overflows the Roche lobe, a dynamical mass loss will occur.

With centrifugal support playing a role of the rope, accretion's efficiency is also determined by the radius $R = R_{\rm in}$ at which the centrifugal support breaks.

[14] Here I borrow a short description of the engine given in [73].

Consider a collection of free particles on Keplerian circular orbits around a black hole. Small viscosity will slowly remove angular momentum, so particles will slowly drift inward. However, in the region $R < R_{\rm ms}$, there are no stable circular orbits, and therefore the centrifugal support breaks: the particles free-fall into the black hole. Thus, similarly as in the case of the Bekenstein engine, the Keplerian binding energy of particles at the location of the marginally stable orbit, $R_{\rm ms}$ (also called ISCO), determines the efficiency of accretion.

5.1 The relativistic Roche lobe overflow

The location of $R_{\rm ms}$ is determined by the minimum of the Keplerian angular momentum $\ell = \ell_K$, shown in Figure 2, left. For a constant angular momentum fluid torus, $\ell = \ell_0$, the combined pressure and centrifugal support breaks at the radius $R_{\rm in} < R_{\rm ms}$, defined by $\ell_K = \ell_0$ and shown in the same Figure, by the dot left of $R_{\rm ms}$ on the angular momentum distribution.

At this location, as discovered by Abramowicz, Jaroszyński and Sikora [1], one of the equipotential surfaces, called the Roche lobe, self-crosses as shown in Figure 2 (right). It should be obvious that if the fluid distribution overflows the Roche lobe, a dynamical mass loss must occur: at the the circle $R = R_{\rm in}$ the centrifugal and pressure support breaks down, and fluid if free falling in the region $R < R_{\rm in}$.

Again, the efficiency is determined by the Keplerian binding energy at breaking point, $R_{\rm in}$, called the *inner edge* of the accretion disk. This name is the source of a confusion, as some wrongly imagine that the name implies that at the inner "edge" velocity, density, and pressure must experience a jump, or a sudden change. Of course they do not. What *does* change in the region close to $R_{\rm in}$ is the nature of the flow: from sub-sonic to super-sonic. Note also that for low angular momentum flows, with $\ell < \ell_K$ everywhere, there is no Roche lobe, and therefore the inner edge cannot be sensibly defined. Such flows differ considerably from the Polish doughnuts, see e.g. [77]. Typically, they assume high viscosity, while Polish doughnuts assume low viscosity, less than about 0.03 in terms of the Shakura-Sunyaev α-parameter.

It was shown [2] that the inner edge must locate between the marginally stable, and marginally bound orbits,

$$R_{\rm mb} < R_{\rm in} < R_{\rm ms}. \tag{16}$$

The marginally bound orbit at $R_{\rm mb}$ has the same binding energy at infinity, $W(\infty) = W(R_{\rm mb})$. This has two important consequences: the efficiency of a torus with $R_{\rm in} = R_{\rm mb}$ is zero, *and* such a torus must have its outer radius at a very large distance, formally at infinity, $R_{\rm out} = \infty$. We have previously shown that the total luminosity of a fat torus increases logarithmically with the outer radius. This, combined with the accretion rate being proportional to the size (13), yields the logarithmic behavior $L_{\rm total}/L_{\rm Edd} \sim \ln(\dot{M}/\dot{M}_{\rm Edd})$. Indeed, Paczyński [4] found that all fat disks calculated by him obey

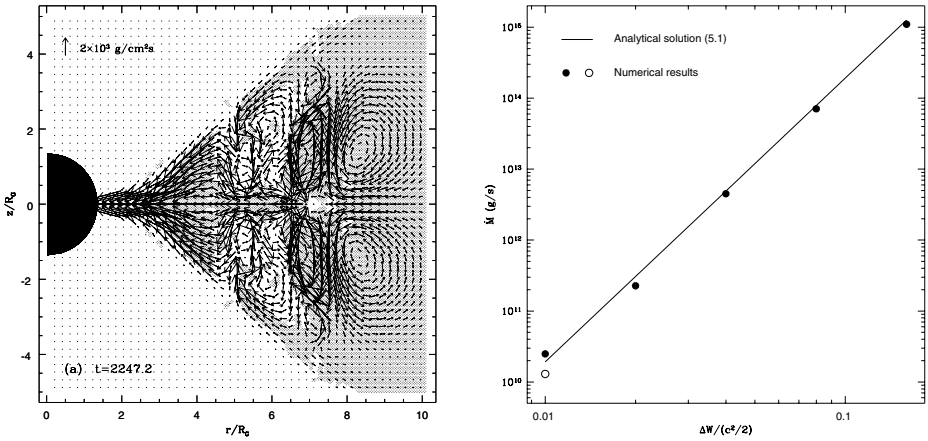

Fig. 3. Left Figure shows a snap-shot of the velocity field inside a time-dependent accretion black hole flow. The nature of the flow clearly changes at the inner edge (although physical characteristics do not experience a jump there). Far away from the inner edge, the flow pattern is very complicated, showing back flows, vortexes, and circulations in convective cells. Close to the inner edge, the Roche lobe overflow mechanism organizes the flow into a highly ordered, almost radial pattern. Right Figure shows that despite all complications, the Roche lobe overflow accretion rate self-regulates according to the simple analytic formula (18). The points are calculated in supercomputer simulations [15] of 3D, viscous, time dependent, black hole accretion flows with different parameters and different boundary conditions. The straight line is given by the formula (18). One should appreciate the nearly perfect agreement between this simple analytic formula and the most sophisticated, indeed today's state-of-art, numerical simulations. Both figures are taken from [15].

$$\frac{L_{\rm total}}{L_{\rm Edd}} = 4.8 \log\left(\frac{16\,\dot{M}}{\dot{M}_{\rm Edd}}\right). \tag{17}$$

This shows that the super-critical accretion is qualitatively different from the standard, sub-Eddington, thin disk accretion. For the standard thin disks, the total luminosity is directly proportional to the accretion rate $L_{\rm total}/L_{\rm Edd} = e(r_{\rm ms})\dot{M}/\dot{M}_{\rm Edd}$, $e(r_{\rm ms}) = {\rm const}$.

The Roche lobe overflow mechanism self-regulates the accretion rate, which for a polytropic equation of state, $P = K\,\rho^{1+1/n}$ equals,

$$\dot{M} = A(n) K^{-n} \frac{R_{in}}{\Omega_K(R_{in})} |\Delta W|^{n+1}, \quad \Delta W \equiv W_S - W_{in} \tag{18}$$

with an analytic expression for $A(n)$ explicitly known in terms of the Euler gamma function, $\Gamma(n)$. Because $n = 3$ for a radiation pressure supported gas, the self-regulation imposed by (18) is a very strong one, $\dot{M} \sim |\Delta W|^4$. Suppose, that in the region close to the inner edge, there is a fluctuation in the thermal

balance, causing overheating. This will induce an expansion, and an increase in the Roche-lobe overflow, which in turn will increase the accretion rate, i.e. the mass loss from the region. The heat contained in the mass that is lost will cool down the region, thus assuring thermal stability. I found [7] that this mechanism of advective cooling caused by the Roche lobe overflow, always stabilizes the innermost region of *any* accretion disk (thin, slim, thick, adaf) against thermal and viscous instability. Roughly speaking, the *local* instabilities have no chance to grow in the innermost region of accretion disks, because they are quickly washed away by advection caused by the Roche lobe overflow.
Stabilization of the *global* Papaloizou-Pringle instability by the Roche lobe overflow, found by Blaes [50], has a different physical reason: almost a perfect reflection of the Papaloizou-Pringle mode at the inner disk edge is a necessary ingredient of the instability. The reflection is not possible in the fast (transonic) flow induced by the Roche lobe overflow. Thus, the non-realistic, non-accreting Polish doughnuts indeed always suffer from the Paploizou-Pingle instability. In a more realistic model of a Polish doughnut, that includes the Roche lobe overflow, the Paploizou-Pringle instability does not operate.

6 Discussion

6.1 Paczyński's pseudo-potential

An accurate and elegant model for a non-rotating black hole's gravity was introduced by Paczyński [5] it terms of a Newtonian gravitational "pseudo-potential",

$$\Phi_{PW}(R) = -\frac{GM}{R - R_S},\ R_S = \frac{2GM}{c^2}. \tag{19}$$

The Paczyński model is remarkably successful: numerous authors used it in their calculations of black hole accretion flows. This clever idea cannot be, however, applied for: (a) rotating black holes, because of the Lense-Thirring effect[15], and (b) self-gravitating fluids, as $\nabla^2 \Phi_{PW} \neq 0$.

6.2 Standard thin disks are inconsistent with $\dot{M} > \dot{M}_{Edd}$

Properties of accretion flows with $\dot{M} > \dot{M}_{\rm Edd}$ are sometime discussed in terms of the standard thin Shakura-Sunyaev model. However, the standard thin disk is inconsistent with the super-Eddington accretion. Indeed, the radiative force cannot be greater than the effective gravity force, and at the surface of the standard disk this condition yields,

$$F_{\rm grav} = \frac{GMm_{\rm P}}{r^2}\left(\frac{H}{r}\right) > F_{\rm rad} = \frac{\sigma_T}{c} f_{\rm rad} = \frac{\sigma_T}{c}\frac{3GM\dot{M}}{8\,\pi r^3}\left[1 - \left(\frac{3r_G}{r}\right)\right]^{\frac{1}{2}}. \tag{20}$$

[15] Indeed, all suggested "Kerr pseudo-potentials", are neither elegant, nor practical.

From (20) Paczyński [60] derived $(H/r)_{max} > \dot{M}/\dot{M}_{\rm Edd}$. This means that for a super-Eddington accretion with $\dot{M}/\dot{M}_{\rm Edd} > 1$ it also must be $H/r > 1$. However, the standard model is a 1D approximation to the 3D accretion physics and assumes $H/r \ll 1$. Its structure equations contain only zero and first order terms in H/r. Therefore, the super-Eddington accretion is outside of the standard model applicability range. Contrary to this, slim disks and Polish doughnuts are suitable to describe super-Eddington accretion: slim disks are accurate up to the second order terms in H/r, and Polish doughnuts are described by the full 3D equations (i.e. contain H/r terms of *all* orders).

6.3 Adios: reasonable conclusions from false arguments

The Blandford & Begelman "adios" paper [79] claims that accretion with small efficiency (Polish doughnuts, adafs) must *necessarily* experience strong outflows, *because* matter in these flows has everywhere a positive Bernoulli constant.

While the very existence of strong outflows from small efficiency accretion black hole flows seems to be supported by observations, and therefore is most probably true, the reasons given by Blandford & Begelman to explain the outflows, are certainly not correct, because, as discussed in [80] by Abramowicz, Lasota & Kluźniak, (1) A positive Bernoulli constant is only a necessary, but certainly not a sufficient, condition for outflows[16]. (2) The very argument that low efficiency accretion has a positive Bernoulli constant everywhere is not correct itself. It follows from an *ad hoc* mathematical assumption (made in order to make the problem easier to solve) that inefficient accretion flows are self-similar. Real flows obey inner and outer boundary conditions and for this reason are not self-similar. The boundary conditions imply *negative* Bernoulli constant at least close to both boundaries.

7 Summary and conclusions

Observations provide a clear evidence for super-Eddington luminosities powered by accretion onto black holes. Theory, solidly based on standard physics, predicts that such super-Eddington luminosities imply highly super-Eddington accretion rates and a very low efficiency of the black hole accretion. The powerful and simple Sołtan argument shows, however, that the efficiency cannot be low all the time, because in the case of AGN this would be in a direct conflict with observations.

Thus, observations and theory together seem to point that highly super-Eddington accretion, that really occur in several black hole sources, is a *transient* "flip-flop" phenomenon. A physical mechanism (or mechanisms ?) for the flip-flop behavior, in which periods of highly supper-Eddington but low efficiency

[16] The *"a-positive-Bernoulli-implies-strong-outflows"* is a wide spread fallacy. Rather surprisingly, as it is plainly incompatible with the well-known classic Bondi solution, in which fluid has a positive Bernoulli constant everywhere, but experiences no outflows [69].

accretion alternate with periods of highly efficient, sub-Eddington or nearly-Eddington accretion is not yet known. Its understanding presents a great challenge for all of us.

Neither "adios", nor any other theoretical model, could at present explain strong outflows and jets that are observed in several super-Eddington black hole sources. Understanding of such outflows is another great challenge.

In the context of the cosmic structure formation, one should conclude that there is no obvious reason for assuming that $\dot{M}_{\rm Edd}$ is the upper limit for the growth rate of the seed black holes.

Acknowledgments: I am grateful for suggestions, advice and help I received when writing this article from Jírka Horak, Igor Igumenshchev, Jean-Pierre Lasota, William Lee, Piero Madau, Paola Rebusco, Martin Rees, Marek Sikora, Rashid Sunyaev and Andrzej Kajetan Wróblewski.

References

1. M.A. Abramowicz, M. Jaroszyński, M. Sikora: A&A **63**, 221 (1978)
2. M. Kozłowski, M. Abramowicz, M. Jaroszyński: A&A **63**, 209 (1978)
3. M. Jaroszyński, M.A. Abramowicz, B. Paczyński: Acta Astr. **30**, 1 (1980)
4. B. Paczyński: Acta Astr. **30**, 347 (1980)
5. B. Paczyński, P.J. Wiita: A&A **88**, 23 (1980)
6. M.A. Abramowicz, M. Calvani, L. Nobili: ApJ **242**, 772 (1980)
7. M.A. Abramowicz: Nature **294**, 235 (1981)
8. M.A. Abramowicz, W.H. Żurek: ApJ **246**, 314 (1981)
9. B. Paczyński, M.A. Abramowicz: ApJ **253**, 897 (1982)
10. M.A. Abramowicz, J.-P. Lasota, C. Xu: in *Quasars* ed G. Swarup, V.K. Kapahi, Reidel, Dordrect, (1986)
11. M.A. Abramowicz, B. Czerny, J.-P. Lasota, E. Szuszkiewicz: ApJ **332**, 646 (1988)
12. E. Szuszkiewicz, M.A. Malkan, M.A. Abramowicz: ApJ **458**, 646 (1996)
13. O.M. Blaes, I. Hubeny, E. Agol, J.H. Krolik: ApJ **553**, 710 (2000)
14. O.M. Blaes, I. Hubeny, J.H. Krolik, E. Agol: ApJ **559**, 680 (2001)
15. I.V. Igumenshchev, X. Chen, M.A. Abramowicz: MNRAS **278**, 236 (1996)
16. I.V. Igumenshchev, M.A. Abramowicz: ApJ.Supp.Ser. **130**, 463 (2000)
17. I.V. Igumenshchev, M.A. Abramowicz, R. Narayan: ApJLett **537**, L27 (2000)
18. I.V. Igumenshchev, R. Narayan, M.A. Abramowicz: ApJ **559**, 1042 (2003)
19. N.I. Shakura, R.A. Sunyaev: A&A **24**, 337 (1974)
20. S. Ichimaru: ApJ **214**, 840 (1977)
21. M.J. Rees, E.S. Phinney, M.C. Begelman, R.D. Blandford: Nature **295**, 17 (1982)
22. R. Narayan, I. Yi: ApJLett **428**, L13 (1994)
23. R. Narayan, I. Yi: ApJLett **452**, 710 (1995)
24. M.A. Abramowicz, X. Chen, S. Kato, J.-P. Lasota, O. Regev: ApJLett **438**, L37 (1995)
25. J.-P. Lasota: *Unmasking Black Holes*, Sci. Amer. **40**, (1999)
26. J.-P. Lasota: Phys. Rep. **311**, 247 (1999)
27. M. Sikora: private communication (1980)
28. A.S. Eddington: MNRAS **77**, 16 (1916) [*The Eddington luminosity paper*]
29. A.S. Eddington: MNRAS **77**, 596 (1917)
30. A.S. Eddington: MNRAS **78**, 113 (1917) [*The famous polemic with Jeans*]

31. A.S. Eddington: MNRAS **79**, 22 (1918) [*An important correction to* P_{rad}]
32. A.S. Eddington: *The Internal Constitution of Stars*, CUP, Cambridge (1926)
33. C. Białobrzeski: Bull. intern. Acad. Polon. Sci. **A 264** (1913)
34. C. Białobrzeski: C.R. Acad. Sci. Paris **782** (1916)
35. C. Białobrzeski: J. Phys. Radium **9**, 237 (1928)
36. C. Białobrzeski: *La thermodynamique des etoiles*, Gauthier-Villars, Paris (1931)
37. C. Białobrzeski: a bibliographical note, Acta Phys. Pol. **13**, 301 (1954)
38. G. Tiercy: *L'equilibre radiatif des etoiles*, Gauthier-Villars, Paris (1935)
39. S. Chandrasekhar: *An introduction to the Study of Stellar Structure*, University of Chicago Press, Chicago (1939)
40. S. Chandrasekhar: *Eddington*, CUP, Cambridge (1983)
41. A.K. Wróblewski: private communication (2004)
42. P.C. Joss, E.E. Salpeter, J.P. Ostriker: ApJ **181**, 429 (1973)
43. M.A. Abramowicz: Observatory **108**, 19 (1988)
44. A.S. Eddington: *Fundamental Theory*, CUP, Cambridge (1928)
45. N.J. Shaviv: ApJLett **494**, 193 (1994)
46. N.J. Shaviv: MNRAS **326**, 126 (2001)
47. A.R. King, R.E. Taam, M.C. Begelman: ApJLett **530**, L25 (2000)
48. I.F. Mirabel, & al. A&A **330**, L9 (1998)
49. J. Madej, B. Paczyński: IAU Coll. **42**, 313 (1977)
50. O.M. Blaes: MNRAS **216**, 553 (1985)
51. J.C.B. Papaloizou, J.E. Pringle: MNRAS **208**, 799 (1984)
52. J.C.B. Papaloizou, J.E. Pringle: MNRAS **213**, 721 (1984)
53. M.J. Rees: private communication (1980)
54. R.D. Blanford, R.L. Znajek: MNRAS **179**, 433 (1977)
55. M. Sikora: MNRAS **196**, 257 (1981)
56. P. Madau: ApJ **243**, 700 (1988)
57. B. Czerny, M. Elvis: ApJ **321**, 305 (1987)
58. M. Malkan: in *Theory of accretion disks*, eds. F. Mayer & al., Reidel, Dordrecht (1989)
59. A.R. King: MNRAS **335**, L13 (2002)
60. B. Paczyński: Seminar at the Copernicus Centre in Warsaw (1980)
61. D. Lynden-Bell: Observatory **102**, 131 (1982)
62. M.A. Abramowicz, T. Piran: ApJLett **241**, L7 (1980)
63. M. Sikora, D.B. Wilson: MNRAS **197**, 529 (1981)
64. M.A. Abramowicz, G.F.R. Ellis, A. Lanza: ApJ **361**, 470 (1990)
65. A.S. Eddington: quoted by S. Weinberg, *Dreams of a Final Theory*, Pantheon Books, New York (1992)
66. O.M. Blaes: MNRAS **227**, 975 (1987)
67. B. Paczyński: Astr. Gesellschaft **57**, 27 (1982)
68. B. Paczyński: Acta Astr. **48**, 667 (1998)
69. J. Frank, A.R. King, D.J. Raine: *Accretion Power in Astrophysics*, CUP, Cambridge (2002)
70. A. Sołtan: MNRAS **200**, 115 (1982)
71. L.-X. Li, B. Paczyński: ApJLett **534**, L197 (2000)
72. M.A. Abramowicz: Nature **294**, 235 (1985)
73. R. Narayan, I.V. Igumenshchev, M.A. Abramowicz: PASJ **55**, L55 (2003)
74. J. Bekenstein: Nouovo Cimento Lett. **4**, 737 (1972)
75. R.P. Geroch: Colloquium at Princeton University, December (1971)
76. G.W. Gibbons: Nature **240**, 77 (1972)

77. M.C. Begelman, D.L. Meier: ApJ **253**, 873 (1982)
78. M.A. Abramowicz: PASJ **37**, 727 (1985)
79. R.D. Blandford, M.C. Begelman: MNRAS **303**, L1 (1999)
80. M.A. Abramowicz, J.-P. Lasota, I.V. Igumenshchev: MNRAS **314**, 775 (2000)

Black Hole Spin-Up in the Light of General Relativistic MHD Simulations

J.H. Krolik

Johns Hopkins University, Baltimore MD 21218, USA

Abstract. Now that the magneto-rotational instability mechanism is well-established as the basis of angular momentum transport in accretion disks, it is possible to do large-scale numerical simulations with reasonable confidence that they are describing actual physical processes in disks. Recently several groups have extended the methods of MHD simulation to incorporate fully general relativistic dynamics. Rapidly-rotating black holes are found to generate strong outward electromagnetic stresses. One consequence is that it may be very difficult to spin up black holes by accretion to greater than some critical a/M that is likely to be rather less than the value, 0.998, suggested many years ago on the basis of photon capture.

1 Background

By the "No Hair Theorem", black holes are characterized solely by their mass M, angular momentum aM, and electric charge Q. Astrophysical black holes are extremely unlikely to have significant net charges, so Q is generally assumed to be effectively zero. For many purposes, the main physical impact of the mass is to set the length scale: $r_g = GM/c^2$. Thus, the only parameter of black holes that distinguishes them qualitatively is the normalized angular momentum, $a/M \equiv a_*$, which determines the rotation rate of the black hole, $\Omega_H = 2a_*/r_H$, where the event horizon $r_H = (1 + \sqrt{1 - a_*^2})r_g$.

Tracking the spin of accreting black holes is therefore of prime interest because the spin parameter should, one expects, govern qualitative properties of the accretion system. Some have suggested, for example, that radio-loud AGN are rapidly-spinning black holes, whereas the more common radio-quiet variety are slowly-spinning [22].

Because of the importance of this question, efforts have been made to predict the spin distribution of black holes from the very beginning of serious work in this field [4] right through to recent years [18]. The critical element in almost all these efforts has been to determine the angular momentum per unit mass brought to black holes as a result of accretion. Generally speaking, it has been assumed hitherto that the specific angular momentum of accreted matter is equal to the specific angular momentum of matter in the innermost stable circular orbit [21]. If this is so, a black hole fed matter with a consistent sense of angular momentum should be spinning very rapidly once it has accreted enough mass to increase its original content by some tens of percent.

In a sense, determining this quantity is the central question of the entire field of accretion disk dynamics. If matter is placed into an orbit at large distance

ESO Symposia: Growing Black Holes, pp. 274–283, 2005.

from a central gravitating object, it must lose angular momentum if it is to move any closer to the central object. Thus, accretion disk dynamics in its most basic form is the study of angular momentum transport in orbiting material. In other words, we will know how much angular momentum accompanies accreting matter to the event horizon when we understand accretion dynamics anywhere in the disk.

A formal answer to this central problem of accretion dynamics can be stated very simply: The stress corresponding to the radial flow of the momentum associated with orbital motion, integrated over a set of nested surfaces centered on the central object, must increase outward. For example, if we imagine a thin disk, so that the natural coordinate system is cylindrical, the r-ϕ component of the stress tensor gives the radial flux of axial angular momentum. This is the component of greatest interest, of course. If this stress, integrated over cylinders parallel to the rotation axis, increases outward, than each successive radius gives more angular momentum to the material just outside it than it receives from matter immediately inside. Each annulus in the disk must then steadily lose angular momentum, and accretion can occur.

Formal solutions, although useful guides, are rarely fully satisfying. We must know the specific physical mechanism acting in order to truly understand this process. That mechanism now appears to be in hand. First suggested more than a decade ago [2,10], there is now extremely good evidence that angular momentum transport in accretion disks is very largely due to MHD turbulence driven by the magneto-rotational instability [3]. This instability grows rapidly in almost all conditions likely to obtain in accretion disks and saturates only when the magnetic field intensity approaches the disk pressure. Whenever the orbital frequency declines outward (i.e., in almost any astrophysically-realized gravitational potential), the orbital shear automatically correlates the radial and azimuthal components of the magnetic field so that the stress associated with the field transports angular momentum outward.

Although the details of MHD turbulence are extremely complicated, its basic principles are straightforward and well-understood. When the MHD approximation is adopted (i.e., it is assumed that the matter's electrical conductivity is good enough to effectively "freeze" relative motion between the fluid and the magnetic field), dynamics under these circumstances can be understood entirely on the basis of three very familiar differential equations – mass conservation, the Euler equation (including gravity, pressure gradient forces, and the Lorentz force), and the induction equation – and a constitutent relation: the fluid's equation of state. No phenomenological guesses (e.g., the α-model of [20]) are required. The details may be messy, but the results are reliable and comprehensible in the sense that they rely only on well-known elementary physics.

2 Simulations

Unfortunately, the level of detail required to capture turbulent dynamics far exceeds what is practical to follow with analytic methods. Numerical simulation

is the only tool in our kit with the power to cope with this problem, and therefore progress in this field has rested very heavily on this technique.

For many years, all such simulations were done in the framework of Newtonian gravity (including "global disk" simulations such as those of [11,12,1,17]). Dynamics in disks centered on many objects of astrophysical interest (protostars, white dwarfs, etc.) are well described by the Newtonian approximation. However, the inner regions of disks centered on black holes or weakly-magnetized neutron stars are certainly relativistic. Moreover, these inner regions are the most interesting ones, for they are where most of the light is emitted. Consequently, fully general relativistic MHD simulation codes are necessary if we are to be confident in our understanding of relativistic accretion.

They are now available. Early versions could simulate accretion flows for only a few orbits [14,15]. Newer codes can run for as long as their owners' computing budgets will allow [5,8]. Both of the two newer codes have been used to investigate the question of spin evolution of accreting black holes. Here I will primarily make use of results from one of these codes; on the question of spin-evolution, there is rough, but not quantitative, agreement between the results from the two codes.

That there is even rough agreement is encouraging because the two codes are very different from one another. The De Villiers-Hawley code [5] is 3-d, follows internal energy but not total energy, and is written in terms of Boyer-Lindquist coordinates. The McKinney-Gammie code [8] is 2-d, follows total energy, and is written in Kerr-Schild coordinates.

We focus first on a suite of four simulations run with the De Villiers-Hawley code [6]. All four began from the same initial condition, a hydrostatic torus centered at $r = 25r_g$ containing a weak poloidal magnetic field. All four also assumed an adiabatic equation of state with index 5/3. They differed in the spin of the central black hole: 0., 0.5, 0.9, or 0.998. In all cases, the equatorial plane of the initial torus coincided with the equatorial plane of the metric and the rotation was prograde. The outer radius for all four simulations was $120r_g$, and the inner radius was placed a short distance outside the event horizon, generally where the lapse function in the equatorial plane was ~ 0.1. All four simulations ran for a time $8100r_g/c$, 10 orbits at the initial pressure maximum, hundreds of orbits near the innermost stable circular orbit.

3 Results

Of the many interesting things found in these simulations [6,13,7,16], two are of particular relevance to black hole spin evolution: the relationship of stress (i.e., angular momentum flux) to pressure, and how the magnitude of the electromagnetic stress depends on the spin of the central black hole.

For thirty years, the compelling dimensional argument of [20] has been used to argue that the ratio of vertically-integrated stress to vertically-integrated pressure is a constant comparable to or somewhat less than unity, labelled α. Our data permit us to investigate the validity of this claim.

Because Boyer-Lindquist coordinates are spherical, it is numerically awkward to integrate anything over cylinders. However, because the typical aspect ratio of matter in these simulations is ~ 0.1 (e.g., in the sense of density scale-height relative to radius), integrals over spherical shells are not bad approximations to integrals over cylinders: near the equatorial plane, where most of the matter is found, they are not too different. A more important redefinition of this ratio is necessitated by the contrast between the Newtonian and relativistic conceptual schemes: in relativity, both the stress and the pressure, not to mention the thickness of the disk, depend on the reference frame in which they are measured. For greatest consistency, therefore, in Figure 1 we plot the ratio of the shell-integrated fluid-frame magnetic stress to the shell-integrated fluid-frame pressure.

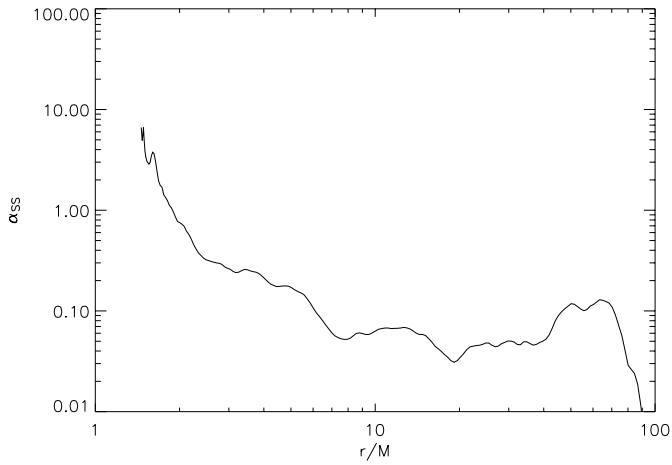

Fig. 1. The ratio of fluid-frame magnetic stress to fluid-frame pressure, both integrated over spherical shells at a particular late time in the simulation with $a/M = 0.9$. Gravitational radii r_g can be measured in units of M when units are chosen so that $G = c = 1$.

As this figure shows clearly, although this ratio is roughly constant at $\simeq 0.05$–0.1 for $r > 8r_g$, it rises sharply with diminishing radius at smaller distances from the black hole. In the simulation from which these data were taken, the black hole's spin parameter was $a/M = 0.9$, so the innermost stable circular orbit was at $2.3r_g$. This radius is often taken to mark the "inner edge" of the disk. Judged by this measure, the "α"-parameter varies systematically with radius throughout those inner regions of the disk where most of the accretion energy is released.

If the stress is measured in units of pressure, its value varies in many other ways as well. In addition to rising systematically with diminishing radius, the ratio of stress to pressure also increases systematically with increasing distance

from the equatorial plane. At any single location, there are large fluctuations in this ratio as a function of time. Some of these fluctuations are correlated over significant spatial volumes and move with a degree of coherence. Thus, from many points of view, simply assuming that the ratio of stress to pressure is a constant can be extremely misleading.

The second class of results to be discussed here has to do with the ability of rotating black holes to inject angular momentum into the accretion flow electromagnetically. It is convenient to describe the stress as a sum of matter and electromagnetic contributions:

$$T^r_\phi = \rho h \boldsymbol{U}^r \boldsymbol{U}_\phi + \frac{1}{4\pi} \boldsymbol{F}^r{}_\alpha \boldsymbol{F}^\alpha_\phi, \tag{1}$$

where ρ is the proper rest-mass density, h is the specific enthalpy, $\boldsymbol{U}^\mu$ is the four-velocity, and $\boldsymbol{F}^{\mu\nu}$ the electromagnetic field tensor. Figures 2–5 show the time-average in each simulation of the spherically-integrated angular momentum flux associated with both the matter and EM contributions as measured in the coordinate frame.

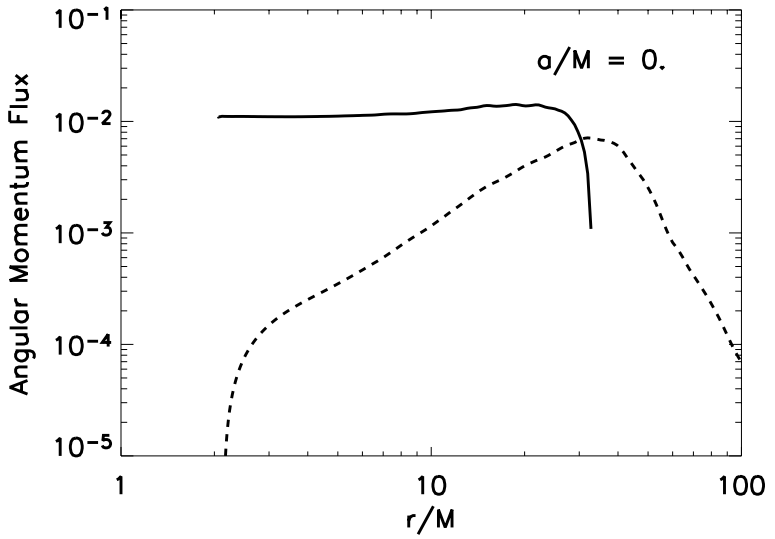

Fig. 2. The time-averaged shell-integrated angular momentum flux due to matter (solid curve) and electromagnetic fields (dashed curve), as seen in the simulation with $a/M = 0$. The sign of the matter contribution has been flipped in order to make it a positive quantity for this logarithmic plot.

These figures display several important properties of angular momentum flow under these circumstances.

First, the integated magnetic torque does indeed increase outward in almost all those portions of the simulations where the existence of stable circular orbits makes steady angular momentum loss a prerequisite of accretion. Thus, the MHD turbulence picture provides the sort of answer expected on the basis of the formal solution to the angular momentum transport question presented at the beginning of this talk. Although it is not easy to see on these logarithmic plots, the gradient in the magnetic stress closely matches the magnitude of the gradient in the matter angular momentum flux.

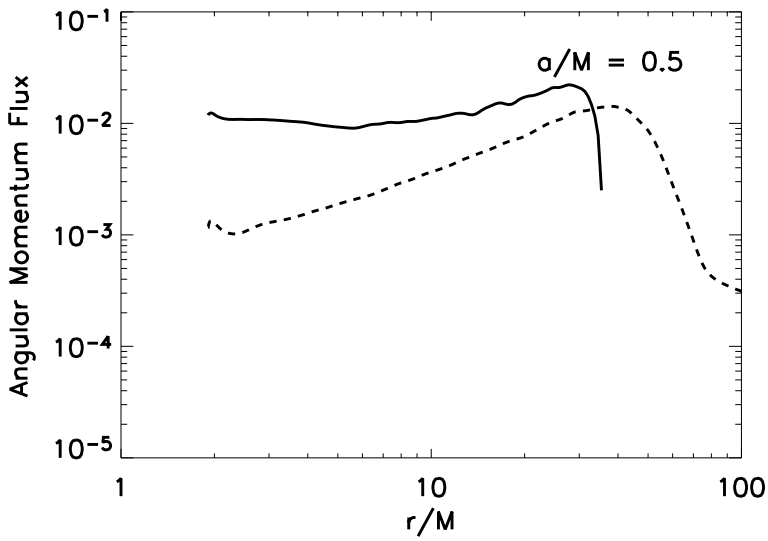

Fig. 3. The time-averaged shell-integrated angular momentum flux, as seen in the simulation with $a/M = 0.5$. The identifications of the curves are as in Figure 2.

Second, contrary to the conventional guess that the stress (other than that due to accretion of matter) ceases at and inside the marginally stable orbit [19], the EM stress continues smoothly through that zone and across the plunging region toward the event horizon (for $a/M = 0$,0.5,0.9,0.998, the marginally stable radius is 6,4.23,2.32,1.23r_g). It is interesting to note in this regard that [19] voiced concern that if magnetic fields were important, their heuristic arguments, based on a purely hydrodynamic picture, might fail. There is a noteworthy contrast, however, between the zero-spin case and the others deep in the plunging region: When the black hole does not rotate, the EM stress drops sharply toward zero as the event horizon is approached, but stays significant all the way to the inner boundary when it does spin. We will return to this point shortly.

The third notable fact is the most interesting: the importance of the magnetic contributions relative to the matter portion rises with increasing black hole spin.

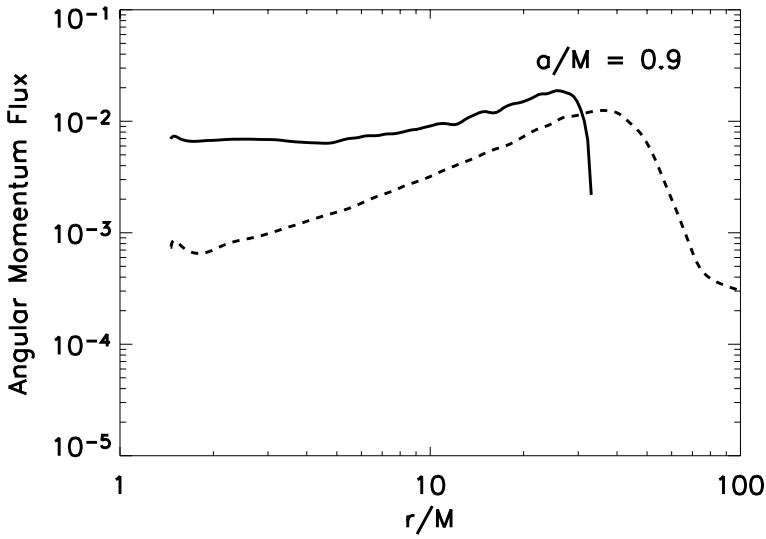

Fig. 4. The time-averaged shell-integrated angular momentum flux, as seen in the simulation with $a/M = 0.9$. The identifications of the curves are as in Figure 2.

Small compared to the matter part when the black hole spins slowly or not at all, the EM angular momentum flux becomes comparable to the angular momentum flux carried by matter when $a/M > 0.9$. In other words, when the black hole spins rapidly, magnetic fields move angular momentum outward at about the same rate as accreting matter carries angular momentum inward! The conclusion reached so facilely in earlier work – that accretion automatically spins up black holes to rapid rotation – is no longer so secure if this is the case.

In fact, we find that this electromagnetic angular momentum flux substantially reduces the net accreted angular momentum per unit rest-mass when the black hole spins rapidly (Table 1). When $a/M \leq 0.5$, the specific accreted angular momentum is only $\sim 10\%$ less than the value at the marginally stable orbit, J_{ms}. However, when the black hole rotates faster, the reduction grows: when $a/M = 0.9$, $\Delta J/\Delta M_0 \simeq 0.85 J_{ms}$, and the ratio falls to $\simeq 0.65 J_{ms}$ for the most rapidly-spinning case.

It is important to recognize that the numbers in the table normalize the accreted angular momentum to the *rest-mass*, not the *mass*. Because matter arrives at the black hole with a significant binding energy, the actual mass accreted is generally rather less than the rest-mass accreted. Consequently, $\Delta J/\Delta M > \Delta J/\Delta M_0$. We quote the rest-mass normalization because it is better-determined in these simulations. We do not explicitly calculate either gas heating or heat loss via radiation, so we are not able to calculate accurately the energy carried by the accreting matter.

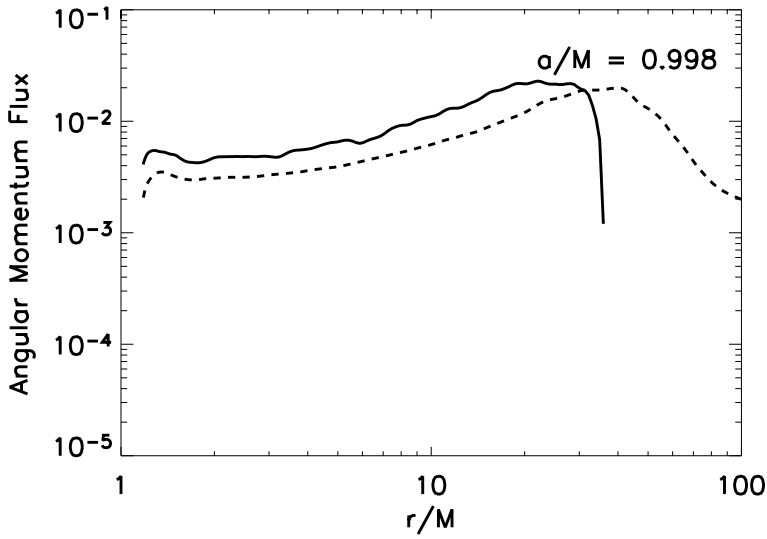

Fig. 5. The time-averaged shell-integrated angular momentum flux, as seen in the simulation with $a/M = 0.998$. The identifications of the curves are as in Figure 2.

Table 1. Net accreted angular momentum per unit rest-mass in the four simulations

Spin	J_{ms}	$\Delta J/\Delta M_0$
0.0	3.46	3.2
0.5	2.90	2.6
0.9	2.10	1.8
0.998	1.39	0.9

One further remark should be made regarding the integrated stress figures. In the two more rapidly-spinning cases, there are significant regions outside the innermost stable circular orbit in which the time-averaged EM angular momentum flux in the disk proper (not separated from the considerable EM stress in the outflow in these figures: see [16] for data taking the two parts separately) *falls* outward rather than rises. Where this is true, there cannot be steady accretion because the angular momentum content of the matter at these radii is growing, not declining. Because the matter cannot accrete if its angular momentum rises, it must pile up in this region. Fixed orbits have fixed specific angular momentum, so the rising angular momentum content of this "inner torus" reflects growth in the mass there as material is fed in from the outside.

4 Implications

As we have shown, the net angular momentum per unit rest-mass delivered to the black hole is always less than that previously expected. When the black hole spins relatively slowly, the effect is not large, but when $a/M > 0.9$, the change becomes significant. The origin of this depression in the angular momentum brought to the black hole is the efficiency of electromagnetic torques moving angular momentum outward. At large radii in the disk body, these are due to the underlying magneto-rotational instability stirring MHD turbulence and the orbital shear correlating the field. However, in the marginally stable and plunging regions, the magnetic field brought in with the accretion flow is further amplified and sheared, particularly when strong frame-dragging is added to the dynamical mix. Moreover, these electromagnetic stresses exist throughout the plunging region. The source of the angular momentum they transport outward is, of course, the rotation of the black hole itself. That the EM stress goes to zero immediately outside the event horizon when $a/M = 0$, but remains finite when the black hole rotates is another signature of this effect.

If the sense of angular momentum of the accreting matter remains constant, the spin parameter of the black hole should approach $\Delta J/\Delta M$ when enough matter has been accreted to increase M by order unity. It is interesting that $\Delta J/\Delta M_0 < a/M$ for our highest spin case, $a/M = 0.998$. Provided the binding energy correction doesn't change the sense of this comparison, this fact suggests that there is a limiting value $(a/M)_*$ to the spin parameter achievable by accretion, and $0.9 < (a/M)_* < 0.998$.

Thorne [21] argued that preferential capture of photons on negative angular momentum orbits would cause spin-up by accretion to halt at $a/M = 0.998$ (this is, of course, why we chose this value of a/M to simulate). What we are now arguing is that the magnetic fields brought into the ergosphere by accretion mediate torques that may be able to limit a/M at a lower value.

We would then expect a pile-up of black holes in the vicinity of this critical spin rate. Black holes spun-up by accretion would approach this value asymptotically from below. Alternatively, if there is another way to create more rapid spins (e.g., mergers of comparable mass black holes in which little angular momentum is lost through gravitational radiation), these more rapidly-spinning black holes, once they begin to accrete, would quickly spin down to $(a/M)_*$. In either case, this would be a favored value for the spin distribution.

Interestingly, the very different simulations of Gammie et al. [9] arrive at a very similar qualitative conclusion. However, the value of $(a/M)_*$ favored by those simulations is $\simeq 0.9$, rather lower than that indicated by ours. The physics in both simulations could be improved, most notably by introducing a more realistic treatment of thermodynamics, so any such estimates must remain preliminary. However, at a qualitative level it does appear very likely that these effects do create a limiting spin-rate, and it is encouraging that two simulations of very different character arrive at estimates of this limiting value that are not grossly different.

References

1. P.J. Armitage, C.S. Reynolds: M.N.R.A.S. **341**, 1041 (2003)
2. S.A. Balbus, J.F. Hawley: Ap.J. **376**, 214 (1991)
3. S.A. Balbus, J.F. Hawley: R.M.P. **70**, 1 (1998)
4. J.M. Bardeen: Nature **226**, 64 (1970)
5. J.-P. De Villiers, J.F. Hawley: Ap.J. **589**, 458 (2003)
6. J.-P. De Villiers, J.F. Hawley, J.H. Krolik: Ap.J. **599**, 1238 (2003)
7. J.-P. De Villiers, J.F. Hawley, J.H. Krolik: submitted to Ap.J. (2004)
8. C.F. Gammie, J.C. McKinney, G. Tóth: Ap.J. **589**, 444 (2003)
9. C.F. Gammie, S.L. Shapiro, J.C. McKinney: Ap.J. **602**, 312 (2004)
10. J.F. Hawley, S.A. Balbus: Ap.J. **376**, 223 (1991)
11. J.F. Hawley, J.H. Krolik: Ap.J. **548**, 348 (2001)
12. J.F. Hawley, J.H. Krolik: Ap.J. **566**, 164 (2001)
13. S. Hirose, J.H. Krolik, J.F. Hawley, J.-P. De Villiers: Ap.J. **606**, 1083 (2004)
14. S. Koide, D.L. Meier, K. Shibata, T. Kudoh: Ap.J. **536**, 668 (2000)
15. S. Koide, K. Shibata, T., T. Kudoh, D.L. Meier: Science **295**, 1688 (2002)
16. J.H. Krolik, S. Hirose, J.F. Hawley: submitted to Ap.J. (2004)
17. M. Machida, R. Matsumoto: Ap.J. **585**, 429 (2003)
18. R. Moderski, M. Sikora, J.-P. Lasota: MNRAS **301**, 142 (1998)
19. D.N. Page, K.S. Thorne: Ap.J. **191**, 499 (1974)
20. N.I. Shakura, R.A. Sunyaev: A. & A. **24**, 337 (1973)
21. K.S. Thorne: Ap.J. **191**, 507 (1974)
22. A.S. Wilson, E.J.M. Colbert: Ap.J. **438**, 62 (1995)

Time Variability of Low Angular Momentum Flows Accreting onto Black Holes: A Natural Mechanism for Radiation Flaring

D. Proga[1,2]

[1] JILA, University of Colorado, Boulder CO 80309, USA
[2] Present address: Department of Astrophysical Sciences, Princeton University, Peyton Hall, Princeton NJ 08544, USA

Abstract. We present results from our magnetohydrodynamical simulations of accretion flows onto black holes. Our main focus is the interplay between inflows and related outflows. We consider applications of such flows to the Galatic center and low luminosity active galactic nuclei.

1 Introduction

Dynamical evidence suggests that the nonluminous matter within 0.015 pc of the Galactic center has a mass of $\approx 2.6 \times 10^6\ M_\odot$ (e.g., [8], [9]). This matter is associated with Sgr A*, a bright, compact radio source [3], and provides very compelling evidence for the existence of a supermassive black hole (SMBH). Observations of Sgr A* in X-ray and radio bands reveal a luminosity substantially below the Eddington limit, $L_{\rm Edd} = 3 \times 10^{44}$ erg s^{-1}. For example, *Chandra* observations show a luminosity in 2-10 keV X-rays of $\approx 2 \times 10^{33}$ erg s^{-1} (ten orders of magnitude below $L_{\rm Edd}$) [1]. *Chandra* observations also revealed an X-ray flare rapidly rising to a level about 45 times as large, lasting for only $\sim 10^4$ s, indicating that the flare must originate near the black hole [1].

It is thought that the Sgr A* radiation is due to gas accretion onto the SMBH. Estimates for the accretion luminosity, L, rely on assumptions about the mass accretion rate, $\dot{M}_a$, and the efficiency of transforming the gas energy into radiation, η (i.e., $L = \eta c^2 \dot{M}_a$). Both $\dot{M}_a$ and η are uncertain and there is no generally accepted model which could explain the low luminosity of Sgr A* by predicting low enough $\dot{M}_a$ or η, or both. For example, Coker & Melia [5] estimated a rate of 10^{-4} M$_\odot$ yr^{-1} from Bondi-Hoyle accretion of winds from nearby stars, while Quataert, Narayan, & Reid [17] estimated the Bondi capture rate of 3×10^{-5} M$_\odot$ yr^{-1}. On the other hand, the best fit spectral models of [13] and [19] have $\dot{M}_a = 10^{-10}$ M$_\odot$ yr^{-1} and 10^{-8} M$_\odot$ yr^{-1}, respectively. Quataert, Narayan, & Reid [17] argue that the low luminosity requires $\dot{M}_a$ to substantially sub-Eddington and sub-Bondi at large radius. However, the rate at which mass is captured into the accretion flow at large radii, the mass supply rate, does not necessarily have to be the same as the rate at which mass is accreted onto a black hole.

Many aspects of spectral models for Sgr A* follow from the simple scaling laws of black hole accretion and will be present in any model, regardless of the

ESO Symposia: Growing Black Holes, pp. 284–289, 2005.

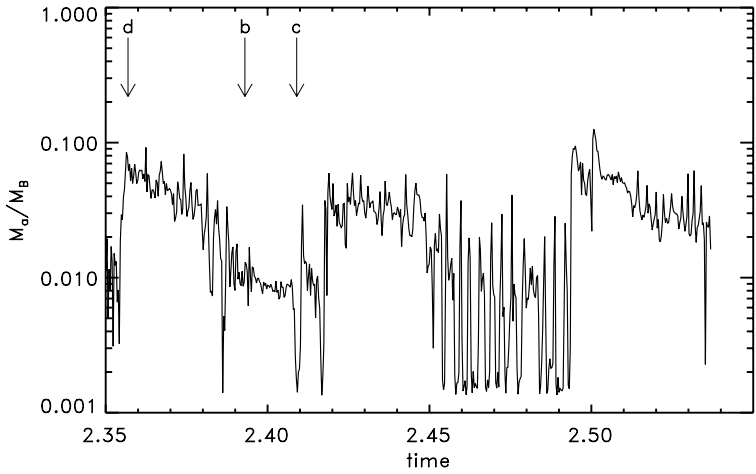

Fig. 1. Late time evolution of the mass accretion rate in units of the Bondi rate, for the fiducial model of MHD accretion flow in [15] (their model D). Time is in units of the Keplerian orbital time at the Bondi radius, which for this simulation was set at 1000 times the black hole radius. The figure shows in detail $\dot{M}_a$ as a function of time toward the end of the simulation. Vertical arrows mark times corresponding to three (out of four) generic states of accretion: accretion is dominated by low-l material which managed to reach the inner boundary despite a blocking corona and outflow from the torus (arrow d), accretion occurs only through the torus (arrow b) and no torus accretion but only very weak accretion through a very low density magnetized polar cylinder (arrow c). See Figs. 2 and 3 for the density maps and the velocity fields of the inner flow corresponding to the times marked.

detailed dynamics. For a steady state model, an impressive range of spectra can be generated with the adjustment of several free parameters: the ratio of electron to ion temperature, the magnetic pressure, the radial density profile, the mass-accretion rate, and the mass-loss rate (e.g., [16]). Thus it is difficult to tightly constrain parameters of a steady state model. However, our recent magnetohydrodynamical (MHD) simulations present a way of constraining the accretion flow models by studying time variability [15]. As we will describe in next section, the simulations show that the inner accretion flow quasi-periodically changes both quantitatively (e.g., $\dot{M}_a$ changes by $\gtrsim 1$ order of magnitude) and qualitatively (e.g., the inner flow can be dominated by an equatorial accretion torus or a polar inflow).

2 Results From MHD Simulations Of Accretion Flows

We have performed axisymmetric, MHD, time-dependent simulations of slightly rotating accretion flows onto black holes [15]. Our simulations are complementary to previous MHD simulations which considered strongly rotating accretion flows and started from a rotationally supported torus (e.g., [2], [6], [7]). We

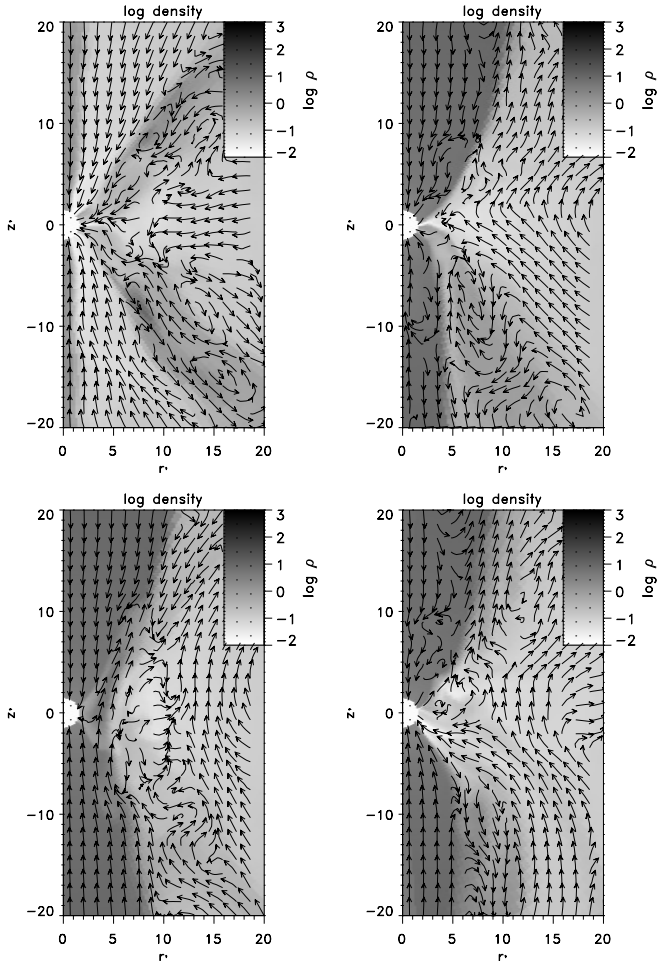

Fig. 2. Maps of logarithmic density overplotted by the direction of the poloidal velocity. This figure compares the inner flow in four different accretion states in our MHD simulations (Fig. 8 in [15]). We express the length scale in units of the black hole radius. The top left panel presents the two-dimensional structure near the beginning of simulations at $t = 0.22$ (not shown in Fig. 1). At this time, accretion onto the black hole occurs through both the torus and the polar funnel. The top right panel presents an example of an inner flow where accretion occurs only through the torus at $t = 2.39$ (marked by arrow b in Fig. 1). The bottom left panel presents an example of an inner flow where there is no torus accretion but only very weak accretion through a very low density magnetized polar cylinder at $t = 2.41$ (marked by arrow c in Fig. 1, note that this state is very short-lived). Finally, the bottom right panel presents an example of an inner flow where accretion is dominated by low-l material (i.e., the inward stream of gas directed present in the lower half of the panel). This material managed to reach the inner boundary despite a blocking corona and outflow from the torus at $t = 2.36$ (marked by arrow d in Fig. 1).

attempt to mimic the boundary conditions of classic Bondi accretion flows as modified by the introduction of a small, latitude-dependent angular momentum at the outer boundary, a pseudo-Newtonian gravitational potential and weak poloidal magnetic fields. A weak radial magnetic field and distribution of the specific angular momentum, l, with latitude allow the density distribution at infinity to approach spherical symmetry. Therefore our outer boundary conditions are consistent with X-ray images taken with *Chandra* which show that the gas distribution in the vicinity of SMBHs is close to spherical.

We find that the material with high l forms an equatorial torus which can accrete onto the black hole because of magnetorotational instability (MRI). The magnetized torus produces a corona and an outflow. The latter two can be strong enough to prevent accretion of low-l material through the polar regions (the source of accretion in the hydrodynamical inviscid case [14]). We find that the net mass accretion rate through the torus is lower than the Bondi rate and also lower than $\dot{M}_a$ in the HD inviscid case.

The accreting torus is the crucial component of our accretion flow. After an initial transient, the inner flow usually consists of a turbulent, gas pressure-dominated MHD torus with an outflow or corona or both, bounded by a magnetic pressure-dominated polar flow. The accretion through the torus is highly variable. In fact, it could be stopped for a relatively short time, by the accumulated poloidal magnetic flux that builds up during accretion and truncates the torus. However, we observe that even when the torus is truncated, there is inflow of material inside the torus and its mass and pressure build up. Consequently, the magnetic field is quickly pushed inward by the torus and the gas from the torus can again fall onto the black hole (note short-lived 'dips' and 'spikes' in the time evolution of $\dot{M}_a$ shown in Fig. 1). Rapid time variability appears to be typical for MHD turbulent torii. Generally, we find that the properties of the inner flow (e.g., the radial density profile in the torus, properties of the corona and outflow) are very similar to those presented by [18] and [10] despite using different initial and outer boundary conditions.

What is new in our simulations is the fact that the torus accretion can be supplemented or even replaced by stream-like accretion of the low-l material occurring outside the torus (e.g., Figs. 1, 2 and 3). When this happens, $\dot{M}_a$ sharply increases and gradually decreases in a quasi-periodic manner. $\dot{M}_a$ due to this 'off torus' accretion can be one order of magnitude larger than that due to the torus (Fig. 1). The off torus accretion is a consequence of our outer boundary and initial conditions which introduce the low-l material to the system. This material can reach the black hole because the torus corona and outflow are not always strong enough to push it away.

One can expect that in the vicinity of SMBHs some gas has very little angular momentum and could be directly accreted. Such a situation occurs likely at the Galactic center where a cluster of young, massive stars losing mass surrounds a SMBH. We propose then that the variability observed in Sgr A* (i.e., flares) could be due to the interplay between gas with a range of specific angular momentum similar to that found in our simulations.

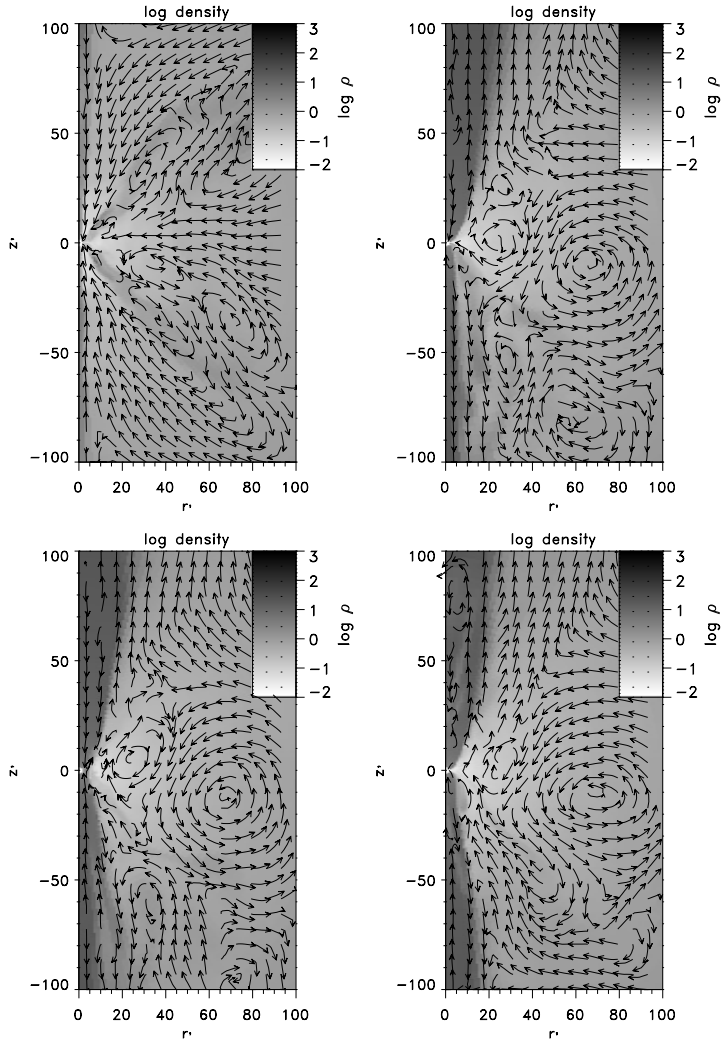

Fig. 3. As Fig. 2 but with the r' and z' ranges increased by a factor of 5. Note the large scale, polar double-sided outflow from the thick equatorial torus in the top right and bottom left panels. The bottom right panel shows an accretion state where the outflow below the equator is replaced by an inflow. We propose that switching between this state and that presented in the top right panel (i.e., in Fig. 1, the states marked by arrows d and b, respectively) can explain radiation flaring in Sgr A*.

3 Conclusions

Our main results can be summarized as follows:

• The properties of the accretion flow depend on an equatorial torus.

• Accretion can be via the torus due to MRI and via the polar funnel where material has zero or low angular momentum.

• The torus outflow and corona are natural mechanisms to narrow or even totally close the polar funnel for the accretion of low-l material.

• The net accretion rate for the MHD, is lower than for the Bondi flow and the HD inviscid flow.

• Time variability of the inner flow may explain light curves in Sgr A*. In particular, we propose that the X-ray flares can be explained by quasi-periodic, off-torus accretion of the low l material.

We acknowledges support from NASA LTSA grant NAG5-11736. We also acknowledge support provided by NASA through grant HST-AR-09947 from the Space Telescope Science Institute, which is operated by the Association of Universities for Research in Astronomy, Inc., under NASA contract NAS5-26555.

References

1. F.K. Baganoff, et at.: Nature **413**, 45 (2001)
2. Baganoff, F.K. et at.: Astrophys. J. **591**, 891 (2003)
3. B. Balick, R. Brown: Astrophys. J. **194**, 265 (1974)
4. H. Bondi: Mon. Not. R. Astron. Soc. **112**, 195, (1952)
5. R. F. Coker, F. Melia: Astrophys. J. Lett. **488**, 149 (1997)
6. T. Di Matteo: Astrophys. J. **582**, 133 (2003)
7. G. Fabbiano et al.: Astrophys. J. **588**, 175 (2003)
8. R. Genzel et al.: Mon. Not. R. Astron. Soc. **317**, 348 (2000)
9. A. M. Ghez, et al.: Nature **407**, 349 (2000)
10. Hawley, J.F., & Balbus, S.A. 2002, Astrophys. J., 573, 749
11. I. V. Igumenshchev, R. Narayan: Astrophys. J. **566**, 137 (2002)
12. I.V. Igumenshchev, R. Narayan, R., M. A. Abramowicz: Astrophys. J. **592**, 1042 (2003)
13. F. Melia, S., Liu, R. Coker: Astrophys. J. **553**, 146 (2001)
    798
14. D. Proga, M. C. Begelman: Astrophys. J. **582**, 69 (2003a)
15. D. Proga, M. C. Begelman: Astrophys. J. **592**, 767 (2003b)
16. E. Quataert, R. Narayan: Astrophys. J. **520**, 298 (1999)
17. E. Quataert, R. Narayan, M. J. Reid: Astrophys. J. Lett. **517**, 101 (1999)
18. J. M. Stone, J. E. Pringle: Mon. Not. R. Astron. Soc. **322**, 461 (2001)
19. F. Yuan, E. Quataert, R. Narayan: Astrophys. J. **598**, 301 (2003)

Narrow-Line Seyfert 1 Galaxies: Growing Black Holes at Supercritical Accretion?

Y. Tanaka[1], T. Boller[1], and L. Gallo[1]

Max-Planck-Institut für Extraterrestrische Physik, D-85748 Garching, Germany

Abstract. The X-ray spectra of NLS1, characterized by a significant soft excess and a steep hard tail analogous to the soft-state black-hole binaries, are systematically studied. If the soft component, best expressed by a blackbody model, is interpreted as an optically-thick disk emission, the X-ray luminosity and the disk temperature indicate, according to the slim disk concept, that these NLS1 are in general relatively low-mass ($10^6 - 10^7 M_\odot$) black holes accreting at highly supercritical rates with the luminosity near or higher than the Eddington limit. The mass-doubling time could be $\lesssim 10^7$ yrs, hence these black holes would be growing rapidly at the recent epoch.

1 Introduction

The recent studies of cosmological evolution of AGN revealed that their spatial density as a function of redshift depends on the X-ray luminosity [1,2], i.e. the higher the luminosity (presumably higher black hole mass) the earlier the spatial density peaks (e.g. see Fig. 12 in [1]) and vice versa. This suggests the presence of a class of the lowest-mass AGN that are most recently in making. If mass accretion were to play a significant role in the growth of black hole mass, these youngest AGN should exhibit higher accretion rates ($\dot{M}/M$) and show different X-ray properties than more massive AGN that passed the space-density peak.

Regarding the effect of mass accretion rate on X-ray properties, it is well known that $\sim 10 M_\odot$ black holes in X-ray binaries undergo transition between two states across a certain accretion rate: the hard state at low accretion rates and the soft state at high accretion rates. The hard state is characterized by a hard power-law spectrum (photon index $\Gamma \sim 1.8$) and rapid flux variation. Whereas, the soft state spectrum consists of a blackbody-type soft component and a significantly steeper ($\Gamma \sim 2.2 - 2.5$) hard tail.

Such distinct, accretion-rate dependent differences may exist in AGN as well. The broad-line Seyfert 1 galaxies (BLS1) show the characteristics of the hard state. In contrast, the narrow-line Seyfert 1 galaxies (NLS1) generally show spectra reminiscent of the soft state, i.e. a steep (significantly steeper than BLS1) hard tail and a soft excess (e.g. [3]). For the analogy to the black-hole binary spectra, and generality of accretion phenomenon, NLS1 are probable candidates for AGN in the soft state. In fact, NLS1 have been considered to be relatively low-mass AGN at high accretion rates from various circumstantial evidence.

In this work, we systematically investigate the X-ray spectral properties of NLS1 using the data obtained with XMM-Newton, and show that they are likely at supercritical accretion. The implications are also discussed.

ESO Symposia: Growing Black Holes, pp. 290–295, 2005.

2 X-ray Properties of Two NLS1: 1H 0707–459 and IRAS 13224–3809

To illustrate some distinct features, the observed XMM EPIC-*pn* spectra of two NLS1, 1H 0707–459 [4] and IRAS 13224–3809 [5] are shown in Fig. 1. As evident from the fit ratio to a power law (bottom panels), both sources show a strong soft excess above a power law with a photon index $\Gamma \sim 2.4 - 2.5$.

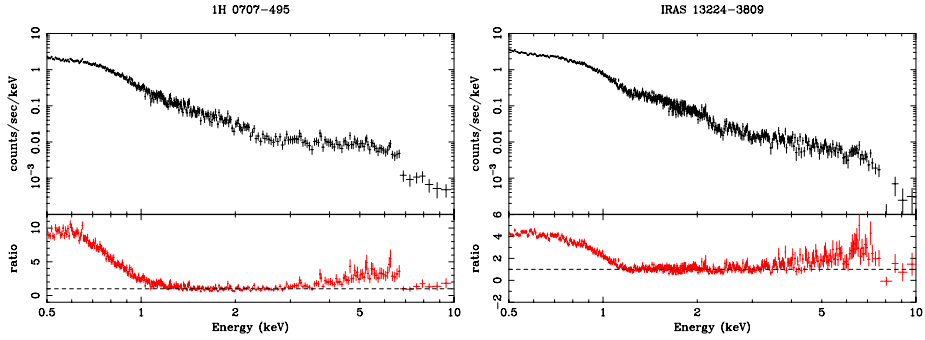

Fig. 1. Observed spectra of 1H 0707-495 (top left) and IRAS 13224-3809 (top right). The bottom panels display the ratio to a power law with a photon index $\Gamma = 2.4$ (left) and 2.5 (right), respectively

In addition, the hard tail gradually flattens towards high energies, and abruptly drops at around ~ 7 keV, suggesting the Fe-K absorption. However, no significant fluorescent line is observed. A flux drop above ~ 7 keV was noticed in several of the NLS1 observed with ASCA [6], hence this feature appears to be fairly common among NLS1.

The above features can be interpreted as a result of *partial covering* [7]. The simplest form of a partial covering model is expressed as

$$[fe^{-\sigma N_{\rm H}} + (1 - f)][F_{\rm soft}(E) + F_{\rm hard}(E)], \quad (1)$$

where f is the covering fraction by an absorber(s) of a column density $N_{\rm H}$. There may be more complex cases involving multiple absorbers [7]. The results of the partial covering fit to the above two NLS1 are shown in Fig. 2 [7,5].

A blackbody model is found to give the best fit to the soft component. For the hard component, a cut-off power law model is employed. If a single power-law is assumed instead, these two NLS1 require an excessive Fe overabundance ($\sim 30\times$solar) [4]. It is shown that a gradual steepening (such as a cutoff power law) can reduce the Fe abundance to $\sim 3\times$ solar [7].

Another distinct property of NLS1 is rapid large-amplitude flux variation (e.g. [3]). Partial covering can also explain the variability as a result of changing covering conditions with time, if more than one absorbing layers of different f and $N_{\rm H}$ are considered, while the intrinsic luminosity remains constant [5,8]. In fact, the blackbody temperature does not change against large flux variation.

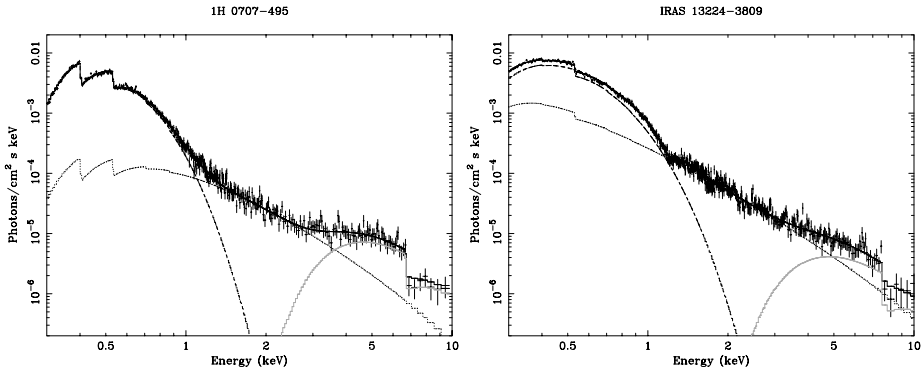

Fig. 2. Partial covering fit to the spectra of 1H 0707–495 (left) and IRAS 13224–3809 (right). The photon spectra unfolding the detector response are presented. The soft and hard components as well as the absorbed component are shown.

3 Partial Covering Analysis of NLS1 Spectra

In order to get a generalized picture of NLS1, we further analyzed a set of archival XMM-Newton EPIC-*pn* spectra of NLS1 based on the partial covering model (Eq. 1). As in Section 2, a blackbody model and a cut-off power law model are used. In addition to 1H 0707–459 and IRAS 13224–3809, fifteen other NLS1

Table 1. The fitting results with partial covering model

Name	kT_{bb} eV	Γ	f	$L_{\rm X}$ [1)] 10^{44}erg s^{-1}	soft excess	edge depth
PKS 0558–504	112	2.6	0.47	120	– –	
PHL 1092	128	∼2.5	0.80	60	++	+
NAB 0205+024	120	2.5	0.43	24	–	
Ton S180	110	2.8	0.56	23	– –	
Mrk 478	106	2.7	0.49	14	– –	
I Zw 1	75	2.5	0.32	11	– –	
IRAS 13349+2438	97	∼2.3	0.48	8.7	++	+
Akn 564	129	2.7	0.28	7	–	
PG 1211+143	117	∼1.9	0.41	3.7	++	+
1H 0707–495	92	∼2.4	0.88	3.5	++	++
IRAS 13224–3809	130	∼2.5	0.78	3.2	++	++
Mrk 335	130	2.3	0.49	2.7	–	
PG 1244+026	147	2.5	0.31	2.7	–	
Mrk 766	104	2.2	0.25	0.8	– –	
Mrk 1044	105	2.4	0.43	0.5	+	
Mrk 359	125	2.1	0.45	0.3	– –	
NGC 4051	130	2.0	0.17	0.015	++	

[1)] Integration of the best-fit model in (0.1–10) keV corrected for absorption and partial covering.

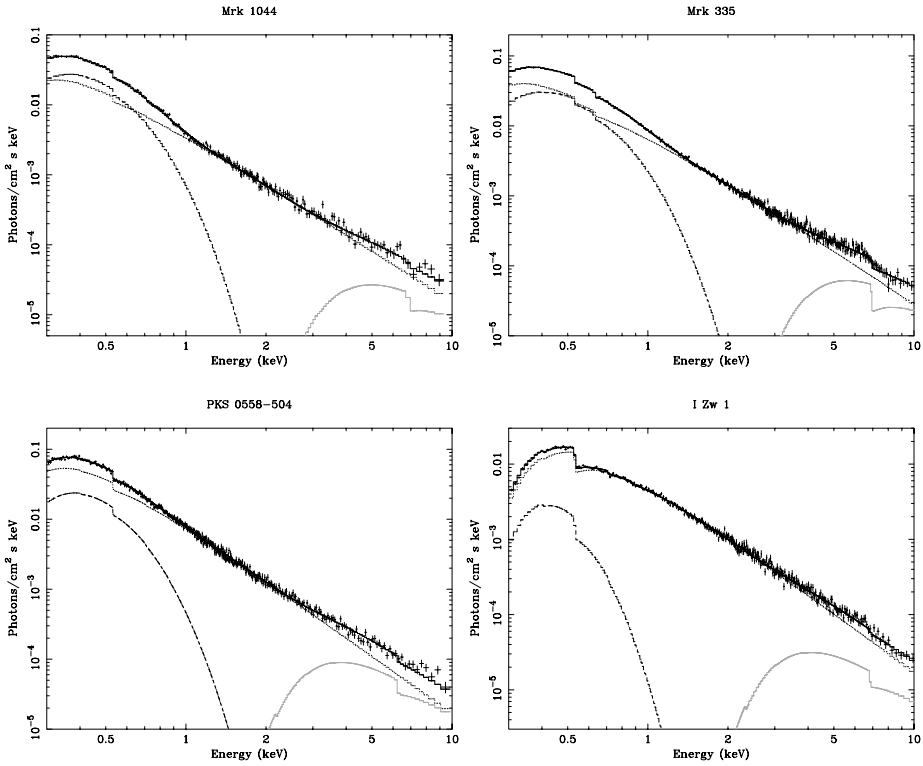

Fig. 3. The photon spectra obtained from partial covering model fits: Mrk 1044 (upper-left), Mrk 335 (upper-right), PKS 0558-504 (lower-left) and I Zw 1 (lower-right), showing differences in flux of the soft component relative to the hard component.

all resulted in satisfactory fits (χ^2/ν within 0.92–1.16) in the energy range 0.3–10 keV. Table 1 lists the best-fit parameter values. Some of the source spectra prefer a significant steepening of the hard component. The steepening is introduced by $\exp(-E/E_{\rm c})$ in the cut-off power law model. For those with $E_{\rm c} < 10$ keV, an average slope over 1.5–4 keV is given (marked "$\sim$"). The X-ray luminosity $L_{\rm X}$ is obtained by integrating the best-fit model over the range (0.1–10) keV, after correcting for absorption and partial covering (f). The flux of the blackbody component relative to that of the hard component is different from source to source. The relative soft excess strength is qualitatively indicated in Table 1 with the marks (– –, –, +, ++), and the edge depth as well with (+, ++).

The photon indices are more than 2.0 for all objects, except PG 1211+143 and NGC 4051, and mostly within ±0.2 of 2.5 independent of the strength of the soft excess, confirming the earlier results. The blackbody temperature of the soft component $T_{\rm bb}$ is found to be distributed in a fairly narrow range, between ~ 70 and ~ 150 eV.

Some of the fit results are shown in Fig. 3. Differences in the relative strength of the soft component are clearly seen.

4 Discussion

4.1 Origin of the soft Component

As shown in Section 3, partial covering models can explain the observed NLS1 spectra well. A blackbody model best reproduces the soft component, which is accurately verified in the cases of particularly strong soft excesses. However, if this blackbody component is the emission from an optically-thick disk, the obtained (color) temperature values are obviously too high for a standard Shakura-Sunyaev disk, even if the color correction is considered (e.g. [9]).

Alternative interpretations of the soft component have been proposed. Fabian et al. [10] consider an X-ray illuminated inner disk. Photoionization produces a line-dominated spectrum below 2 keV, which is relativistically blurred and mimics a blackbody spectrum. The shape depends on the ionization parameter.

Gierlinski and Done [11], systematically studying PG quasar spectra, propose that the soft excess, commonly seen at a similar temperature, is an artifact of strong, ionized absorption due to O VII, O VIII, and Fe-L. Relativistic smearing will produce a broad absorption trough which leads to an apparent soft excess.

Although the origin of the soft component remains a fundamental question, here we proceed still based on the interpretation of the optically-thick disk emission in view of the excellent fit with a blackbody spectrum.

4.2 Results Based on the Slim Disk Model

The too-high blackbody temperature can be explained by the "slim disk model", first proposed by Abramowicz [12], which applies at very high accretion rates such as $\dot{M} \gg L_{\rm E}/c^2$, where $L_{\rm E}$ is the Eddington limit. A slim disk allows for a much higher disk temperature than the limit for a standard thin disk. The slim disk model has recently been developed extensively (e.g. [13,14,15]). We shall interpret the results of the present analysis based on the slim disk model.

If the bolometric luminosity $L_{\rm b}$ and the innermost disk temperature $T_{\rm bb}$ are known, one can derive the black hole mass M and $\dot{M}$ (or $L_{\rm b}/L_{\rm E}$). However, since the SED is complex (e.g. [9]) and still uncertain, reliable estimation of $L_{\rm b}$ is difficult. Here we use $L_{\rm X}$ as an absolute minimum of $L_{\rm b}$. We adopt the color correction factor $T_{\rm bb}/T_{\rm eff} = 2.4$ according to [9].

The results obtained by utilizing an extrapolation of Fig. 1 in [14] are listed in Table 2. Evidently, all except NGC 4051 are near or exceeding the Eddington limit. M will be substantially underestimated by substituting $L_{\rm X}$ for $L_{\rm b}$. For a given $T_{\rm bb}$, true M will be larger approximately by a factor $(L_{\rm b}/L_{\rm X})^{1/2}$. $L_{\rm b}/L_{\rm E}$ is also underestimated, but to a less degree than M. On the other hand, $T_{\rm bb}/T_{\rm eff}$ could be larger than 2.4 (see [15]). If so, $L_{\rm b}/L_{\rm E}$ becomes somewhat smaller.

In conclusion, a total of seventeen NLS1 spectra are all explained satisfactorily based on the partial covering scenario. Several of them showed a large Fe overabundance. This would imply a contribution from matter of Type 1a supernova origin, which suggests active formation of massive stars creating a gas-rich environment.

Table 2. The results based on the slim disk model

Name	kT_{bb} eV	$L_{\rm X}$ 10^{44}erg s^{-1}	$M_{\rm min}$ $10^6 M_\odot$	$L_{\rm X}/L_{\rm E}$
PKS 0558–504	112	120	$\sim$20	> 3
PHL 1092	128	60	$\sim$10	> 3
NAB 0205+024	120	24	~ 6	~ 3
Ton S180	110	23	~ 7	~ 3
Mrk 478	106	14	~ 5	~ 3
I Zw 1	75	11	~ 7	~ 1.5
IRAS 13349+2438	97	8.7	~ 4	~ 2
Akn 564	129	7	~ 2	~ 2
PG 1211+143	117	3.7	~ 1.5	~ 2
1H 0707–495	92	3.5	~ 2	~ 1
IRAS 13224–3809	130	3.2	~ 1.5	~ 2
Mrk 335	130	2.7	~ 1	~ 2
PG 1244+026	147	2.7	~ 1	~ 2
Mrk 766	104	0.8	~ 0.8	~ 1
Mrk 1044	105	0.5	~ 0.4	~ 0.7
Mrk 359	125	0.3	~ 0.3	~ 0.8
NGC 4051	130	0.015	~ 0.1	~ 0.2

If the soft blackbody component is interpreted as the emission from an optically-thick disk, the high disk temperature is explained by the slim disk model as expected when the accretion rate is highly supercritical ($\dot{M} \gg L_{\rm E}/c^2$), which is found indeed to be the case.

For such near- or super-Eddington luminosities, also taking reduced radiation efficiency into account, the mass-doubling time would be only $\lesssim 10^7$ yrs. Thus, NLS1 are probably the most rapidly growing black holes in the recent era.

References

1. Y. Ueda, M. Akiyama, K. Ohta, T. Miyaji: ApJ **598**, 886 (2004)
2. G. Hasinger: 'The Emergence of Cosmic Structure', ed. by S.S. Holt, C. Reynolds, AIP Conf. Proc. **666**, 227 (2003)
3. Th. Boller: New Astron. Rev. **44**, 387 (2000)
4. Th. Boller, A.C. Fabian, R. Sunyaev, J. Trümper et al.: MNRAS **329**, L1 (2002)
5. Th. Boller, Y. Tanaka, A.C. Fabian, W.N. Brandt et al.: MNRAS **343**, L89 (2003)
6. S. Vaughan, J. Reeves, R. Warwick, R. Edelson: MNRAS **309**, 113 (1999)
7. Y. Tanaka, Th. Boller, L. Gallo, R. Keil, Y. Ueda: PASJ **56**, L9 (2004)
8. L. Gallo, Y. Tanaka, Th. Boller, A.C. Fabian et al.: MNRAS (2004) in press
9. R.R. Ross, A.C. Fabian, S. Mineshige: MNRAS **258**, 189 (1992)
10. A.C. Fabian, G. Miniutti, L. Gallo, Th. Boller et al.: MNRAS (2004) in press
11. M. Gierlinski, C. Done: MNRAS **349**, L7 (2004)
12. M.A. Abramowicz, B. Czerny, J.P. Lasota, E. Szuszkiewicz: ApJ. **332**, 646 (1988)
13. S. Mineshige, T. Kawaguchi, M. Takeuchi, K. Hayashida: PASJ **52**, 499 (2000)
14. K. Watarai, T. Mizuno, S. Mineshige: ApJ. **549**, L77 (2001)
15. T. Kawaguchi: ApJ **593**, 69 (2003)

Probing the Magnetic Field at Sub-Parsec Radii in the Accretion Disk of NGC 4258

M. Modjaz[1], J.M. Moran[1], L.J. Greenhill[1], and P.T. Kondratko[1]

Harvard-Smithsonian Center for Astrophysics, 60 Garden Street, Cambridge MA 02138, USA

Abstract. We present an analysis of polarimetric observations of the water vapor masers in NGC 4258 obtained with the GBT at 22 GHz. We do not detect any circular polarization in the spectrum indicative of Zeeman-induced splitting of the maser lines of water. We have improved the 1-σ upper limit estimate on the toroidal component of the magnetic field in the circumnuclear disk of NGC 4258 at a radius of 0.2 pc from 300 mG to 90 mG. We have developed a new method for the analysis of spectra with blended features and derive a 1-σ upper limit of 30 mG on the radial component of the magnetic field at a radius of 0.14 pc. Assuming thermal and magnetic pressure balance, we estimate an upper limit on the mass accretion rate of $\sim 10^{-3.7}$ $M_{\odot}yr^{-1}$. We discuss the ramifications of our results on current accretion theories that have been used to explain low luminosity active galactic nuclei.

1 Introduction

Magnetic fields appear to be important for many aspects of material-inflow and outflow in active galactic nuclei (AGNs). Magnetic fields are thought to provide outward angular momentum transport in the accretion process via the magneto-rotational-instability, with accompanied dissipative heating, allowing further mass-inflow [1,2]. Strong poloidal magnetic fields may thread centrifugal winds, which could carry away angular momentum, while confining and collimating large-scale outflows and jets seen in radio-loud AGNs [3,16]. Furthermore, broad-line region clouds may be constrained by magnetic pressure [22] or accelerated in magnetized winds (e.g., [5]; [4]).

NGC 4258 is a low-luminosity Seyfert II galaxy at a distance of about 7.2 Mpc [14], which harbors water masers. The spatial distribution and line-of-sight velocities of the masers delineate the molecular portion of a thin, Keplerian (better to 1%) accretion disk that is nearly edge-on and slightly warped [17,11]. Its inner radius is approximately 0.14 pc and its outer radius approximately 0.28 pc from the central black hole with $M_{BH} = (3.9 \pm 0.4) \times 10^7 M_{\odot}$ [19]. The masers fall into three groups: a dense cluster of lines near the systemic velocity of the galaxy, which lie close to the line-of-sight to the black hole; and two groups of less densely packed lines offset by $\pm \sim 1000$ km s^{-1}. These high-velocity masers are distributed along a line perpendicular to the line-of-sight at different radii.

ESO Symposia: Growing Black Holes, pp. 296–301, 2005.

2 Measuring Magnetic Fields: the Zeeman Method

The Zeeman technique constitutes the most direct way of obtaining the magnitude and direction of the magnetic field. Magnetic field estimates in accretion disks have been derived from other techniques (e.g., [15]), but they are relatively indirect and model dependent, relying on assumptions of equipartition between thermal and magnetic energy, and adopted values of electron density and temperature at various radii.

Since the water molecule is non-paramagnetic, an external magnetic field couples to the nuclear magnetic moment, giving rise to line emission that has the characteristic Zeeman pattern. Hence, the splitting is much less than the maser linewidth for sub-Gauss magnetic fields, around 10^{-3} or 10^{-4} of the linewidth $\Delta v_{\rm L}$. For a simple Gaussian line profile, the slight frequency separation of the left-circular polarization (LCP) and right-circular polarization (RCP) profiles of the σ components can be detected as an "S" shaped profile in the Stokes V [(LCP − RCP)/2] spectrum. This S profile is proportional to the derivative of the Stokes I [(LCP + RCP)/2] spectrum in the small splitting case. Modeling of the theoretical H_2O Zeeman pattern by e.g. [8] and [23] showed the following relation for circular polarization in the simple LTE case:

$$\frac{V_{\rm max}}{I_{\rm max}} = \frac{A_{\rm F-F'} B_{\rm los}}{\Delta v_{\rm L}} \ , \tag{1}$$

where $V_{\rm max}$ is the maximum of the S curve, $B_{\rm los}$ is the magnetic field along the line-of-sight, and $A_{\rm F-F'}$ is a coefficient that depends on which hyperfine component is assumed to be masing. We adopt $\rm A_{F-F'} = 0.020\ km\ s^{-1}\ G^{-1}$, appropriate for the merger of the three strongest hyperfines as derived by [21] from radiative transfer calculations.

There are two types of maser lines in the spectrum of NGC 4258, which require different treatments to measure the Zeeman effect. For the well-isolated redshifted and blueshifted high-velocity maser lines, the standard S-curve analysis method as outlined above works well. For the systemic features, which are heavily blended in velocity space, we developed a variant of the S-curve method. Our new technique is more appropriate since it does not require the a priori knowledge of the velocity components. In this procedure, we cross correlate the LCP and RCP spectra to determine the net velocity offset. This cross correlation method is based on the assumption that the B field strength and direction remain constant over the emission region, i.e. that the Zeeman-induced velocity shift is constant across the spectrum. Thus, both the *toroidal* component of the B field (via the high-velocity features) can be probed and the *radial* component (via the systemic features).

3 Results

We took eight hours of spectral line data in RCP and LCP on 2003, October 23 with the Robert C. Byrd Green Bank Telescope (GBT)[1] at 22.2 GHz. The

[1] The GBT is operated by the NRAO.

spectrometer had a bandwidth of 200 MHz configured to provide a channel spacing of 0.164 km s^{-1} with its 16384 channels over 200 MHz (2700 km s^{-1}). Our spectrum of NGC 4258 probably constitutes the most sensitive spectrum ever taken, and shows the complete velocity range of water maser emission in NGC 4258 simultaneously.

3.1 Magnetic Field

We did not detect any circular polarization in the spectrum indicative of Zeeman-induced splitting of the maser lines of water. Using the S-curve technique, we calculated a 1-σ upper limit to any circular polarization in the strongest red-shifted high-velocity feature, located at 1303 km s^{-1}, of $< 0.1\%$, which implies that $|B_{\rm los}| < 90$ mG (Fig. 1). Here $B_{\rm los}$ represents the average toroidal magnetic field over the maser emission region of < 0.003 pc at a radial distance of 0.2 pc from the black hole. This result is an improvement of the upper limit of $|B_{\rm los}| < 300$ mG derived by [12] on the 1306 km s^{-1} feature using the same method.

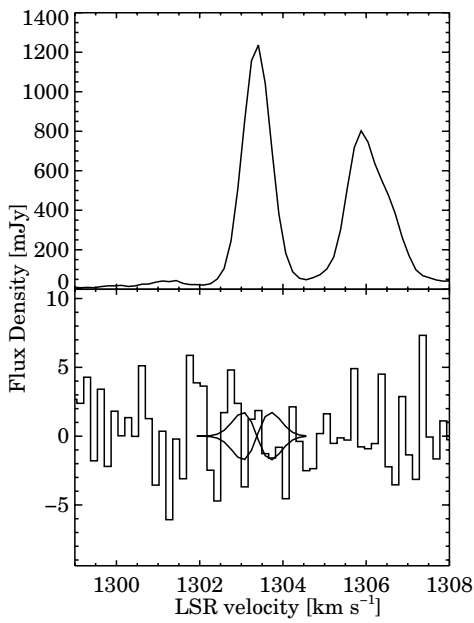

Fig. 1. GBT data of the high-velocity feature at 1303 km s^{-1} , which has a linewidth of 0.79 km s^{-1}, with Zeeman analysis. *Top:* Stokes I [= (LCP + RCP)/2] spectrum. *Bottom:* The Stokes V [= (LCP − RCP)/2] spectrum with superimposed Zeeman S curve for the upper limit of 91 mG on $B_{\rm los}$

We performed the cross correlation method on the systemic features (at $470 - 510$ km s^{-1}, Fig. 2), which are stronger, more numerous, but have broader line widths than the high-velocity features, and estimated a 1-σ upper limit of $|B_{\rm los}| < 30$ mG. Here, $|B_{\rm los}|$ refers to the ordered radial component of the B field, at a distance of 0.14 pc from the central black hole.

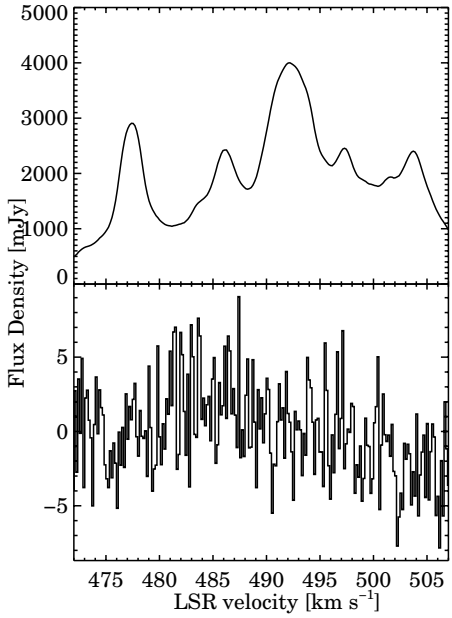

Fig. 2. Similar to Fig. 1, except for the systemic features and no S curve analysis performed. The slow drift in Stokes V (lower panel) is due to imperfect baseline subtraction

We did simulations to estimate the limit on the total magnetic field given our limits on two different components. Although the two components were probed at only slightly different radii, but different locations in the disk, we regard them as representative values for the disk and thus assume they come from the same point. We found that the simulated orientations for the B field would exceed measurements 50% of the time for a $|B_{\rm tot}|$ value of 130 mG. Thus, we adopted the estimate of 130 mG as the upper limit on the total B field.

3.2 Mass Accretion Rate

Relating the thermal pressure at the midplane of the accretion disk to the magnetic pressure, the mass accretion rate can be estimated from the magnetic field

strength. We assumed that magnetic fields provide the kinematic viscosity and thus set $\alpha = C/(1+\beta)$ [20], where α is the standard Shakura-Sunyaev parameter, $\beta = P_{\rm gas}/P_{\rm mag}$ and $C = 0.5 - 0.6$. Adopting a temperature of 400 K in the masing medium [21,23], equipartition between magnetic and thermal pressure ($\beta = 1$), and an upper limit on the total B field of 130 mG, we obtained at the radius of $r = 0.14$ pc a mass accretion rate of (e.g., [7])

$$\dot{M} < 10^{-3.7} \left(\frac{0.6\ \beta}{1+\beta}\right) \left(\frac{B_{\rm tot}}{130\ {\rm mG}}\right)^2 \left(\frac{T_{\rm k}}{400\ {\rm K}}\right)^{1/2} \left(\frac{r}{0.14\ {\rm pc}}\right)^3 \left(\frac{M_{\rm BH}}{3.9\ M_7}\right)^{-1} , \quad (2)$$

in units of $\mathrm{M_\odot yr^{-1}}$, where M_7 stands for 10^7 $\mathrm{M_\odot}$. Local 3D MHD simulations of accretion disks [9] predict $\beta \sim 60$ (and thus $\alpha = 0.01$) and $B_{\rm tot} = \sqrt{16/5}\ B_{\rm radial} < 54$ mG ; if we adopted those values, we obtained at a radius of 0.14 pc, $\dot{M} < 10^{-4.2}$ $\mathrm{M_\odot yr^{-1}}$. The estimate in (2) reflects an improvement by one order of magnitude from the previous estimate of the mass accretion rate in NGC 4258's disk (scaled to the presently estimated and measured values of $M_{\rm BH}$, $T_{\rm k}$ and D) using the same methods [12].

Several accretion models have been proposed to explain the sub-Eddington nature of the central source of NGC 4258 and include the standard thin disk, the Advection-Dominated Accretion Flows (ADAF), and the Jet-Dominated-Accretion Flow (JDAF) model. Figure 3 shows a comparison of the $\dot{M}$ values predicted by the different accretion models for NGC 4258 and includes our upper limit on the mass accretion rate from our measurements in conjunction with statistical considerations and from MHD predictions. Provided accretion has been steady over the time span needed for material to reach the galactic nucleus from the maser disk, our results do not favor the ADAF model, but are consistent with the simple thin disk and the JDAF model.

References

1. S.A. Balbus, J.F. Hawley: ApJ **376**, 214 (1991)
2. S.A. Balbus: Ann. Rev. A&A **41**, 555 (2003)
3. R.D. Blandford, D.G. Payne: MNRAS **199**, 883 (1982)
4. M. Bottorff, K.T. Korista, I. Shlosman, R.D. Blandford: ApJ **479**, 200 (1997)
5. R.T. Emmering, R.D. Blandford, I. Shlosman: ApJ **385**, 460 (1992)
6. H. Falcke, P.L. Biermann: A&A **342**, 49 (1999)
7. J. Frank, A. King, D. Raine: *Accretion Power in Astrophysics*, 3rd edn. (Camridge University Press, Cambridge 2002)
8. D. Fiebig, R. Güsten: A&A **214**, 333
9. J.F. Hawley, C.F. Gammie, S.A. Balbus: ApJ **464**, 690 (1996)
10. C.F. Gammie, R. Narayan, R. Blandford: ApJ **516**, 177 (1999)
11. J.R. Herrnstein, L. J. Greenhill, J. M. Moran: ApJ **468**, L17 (1996)
12. J.R. Herrnstein, J.M. Moran, L.J. Greenhill, E.G. Blackman, P.J. Diamond: ApJ **508**, 243 (1998)
13. J.R. Herrnstein, L.J. Greenhill, J.M. Moran, P.J. Diamond, M. Inoue, N. Nakai, M. Miyoshi: ApJ **497**, L69 (1998)
14. J.R. Herrnstein et al.: Nature **400**, 539 (1999)

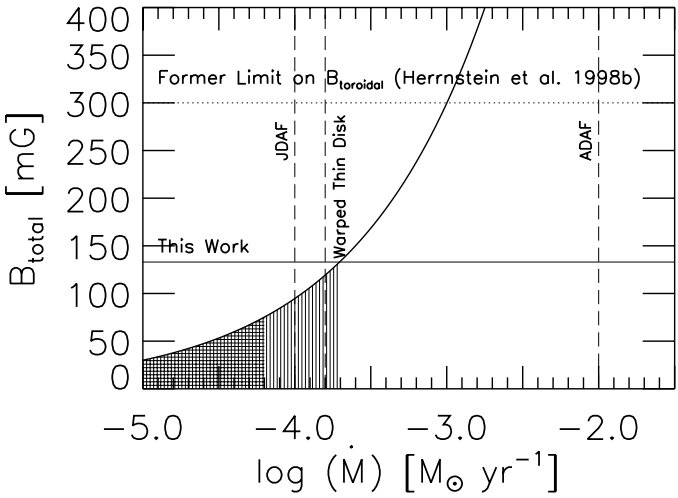

Fig. 3. Expected strength of the total equipartition B field as a function of mass accretion rate at a radius of 0.14 pc for $T_{\rm k} = 400$ K and $\beta = 1$ (Eq. 2). The accretion rates predicted by the jet-disk model of [6] (JDAF), the thin disk and the ADAF models of [10] are shown (*dashed vertical lines*), as well as the upper limit by [12] and that from the present experiment (*horizontal lines*). The *vertically* shaded region shows the constraint on the accretion rate assuming equipartition magnetic fields (i.e., $B_{\rm tot} < 130$ mG, $\beta = 1$ and, thus $\alpha = 0.3$) and the *cross hatch* shaded region depicts the constraint having incorporated the MHD predictions by [9] (i.e., $\rm B_{tot} = \sqrt{16/5}\ B_{radial} < 54$ mG, $\beta = 60$ and, thus $\alpha = 0.01$)

15. D.L. Jones, A.E. Wehrle, D.L. Meier, B.G. Piner: ApJ **534**, 165 (2000)
16. R. Krasnopolsky, Z. Li, R.D. Blandford: ApJ **526**, 631 (1999)
17. J.M. Moran, L.J. Greenhill, J.R. Herrnstein, P. Diamond, M. Miyoshi, N. Nakai, M. Inque. In *Proceedings of the National Academy of Sciences* **92**, 11427 (1995)
18. J.M. Moran, L.J. Greenhill, J.R. Herrnstein: Journal of Astrophysics and Astronomy **20**, 165 (1999)
19. M. Miyoshi, J.M. Moran, J.R. Herrnstein, L.J. Greenhill, N. Nakai, P. Diamond, M. Inoue: Nature **373**, 127 (1995)
20. R. Narayan, R. Mahadevan, E. Quataert: 'Advection-Dominated Accretion around Black Holes'. In: *Theory of Black Hole Accretion Disks*, ed. M.A. Abramowicz, G. Björnsoon, J.E. Pringle (Cambridge University Press, Cambridge 1998) pp. 148-182
21. G.E. Nedoluha, W.D. Watson: ApJ **384**, 185 (1992)
22. M.J. Rees: MNRAS **228**, 47P (1987)
23. W. Vlemmings, P.J. Diamond, H.J. van Langevelde: A&A **375**, L1 (2001)

Mass and Angular Momentum of Sgr A*

B. Aschenbach

Max-Planck-Institut für extraterrestrische Physik, Garching, 85740, Germany

Over the past four years it has become increasingly clear that Sgr A* is not a steady source but is more or less continuously flaring. The first large flare was observed in X-rays on October 26, 2000 with *Chandra* [1]. A second, even brighter X-ray flare went off on October 3, 2002 and was recorded by *XMM-Newton* [2]. In the near infrared (NIR) two bright flares were observed on June 15 and 16, 2003 with the VLT *NACO* [3]. The two NIR flares showed quasi-periodic oscillations with a period of 16.8±2 min which if interpreted as the Kepler period of the last, marginally stable orbit implies a spin of the Sgr A* black hole (BH) of $a = 0.52$ adopting a BH mass of $3.6{\times}10^6 \mathrm{M}_\odot$ [3]. The two X-ray flares did not only show a quasi-period consistent with the NIR period but indicated additional quasi-periods, which fall into four groups [4] (c.f. Fig. 1). In a first attempt we associated these quasi-periods with the three fundamental oscillation modes a particle can have when orbiting a rotating BH representative for an accretion disk [4]. These are the Kepler frequency Ω_K (azimuthal), the radial epicyclic frequency Ω_R (radial) and the vertical epicyclic frequency Ω_V (polar). For the first three quasi-periods a consistent solution was found for $\mathrm{M_{BH}} = 2.72^{+0.12}_{-0.19}{\times}10^6\ \mathrm{M}_\odot$ and $a = 0.9939^{+0.0026}_{-0.0074}$. However, it had to be assumed that the oscillations originate from two different orbit radii, and for the fourth period no satisfactory explanation was found [4].

A closer look reveals that the average frequencies of the first three groups are consistent with a frequency ratio of 1:2:3 (c.f. Fig. 1). Similar to what Abramowicz & Kluźniak [6] have proposed to explain the 3:2 frequency ratio observed in microquasars I suggest that the 3:1 frequency ratio is due to a resonance between Ω_V and Ω_R at some orbital radius r_{31}. The frequency in between is either the beat frequency of Ω_V and Ω_R or the first harmonic of Ω_R. This assumption results in a relation between r_{31} and a. The additional requirement of the existence of a 3:2 resonance of Ω_V and Ω_R at a radius r_{32} and the same a such that r_{31} and r_{32} are commensurable orbits, i.e. $\Omega_\mathrm{V}(\mathrm{r}_{31}) = 3 \times \Omega_\mathrm{R}(\mathrm{r}_{32})$, produces a single solution for $\mathrm{r}_{31} = 1.546$, $\mathrm{r}_{32} = 3.919$ and $a = 0.99616$ [5]. r is measured in units of the gravitational radius. Interestingly, the same values of r_{31} and a can be derived in a totally different way. The inspection of the Boyer-Lindquist functions show that the orbital velocity $\mathrm{v}^{(\Phi)}$ described in the ZAMO-frame is no longer a monotonic function of r for $a > 0.9953$. In a small range of r $\partial \mathrm{v}^{(\Phi)}/\partial \mathrm{r} > 0$. This is a new effect of General Relativity which has been overlooked so far. For $2\pi \frac{\partial \mathrm{v}^{(\Phi)}}{\partial \mathrm{r}} = \Omega_\mathrm{R}$ and $\Omega_\mathrm{V} = 3 \times \Omega_\mathrm{R}$ the same values for r_{31} and a are obtained as above. With r_{31} and a fixed $\mathrm{M_{BH}}$ is given by just the observed frequencies, so that $\mathrm{M_{BH}}/\mathrm{M}_\odot = 4603/\nu_\mathrm{up}$, with ν_up the highest frequency of the triplet in Hz. For Sgr A* $\mathrm{M_{BH}} = (3.28 \pm 0.13) \times 10^6\ \mathrm{M}_\odot$ and $a = 0.99616$ [5]. This

ESO Symposia: Growing Black Holes, pp. 302–303, 2005.

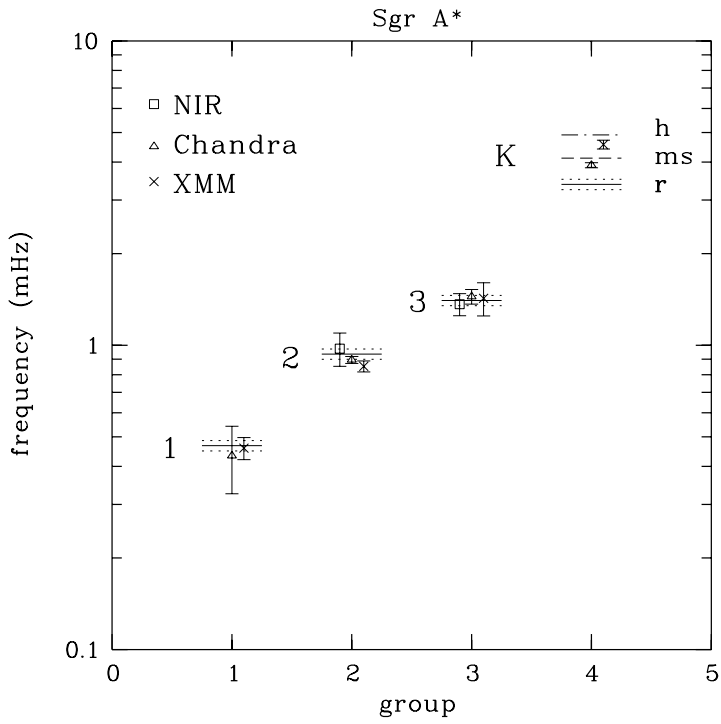

Fig. 1. The four groups of frequencies found in the NIR and X-ray flares of Sgr A*. The solid horizontal lines indicate the best fit to the measured frequencies of groups 1, 2 and 3 for a frequency ratio of 1:2:3; the associated dashed lines correspond to $\pm$ 1σ errors. The best fit Kepler frequencies (K) for the resonance orbit (r_{31}), the marginally stable orbit (ms) and at the event horizon (h) are compared with the two high frequency measurements [4, 5]. Apparently Kepler frequencies for radii below the marginally stable orbit exist, at least over the duration of a flare

value of M_{BH} may be compared with the dynamically determined masses of $M_{BH} = (3.59 \pm 0.59) \times 10^6$ $M_\odot$ [7], $(4.07 \pm 0.62) \times 10^6$ $M_\odot$ [8] and $(3.6 \pm 0.4) \times 10^6$ $M_\odot$ [9]. The latter two measurements are for a distance of 8 kpc to Sgr A*.

References

1. F. K. Baganoff, M. W. Bautz, W. N. Brandt et al.: Nature **413**, 45 (2001)
2. D. Porquet, P. Predehl, B. Aschenbach et al.: A&A **407**, L17 (2003)
3. R. Genzel, R. Schödel, T. Ott et al.: Nature **425**, 934 (2003)
4. B. Aschenbach, N. Grosso, D. Porquet, P. Predehl: A&A **417**, 71 (2004)
5. B. Aschenbach: A&A in press (2004), astro-ph/0406545
6. M. A. Abramowicz & W. Kluźniak: A&A **374**, L19 (2001)
7. F. Eisenhauer, R. Schödel, R. Genzel et al: ApJ **597**, L121 (2003)
8. A. M. Ghez, G. Duchêne, K. Matthews et al.: ApJ **586**, L127 (2003)
9. A. M. Ghez, E. Becklin, G. Duchêne et al.: AN **324**, 527 (2003)

What Triggers the Activity Cycle in Galactic Nuclei?

A. Janiuk[1], B. Czerny[1], and A. Siemiginowska[2]

[1] Copernicus Astronomical Center, 00-716 Warsaw, Poland
[2] Harvard Smithsonian Center for Astrophysics, MA 02138, Cambridge, USA

Abstract. The cyclic activity of AGN may either be caused by the changes of fuel supply to the central engine, or by the processes intrinsic to the accretion disk. Here we consider the latter possibility, assuming that the mean accretion rate is constant, and the periodic changes of the disk luminosity appear due to the instability cycle operating in its inner parts, with possible transition to advective flow (ADAF).

In the regions of partial Hydrogen ionization opacity changes affect the energetic balance of the gas. The limit-cycle oscillations between the hot and cold states of the disk are known to be responsible e.g. for Dwarf Nova eruptions. In order to explain the observed outburst amplitudes of DN, the viscosity parameter has to vary between the disk states: $\alpha_{\rm cold} \ll \alpha_{\rm hot}$. Then the disk can oscillate between the two solutions: small viscosity in quiescence and large viscosity in the outburst.

The changing viscosity parameter in DN disks is supported by the strength of magneto-rotational (MRI) turbulences [2]. Due to the diffusion of magnetic field in the cold disk, the turbulence may die away, while being efficient in the active phase [4]. However, in AGN the situation is different: the magnetic field is always frozen into the gas, even in the cold disk, so we should rather keep $\alpha_{\rm cold} \approx \alpha_{\rm hot}$ [3].

We perform a self-consistency check of the constant α parameterization in AGN: (i) assume a single value of α in both cold and hot states of the disk; (ii) check the strength of MRI: calculate Reynolds numbers in a cold and hot disk, solving the disk vertical structure equations; (iii) confirm that in AGN disks MRI is always efficient, since the Reynolds numbers are above critical; (iv) calculate the time-dependent evolution driven by the ionization instability [6], keeping the constant α parameter.

As a result of the constant α, the oscillations of an AGN disk lead only to a small amplitude flickering, rather than prominent on-off activity cycle. However, below a certain value of the local accretion rate the innermost parts of the disk can evaporate [5] and form the advectively-dominated accretion flow (ADAF). The disk evaporation radius is determined by $R_{\rm ADAF} = 1.9\dot{m}^{-2}\alpha_{0.1}^4 R_{\rm Schw}$ [1].

Temporal variations of the local accretion rate, induced by the instability cycle, may result in the inner disk evaporation. The inner flow is radiatively inefficient, since the bulk of energy dissipated in the disk is advected into the black hole. Thus the ADAF does not contribute to the disk luminosity. In the time-dependent calculations we therefore include the transition into ADAF, still

ESO Symposia: Growing Black Holes, pp. 304–305, 2005.

keeping a constant α parameter. This is sufficient to explain the intermittent activity of AGN, both in terms of amplitudes and timescales. The latter depend quadratically on the black hole mass.

Conclusions

- Instability of the accretion disk due to the partial hydrogen ionization leads to periodic changes of the thermal state of the disk and intermittent activity of the source.
- Parameterization of viscosity dependent on the disk state, $\alpha_{\rm cold} << \alpha_{\rm hot}$, is justified only in case of stellar mass accreting objects (DN, SXTs).
- In AGN the magneto-rotational turbulences are very efficient mechanism of angular momentum transport even in the cold disk. Therefore we can adopt $\alpha_{\rm cold} = \alpha_{\rm hot}$.
- Large amplitudes of luminosity variations in AGN that can explain their intermittent activity are obtained if we take into account evaporation of the inner disk and transition to ADAF.

References

1. Abramowicz M.A., et al., ApJ, **438**, L37 (1995)
2. Balbus S.A., Hawley J.F., ApJ, **376**, 214 (1991)
3. Janiuk A., et al., ApJ, **602**, 595 (2004)
4. Menou K., Quataert E., ApJ, **552**, 204 (2001)
5. Meyer F., Meyer-Hofmeister E., A&A, **392**, L5 (2002)
6. Siemiginowska A., et al., ApJ, **458**, 491 (1996)

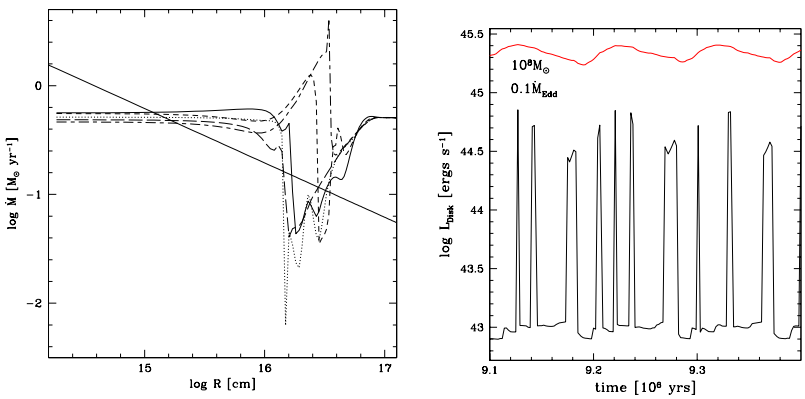

Fig. 1. Left: The accretion rate variations during the instability cycle. The disk evaporation occurs when $\dot{M}$ drops below the critical value (straight line). **Right:** The exemplary disk lightcurve for constant $\alpha = 0.1$, $M_{\rm BH} = 10^8 M_\odot$. The minima are much deeper when we allow for the inner disk evaporation; resulting sharp outbursts are compared here with small flickering (*upper line*) produced when no evaporation occurs

A Simple Test for two Accretion Modes in AGN

S. Jester

Fermilab, MS 127, PO Box 500, Batavia IL, 60510, USA

Abstract. By analogy to the different accretion states observed in black-hole X-ray binaries (BHXBs), it appears plausible that accretion disks in active galactic nuclei (AGN) undergo a state transition between a radiatively efficient and inefficient accretion flow. If the radiative efficiency changes at some critical accretion rate, there will be a change in the distribution of black hole masses and bolometric luminosities at the corresponding transition luminosity. To test this prediction, I consider the joint distribution of AGN black hole masses and bolometric luminosities for a sample taken from the literature. The small number of objects with low Eddington-scaled accretion rates $\dot{m} < 0.01$ and black hole masses $M_{\rm BH} < 10^9\,M_\odot$ constitutes tentative evidence for the existence of such a transition in AGN. Selection effects, in particular those associated with flux-limited samples, systematically exclude objects in particular regions of the $(M_\bullet, L_{\rm bol})$ plane. Therefore, they require particular attention in the analysis of distributions of black hole mass, bolometric luminosity, and derived quantities like the accretion rate. I suggest further observational tests of the BHXB-AGN unification scheme which are based on the jet domination of the energy output of BHXBs in the *hard* state, and on the possible equivalence of BHXB in the *very high* (or *steep power-law*) state showing ejections and efficiently accreting quasars and radio galaxies with powerful radio jets.

Abstract of a paper submitted to the Astrophysical Journal

ESO Symposia: Growing Black Holes, p. 306, 2005.

Super-Eddington Active Galctic Nuclei: Spectral Modeling and Black Hole Growth

T. Kawaguchi

National Astronomical Observatory of Japan, Mitaka, Tokyo, Japan

1 Modeling Broadband Spectral Distribution of Narrow-Line Seyfert 1 Galaxies

Among Active Galactic Nuclei (AGN), narrow line Seyfert 1 galaxies (NLS1s) are supposed to have high accretion rates [1,2]. The gas accretion rate $\dot{M}$ for those objects is expected to be larger than $10\,L_{\rm Edd}/c^2$, where $L_{\rm Edd}$ is the Eddington luminosity.

We have explored some physical aspects that become important when an accretion rate becomes super-Eddington; electron scattering (in opacity and Comptonization), relativistic effect (gravitational and transverse Doppler redshift) and self-gravity of accretion disks. It is found that the outer edge of the non self-gravitating part of the disc radiates optical/UV continuum emission when $\dot{M} \gg L_{\rm Edd}/c^2$ [3]. In other words, outer region, where optical continuum is emitted, must be solved with the effect of self-gravity of the disks.

Fig. 1 presents an example of successful fits [4]. We are also trying to fit another NLS1 with our own XMM observational data [5]. Currently, these models are the only ones that explain broadband spectral energy distribution of NLS1s, in our best knowledge. Near-IR emission is dominated by radiation from a dusty torus existing at $r > 3\times10^5 R_{\rm Sch}$, where $R_{\rm Sch}$ is the Schwarzschild radius. Clouds in the broad line region are apart from the central black hole (BH) by $\sim 1.4 \times 10^5 R_{\rm Sch}$ (using a relation in [6]), thus they are apparently located between the self-gravitating disk and the dusty torus.

2 Growth of Massive Black Holes by Super-Eddington Accretion

NLS1s and Narrow-Line quasars (NLQs) seem to amount to $\sim 10-30\%$ of AGNs in the local universe.

In general, the duration (or the sum of multiple episodic phases) of an AGN is thought to be $\sim 10^8$ yr from several independent arguments [7]. Then, let us simply assume that each NLS1 (or NLQ) has a duration of $\sim (1-3)\times10^7$yr.

Together with their average accretion rate ($\sim 100 L_{\rm Edd}/c^2$; [3]), we argue that a BH growth by factor of $8-800$ happens in these super-Eddington accretion phase of AGNs [8]. Moreover, there is a possible, systematic underestimation of accretion rates (in the Eddington unit) due to an overestimation of BH mass by massive accretion discs for super-Eddington objects [4]. If it is true, the factor of

ESO Symposia: Growing Black Holes, pp. 307–308, 2005.

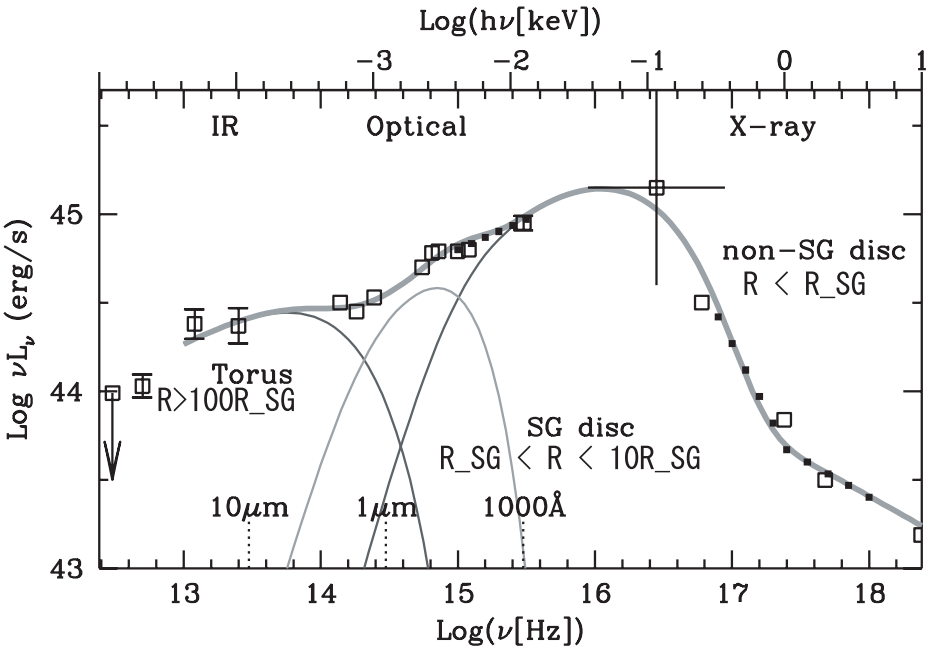

Fig. 1. Spectral modeling of Ton S 180 [4], with an inner non self-gravitating disk ("non-SG disc"; at $r < R_{\rm SG}$), an outer self-gravitating disk ("SG disc"; at $R_{\rm SG} < r < 10R_{\rm SG}$), and dusty torus (at $r < 100R_{\rm SG}$). Here, $R_{\rm SG}$ stands for the outer edge of the non self-gravitating disk, and is about $3000R_{\rm Sch}$ ($= 0.002$pc).

BH growth above may be larger by order(s) of magnitude. In contrast, the growth factor expected in sub-Eddington phase is only ~ 2. Therefore, the cosmic BH growth by accretion is likely dominated by super-Eddington phase, rather than sub-Eddington phase which is the majority among AGNs.

This analysis is based on the fraction and the average accretion rate of NLS1s and NLQs obtained for $z < 0.5$. If those numbers are larger at higher redshift (where BHs were probably less grown), super-Eddington accretion would be even more important in the context of cosmic BH growth history.

References

1. N. Brandt, Th. Boller: Astronomische Nachrichten, **319**, 163 (1998)
2. S. Mineshige, T. Kawaguchi, M. Takeuchi, & K. Hayashida: PASJ, **52**, 499 (2000)
3. T. Kawaguchi: ApJ, **593**, 69 (2003)
4. T. Kawaguchi, A. Pierens, J.M. Huré: A&A, **415**, 47 (2004)
5. T. Kawaguchi, C. Matsumoto, K.M. Leighly, in preparation
6. S. Kaspi, P.S. Smith, H. Netzer et al.: ApJ, **533**, 631 (2000)
7. P. Martini: in *Coevolution of Black Holes and Galaxies, from the Carnegie Observatories Centennial Symposia* ed. by L. Ho (CUP, Cambridge) p. 170 (2004)
8. T. Kawaguchi, K. Aoki, K. Ohta, S. Collin: A&A, **420**, L23 (2004)

Global Three-Dimensional MHD Simulations of Co-existence of Hard State and Soft State Disks in Black Hole Accretion Flows

M. Machida[1], K. Nakamura[2], K. Ohsuga[3], and R. Matsumoto[4]

[1] Division of Theoretical Astronomy, NAOJ, Mitaka, Tokyo, 181-8858, Japan
[2] Dept. of Sci., Matsue National College of Thech., Matsue, Shimane 690-8518, Japan
[3] Dept. of Phys., Rikkyo Univ.,Toshima-ku, Tokyo 171-8501, Japan
[4] Dept. of Phys., Chiba University, Chiba, Chiba 263-8522, Japan

Abstract. We present the results of 3D global resistive magnetohydrodynamic (MHD) simulations of black hole accretion flows. General relativistic effects are simulated by using the pseudo-Newtonian potential. We included optically thin bremsstrahlung cooling to simulate the transition from low state to high state. We found that the outer disk cooled down by radiative cooling becomes dominated by magnetic pressure. Hard-state disks in the inner region co-exists with soft-state disks in the outer region. We computed radiation spectrum of the disk by including synchrotron emission and compton cooling, and reproduced the observed X-ray spectrum of black hole candidates.

1 Introduction

State transitions are obserbed in galactic black hole candidates such as Cyg X-1 and GRS 1915+105. The low state is characterized by violent X-ray fluctuations and by the absence of soft black body component. The spectrum of the high state is composed of a blackbody like component and a hard tail. Now it is considered that the low state correnspods to optically thin advection dominated accretion flows (ADAF) and the high state corresponds to the standard disk. Although the cause of these state transitions is not clear, radiative cooling should play essential role in the low-high state transition. We study the state transition from low state to high state by global 3D MHD simulations.

2 Numerical Model and Results

The initial state is an equilibrium torus threaded by weak toroidal magnetic field. This model is the same as model L in [1]. After the accretion disk becomes quasi-steady, we include optically thin bremsstrahlung cooling term in the energy equation. We assume that the bremsstrahlung cooling is negligible in the coronal region where the density is lower than $\rho_{\rm crit}$.

Figures 1a and 1b show the logarithmic temperature distribution averaged in azimuthal direcition at $T = 24450$ and at $T = 33900$. Since the gas density in the outer region is larger than that in the inner region, the transition takes place from the outer region of the disk. As the disk shrinks in the vertical direction,

ESO Symposia: Growing Black Holes, pp. 309–310, 2005.

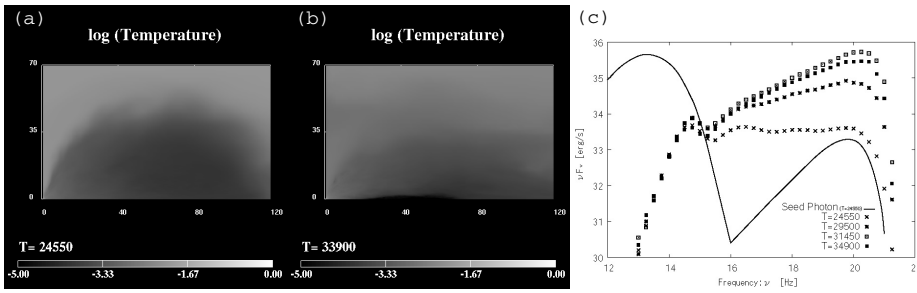

Fig. 1. Logarithmic temperature distribution averaged in azimuthal direction before (a) and after (b) the transition to a cool disk. (c) Spectral energy density computed from numerical results.

the magnetic pressure increases because the magnetic field is frozen to plasma. The equatorial plasma β ($\beta = P_{\rm gas}/P_{\rm mag}$) at the outer region becomes as small as $\beta \sim 0.1$. Vertical contraction of the disk stops when the magnetic pressure dominates in the disk. Since turbulence is suppressed in low-β region, mass accretion rate decreases. Thus, the inner region of the disk still stays in optically thin, hot ADAF.

Figure 1c shows the spectral energy density (SED) obtained by post-processing numerical results. As seed photons, we included thermal synchrotron emission and free-free emission. 3D monte Carlo code is used to take into account the inverse Compton scattering. Solid curve shows the distribution of seed photon at $T = 24550$. Symbols show the numerical results at $T = 24450$, 29000, 31450 and 34900. X-ray luminosity increases as the surface density increases. Even after the onset of transition in the outer region, the SED stays in X-ray hard state because hot inner disk and corona co-exsists with the cool disk.

3 Summary and Discussion

We presented the results of three-dimensional MHD simulation of an optically thin accretion disk including optically thin cooling. When the mass accretion rate exceeds the threshold of the onset of thermal instability, the disk temperature decreases until the enhanced magnetic pressure supports the disk. We expect that the magnetic field enhanced in the outer cool disk will buoyantly escape from the disk and create magnetically active disk corona. Observation of XTE J1550-564 indicates that low state disk makes transition to the high state disk via intermediate very high state [2]. The intermediate state is composed of an optically thick disk and a surrounding hot corona.

References

1. M. Machida, K. Nakamura, R. Matsumoto: PASJ, **56**, 671, (2004)
2. A. Kubota, C. Done: MNRAS, **353**, 980 (2004)

Super-Eddington Luminosity from Fragmented Accretion Disks

F. Meyer

Max-Planck-Institut für Astrophysik, Garching, Germany

Abstract. In order to resolve the problem of apparent super-Eddington luminosities from accretion disks around black holes in super-luminous X-ray sources we propose that in strong magnetic fields under radiation pressure such disks fragment into individual magnetically aligned columns of cool disk gas and that radiation escapes through the gaps between them at super-Eddington luminosity.

1 Super-Eddington radiation from accretion disks

In order not to exceed the Eddington limit the ultra-luminous X-ray sources (ULXs) would have to be of intermediate mass, 50-100 $M_{\odot}$. But the observed disk temperatures are too high for such black hole masses [1]. Various suggestions have been made to resolve this problem.

Radiation pressure supported disks in magnetic fields are unstable against a "photon-bubble instability", in which over-stable oscillations enhance vertical energy transport [2]. In a non-linear version such radiation driven inhomogeneities can allow the escaping flux to exceed the Eddington limit and are suggested as resolution of the ULX problem [3,4]. We here suggest that radiation pressure leads to a complete fragmentation of accretion disks in magnetic fields around black holes and that radiation escapes through the gaps between fragments at super-Eddington luminosity [5]. Essential for the gap formation is the heating in the overlying disk corona into which gas of too low a density evaporates.

2 Model

If magnetic pressure exceeds gas pressure the magneto-rotational instability [6] is quenched. But there is still heating of disk gas: Coronal magnetic fields penetrating the disk are sheared by Kepler motion of their foot points in the disk. This energy input is dissipated in the corona by reconnection instabilities. Dynamical reconnection in a low gas pressure coronal plasma predominantly accelerates ions in collision-free shocks. At low density the coronal plasma radiates inefficiently. However the ions penetrate along field lines into the accretion disk to high optical depth. There they release their energy and heat the accretion disk. Radiation transports this energy to the surface where it is radiated away. For high accretion rate or a rapidly spinning black hole and close to the central accretor the energy input is high. As a result radiation pressure dominates over gas pressure and expands the disk against gravity in the vertical direction.

ESO Symposia: Growing Black Holes, pp. 311–312, 2005.

If now in an originally homogeneous disk one of the magnetic columns accidentally has a smaller density than its neighbors radiation will preferentially choose this pathway for escape thereby expanding it and lifting its upper part into a density regime for which evaporation into the corona occurs by the predominance of heating over cooling at low density. As a result the column looses mass and the process accelerates until the whole column is evaporated and a gap has formed. The radiation then escapes rather sidewise from the remaining columns and can easily surpass the Eddington luminosity.

An essential element in this fragmentation is thus that the density at the transition between disk and corona is determined by the coronal heating. At higher density gas is able to cool efficiently and remain in the disk. At lower density gas is heated up to coronal temperatures.

3 Discussion

This fragmentation process eliminates the Lightman-Eardly instability of the radiation pressure supported disk theoretically expected, but observationally not evident. Further a blobby disk suggested here is an ideal configuration for modeling quasi-periodic oscillations at near Kepler frequencies and has the potential to resolve many other problems.

In particular it may lead to understanding of the so called very high state in which Comptonization of disk photons by coronal electrons appears to produce a power law rather than a disk black body spectrum [7]. Mass equilibrium between disk and corona is reached when the rate of coronal ions stopped in the blobby disk equals the rate at which blob mass enters the corona by shearing away the blob skins through the radiative flux in the gaps. At higher accretion rate and luminosity more mass will reside in the corona until at very high rates coronal density is high enough to efficiently heat coronal electrons by electron ion collisions and radiate large parts of the coronal energy by Comptonizing cool disk photons rather than through disk radiation directly.

References

1. K. Makishima, A. Kubota et al.: ApJ, **535**, 632 (2000)
2. C.F. Gammie: MNRAS, **(**297), 929 (1998)
3. M.C. Begelman: ApJ, **551**, 897 (2000)
4. M.C. Begelman: ApJ, **568**, L97 (2002)
5. F. Meyer: In: *Stellar-Mass, Intermediate-Mass, and Supermassive Black Holes*, Conference Kyoto 2003, ed. by K. Makishima, S. Mineshige, Progress of Theor. Phys., Suppl. in press (2004)
6. S.A. Balbus, J.F. Hawley: Rev.Mod.Phys., **70**, 1 (1998)
7. A. Kubota, C. Done: MNRAS, **353**, 980 (2004)

Oscillations of Thick Accretion Disks Around Black Holes

E. Rubio-Herrera and William H. Lee

Instituto de Astronomía, UNAM. Apartado Postal 70–264
C.P. 04510 México D.F. México.

Abstract. We present a numerical study of the response of a thick accretion disk to a localized, external perturbation with the aim of exciting internal modes of oscillation. We find that the perturbations efficiently excite global modes recently identified as acoustic p–modes, and closely related to the epicyclic oscillations of test particles. The two strongest modes occur at eigenfrequencies which are in a 3:2 ratio. We have assumed a constant specific angular momenutm distribution within the disk. Our models are in principle scale–free and can be used to simulate accretion tori around stellar or super massive black holes.

1 Introduction and description of this work

Observations in the X–ray band have revealed millisecond oscillations in systems containing neutron stars and black hole candidates surrounded by an accretion disk[5]. In four of these sources, probably containing a black hole (BH), there are two peaks (kHz Quasi Periodic Oscillations) whose frequencies are in a 3:2 ratio. This supports the conjecture[1] that a resonance mechanism is responsible for this phenomenon. It has also been suggested[4] that this 3:2 ratio could be related to acoustic p–modes within the torus, excited by a global external perturbation. We show here that this frequency ratio could be produced by a localized periodical perturbation.

To study these oscillations, we consider pressure supported disks in hydrostatic equilibrium. Using a polytropic EOS $P = K\rho^{\gamma}$, the Paczyński–Wiita[3] pseudo Newtonian potential and a constant specific angular momentum distribution, we have the following equation for the profile of the torus:

$$\frac{\gamma}{\gamma - 1}\frac{P}{\rho} = \frac{-GM_{bh}}{R - r_g} + \int \frac{l(r')^2}{2r'^3}dr + \Phi_0. \tag{1}$$

For the simulations, we use Smoothed Particle Hydrodynamics[2]. The initial conditions are generated by distributing N fluid elements over the torus volume and relaxing them for several dynamical times to obtain a distribution close to equilibrium. Our dynamical calculations are performed by introducing perturbations of the form:

$$a_{pert} = -\eta a_g \exp\left(\frac{r_o - r}{\delta r}\right)\sin(2\pi\nu_s t). \tag{2}$$

ESO Symposia: Growing Black Holes, pp. 313–314, 2005.

Here a_g is the acceleration due to gravity, r_o is the outer edge of the torus and $\eta \ll 1$. The analysis of the data is carrried out by performing the Fourier decomposition of the main hydrodynamical variables as function of time (disk's center, the maximum and mean densities, and the various total energies).

2 Results and conclusions

The Fourier analysis of the total kinetic and potential energies in the torus is shown in Fig. 1 for a case using a black hole of $2.5M_\odot$ and a perturbation with a frequency $\nu_s = 200$ Hz, which is clearly seen as the narrow peak in Fig.1. Two more peaks are observed at $\nu_1 \approx 300$ Hz, related with the radial epicyclic frecuency (which for a test particle at the same radius is $\kappa = 426$ Hz); and $\nu_2 \approx 450$ Hz, related to the sequence 2:3:4:..., of acoustic p–modes. From these results we conclude that: (1) global modes of oscillation in thick tori [6] can be efficiently excited by a localized perturbation, and, (2) the most strongly excited mode is the one that corresponds to the radial epicyclic frequency, shifted to lower frequencies because of the finite extent of the torus.

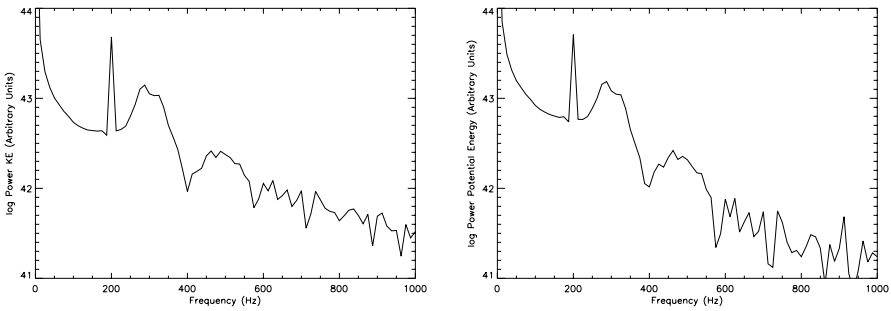

Fig. 1. FFT spectra for the kinetic (left) and potential energy (right). In each panel, the first peak corresponds to the perturbation introduced at 200 Hz, the second to the modified epicyclic frequency, and the third one to 1.5 times the second.

It is a pleasure to acknowledge suggestions and discussions with L. Rezzolla. Financial support for this work was provided by CONACyT (36632E) and the I.A./UNAM Graduate Office.

References

1. Abramowicz, M., Kluźniak, W., A&A. **374**, L19 (2001)
2. Monaghan, J. ARA&A. **30**, 543 (1992)
3. Paczyński, B., Wiita, J., A&A. **88**, 23 (1980)
4. Rezzolla, L., Yoshida, S., Zanotti, O., MNRAS. **344**, 978 (2003)
5. van der Klis, M. ARA&A **38**, 717 (2000)
6. Zanotti, O., Rezzolla, L., Font, J., MNRAS **341**, 832 (2003)

AGN Outbursts and Accretion Disks

A. Siemiginowska[1], A. Janiuk[2], and B. Czerny[2]

[1] Center for Astrophysics, Cambridge MA, 02138, USA
[2] Copernicus Astronomical Center, Warsaw, Poland

Abstract. We discuss the AGN intermittent activity. Accretion onto a supermassive black hole (SMBH) is generally accepted as the basis of AGN activity, however there are still many questions about properties of the accretion flow as well as the fuel supply to the innermost regions of the host galaxy. There is growing evidence that the AGN activity could be intermittent, however the origin of this intermittency has not been identified. Several large scale processes have been discussed including mergers and feedback. However, processes related directly to the accretion disk can influence AGN activity as well. Here we link evolution of the accretion disk to AGN activity and describe different stages of AGN activity and corresponding timescales. This evolution scenario is decoupled from any external fuel supply, although it requires a continuous fuel supply into an accretion region. The amount of radiative energy and the duration of outbursts depend on the model parameters. [1]

1 Observational Motivation and Model

Recent *Chandra* observations of X-ray clusters suggest that repetition timescales of AGN outbursts should be of order $10^5 - 10^7$ yrs [2][3]. The Perseus cluster data imply that the central AGN should have about 270 outbursts over $2{\times}10^9$ years and the total energy supply to the cluster by these outbursts is equal to $\sim 10^{60}$ ergs [2].

Other observational evidence for intermittency comes from the morphology of large double-double radio galaxies that indicates multiple phases of the nuclear activity [10]. Some Compact Symmetric Objects have measured expansion velocities pointing to their young age ($< 10^4$yrs) while their large scale radio emission indicates a relic of past activity [1]. Stawarz et al[9] suggested recently that also large scale X-ray jets may require intermittent supply of relativistic particles and possibly AGN intermittency on timescales of 10^5 years.

The origin of the intermittent activity has not been identified thus far. Mergers, or feedback between the activity of the central AGN and a fuel supply, are linked to processes outside of the nucleus. We consider a process directly related to the accretion flow in the close vicinity of a SMBH. We assume a non-steady accretion and study effects of thermal-viscous instabilities in the disk [8]. Such instabilities can provide a large amplitude variability ($\Delta L \sim 10^4$-10^5) on timescales of 10^4-10^8yrs depending on the SMBH mass[4]. However, large outbursts occur

[1] This work was supported in part by NASA grants GO-09820.01-A, NNG04GF98G and NAS8-39073.

ESO Symposia: Growing Black Holes, pp. 315–316, 2005.

when the viscosity is drastically reduced in the quiescence. The MHD simulations suggest that the change in the viscosity between an outburst and quiescence is not so significant [6][5] [7].

The key new feature of the model considered here is a transition to a low efficiency accretion state in the quiescence [5]. When the local accretion rate drops below the critical value (left in Fig.1) the disk evaporates, and the radiation efficiency of the accretion flow is dramatically reduced [5]. Large amplitude luminosity variations for $10^8 M_\odot$ SMBH occur on the timescale of $\sim 10^4$yrs as indicated in Fig.1 (right).

We conclude that accretion disk instability can cause a quasi-periodic AGN variability. The variability timescales scale with the BH mass and are of the order of the observed repetition timescales. Energy of the outbursts is also consistent with the observations. Detailed evolution model needs to be developed to properly calculate the evolution of the evaporated disk.

References

1. Baum, S. A. et al 1990, A&A, 232, 19
2. Fabian, A. C. et al 2003, MNRAS, 344, L43
3. Forman, W., et al. 2004, astro-ph/0312576
4. Hatziminaoglou, E., Siemiginowska, A., & Elvis, M. 2001, ApJ, 547, 90
5. Janiuk, A., Czerny,B., Siemiginowska, & Szczerba, 2004, ApJ, 602, 595
6. Janiuk, A., Czerny, B. & Siemiginowska, A., 2004, this Proceedings
7. Menou, K. & Quataert, E. 2001, ApJL, 562, L137
8. Siemiginowska, A., Czerny, B., & Kostyunin, V. 1996, ApJ, 458, 491
9. Stawarz, Ł., Sikora, M., Ostrowski, M., & Begelman, M. C. 2004, ApJ, 608, 95
10. Subrahmanyan, R., Saripalli, L., & Hunstead, R. W. 1996, MNRAS 279, 257

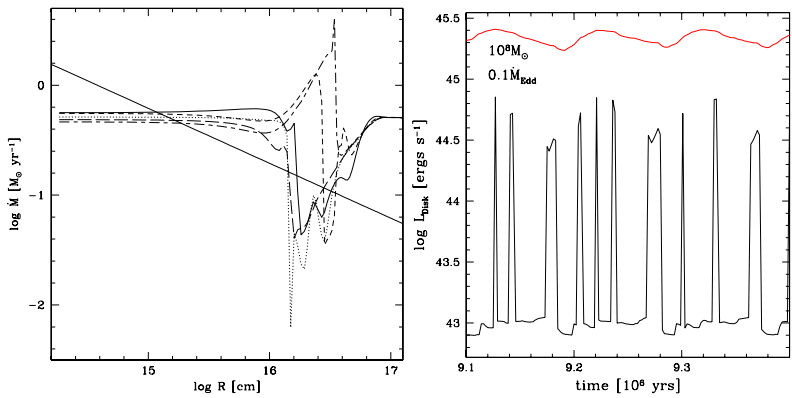

Fig. 1. Left: The local accretion rate during a disk evolution cycle The thick solid line marks the critical accretion rate below which the disk is evaporated. **Right:** The disk lightcurve. The upper curve shows flickering of the disk luminosity of the evolving standard disk with no evaporation. The lower curve shows sharp outbursts for the disk with the evaporated inner part in quiescence. $M_{\rm BH} = 10^8 M_\odot$, $\alpha = 0.1$, $\dot{M} = 0.1\dot{M}_{\rm Edd}$.

Shocks Near a Black Hole of an Accretion-Powered AGN

S. Tsuruta and K. Fukumura

Montana State University, Bozeman MT 59717, USA

1 Introduction

A realistic model of the AGN central engine probably should include the effects of the magnetic field. The black hole magnetosphere is studied first by Blandford and Znajek 1977 [1] in the context of winds and jets from radio-loud AGNs. The work has been extended to magnetospheric physics of accreting AGNs by various authors [2–6]. In this case, plasma particles will be *frozen-in* to the magnetic field lines, and hence the accreting fluid will fall onto the black hole from regions above the equatorial plane along the field lines (see, e.g., Figure 1 of Ref. [6] and Figure 2 of Ref. [5]). Then, magnetohydrodynamics (MHD) will become important to describe the motion of the particles associated with the background field. Recently the resulting relativistic MHD shocks were explored by our group [5]. In general, the MHD shocks can be hydro-dominated or magneto-dominated [4]. Obviously the MHD case is, however, very complicated. Owing to these complexities, it was not straightforward for us to study the exact global shock-included accreting MHD flow solutions further in detail in a wider parameter/solution space [5]. Therefore, in our most recent paper [7], as a starting point, we investigated the hydrodynamic limit, which should be valid in the case of small magnetization. Our model should apply to the hydro-dominated shocks where the magnetic field does not make a significant contribution to the properties of the shocks under a weak field limit. Here we briefly report on our findings. Further details are found in Fukumura and Tsuruta [7].

One-dimensional (1D), hot accretion flows around a black hole, generally treated as ideal hydrodynamical fluid, have been investigated by various authors. In the case of isothermal shocks, the postshock fluid can lose substantial energy and entropy across the shock while the fluid temperature is continuous across the shock location. Lu and Yuan [8] examined the isothermal shock formation in one-dimensional (1D) adiabatic hot flows in the Kerr geometry, for various flow parameters including black hole rotation. In our paper [7] we investigated the geometrical effects by extending the work by Lu and Yuan [8] on standing isothermal shock formation in 1D adiabatic flows in the equatorial plane, to two dimensional (2D) calculations for flows above the equatorial plane.

2 Methods

The isothermal shock jump conditions as well as the regularity condition, previously developed in the past literature for one-dimensional (1D) flows in the equa-

ESO Symposia: Growing Black Holes, pp. 317–318, 2005.

torial plane [8], are extended to two-dimensional (2D), non-equatorial flows. The basic hydrodynamic equations with these conditions are self-consistently solved in the context of general relativity to explore the formation of stable isothermal shocks.

3 Results and Concluding Remarks

Our results will offer the possibility of a high energy source in various broad regions (0 degrees $< \theta_{sh} <$ 90 degrees) above the disk plane. (θ_{sh} is the angle from the polar axis toward the equatorial plane.) However, we find that the strongest shocks, with high Mach number ratio M_1/M_2 with large E_{sh} (shock-induced release energy), should develop near the equator (large θ_{sh}), although the quasi-polar shock (small θ_{sh}) is also possible. (Here subscripts 1 and 2 refer to the pre and post shock quantity.) We find no shocks in the polar region (e.g., $\theta_{sh} <\sim 5$ degrees) when the preshock fluid energy is relatively large, although the shock-free accretion is physically allowed. The magnitude of the energy released from the shock roughly increases as the shock location gets closer towards the black hole, as already found by 1D studies [8]. In addition, however, we further find, from our 2D calculations, that E_{sh} greatly depends, not only on the fluid energy E_1 and angular momentum ℓ, but also on *the angle of the shock location* θ_{sh}. The average shock strength (thus energy release) tends to be weaker towards the polar region.

We found that strong shocks are formed in various locations above the equatorial plane especially around a rapidly-rotating black hole with the prograde flows (rather than a Schwarzschild black hole), but the retrograde flows develop weaker shocks.

One of our major motivations was to explore the possibility that shocks produced in such flows act as the radiation source for some reprocessed features, such as the iron fluorescent lines, which are observed from some AGNs [9]. It is generally considered that a hot illuminating source *above* the cooler disk is required, to produce such features. Sufficient energy dissipation we found across the shock in the hot non-equatorial flows above the cooler accretion disk may offer an attractive candidate for such an illuminating source.

References

1. R.D. Blandford, R.L. Znajek: MNRAS **179**, 433 (1977)
2. E.S. Phinney: Ph.D. Thesis, Cambridge University, Cambridge, UK (1983)
3. M. Takahashi, S. Nitta, Y. Tatematsu, A. Tomimatsu: ApJ **363**, 206 (1990)
4. M. Takahashi: ApJ **570**, 264 (2002)
5. M. Takahashi, D. Rilett, K. Fukumura, S. Tsuruta: ApJ **572**, 950 (2002); also Rilett et al. (2004) in preparation.
6. A. Tomimatsu, M. Takahashi: ApJ **552**, 710 (2001)
7. K. Fukumura, S. Tsuruta: ApJ **611**, 964-976 (2004) (Astro-ph/0405269)
8. J.-F. Lu, F. Yuan, F. 1998, MNRAS **295**, 66 (1998)
9. K. Nandra, K.A. Pounds: MNRAS **268**, 405 (1994)

The Art and Science of Black Hole Mergers

B.F. Schutz[1,2]

[1] Max Planck Institute for Gravitational Physics (Albert Einstein Institute), 14476 Potsdam Germany
[2] Department of Physics and Astronomy, Cardiff University, Wales

Abstract. The merger of two black holes is one of the most extraordinary events in the natural world. Made of pure gravity, the holes combine to form a single hole, emitting a strong burst of gravitational radiation. Ground-based detectors are currently searching for such bursts from holes formed in the evolution of binary stars, and indeed the very first gravitational wave event detected may well be a black-hole merger. The space-based LISA detector is being designed to search for such bursts from merging massive black holes in the centers of galaxies, events that would emit many thousands of solar masses of pure gravitational wave energy over a period of only a few minutes. To assist gravitational wave astronomers in their searches, and to be in a position to understand the details of what they see, numerical relativists are performing supercomputer simulations of these events. I review here the state of the art of these simulations, what we have learned from them so far, and what challenges remain before we have a full prediction of the waveforms to be expected from these events.

1 Black-hole coalescence systems

Black holes are the ultimate in strong gravity, and the details of their merging require general relativity for any kind of even approximate description. Nevertheless, it is one of the remarkable consequences of general relativity that, during the orbital phase before coalescence, the black holes follow orbits that are described to first order by Newtonian gravity: their interaction when separated by a significant distance does not reflect the enormously strong gravity inside and near them. Only when they come within a few tens of gravitational radii do we require full general relativity to describe the dynamics.

Before that, the post-Newtonian approximation – an asymptotic approximation to general relativity valid for small orbital velocity ($v/c \ll 1$) in gravitationally bound systems – provides a systematic approach to studying the orbital inspiral phase, where orbits shrink and lose eccentricity through the radiation of energy and angular momentum in gravitational waves.[1] The classic test of gravitational wave theory, the Hulse-Taylor binary neutron-star system, is very accurately described by such an approximation.[2]

The gravitational radiation emitted by orbiting black holes comes out at multiples of the orbital frequency $f_{\rm orb}$, starting at $f_{\rm gw} = 2f_{\rm orb}$. Higher harmonics are important only if the orbit is highly eccentric. Other frequencies, including $f_{\rm orb}$ itself, can appear in the spectrum from the coupling of black-hole spins to the orbital angular momentum and to each other, but this is significant only

ESO Symposia: Growing Black Holes, pp. 321–332, 2005.

when the holes are very close to one another. When they are well separated, the orbital frequency is the Newtonian one,

$$f_{\rm orb} = \frac{1}{2\pi}\left(\frac{GM}{R^3}\right),$$

where M is the total mass and R the separation of the holes. Putting in some numbers, this gives for the dominant gravitational wave frequency

$$f_{\rm gw} = 2\times 10^3 {\rm Hz}\left(\frac{M}{10M_\odot}\right)^{-1}\left(\frac{R_g}{R}\right)^{3/2},$$

where R_g is the gravitational radius (radius of the horizon) of a black hole of the total mass M, *i.e.* of the final merged black hole.

From this it is clear that ground-based detectors, which are most sensitive around 100 Hz and which will eventually reach down to around 10 Hz, will be looking at mergers of black holes produced by stellar evolution, up to about $100M_\odot$. Even black holes formed in the first generation of stars, which could have masses of a few hundred solar, may be visible to advanced detectors only in the final merger event, but not during the long inspiral phase. Most merger events in the ground-based frequency window probably result from the long-term evolution of stellar binary systems, in which the mass-ratio between the holes is probably not very large and the orbits have circularized early.

For the LISA gravitational wave detector, the most sensitive frequency window is between 1 and 10 mHz, which places the masses of the holes in the 10^4–$10^6 M_\odot$ range: black holes in the centers of galaxies. For these, two kinds of merger events that seem promising sources and have received the most attention from theorists.[3] In one scenario, two comparable-mass black holes are brought together by dynamical friction with the background stellar population. Here the orbital eccentricity during the observation period might be very small.

In the second scenario, a compact object like a neutron star or (even better) a $10M_\odot$ black hole is placed by random collisions into a plunge orbit that takes it close enough to the black hole to be captured on the first pass, due to the loss of energy to gravitational radiation. After that it may take millions of orbits before its distance of closest approach inches close enough to the horizon for it finally to get captured. Studies suggest that in this case the orbit remains substantially eccentric right up to the end.

These two scenarios require very different techniques to study them theoretically. In the capture scenario, the mass ratio should be smaller than 0.1%, which means that the inspiralling hole can be treated as a small perturbation on the background of the larger hole. This perturbation study is a hot topic in theoretical research today and is far from solved. However, the problem has been understood well enough for theorists to have confidence that LISA will see hundreds of these events.[4] Given that the inspiralling object spends so much time probing the geometry near the central black hole, these capture events will provide an ideal test of the Kerr metric and general relativity's theorems about black-hole uniqueness.[3]

The first scenario, where two holes merge with a mass ratio that is not very different from unity, must be studied by numerical techniques. Post-Newtonian orbital approximations may apply up to very small separations ($R/R_g \sim 10$?), but the final plunge and merger phase must be studied numerically. This is another hot topic in relativity theory. The focus of this article is to describe what we have learned about this process so far.

2 The three phases of black hole merger

Provided that the black holes start far enough apart, the lifetime of the system is dominated by the lowest-order radiation reaction corrections. From this we learn that the time to coalescence of a circular binary whose component masses are m_1 and m_2, whose total mass is $M = m_1 + m_2$, and whose initial separation in a circular orbit is R, is

$$t_c = \frac{5}{256\delta(1-\delta)} \frac{R}{c} \left(\frac{GM}{c^2 R}\right)^{-3}, \tag{1}$$

where δ is the *mass fraction*:

$$\delta = m_1/M.$$

Solving for the separation, we see that for holes to coalesce due to gravitational radiation reaction within a time short compared to a Hubble time, their separation must be small:

$$R_c = 2 \times 10^{-3} \delta^{1/4} (1-\delta)^{1/4} \left(\frac{t_c}{10^{10}\mathrm{yr}}\right)^{1/4} \left(\frac{M}{10^6 M_\odot}\right)^{3/4} \quad \mathrm{pc}. \tag{2}$$

The stellar dynamics in the central star cluster that are required to bring holes this close are discussed elsewhere in this volume by a number of authors.

The black holes spend almost all their time, and (for 10^4–$10^6 M_\odot$ holes) almost all the time they are visible to LISA, in this first phase of the dynamics, where the stars orbit one another and gradually spiral together.

Eventually the post-Newtonian description of the orbit breaks down, and the holes cannot be treated as point particles any more. What is more, it is expected that the holes will reach the *innermost stable circular orbit* (ISCO), at which the gradual inspiral ends and the holes plunge together. This is what happens to point particles in the Kerr geometry: the location of the ISCO depends on the spin of the hole, and it can be anywhere from 3 times the horizon size (non-spinning Schwarzschild hole) to just above the horizon (maximally spinning Kerr hole). Once the holes begin to plunge together, they rapidly meet and merge into a single black hole. This second phase of the merger process cannot be understood analytically and is the object of the numerical work that I will describe below. We don't even have a very good idea of where the transition occurs between the first and second stages.

The final stage of the merger is better understood: very quickly the final black hole radiates away all its non-axisymmetry and settles into a Kerr black

hole. The radiation is dominated by the excited quasi-normal modes of the black hole, which have strong damping: within a few cycles (a few light-crossing times) the hole is substantially axisymmetric. This process is understood at the level of perturbation theory of black holes and has been studied numerically, with no surprises.

3 Why study mergers numerically?

Of these phases, the one that is least understood is the second. At the moment, numerical studies only handle black holes that are very close to one another, near the ISCO. Studies have been able to follow holes from such an orbit through to merger and ringdown, but we do not yet know if the starting conditions are physically appropriate. I will come back to this key issue below. The computer resources needed to study this problem are substantial. Why, then, should we be trying so hard to understand this process?

There are at least four reasons:

1. Gravitation theory. Although we have good theoretical reasons for believing that general relativity's description of time-independent black holes is correct, we do not know what the theory says in detail about dynamical horizons and mergers. The process is strongly nonlinear, and it appears therefore that numerical experiments are the only way of doing *experiments* in this regime.
2. Simplest dynamical problem in general relativity. Black hole mergers are in some sense the least complicated strong-field process, since they are not complicated by the need to include fluid dynamics, atomic or nuclear physics, or magnetic fields. They do have a complication that stars do not: the singularity at the center. This challenges the numerical formulation of the problem, but it is nevertheless true that the "parameter space" of merger models will be small compared to that of stars.

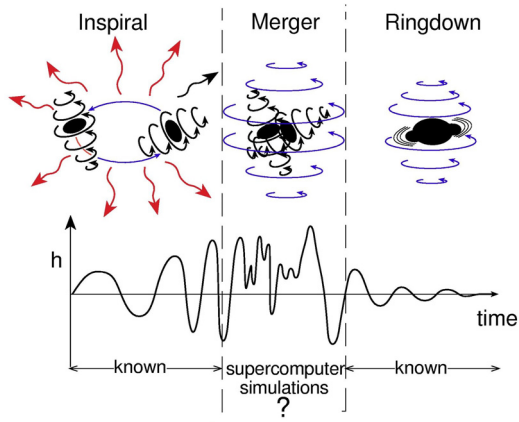

Fig. 1. The three phases of black hole merger (courtesy Kip Thorne).

3. Gravitational wave detection. One of the principal motivations for studying this problem is the need for good numerical waveform predictions as an aid to the detection of these events. Ground-based detectors will be operating in one year at the level of sensitivity where the first black-hole coalescences could potentially be seen, but only if the signal waveform can be predicted well enough. Waveform predictions are used to construct *matched filters* for the data, which find weak signals buried in the noise if the incoming waveform correlates well with the predicted one. For the first stage of inspiral, our predicted waveforms are adequate. But much of the signal is expected to come from the second stage, and so there is considerable pressure from the detector community to make useful predictions. And when signals are detected, the predictions will be needed for their interpretation: what do they say about the mass ratio and spins of the holes? Finally, for LISA, there is an additional problem, that the signals will be so strong that they will contaminate the data and must be removed in order to search for weaker signals, such as those from the capture of smaller black holes. This removal can only be done adequately if there is a good waveform prediction.
4. Astrophysically interesting predictions. Simulations could help fill in the answers to a number of important astrophysical questions. The angular momentum radiated in the second phase (plunge and merger) determines the spin of the final black hole. Can holes with extreme spin be formed by mergers? The linear momentum radiated determines the recoil velocity of the final black hole. Will such holes remain bound in their star clusters or galaxies after merger? (See the article by Scott Hughes in this volume.)

4 Practical numerical simulations: what are the issues?

A glance at some numbers will show why the simulation of the merger of two black holes is a challenging task.

Grid meshes must be large but at the same time fine. The horizon must be well resolved, requiring a fine mesh. But the speed of the black holes in their orbits before the plunge is actually nonrelativistic, so the gravitational wavelength is long. To resolve the waves, one needs to place the grid boundary several wavelengths away. In three dimensions, this can be costly. Using the mass M as a distance unit (in ordinary units this is GM/c^2), a mesh resolution of $0.01M$ and an outer boundary distance of $100M$ (which is only 1.5λ if the initial orbit is the Schwarzschild ISCO) already requires 10^{12} grid points.

In addition, there is a big memory requirement per grid point, because modern formulations of the field equations, specially designed for numerical stability, require between 50 and 80 double-precision variables per grid point. A single time-step could therefore require 400 to 600 TB of main memory to store the mesh described above.

The nonlinearity of the Einstein field equations means that computing the functions needed to advance the simulation by one time-step is costly. The equation for each variable can involve all the others at neighboring points (7 points

in second-order-accurate methods, many more in more accurate schemes), in non-linear combinations (polynomials, matrix inversions). The result can require thousands of floating-point operations per variable per grid point per time step. A single time-step on the mesh described above could demand 10^{17} operations. A teraflop computer would take a day to do just one time-step!

Finally, there need to be a lot of time-steps. The time-step size is set by the Courant condition, at least in the explicit finite-difference methods used by the AEI group and most others. Since the horizon must be resolved with hundreds of cells, a single orbit will traverse thousands of grid cells, and will therefore require thousands of time-steps. A single orbit on our hypothetical mesh and hypothetical teraflop computer would therefore take three years to compute!

It is clear from these numbers that calculations done at present must make compromises or use clever tricks to get around these problems. I will discuss these approaches in the next section. But first it is important also to understand that the problems facing groups doing these simulations are not just brute-force computing power issues. They also involve a host of subtle, theoretical issues associated with Einstein's equations.

For example, inside the black holes there are singularities. These must be avoided somehow, since the computer cannot compute accurately near them. The method of choice today (a big advance over even 5 years ago) is excision: a region of the grid mesh containing the singularity is simply left out of the numerical integration. This is possible because, as long as this region is entirely contained inside the horizon, no errors made in the solution inside the horizon can leak out and affect the solution outside: the interior of the black hole is causally decoupled from the exterior. However, that is only true of the exact Einstein equations. Their finite-difference approximation may well be able to transfer information (and errors) from inside the horizon to outside. So excision needs to be handled with care, and at present there is a strong suspicion that some slowly growing instabilities seen in codes that use excision may be caused by non-causal effects in the finite-difference equations.

Most formulations of Einstein's equations restrict the integration to a finite domain, so not only is there an inner boundary at the excision surface, but there is also an outer boundary at the edge of the grid. Remarkably, it is not known how to set an accurate boundary condition there. Unlike the simple case of a scalar wave equation, where an outgoing wave boundary condition is simple to impose and does a good job of imposing causality on the system, in general relativity there are too many wave-like degrees of freedom and many non-radiative variables, all coupled together. So far, the only remedy has been to try to put the boundary and its over-simplified boundary condition so far away that unwanted reflected waves and information arrive back in the center of the integration domain only after the most interesting events (plunges, mergers) have happened.

What is more, there is not even a unique formulation of the Einstein equations. Coordinate freedom means that one can change the variables one integrates and the way they couple to one another, and one can even change the slicing of spacetime into space sections. And among Einstein's equations there are four

so-called constraint equations that have an elliptical structure. This means that it is possible to insert them into the remaining six dynamical equations in any number of ways (via linear combinations or more complicated insertions) without changing the physical solution of the equations. This freedom has been seen to have a big effect on the stability of the integration methods, and therefore is a useful but complicating measure.[6]

Once one has some output from a numerical simulation, there remains the important challenge of interpreting it: finding horizons, discovering causes of instabilities, visualizing the physical and geometrical variables. The AEI group has put a great deal of effort into this problem, producing along the way many beautiful images and movies. But it is fair to say that the subject of visualization of three-dimensional simulations in general relativity is in its infancy and could reqard a systematic study.

Perhaps the most troubling problem of all, at least at present, is the correct formulation of the initial data for a numerical integration. I will describe this in detail in a later section.

All of this makes clear that the problem is a complex one, and there is a premium on collaboration. Many different approaches need to be explored, but at the same time one needs a framework in which they can be compared. Moreover, there is much commonality in the computational infrastructure required for many of these otherwise different approaches.

The AEI group recognized this long ago and began to develop the Cactus Computational Toolkit to enable teams of scientists to collaborate more effectively, even over large distances.[5] Recently a group of leading scientists working in numerical relativity, most of them Cactus users, formed a quality-assurance organization called Apples with Apples.[7] The aim is develop a set of specific tests that could be applied to all variants, all approaches to the numerical relativity problem. This then allows one to compare "apples with apples" rather than "apples with pears" in deciding which approach is more promising.

5 Addressing the issues

I described the computer-power challenges in the previous section as starkly as I could, but it is clear that there are methods to reduce the size of the problem. All the demands are driven by the size of the grid mesh. This can be reduced in a number of ways. Mesh refinement is an obvious one, in which there is not a uniform mesh spacing everywhere. Near the horizon one needs finely spaced grid points, but these are wasted far away. Groups have now begun to do numerical integrations in meshes consisting of a series of concentric boxes, with coarser and coarser resolution as one goes out.[8,9] This can dramatically reduce the number of grid points by factors of 1000 or more. Then a three-year integration becomes the work of one day.

Even more radical solutions are possible in the framework of spectral methods, which dispose of grid points in favor of representing variables by sums of basis functions, whose coefficients become the numerical variables of the prob-

lem. This global approach offers considerable promise, not only in reducing the size of the problem but also in curing instabilities.[10,11]

Studies of singularity excision are beginning to understand how they might create weak instabilities. Excision seems to work best, at least at present, in comoving coordinates, where the black holes do not move across the mesh but rather the mesh follows them as they merge together. The coordinate freedom of general relativity permits this, and in fact the fixed mesh refinement techniques referred to above also work best in this kind of coordinate system.

To solve the boundary condition problem, one may need a radical reformulation of the basic equations. One approach, devised originally by H Friedrich,[12] is being investigated intensively by a group of scientists at the AEI and their collaborators at other institutions.[13] In this idea, the field equations are expressed in a conformally compactified way, which means that the spacetime is mapped onto a computational domain in which the outgoing light rays reach "infinity" in a finite coordinate distance. There is a natural boundary condition there, and the result is a simulation of the whole spacetime with automatically varying refinement. As promising as this is in the long run, it has only recently begun and will require a number of years to reach the level of robustness of the standard spacetime-slicing approaches.

Instabilities still plague the current generation of simulations, although they grow much more slowly than in earlier codes (say, 5 years ago), thus permitting longer runs. Some seem to be associated with violations of the constraint equations, which must hold for any valid solution. Thus, methods are being studied that re-solve the constraints every time-step, which is considerable work but may be worthwhile. Another possibility is that at least some instabilities comes from bad coordinate choices, so there is considerable experimentation on this front.

Visualization is constantly being improved. A new generation of horizon finders has joined the Cactus code.[14] Finding the black hole horizon is not a trivial task, because the horizon is not locally defined. It consists of the light-rays that are marginally trapped after the entire evolution has settled down. Thus, one finds the horizon by "shooting" photons backwards in time to find the last one that manages to escape. This requires one to save the geometry at all the relevant time-steps, for example, which adds to the computational problems. Figure 2 below is a visualization of the result of this horizon finder.

Finally, recognizing that collaboration is ever more important in this field, numerical relativists have been among the leaders in the Grid computing movement. The GridLab collaboration,[15] supported by an EU research grant, has developed a suite of tools that allow Cactus users to access computing resources all over the world. Another EU grant supports a network of scientists working together on gravitational radiation source problems.[16] In Germany, a special research grant links the AEI with the Universities of Hannover, Jena, and Tübingen in studies of gravitational radiation, including numerical studies.[17]

6 Key issue: the problem of initial data

A numerical simulation must start with a representation of the black holes at some point late in their inspiral phase. Since our knowledge of their location at this time is a result of solving the post-Newtonian approximation, we do not have a complete description of the spacetime metric at this initial time. In particular, the initial gravitational-wave content of the metric is poorly known. This is made worse by the fact that our current methods for solving the constraint equations at the initial moment of time make certain simplifying assumptions that essentially freeze the gravitational wave content in an uncontrollable way. There is thus the possibility that the initial configuration for the numerical integration does not represent two black holes after a long inspiral phase.

One way around this would be to let the holes orbit once numerically, during which any unwanted gravitational radiation (and also any other unwanted irregularities imposed by the initial value formulation, such as distorted horizons) would have time to go away. At present we do not have the luxury of such long integration times, but in the future this may well be the way to cure this aspect of the initial-value problem.

However, a far more worrying aspect of the problem faces groups today. Simply put, they don't know where to start the holes and what velocities to give them. There is no analytic solution to the Kepler problem, so when a group decides to start with holes at a separation of, say, $7M$, they have no exact guide to what circular velocities to give the holes to ensure that they are actually in a quasi-circular orbit. Moreover, they do not even know at present whether $7M$ is inside or outside the ISCO. If it is inside, then the holes will plunge together rapidly. If it is outside, then they may orbit stably until the group runs out of computer time! And we don't yet know whether the ISCO is so well-defined: maybe there is a broad region where the circular orbit begins to go unstable.

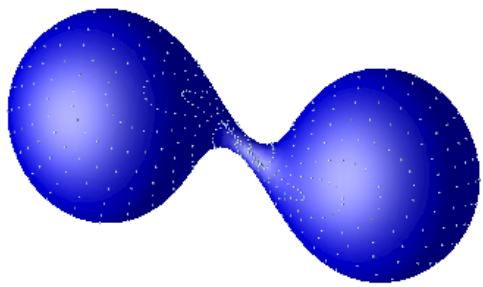

Fig. 2. One frame from a reconstruction of the true horizons during a black hole merger simulation. The holes are orbiting as they merge. Courtesy P Diener.

Even if we knew where the place the holes to start them off, the uncertainty in their orbital speeds would also be a problem. Taking a speed smaller than they would actually arrive with would again cause them to plunge together too rapidly. Taking too large a speed would cause them to separate again.

While it is possible to explore these issues numerically, this would take a huge amount of computer resource. At present several groups are trying to use heuristic models of the circular-orbit problem as a guide to the right data.[18] And numerical data found by a new technique based on spectral methods seems to be in good agreement with these heuristics.[19] But this problem is far from being solved, and until we have a better understanding of it, it will be difficult to trust any waveform predictions.

7 Numerical evolutions

The most ambitious black hole simulation attempted to date was the AEI's "Discovery Channel" simulation, so-called because it was performed and visualized for a program aired by the Discovery Channel network in 2003. It followed two equal-mass Schwarzschild black holes from what was then our best guess as to the location and orbital velocities of the ISCO. The simulation showed that the holes immediately plunged together and merged in less than half an orbit. This was not expected, and it suggests that the initial position was actually inside the ISCO and/or that the initial velocities were too small.

The evolution itself was very successful, and the group could follow the merger through ringdown of the final black hole. The excision regions remained stable throughout. The merger of the horizons was also very smooth, as has been shown by Diener: see Figure 2.

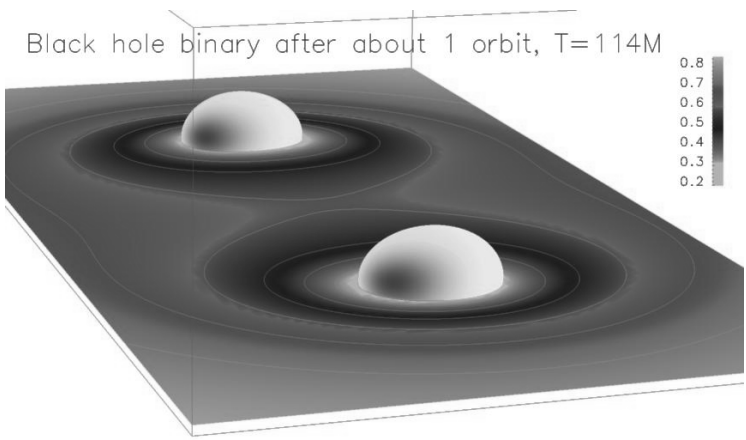

Fig. 3. The state of the Brügmann et al [20] simulation after one complete orbit. Courtesy B Brügmann.

The record for the longest stable simulation of two black holes in orbit belongs was set late last year with a simulation by Brügmann and collaborators.[20] Figure 3 shows the horizons of the black holes *after* one complete orbit. They show little distortion and have kept their distance well. The simulation used the group's own mesh refinement code and a number of advances devised jointly with the AEI group. The orbit took $114M$ of time, and the simulation actually remained stable for $150M$. Even more remarkably, it took only 24 hours to perform on a single processor! The performance of a single stable circular orbit is indeed a major step forward in the current state of this field!

More groups can be expected to attempt to emulate the success of this simulation, both using finite differences and in the realm of spectral methods. It encourages me to be optimistic that in two to three years we will have reasonably accurate waveforms for extracting the merger signals of non-spinning black holes from the data of ground-based gravitational wave detectors. Hopefully, that will be rapidly followed by further improvements. Spin will be important for the merger signal, and most merging black holes can be expected to have a substantial spin. And even more important, especially for LISA, will be simulations of unequal-mass mergers. These are currently being developed in a number of groups.

Nevertheless, progress in this field will not speed up overnight. It is limited by a shortage of people, and in recognition of this, NASA and NSF have been discussing a joint initiative to fund more effort in the USA. If this should materialize, it would bring the day when these simulations provide really useful results considerably closer.

References

1. Luc Blanchet, "Gravitational Radiation from Post-Newtonian Sources and Inspiralling Compact Binaries", Living Rev. Relativity 5, (2002), 3. [Online article]: cited on 24 October 2004, http://www.livingreviews.org/lrr-2002-3
2. Ingrid H. Stairs, "Testing General Relativity with Pulsar Timing", Living Rev. Relativity 6, (2003), 5. [Online article]: cited on 24 October 2004 http://www.livingreviews.org/lrr-2003-5/
3. C. Cutler and K.S. Thorne, "An overview of gravitational wave sources", in *Proceedings of the GR16 Conference on General Relativity and Gravitation*, ed. N. Bishop (World Scientific, 2002).
4. J R Gair, L Barack, T Creighton, C Cutler, S L Larson, E S Phinney, M Vallisneri, *Class. Quant. Grav.* **21** S1595-S1606 (2004)
5. See the website http://www.cactuscode.org/.
6. M Alcubierre, et al, *Phys. Rev.* **D62** 044034 (2000)
7. M Alcubierre, et al, *Class. Quant. Grav.* **21** 589 (2004). See also the website http://www.appleswithapples.org/.
8. E Schnetter, S H Hawley, I Hawke, *Class. Quant. Grav.* **21** 1465-1488 (2004).
9. B Imbiriba, et al, gr-qc/0403048.
10. L E Kidder, M A Scheel, S A Teukolsky, E D Carlson, G B Cook, *Phys. Rev.* **D62** 084032 (2000).
11. J Novak, S Bonazzola *J. Comp. Phys.* **197** 186-196 (2004).

12. H Friedrich, *Lect. Notes Phys.* **604** 1-50 (2002).
13. S Husa, *Lect. Notes Phys.* **617** 159-192 (2003).
14. J Thornburg, *Class. Quant. Grav.* **21**, 743-766 (2004).
15. See the website http://www.gridlab.org/.
16. See the website http://www.eu-network.org/.
17. See the website http://www.tpi.uni-jena.de/SFB/.
18. A Buonanno, *Class. Quant. Grav.* **19** 1267-1278 (2002).
19. E Gourgoulhon, P Grandclement, S Bonazzola *Int. J. Mod. Phys.* **A17** 2689-2694 (2002).
20. B Brügmann, W Tichy, N Jansen *Phys. Rev. Lett.* **92** 211101 (2004)

How Black Holes Get Their Kicks: Radiation Recoil in Binary Black Hole Mergers

S.A. Hughes[1], M. Favata[2], and D.E. Holz[3]

[1] Department of Physics and Center for Space Research, Massachussets Institute of Technology, 77 Massachusetts Avenue, Cambridge, MA 02139
[2] Department of Astronomy, Cornell University, 611 Space Sciences Building, Ithaca, NY 14853
[3] Center for Cosmological Physics, University of Chicago, Chicago, IL 60637

Abstract. Gravitational waves from the coalescence of binary black holes carry linear momentum, causing center of mass recoil. This "radiation rocket" has important implications for systems with escape speeds of order the recoil velocity. We describe new recoil calculations using high precision black hole perturbation theory to estimate the magnitude of the recoil for the slow "inspiral" coalescence phase; coupled with a cruder calculation for the final "plunge", we estimate the total recoil imparted to a merged black hole. We find that velocities of many tens to a few hundred km/sec can be achieved fairly easily. The recoil probably never exceeds about 500 km/sec.

It is very well known that gravitational waves (GWs) carry energy and angular momentum from a binary system, causing decay of the binary's orbit and eventually driving the system to merge into a single object. Although it has been understood for quite some time (e.g., [1]), it is somewhat less well-appreciated that these waves can carry *linear* momentum from the system as well. The center of mass in this case must recoil in order to enforce global conservation of momentum. If the recoil velocity is comparable to or greater than the escape velocity of the binary's host structure, there could be important dynamical consequences, such as ejection of the merged black hole remnant.

The recoil arises because the radiation field generated by a binary is typically asymmetric. As a helpful cartoon, consider the following argument due to Alan Wiseman. In an unequal mass binary (Fig. 1), the smaller member, m_1, moves with a higher speed than the larger member, m_2. It is thus more effective at "forward beaming" its wave pattern. This means that there is an instantaneous net flux of momentum ejected from the system parallel to the velocity of the smaller body, and a concomitant recoil opposing this.

Over an orbit, the recoil direction continually changes. If the orbit were perfectly circular, this means that there would be no net interesting effect — the binary's center of mass would run around in a circle, and the *net* recoil would sum to zero. However, when GW emission is strong, the orbit is *not* perfectly circular: Because of the secular, dissipative evolution of the binary's energy and angular momentum, the black holes slowly spiral towards one another. Since the orbit does not close, the recoil does not sum to zero. The recoil accumulates until the holes merge and settle down to a quiescent state, shutting off the momentum flux and yielding a net, non-zero kick.

ESO Symposia: Growing Black Holes, pp. 333–339, 2005.

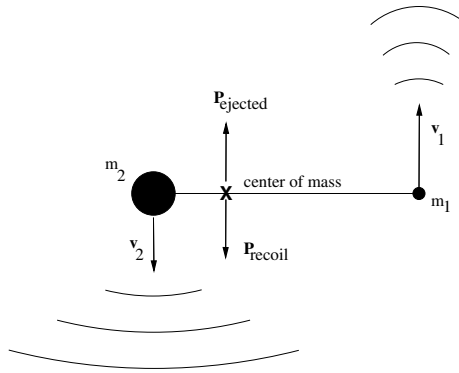

Fig. 1. GW emission from an unequal mass binary. Momentum is ejected parallel to the smaller body's velocity ($\boldsymbol{v}_1$). Conservation of momentum requires that the system recoil in the opposite direction.

This recoil is not a wierd property of GWs — it holds for *any* form of radiation[1]. This can be brought out by considering a multipolar decomposition. Suppose we build a distribution of charges that has a non-zero electric dipole and quadrupole moment, as in Fig. 2. Suppose further that we spin this charge arrangement about its center point, driving the system to radiate electromagnetic waves. What does this radiation distribution look like from far away?

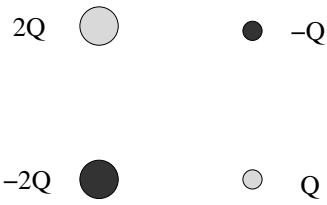

Fig. 2. Charge distribution with non-zero dipole and quadrupole moment. Spinning this distribution about its center point produces radiation carrying non-zero linear momentum due to beating between the dipolar and quadrupolar radiation fields.

The radiation's *amplitude* has two pieces, dipole and quadrupole:

$$\boldsymbol{E} = \boldsymbol{E}^{\rm dip} + \boldsymbol{E}^{\rm quad} , \qquad \text{where} \tag{1}$$

$$\boldsymbol{E}^{\rm dip} \propto e^{i(\phi-\omega t)} , \qquad \boldsymbol{E}^{\rm quad} \propto e^{2i(\phi-\omega t)} . \tag{2}$$

Since the intensity $I \propto |\boldsymbol{E}|^2$, it will contain three pieces:

$$I = I^{\rm dip} + I^{\rm quad} + I^{\rm dip-quad} , \tag{3}$$

[1] Indeed, electromagnetic or neutrino recoil may impact neutron star kicks [2,3].

where

$$I^{\rm dip} \propto |\boldsymbol{E}^{\rm dip}|^2 \propto \text{constant} ; \qquad I^{\rm quad} \propto |\boldsymbol{E}^{\rm quad}|^2 \propto \text{constant} \tag{4}$$

$$I^{\rm dip-quad} \propto \text{Re}\left[\boldsymbol{E}^{\rm dip}\bar{\boldsymbol{E}}^{\rm quad}\right] \propto \cos(\phi - \omega t) . \tag{5}$$

The intensity has a preferred direction, which rotates as the charge distribution rotates. The energy from the system is instantaneously beamed in a preferred direction, and so there is a net flux of momentum in that direction as well.

Since the lowest order GWs are quadrupolar, recoil from GW emission must come (at lowest order) from a beating of the mass quadrupole with mass octupole and current quadrupole moments. The mass octupole and current quadrupole vanish for an equal mass binary, demonstrating — in accord with our "forward beaming" intuition — that unequal masses are needed for there to be any recoil. This also demonstrates that GW recoil must be a very small effect, except perhaps in the very late stages of coalescence — the octupole radiation amplitude is smaller than the quadrupole by a factor of order v/c (where v is orbital speed).

The first careful analysis of recoil in binary systems due to GW emission is that of Michael Fitchett [5]. Fitchett's analysis described the orbital dynamics of the binary using Newtonian gravity and only included the lowest radiative multipoles which contribute to the recoil. His analysis predicted that the recoil of the merged remnant took the form

$$v_{\rm F} \simeq 1480\,{\rm km/sec}\frac{f(q)}{f_{\rm max}}\left(\frac{2G(m_1+m_2)/c^2}{R_{\rm term}}\right)^4 , \tag{6}$$

where $R_{\rm term}$ is the orbital separation at which GW emission terminates, $q = m_1/m_2$ is the binary's mass ratio, and $f(q) = q^2(1-q)/(1+q)^5$ is a function whose maximum is at $q \simeq 0.38$, and has the limit $f(q) \simeq q^2$ for $q \ll 1$.

Three features of this formula are particularly noteworthy. First, this result does not depend on total mass — only on the mass *ratio* (bearing in mind that $R_{\rm term}$ scales with total mass M). Thus, this scaling holds for any binary black hole merger — stellar mass mergers through supermassive mergers. Second, the overall scale is quite high. Although there is an important dependence on mass ratio and the termination radius $R_{\rm term}$ is somewhat uncertain, Eq. (6) indicates that kicks of hundreds of km/sec are not difficult to achieve; kicks $\gtrsim 1000$ km/sec are plausible. This is high enough that we might expect black hole ejection following a merger to be common.

Notice, however, that the recoil becomes very strong when the separation of the bodies is small. This is a strong hint that we cannot take Eq. (6) at face value — the strong gravity physics neglected by Ref. [5] is likely to be very important.

A few efforts have improved on Fitchett's analysis over the years. Fitchett and Detweiler [6] first made a strong field analysis, treating the binary as a Schwarzschild black hole M orbited by a point mass μ. The orbiting body's influence can then be studied using black hole perturbation theory. Their results suggested that Eq. (6) describes the recoil fairly well. Wiseman [4] analysed the recoil with post-Newtonian theory (roughly, an expansion in $v \sim \sqrt{GM/rc^2}$).

He found that Fitchett's formula tended to systematically overestimate the recoil by $\gtrsim 10\%$. Unfortunately, his results behave somewhat pathologically for $r \lesssim 9GM/c^2$ due to ill behavior of the expansion in the very strong field.

This motivates our analysis of this problem. Our formal setup is quite similar to that of Fitchett and Detweiler: We model the binary as a pointlike body μ moving on the exact, geodesic orbits of a Kerr black hole with mass M and spin parameter a. We compute the GWs emitted from such orbits very accurately using black hole perturbation theory [7–9], and extract the recoil from the wave pattern [10]. The perturbative approach allows us to study the dynamics of the binary's spacetime with high accuracy. Schematically, we treat this spacetime as that of the Kerr black hole plus a small perturbation:

$$g_{\alpha\beta} = g^{\rm Kerr}_{\alpha\beta}(M,a) + h_{\alpha\beta}(\mu) \; . \tag{7}$$

By requiring that this spacetime satisfy the Einstein field equations, it can be shown [7] that $h_{\alpha\beta}$ is governed by a wave-like equation. The wave operator automatically captures the most important properties of the strong field physics.

This approach is strictly accurate only when $\mu \ll M$ — the smaller body cannot significantly distort the spacetime if we want the exact Kerr orbits to describe our binary. We believe, though, that we can extrapolate out of this regime with accuracy good enough for most astrophysical purposes — our extrapolation errors are estimated to be at most several tens of percent, at least up to a mass ratio $q \simeq 0.3$, and to scale with the squared mass ratio.

We focus upon circular, equatorial orbits of Kerr black holes. Circularity is surely a good approximation, since eccentricity is rapidly reduced during coalescence. The equatorial assumption is not so good; since the binaries of interest form through captures, we expect no particular alignment between the spin and orbit. We are working to lift this approximation, which requires moderately substantial modifications to our code; early indications are that the inclination does not have a very large effect on the recoil, other than to change the radius at which a transition in the orbital dynamics occurs. Results from the prograde and retrograde equatorial orbits appear to bound the recoil at any spin.

One technical detail of our code is important enough that it requires some explanation. Our calculation expands the perturbation as

$$\Psi_4 = \frac{1}{r} \sum_{lm} Z_{lm} S_{lm}(\theta) e^{im(\phi - \Omega t)} \; . \tag{8}$$

Ψ_4 represents a curvature perturbation, and serves as a surrogate for $h_{\alpha\beta}$. $S_{lm}(\theta)$ is a spheroidal harmonic (very similar to a spherical harmonic), and Z_{lm} is a complex number found by solving a certain differential equation [7,8]. The most important aspect of this equation for our purposes is the presence of the orbital frequency Ω: We assume that the orbit is well-described by a Fourier expansion. This is only true if the orbit is periodic (or nearly so). This in turn is only true when the separation r of the black holes is greater than the radius of the "last stable orbit" (LSO), $r_{\rm LSO}(a)$. (For Schwarzschild holes, $a = 0$, $r_{\rm LSO} = 6GM/c^2$.)

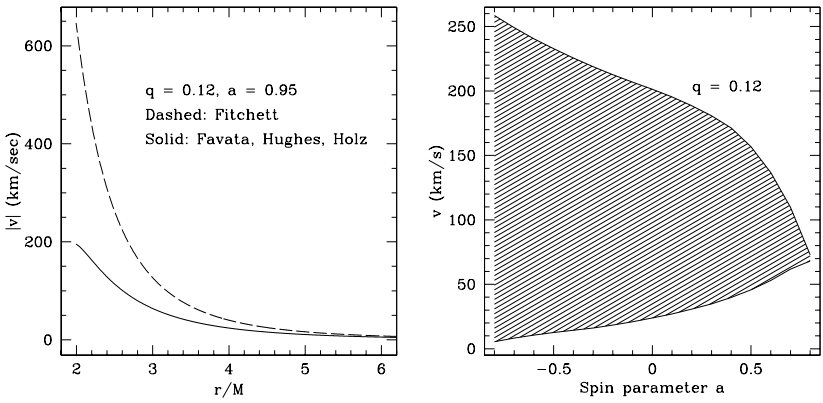

Fig. 3. Left: Fitchett's accumulated recoil and our results, versus binary separation r. This illustrates the importance of a proper treatment of strong-field physics. Right: Total recoil versus black hole spin a. The upper curve is our overestimate, the lower our underestimate. The span between them shows the importance of the final plunge.

In the regime $r > r_{\rm LSO}(a)$, dynamically stable orbits exist. GWs slowly evolve the system through a sequence of stable orbits of ever decreasing radius. At any instant in this regime, the orbit is well modeled as periodic with a well-defined frequency Ω. The recoil is then simply related to the coefficients Z_{lm} and to an overlap integral involving the harmonics $S_{lm}(\theta)$; see Ref. [10] for details.

As we approach and cross $r_{\rm LSO}(a)$, the orbit becomes a rapid "plunge" in which the small body quickly falls into the event horizon. This final plunge *cannot* be treated using this Fourier expansion, so our calculation breaks down. We are currently developing techniques to model this regime accurately. For the present analysis, we compute a probable overestimate (based on an extrapolation of the inspiral momentum flux beyond its range of validity) and a probable underestimate (based on a low-order flux formula coupled to the plunging motion) in order to provide a reasonable range for the likely recoil.

Our analysis shows that Fitchett's calculation *consistently overestimates* the recoil velocity, especially as the LSO is approached; see the left-hand panel of Fig. 3. This is due to strong-field physics: A wave packet released near the horizon redshifts as it propagates to large radius, reducing the energy and momentum that it carries. This effect is not present in calculations which neglect curved spacetime physics, as in Ref. [5]. Also, when radiation propagates through a curved spacetime, the anisotropy of the radiation pattern tends to be somewhat reduced due to the phenomenon of *tails* — essentially, the backscatter of the radiation from spacetime curvature itself. Both the redshifting and the anisotropy reduction reduce the recoil relative to Fitchett's original analysis.

The right-hand panel of Fig. 3 summarizes our results for the total recoil that can be expected in a merger; the curves shown are for $q = 0.12$, but can be rescaled using $f(q)$ [Eq. (6) and subsequent text]. The range shown here shows the uncertainty that results from our inability to model the plunge very well. It

is largest for retrograde orbits ($a < 0$) of rapidly rotating black holes because the transition to plunge occurs at relatively large radius there — the smaller body plunges quite a distance before passing through the event horizon. By contrast, for prograde orbits ($a > 0$), the transition occurs at small radius, so the plunge does not matter quite so much. Our uncertainty is much smaller for those cases.

A very notable feature of this plot is that the recoil, though substantial, *never* exceeds about 500 km/sec, even when the mass ratio is "tuned" to maximize the recoil. On the other hand, it is not difficult for the recoil to reach several tens of km/sec, even for our underestimate. Indeed, when we convolve our over- and underestimates with a distribution of likely mass ratios and spin values (cf. Ref. [11]) we find that recoils of several tens of km/sec are quite easy to achieve; recoils ~ 100 km/sec are likely for an interesting fraction of recoils; and recoils of several hundred km/sec, though possible, are probably rather rare.

In the near future we hope to reduce our error bars, but for now we understand the recoil with sufficient accuracy that these results can be used for many astrophysical applications The most likely recoil range — several tens to a few hundred km/sec — is particularly interesting: While not large enough to eject black holes from massive galaxies, kicks in this range can lead to ejection in dwarf galaxies and dark matter halos, affect the nuclear density profiles of galaxies with SMBHS, and influence the hierarchical growth of supermassive and intermediate mass black holes [11–17].

It is a pleasure to thank Saul Teukolsky and Jerry Ostriker for bringing this problem to our attention, and Éanna Flanagan, Avi Loeb, David Merritt, Miloš Milosavljević, Martin Rees, Joseph Silk, Alan Wiseman, and Yanqin Wu for many useful discussions. SAH would especially like to thank the organizers of this conference for a fantastic meeting. MF is supported by NSF grant PHY-0140209; SAH by NSF grant PHY-0244424 and NASA grant NAG5-12906; and DEH by NSF grant PHY-0114422.

References

1. J. D. Bekenstein: Astrophys. J. **183**, 657 (1973).
2. E. R. Harrison and E. Tademaru: Astrophys. J. **201**, 447 (1975).
3. D. Lai, D. F. Chernoff and J. M. Cordes: Astrophys. J. **549**, 1111 (2001).
4. A. G. Wiseman: Phys. Ref. D **46**, 1517 (1992).
5. M. J. Fitchett: Mon. Not. R. Astron. Soc. **203**, 1049 (1983).
6. M. J. Fitchett and S. D. Detweiler: Mon. Not. R. Astron. Soc. **211**, 933 (1984).
7. S. A. Teukolsky: Astrophys. J. **185**, 635 (1973).
8. S. A. Hughes: Phys. Rev. D **61**, 084004 (2000).
9. S. A. Hughes: Phys. Rev. D **64**, 064004 (2001).
10. M. Favata, S. A. Hughes, and D. E. Holz: Astrophys. J. Lett. **607**, L5 (2004).
11. D. Merritt, M. Milosavljević, M. Favata, S. A. Hughes, and D. E. Holz: Astrophys. J. Lett. **607**, L9 (2004).
12. P. Madau and E. Quataert: Astrophys. J. Lett. **606**, L20 (2004).
13. M. Volonteri, F. Haardt, P. Madau: Astrophys. J. **582**, 559 (2003).
14. K. Gultekin, M. C. Miller, and D. P. Hamilton, Astrophys. J., submitted; astro-ph/0402532.

15. Z. Haiman: Astrophys. J., submitted; astro-ph/0404196.
16. J. Yoo and J. Miralda-Escudé: Astrophys. J. Lett., submitted; astro-ph/0406217.
17. M. Boylan-Kolchin, C.-P. Ma, and E. Quataert: Astrophys. J. Lett., submitted; astro-ph/0407488.

Black Holes in Galaxy Mergers

T. Di Matteo[1], V. Springel[1], and L. Hernquist[2]

[1] Max-Planck-Institut für Astrophysik, Karl-Schwarzschild-Straße 1, 85740 Garching bei München, Germany
[2] Harvard-Smithsonian Center for Astrophysics, 60 Garden Street, Cambridge, MA 02138, USA

Abstract. Here we report on simulations which, for the first time, simultaneously track star formation and black hole growth, and associated feedback processes, during collisions of galaxies. We show that encounters and mergers of galaxies lead to strong nuclear gas inflows, fueling both powerful starbursts and rapid growth of central black holes. Energetic feedback from accretion onto black holes eventually expels sufficient amount of gas from the merger remnant to quench star formation as well as further black hole growth. At the completion of such an event, the stellar velocity dispersion of the remnant spheroid correlates with the final black hole mass in the manner indicated by observations of the $M_{\rm BH} - \sigma$ relation.

1 Introduction

In recent years, strong dynamical evidence has been accumulated that indeed indicates that supermassive black holes reside at the center of most galaxies [5,6]. In particular, a remarkable connection between supermassive black holes and the properties of their host galaxies has been discovered which shows that the central black hole mass is tightly correlated with the stellar velocity dispersion of its host galaxy bulge [2,3] and to the mass of the spheroidal component [6,8,4]. The strong link implied by these relations, between the masses of black holes and the gravitational potential wells that host them suggests a fundamental connection between the growth of black holes and the formation of stellar spheroids in galaxy halos.

It is also evident that a large fraction of the black hole mass in galaxies today must have been assembled by gas accretion, predominantly during the peak of the quasar phase in the early Universe [11,13]. While the detailed physics of accretion is highly complex and only partially understood, it is likely that conditions on galactic scales ultimately determine the supply of gas near a supermassive black hole. Interactions and mergers between galaxies are known to trigger large-scale nuclear gas inflows, which is a prerequisite for growth of central black holes.

2 Hydrodynamical simulations

We have, therefore, performed simulations of isolated and merging galaxies that describe the processes of radiative cooling, star formation, black hole growth, and feedback from supernovae and accretion onto black holes, together with

ESO Symposia: Growing Black Holes, pp. 340–345, 2005.

the gravitational dynamics of gas, stars, and dark matter and their non-linear coupling.

In particular, we include a novel treatment of gas accretion onto supermassive black holes and associated feedback in the centres of merging galaxies. Briefly, we incorporate star formation and black hole growth into simulations of entire galaxies using a sub-resolution approach, by forming "macroscopic" representations of simple physical models that capture the large-scale impact of these effects on resolved scales. We describe black holes using collisionless "sink" particles that can grow in mass by accreting gas. The accretion rate is estimated by relating the small-scale, unresolved flow around the black hole to the large-scale, resolved gas properties using a Bondi-Hoyle model:

$$\dot{M}_B = 4\pi\alpha G^2 \frac{M_{\rm BH}^2 \rho}{(c_s^2 + v_{\rm rel}^2)^{3/2}}. \quad (1)$$

Here, ρ and c_s are the density and sound speed of the gas, respectively, $v_{\rm rel}$ is the velocity of the black hole relative to the gas and α is a dimensionless parameter. If the Bondi-Hoyle rate exceeds the Eddington value we limit the accretion to this critical value, $\dot{M} = \min(\dot{M}_B, \dot{M}_{\rm Edd})$, where $\dot{M}_{\rm Edd} = 4\pi G M_{\rm BH} m_p / \eta \sigma_T c$ and m_p is the proton mass, σ_T is the Thomson cross section, and η is the radiative efficiency which is related to the luminosity by $\eta = L/(\dot{M}c^2)$. We further assume that a small fraction f of the radiated luminosity L couples thermodynamically to the surrounding gas. This gives an effective heating rate,

$$\dot{E}_{\rm feed} = fL = f\eta\dot{M}c^2, \quad (2)$$

where we take $\eta = 0.1$, the typical value derived from Shakura-Sunyaev accretion models onto a Schwarzschild black hole. We take $f = 0.05$, so that $\sim 0.5\%$ of the accretion energy is available to heat the gas.

3 Simulations with and without black holes

Figure 1 illustrates the impact of central, supermassive black holes on representative mergers of two disk galaxies. We compare the gas evolution between two simulations with the same orbits and galaxies. Star formation and supernova feedback are included in both simulations, but we add our black hole growth and feedback in one (top four panels of Fig. 1) and neglect it in the other (bottom four panels). The first image ($t = 1.1$ Gyr) shows the systems after the first passage of the two galaxies. At this time, the black holes in the centres of each galaxy (top) have already grown significantly from their initial masses and are accreting at a moderate level. However, the overall star formation rate is essentially unaffected by the presence of the black holes, as indicated by Figure 2, which plots the star formation rate (in both cases), black hole accretion rate, and black hole mass (for the top panels), as a function of time. The second snapshot ($t = 1.4$ Gyr) depicts the galaxies distorted by their mutual tidal interaction, just before they merge. The peak in the star formation and black hole accretion (see also Fig. 2)

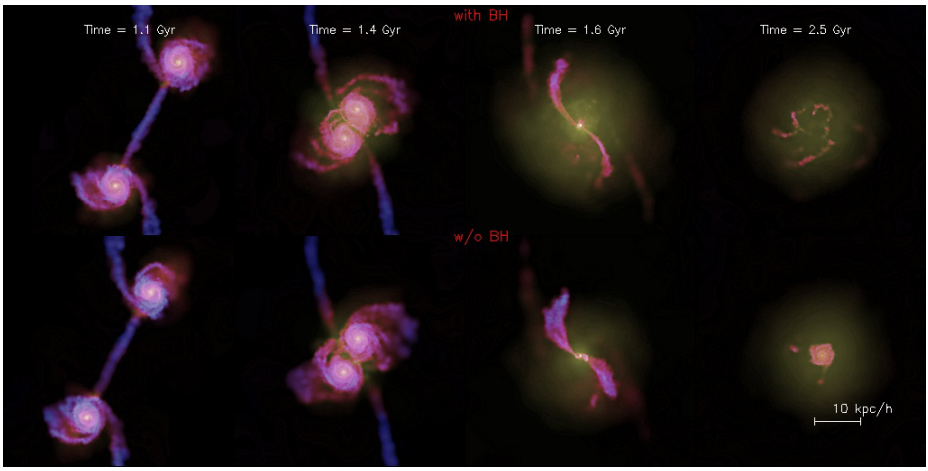

Fig. 1. Overview of the time evolution in mergers of two galaxies in models with and without black holes, shown in the panels of the top and bottom row, respectively. The images visualise the projected gas distribution in the two galaxies, colour-coded by temperature. The colliding galaxies have the same initial mass corresponding to a 'virial velocity' of $V_{\rm vir} = 160$ km/s, and consist of an extended dark matter halo, a stellar bulge, and a disk made up of stars and 20% gas. Each individual galaxy in the simulations is represented with 30000 particles for the dark matter, 20000 for the stellar disk, 20000 for the gaseous disk, and 10000 for the bulge component. Two such galaxies were set up on a parabolic, prograde collision course, and then evolved forward in time numerically with GADGET-2[9], a parallel TreeSPH simulation code.

is reached at the time of the third snapshot ($t = 1.6$ Gyr), when the galaxies finally coalesce. At this time, a strong wind driven by feedback energy from the accretion expels much of the gas from the inner regions in the simulation with black holes. Finally, the last snapshots show the systems after the galaxies have merged ($t = 2.5$ Gyr), leaving behind quasi-static spheroidal galaxies. In the simulation with black holes, the remnant is very gas poor and has little gas left dense enough to support ongoing star formation, which is highlighting the fact that the presence of supermassive black holes accreting from the surrounding gas and heating it with the associated feedback energy dramatically alters the merger remnant. In fact, the star formation rate drops by about three orders of magnitude after the completion of the merger compared to the model which neglects black holes (see top panel of Fig. 2).

4 Black hole growth and the $M_{\rm BH} - \sigma$ relation

In Figure 2, we also show examples of the evolution of star formation rate, black hole accretion rate, and black hole mass in mergers when the progenitor galaxy mass is varied, parameterised in terms of the 'virial velocity', $V_{vir} = 80, 160, 320$ kms^{-1}. All the models start with an initial black hole of mass $M_{\rm BH} = 10^5 M_{\odot}$,

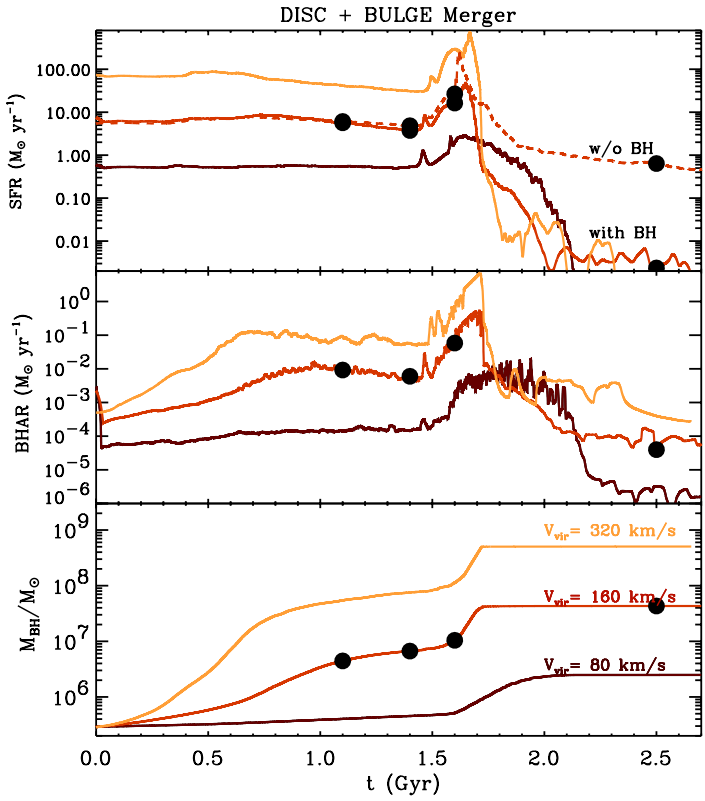

Fig. 2. Evolution of the global star formation rate (top panel), black hole accretion rate (middle panel; in solar masses per year) and black hole mass (bottom panel; in units of solar masses) in models with galaxies of virial velocity $V_{\rm vir} = 80, 160, 320$ km/s, (bottom to top lines in each panel, also labelled in the bottom panel). For comparison, we also show the evolution of the star formation rate for the model without a black hole (dashed line – for the $V_{\rm vir} = 160$km/s galaxy).

and they all qualitatively reproduce the key features of the evolution shown in Figure 1: the star formation and black hole accretion rates are both quenched in the remnant, and black hole growth saturates owing to feedback provided by accretion energy. However, the damping of star formation and black hole activity is more abrupt in the more massive systems. Here, the total gas supply for accretion is larger, and the gravitational potential well is deeper, and so the black hole has to grow much more before its released energy is sufficient to expel the gas in a quasar driven wind, which then terminates further nuclear accretion and star formation. For the same reasons, the initial growth of the black holes, which is regulated by the properties of nearby gas, depends on the total mass.

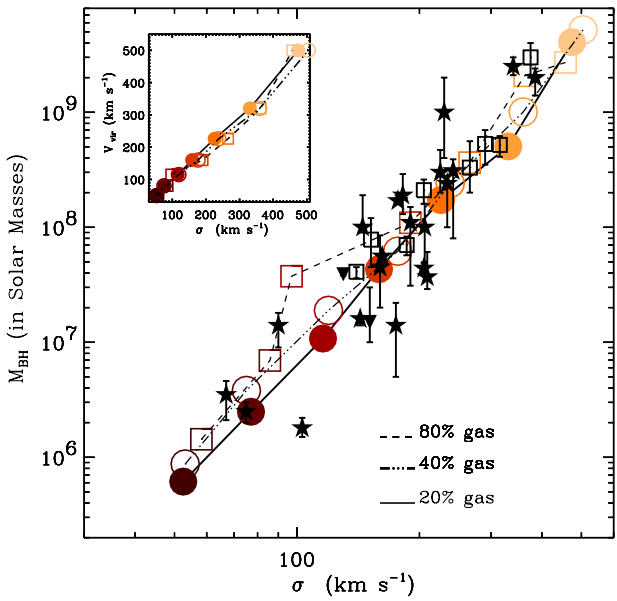

Fig. 3. The $M_{\rm BH} - \sigma$ relation of our galaxy merger simulations compared with observational measurements. The solid circles show the masses of the black holes and the bulge velocity dispersions measured for the final remnants of six merger simulations of galaxies with disk gas fraction of 20%, but different virial velocities of $V_{\rm vir} = 50$, 80, 160, 320, and 500 km/s. Open circles and open squares with the same colour give results for gas fractions of 40% and 80%, respectively. We calculate σ as the line-of-sight stellar velocity dispersion of stars in the bulge within the effective radius, R_e, of the galaxy. Black symbols show observational data for the masses of supermassive black holes and the velocity dispersions of their host bulges taken from[12]. Measurements based on stellar kinematics are denoted by filled stars, those on gas kinematics by open squares, and those on maser kinematics by filled triangles. The inset shows the relation between the circular velocity $V_{\rm vir}$ and σ measured for the merger remnants in the simulations

It is faster in more massive systems, which can therefore reach the exponential, Eddington-limited growth phase more easily.

The dependence of black hole growth on galaxy mass yields a relation between the stellar spheroid of the remnant and its central black hole. Figure 3 shows the black hole mass versus the stellar velocity dispersion of the merger remnants from our simulations, compared with observationals. We include simulations with six different galaxy masses, corresponding to $V_{\rm vir} = 50, 80, 160, 320,$ and 500 km s^{-1}. We also varied the initial gas mass fraction $f_{\rm gas}$ of the galaxies' disks from 0.2 (as in Figs. 1 and 2), to 0.4 and 0.8. Remarkably, our simulations reproduce the observed $M_{\rm BH}$–σ correlation very well. We have also checked that this result is insensitive to the orbits of the galaxy collisions. Note that black holes in

more gas-rich mergers reach somewhat larger masses than those growing in gas-poorer environments (which is expected from our prescription for the accretion rate), but this is partly compensated by an increase in the velocity dispersion of the corresponding bulges, maintaining a comparatively tight $M_{\rm BH}$–σ relation. However, this suggests that part of the intrinsic scatter in the observed relation can be ascribed to different gas fractions of the galaxies during black hole growth. Our lowest mass galaxy models probe a region of the $M_{\rm BH}$–σ relation where few measurements are available and predict that this correlation should hold towards small black hole masses and velocity dispersions, in tentative agreement with recent observations[4].

5 Conclusions

Black hole growth is self-regulated in our models. As galaxies merge to form spheroids, the dynamical response of the gas to the energy supplied by accretion halts further growth once the black holes have reached a critical size for the gravitational potential of the bulge[1]. At this saturation point, the AGN generate outflows that drive away gas and inhibit further star formation[10].

References

1. T. Di Matteo, V. Springel, & L. Hernquist: ApJ, submitted, (2004)
2. L. Ferrarese & D. Merritt: ApJ, **539**, L1, (2000)
3. Gebhardt et al.: ApJ,**539**, L13, (2000)
4. J. E. Greene, L.C. Ho: ApJ, in press, (2004)
5. J. Kormendy & D. Richstone: ARA&A, **33**, 581, (1995)
6. J. Magorrian et al.: AJ, **115**, 2285, (1998)
7. A. Marconi & L. Hunt: ApJ, **589**, L21, (2003)
8. R. J. McLure & J. S. Dunlop: MNRAS, **331**, 795 (2002)
9. V. Springel, L. Hernquist: MNRAS, **339**, 289–311, (2003)
10. V. Springel, T. Di Matteo, L. Hernquist: ApJ, submitted, (2004)
11. A. Soltan: MNRAS, **200**, 115 (1982)
12. S. Tremaine, et al.: ApJ, **574**, 740 (2002)
13. Q. Yu, S. Tremaine: MNRAS, **335**, 965 (2002)

The Effect of Gaseous Dissipation on the Fate of Supermassive Black Holes in Merging Galaxies

S. Kazantzidis[1], L. Mayer[1], M. Colpi[2], P. Madau[3], V.P. Debattista[4], T. Quinn[6], J. Wadsley[5], J. Stadel[1], and B. Moore[1]

[1] Institute for Theoretical Physics, University of Zürich, Winterthurerstrasse 190, CH-8057 Zürich, Switzerland
[2] Dipartimento di Fisica G. Occhialini, Università di Milano Bicocca, Piazza della Scienza 3. I-20126 Milano, Italy
[3] Department of Physics, University of California at Santa Cruz, 1156 High Street, Santa Cruz, CA 95064
[4] Institut für Astronomie, ETH Zürich, Scheuchzerstrasse 7, CH-8093 Zürich, Switzerland
[5] Department of Physics and Astronomy, McMaster University, 1280 Main Street West, Hamilton, ON L8S 4M1, Canada
[6] Department of Astronomy, University of Washington, Seattle, WA 98195

Abstract. We analyze the effect of dissipation on the orbital evolution of supermassive black holes (SMBHs) using high-resolution gasdynamical simulations of binary equal- and unequal-mass mergers of disk dominated galaxies that include the effects of radiative cooling and star formation. We find that equal-mass mergers *always* lead to the formation of a *close* SMBH pair at the center of the remnant with separations limited solely by the adopted force resolution of ~ 100 pc. Instead, the final separation of the SMBHs in unequal-mass mergers depends sensitively on how the central structure of the merging galaxies is modified by dissipation. In the absence of dissipation, the companion galaxy is entirely disrupted before the merger is completed leaving its SMBH wandering at a distance too far from the center of the remnant for the formation of a close pair. In contrast, gas cooling facilitates the pairing process by increasing the resilience of the companion galaxy to tidal disruption. Our results suggest that semi-analytic models of hierarchical SMBH growth that neglect the effect of dissipation likely overestimate the number of wandering SMBHs in massive galaxies. The large gas inflows associated with the strong tidal torques during the merger lead to the formation of massive, rotationally supported nuclear disks with sizes, masses and rotational velocities similar to the ones observed spectroscopically for few AGNs and ULRIGs. These disks are gravitationally unstable and likely provide the necessary fuel for feeding the SMBHs and bridging the gap between the large scale flows and the viscous accretion taking place once the gas has reached the AGN accretion disk at subparsec scales.

1 Introduction

Since the pioneering work of Toomre, binary mergers of gas-rich disk galaxies have been suggested as the main mechanism for the formation of bright elliptical galaxies. Mergers destroy rotational equilibria, transform stellar disks into more spheroidal configurations supported by random velocities, and drive large-scale

ESO Symposia: Growing Black Holes, pp. 346–351, 2005.

gas flows that may result into massive starbursts. If a nuclear supermassive black hole (SMBH) is present in one of the interacting systems, gas inflows toward the former can drive accretion powered energy outflows.

HST spectroscopic observations have indicated that most of the bright elliptical galaxies and spirals with prominent bulges in the local Universe host SMBHs, fossil records of an earlier quasar phase. The SMBH masses seem to correlate tightly with the mass of the stellar spheroid, and thus with the depth of the potential well that is measured by the line-of-sight stellar dispersion velocity, σ. This is suggestive of a strong link between galaxy and SMBH formation and evolution ([7], [8]). AGN feedback can quench star formation when sufficient energy or momentum is injected into the gas on a dynamical time scale shaping the bulge properties farther away from the SMBH gravitational sphere of influence $r_{\rm BH} \sim {\rm G}M_{\rm BH}/\sigma^2$ ([20], [3]). Even on much larger scales, AGN energy outflows can deposit entropy in the hot intracluster medium [2]. This phenomenon has thus important implications for studies whose main goal is to trace the history of cosmic structures (for a physical model of the coevolution of QSOs and their spheroidal hosts see [10]).

The formation and growth of SMBHs has been recently studied in a cosmological context using a statistical formulation (e.g., [21], [15]). These models trace back the evolution of SMBHs nested inside the cores of dark matter (DM) halos. Simple physical recipes are added in a merger tree diagram to describe the history of the baryonic component and the evolution of accreting SMBHs in galactic subunits. The AGN luminosity function at different cosmic times, the $M_{\rm BH}$ versus σ relation, and the QSO luminosity and local SMBH mass density are explained in this context, under the condition that the SMBH mass grows mainly by accretion of gas funneled into the core at a rate close to the Eddington limit. Volonteri, Haardt & Madau [21] were the first to follow the assembly of seed BHs born in population III objects, tracing their dynamics in detail, i.e., including time scales for their sinking by dynamical friction, and keeping non obvious dependences such as eccentricity corrections and mass loss by underlying tidal fields [4]. These authors included the possibility that tidal stripping of mass around the nuclear SMBHs may give rise to "wandering" SMBHs, as it was first suggested by [9].

Hence, the formation of SMBH binaries in a cosmological context is becoming an issue of growing importance: coalescing SMBH binaries with masses between $10^5 - 10^7 {\rm M}_\odot$ are expected to generate the strongest gravitational wave signals that will become detectable with the space-based interferometer LISA. LISA can potentially provide information of the entire process of clustering of structures up to redshift $z \sim 20$ probing the Universe at its cosmic dawn [19]. It is our aim to explore in detail the hydrodynamical processes taking place in a merger between galaxies hosting SMBHs and to study the effect of a gaseous dissipation in the orbital evolution and fueling of the SMBHs. Our approach is thus complementary to the semianalytical studies.

The formation and subsequent dynamical evolution of SMBH pairs depend on how efficiently the galactic cores lose angular momentum on account of dy-

namical friction during the merging process. Four main stages in this process have been highlighted by [1]: (1) SMBH drag toward the center of the common mass distribution by dynamical friction acting on both interacting systems; (2) formation of a SMBH pair as the SMBHs loose angular momentum due to the interaction with the background; (3) slow hardening of the binary SMBH by three-body scattering with the surrounding stars plunging along low angular momentum orbits; (4) further shrinking of the binary SMBH orbit due to emission of gravitational waves and eventual coalescence.

The early phases (1) and (2) have been investigated numerically in the past by a number of authors (e.g., [9], [16]). However, the galaxy models in these studies were idealized, spherical stellar systems with no link to current models of structure formation. These models could at most faithfully represent just the central bulges of real galaxies. Hence, the depiction of the first two phases was incomplete and both the larger scale dynamical evolution of the merging systems and the cosmological framework were missing. Moreover, these studies included no dissipative component, and thus did not explore the role of gas in the formation and evolution of a SMBH pair. Notable exceptions are the studies by [6], who showed that the presence of gas in phase (3) causes continuing loss of orbital angular momentum rapidly reducing the SMBH relative separation to distances where gravitational radiation and coalescence is efficient. However, if and how their initial conditions are related to the larger scale dynamics involved in galaxy merging is still unclear.

2 Numerical Simulations

We performed a number of high-resolution binary merger simulations of disk dominated galaxies with mass ratios of 1:1 and 4:1. We simulate mergers in which gas behaves adiabatically, and mergers in which we include radiative cooling and star formation. For details we refer to [12] . The simulations were performed with GASOLINE, a multi-stepping, parallel TreeSPH N-body code [22]. Each galaxy consists of a spherical and isotropic [18] DM halo, an exponential disk (with gas fraction between 10 and 50% of the total disk mass), and a spherical, [11] non-rotating bulge. For the basic galaxy model we adopted parameters from Milky Way model A1 of [13]. Specifically, the DM halo had a virial mass of $M_{\rm vir} = 7 \times 10^{11}\, h^{-1}{\rm M}_{\odot}$, a concentration $c = 12$, and a dimensionless spin parameter of $\lambda = 0.031$. The mass, thickness and scale length of the disk were $M_{\rm d} = 0.04 M_{\rm vir}$, $z_0 = 0.1 R_{\rm d}$, and $R_{\rm d} = 2.45 h^{-1}$ kpc, respectively. The bulge mass and scale radius were $M_{\rm b} = 0.008 M_{\rm vir}$ and $a = 0.2 R_{\rm b}$, respectively. The companion galaxy is either a replica of the same model in equal-mass mergers or a system containing one-fourth of the mass in each component in which lengths and velocities are renormalized according to the cosmological scaling for virialized systems [17]. To each of the galaxy models was added a particle at the center of the bulge component that represents a central SMBH. For the largest galaxy model we used a mass equal to $M_{\rm BH} = 3 \times 10^6 M_{\odot}$.

3 The dynamics of SMBH pairing

We find that the galaxies merge in three to five orbits (between 5.5 to 7 Gyr). In equal-mass mergers, the cuspy potentials of both galaxies are deep enough to allow the survival of their inner regions until orbital decay by dynamical friction is complete. This result holds for both adiabatic and dissipational mergers. In gasdynamical runs large gas inflows are observed. During the first two orbits a strong spiral pattern appears in both the stellar and the gaseous component and mild non-axisymmetric torques redistribute mass and angular momentum, driving approximately 20% of the gas towards the center. The central bulges stabilize the galaxies against bar formation. Shortly before the galaxies merge, a second much stronger inflow occurs caused by strong tidal torquing. This inflow results in a significant central concentration of cold gas. In this case, more than 80% of the gas that was originally in the disks is collected within the central 500 pc. In runs with star formation these large inflows are associated with a central starburst and more than 90% of the central gas distribution is converted into stars in less than 10^8 yr. The peak star formation rates range from 30 to $> 100\,\mathrm{M_\odot yr^{-1}}$, comparable to those of luminous infrared galaxies. As illustrated in Figure 1, the two SMBHs end up orbiting at the center of the remnant on eccentric orbits and at a separation comparable to the resolution of our simulations of ~ 100 pc.

In unequal-mass mergers, the outcome depends sensitively on the presence or not of dissipation, as shown in Figure 1. In adiabatic runs, the tidal disruption of the satellite galaxy at about 6 kpc from the center leaves its SMBH wandering at a distance that prohibits the formation of a close pair. In dissipational runs, the situation is reversed as the gas inflow becomes particularly strong in the light galaxy. We measured an inflow of about $3\,\mathrm{M_\odot yr^{-1}}$ within the central kiloparsec compared with $< 0.5\,\mathrm{M_\odot yr^{-1}}$ for the larger galaxy. This striking difference in the gas inflows is attributed to a tidally induced stellar bar observed in the satellite galaxy approximately 1.5 Gyr before the final passage. More than 90% of the gas is funneled into the center owing to gas shocking in the bar potential. At this stage the companion galaxy has about 20% more gas within its central ~ 1 kpc relative to the larger galaxy. This is strongly suggestive that dynamical destabilization of the satellite galaxy during the merger may trigger some nucler activity in it, before the merger is completed. Thus, dissipation enables the core of the lighter galaxy to survive complete tidal disruption by deepening its potential well and facilitates the formation of a SMBH pair separated by ~ 100 pc similarly to the equal-mass mergers.

3.1 Massive Nuclear Disks

The large inflows observed in the cooling and star formation simulations always produce a rotationally supported nuclear disk with a size in the range $1 - 2$ kpc, as illustrated in the right panels of Figure 1. The nuclear disks at the center of the remnants show significant spiral patterns (Figure 1) and likely provide the necessary fuel for feeding the SMBHs. These disks are tilted by

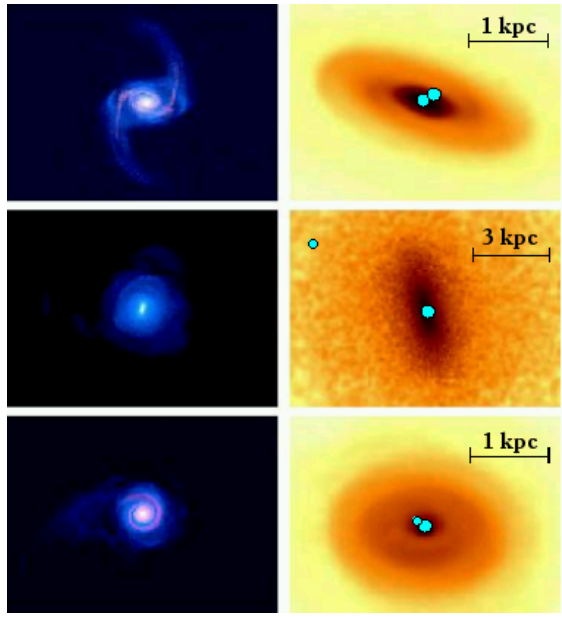

Fig. 1. Final position of supermassive BHs (*filled circles*) in a subset of merger simulations. The large scale (*left*) and small-scale (*right*) structure of the remnants projected onto the orbital plane is also shown. All frames correspond to remnants that were allowed to relax for several dynamical times after the merger was complete. The top and bottom rows of panels present results for the coplanar 1:1 and 4:1 mergers with gas cooling, respectively. The middle rows of panels corresponds to the coplanar adiabatic 4:1 merger. The frames on the left show the logarithmic baryonic surface density maps and are 320×230 kpc. Blue and red maps are used for the stellar and gaseous component, respectively, and adaptive smoothing is used to preserve details in high-density regions. The top and bottom frames on the right are enlarged by a factor of 100 and show the central nuclear gaseous disks. The middle frame on the right shows the stellar distribution of the merger remnant and is enlarged by a factor of 30.

several to a few tens of degrees relative to the orbital plane of the galaxies. They have peak rotational velocities and gas masses in the range of $250 - 300$ km s^{-1} and $\sim 10^8 - 10^9 M_{\odot}$, respectively, and they are resolved by more than 10^4 particles. Nuclear disks of *molecular* gas of a few hundred parsec to a kiloparsec scale have been identified spectroscopically for few AGNs and ULRIGs ([5]), whose observed sizes, masses, and rotational velocities are comparable to those measured in our simulations.

4 Conclusions

Gaseous dissipation influences considerably the outcome of binary mergers of disk dominated galaxies containing SMBHs. Most importantly, it controls the

SMBH pairing process in unequal-mass mergers by modifying the central structure of the companion galaxy and enabling it to survive complete tidal disruption. This result suggests that semi-analytic models of hierarchical SMBH growth that neglect the effect of dissipation likely overestimate the number of wandering SMBHs in MW-sized galaxies [19], since the majority of these result from mergers with mass ratios less than 3:1. Quantifying the number of wandering SMBHs in account of our new results will be of great interest for the LISA experiment.

Moreover, the simulations of dissipative unequal-mass mergers show that the timing of central inflows in the two galaxies can be quite different. Indeed, approximately 1 Gyr before the completion of the merger, we measured in the core of the companion galaxy a factor of ~ 2 larger gas mass compared to that in the larger galaxy. Thus, the satellite galaxy may experience nuclear activity long before the coalescence of the two cores. This might explain the existence of galaxies like Markarian 231 that has two nuclei, yet only one of them hosts an AGN and undergoes intense star formation.

References

1. Begelman, M. C., Blandford, R. D., & Rees, M. J.: Nature, **287**, 307 (1980)
2. Begelman, M. C.: in *Coevolution of Black Holes and Galaxies, from the Carnegie Observatories Centennial Symposia* ed. by L. Ho (CUP, Cambridge) p. 375 (2004)
3. Burkert, A. & Silk, J.: ApJL, **554**, L151 (2001)
4. Colpi, M., Mayer, L., & Governato, F.: ApJ, **525**, 720 (1999)
5. Davies, R. I., Tacconi, L. J., & Genzel, R.: ApJ, **602**, 148 (2004)
6. Escala, A., Larson, R. B., Coppi, P. S., & Mardones, D.: ApJ, **607**, 765 (2004)
7. Ferrarese, L. & Merritt, D.: ApJL, **539**, L9 (2000)
8. Gebhardt, K., et al.: ApJL, **539**, L13 (2000)
9. Governato, F., Colpi, M., & Maraschi, L.: MNRAS, **271**, 317 (1994)
10. Granato,G. L., De Zotti, G., Silva, L., Bressan, A., & Danese, L.: ApJ, **600**, 580 (2004)
11. Hernquist, L.: ApJ, **356**, 359 (1990)
12. Kazantzidis, S., et al.: submitted to ApJL (2004)
13. Klypin, A., Zhao, H., & Somerville, R. S.: ApJ, **573**, 597 (2002)
14. Komossa, S., Burwitz, V., Hasinger, G., Predehl, P., Kaastra, J. S., & Ikebe, Y.: ApJL, **582**, L15 (2003)
15. Menci, N. et al.: ApJ **587**, L63 (2003)
16. Milosavljević, M. & Merritt, D.: ApJ, **563**, 34 (2001)
17. Mo, H. J., Mao, S., & White, S. D. M.: MNRAS, **295**, 319 (1998)
18. Navarro, J. F., Frenk, C. S., & White, S. D. M.: ApJ, **462**, 563 (1996)
19. Sesana, A., Haardt, F., Madau, P., & Volonteri, M.: ApJ, **611**, 623 (2004)
20. Silk, J. & Rees, M. J.: A&A, **331**, L1 (1998)
21. Volonteri, M., Haardt, F., & Madau, P.: ApJ, **582**, 559 (2003)
22. Wadsley, J. W., Stadel, J., & Quinn, T.: New Astronomy, **9**, 137 (2004)

The Role of Gas in the Merging of Massive Black Holes in Galactic Nuclei

A. Escala[1,2], P.S. Coppi[2], R.B. Larson[2], and D. Mardones[1]

[1] Departamento de Astronomía, Universidad de Chile, Casilla 36-D, Santiago, Chile
[2] Department of Astronomy, Yale University, New Haven, CT06520-8101, USA

Abstract. Using high-resolution SPH numerical simulations, we investigate the effects of gas on the inspiral and merger of a massive black hole binary. This study is motivated by the very massive nuclear gas disks observed in the central regions of merging galaxies. Here we present results that expand on the treatment in a previous work [1], by studying more realistic models in which the gas is in a disk with significant clumpiness. In the variety of simulations that we perform, we find that gravitational drag is able to reduce the separation to distances where gravitational radiation is efficient in a timescale that varies between 5×10^6yr and 2.5×10^7yr.

1 Results

We run a variety of models, ranging from simulations with a relatively smooth gas disk to cases in which the gas has a more clumpy spatial distribution. We also vary the inclination angle between the plane of the binary and the plane of the disk, and the mass ratio between the MBHs and the gaseous disk.

We start by varying the level of clumpiness, controled by the parameter K in the E.O.S. ($P = K\,\rho^{5/3}$). We consider first an MBH binary in which each black hole has a mass equal to 1% of the total gas mass, initially in a circular orbit with a binary separation of 400 pc. Figure 1 shows the evolution of the binary separation in these four cases over several orbits. In the early evolution of the system, the separation diminishes due to the gravitational drag exerted by the background medium; this regime lasts until the binary separation is approximately 40 pc. The marked increase of the coalescence timescale when the binary separation is less than 40 pc happens because the MBHs then come close enough that the wake formed by each MBH is disrupted by the gravity of the other MBH, and therefore the gravitational drag decreases. After this temporarily slow transition regime, the subsequent evolution of the binary leads to rapid coalescence in only another $\sim 10^6$yr.

The binary evolution has a strong dependence on the parameter K, and the cases with lower K (higher clumpiness) suffer a stronger deceleration. The explanation involves the gas density close to each MBH, which is higher for lower K. As a result, because the gravitational drag is stronger in a denser environment, the binary MBH separation shrinks faster in the cases with lower K.

We also study the effect of varying the ratio between the mass of the MBHs and the mass of the gas disk. We consider four cases with black hole masses of 1%, 3%, 5% & 10% of the total gas mass (Figure 2). Initially the separation

ESO Symposia: Growing Black Holes, pp. 352–353, 2005.

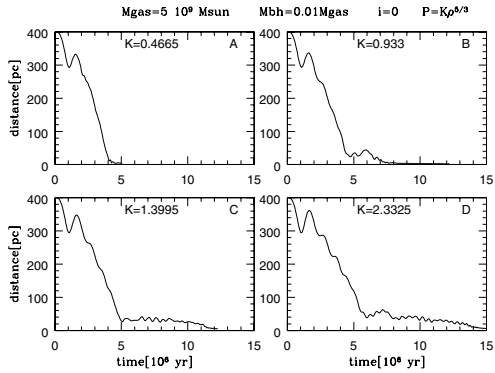

Fig. 1. This plot shows the evolution of the binary separation for runs with four different values of K, as indicated. In all cases the mass of each MBH is 1% of the mass of the gas, and the orbit of the binary is in the plane of the disk.

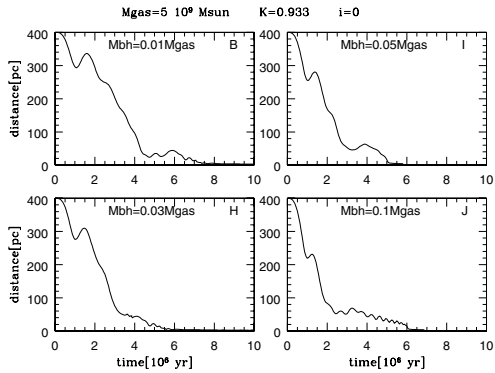

Fig. 2. This plot shows the evolution of the binary separation for runs which assume 4 different ratios between the mass of each MBH and the mass of the gas disk: 0.01, 0.03, 0.05, 0.1. For these runs we adopt an equation of state with K=0.933, and the orbit of the binary is in the plane of the disk.

diminishes due to the gravitational drag exerted by the background medium, the binary coalescence timescale depends on the black hole mass, with the more massive cases suffering a stronger deceleration. But when the binary arrives to the transition regime, Figure 2 shows that there is no longer a clear dependence on the black hole mass; this is because as we increase the black hole mass, the wake formed is stronger, but the disruption of the wake by the gravity of the other MBH is also stronger.

References

1. A. Escala, R. B. Larson, P. Coppi & D. Mardones: ApJ, **607**, 765 (2004)

Mergers and Binary Systems of SMBH in the Contexts of Nuclear Activity and Galaxy Evolution

A. Lobanov

Max-Planck-Institut für Radioastronomie, Auf dem, Hügel 69, 53121 Bonn, Germany

Abstract. The dynamic evolution of binary systems of supermassive black holes (SMBH) may be a key factor affecting a large fraction of the observed properties of active galactic nuclei (AGN) and galaxy evolution. Different classes of AGN can be related in general to four evolutionary stages in a binary SMBH: 1) early merger stage; 2) wide pair stage; 3) close pair stage; and 4) pre-coalescence stage.

Mergers are expected to occur frequently over the course of galaxy evolution. Formation of binary (or multiple) systems of SMBH is a likely outcome of galactic mergers. Binary black hole (BBH) systems should therefore play an important role in the nuclear activity of galaxies, since the latter is believed to be closely related to SMBH. Analytical work may help identifying main trends of the co-evolution of AGN and BBH. A good starting point for this work is provided by a number of studies of BBH dynamics (e.g., [1] and subsequent works) and interaction of supermassive black holes with nuclear environment in galaxies [2,4]. Based on these studies, a scheme can be proposed that connects distinct stages of the binary evolution to characteristic types of AGN and galactic morphology associated with them.

1. Early merger — Low-power AGN: Individual galaxies or early mergers (while both BH retain their accretion disks). Timescale and magnitude of nuclear activity depend on the conditions in the central regions, and it is likely that a cavity is formed around the BH, producing a "starving", low–power AGN [2]. If galaxies were formed at redshifts $z \sim 5-10$, the peak of single BH activity in galaxies is likely to occur at $z \sim 1$. Around this redshift, AGN with single SMBH may represent a (probably small) fraction of quasars and FR II type radio galaxies. At later epochs a single SMBH in the center of a galaxy is expected to reduce its fueling rate to $F \leq 10^{-3}\,[\dot{\mathrm{M}}_{\mathrm{Edd}}]$, and support a typical luminosity of $L \leq L_{\mathrm{Edd}}\,F \approx 10^{43} M_8\,\mathrm{erg/s}$. ($M_8 = M_{\mathrm{bh}}/10^8\,M_\odot$). This activity would be similar to that found in a typical Seyfert galaxy. The activity should remain weak during an early merger and relaxation of the galactic cores, which is expected to last for $\sim 10^8$ years, [4,5]. An AGN at this stage would have weak pc-scale and (FR I) kpc-scale jets, weak broad line regions, and very weak variability.

2. Wide pair — High-power AGN: After the merger, the BHs sink toward the center of the stellar distribution and form a gravitationally bound system, with typical orbital separations $r_{\mathrm{b}} \sim 1 - 10\,\mathrm{pc}$ and initial orbital velocities $v_{\mathrm{init}} \sim 10 - 100\,\mathrm{km/s}$. The dynamical friction would reduce the orbital separation to $r_{\mathrm{b}} \sim 0.1-1\,\mathrm{pc}$, and the smaller BH would eventually lose its accretion disk. The accretion disk is aligned with the orbital plane and disrupted by

ESO Symposia: Growing Black Holes, pp. 354–355, 2005.

the secondary BH. Interaction of the BBH with the stars and gas would increase the fueling rate by a factor of 10–100 [2], bringing it close to $\dot{M}_{\rm Edd}$ and supporting a luminosity of $\leq 10^{46}$ erg/s on timescales of $\sim 10^8$ years. BBH systems at this stage should produce strong pc-scale and (FR II) kpc-scale jets; strong broad line regions, and variability on timescales $\tau_{\rm var} \sim 10^2$–10^4 days.

3. Close pair — Radio-quiet AGN: At orbital separations $r_{\rm b} \sim 10^{-2} - 1$ pc, the interaction of the secondary BH with the accretion disk intensifies so that it may even lead to a complete destruction of the disk. A turbulent activity in the nuclear region would result in strong thermal emission in the optical and high-energy band, varying on timescales $\tau_{\rm var} \sim 10^0$–10^3 days. The jet production stops, and the level of radio emission is reduced substantially. The fueling rate is also reduced, and the resulting luminosities would reach up to $\leq 10^{45}$ erg/s. This stage lasts for $\leq 10^8$ years. An AGN at this stage is a "radio quiet" QSO (one should remember, however, that there are several possible factors potentially capable of quenching the jet production in AGN).

4. Pre-coalescence — Intraday variable AGN: At separations $r_{\rm b} \leq 10^{-2}$ pc, gravitational radiation becomes the most important evolutionary factor. With $r_{\rm b} \gg r_{\rm acc}$, it is possible that an accretion disk is formed again around the BBH. Luminosities of up to $\leq 10^{45}$ erg/s should be expected. This stage would last for $\sim 10^7$ years. A typical AGN at this stage would be an intraday variable source (with prominent variability on timescales $\tau_{\rm var} \sim 10^{-1}$–$10^3$ days), with "re-started" pc-scale radio jets, (and possible kpc-scale relics), and a prominent broad line region. The relativistic effects and orbital motion will result in variability on timescales that correspond to brightness temperatures of up to

$$T_{\rm b,max} = 5.58 \cdot 10^{11} \Delta S_{\rm var} \delta^{2-\alpha} \left[\frac{\lambda_{\rm obs} D_{\rm L} (\mu^3 + \mu^2)^{1/5}}{M_8 (1+z)^2} \right]^2 \,[{\rm K}]\,,$$

where μ is the mass ratio of the binary and δ is the Doppler factor of the emitting material. Example: 0917+624: $z = 1.446$, $\Delta S_{\rm var} = 0.14\,{\rm Jy}$, $\tau_{\rm min} = 0.285\,d$ at $\lambda_{\rm obs} = 6\,{\rm cm}$ $T_{\rm b,obs} = 1.4 \cdot 10^{19}\,{\rm K}$ [3]. Model estimate: $T_{\rm b,max} = 4 \cdot 10^{20}\,{\rm K}$, for $M_{\rm bh} = 10^7 {\rm M}_\odot$, $\mu = 1$, $\delta = 1$.

The proposed connection between BBH evolution and AGN is not necessarily unique and exclusive, but it should provide a viable skeleton for building up more complex and detailed models relating nuclear activity to the properties of multiple black holes in active galaxies. In particular, it would be important to investigate joint cosmological evolution of active galaxies and supermassive BBH embedded into their nuclei.

References

1. M.C. Begelman, R.C. Blandford, M.J. Rees: Nature **287**, 307 (1980)
2. V.I. Dokuchaev: MNRAS, **251**, 564 (1991)
3. A. Kraus et al: A&A, **352**, 107 (1999)
4. A.G. Polnarev, M.J. Rees: A&A, **283**, 301 (1994)
5. N. Roos: A&A, **104**, 218 (1991)

Gravitational Waves from Massive Black Holes Binaries

A. Sesana[1], F. Haardt[1], P. Madau[2], and M. Volonteri[2]

[1] Dipartimento di Fisica e Matematica, Università dell'Insubria, via Valleggio 11, 22100 Como, Italy
[2] Department of Astronomy & Astrophysics, University of California, 1156 High Street, Santa Cruz, CA 95064

Abstract. We compute the expected gravitational wave (GW) signal from coalescing massive black hole (MBH) binaries in a hierarchical structure formation scenario based on the standard ΛCDM cosmology. The integrated emission from the MBH binaries results in a gravitational wave background (GWB). We discuss observability of such GWB by planned Laser Interferometer Space Antenna (*LISA*) [1,2].

1 Model Description

We track backwards [3] the merger history of parent halos (and associated MBHs) with present day mass in the range $10^{11} - 10^{15}\,\mathrm{M}_{\odot}$ using a Monte Carlo algorithm based on the extended Press-Schechter formalism up to $z = 20$. We simulate a total of 220 halos weighting the results with the Press-Schechter halo mass function.
We place seed holes with $m_{\rm seed} = 150\,\mathrm{M}_{\odot}$ within halos above $M = 10^7\,\mathrm{M}_{\odot}$ collapsing at z=20 from rare 3.5 σ density peaks. We assume that in each major merger the more massive hole accretes, at the Eddington rate, a gas mass such to recover the $m_{BH} - \sigma$ relation. During mergers, dynamical evolution of forming MBH binaries is followed taking into account for the main physical processes involved, such as dynamical friction against the dark matter halos, the hardening of MBH pairs via three-body scattering of background stars, GW emission, triple MBH interactions, and the "gravitational rocket'. GW emission takes over at small radii and lead MBH pairs to coalescence.

2 Results

We model GW emission from each binary with quadrupole formalism, integrating contribution of all systems in order to evaluate the total GWB [1]. The result is shown, in terms of the characteristic GW strain amplitude h_c [4], in fig. 1. We discuss the nature of such a background, discriminating resolvable sources from confusion noise [5]. We find that *LISA* will resolve the GWB into discrete sources detecting ≈90 events over a 3 yr observation period (fig. 2, left panel). Once subtracted resolvable sources, the remaining confusion noise is expected to be well below planned *LISA* sensitivity (fig. 2, right panel).

ESO Symposia: Growing Black Holes, pp. 356–357, 2005.

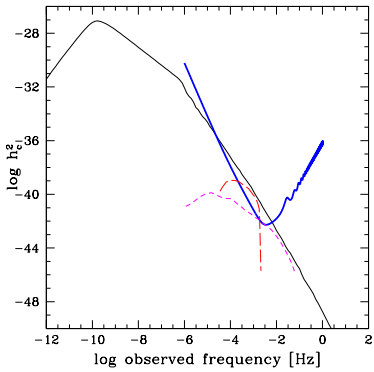

Fig. 1. Total GWB from inspiraling MBH binaries. The square of the characteristic strain is plotted vs. wave frequency (*thin solid line*). *Thick solid line: LISA* sensitivity curve. Expected strain from extragalactic [6](*short-dashed line*) and galactic [7] (*long-dashed line*) white dwarf binaries are also plotted .

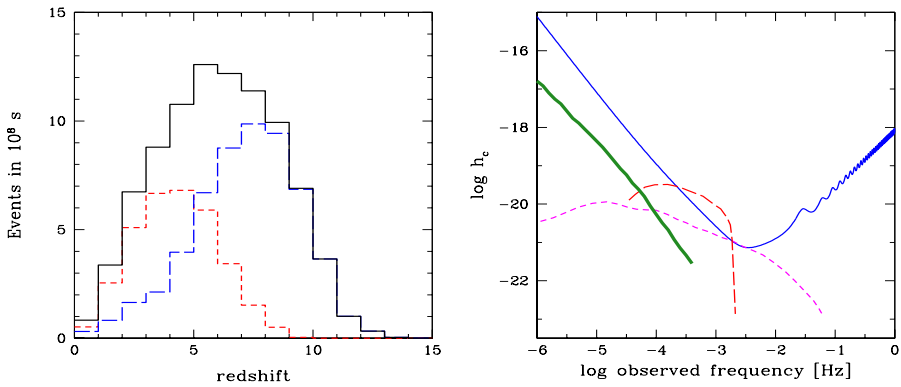

Fig. 2. Left panel: Total number counts of sources as a function of redshift (*solid line*), divided into coalescences (*short-dashed line*) and shifting sources (*Long-dashed line*) [2]. Right panel: h_c level of confusion noise due to MBH binaries against frequency (*thick solid line*). Other lines have the same meaning as in fig. 1.

References

1. Sesana, A., Haardt, F., Madau, P., Volonteri, M.: ApJ, 611, 623 (2004)
2. Sesana, A., Haardt, F., Madau, P., Volonteri, M.: in preparation (2004)
3. Volonteri, M., Haardt, F., & Madau, P.: ApJ, 582, 599 (2003)
4. Thorne, K. S.: in 300 Years of Gravitation, ed. S. Hawking & W. Israel (Cambridge: Cambridge Univ. Press), 330 (1987)
5. Cornish N. J.: arXiv:gr-qc/0304020 (2003)
6. Farmer, A. J., & Phinney, E. S.: MNRAS, in press (astro-ph/0304393) (2003)
7. Nelemans, G., Yungelson, L. R., & Portegies-Zwart, S. F.: A&A, 375, 890 (2001)

At the Beer and brezen' party on Tuesday

At the Beer and brezen' party on Tuesday

Outbursts from Supermassive Black Holes and Their Impacts on the Hot Gas in Elliptical Galaxies

W. Forman[1], C. Jones[1], E. Churazov[2,3], S. Heinz[4], R. Kraft[1], M. Markevitch[1], P. Nulsen[1], and A. Vikhlinin[1,3]

[1] Smithsonian Astrophysical Observatory, CFA Cambridge, MA, USA
[2] Max Planck Institute for Astrophysics, Garching, Germany
[3] IKI, Space Research Institute, Moscow, Russia
[4] MIT, Cambridge, MA, USA

1 AGN, Cluster Cores, and Cooling Flows

Many clusters have surface brightness distributions that are regular with strong peaks on a bright, central, often cD, galaxy. In the Einstein X-ray survey of 215 clusters, 64% of clusters contained a bright X-ray peak, centered on an optically bright galaxy [27]. These systems, described as **X**-ray **D**ominant (XD) clusters, are those that have high central gas densities and hence short cooling times. In the absence of energy input, the most remarkable XD systems are calculated to be depositing mass at rates as high as 1000 $M_\odot$ yr^{-1} (e.g., [14]). For many years, these centrally peaked, XD clusters have been described with a "cooling flow" model, first developed by Fabian & Nulsen [16] and Cowie & Binney [11]. However, observations with XMM-Newton have shown that mass deposition rates in cooling flow clusters, although still significant, are at least five times smaller than expected in the standard model ([37] and references therein). This requires considerable energy input to compensate for radiative losses.

The phenomenon of "cooling flows", described for luminous clusters, also applies to other systems with gaseous atmospheres. In particular, galaxy groups, the poorer cousins of rich clusters [25] and individual early type galaxies with their luminous X-ray coronae [20] also frequently have short gas cooling times at their centers [40].

To compensate for the radiative losses, a variety of mechanisms have been proposed including cluster mergers, thermal conduction [43,2,22,12,47], and energy input from AGN in the central galaxy [39,5,44,24,38,9,10]. In this contribution, we discuss the interaction between energy output from AGN and the surrounding, hot gaseous atmospheres.

2 Energy Input from Active Nuclei

One of the most promising energy sources for replenishing the energy radiated by hot gas in clusters, groups, and individual early type galaxies is energy input from supermassive black holes that lie in galaxy nuclei. One early clue that AGN

ESO Symposia: Growing Black Holes, pp. 363–370, 2005.

were an important source of energy was the high frequency of radio activity in the central cluster galaxy of XD clusters (70%) compared to that in galaxies with non-peaked X-ray emission (20%) [8].

Using radio studies, Owen, Eilek & Kassim [36] pioneered the view that the mechanical power produced by the supermassive black hole at the center of M87 was more than sufficient to compensate for the energy radiated in X-rays. Churazov et al. [9] (see also [29,7,13,28]) argued that the morphology of the X-ray and radio observations could be explained by radio emitting plasma bubbles buoyantly rising through the hot X-ray emitting gas. These buoyant bubbles could uplift the coolest gas and provide energy input, as bubble enthalpy is converted to kinetic energy, then thermalized in the bubble wake.

2.1 Cavities and Buoyant Bubbles

With Chandra, more direct evidence for the importance of AGN energy input to hot gas in early type galaxies, groups, and clusters was manifest in the frequent detection of plasma cavities in the hot gas. For NGC1275, the active galaxy at the center of the Perseus cluster, the cavities evacuated of hot gas by the radio emitting relativistic plasma where first detected with ROSAT [6] while Chandra observations mapped the structure of these cavities in great detail [17]. With Chandra, similar cavities were detected around galaxies e.g., M84, [19], in groups e.g., [45,33], and in other rich clusters e.g., [34,17,4].

Since the cavities were found to be surrounded by bright rims of cool gas (e.g., [17]), alternatives to shock heating models were proposed. Churazov et al. [9] (see also [29,7,13,28]) used M87 to study the effects of buoyant bubbles on the surrounding gas. They showed that the structure seen in the radio and X-ray images was consistent with that expected from multiple outbursts that inflate buoyant bubbles which rise through the gaseous atmosphere and produce mushroom-shaped structures. Many of these features are seen in Fig. 2 (discussed in more detail below). Thus, a self-regulated system, with intermittent outbursts creating buoyant bubbles, can produce the observed X-ray and radio structures and can replenish much of the energy radiated by the X-ray luminous gas, and thereby significantly reduce the expected mass deposition in "cooling flows".

Churazov et al. developed a model to explain the self-regulation of the accretion process around supermassive black holes [10]. In this simple model, the supermassive black hole lies at the bottom of the gravitational potential surrounded by the lowest entropy gas. When cooling dominates, the gas entropy decreases and accretion increases. The higher accretion rate increases the energy ouput of the central black hole and the energy input to the gas increases, its entropy increases, and the accretion declines.

2.2 Shocks and Buoyant Bubbles in M87

While bouyant bubbles and cavities are becoming a commonly observed feature in "cooling flow" clusters, there is increasing evidence for weak shocks that contribute to heating the X-ray emitting gas. Fabian et al. [18] first reported

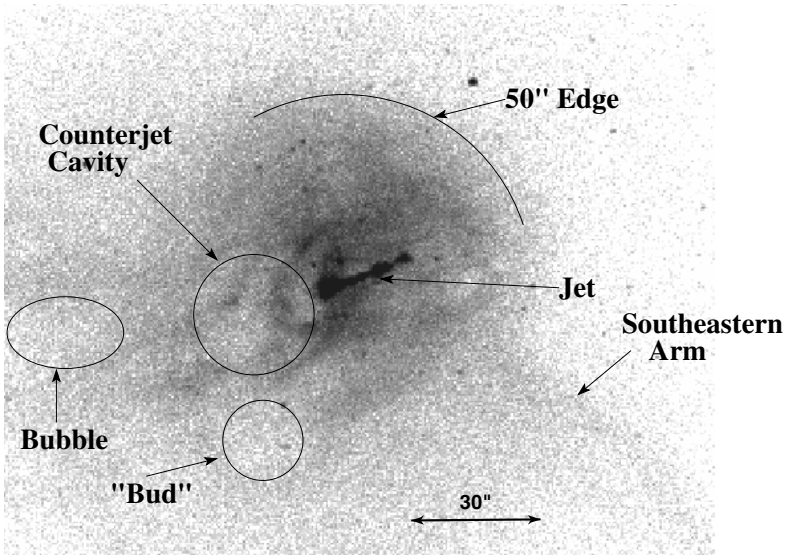

Fig. 1. The central region of M87 as seen by the Chandra ACIS-S detector in the energy band 0.5 to 2.5 keV. The core region shows the jet, the counterjet cavity, a "bud" emanating from the southeastern edge of the counterjet cavity, and the beginning of the southwestern arm.

evidence for repeated shocks surrounding NGC1275 in Perseus. The Chandra observations showed faint ripples interpreted as sound waves or weak shocks, having been produced by multiple outbursts from the central AGN [41]. With a sound speed of 1170 km $s^{-1}$and a period of about 10^7 years, Fabian et al. argued that these shocks could provide sufficient energy to balance the radiative energy losses from the the central 100 kpc cluster core.

A second and more detailed view of the interaction of AGN outbursts with a cluster atmosphere came from observations of M87, the dominant central galaxy in the nearby Virgo cluster [46,21]. The M87 Chandra observations show (Fig. 1) the counterjet cavity and a bubble (labeled "bud" in Fig. 1) erupting from the counterjet cavity, corresponding to the southeastern extension of the bright core in the 6 cm radio observations [26]. Other cavities in the eastern arm (labeled "bubble" in Fig. 1) have no detected radio emission and are "ghost" cavities, a term coined by Ensslin [15].

On larger scales, Fig. 2 shows a remarkable variety of structure including:

- a nearly azimuthally symmetric ring of emission with a leading edge at a radius of 14 kpc (3′), most prominent to the north and northwest
- a second partial ring of enhanced emission, just beyond the 14 kpc ring, at a radius of 17 kpc
- the prominent eastern and southwestern arms. These arms are seen as cooler gas in the XMM-Newton temperature map [35,21]

- at radii beyond the 14 kpc ring, the division of each arm into two filaments. For the southwestern arm, the filaments (labeled **S1** and **S2** in Fig. 2) turn east while for the eastern arm, the two filaments (labeled **E1** and **E2** in Fig. 2) turn north.
- a southern arc, at a radius of approximately 37 kpc ($\sim 8'$) (also seen in the ROSAT HRI and XMM-Newton images [21]).

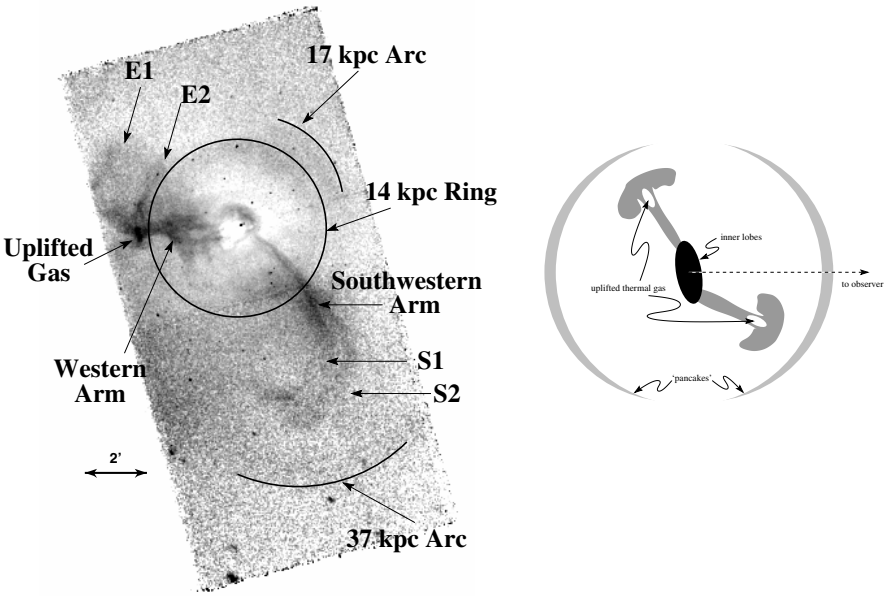

Fig. 2. (left) The flat-fielded Chandra image in the energy band 0.5-2.5 keV with a King model subtracted to remove the large scale radial surface brightness gradient. Many faint features are seen including 1) the prominent eastern and southwestern arms and their bifurcation (**E1, E2** and **S1, S2** identify the extensions of the eastern and southwestern arms), 2) the 14 kpc ($3'$) ring, 3) the 17 kpc ($3.75'$) arc, and 4) the faint southern 37 kpc ($8'$) arc. (right) A schematic of M87. The black region in the center denotes the inner radio lobes, gray "mushrooms" correspond to the buoyant bubbles, and the gray lens-shaped structures are flattened older bubbles (see Churazov et al. for a detailed discussion [9]).

The 14 kpc ring is the clearest example of a shock-driven feature in M87 (Fig. 2). A simple model was used to calculate the energy in an initial outburst that gave rise to the 14 kpc ring. Assuming a single outburst into a hydrostatic, isothermal atmosphere, described by a power-law gas density profile which matches that observed, we found that an energy deposit of 8×10^{57} ergs about 10^7 yrs ago can produce both the observed gas density and gas temperature profiles.

A second partial ring is seen to the northwest at a radius of 17 kpc (3.75′) extending over $\sim 60^\circ$ in azimuth (see Fig. 2). To form this surface brightness enhancement, a disturbance traveling at the sound speed would have originated approximately 4×10^6 years before the event that created the 14 kpc ring. The amplitude of the 17 kpc ring is comparable to that of the 14 kpc ring and therefore would require a similar amount of injected energy.

These two rings at radii of 14 and 17 kpc in M87 are very similar to the structures seen by Fabian et al. [17] in Perseus. As in Perseus, they can provide sufficient energy to balance the radiative cooling in the core, if the outbursts recur with time averaged outputs similar to that observed over the past 10^7 years.

While the rings and arcs around M87 and NGC1275 probably owe their origins to shocks produced by AGN outbursts, other structures seen in M87 clearly show the effects of the buoyant bubbles. In particular, the eastern and southwestern arms (seen in the X-ray and radio images [21,36]; see Fig. 2) are likely the result of rising buoyant bubbles, since their gas temperatures are cooler than the ambient atmosphere [35,1] as first described by Churazov [9].

We have described several of the remarkable structures seen in the Chandra and XMM-Newton observations of M87. Many of these, particularly the bubbles emanating from the central region, the nearly circular rings of enhanced emission at 14 kpc and 17 kpc, and the brightening of the X-ray arms at these radii, can be attributed to AGN outbursts. The 14 kpc and 17 kpc rings can be interpreted as shock waves driven by the current outburst that began about 10^7 years ago. The outburst also inflated the inner radio lobes (and cocoon). Outbursts like those that produced these shocks can quench the M87 cooling flow, if they occur approximately every 3×10^7 years.

The hot X-ray emitting gas contains reflections of previous episodes of AGN activity in the form of bubbles and their bright rims, shocks, and buoyantly uplifted gas structures. With the detailed observations at X-ray and radio wavelengths of M87, we can probe the interaction between the central AGN, the relativistic plasma, and the X-ray gas. We are beginning to understand the cyclic heating of the X-ray gas and the energy transfer mechanisms between the central supermassive black hole and the hot gaseous atmosphere that surrounds central cluster galaxies.

2.3 Centaurus A – Jets in a Cool ISM

Centaurus A is a spectacular example showing energy input from an active nucleus into a hot galactic corona (see the series of papers by Kraft et al. [30–32]; also [23]). At a distance of only 3.5 Mpc, Cen A provides a unique look at an active galaxy undergoing a merger. Fig. 3 shows a recent "raw" Chandra image with several hundred compact binary sources, the X-ray jet extending to the northeast and an X-ray lobe extending in the counter jet (southwest) direction.

X-ray modelling of the southwestern lobe yields a measurement of the expansion velocity of the lobe. Kraft et al. showed that the southern radio lobe was expanding into a 0.3 keV galaxy corona and that the gas temperature of the

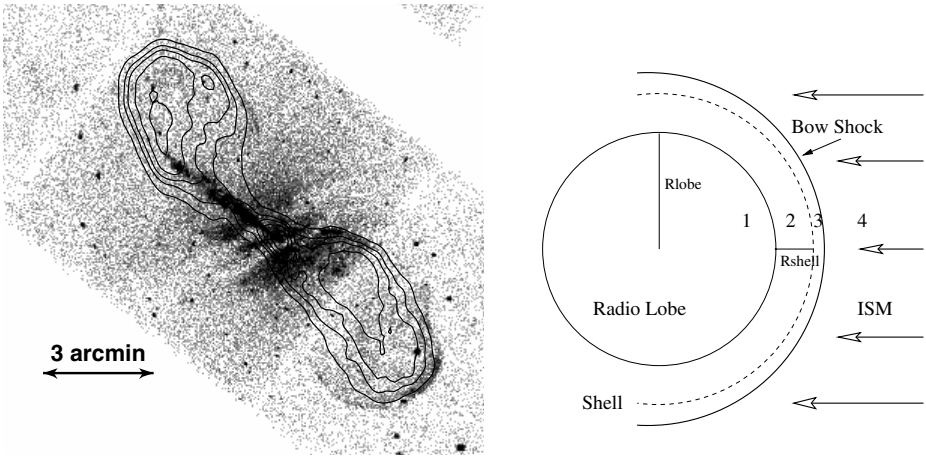

Fig. 3. (**left**) The "raw" Chandra image of Cen A showing the jet, compact X-ray sources, diffuse emission from the galactic corona, and the southwestern lobe. Contours from the 13cm radio image of Cen A are superposed to show that the southwestern radio lobe is driving the leading edge of the X-ray shell. (**right**) Region 1 is the radio lobe, region 2 the observed X-ray enhancement region, region 3 is a physically thin layer where the Rankine-Hugoniot shock conditions are met, and region 4 is the ambient ISM into which the radio emitting plasma bubble is expanding.

bright leading edge of the lobe (see Fig. 3) had a temperature of about ~ 3 keV. The relativistic, radio emitting plasma in the lobe is expanding into an ISM described as a β-model with a=0.5 kpc and $n_H(0)$=$(3.7\pm0.4)\times10^{-2}$ cm $^{-3}$.

The model proposed for the lobe (see Fig. 3) includes 1) a volume of relativistic plasma, 2) the "bright" observed X-ray shell (3 keV), 3) a thin, hot boundary layer between the X-ray shell and the external 0.3 keV ISM where the Rankine-Hugoniot conditions are satisfied, and 4) the external ISM. By matching the thermal pressure in the X-ray shell (region 2) with the thermal and ram pressure in the hot boundary layer (region 3), we find a gas temperature in the boundary layer of $T \sim$6.5 keV. In turn, this yields the expansion velocity of the lobe of Mach ~ 8.5, or $\sim$2400 km s^{-1}.

We do not directly observe the bow shock, but rather the cooler, denser material that is accumulating ahead of the contact discontinuity. The thermal energy in the shell is a significant fraction of the thermal energy of the hot ISM, demonstrating the possibility that the hot ISM of early galaxies can be re-energized by outflows from nuclear activity.

3 Conclusion

With the detailed cluster, group, and early type galaxy observations from Chandra and XMM-Newton, we are unravelling the puzzle posed by cooling flows and understanding how supermassive black holes are able to re-energize and heat the atmospheres in their parent galaxies, groups, and clusters. We are beginning

to see how energy is transferred from the SMBH to the hot gas. We see shocks, driven by multiple nuclear outbursts, and extensive networks of buoyant bubbles of relativistic plasma transferring energy to the ambient gas as they rise through hot gaseous atmospheres.

Acknowledgments

This work was supported by the Smithsonian Astrophysical Observatory, the Max Planck Institute for Astrophysics, the Space Research Institute of the Russian Academy of Sciences, and the Massachusetts Institute of Technology.

References

1. Belsole, E. et al.: A&A, 365, L188 (2001)
2. Bertschinger, E. & Meiksin, A.: ApJL, 306, L1 (1986)
3. Binney, J. & Tabor, G.: MNRAS, 276, 663 (1995)
4. Blanton, E., Sarazin, C., McNamara, B.: ApJ, 585, 227 (2003)
5. Böhringer, H. & Morfill, G.: ApJ, 330, 609 (1988)
6. Böhringer, H., Voges, W., Fabian, A., Edge, A. & Neumann, D.: MNRAS, 264, L25 (1993)
7. Bruggen, M.: ApJ, 592, 839 (2003)
8. Burns, J.: AJ, 99, 14 (1990)
9. Churazov, E., Bruggen, M., Kaiser, C., Böhringer, H. & Forman, W.: ApJ, 554, 261 (2001)
10. Churazov, E., Sunyaev, R., Forman & Böhringer, H.: MNRAS, 332, 729 (2002)
11. Cowie, L. & Binney, J.: ApJ, 215, 723 (1977)
12. David, L., Hughes, J. & Tucker, W.: ApJ, 394, 452 (1992)
13. De Young, D.: MNRAS, 343, 719 (2003)
14. Edge, A. et al.: MNRAS, 270, L1 (1994)
15. Ensslin, T. A.: in Diffuse Thermal and Relativistic Plasma in Galaxy Clusters, p. 275, astro-ph/9906212, (1999)
16. Fabian, A. & Nulsen, P.: MNRAS, 180, 479 (1977)
17. Fabian, A. et al.: MNRAS, 318, L65 (2000)
18. Fabian, A. et al.: MNRAS, 334, L43 (2003)
19. Finoguenov, A. & Jones, C.: ApJL, 547, L107 (2001)
20. Forman, W., Jones, C. and Tucker, W.: ApJ, 293, 102 (1985)
21. Forman, W. et al.: submitted to ApJ, astro-ph/0312576 (2004)
22. Gaetz, T.: ApJ, 345, 666 (1989)
23. Hardcastle, M. et al.: ApJ, 593, 169 (2003)
24. Heinz, S., Reynolds, C., Begelman, M.: ApJ, 501, 126 (1998)
25. Helsdon, S., Ponman, T., O'Sullivan, E. & Forbes, D.: MNRAS, 325, 693 (2001)
26. Hines, D., Owen, F. & Eilek, J.: ApJ, 347, 713 (1989)
27. Jones, C. and Forman, W.: ApJ, 511, 65 (1999)
28. Kaiser, C.: MNRAS, 343, 1319 (2003)
29. Kaiser, C. & Binney, J.: MNRAS, 338, 839 (2003)
30. Kraft, R. et al.: ApJ, 560, 675 (2001)
31. Kraft, R. et al.: ApJ, 569, 64 (2002)
32. Kraft, R. et al.: ApJ, 592, 129 (2003)
33. Mazzotta, P. et al.: ApJL, 567, L37 (2002)
34. McNamara, B. et al.: ApJL, 534, L135 (2000)

35. Molendi, S.: ApJ, 580, 815 (2002)
36. Owen, F., Eilek, J. & Kassim, N.: ApJ, 543, 611 (2000)
37. Peterson, J. et al.: Proceedings of "The Riddle of Cooling Flows in Clusters of Galaxies" eds. Reiprich, Kempner, Soker, astro-ph/0310008 (2003)
38. Reynolds, C., Heinz, S., Begelman, M.: ApJL, 549, L179 (2001)
39. Rosner, R. & Tucker, W.: ApJ, 338, 761 (1989)
40. Thomas, P., Fabian, A., Arnaud, K., Forman, W. & Jones, C.: MNRAS, 222, 655 (1986)
41. Ruszkowski, M., Bruggen, M., Begelman, M.: ApJ, 611, 158 (2004)
42. Tucker, W., Tananbaum, H., and Remillard, R.: ApJ, 444, 532 (1995)
43. Tucker, W. & Rosner, R.: ApJ, 267, 547 (1983)
44. Tucker, W. & David, L.: ApJ, 484, 602 (1997)
45. Vrtilek, J., Grego, L., David, L., Ponman, T., Forman, W., Jones, C. & Harris, D.: APRB17107 (2002)
46. Young, A., Wilson, A., Mundell, C.: ApJ, 579, 560 (2002)
47. Zakamska, N. & Narayan, R.: ApJ, 582, 162 (2003)

The Importance of Jets for Black Hole Growth

S. Heinz[1,2], R. Sunyaev[3], A. Merloni[3], and T. Di Matteo[3]

[1] Center for Space Research, MIT,77 Mass. Ave., Cambridge, MA 02139, USA
[2] Chandra Fellow
[3] Max-Planck-Institute for Astrophysics, Karl-Schwarzschild-Str. 1, Garching 85741, Germany

Abstract. The scale invariance model [10] can be used to derive robust scaling relations between the radio luminosity from accreting black holes and the black hole mass and accretion rate. These relations agree well with the recently found "fundamental plane" of black hole activity [12]. Using these relations and the well known radio luminosity function, we derive estimates of the current and integrated power input by jets from growing black holes. Comparison with the estimated black hole mass density shows that the conversion efficiency from accreted rest mass to jet energy should be about 10% (with rather large uncertainties).

1 Introduction

Jets play a two-fold role in regulating and facilitating black hole growth. Firstly, they energize and transform the surrounding medium and are one of the primary candidates for large scale feedback in structure formation. See the contributions from Begelman and from Di Matteo and Springel in these proceedings for details on how AGN jet heating might occur.

The second role jets play in the process of structure formation and black hole growth is less well understood, but nonetheless important: it seems plausible now that some modes of accretion onto black holes not only facilitate jet formation, but actually require it [2] and there is mounting evidence from the X-ray binary community that steady jets are universally present in objects that are in the so-called low/hard state. This necessity might arise from the fact that jets can carry away mass, energy, and angular momentum from the accretion flow. Furthermore, jets offer a direct probe of the innermost regions around black holes where they are formed, and are thus important probes of strong gravity.

Despite the seeming importance of jets for cosmological studies of black holes, we still lack some of the most fundamental information about the nature of jets. Their particle and magnetic field content is still not known definitively, as are the processes that collimate and accelerate them and the actual bulk velocities of the jet plasma. The single most important variable for feedback studies, the kinetic power of the jet $L_{\rm kin}$, is therefore not known well at all. In this article, we will point out a new method to estimate this important parameter.

ESO Symposia: Growing Black Holes, pp. 371–376, 2005.

2 A New Diagnostic Tool for Accreting Black Holes

The recent discovery of a fundamental relation between the radio emission from jets in X-ray binaries (XRBs) and the X-ray luminosity in these objects [4,8] has inspired a new approach to study the nature of jets, which tries to determine important jet properties without the necessity to understand every complex detail of jet structure and evolution in detail. We will lay out below how this method can be used to study jets and how it can be useful for understanding the impact of jets on black hole growth.

In [10], we presented the scale invariance model, which builds the basis of the following arguments. The main idea of the model is that only very few parameters govern the physics of the inner accretion disk, namely the black hole mass M, the accretion rate $\dot{m}$, and possibly black hole spin (which we will neglect in the following).

The only relevant scale imposed by these parameters is assumed to be the gravitational radius $r_{\rm g}$ and we will assume that all relevant jet physics is invariant under changes of this scale. In other words, a jet from a black hole of mass M_1 will have the same proportions and spatial evolution of dynamical variables as a jet from a black hole of mass M_2, but its spatial scales will be different by a factor of M_1/M_2. Mathematically, this means that any quantity f relevant to jet dynamics can be expressed in the form

$$f(\mathbf{r}, M, \dot{m}, a) = \Phi_f(M, \dot{m}, a)\Psi_f(\mathbf{r}/r_{\rm g}, a) \tag{1}$$

(see [10] for details). Φ_f are functions describing the normalization of variable f at the base of the jet, and they are typically provided by accretion disk theory. We will take $\Phi_B = \sqrt{\dot{m}/M}$ as our fiducial expression for how the magnetic field strength at the base of the jet varies with M and $\dot{m}$. The functions ψ_f are structure functions that describe the spatial variation of f, i.e., collimation, acceleration, etc. They are currently not well known. We will further assume that the electrons responsible follow a powerlaw distribution in energy: $f(\gamma) = C\gamma^{-p}$, with $\Phi_C = \Phi_B^2$, with a fiducial value of $p = 2$. Finally, by dimensional analysis we will assume that the kinetic jet power follows the proportionality $L_{\rm kin} \propto B^2M^2 \propto M\dot{m}$.

By inserting eq. (1) into the expressions for the synchrotron radio luminosity of the jet, it is straightforward to show that the radio luminosity from the jet follows the relation

$$L_{\rm r} \propto M^{17/12-\alpha_{\rm r}/3}\dot{m}^{17/12+2\alpha_{\rm r}/3} \propto L_{\rm kin}^{1.42+2\alpha_{\rm r}/3}M^{-\alpha_{\rm r}} \tag{2}$$

where $\alpha_{\rm r}$ is the radio spectral index. The functions Φ_f determine the powerlaw index, while the unknown functions Ψ_f are subsumed into $\alpha_{\rm r}$, which is an observable. Typically, $\alpha_{\rm r} \sim 0$ for the optically thick, flat spectrum cores of jets we are interested in here, so $L_{\rm r} \propto M^{1.42}\dot{m}^{1.42} \propto L_{\rm kin}^{1.42}$.

This relation is robust and model independent, since the functions Ψ_f drop out. It is valid both for optically thick radiation with $\alpha_{\rm r} \sim 0$ and optically thin radiation at higher frequencies with $\alpha = (p-1)/2 \sim 0.5$. As recently shown

by [9], it is possible to extend this analysis to include synchrotron losses of the radiating electrons. This allows us to treat synchrotron X-rays from the jet and derive the scaling relations governing them. In this case,

$$L_{\rm x} \propto M^{(3\alpha_{\rm x})/2}\dot{m}^{(5-3\alpha_{\rm x})/2} \propto L_{\rm kin}^{(5-3\alpha_{\rm x})/2}M^{\alpha_{\rm x}-1} \tag{3}$$

To test these relations observationally, we must make a connection between the accretion rate $\dot{m}$ and an observable. Since we are particularly interested in low luminosity objects, we will consider the hard (2-10 keV) X-ray luminosity as a proxy of the accretion activity, because it is not affected significantly by absorption, and because it is known to correlate with the radio emission in XRBs.

In order to look for evidence of any relation between $L_{\rm r}$, M, and $\dot{m}$, we collected a large sample of black holes with measured masses and radio and X-ray luminosities. The sample contains 99 AGNs and 8 XRBs at 50 different epochs for a total of 149 data points. The details of this sample can be found in [12], we do want to point out, though, that the sample was selected with the goal to avoid selection effects induced by relativistic beaming (Blazars and BL Lac objects were excluded, and the only powerful quasar included is 3C273, most objects are at low luminosities).

Partial correlation tests show that there is strong evidence that $L_{\rm r}$ correlates with both M and $L_{\rm x}$. Thus, a multivariate correlation analysis is necessary to find the dependence of $L_{\rm r}$ on M and $L_{\rm x}$. Looking for a correlation between, say, $L_{\rm r}$ and M is not sufficient and will not yield meaningful results. We have performed such an analysis [12], and found the following relation:

$$\log L_{\rm r} = 0.78\log M + 0.6\log L_{\rm x} + 7.33 \tag{4}$$

with a scatter of $\sigma \sim 1\,$dex.

It is worth noting that the dependence of $L_{\rm r}$ on M is well constrained to be $L_{\rm r} \propto M^{1.4}$ (note that $L_{\rm x}$ depends on M, presumably through $L_{\rm x} \propto M$, thus eq. (4) is consistent with this statement), which confirms the predictions from eq. (2) very nicely.

Finally, we can attempt to make a connection between $L_{\rm x}$ and the accretion rate. For different emission mechanisms and accretion disk scenarios, the dependence of $L_{\rm x}$ on $\dot{m}$ will differ. For example, inefficient accretion flows tend to have steep dependences of the form $L_{\rm x} \sim \dot{m}^2$, X-ray synchrotron emission from the jet follows eq. (3), while for efficient accretion disks, $L_{\rm x} \sim \dot{m}$. Fitting the predicted scaling relations from eqs. (2) and (3) leads to the following results: Inefficient flows with steep $L_{\rm x}$-$\dot{m}$ dependences (such as ADAFs) can reproduce the fundamental plane relation from eq. (4) very well. X-ray synchrotron radiation is marginally consistent with this relation, but requires rather steep electron spectra and absence of radiative cooling (however, steep spectra and cooling typically go together and such steep electron spectra are also inconsistent with the observed X-ray spectra of most of the sources) to fit the relation, [9]. Finally, efficient accretion is ruled out completely.

3 Estimating Jet Power

In the previous section we showed that there is a simple, generic, and observationally tested relation between the jet power $L_{\rm kin}$, the black hole mass M, and the core radio luminosity $L_{\rm r}$, and that for flat spectrum jets, the mass drops out of this relation completely. Therefore, a simple relation between the radio luminosity and the kinetic jet power exists:

$$L_{\rm kin} = \eta L_{\rm Edd} \times (L_{\rm r}/L_{\rm Edd})^{12/17} \tag{5}$$

However, the normalization constant η is not know from the scale invariance model alone.

The fundamental plane relation is a good indication that this relation holds. There are a number of sources on the relation for which reasonably reliable estimates of the jet power exist, namely M87, Cygnus A, and Perseus A. We can use these sources to normalize eq. (5). We should keep in mind that the sources each have some offset from the fundamental plane relation due to the intrinsic scatter around the plane. Furthermore, the large scale power estimates are time averaged and might not be representative of the current jet power, with the exception of the M87 jet, where direct power estimates for the kpc scale jet do exist.

The rough power estimates for the three sources are: $10^{45.7}$, 10^{43}, and $10^{44.5}$ ergs s^{-1} for Cyg A, M87, and Per A respectively [3,1,6], while their radio luminosities are $10^{41.4}$, $10^{39.8}$, and $10^{41.7}$ ergs s^{-1}. Thus, the normalization constants we derive for the sources are $\eta_{\rm CygA} \sim 1.8 \times 10^5$, $\eta_{\rm M87} \sim 5 \times 10^4$, and $\eta_{\rm PerA} \sim 7 \times 10^3$, each carrying considerable uncertainty from the estimate of the kinetic power (which is very difficult to achieve).

Given the "fundamental plane" relation, we can also calculate what the radio power should be if there were no scatter around the relation, based on the X-ray luminosity and the mass of the objects. In this case, the normalization constants are $\eta_{\rm CygA} \sim 2.7 \times 10^5$, $\eta_{\rm M87} \sim 1.7 \times 10^5$, and $\eta_{\rm PerA} \sim 10^5$, which is significantly more homogeneous. This expression is more appropriate to use in an average sense when using a large sample of sources, since the radio emission carries a significant fraction of the scatter in the fundamental plane relation due to variations in relativistic beaming, black hole spin, and spectral index. We will thus use this corrected estimate of the efficiency, which averages to $\eta \sim \eta_{5.2}\, 1.6 \times 10^5$, with about an order of magnitude uncertainty.

Given this normalization, we can now use the measured radio luminosity function $\rho(L_{\rm r}, z)$ for flat spectrum sources (model 1, [5]) and convert it into a kinetic LF:

$$\rho(L_{\rm kin}, z) = 5.5 \times 10^{-8} \left(\frac{L_{\rm kin}}{L_{\rm Edd}}\right)^{5/12} \rho(L_{\rm r}(L_{\rm kin}), z) \tag{6}$$

with $L_{\rm r}(L_{\rm kin})$ from eq. (5).

Integrating this over $L_{\rm kin}$ (corresponding to the observed range in $L_{\rm r}$), we arrive at the total kinetic energy input by flat spectrum jets into the IGM per

Mpc^3 at zero redshift:

$$L_{\mathrm{kin,flat}} \approx 7 \times 10^{39}\,\mathrm{ergs\,s^{-1}\,Mpc^{-3}}\,\eta_{5.2} \tag{7}$$

We should note that there are many more steep spectrum sources than there are flat spectrum sources in any given luminosity bin of the [5] luminosity function (LF), and these sources are not counted in this estimate. Because the flat spectrum core of these sources is hidden under the more luminous steep spectrum component, the actual flat spectrum luminosity of these sources is smaller than the radio luminosity used to derive the steep spectrum LF function of [5].

Using the steep spectrum LF to calculate the same estimate as that of eq. (7) will thus result in a gross overestimate of the actual kinetic power and will thus be an upper limit on the actual current heating rate. This value is $L_{\mathrm{kin,steep}} \approx 9 \times 10^{40}\,\mathrm{ergs\,s^{-1}\,Mpc^{-3}}\,\eta_{5.2}$. Since the flat spectrum part is a lower limit, we can write $7 \times 10^{39}\,\mathrm{ergs\,s^{-1}\,Mpc^{-3}} < L_{\mathrm{kin}} < 10^{41}\,\mathrm{ergs\,s^{-1}\,Mpc^{-3}}$. It is plausible that the steep spectrum sources actually contribute at about the same level to the total kinetic power input as the flat spectrum ones, so we will use $L_{\mathrm{kin}} \approx 2 \times L_{\mathrm{kin,flat}}\xi_{\mathrm{steep}}$ as our best guess (where ξ_{steep} is the fudge factor accounting for the actual ratio of steep to flat spectrum source power).

Integrating eq. (7) over the redshift interval considered by [5] ($z = 0 - 5$), we finally arrive at the mean energy density contributed by the jets from radio sources:

$$e_{\mathrm{kin}} \approx 10^{59}\,\mathrm{ergs\,Mpc^{-3}}\,\eta_{5.2}\,\xi_{\mathrm{steep}} \tag{8}$$

with about an order of magnitude uncertainty. Comparing this to the estimated mean black hole mass density at zero redshift of $\rho_{\mathrm{BH}} \approx \zeta_{2.5}\,2.5 \times 10^5\,M_\odot\,\mathrm{Mpc^{-3}}$, this corresponds to an energy conversion efficiency of

$$\frac{e_{\mathrm{kin}}}{\rho_{\mathrm{BH}}c^2} \approx 12\%\eta_{5.2}\,\xi_{\mathrm{steep}}/\zeta_{2.5} \tag{9}$$

with about an order of magnitude uncertainty in each direction (see also [11] for an alternative, but consistent, estimate).

This number is on the large side of traditional estimates of how much power can be extracted from accreting black holes, comparable to the total radiative power that is typically assumed to be released by efficient accretion disks. Thus, this estimate provides an interesting argument for what has recently been called "jet domination" in low luminosity accretion flows [7]. It also demonstrates that kinetic power input by growing black holes needs to be considered as an important feedback mechanisms in structure formation and that the "fundamental plane" of black hole activity can provide important assistance in pinning down critical jet parameters. As a note of caution, it should be kept in mind that the LF likely contains many beamed sources. However, most of the kinetic power is actually contributed by low luminosity sources in this scenario, where beaming selection effects might not be so important. Clearly, further study is necessary to treat selection effects and relativistic beaming properly and improve the rough estimates presented above.

4 Conclusions

We argued that the assumption of scale invariance of jets from black holes can be used to derive robust, model independent scaling relations between the jet radio luminosity and the black hole mass and accretion rate. The recently found "fundamental plane" relation between radio luminosity, black hole mass, and X-ray luminosity confirms the predictions from the scale invariance hypothesis. Based on the scale invariance scaling, we showed how the radio luminosity function of flat spectrum sources can be used to estimate the total power released by jets from growing black holes. Comparing this power to the local black hole density, we find that of the order of 10 percent of the rest mass accreted by the black hole should have been converted into jet kinetic energy.

Acknowledgements. Support for this work was provided by NASA Chandra Fellowship grant, Award Number PF3-40026, under NASA contract NAS8-39073.

References

1. G. V. Bicknell, M. C. Begelman: ApJ **467**, 597 (1996)
2. R. D. Blandford, M. C. Begelman: MNRAS **303**, L1 (1999)
3. C. L. Carilli, P. D. Barthel: MNRAS **7**, 1 (1996)
4. S. Corbel, et al.: A&A **400**, 1007 (2003)
5. J. S. Dunlop, J. A. Peacock: MNRAS **247**, 19 (1990)
6. A. C. Fabian, et al.: MNRAS **331**, 369 (2002)
7. R. P. Fender, E. Gallo, P. G. Jonker: MNRAS **343**, L99 (2003)
8. E. Gallo, R. P. Fender, G. G. Pooley: MNRAS **344**, 60 (2003)
9. S. Heinz: MNRAS in press. astro-ph/0409029 (2004)
10. S. Heinz, R. A. Sunyaev: MNRAS **343**, L59 (2003)
11. A. Merloni: MNRAS, **353**, 1035 (2004)
12. A. Merloni, S. Heinz, T. Di Matteo: MNRAS **345**, 1057 (2003)

Properties of Jets at Different Scales and the Connection with Accretion

L. Maraschi and F. Tavecchio

Osservatorio Astronomico di Brera, Via Brera 28, Milano, Italy

Abstract. Results of a *Chandra*/*HST* survey for resolved high frequency emission from radio bright AGN jets are summarized. The multifrequency mapping and modelling indicates that powerful jets generally remain relativistic up to very large scales (10^{22-24} cm). The X-ray to radio flux ratios of emission "knots" along the large scale jets are found to decrease systematically, which can be interpreted as moderate deceleration of the bulk flow near the jet end. In two cases the physical parameters and kinetic power at large scales can be compared with those deduced in a consistent way for the blazar emission region (10^{16-17} cm) suggesting that the propagation is essentially free with little power dissipation between the two scales. Finally, connecting the jet properties with those of the presumed associated accretion disk (10^{14-15} cm) a unified scenario is suggested whereby the most powerful jets are produced by rapidly spinning black holes with bright, near Eddington accretion disks. Significantly lower accretion rates (in Eddington units) lead to jets of lower absolute power and very underluminous disks (as predicted in ADAF–like models) thus with a higher ratio of jet to disk luminosity.

1 Introduction

The existence of relativistic jets in extragalactic radiosources was hypothesised already in the 60s on the basis of the radio lobe energetics and the absence in most cases of a visible connection with the nucleus [21]. Since then, a wealth of initially puzzling observations at all frequencies from radio to gamma-rays have been understood within this framework and have allowed insight in the underlying physics (e.g.[17]). Nevertheless, the main mode of energy transport along the jet, whether electromagnetic or supported by protons, is still a matter of debate [5]. Here we will assume the latter scenario.

Due to relativistic amplification, the radiation emitted by jets is most conspicuous and therefore best studied for jets pointing at small angles to the line of sight (blazars). Then, in most cases the radiation from the inner (unresolved) part of the jet outshines the nucleus.

The discovery of high energy gamma-rays from blazars, in the GeV and TeV range ([14], [20]) was critical in enlightening the spectral energy distribution (SED) of the inner jet. It is now clear that the blazar SEDs consist of two main components of comparable luminosity that can be produced via the synchrotron and Inverse Compton mechanisms respectively *by the same population of relativistic electrons* . Within this simple model multifrequency observations allow to constrain significantly the physical properties of the jet plasma [26]. The variability timescales indicate that the blazar emission derives from regions of sizes 10^{16-17} cm at distances 10^{17-18} cm from the nucleus.

ESO Symposia: Growing Black Holes, pp. 377–385, 2005.

At much larger distances jets terminate and deposit their power in the surrounding medium, in some cases giving rise to conspicuous radio lobes. Today, thanks to the *Chandra and HST* resolution and sensitivity, we can access X-ray and optical emission in addition to radio from jets at large scales (see [13] and references therein), opening up a whole new "dimension" which can resolve the degeneracy of pure synchrotron models also for the outer jet regions.

In fact the serendipitous discovery with *Chandra* of X-ray emission associated with the radio jet of PKS 0637-752 (z=0.651) at a projected distance of ~ 100 kpc [9] immediately showed that X-rays derive from a spectral component different from the synchrotron one. While a synchrotron self Compton (SSC) model leads to an implausibly high requirement for the jet power and to conditions far from equipartition [25], the X-ray emission can be explained as upscattering of the CMB photons by the same electron population which produces the radio emission via synchrotron, if the jet is still relativistic on very large scales [27,8]. The latter model can accomodate conditions close to equipartition and a less extreme requirement for the total power.

Here we will discuss the general results of a survey with *Chandra* and *HST* of 17 jets, selected for their radio properties (surface brightness and angular size) carried out by Sambruna et al. [23,24] showing that powerful jets have indeed common properties (Section 2).

Moreover, two objects in the sample were (serendipitously) well studied blazars. For these two sources we can consistently derive the jet physical properties (e.g. energy densities and bulk motion) *at different scales in the same jet* (Section 3).

Finally, comparing the jet power estimated at the blazar region with the accretion power estimated from signatures of an accretion disk for sources with sufficient data we derive elements pointing to a "fundamental plane" for AGN unification.

2 Large Scale X-ray Emission from Powerful Radio Jets

Following the discovery of X-ray emission along the radio jet of PKS 0637-752 systematic studies were clearly needed. From the few jets initially known to emit at X-rays and/or optical it was also clear that the optical flux would be critical in discriminating between a synchrotron or Inverse Compton origin for the X-ray radiation. We thus initiated a "snapshot" survey with *Chandra* and *HST* to investigate the range of X-ray and optical properties of a pre-defined jet sample.

The targets were selected from two reference lists of known radio jets with criteria based only on radio morphology and surface brightness, to match the resolution and sensitivity of *Chandra* for an X-ray to radio spectral index $\alpha_{rx} \simeq 0.8$. At least one radio-knot was required to be present at more than 3 arcsec from the nucleus, yielding 17 targets. All were observed and the results are fully described in [24]. All objects except one turned out to be luminous FRII quasars, with rather high core dominance parameter and strongly asymmetric jets. This

means that, the very requirement of bright radio emission close to but separated from the core yields jets closely aligned to the line of sight.

The only FRI target shows two quasisymmetrical radio hotspots which are clearly detected in both X-rays and optical with synchrotron SEDs. The small radio-jet is marginally detected in X-rays, at the same level as other X-ray regions close to the nucleus not associated with radio features.

Of the 16 quasar jets, 12 have at least 1 feature detected in X-rays and/or in the optical band. The remaining 4 radio-jets (of which one at z=1.9) are undetected. The high detection rate does not conflict with beamed models for the X-ray radiation, since, as mentioned above, the survey sample, is intrinsically biased towards beamed objects.

The morphology of the detected jets is quite complex, usually more than one feature ("knot") along the jet is observed. Space prevents here a more detailed discussion. Note that emission from the lobes is also observed in a number of objects, but will not be discussed here.

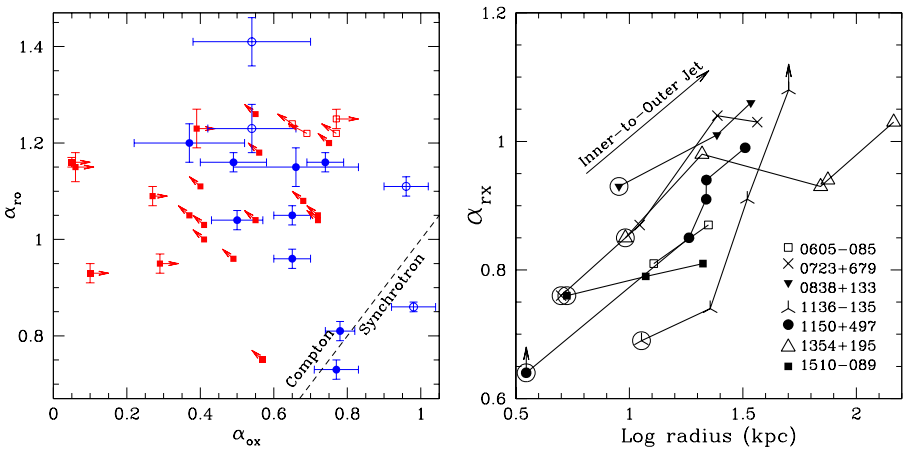

Fig. 1. *Left panel:* α_{ro} vs. α_{ox} for jet knots (filled symbols) (open symbols refer to features outside the jet, not discussed here); squares indicate upper limits (horizontal arrows: X-ray u.l.; diagonal arrows: optical u.l.). *Right panel:* α_{rx} is plotted vs. projected distance from the nucleus for different emission features along the same jet.

We wish to stress few "general" results. The first concerns the SEDs of the emission knots, which are generally unresolved by *Chandra*. Fluxes were extracted in all bands using an extraction radius of 1 arcsec to match the *Chandra* resolution. The broad band spectral indices α_{ro}, α_{ox} are shown in Fig. 1 (left panel) for all the jet knots detected in at least two bands (28). Within the X-ray detected knots (22) the SEDs are consistent with a single synchrotron spectrum ($\alpha_{ox} \geq \alpha_{ro}$) in only two cases, while in the others (20/22) the SEDs are concave, indicating that X-rays are produced by a separate spectral component. For

6 knots detected in the optical but not in X-rays the present upper limits are insufficient to discriminate.

Thus, the behaviour exhibited by the PKS 0637-752 jet is indeed common, at least among powerful jets. Spectral fits of the derived concave SEDs with the IC-CMB model yield similar physical parameters. On this regard we recall that the main source of uncertainty in the results is the actual size of the emission region, for which X-rays provide only an upper limit.

The second important result of the survey is the evidence of a systematic trend of the radio to X-ray flux ratio to increase with increasing distance from the nucleus. This is shown in Fig. 1 (right panel), where the index α_{rx} is plotted for individual knots along the same jet vs. projected distance. A similar trend though with larger scatter can be seen also in the run of the α_{ro} index vs. distance. This behaviour, already noted in specific objects like 3C 273 and PKS 1136-135 [22,1,23] appears then to be present in all the FR II jets for which we have sufficient information, suggesting a common physical cause.

A first possibility is that the synchrotron mechanism systematically extends to higher energies in the innermost knots providing an additional contribution to the X-ray flux, as shown directly in the case of 3C273 and PKS1136-135. Another contribution to X-ray emission from the inner regions of the galaxy could come from IC of starlight photons. Alternatively, in a pure IC/CMB scenario, the plasma could undergo deceleration in shocks, associated with an increase of the magnetic field (as proposed in the case of 3C 273 [22]).

Deeper multifrequency images of two of the survey objects were obtained to gain insight in some of these problems. A preliminary analysis of the long exposures of 1136-135 and 1150+497 yielded the sequence of SEDs shown in Fig. 2. Fitting the SEDs with the IC+CMB model and adopting the equipartiton assumption, yields decreasing Doppler factors and increasing magnetic field and relativistic electron densities, plausibly supporting the deceleration scenario.

3 The outer jet – inner jet connection

Two objects in the survey (PKS 1510-089 and 1641+399), serendipitously turned out to be well studied blazars whose SED was measured up to hard X-rays with BeppoSAX and in gamma-rays with EGRET. Reliable estimates of physical parameters and of the power transported at small scale (see [28] for more detail) could then be compared with the values obtained from the SEDs of the large scale emission regions detected in the survey. For the latter case, since the SEDs are much less detailed, we chose equipartition as an additional hypothesis to determine the parameters, checking a posteriori that, even relaxing to some extent the equipartition requirement, the model parameters did not change dramatically.

We find that: *i)* the jet maintains a nearly constant relativistic velocity (to within a factor 2) from the subparsec to 100 kpc scale; *ii)* the transported power inferred for the outer jet is remarkably similar to that estimated close to the nucleus; *iii)* the pressure at the two scales is consistent with a simple inverse

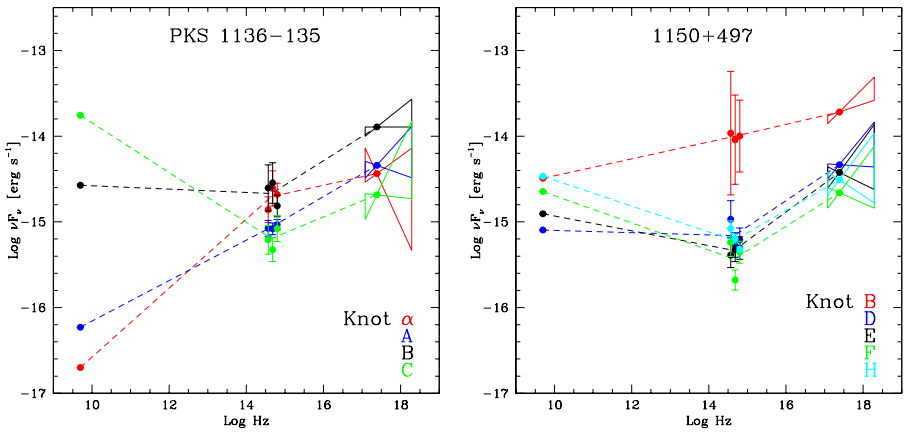

Fig. 2. *Left panel:* Spectral energy distributions for different knots along the jets of PKS 1136-135 (*Left panel*) and 1150+497 (*Right panel*) measured in deep exposures of these two sources.

scaling relation with the jet cross section. Although the quantitative results are uncertain within factors of a few they are consistent with the simplest possible scenario for the jet propagation, i.e. free expansion [29]. Plausibly the conditions for free expansion are met only by the most powerful jets. The physical consistency of the parameters determined from spectral modelling at widely different scales gives us confidence in the derived values.

4 The jet - accretion disc connection

The origin of relativistic jets is an open problem in astrophysics. Two basic alternatives were first studied in [3] and [2]. We refer to the paper by J. Krolik at this conference for a discussion of the problem and very interesting results from magneto hydrodynamic, fully relativistic simulations of the interaction of a spinning black with a disk accretion flow.

We simply recall that even in the Blandford and Znajek model, where the black hole spin plays an essential role, the production of the jet is related to the accretion flow which should provide the necessary magnetic field.

A simple estimate through the BZ formula in the case of a purely spherical accretion model in equipartition gives the following relation

$$P_{BZ} \simeq g\dot{M}c^2a^2 \tag{1}$$

where P_{BZ} is the extracted (jet) power, $P_{acc} = \dot{M}c^2$ is the accretion power, a is the adimensional hole angular momentum and g is of order 1/64 in the spherical case, but in fact it is a highly uncertain number since it depends strongly on the field configuration. Eq.(1) shows that the extracted power depends on the accretion rate, in the simplest approximation the two are proportional.

Following an observational approach, one can work backwards estimating the jet power from the SEDs of the blazar region (inner jet) and the accretion power from the traditional signatures of the accretion disk (the blue bump and/or the emission lines) in the SEDs of the nuclei, and compare the two. This was done for a small "sample" of FSRQ with a good measure of the non thermal (blazar) SEDs up to at least hard X-rays obtained with BeppoSAX [18]. For BL Lac sources (again selected to have adequate observational coverage of their SEDs) upper limits on the disk luminosity were inferred, except for BL Lac itself, which showed a measurable H_α line. The results are summarized in Fig. 1, where the (rest frame) luminosity of the jet, $L_{\rm jet}$, is compared with the luminosity of the disk, $L_{\rm disk}$. The figure shows that *at high luminosities the two values are of the same order*.

At such high luminosities the estimated radiative efficiencies of the jet [18] are of order 10% as is the efficiency of a "standard" optically thick disk, thus the power transported by the jet, P_{jet}, is *of the same order as the accretion power*, P_{acc}. This already poses a stringent requirement as to how to supply a strong enough field for the BZ process even for maximal rotation ($a \simeq 1$, (e.g. [12], [15]).

On the other hand, assuming that the near equality above for the respective powers holds, the dominance of the jet luminosity for lower power objects could be understood if the disk is radiatively inefficient, as expected for low accretion rates (in Eddington units). On the equality line drawn for reference in the figure we mark (empty circles) the position of a 10^{-2} $\dot{m}_{\rm Edd}$ for 10^9 and 10^8 $M_\odot$ respectively (with 10% efficiency), while the points for 10^{-3} $\dot{m}_{\rm Edd}$ for the same

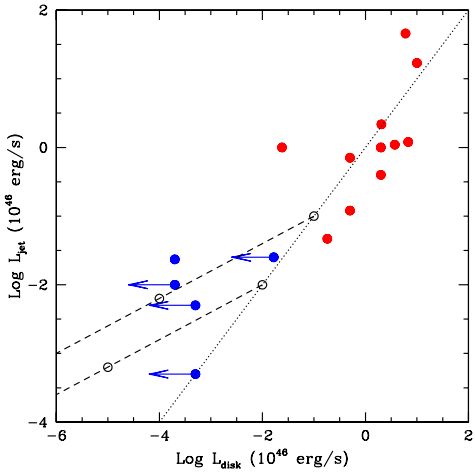

Fig. 3. Luminosities of blazar jets are plotted vs. luminosities of the associated accretion disks (filled simbols). For open simbols see text.

masses are computed assuming for the disc radiative efficiencies predicted by ADAF models [16].

In summary, the luminosity range spanned by the objects in Fig. 3 can be interpreted as a sequence of decreasing accretion rates, for objects of essentially similar (large) mass [17]. Mass measurements of a number of nearby BL Lacs directly support this hypothesis [1],[10]. It would be interesting to provide reliable mass estimates for all the objects so that the diagram could be best drawn in normalised luminosities.

The larger photon energy density around the most powerful jets, a result derived from radiative modeling of the "blazar sequence", i.e. the systematic trend of the blazar SEDs to peak at higher energies with decreasing luminosities, [11], [6], can then be accounted for in terms of a larger radiative efficiency of more powerful disks, and fits in with the evolutionary scheme proposed in [7].

5 A unified physical model for AGN

The scenario envisaged above can be summarized in a "fundamental plane" for AGN where the two axis are the dimensionless black hole spin and the accretion rate in Eddington units [4] (see Fig. 2).

At high (in Eddington units) accretion rates and close to maximal spin we find objects with bright accretion disks, strong emission lines and powerful jets. When seen on axis these are the powerful blazars (Flat Spectrum Quasars), at larger angles they appear as radio loud quasars or FR II radiogalaxies. At low accretion rates and high spin we find objects with radiatively inefficient accretion disks and therefore little trace of thermal radiation (no emission lines)

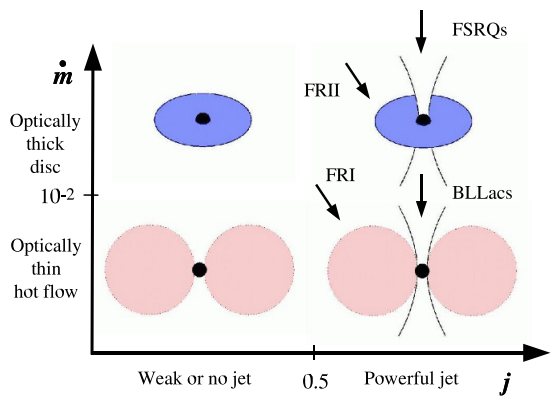

Fig. 4. The fundamental AGN plane (see text).

but still relatively powerful jets. The magnetic field sustaining the BZ effect is determined by the accretion flow (not by its radiation) and possibly profits of a geometrically thick disk. Such objects seen on axis appear as BL Lacs and at large angles as radio galaxies with optically dull nuclei. *If the accretion disk were the only responsible for the jet origin it would be difficult to understand why among quasars with comparable blue bumps and emission lines (presumably due to similar accretion disks) only a minority show strong radio emission implying the presence of a powerful jet.*

The possibility of a "dicothomy" between the radio loud and radio quiet regimes is far from settled: radio loud AGN could simply be the high spin tail of an angular momentum distribution which is at present unknown. On the other hand a spin "threshold" may be required to launch a relativistic jet. The value of this threshold would probably depend on the accretion rate, magnetic structure and angular momentum in the inner disk and could be lower for largely sub-Eddington, radiatively inefficient disks.

Grants from the Ministry of University and Research (MIUR-COFIN 2002 027 145–007) and from the Italian Space Agency (ASI I/R/047/02) are acknowledged.

References

1. Barth, A. J. et al.: ApJ, **566**, L13 (2002)
2. Blandford, R. D. & Znajek, R. L.: MNRAS, **179**, 433 (1977)
3. Blandford, R. D. & Payne, D. G.: MNRAS, **199**, 883 (1982)
4. Blandford, R. D.: Saas-Fee Advanced Course 20. Lecture Notes, XII, 280 pp. 97, Springer-Verlag (1990)
5. Blandford, R.: ASP Conf. Ser. **290**, 2 (2003)
6. Böttcher, M. & Dermer, C. D.: ApJ, **564**, 86 (2002)
7. Cavaliere, A. & D'Elia, V.: ApJ, **571**, 226 (2002)
8. Celotti, A., Ghisellini, G., & Chiaberge, M.: MNRAS, **321**, L1 (2001)
9. Chartas, G. et al.: ApJ, **542**, 655 (2000)
10. Falomo, R. et al.: MNRAS, **343**, 505 (2003)
11. Ghisellini, G., et al.: MNRAS, **301**, 451 (1998)
12. Ghosh, P. & Abramowicz, M. A.: MNRAS, **292**, 887 (1997)
13. Harris, D. E. & Krawczynski, H.: ApJ, **565**, 244 (2002)
14. Hartman, R. C. et al.: ApJ, **385**, L1 (1992)
15. Livio, M., Ogilvie, G. I., & Pringle, J. E.: ApJ, **512**, 100 (1999)
16. Mahadevan, R.: ApJ, **477**, 585 (1997)
17. Maraschi, L.: AIP Conf. Proc., **586**, 409 (2001)
18. Maraschi, L. & Tavecchio, F.: ApJ, **593**, 667 (2003)
19. Marshall, H. L. et al.: ApJ, **549**, L167 (2001)
20. Punch, M. et al.: Nature, **358**, 477 (1992)
21. Rees, M. J.: Nature, **211**, 468 (1966)
22. Sambruna, et al.: ApJ, **549**, L161 (2001)
23. Sambruna, R. M. et al.: ApJ, **571**, 206 (2002)
24. Sambruna, R. M. et al.: ApJ, **608**, 698 (2004)
25. Schwartz, D. A. et al.: ApJ, **540**, L69 (2000)

26. Tavecchio, F., Maraschi, L., & Ghisellini, G.: ApJ, **509**, 608 (1998)
27. Tavecchio, F. et al.: ApJ, **544**, L23 (2000)
28. Tavecchio, F. et al.: ApJ, **543**, 535 (2000)
29. Tavecchio, F. et al.: ApJ, in press (2004)

Radiative Feedback from Quasars and the Growth of Supermassive Black Holes

S.Yu. Sazonov[1,2], J. P. Ostriker[3], L. Ciotti[4], and R. A. Sunyaev[1,2]

[1] Max-Planck-Institut für Astrophysik, Karl-Schwarzschild-Str. 1, 85740 Garching, Germany
[2] Space Research Institute, Profsoyuznaya 84/32, 117997 Moscow, Russia
[3] Institute of Astronomy, Madingley Road, CB3 0HA Cambridge
[4] Department of Astronomy, University of Bologna, via Ranzani 1, I-40127 Bologna, Italy

Abstract. We discuss the role of feedback via photoionization and Compton heating in the co-evolution of massive black holes at the center of spheroidal galaxies and their stellar and gaseous components. We first assess the energetics of the radiative feedback from a typical quasar on the ambient interstellar gas. We then demonstrate that the observed $M_{\rm BH}$–σ relation could be established at a relatively early epoch in galactic evolution when the formation of the stellar bulge was almost completed and the gas-to-stars mass ratio was reduced to a low level $\sim$0.01 such that cooling could not keep up with radiative heating. A considerable amount of gas was expelled at that time and black hole accretion proceeded at a much lower rate thereafter.

1 General Picture

Most elliptical galaxies are poor with respect to interstellar gas. Also, elliptical galaxies invariably contain central massive black holes (BHs), and there exists a tight relationship between the characteristic stellar velocity dispersion σ and the BH mass $M_{\rm BH}$ [4,2], and between $M_{\rm BH}$ and the host spheroid mass in stars, M_* [3]. Are these two facts related? Here we focus on a scenario in which the mass of the central BH grows within gas rich elliptical progenitors until star formation has reduced the gas fraction in the central regions to of order 1% of the stellar mass. Then radiative feedback during episodes when the BH luminosity approaches its Eddington limit drives much of the gas out of the galaxy, limiting both future growth of the BH and future star formation to low levels.

Many works already recognized the importance of feedback as a key ingredient of the mutual BH and galaxy evolution [4–16]. What is new about this work is the stress on one component of the problem that has had relatively little attention: the radiative output of the central BH is not conjectural – it must have occured – and the high energy component of that radiative output will have a dramatic and calculable effect in heating the gas in ellipticals.

Using the average quasar spectral output derived in [17], we show below and in more detail in [18] that the limit on the central BH produced by the above argument coincides accurately with the observed $M_{\rm BH}$–σ relation. Not only the slope, but also the small normalization factor is nicely reproduced.

ESO Symposia: Growing Black Holes, pp. 386–392, 2005.

The present work is complementary to [5,8] in that, while it does not attempt to model the complex flaring behavior of an accreting BH with an efficient hydrodynamical code, it does do a far more precise job of specifying the input spectrum and the detailed atomic physics required to understand the interaction between that spectrum and the ambient interstellar gas in elliptical galaxies.

2 Radiative Heating of ISM in Spheroids

Below we assess the conditions required for the central BH radiation to significantly heat the ISM over a substantial volume of the galaxy. In this section we shall *assume* that the central BH has a mass as given by the observed $M_{\rm BH}$–σ relation for local ellipticals and bulges [2]:

$$M_{\rm BH} = 1.5 \times 10^8 M_\odot \left(\frac{\sigma}{200\ {\rm km\ s^{-1}}}\right)^4. \tag{1}$$

This assumption will be dropped in §3, where we *predict* the $M_{\rm BH}$–σ relation.

In [17] we computed for the average quasar spectrum the equilibrium temperature $T_{\rm eq}$ (at which heating due to Compton scattering and photoionization balances cooling due to line and continuum emission) of gas of cosmic chemical composition as a function of the ionization parameter $\xi \equiv L/nr^2$, where L is the BH bolometric luminosity. In the range 3×10^4–10^7 K,

$$T_{\rm eq}(\xi) \simeq 2 \times 10^2 \xi\,{\rm K}, \tag{2}$$

while at $\xi \ll 10^2$ and $\xi \gg 10^5$, $T_{\rm eq} \approx 10^4$ K and 2×10^7 K, respectively. On the other hand, the galactic virial temperature is given by

$$T_{\rm vir} \simeq 3.0 \times 10^6\,{\rm K} \left(\frac{\sigma}{200\ {\rm km\ s^{-1}}}\right)^2. \tag{3}$$

We can then find the critical density $n_{\rm crit}$ defined by

$$T_{\rm eq}(L/n_{\rm crit} r^2) = T_{\rm vir} \tag{4}$$

as a function of distance r from the BH. Gas with $n < n_{\rm crit}(r)$ will be heated above $T_{\rm vir}$ and expelled from the galaxy. We show in Fig. 1 the resulting (r, n) diagrams for a small and large BH/galaxy.

In reality, provided that $T_{\rm eq} > T_{\rm vir}$, significant heating will take place only out to a certain distance that depends on the luminosity and duration of the quasar outburst. Since the BH releases via accretion a finite total amount of energy, $\epsilon M_{\rm BH} c^2$, there is a characteristic limiting distance:

$$R_{\rm C} = \left(\frac{\sigma_{\rm T} \epsilon M_{\rm BH}}{3\pi m_{\rm e}}\right)^{1/2} = 400\,{\rm pc} \left(\frac{\epsilon}{0.1}\right)^{1/2} \left(\frac{M_{\rm BH}}{10^8 M_\odot}\right)^{1/2}. \tag{5}$$

Inside this radius, a low density, fully photoionized gas will be heated to the Compton temperature $T_{\rm C} \approx 2\,{\rm keV}$ characteristic of the quasar spectral output.

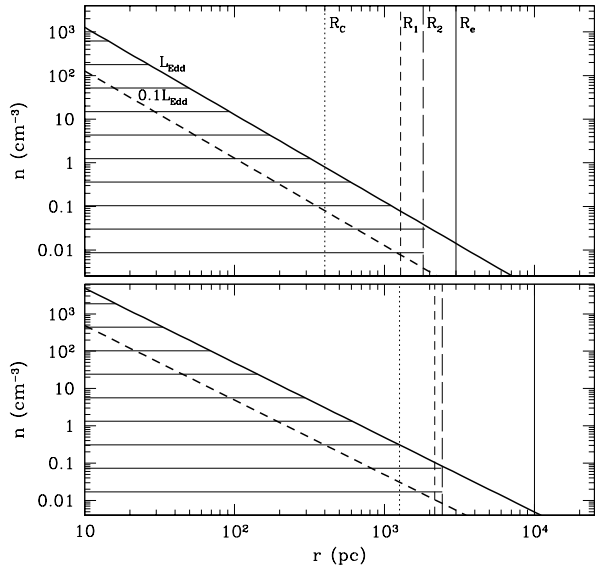

Fig. 1. The (r, n) plane for a galaxy with $\sigma = 180\,\mathrm{km\,s^{-1}}$ ($T_{\rm vir} = 2.4 \times 10^6\,\mathrm{K}$, $M_{\rm BH} = 10^8 M_\odot$, upper panel), and with $\sigma = 320\,\mathrm{km\,s^{-1}}$ ($T_{\rm vir} = 7.7 \times 10^6\,\mathrm{K}$, $M_{\rm BH} = 10^9 M_\odot$, lower panel). In the dashed area, gas can be heated above $T_{\rm vir}$ by radiation from the central BH emitting at the Eddington luminosity. The upper boundary of this area scales linearly with luminosity. Vertical boundaries are $R_{\rm C}$, R_1, R_2 and $R_{\rm e}$.

More relevant for the problem at hand is the distance out to which low density gas will be Compton heated to $T \gtrsim T_{\rm vir}$:

$$R_1 = R_{\rm C}\left(\frac{T_{\rm C}}{T_{\rm vir}}\right)^{1/2} = 1,300\,\mathrm{pc}\left(\frac{\epsilon}{0.1}\right)^{1/2}\frac{\sigma}{200\ \mathrm{km\ s^{-1}}}. \tag{6}$$

Yet another characteristic radius is out to which gas of critical density $n_{\rm crit}$ will be heated to $T \gtrsim T_{\rm vir}$ via photoinization and Compton scattering:

$$R_2 = R_1[\Gamma(n_{\rm crit})/\Gamma_{\rm C}]^{1/2}, \tag{7}$$

where $\Gamma_{\rm C}$ and Γ are the Compton and total heating rates, respectively. Depending on gas density ($0 < n < n_{\rm crit}$), the outer boundary of the "blowout region" will be located somewhere between R_1 and R_2. The size of the heating zone can be compared with the galaxy effective radius

$$R_{\rm e} \sim 4,000\,\mathrm{pc}\left(\frac{\sigma}{200\ \mathrm{km\ s^{-1}}}\right)^2. \tag{8}$$

The different characteristic distances defined above are shown as a function of $M_{\rm BH}$ in Fig. 2. One can see that a BH of mass $< 10^7 M_\odot$ should be able to unbind the ISM out to several $R_{\rm e}$. In the case of more massive BHs/galaxies with $M_{\rm BH} \sim 10^8$–$10^9 M_\odot$, the heating will be localized to innermost $\sim$0.3–0.5$R_{\rm e}$.

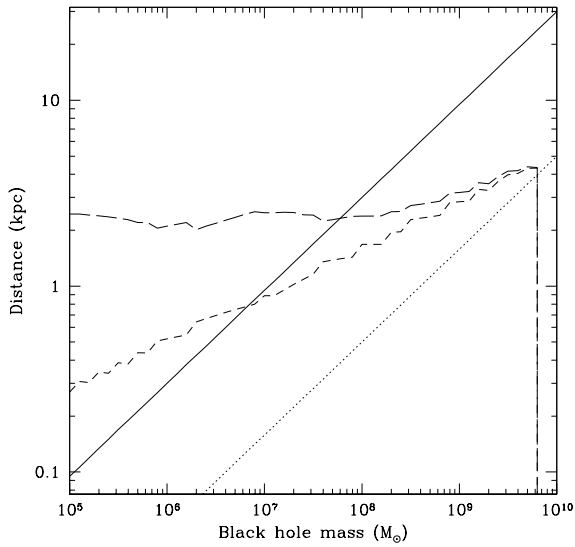

Fig. 2. Different heating radii: $R_{\rm C}$ (dotted line), R_1 (short-dashed line), and R_2 (long-dashed line), and the galactic effective radius (solid line), as a function of $M_{\rm BH}$.

3 Possible Origin of the $M_{\rm BH}$–σ Relation

We now consider the following general idea. Before the BH grows to a certain critical mass, $M_{\rm BH,crit}$, its radiation will be unable to efficiently heat the ambient gas, and the BH will accrete gas efficiently. Once the BH has grown to $M_{\rm BH,crit}$, its radiation will heat and expell a substantial amount of gas from the central regions. Feeding of the BH will then become self-regulated on a time scale of order the cooling time of the low density gas. Subsequent central activity will be characterized by a very small duty cycle ($\sim$0.001), as predicted by hydrodynamical simulations [5,8] and suggested by observations [14]. BH growth will be essentially terminated.

Suppose that the galaxy density distribution is that of a singular isothermal sphere, with the gas density following the total density:

$$\rho_{\rm gas}(r) = \frac{M_{\rm gas}}{M}\frac{\sigma^2}{2\pi G r^2}. \tag{9}$$

Here $M_{\rm gas}$ and M are the gas mass and total mass within the region affected by radiative heating. The size of the latter is uncertain but is less than a few kpc (see §2), so that M is dominated by stars rather than by dark matter.

Radiation from the central BH can heat the ambient gas up to

$$T_{\rm eq} \approx 6.5\times10^3\,{\rm K}\frac{L}{L_{\rm Edd}}\left(\frac{M_{\rm gas}}{M}\right)^{-1}\frac{M_{\rm BH}}{10^8 M_\odot}\left(\frac{200\,{\rm km\ s^{-1}}}{\sigma}\right)^2, \tag{10}$$

this approximate relation being valid in the range 3×10^4–10^7 K. Remarkably, $T_{\rm eq}$ does not depend on distance for the adopted r^{-2} density distribution. We

then associate the transition from rapid BH growth to slow, feedback-limited BH growth with the critical condition

$$T_{\rm eq} = \eta_{\rm esc} T_{\rm vir}, \tag{11}$$

where $\eta_{\rm esc} \gtrsim 1$ and $T_{\rm vir}$ is given by (3). Once heated to $T_{\rm eq} \gtrsim T_{\rm vir}$, the gas will stop feeding the BH. The condition (11) will be met for

$$M_{\rm BH,crit} = 4.6 \times 10^{10} M_\odot \eta_{\rm esc} \left(\frac{\sigma}{200\,{\rm km\ s^{-1}}} \right)^4 \frac{L_{\rm Edd}}{L} \frac{M_{\rm gas}}{M}. \tag{12}$$

Therefore, for fixed values of $\eta_{\rm esc}$, $L/L_{\rm Edd}$ and $M_{\rm gas}/M$ we expect $M_{\rm BH,crit} \propto \sigma^4$, similarly to the observed $M_{\rm BH}$–σ relation. Equally important is the normalization of the $M_{\rm BH}$–σ relation. By comparing (12) with (1) we find that the observed correlation will be established if

$$M_{\rm gas}/M = 3 \times 10^{-3} \eta_{\rm esc}^{-1} L/L_{\rm Edd}. \tag{13}$$

The gas-to-stars ratio is thus required to be low and approximately constant for spheroids of different mass at a certain stage of their evolution. As for the Eddington ratio, it is reasonable to expect $L/L_{\rm Edd} \sim$0.1–1 during quasar outbursts.

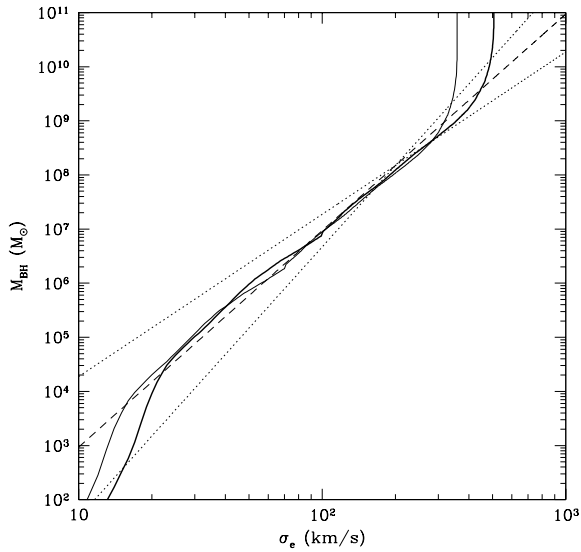

Fig. 3. Thick solid line shows the predicted $M_{\rm BH}$–σ correlation resulting from heating of the ISM by the radiation from the central BH assuming $M_{\rm gas}(R_{\rm e})/M = 0.003$ and $\eta_{\rm esc} = 1$. Thin solid line corresponds to $M_{\rm gas}(R_{\rm e})/M = 0.0015$ and $\eta_{\rm esc} = 2$. Dashed line is the observed $M_{\rm BH} \propto \sigma^4$ correlation in the range 10^6–a few $10^9 M_\odot$, extrapolated to lower and higher BH masses. Dotted lines are $M_{\rm BH} \propto \sigma^3$ and $M_{\rm BH} \propto \sigma^5$ laws.

The approximately linear $T_{\rm eq}(\xi)$ dependence [see (2)] was crucial to the above argument leading to the $M_{\rm BH,crit} \propto \sigma^4$ result. However, the $T_{\rm eq}(\xi)$ function

becomes nonlinear outside the range $3 \times 10^4\,\mathrm{K} < T_{\rm eq} < 10^7\,\mathrm{K}$ [17]. In Fig. 3 we show the predicted correlation between $M_{\rm BH,crit}$ and σ for $L/L_{\rm Edd} = 1$ and $M_{\rm gas}/M = 3 \times 10^{-3}$. It can be seen that the $M_{\rm BH} \propto \sigma^4$ behavior is expected to break down for $M_{\rm BH} < 10^4 M_\odot$ and for $M_{\rm BH} \gtrsim$ a few $10^9 M_\odot$. It is perhaps interesting that the range of masses shown in Fig. 3 for which $M_{\rm BH} \propto \sigma^4$ is obtained from considerations of atomic phyisics (and the observed AGN spectra) corresponds closely with the range of masses for which this power law provides a good fit to the observations. Exploring the $M_{\rm BH}$–σ relation observationally near $10^9 M_\odot$ would be a sensitive test of the importance of radiative feedback.

4 Detailed Modelling of the BH-Galaxy Co-evolution

In [18–20] we addressed in a more quantitative way the BH growth in the context of the parent galaxy evolution. We adopted a physically-motivated one-zone model, taking into account the mass and energy return from the evolving stellar population. This model predicts that after an initial "cold" phase dominated by gas infall, once the gas density becomes sufficiently low the gas heating dominates and the galaxy switches to a "hot" solution. The gas mass/stellar mass ratio at that epoch ($\sim$0.003) is remarkably close to the value inferred above from the argument leading to the right $M_{\rm BH}$–σ relation. Other predictions of the toy model are also in satisfactory agreement with observations. The "cold" phase would probably be identified observationally with the Lyman Break and SCUBA galaxies, while the "hot" phase with normal, local ellipticals.

A proper investigation of the importance of radiative heating on the BH/galaxy co-evolution, based on hydrodynamical numerical simulations, is now in progress.

References

1. L. Ferrarese, D. Merritt: ApJ **539**, L9 (2000)
2. S. Tremaine, K. Gebhardt, R. Bender et al.: ApJ **574**, 740 (2002)
3. J. Magorrian, S. Tremaine, D. Richstone et al.: AJ **115**, 2285 (1998)
4. J. Binney, G. Tabor: MNRAS **276**, 663 (1995)
5. L. Ciotti, J.P. Ostriker: ApJ **487**, L105 (1997)
6. J. Silk, M.J. Rees: A&A **331**, L1 (1998)
7. A. Fabian: MNRAS **308**, L39 (1999)
8. L. Ciotti L., J.P. Ostriker: ApJ **551**, 131 (2001)
9. A. Burkert, J. Silk: ApJ **554**, L151 (2001)
10. L. Ciotti, T. van Albada: ApJ **552**, L13 (2001)
11. A. Cavaliere, V. Vittorini: ApJ **570**, 114 (2002)
12. A. King: ApJ **596**, L27 (2003)
13. J.S.B. Wyithe, A. Loeb: ApJ **595**, 614 (2003)
14. Z. Haiman, L. Ciotti, J.P. Ostriker: ApJ **606**, 763 (2004)
15. G.L. Granato, G. De Zotti, L. Silva, A. Bressan, L. Danese: ApJ **600**, 580 (2004)
16. N. Murray, E. Quataert, T.A. Thompson: astro-ph/0406070
17. S.Yu. Sazonov, J.P. Ostriker, R.A. Sunyaev: MNRAS **347**, 144 (2004)

18. S.Yu. Sazonov, J.P. Ostriker, L. Ciotti, R.A. Sunyaev: MNRAS submitted. astro-ph/0411086 (2004)
19. L. Ciotti, J.P. Ostriker, S.Yu. Sazonov: these proceedings
20. J.P. Ostriker, L. Ciotti: Phil. Trans. of Roy. Soc., part A (2004, in press)

Feedback from Quasars in Galaxy Formation

P. Monaco

Dipartimento di Astronomia, via tiepolo 11, 34131 Trieste, Italy

1 Introduction

Several observational pieces of evidence and theoretical arguments suggest that feedback from accreting black holes is an unavoidable ingredient in the formation of galaxies. Many of these arguments are very well addressed in this volume; here I only mention the recent result of a dearth of low-luminosity AGN in the GOODS deep fields[1]. Taken together with other datasets, like the recent COMBO17[3] and SDSS[4] surveys, this result allows to reconstruct the AGN luminosity function at $z \sim 4$ from $M_{1450} = -21$ to -28. This is roughly fit by a simple (negative) density evolution of the $z = 3$ luminosity function[2]. This fact highlights the apparently "anti-hierarchical" behaviour of AGN (see also A. Merloni, these proceedings), in the sense that the peak of bright quasars aniticipates that of fainter objects, at variance with what is expected if AGN simply followed the assembly of dark matter halos.

The failure of models based on a simple connection between dark matter halos and black hole accretion is not unexpected, due to the complexity of the problem. A more physical picture is needed to investigate the feedback from quasars, in particular the effect that a shining quasar has on the ISM of a star-forming galaxy.

2 Facing the "gastrophysics" of feedback

I have recently proposed a model for feedback in galaxy formation[5], where the efficiency of energy injection by supernovae (SNe) and the timescale of star formation are computed from a self-consistent model that takes into account (though in a simplified way) the multi-phase nature of the ISM. Here I list the main properties of this model.

The ISM is assumed to be composed of two phases in pressure equilibrium. The cold phase grows by cooling of the hot phase and by infall from an external halo, here considered as a passive reservoir of gas. It is fragmented into clouds, with a power-law mass spectrum (whose slope is a parameter) truncated below at some small mass. Clouds larger than a Jeans mass (which takes into account the non-spherical geometry of clouds) collapse and form stars in a few dynamical times; in the meantime they accrete mass through anelastic encounters with other clouds. The high-mass cut of the cloud mass function is then set to the

ESO Symposia: Growing Black Holes, pp. 393–398, 2005.

mass reached by a Jeans-mass collapsing cloud before it is destroyed by star formation.

In a companion paper[6] I have shown that SN explosions in a star-forming cloud (presumably pre-heated by HII regions) can destroy the cloud in ~ 3 Myr, and most (~ 90 per cent) of the energy budget is available for feedback.

The SNe exploding in a collapsing cloud gives rise to a single superbubble (SB), that sweeps the hot phase and hardly affects the cold phase (whose filling factor is low). The propagation of the blast is halted either by blowing-out of a thin structure (like a spiral disc) or by being pressure-confined. The effect of the blast on the hot phase depends dramatically on whether the hot interior gas is able to cool and collapse to a cold shell (called Pressure Driven Snowplow, PDS) before being destroyed; in the adiabatic stage the hot phase is shock-heated, in the PDS phase it is swept by the snowplow and cooled. Four different feedback regimes are then possible: SBs can blow-out or be confined, in the adiabatic or in the PDS regime.

The adiabatic blow-out regime is typical of spiral discs; in a Milky Way-like case the main properties of the local ISM are reproduced. Thick structures like spheroids are typically in the adiabatic confinement regime. In this case feedback is very efficient, as all the energy coming from SNe (after the destruction of the cloud) is injected into the hot phase. Figure 1 shows the evolution in this regime of a toy spheroid of $10^{11}\,M_\odot$. The ISM regulates to a high pressure, $P/k \sim 10^6$

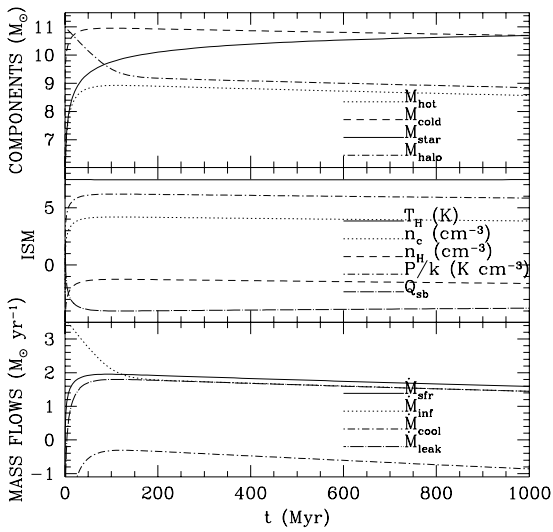

Fig. 1. Evolution of a toy spheroid of mass $10^{11}\,M_\odot$ and half-mass radius 4.9 kpc. The mass, initially in the external halo, is let infall in a timescale of 2.5×10^7 yr. Upper panel: mass components (see labels). Mid panel: ISM structure. Lower panel: Mass flows

K cm^{-3}, the hot phase is very hot ($T \sim 3 \times 10^7$ K), while the cold phase is fragmented into small clouds with a low filling factor. As a result, the star formation timescale is of order of a Gyr, and the porosity $Q_{\rm SB}$ of the expanding SBs is very low.

3 The effect of a shining quasar

A quasar affects the ISM of the host galaxy mainly through radiative heating and radiation pressure. Taken alone, both processes are unlikely to trigger a strong wind able to remove most ISM from a big spheroid[8]. Radiative heating (see also the paper by Sazonov et al. in this volume) will anyway perturb the ISM. In particular, runaway heating by a quasar can heat part of the cold phase to nearly the inverse Compton temperature of the AGN[9], $T \sim 2 \times 10^7$ K, very similar to the temperature of the hot phase. The effect of this evaporation on the system is illustrated in Figure 2, where we have added black hole, accreting at the Eddington rate, which evaporates 50 $M_\odot$ of the cold phase for each $M_\odot$ of accreted mass[10]. As soon as the evaporated mass overtakes the (unperturbed) star formation rate by a factor of ~ 10, the system switches from the adiabatic confinement to the PDS confinement regimes. When this happens, snowplows start to collapse the hot phase (which has gained a significant amount of mass) back into cold clouds. This causes a sudden drop in pressure and an explosive increase of the porosity of SBs, which reaches values larger than unity.

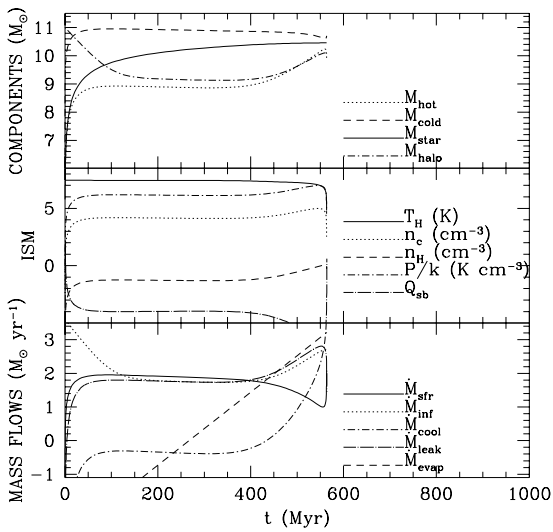

Fig. 2. As in figure 1, with the addition of an evaporation term due to a black hole accreting at the Eddington rate. 50 $M_\odot$ are evaporated for each accreted $M_\odot$[10]

The percolation of the expanding cold shells will lead to (i) a roughly spherical shell expanding out of the galaxy at $\sim$ 200 km s^{-1}, (ii) an intermediate region dominated by very hot and tenuous gas, (iii) a concentration of cold gas compressed toward the centre of the galaxy. The expanding cold shell will be pushed effectively by radiation pressure from the shining quasar. Besides, the black hole will be fuelled by the cold gas compressed to the centre by the blasts. The main shining phase of the quasar then follows the triggering of the wind.

It is possible to show[10] that radiation pressure from an Eddington accreting black hole of mass $M_\bullet$ is able to remove from a bulge of mass $M_{\rm bulge}$ an amount of gas:

$$M_{\rm wind} = 0.21 \left(\frac{M_\bullet / 1.8 \times 10^8\, M_\odot}{(M_{\rm bulge}/10^{11}\, M_\odot)^{1.1}} \right)^{1.5} \times M_{\rm bulge}. \quad (1)$$

This process can then create a black hole–bulge correlation very similar to that observed.

4 Quasars in a galaxy formation model

The toy model presented in Figures 1 and 2 does not take into proper account the hierarchical nature of galaxy formation, and the assembly of a low-angular momentum reservoir of gas able to accrete onto the black hole. To produce more realistic predictions, we have inserted black hole accretion into a galaxy formation model. This is still under construction, so the results presented here must be considered as only illustrative. A brief description of this model is contained in this reference[10].

A seed black hole of 1000 $M_\odot$ is put at the centre of each newly formed dark matter halo. The first loss of angular momentum of the gas is due to the same tidal fields responsible for the formation of spheroids, due to galaxy mergers and disc instabilities. Umemura and collaborators[13] suggested that radiation drag by the UV field of young stars is a likely responsible for a nearly complete loss of angular momentum, in which case the gas would accumulate at a rate proportional to the star-formation rate. Accepting this reasonable recipe (that can be caused by other processes), we let the cold gas in the bulge fall onto the black hole at a some fraction of the bulge star formation rate. If this accretion rate is larger than the Eddington limit, we put the excess gas into a reservoir an let it accrete later. A similar scheme is used by Danese and collaborators (see his contribution in this volume and this reference[11]).

Figure 3 shows as an example the evolution of the main progenitor of a spheroid, contained in a $1.1 \times 10^{13}\, M_\odot$ dark matter halo, if winds are absent, and if 0.3 per cent of the star formation rate is accreted by the black hole. At very high redshift the black hole grows at the Eddington rate from its initial mass to $\sim 10^8\, M_\odot$. Later, it grows at each merger event, generally at a sub-Eddington rate. The final black hole mass is compatible with the observed black hole–bulge relation. Figure 4 shows what happens if the accretion rate is 2 per cent of the star-formation rate, and galaxy winds are allowed. In this case winds (denoted by

a cross) quench star formation and black hole accretion at each accretion event at $z < 4$. As a result, larger black holes are available at high redshift, while the low-redshift activity is quenched (the shining phases are however Eddington-limited).

The effect of winds on the properties of the host galaxy are likely to be modest. However, the quenching of star formation at low redshift and the consequent ejection of metals will make the galaxy appear older, redder and more α-enhanced. This can help in reproducing the observed assembly of spheroids[12].

5 Conclusions

The shining of quasars is likely to affect deeply the ISM of the host, star-forming spheroid. In particular, it perturbs the ISM by evaporating part of the cold phase. This can change the way feedback works in the galaxy. This change can lead to the percolation of the expanding shells of dense, cold gas created by SN explosions. The resulting galaxy-wide shell is effectively pushed by radiation pressure; in this way the wind can eject up to ~ 20 per cent of the mass of the spheroid, in the case of an Eddington-limited black hole hole that follows the observed black hole–bulge relation.

The preliminary inclusion of quasar winds in a galaxy formation model shows that they may be responsible for the black hole–bulge relation (that can however be as well set by the mechanism responsible for the creation of a low-angular momentum reservoir) and that their influence on the properties of quasars and galaxies can help in reproducing the available observational evidence.

Acknowledgements

The author thanks F. Fontanot, S. Cristiani and G. Taffoni for discussions.

References

1. S. Cristiani, D.M. Alexander, F. Bauer, et al.: ApJ **600**, L119 (2004)
2. S. Cristiani, D. M. Alexander, F. Bauer, et al.: in *Multiwavelength mapping of galaxy evolution*, ed. by A. Renzini, R. Bender. In press (astro-ph/0403494)
3. C. Wolf, L. Wisotzki, A. Borch, S. Dye, M. Kleinheinrich, K. Meisenheimer: A&A **408**, 499 (2003)
4. X. Fan, M.A. Strauss, D.P. Schneider, et al.: AJ **121**, 54 (2001)
5. P. Monaco: MNRAS **352**, 181 (2004)
6. P. Monaco: MNRAS in press (astro-ph/0407052)
7. C.F. McKee, J.P. Ostriker: ApJ **218**, 148 (1977)
8. M. Begelman: in *Coevolution of Black Holes and Galaxies*, ed. by L. Ho (Cambridge: Cambridge University Press 2003)
9. M.C. Begelman, C.F. McKee, G.A. Shields: ApJ **271**, 70 (1983)
10. P. Monaco, F. Fontanot, in preparation
11. G.L. Granato, G. De Zotti, L. Silva, A. Bressan, L. Danese: ApJ **600**, 580 (2004)
12. A. Cimatti, L. Pozzetti, M. Mignoli, et al.: A&A **391**, L1 (2002)
13. M. Umemura, J. Fukue, S. Mineshige: ApJ **479**, L97 (1997)

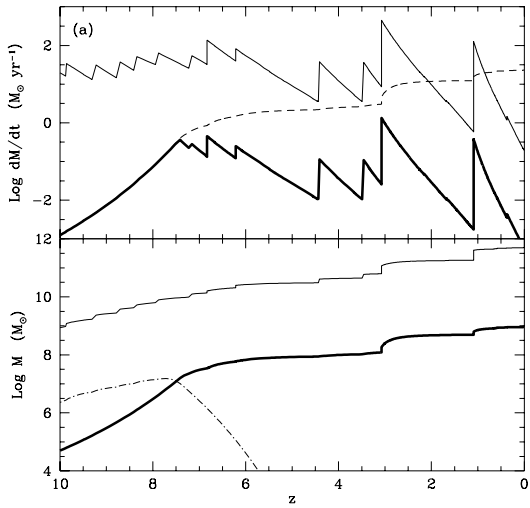

Fig. 3. Evolution as a function of redshift of the main progenitor of an elliptical hosted in a $1.1 \times 10^{13}\, M_\odot$ dark matter halo, as predicted by the galaxy formation model. Winds are absent. Upper panel: star-formation rate (*continuous line*), accretion rate (*continuous thick line*), Eddington limit (*dashed line*). Lower panel: bulge star mass (*continuous line*), black hole mass (*continuous thick line*), black hole reservoir (*dot-dashed line*)

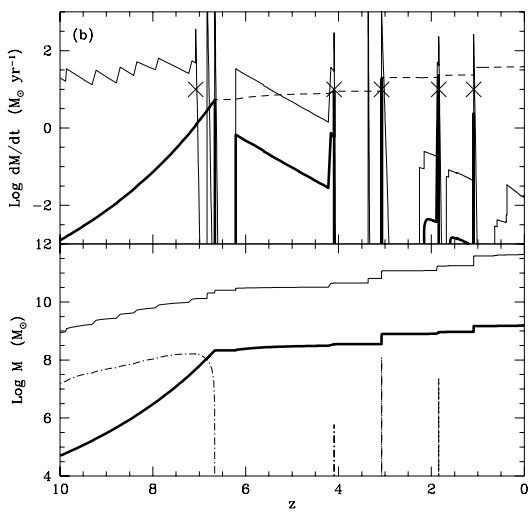

Fig. 4. As in figure 4, for the case of quasar-triggered winds. Crosses denote the redshifts at which winds are triggered

A Possible Feature of the Thermal Matter in Relativistic Jets in Radio-Loud Quasars

J.-M. Wang[1], R. Staubert[2], and T.J.-L. Courvoisier[3]

[1] Laboratory for High Energy Astrophysics, Institute of High Energy Physics, Chinese Academy of Sciences, Beijing 100039, P.R. China
[2] Institut für Astronomie und Astrophysik – Astronomie, Sand 1, D-72076 Tübingen, Germany
[3] INTEGRAL Science Data Center, Chemin d'Ecogia 16, CH-1290 Versoix, and Geneva Observatory, 51 ch. des Maillettes, CH-1290 Sauverny, Switzerland.

Abstract. We explore the possibility that the Kα line from the thermal matter may appear at tens of keV due to a high Doppler blue-shift. In the jet comoving frame, the energy density of photons originally emitted by the accretion disk and reflected off the broad line region clouds dominates over that of photons of other origin. We discuss the photoionization states of the thermal matter and find that the irons elements are neutral. The high metallicity in quasars enhances the possibility to detect the thermal matter in the relativistic jet in some radio-loud quasars. A highly Doppler blue-shifted Kα line may be detected. We make a prediction for 3C 273, in which the Kα line luminosity might be of the order 3.0×10^{44}erg s^{-1} with an equivalent width of 2.4 keV. Such a line could be detected in a future mission.

1 Introduction

Thermal matter generally exists in relativistic jets in radio-loud quasars [2,7,3], however, little attention has been paid to questions related to the thermal matter. *Chandra* discovered several lines from highly ionized atoms, such as Fe XXV, Fe XXIV, Co XIV, S XVI, Lyα and Lyβ, Ne X and Mg XI etc. in SS 433 [1]. The chemical composition in these jets definitely includes heavy elements rather than pure pair plasma. In radio-loud quasars, the case is highly uncertain [2,7]. We show that the thermal matter in the jet is neutral and the observational features of the thermal matter will mainly be the presence of a highly Doppler shifted Kα line, which could be detected in some radio-loud quasars by future instruments.

2 Emission from Thermal Matter

There are some constraints on temperature, density and size of the thermal matter in relativistic jets [2,3]. We calculate the iron Kα line from the thermal matter in the jet in radio-loud quasars based on the reflection model [6] via clouds in broad lineregion [4]. The line is highly blueshifted due to the motion of the jet. We find [10]

$$L_{\mathrm{K}\alpha}^{\mathrm{obs}} = 3.0 \times 10^{44}\ (\mathrm{erg/s}) \Gamma_{10}^{6} \mathcal{A}_{10} L_{\mathrm{X},44}^{\mathrm{ref}} \qquad (1)$$

ESO Symposia: Growing Black Holes, pp. 399–400, 2005.

where Lorentz factor $\Gamma_{10} = \Gamma/10$, iron abundance $\mathcal{A}_{10} = Z_{\rm QSO}/10Z_\odot$ and the reflected X-ray luminosity $L^{\rm ref}_{\rm X,44} = L^{\rm ref}_{\rm X}/10^{44}{\rm erg\ s^{-1}}$. The criteria for potential candidates are

$$\frac{L_\gamma}{L_{\rm syn}} > 1; \quad \frac{\rm N\ V}{\rm C\ IV} \geq 0.4. \tag{2}$$

implying the metal-rich quasars with γ-ray dominated emission [8], which are common [9].

For the parameters of 3C 273, we estimate a Kα line luminosity $L^{\rm obs}_{\rm K\alpha} \approx 3.0 \times 10^{44}$ erg s^{-1} and the flux $F_{\rm K\alpha} = 3.9\times10^{-12}$ erg cm^{-2} s^{-1}. With the *INTEGRAL* continuum spectrum, $F_E = 3.6 \times 10^{-11}E^{-0.73}$ erg cm^{-2} s^{-1} keV^{-1} [5], the equivalent width is estimated by $EW({\rm K}\alpha) \approx F_{\rm K\alpha}/F_E \approx 2.4$ (keV).

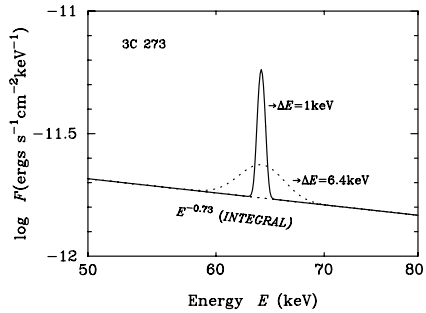

Fig. 1. A plot of the line profiles with future missions. A Gaussian profile for the line is assumed in the jet comoving frame. We assume two cases with energy resolution of $\Delta E = 1$keV and $\Delta E = 6.4$keV, respectively.

This feature would allow a direct measurement of the jet gamma factor and give very important indications on the as of yet not clear nature of the jet. The next generation hard X-ray instruments, such as, *NEXT* with energy resolution $\Delta E = 1$keV, may well measure this component.

References

1. Marshall, H. L., et al.: ApJ, 564, 941 (2002)
2. Celotti, A. & Fabian, A. C.: MNRAS, 264, 228 (1993)
3. Celotti, A., et al.: MNRAS, 293, 288 (1998)
4. Collin-Soufrrin, S., et al.: A&A, 314, 393 (1996)
5. Courvoisier, T.J.-L., et al.: A&A, 411, L343 (2003)
6. Sikora, M., Begelman, M.C. & Rees, M.J.: ApJ, 421, 153 (1994)
7. Sikora, M., et al.: ApJ, 484, 108 (1997)
8. Dondi, L. & Ghisellini, G.: MNRAS, 273, 583 (1995)
9. Hamann, F. & Ferland, G.: ARAA, 37, 487 (1999)
10. Wang, J.-M., Staubert, R. &Courvoisier, T.J.-L.: A&A, 419, L9 (2004)

The Influence of Black Hole Mass and Accretion Rate on the FRI/FRII Radio Galaxy Dichotomy

M. Wold[1,2], M. Lacy[2], and L. Armus[2]

[1] European Southern Observatory, D-85748 Garching bei München, Germany
[2] Spitzer Science Center/Caltech, 1200 E. California Blvd., Pasadena, CA 91125

Abstract. We use medium resolution optical spectra of 3CR radio galaxies to estimate their black hole masses and accretion rates. Black hole masses are found from central stellar velocity dispersions, and accretion rates are derived from narrow emission-line luminosities. The sample covers both Fanaroff-Riley (FR) classes; the more powerful FRIIs and the less powerful FRIs. We find that FRIs and FRIIs separate in diagrams of radio luminosity and narrow-line luminosity versus black hole mass. This suggests that, at a given black hole mass, the FRIIs accrete more efficiently, or accrete more matter, than FRIs.

1 Introduction

The classification of radio galaxies into FRIs and FRIIs is morphological in origin. Whereas FRIIs have knotty jets and radio lobes that end in bright hot-spots, the less powerful FRIs have smooth jets and large lobes that grow dimmer outward. The FRI/FRII transition is relatively sharp in terms of radio luminosity, with sources at $\log P_{178\mathrm{MHz}} > 25$ ($\mathrm{W\,Hz^{-1}\,sr^{-1}}$) being almost exclusively FRIIs, and sources at lower radio luminosities possessing FRI morphology [4]. Interestingly, the FRI/FRII transition radio luminosity, L_{rad}, is an increasing function of the optical luminosity, L_{opt}, of the host galaxy, $L_{\mathrm{rad}} \propto L_{\mathrm{opt}}^2$ [10]. The separation of FRIs and FRIIs in the radio-optical luminosity plane is surprisingly sharp, and several explanations have been offered including environmental differences [3,8], different physical processes [11] and differences in AGN parameters such as black hole mass and accretion rate [2,7].

2 Results

Here we investigate the influence of black hole mass and accretion rate on the FRI/FRII dichotomy. Spectra were obtained with the Double Spectrograph on the Palomar 5m, and sources having $P_{178\mathrm{MHz}} \leq 10^{26.5}$ $\mathrm{W\,Hz^{-1}\,sr^{-1}}$ (assuming $H_0 = 70$ $\mathrm{km\,s^{-1}\,Mpc^{-1}}$, $\Omega_m = 0.2$, $\Omega_\Lambda = 0.8$) were selected.

The spectra cover the regions around the Ca H&K $\lambda\lambda$3934,3969 Å and the MgI*b* λ5175 Å absorption. Template stars were observed and broadened with Gaussians and fit to the galaxy spectra using a direct fitting routine [1]. The best-fit velocity dispersions were converted to black hole masses using the M_{bh}–σ_* relation [4,6]. From the literature, but also from wide-slit spectra, we obtain the luminosity in the narrow [OII]3727 and/or [OIII]5007 Å emission lines.

ESO Symposia: Growing Black Holes, pp. 401–402, 2005.

In Fig. 1, we show the radio and the narrow-line [OII] luminosity as a function of black hole mass for some of the galaxies in our sample. FRIs and FRIIs separate fairly well, populating different regions of the diagrams. The [OII] narrow-line luminosity probes the total luminosity in the narrow-line region [12], and taking into account a covering factor, the narrow line luminosity scales with the photoionizing luminosity, and hence the accretion rate. The separation of FRIs and FRIIs in these diagrams may therefore imply that, at a given black hole mass, FRIs accrete less efficiently (or accrete less matter) than FRIIs. Sources that do not follow the general separation so well may be low-excitation radio galaxies [9]. One such example is 3C 35, which we find to have much weaker [OIII] than [OII]. In this case the environment, rather than accretion rate and black hole mass, may have determined the radio morphology of the source.

References

1. A.J. Barth, L.C. Ho, L.W. Sargent: AJ, **124**, 2607 (2002)
2. S.A. Baum, E.L. Zirbel, C.P. O'Dea: ApJ, **451**, 88 (1995)
3. D.S. De Young: ApJ, **405**, L13 (1993)
4. B.L. Fanaroff, J.M. Riley: MNRAS, **167**, 31P (1974)
5. L. Ferrarese, D. Merritt: ApJ, **539**, 9L (2000)
6. K. Gebhardt, et al.: ApJ, **539**, L13 (2000)
7. G. Ghisellini, A. Celotti: A&A, **379**, L1 (2001)
8. Gopal-Krishna, P.J. Wiita: A&A, **373**, 100 (2001)
9. R. Laing, C.R. Jenkins, J.V. Wall, S.W. Unger: 'Spectrophotometry of a complete sample of 3CR radio sources: Implications for Unified Models'. In: *ASP Conf. Ser., Vol 54, 1994*, ed. by G.V. Bicknell, M.A. Dopita, P.J. Quinn, pp. 201–208
10. M.J. Ledlow, F.N. Owen: AJ, **112**, 9 (1996)
11. D.L. Meier: ApJ, **522**, 753 (1999)
12. C.J. Willott, S. Rawlings, K.M. Blundell, M. Lacy: MNRAS, **309**, 1017 (1999)

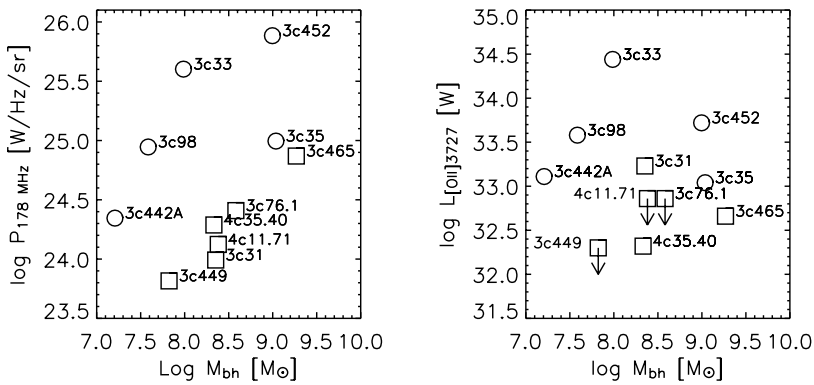

Fig. 1. Radio luminosity (left) and narrow-line [OII]3727 luminosity (right) as a function of black hole mass. FRI sources are plotted with squares, and FRIIs with circles.

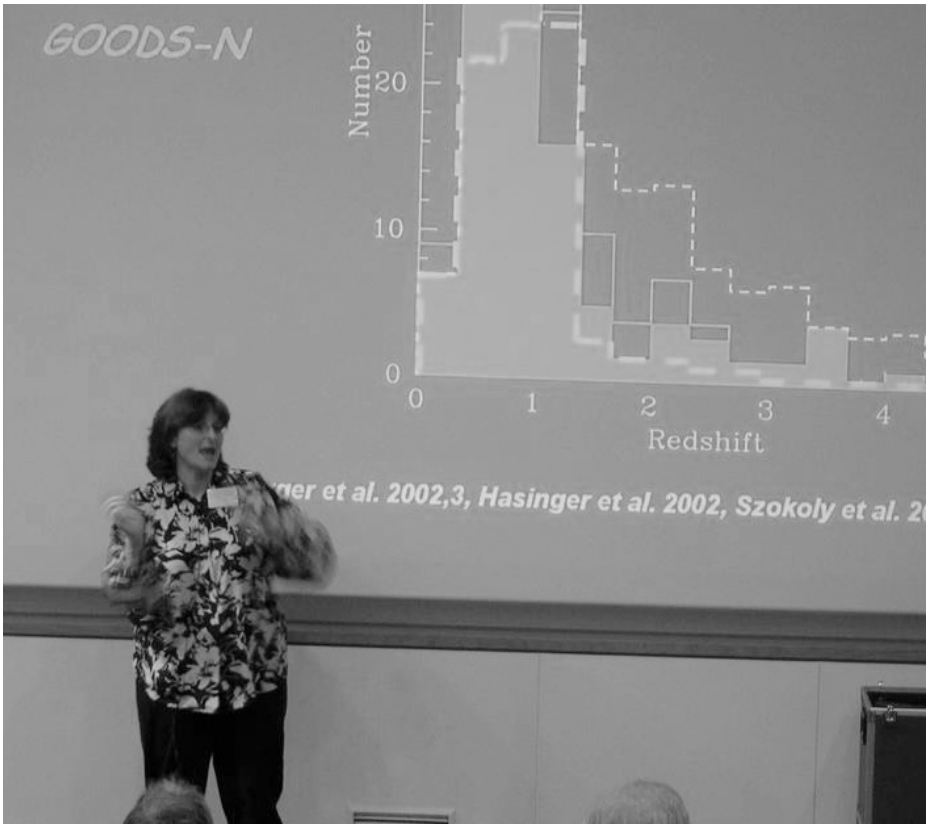
GOODS-N
Number
20
10
0
0
1
2
3
4
Redshift
ger et al. 2002,3, Hasinger et al. 2002, Szokoly et al. 2


PI: N. Brandt (PS

The Obscured X-ray Background and Evolution of AGN

A.C. Fabian and M.A. Worsley

Institute of Astronomy, Madingley Road, Cambridge CB3 0HA, UK

Abstract. The X-ray Background has been resolved in the 0.5–5 keV band and found to consist mostly of both unabsorbed and absorbed AGN with column densities $< 10^{23}\,\mathrm{cm}^{-2}$. This contrasts with the local AGN population where the column density range extends to Compton-thick objects and beyond ($> 1.5 \times 10^{24}\,\mathrm{cm}^{-2}$). Stacking analysis of the integrated emission of sources detected by XMM-Newton in the Lockman Hole, and by Chandra in the CDF-N and S reveals that the resolved fraction of the X-ray Background drops above 6 keV and is about 50% above 8 keV. The missing flux has the spectrum of highly absorbed AGN, making it likely that the range of column density at redshift one is similar to that locally, and that many AGN are as yet undetected in well-studied fields.

1 Introduction

Deep images with Chandra and XMM-Newton have shown that the X-ray Background (XRB) is composed, at least in the 2–5 keV band, of the emission of many active galactic nuclei (AGN) [1][2][3][4]. This was anticipated by earlier work with ROSAT [5] which resolved the 0.5–2 keV XRB in a similar manner. The XRB therefore reveals the integrated X-ray emission of AGN and is an important tool for studying the accretion history of the Universe and the evolution of AGN.

The background spectrum in the 2–10 keV band is flatter than typical AGN and requires that most are absorbed [6][7][8]. This ties in with what we know of AGN locally where absorbed Seyfert II galaxies outnumber Seyfert Is. What remains to be determined is whether powerful objects such as quasars have a significant obscured fraction, how the obscuration evolves with time in an object and how obscuration evolves with redshift within the population.

2 Local obscured AGN

Absorbed AGN are very common in the local Universe [9]. The three nearest AGN with X-ray luminosities exceeding $10^{40}\,\mathrm{erg\ s}^{-1}$, NGC4945 [10][11], the Circinus Galaxy [12] and Cen A [13] all lie behind absorbing column densities $N_\mathrm{H} > 10^{23}\,\mathrm{cm}^{-2}$. The first two are Compton thick with $N_\mathrm{H} > 1.5 \times 10^{24}\,\mathrm{cm}^{-2}$. The ratio of absorbed to unabsorbed nuclei is at least 3–5, with the column density distribution being fairly flat [14]. The large ratio suggests that the geometry is more complex than the simple unification torus model.

ESO Symposia: Growing Black Holes, pp. 407–417, 2005.

At greater distances where higher luminosity objects are sampled there are some clearly highly absorbed AGN (e.g., NGC6240, [15]; IRAS09014, [16]; 3C294 nucleus, [17]). In particular, the nuclei of many radio galaxies lie behind large column densities.

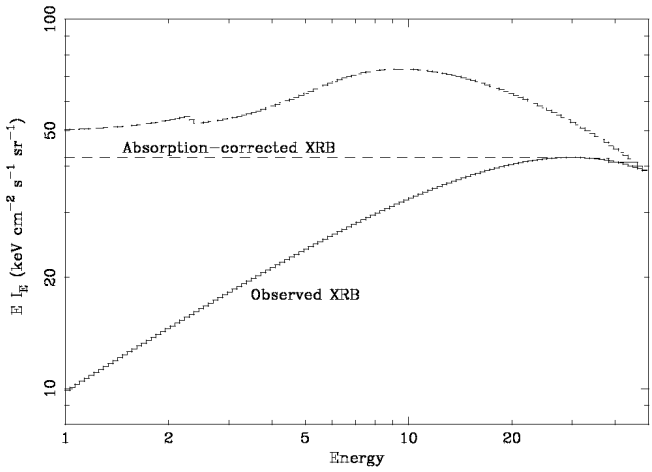

Fig. 1. The extragalactic XRB intensity as observed and the minimum absorption-corrected spectrum required assuming a typical intrinsic spectrum with $\Gamma = 2$. Compton-thick obscuration or reflection could make the corrected intensity higher.

3 Tying the evolution of AGN and the XRB in with the local black hole mass density

If η is the efficiency with which mass is turned into radiation during accretion ($\eta = 0.06$ for a standard thin disc around a non-spinning black hole and a typical assumed value for an accreting black hole is 0.1), then

$$\varepsilon_{\rm rad}(1+z) = \eta \rho_{\rm h} c^2$$

[18] $\varepsilon_{\rm rad}$ is the observed energy density in that radiation now, $\rho_{\rm h}$ is the mean mass density added to the black holes and z is the mean redshift of the population. Applying this formula to the *intrinsic* absorption-corrected spectrum of the XRB with a 2–10 keV bolometric correction factor of 30 and a mean source redshift of 2 gave a mean black hole mass density of about $\rho_{\rm h} \sim 8 \times 10^5\,{\rm M}_\odot\ {\rm Mpc}^{-3}$ [19].

This is significantly larger than $\rho_{\rm h} \sim 3 \times 10^5\,{\rm M}_\odot\ {\rm Mpc}^{-3}$ found by [22] from the black hole mass – stellar velocity correlation applied to the local galaxy luminosity function. Elvis et al [21] suggest that this requires the radiative efficiency $\eta > 0.15$ and thus that most black holes are spinning rapidly (which boosts η).

A major new result for AGN from X-ray surveys is the peak in number density around $z \sim 0.8$, not at $z \sim 2$ as found for quasars [22][23][9]. Simply put, the population of AGN with X-ray luminosities above 3×10^{44} erg s^{-1}, which are traditionally quasars, began dying at $z \sim 2$ whereas the population of less luminous objects, akin to nearby Seyferts, carried on to $z \sim 0.8$ before dying. This means we should rework the Seyfert part of the Soltan equation with a mean $z \sim 0.8$. That changes the bolometric correction to 15 [17] and brings the predicted black hole mass density into line with observations at $4 - 5 \times 10^5\,\mathrm{M}_\odot\ \mathrm{Mpc}^{-3}$ for $\eta \sim 0.1$ [17][25][26].

The situation therefore looks fair for $\eta \sim 0.1$ provided that all populations have been accounted for. A possible problem lies in the column density distribution of local sources compared with distant ones, such as are commonly resolved in deep X-ray surveys. The sources found in the latter overwhelmingly have column densities $< 10^{23}\,\mathrm{cm}^{-2}$ [27] whereas locally this accounts for only about 40% [14]. Does the column density distribution evolve with redshift or have the surveys failed to find AGN with larger column densities? To study that we have examined just how well the spectrum of the resolved sources in deep X-ray fields matches the spectrum of the XRB and so whether a population of sources remains unresolved [28][29].

4 Resolving the XRB with Deep Surveys

The deep, pencil-beam X-ray surveys have confirmed that the XRB is made up of point sources. The XMM-Newton observation of the Lockman Hole (XMM-LH; [30], as well as the Chandra Deep Field North (CDF-N; [3]) and Chandra Deep Field South (CDF-S; [1]), are able to resolve $\sim 70 - 90\%$ of the XRB in the broad 0.5–2 keV and 2–10 keV bands. The variation in this fraction is dependent on the XRB normalisation[1] chosen.

These high resolved fractions are often used as the basis for claims that the XRB has been completely resolved up to 10 keV. Such optimistic statements are misleading, since it is counts in the 2–5 keV regime that dominate the 2–10 keV band. In order to investigate more carefully the behaviour of the resolved fraction with energy we carried out a source-stacking analysis using the XMM-LH data [28]. We employed a straightforward photometric approach to find the total resolved flux in a number of narrow energy bands. XMM-Newton was particularly suited to the study since it has good sensitivity up to 12 keV.

The Lockman Hole is one of the most well-studied regions of the sky and has received multi-wavelength attention. The unusually low level of neutral Galactic absorption ($\sim 5 \times 10^{-19}\,\mathrm{cm}^{-2}$) makes it particularly well-suited to deep X-ray surveys. The total accumulated XMM-Newton exposure time has now reached $\sim$ 700 ks from 17 different observations. We restricted our analysis to sources within

[1] [31] summarize their own and previous work on the spectrum of the XRB which indicates that the normalization is probably a factor of 1.3 times greater than the HEAO-A2 all-sky study of [32]. See also [33]

a central 10-arcmin radius with the lowest background levels and maximum exposure time.

4.1 Source Detection, Photometry and Stacking

We cleaned the raw event files to exclude background flares and bad pixels before extracting images in five different energy bands; 0.2–0.5 keV, 0.5–2 keV, 2–4.5 keV, 4.5–7.5 keV and 7.5–12 keV. We carried out sliding-box source detection to generate an initial list of bright sources. These were then masked-out of the images and further source-fitting carried out with maximum-likelihood point spread function (PSF) fitting. The final source list was verified manually, resulting in a final list of 126 detected sources located within 10' of the observation. (Since this early work our subsequent re-analysis has made use of a more complete source list of 156 objects although the additional 30 sources make no significant difference to our results.)

We adopted straightforward aperture photometry to determine the count-rate of each source and in each energy band. The three XMM-Newton instruments were processed separately to provide robustness and because of differences in background level and PSF. For each instrument and energy band an exposure-corrected image was made by dividing by the exposure map. In each case we also created a source-free image by masking out all the detected sources. For each source and in each energy band, the total count-rate was extracted from within a circular aperture centred on the source position. The local background level was measured in an annulus surrounding the source but here we used the source-free version of the images to avoid contamination. Given the aperture-measured and annulus-measured count-rates the true source and background count-rates can be easily determined.

When calculating the true source and background count-rates we assumed an analytical fit to the PSF. Tests of the quality of the analytical model on a number of sources found it to be acceptable within the energy bands and off-axis angles required. The radius of the circular extraction aperture was chosen to maximise signal-to-noise in the final source count-rate. The background- and exposure-corrected count-rates for each source were converted to fluxes using conversion factors computed with XSPEC assuming a $\Gamma = 1.4$ source plus $N_{\rm H} = 5 \times 10^{19}\,{\rm cm}^{-2}$ Galactic absorption.

The total resolved flux in each energy band was calculated by summing the measured flux for each source. Every source is included regardless of whether or not it is detected in the band. Flux errors were added appropriately and combined with the estimated error in the counts-to-flux conversion. A correction for Galactic absorption was made; this is $\sim 15\%$ in the 0.2–0.5 keV band and $\lesssim 1\%$ in the harder bands.

4.2 XMM-Newton Results

Figure 2 shows the resolved XRB intensity for each of the XMM-Newton instruments along with the total XRB. From 0.5–12 keV we took the total XRB to be a

$\Gamma = 1.41$ power-law with a normalisation of 11.6 keV cm^{-2} s^{-1} sr^{-1} keV^{-1} [31]. In the softest band, 0.2–0.5 keV the extragalactic background level is uncertain and is estimated to lie at 20–35 keV cm^{-2} s^{-1} sr^{-1} keV^{-1} [34].

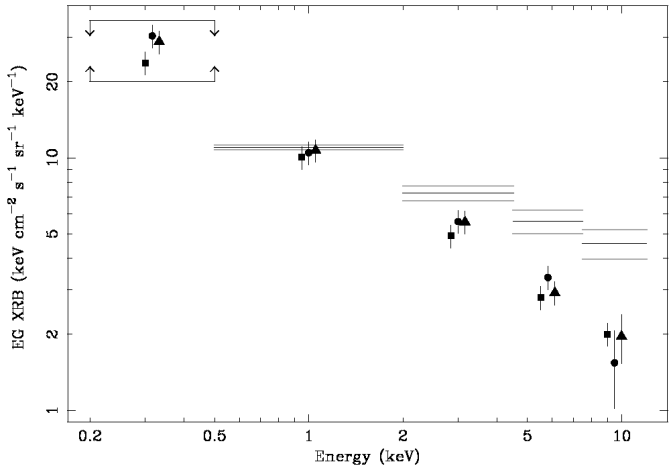

Fig. 2. The extragalactic XRB intensity resolved from detected sources in the energy bands. The values from the three instruments are plotted, for clarity, as points in the centre of each band and offset horizontally with respect to each other. Squares, circles and triangles represent the PN, MOS-1 and MOS-2 instruments respectively. Errors are one sigma. The bars represent the total extragalactic XRB intensity.

From 0.2–2 keV the resolved fraction of the background is consistent with $\sim 90\%$. The 2–4.5 keV band also shows a high resolved fraction of 70–80% but the harder bands > 4.5 keV only resolve $\lesssim 60\%$. The missing XRB component has a spectral signature consistent with what would be expected from an undetected population of highly obscured sources.

The level of the unresolved fraction depends upon the Lockman Hole being a representative sample of the sky, as well as the normalisation taken for the total XRB, which itself is still subject to errors of 10–15%. We do not correct for the bright-end source population: the pencil-beam nature of the field means that bright sources ($\gtrsim 5 \times 10^{-14}$ erg cm^{-2} s^{-1}) are not well-sampled whilst those brighter than $\sim 10^{-13}$ erg cm^{-2} s^{-1} are not seen at all. The additional contribution by these bright objects would increase the resolved fraction by $\sim$ 10–20%, but this is only comparable to the effect of field-to-field variations. Critically, since bright sources typically have very soft spectral slopes, no additional contribution can account for the missing XRB above 5 keV, nor could any adjustments to XRB normalisation.

4.3 The Chandra Deep Fields

Although Chandra has low effective area at energies exceeding 7 keV, the CDF-N and CDF-S probe much deeper than the XMM-LH. We used the CDFs to assess whether the contribution from the fainter sources detected by Chandra were able to explain the XMM-Newton results. To aid comparison, as well as to take advantage of numerous software improvements and the complete XMM-LH source catalogue, we re-analysed the XMM-Newton data using identical energy bands to the Chandra work (see [29]).

The CDF-N and CDF-S cover 447.8 and 391.3 arcmin^2 respectively. We used the catalogues from [3] which contain 503 and 326 sources respectively for the fields as well as photometry. Source-extraction apertures enclosing 90–100% of the counts were used and the local background correction was determined from Poisson statistics. Counts-to-flux conversion was performed, where possible, using conversion factors appropriate to the hardness ratio of the source. For sources with an insufficient number of counts to permit this, a $\Gamma = 1.4$ spectrum was assumed.

Prior to our stacking analysis we applied corrections for Galactic absorption as well as several systematic effects which have been recently quantified [3]. The total resolved flux in each of five photometric bands (0.5–1 keV, 1–2 keV, 2–4 keV and 4–6 keV) was calculated by summing the measured flux for each detected source. In order to calculate a resolved intensity the flux from each source must be divided by a solid angle on the sky; however, since the CDFs show a substantial increase in sensitivity towards the centre of the fields, this solid angle is a function of source brightness. The total solid angles of 447.8 and 391.3 arcmin^2 are only applicable to the brightest objects, whereas fainter sources are only detectable over a fraction of these regions and the appropriate solid angle to take is smaller. We use the sensitivity functions from [3] when calculating source intensities.

4.4 Bright-End Correction

In order to remove the 'noise' in the resolved fluxes that is due to poor sampling of the brighter sources (which only occur with sky densities of $\sim$ a few on the size of the deep surveys), we ignored sources with 0.5-8 keV fluxes greater than 5×10^{-14} erg cm^{-2} s^{-1}. We then used number counts from wide-area surveys to replace the missing flux due to all the sources brighter than this. We used the the $\log N$–$\log S$ functions from [36], compiled in for the 0.5–2 keV and 2–10 keV bands.

A number of studies have confirmed a strong dependence of source spectral shape with flux. At the bright-end sources have spectral slopes much softer than the $\Gamma = 1.4$ of the XRB. We took a linear fit to the relationship as observed by [37], although we conservatively impose a maximum of $\Gamma = 2$. Given this relation we can compute the bright-source contribution for each energy band, using the appropriate spectral index at each source flux and integrating the $\log N$–$\log S$ function.

4.5 Results

Figure 3 shows the bright-end corrected and resolved XRB as seen in the CDF-N, CDF-S and XMM-LH. The extragalactic XRB level is taken to be the spectrum measured by [31], but at high energies we take account of the slight turn-over, and below 1 keV we take account of the steeping over the spectrum implied by AGN-shadowing observations (for details refer to [29]).

The resolved fraction is $\sim$ 70–90% up to $\sim$ 4 keV. XMM-Newton sees a decrease in the 4–6 keV band whereas the CDFs remain consistent with a high resolved fraction of $\sim$ 80–90%. This difference is due to the faint, hard sources which are detected in the CDFs but not the (shallower) XMM-LH. In the 6–8 keV range all three surveys only resolve 50–70%, whilst in the 8–12 keV band XMM-Newton only resolves 40-60% of the background. The total resolved flux in the broad 0.5–8 range remains high (80–85%), and illustrates the need for narrow-band stacking to reveal the decrease > 6 keV.

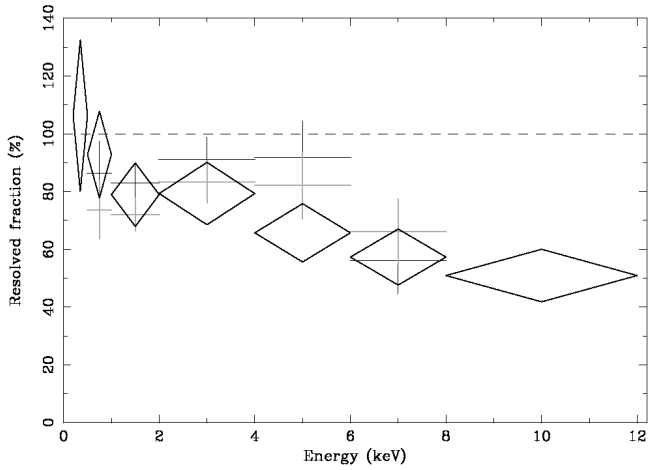

Fig. 3. The resolved fraction of the XRB as seen in the CDF-N (black crosses), CDF-S (grey crosses) and XMM-LH (the combined PN/MOS-1/MOS-2 result; black diamonds), as a function of energy.

4.6 The Missing Source Population

We have modelled the spectral shape of the missing XRB fraction as a single population of sources. We assumed an underlying $\Gamma = 2$ power-law, inclusive of an $R = 1$ reflection component, plus intrinsic photoelectric absorption. A grid of spectra was constructed over the range $z = 0.1$–3 and $N_{\rm H} = 10^{22}$–$10^{25}\,{\rm cm}^{-2}$ and for each we calculated the goodness-of-fit between the model spectrum and the unresolved XRB spectrum. The confidence contours in source spectral shape are shown in Figure 4.

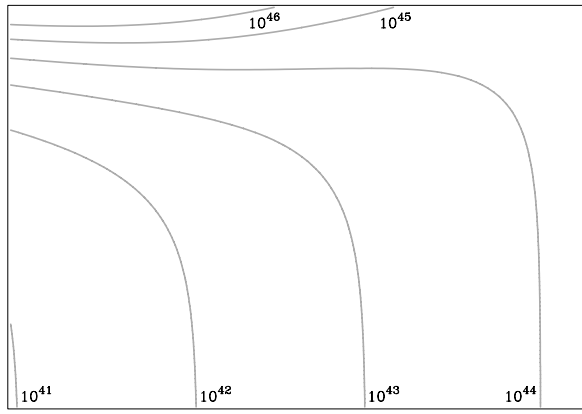

Fig. 4. Confidence contours (horizontal) of fits between the missing XRB spectrum and an obscured power-law model for the XMM-Newton data. 68, 90 and 95% contours are shown. The best-fitting model has $z \sim 0.8$ and $N_{\rm H} \sim 4.5 \times 10^{23}\,{\rm cm}^{-2}$.The other contours indicate the maximum, unobscured, rest-frame 2–10 keV luminosity of a single source in the population.

The XMM-LH and CDFs show similar contours for the characteristics of the missing population, although it is the XMM-Newton results, which extend up to 12 keV, which provide the best constraints. The best-fitting models have $z = 0.5$–1.5 and $N_{\rm H} = 10^{23}$–$10^{24}\,{\rm cm}^{-2}$, pointing to a highly obscured population of AGN. Since the missing sources are undetected, the survey sensitivity allows an upper limit to be placed on the luminosity of each object. For the best-fitting source models this upper limit is $\lesssim 5 \times 10^{43}\,{\rm erg\ s}^{-1}$. The sources must occur with areal densities of $\gtrsim 2800\,{\rm deg}^{-2}$ – a considerable number. This would correspond to at least ~ 350 undetected AGN in the CDF-N, and suggests that there must be $\gtrsim 3$ times more undetected, obscured sources than detected, unobscured ones. Figure 5 shows the resolved and total XRB with the typical shape of the sources required to account for the missing intensity.

The absorption-corrected flux of the missing population can be used to estimate the black hole mass density of the obscured population. Assuming an accretion efficiency of 0.1, and a bolometric correction of 0.1, the missing population would correspond to a black hole mass density of ~ 0.5–$1 \times 10^5\,{\rm M}_\odot\ {\rm Mpc}^{-3}$; ~ 10–20% of the total local value.

5 Summary

Studies of the XRB continue to reveal the evolution and properties of AGN. Most of the XRB is resolved up to an energy of 5 keV and is due to AGN – Seyferts and quasars – with absorbing column densities $< 2 \times 10^{23}\,{\rm cm}^{-2}$. The

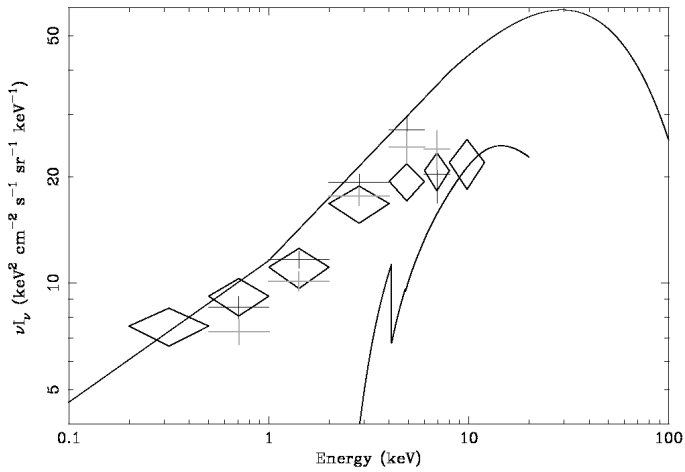

Fig. 5. The total extragalactic XRB (upper solid curve) along with that resolved in the XMM-LH (black diamonds), CDF-N (black crosses) and CDF-S (grey crosses). The lower solid curve shows the spectrum of the best-fitting model for the missing source population at $z \sim 0.8$ and with $N_{\rm H} \sim 4.5 \times 10^{23}\,{\rm cm}^{-2}$.

identification of large samples of such objects shows that the lower luminosity ones (Seyfert-like) evolve rapidly to $z \sim 0.8$ while quasars evolve more slowly to $z \sim 2$. Assuming that the Seyfert-like ones have lower black hole masses, those black holes continued to grow at later stages of the Universe than the more massive ones associated with quasars.

The resolved fraction of the XRB drops to 60–70% above 6 keV and 50% above 8 keV. The missing fraction between 6–8 keV is not due to the known faint sources in the 2–5 keV band since it would have been detected by the stacking analysis which corresponds to an exposure time of 0.5 Gs or more. The missing fraction is most simply explained as due to the high column density ($N_{\rm H} > 2 \times 10^{23}\,{\rm cm}^{-2}$) extension to the observed Seyfert-like objects evolving rapidly to $z \sim 1$. Such a population was implicit in XRB synthesis models such as that of [38] or [39].

Presumably there is also a Compton-thick population as well, which would make less of an impact on the XRB since Compton down-scattering then depletes the emergent X-ray luminosity. The total black hole density due to Compton-thin sources is then about $\rho_{\rm h} \approx 5 \times 10^5 \eta_{-1}^{-1}\,{\rm M}_\odot\ {\rm Mpc}^{-3}$, where $\eta = 0.1\eta_{-1}$. This is consistent with recent estimates of the local value of $\rho_{\rm h}$ [25] [26] for $\eta = 0.1$.

The issue of highly obscured and Compton-thick quasars remains unresolved [40]. Powerful radio galaxies represent one, relatively small, population. Some powerful, highly obscured, radio-quiet quasars have been found [41][42][43][44], with [45] estimating a surface density of at least 10 deg^{-2}, The uncertainties are currently too large to assess their general importance. Future work combining X-ray and Spitzer data will be instructive.

References

1. R. Giacconi, A. Zirm, J. Wang, P. Rosati, M. Nonino, P. Tozzi, R. Gilli, V. Mainieri, G. Hasinger, L. Kewley, J. Bergeron, S. Borgani, R. Gilmozzi, N. Grogin, A. Koekemoer, E. Schreier, W. Zheng, C. Norman: ApJS **139**, 369 (2002)
2. R.F. Mushotzky, L.L. Cowie, A.J. Barger, K.A. Arnaud: Nat **404**, 459 (2000)
3. D.M. Alexander, F.E. Bauer, W.N. Brandt, D.P. Schneider, A.E. Hornschemeier, C. Vignali, A.J. Barger, P.S. Broos, L.L. Cowie, G.P. Garmire, L.K. Townsley, M.W. Bautz, G. Chartas, W.L.W. Sargent: AJ **126**, 539 (2003)
4. A.J. Barger, L.L. Cowie, W.N. Brandt, P. Capak, G.P. Garmire, A.E. Hornschemeier, A.T. Steffen, E.H. Wehner: AJ **124**, 1839 (2002)
5. G. Hasinger, R. Burg, R. Giacconi, M. Schmidt, J. Trumper, G. Zamorani: A&A **392**, 482 (1998)
6. G. Setti, L. Woltjer: A&A **224**, L21 (1989)
7. P. Madau, G. Ghisellini, A.C. Fabian: MNRAS **270**, L17 (1994)
8. A. Comastri, G. Setti, G. Zamorani, G. Hasinger A&A **296**, 1 (1995)
9. G. Matt, A.C. Fabian, M. Guainazzi, K. Iwasawa, L. Bassani, G. Malaguti: MNRAS **318**, 173 (2000)
10. K. Iwasawa, K. Koyama, H. Awaki, H. Kunieda, K. Makishima, T. Tsuru, T. Ohashi, N. Nakai: ApJ **409**, 155 (1993)
11. C. Done, G.M. Madejski, D.A. Smith: ApJ **463**, L63 (1996)
12. G. Matt, M. Guainazzi, R. Maiolino, S. Molendi, G.C. Perola, L.A. Antonelli, L. Bassani, W.N. Brandt, A.C. Fabian, F. Fiore, K. Iwasawa, G. Malaguti, A. Marconi, J. Poutanen: A&A **341**, L39 (1999)
13. R.E. Rothschild, D.L. Band, P.R. Blanco, D.E. Gruber, W.A. Heindl, D.R. MacDonald, D.C. Marsden, K. Jahoda, D. Pierce, G. Madejski, M. Elvis, D.A. Schwartz, R. Remillard, A.A. Zdziarski, C. Done, R. Svensson: ApJ **510**, 651 (1999)
14. G. Risaliti, R. Maiolino, M. Salvati: ApJ **522**, 157 (1999)
15. P. Vignati, S. Molendi, G. Matt, M. Guainazzi, L.A. Antonelli, L. Bassani, W.N. Brandt, A.C. Fabian, K. Iwasawa, R. Maiolino, G. Malaguti, A. Marconi, G.C. Perola: A&A **349**, L57 (1999)
16. K. Iwasawa, A.C. Fabian, S. Ettori: MNRAS **321**, L15 (2001)
17. A.C. Fabian: 'Carnegie Observatories Astrophysics Series, Vol. 1: Coevolution of Black Holes and Galaxies' ed. L.C. Ho (Cambridge: Cambridge Univ. Press) (astro-ph/0304122) (2003)
18. A. Soltan: MNRAS **200**, 115 (1982)
19. A.C. Fabian, K. Iwasawa: MNRAS **303**, L34 (1999)
20. Q. Yu, S. Tremaine: MNRAS **335**, 965 (2002)
21. M. Elvis, G. Risalti, G. Zamorani: ApJ **565**, L75 (2002)
22. G. Hasinger: Proc. Symposium 'New Visions of the X-ray Universe in the XMM-Newton and Chandra Era' 26-30. November, ESTEC, The Netherlands (2001)
23. Y. Ueda, M. Akiyama, K. Ohta, T. Miyaji: ApJ **598**, 886 (2003)
24. F. Fiore, M. Brusa, F. Cocchia, A. Baldi, N. Carangelo, P. Ciliegi, A. Comastri, F. La Franca, R. Maiolino, G. Matt, S. Molendi, M. Mignoli, G.C. Perola, P. Severgnini, C. Vignali: A&A **409** 79 (2003)
25. A. Marconi, G. Risaliti, R. Gilli, L.K. Hunt, R. Maiolino, M. Salvati: MNRAS **351** 169 (2004)
26. F. Shankar, P. Salucci, G.L. Granato, G. De Zotti, L. Danese: MNRAS, in press (astro-ph/0405585)

27. D.M. Alexander, W.N. Brandt, A.E. Hornschemeier, G.P. Garmire, D.P. Schneider, F.E. Bauer, R.E. Griffiths: AJ **122**, 2156 (2001)
28. M.A. Worsley, A.C. Fabian, X. Barcons, S. Mateos, G. Hasinger, H. Brunner: MNRAS **352**, L28 (2004)
29. M.A. Worsley, A.C. Fabian, F.E. Bauer, D.M. Alexander, G. Hasinger, S. Mateos, H. Brunner, W.N. Brandt, D.P. Schneider: MNRAS, submitted (2004)
30. G. Hasinger, B. Altieri, M. Arnaud, X. Barcons, J. Bergeron, H. Brunner, M. Dadina, K. Dennerl, P. Ferrando, A. Finoguenov, R.E. Griffiths, Y. Hashimoto, F.A. Jansen, D.H. Lumb, K.O. Mason, S. Mateos, R.G. McMahon, T. Miyaji, F. Paerels, M.J. Page, A.F. Ptak, T.P. Sasseen, N. Schartel, G.P. Szokoly, J. Trümper, M. Turner, R.S. Warwick, M.G. Watson: A&A **365**, L45 (2001)
31. A. De Luca, S. Molendi: A&A **419**, 837 (2004)
32. F.E. Marshall, E.A. Boldt, S.S. Holt, R.B. Miller, R.F. Mushotzky, L.A. Rose, R.E. Rothschild, P.J. Serlemitsos: ApJ **235**, 4 (1980)
33. M. Revnivtsev, M. Gilfanov, R. Sunyaev, K. Jahoda, C. Markwardt: A&A **411**, 329 (2003)
34. R.S. Warwick, T.P. Roberts: AN **319**, 59 (1998)
35. F.E. Bauer, D.M. Alexander, W.N. Brandt, D.P. Schneider, E. Treister, A.E. Hornschemeier, G.P. Garmire: AJ, in press (astro-ph/0408001) (2004)
36. A. Moretti, S. Campana, D. Lazzati, D. Tagliaferri: ApJ **588**, 696 (2003)
37. A. Streblyanska, J. Bergeron, H. Brunner, A. Finoguenov, G. Hasinger, V. Mainieri: Nucl. Phys. B., **132**, *Proceedings of the 2nd BeppoSAX Conference: The Restless High-Energy Universe*, Eds. E.P.J. van den Heuvel, R.A.M.J. Wijers, J.J.M. in 't Zand, p. 232 (2004)
38. P. Gandhi, A.C. Fabian: MNRAS **339**, 1095 (2003)
39. R. Gilli, M. Salvati, G. Hasinger: A&A **366**, 407 (2001)
40. A. Comastri, F. Fiore, C. Vignali, M. Brusa, F. Civano: these proceedings. (astro-ph/0410272) (2004)
41. C.S. Crawford, P. Gandhi, A.C. Fabian, R.J. Wilman, R.M. Johnstone, A.J. Barger, L.L. Cowie: MNRAS **333**, 809 (2002)
42. C. Norman, G. Hasinger, R. Giacconi, R. Gilli, L. Kewley, M. Nonino, P. Rosati, G. Szokoly, P. Tozzi, J. Wang, W. Zheng, A. Zirm, J. Bergeron, R. Gilmozzi, N. Grogin, A. Koekemoer, E. Schreier: ApJ **571**, 218 (2002)
43. D. Stern, E.C. Moran, A.L. Coil, A. Connolly, M. Davis, S. Dawson, A. Dey, P. Eisenhardt, R. Elston, J.R. Graham, F. Harrison, D.J. Helfand, B. Holden, P. Mao, P. Rosati, H. Spinrad, S.A. Stanford, P. Tozzi, K.L. Wu: ApJ **568**, 71 (2002)
44. R.J. Wilman, A.C. Fabian, C.S. Crawford, R.M. Cutri: MNRAS **338**. L19 (2003)
45. P. Gandhi, C.S. Crawford, A.C. Fabian, R.M. Johnstone: MNRAS **348**, 529 (2004)

When Supermassive Black Holes Were Growing: Clues from Deep X–ray Surveys

G. Hasinger

Max-Planck-Institute for Extraterrestrial Physics, 84571 Garching, Germany

Abstract. Merging the *Chandra* and *XMM–Newton* deep surveys with the previously identified *ROSAT* surveys a unique sample of almost 1000 AGN–1 covering five orders of magnitude in 0.5–2 keV flux limit and six orders of magnitude in survey solid angle with $\sim$ 95% completeness has been constructed. The luminosity–redshift diagram is almost homogeneously filled. AGN–1 are by far the largest contributors to the soft X–ray selected samples. Their evolution is responsible for the break in the total 0.5–2 keV source counts. The soft X–ray AGN–1 luminosity function shows a clear change of shape as a function of redshift, confirming earlier reports of luminosity–dependent density evolution for optical quasars and X–ray AGN. The space density evolution with redshift changes significantly for different luminosity classes, showing a strong positive evolution, i.e. a density increase at low redshifts up to a certain redshift and then a flattening. The redshift, at which the evolution peaks, changes considerably with X–ray luminosity, from $z \approx$0.5–0.7 for luminosities $\log L_x$=42–43 erg s^{-1} to $z \approx 2$ for $\log L_x$=45–46 erg s^{-1}. The amount of density evolution from redshift zero to the maximum space density also depends strongly on X–ray luminosity, more than a factor of 100 at high luminosities, but less than a factor of 10 for low X–ray luminosities. For the first time, a significant decline of the space density of X–ray selected AGN towards high redshift has been detected in the range $\log L_x$=42–45 erg s^{-1}, while at higher luminosities the survey volume at high–redshift is still too small to obtain meaningful densities. A comparison between X–ray and optical properties shows now significant evolution of the X–ray to optical spectral index for AGN–1. The constraints from the AGN luminosity function and evolution in comparison with the mass function of massive dark remnants in local galaxies indicates, that the average supermassive black hole has built up its mass through efficient accretion ($\epsilon \sim 10\%$) and is likely rapidly spinning.

1 Introduction

In recent years the bulk of the extragalactic X–ray background in the 0.1-10 keV band has been resolved into discrete sources with the deepest *ROSAT*, *Chandra* and *XMM–Newton* observations [32,55,14,27,33,1,35,8]. Optical identification programmes with Keck [61,40,5,4] and VLT [29,12] find predominantly unobscured AGN–1 at X–ray fluxes $S_X > 10^{-14}$ erg cm^{-2} s^{-1}, and a mixture of unobscured and obscured AGN–2 at fluxes $10^{-14} > S_X > 10^{-15.5}$ erg cm^{-2} s^{-1} with ever fainter and redder optical counterparts, while at even lower X–ray fluxes a new population of star forming galaxies emerges [35,58,1,36,56,8]. At optical magnitudes R>24 these surveys suffer from large spectroscopic incompleteness, but deep optical/NIR photometry can improve the identification

ESO Symposia: Growing Black Holes, pp. 418–431, 2005.

completeness significantly, even for the faintest optical counterparts [75,43]. A recent review article [12] summarizes the current status of X–ray deep surveys.

The AGN/QSO luminosity function and its evolution with cosmic time are key observational quantities for understanding the origin of and accretion history onto supermassive black holes, which are now believed to occupy the centers of most galaxies. X–ray surveys are practically the most efficient means of finding active galactic nuclei (AGNs) over a wide range of luminosity and redshift. Enormous efforts have been made by several groups to follow up X–ray sources with major optical telescopes around the globe, so that now we have fairly complete samples of X–ray selected AGNs. The most complete and sensitive sample was compiled recently by Hasinger, Miyaji and Schmidt [34], concentrating on unabsorbed (type–1) AGN selected in the soft (0.5–2 keV) X–ray band, where due to the previous *ROSAT* work [50,51] complete samples exist, with sensitivity limits varying over five orders of magnitude in flux, and survey solid angles ranging from the whole high galactic latitude sky to the deepest pencil-beam fields. These samples allowed to construct luminosity functions over cosmological timescales, with an unprecedented accuracy and parameter space.

Table 1. The soft X–ray sample

Survey[a]	Solid Angle [deg^2]	$S_{\rm X14,lim}$ [cgs]	$N_{\rm tot}$	$N_{\rm AGN-1}$[b]	$N^{\rm c}_{\rm unid}$
RBS	20391	≈ 250	901	203	0
SA–N	684.0–36.0	47.4–13.0	380	134	5
NEPS	80.7–1.78	21.9–4.0	262	101	9
RIXOS	19.5–15.0	10.2–3.0	340	194	14
RMS	0.74–0.32	1.0–0.5	124	84	7
RDS/XMM	0.126–0.087	0.38–0.13	81	48	8
CDF–S	0.087–0.023	0.022–0.0053	293	113	1
CDF–N	0.048–0.0064	0.030–0.0046	195	67	21
Total			2566	944	57

[a] Abbreviations – RBS: The *ROSAT* Bright Survey [62]; SA–N: *ROSAT* Selected Areas North [4]; NEPS: *ROSAT* North Ecliptic Pole Survey [29]; RIXOS: *ROSAT* International X–ray Optical Survey [47], RMS: *ROSAT* Medium Deep Survey, consisting of deep PSPC pointings at the North Ecliptic Pole [9], the UK Deep Survey [48], the Marano field [74] and the outer parts of the Lockman Hole [61,39]; RDS/XMM: *ROSAT* Deep Survey in the central part of the Lockman Hole, observed with *XMM–Newton* [40,42,19]; CDF–S: The *Chandra* Deep Field South [29,75,43]; CDF–N: The *Chandra* Deep Field North [5,4].

[b] Excluding AGNs with $z < 0.015$.

[c] Objects without redshifts, but hardness ratios consistent with type–1 AGN.

2 The X–ray selected AGN–1 sample

For the derivation of the X–ray luminosity function and cosmological evolution of AGN well–defined flux–limited samples of active galactic nuclei have been chosen, with flux limits and survey solid angles ranging over five and six orders of magnitude, respectively (see Table 1). To be able to utilize the massive amount of optical identification work performed previously on a large number of shallow to deep *ROSAT* surveys, the analysis was restricted to samples selected in the 0.5–2 keV band. In addition to the *ROSAT* surveys already used in [50,51], data from the recently published *ROSAT* North Ecliptic Pole Survey (NEPS) [29,54], from an *XMM–Newton* observation of the Lockman Hole [42] as well as the *Chandra* Deep Fields South (CDF–S) [29,75,43] and North (CDF–N) [5,4] were included. In order to avoid systematic uncertainties introduced by the varying and a priori unknown AGN absorption column densities only unabsorbed (type–1) AGN, classified by optical and/or X–ray methods were selected. We are using here a definition of type–1 AGN, which is largely based on the presence of broad Balmer emission lines and small Balmer decrement in the optical spectrum of the source (optical type–1 AGN, e.g. the ID classes a, b, and partly c in [61], which largely overlaps the class of X–ray type–1 AGN defined by their X–ray luminosity and unabsorbed X–ray spectrum [29]. However, as Szokoly et al show, at low X–ray luminosities and intermediate redshifts the optical AGN classification often breaks down because of the dilution of the AGN excess light by the stars in the host galaxy (see e.g. [52]), so that only an X–ray classification scheme can be utilized. Schmidt et al. [61] have already introduced the X–ray luminosity in their classification. For the deep XMM–Newton and *Chandra* surveys in addition the X–ray hardness ratio was used to discriminate between X–ray type–1 and type–2 AGN, following [29].

Most ($\approx$ 70–100%) of the extragalactic X–ray sources found in both the deep and wider X–ray surveys with Chandra and XMM-Newton are AGN of some type. Starburst and normal galaxies make increasing fractional contributions at the faintest X–ray flux levels, but even in the CDF-N they represent $\sim$ 20–30% of all sources (and create $\sim$ 5% of the XRB). The observed AGN sky density in the deepest X–ray surveys is ≈ 7200 deg^{-2}, about an order of magnitude higher than that found at any other wavelength [8]. This exceptional effectiveness at finding AGN arises because X–ray selection (1) has reduced absorption bias and minimal dilution by host-galaxy starlight, and (2) allows concentration of intensive optical spectroscopic follow-up upon high-probability AGN with faint optical counterparts (i.e., it is possible to probe further down the luminosity function).

3 Number Counts and Resolved Background Fraction

Based on deep surveys with Chandra and XMM-Newton, the X–ray log(N)–log(S) relation has now been determined down to fluxes of 2.4×10^{-17} erg cm^{-2} s^{-1}, 2.1×10^{-16} erg cm^{-2} s^{-1}, and 1.2×10^{-15} erg cm^{-2} s^{-1} in the 0.5–2, 2-10

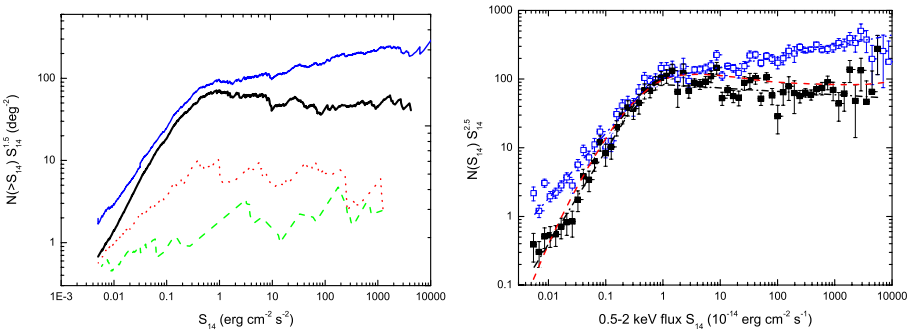

Fig. 1. (a) Cumulative number counts N(>S) for the total sample (upper blue thin line), the AGN–1 subsample (lower black thick line), the AGN–2 subsample (red dotted line) and the galaxy subsample (green dashed line). (b) Differential number counts of the total sample of X–ray sources (open squares) and the AGN–1 subsample (filled squares). The dot-dashed lines refer to broken powerlaw fits to the differential source counts (see text). The dashed red line shows the prediction for type–1 AGN (from [34]).

and 5-10 keV band, respectively [10,33,58,53,8]. Figure 1a shows the normalized cumulative source counts $N(> S_{\rm X14})S_{\rm X14}^{1.5}$. The total differential source counts, normalized to a Euclidean behaviour ($\mathrm{d}N/\mathrm{d}S_{\rm X14} \times S_{\rm X14}^{2.5}$) is shown with open symbols in Figure 1b. Euclidean source counts would correspond to horizontal lines in these graphs. For the total source counts, the well-known broken powerlaw behaviour is confirmed with high precision. A broken power law fitted to the differential source counts yields power law indices of $\alpha_b = 2.34 \pm 0.01$ and $\alpha_f = 1.55 \pm 0.04$ for the bright and faint end, respectively, a break flux of $S_{\rm X14} = 0.65 \pm 0.10$ and a normalisation of $\mathrm{d}N/\mathrm{d}S_{\rm X14} = 103.5 \pm 5.3$ deg^{-2} at $S_{\rm X14} = 1.0$ with a reduced χ^2=1.51. We see that the total source counts at bright fluxes, as determined by the *ROSAT* All-Sky Survey data, are significantly flatter than Euclidean, consistent with the discussion in [31]. Moretti et al. [53], on the other hand, have derived a significantly steeper bright flux slope ($\alpha_b \approx 2.8$) from *ROSAT* HRI pointed observations. This discrepancy can probably be attributed to the selection bias against bright sources, when using pointed observations where the target area has to be excised.

The ROSAT HRI Ultradeep Survey had already resolved 70-80% of the extragalactic 0.5–2 keV XRB into discrete sources, the major uncertainty being in the absolute flux level of the XRB. The deep Chandra and XMM-Newton surveys have now increased the resolved fraction to 85-100% [53,35]. Above 2 keV the situation is complicated on one hand by the fact, that the HEAO-1 background spectrum [46], used as a reference over many years, has a $\sim 30\%$ lower normalization than several earlier and later background measurements (see e.g. [53]). Recent determinations of the background spectrum with XMM-Newton [15] and RXTE [57] strengthen the consensus for a 30% higher normalization, indicating that the resolved fractions above 2 keV have to be scaled down correspondingly. On the other hand, the 2-10 keV band has a large sensitivity gradient across the

band. A more detailed investigation, dividing the recent 770 ksec XMM-Newton observation of the Lockman Hole into finer energy bins, comes to the conclusion, that the resolved fraction decreases substantially with energy, from over 90% below 2 keV to less than 50% above 5 keV [35].

Type–1 AGN are the most abundant population of soft X–ray sources. For the determination of the AGN–1 number counts we include those unidentified sources, which have hardness ratios consistent with AGN–1 (a contribution of $\sim 6\%$, see Table 1). Figure 1 shows, that the break in the total source counts at intermediate fluxes is produced by type–1 AGN, which are the dominant population there. Both at bright fluxes and at the faintest fluxes, type–1 AGN contribute about 30% of the X–ray source population. At bright fluxes, they have to share with clusters, stars and BL-Lac objects, at faint fluxes they compete with type–2 AGN and normal galaxies (see Fig. 1a and [8]). A broken power law fitted to the differential AGN–1 source counts yields power law indices of $\alpha_b = 2.55 \pm 0.02$ and $\alpha_f = 1.15 \pm 0.05$ for the bright and faint end, respectively, a break flux of $S_{\rm X14} = 0.53 \pm 0.05$, consistent with that of the total source counts within errors, and a normalisation of of $\mathrm{dN/d}S_{\rm X14} = 83.2 \pm 5.5$ deg^{-2} at $S_{\rm X14} = 1.0$ with a reduced χ^2=1.26. The AGN–1 differential source counts, normalized to a Euclidean behaviour ($\mathrm{dN/d}S_{\rm X14} \times S_{\rm X14}^{2.5}$) is shown with filled symbols in Figure 1.

4 The Soft X–ray Luminosity Function and Space Density Evolution

Hasinger, Miyaji and Schmidt [34] have employed two different methods to derive the AGN–1 X–ray luminosity function and its evolution. The first method uses a variant of the $\frac{1}{V_a}$ method, which was developed in [50]. The binned luminosity function in a given redshift bin z_i is derived by dividing the observed number $N_{obs}(L_x, z_i)$ by the volume appropriate to the redshift range and the survey X–ray flux limits and solid angles. To evaluate the bias in this value caused by a gradient of the luminosity function across the bin, each of the luminosity functions is fitted by an analytical function. This function is then used to predict $N_{mdl}(L_x, z_i)$. Correcting the luminosity function by the ratio N_{obs}/N_{mdl} takes care of the bias to first order.

The second method uses unbinned data. Individual $V_{\rm max}$ of the RBS sources are used to evaluate the zero-redshift luminosity function. This is free of the bias described above: using this luminosity function to derive the number of expected RBS sources matches the observed numbers precisely. In the subsequent derivation of the evolution, i.e., the space density as a function of redshift, binning in luminosity and redshift is introduced to allow evaluation of the results. Bias at this stage is avoided by iterating the parameters of an analytical representation of the space density function. Together with the zero-redshift luminsity function this is used to predict $N_{mod}(L_x, z_i)$ for the surveys. The observed densities in the bins are derived by multiplying the space density value by the ratio

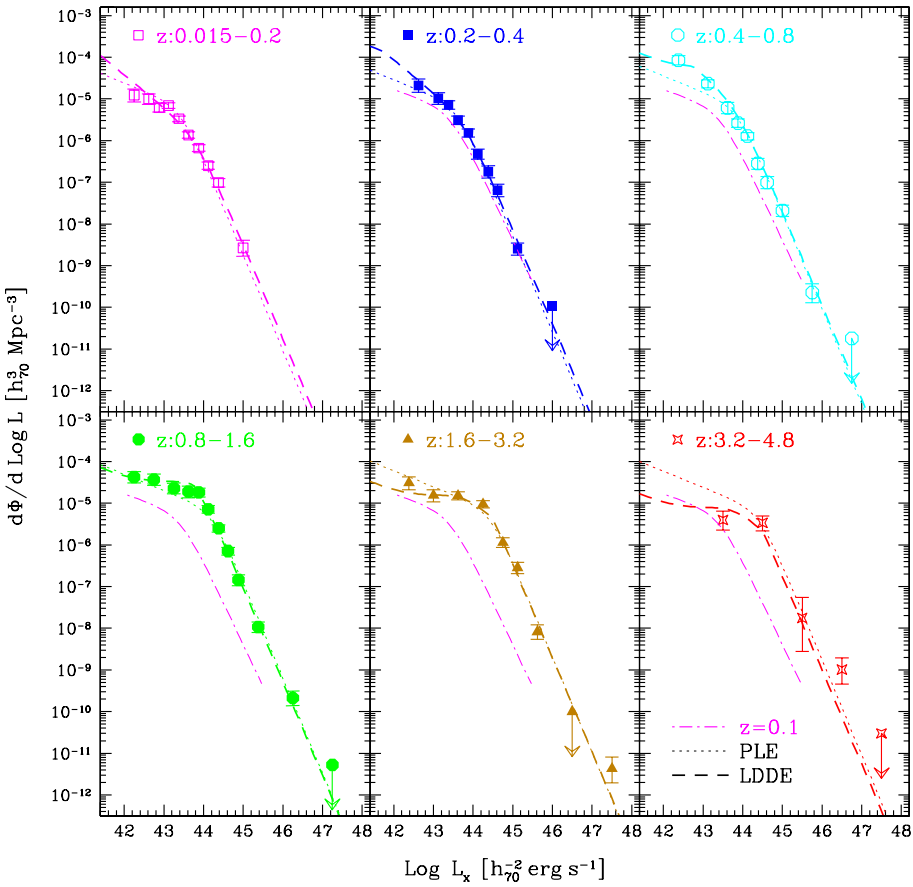

Fig. 2. The soft X–ray luminosity function of the type–1 AGN sample in different redshift shells for the nominal case as labelled. The error bars correspond to 68% Poisson errors of the number of AGNs in the bin. The best–fit two power-law model for the $0.015 < z < 0.2$ shell are overplotted in the higher redshift panels for reference. The dotted and dashed lines give the best–fit PLE and LDDE models (from [34]).

$N_{obs}(L_x, z_i)/N_{mod}(L_x, z_i)$. At this stage, none of the densities are derived by dividing a number by a volume.

The other difference between the two methods is in the treatment of missing redshifts for optically faint objects. In the binned method, all AGN without redshift with $R > 24.0$ were assigned the central redshift of each redshift bin to derive an upper boundary to the luminosity function. In the unbinned method, the optical magnitudes of the RBS sources were used to derive the optical redshift limit corresponding to $R = 24.0$. The $V_{\max}$ values for surveys (such as CDF–N) spectroscopically incomplete beyond $R = 24.0$ were based on the smaller of the X–ray and optical redshift limits.

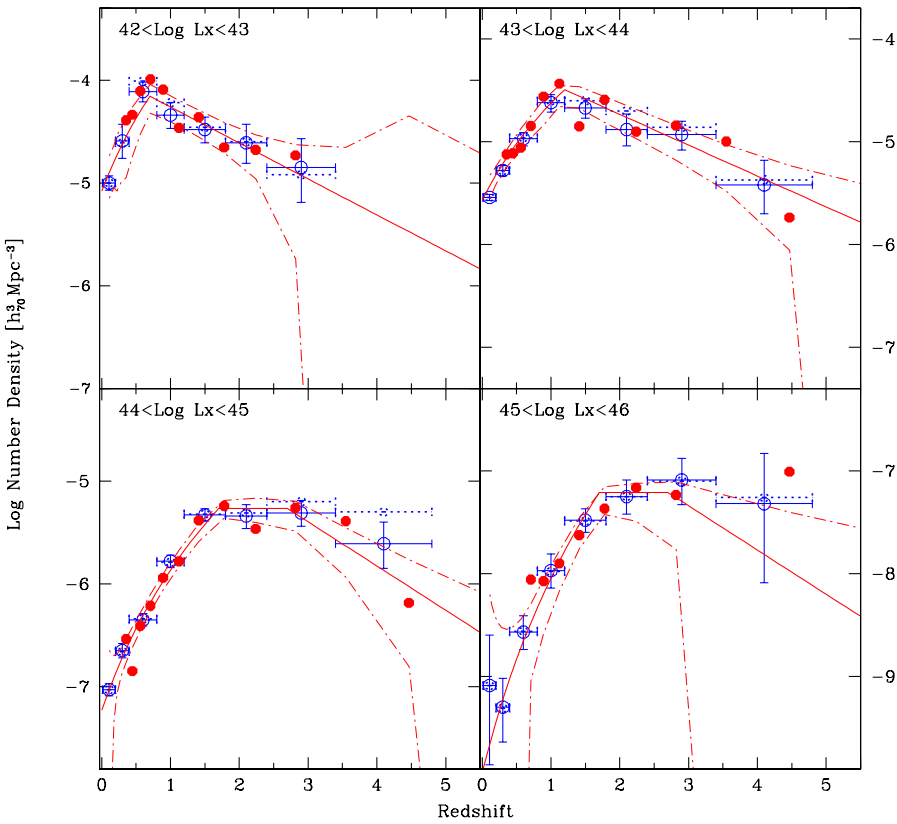

Fig. 3. Comparison between the space densities derived with two different methods. The blue datapoints with error bars refer to the binned treatment using the N_{obs}/N_{mdl} method, the dashed horizontal lines corresponding to the maximum contribution of unidentified sources. The thin and thick red lines and dots refer to the unbinned method (from [34]).

Figure 2 shows the luminosity function derived this way in different redshift shells. A change of shape of the luminosity function with redshift is clearly seen and can thus rule out simple density or luminosity evolution models. In a second step, instead of binning into redshift shells, the sample has been cut into different luminosity classes and the evolution of the space density with redshift was computed. Figure 3 shows a direct comparison between the binned and unbinned determinations of the space density, which agree very well within statistical errors.

The fundamental result is, that the space density of lower–luminosity AGN–1 peaks at significantly lower redshift than that of the higher–luminosity (QSO–

type) AGN. Also, the amount of evolution from redshift zero to the peak is much less for lower–luminosity AGN. The result is consistent with previous determinations based on less sensitive and/or complete data, but for the first time our analysis shows a high-redshift decline for all luminosities $L_X < 10^{45}$ erg s^{-1} (at higher luminosities the statistics is still inconclusive). Albeit the different approaches and the still existing uncertainties, it is very reassuring that the general properties and absolute values of the space density are very similar in the two different derivations in.

A luminosity-dependent density evolution (LDDE) model has been fit to the data. Even though the sample is limited to soft X–ray-selected type–1 AGN, the parameter values of the overall LDDE model are surprisingly close to those obtained by Ueda et al. 2003 for the intrinsic (de-absorbed) luminosity function of hard X–ray selected obscured and unobscured AGN, except for the normalization, where Ueda et al. reported a value about five times higher.

These new results paint a dramatically different evolutionary picture for low–luminosity AGN compared to the high–luminosity QSOs. While the rare, high–luminosity objects can form and feed very efficiently rather early in the Universe, with their space density declining more than two orders of magnitude at redshifts below z=2, the bulk of the AGN has to wait much longer to grow with a decline of space density by less than a factor of 10 below a redshift of one. The late evolution of the low–luminosity Seyfert population is very similar to that which is required to fit the Mid–infrared source counts and background [24] and also the bulk of the star formation in the Universe [41], while the rapid evolution of powerful QSOs traces more the merging history of spheroid formation [23].

This kind of anti–hierarchical Black Hole growth scenario is not predicted in most of the semi–analytic models based on Cold Dark Matter structure formation models (e.g. [37,71]). This could indicate two modes of accretion and black hole growth with radically different accretion efficiency (see e.g. [16]). A self–consistent model of the black hole growth which can simultaneously explain the anti–hierarchical X–ray space density evolution and the local black hole mass function derived from the $M_{BH} - \sigma$ relation assuming two radically different modes of accretion has recently been presented in [7].

5 Optical versus X–ray selection of AGN–1

The space density of soft X–ray selected QSOs from the Hasinger et al. sample is compared to the one of optically-selected QSOs at the most luminous end in Fig. 4. The $z < 2$ number density curve for optically selected QSOs ($M_{b_J} < -26.0$) is from the combination of the 2dF and 6dF QSO redshift surveys [14]. The $z > 2.7$ number densities from [60] and [20] have been originally given for H_0=50 km s^{-1} Mpc^{-1}, $\Omega_m = 1, \Omega_\Lambda = 0$. Their data points have been converted to H_0=70 km s^{-1} Mpc^{-1}, $\Omega_m = 0.3, \Omega_\Lambda = 0.7$ and the $M_{\rm B}$ threshold has been re-calculated with an assumed spectral index of $\alpha_o = -0.79$ ($f_\nu \propto \nu^{\alpha_o}$), following e.g. [69]. The plotted curve from [60,20] is for $M_B < -26.47$ under these assumptions. A small correction of densities due to the cosmology conversion

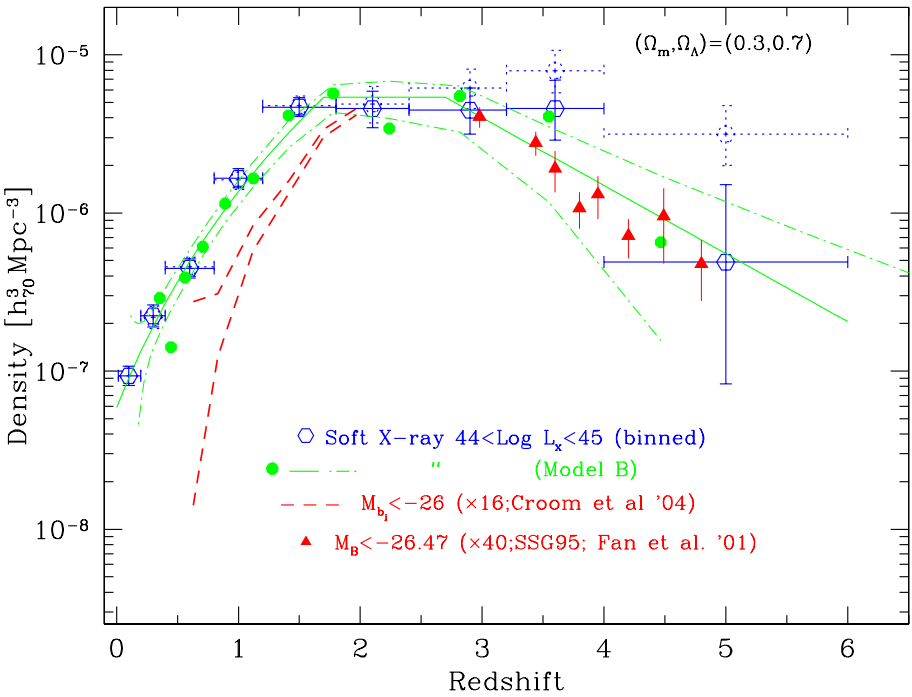

Fig. 4. Comparison of the space density of luminous QSOs between optically selected and soft X–ray selected samples (from [34]). The X–ray number densities are plotted for the luminosity class $\log L_{\rm x} = 44 - 45$, both for the binned and unbinned analysis with the same symbols as in Fig. 3. The dashed lines represent the one sigma range for $M_{b_{r,j}} < -26.0$ from [14], multiplied by a factor of 16 to match the X–ray space density at z=2. The triangles at $z > 2.7$ with 1σ errors are from [60] (SSG95) and [20] after a cosmology conversion (see text) and a scaling by a factor of 40 to match with the soft X–ray density at $z \sim 2.7$. As discussed in this paper, both the rise and the decline of the space density, behavior changes with L_x and therefore that the comparison can only be illustrative.

causing redshift-dependent luminosity thresholds has also been made, assuming $d\Phi/dlogL_B \propto L_B^{-1.6}$ [20]. The space density for the soft X–ray QSOs for the luminosity class $44 < logL_x < 45$ has been plotted both for the binned and unbinned determination. The Croom et al. [14] space density had to be scaled up by a factor of 16 in order to match the X–ray density at $z \sim 2$. The Schmidt, Schneider & Gunn / Fan et al. data points have been scaled by a factor of 40 to match the soft X–ray data at $z = 2.7$ in the plot. There is relatively little difference in the density functions between the X–ray and optical QSO samples, although we have to keep in mind, that both the rise and the decline of the space density is varying with X–ray luminosity, so that this comparison can only be illustrative until larger samples of high–redshift X–ray selected QSOs will be available.

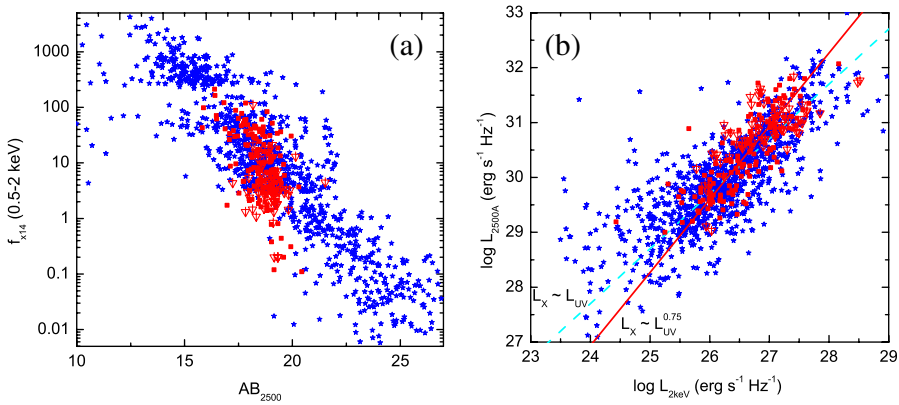

Fig. 5. (a): comparison of X–ray fluxes and AB_{2500} UV magnitudes for the sample of $\sim$ 1000 X–ray selected type-1 AGN from [34] (blue points) with the ROSAT-observed optically selected SDSS QSOs [69]. Filled red squares give the standard SDSS QSO, while open red squares give the specifically selected high-redshift SDSS sample (see [69]). (b): Monochromatic 2 keV X–ray versus 2500 ÅUV luminosity for the same samples. The blue (dark) solid line shows a linear relation between the two luminosities, while the yellow (light) solid line gives the non-linear relation $L_X \sim L_{UV}^{0.75}$ from the literature [69].

As a next step we directly study the X–ray and optical fluxes and luminosities of our sample objects and compare this with the optically selected QSO sample of Vignali et al. [69] based on SDSS-selected AGN serendipitously observed in ROSAT PSPC pointings. Because of the inhomogeneous nature and different systematics of the different surveys entering our sample, the optical/UV magnitudes of our objects have unfortunately much larger random and systematic errors and are based on fewer colours than the excellent SDSS photometry. In our preliminary analysis we therefore calculated the AB_{2500} magnitudes simply extrapolating or interpolating the observed magnitudes in the optical filters closest to the redshifted 2500 Åband, assuming an optical continuum with a power law index of -0.7, i.e. not utilizing the more complicated QSO spectral templates including emission lines which have been used in [69]. A spectroscopic correction for the host galaxy contamination, as done for the SDSS sample, was also not possible for our sample, however, for a flux and redshift-selected sample of 94 RBS Seyferts [59] we have morphological determinations of the nuclear versus host magnitudes (see below). In all other aspects of the analysis we follow the Vignali et al. treatment. Figure 5a shows 0.5–2 keV X–ray fluxes versus AB_{2500} magnitudes for our sample objects (blue stars) in comparison with the Vignali et al. SDSS sample (X–ray detections are shown as filled red squares, upper limits as down–pointing triangles). It is obvious, that our multi-cone survey sample covers a much wider range in X–ray and optical fluxes than the magnitude-limited SDSS sample. Unlike the SDSS sample, our sample shows a very clear

correlation between X–ray and optical fluxes, but also a wider scatter in this correlation.

Figure 5b shows the monochromatic X–ray versus UV luminosity for the same data. Now the X–ray and optically selected samples cover a similar parameter range at the high luminosity end, but the X–ray selected data reach significantly lower X–ray and UV luminosities than the optically selected sample. Again, there is a larger scatter in the X–ray selected sample. The figure also shows two analytic relations between X–ray and UV luminosity: a linear relation $L_X \propto L_{UV}$ and the non–linear behaviour $L_X \propto L_{UV}^{0.75}$ found in the literature (e.g. [69]). While the Vignali et al. optically selected sample clearly prefers the non-linear dependence (see also [11]), this is not true for the X-ray selected sample, which is consistent with a linear relation, apart from the behaviour at low luminosities, where significant contamination from the host galaxy is expected.

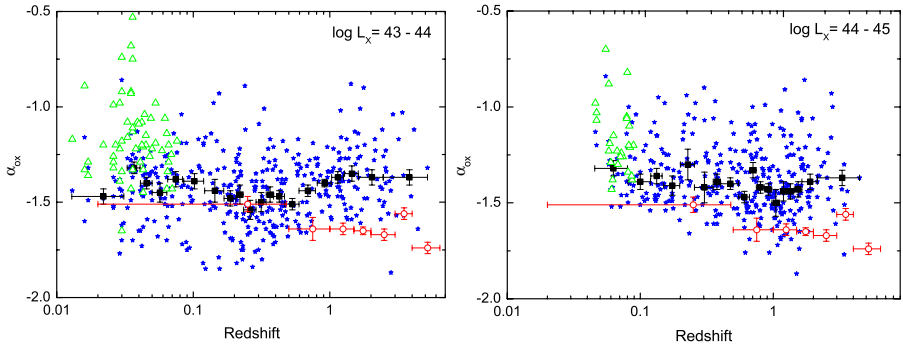

Fig. 6. X–ray to optical spectral index α_{ox} as a function of redshift for different luminosity classes for the Hasinger et al. sample of $\sim$ 1000 soft X–ray selected type-1 AGN. Blue (dark) stars give the values derived using the total integrated optical light, while the green triangles give the values using only the nuclear component from 93 RBS AGN, derived by Salvato [59] from detailed imaging decomposition. The solid black squares with error bars give the median and variance of the X-ray selected sample. Open red squares with error bars show the average α_{ox} values for the Vignali et al. optically selected QSOs.

To check on any evolution of the optical to X–ray spectral index with redshift we calculated α_{ox} values, following [69] for all our sample objects. In order to see possible luminosity–dependent evolution effectssimilar to those observed in the space density evolution, we divided our sample into the same luminosity classes as in Section 4. Figure 6 shows the α_{ox} values determined for objects in the luminosity class 43–44 and 44–45, respectively, as a function of redshift. Apart from a few wiggles, which are likely due to the omission of the emission lines in the optical AGN continuum, there is no significant evolution with redshift. The optically selected sample, on the other hand, shows a significant trend with redshift and average values inconsistent with the X-ray selected sample for most

of the redshift range. The diagram also shows, that this discrepancy is likely not caused by the missing host galaxy contamination correction in our analysis. From the relatively small number of nearby (z<0.1) of RBS sources, where a morphological fitting procedure has been used to subtract the host emission from the total magnitude [59] we can estimate the host dilution effect, which is clearly larger at lower X–ray luminosities and makes the discrepancy even larger. The immediate conclusion is, that the average optical to X-ray sample properties are dependent on systematic sample selection effects.

6 X–ray Constraints on the Growth of SMBH

The AGN luminosity function can be used to determine the masses of remnant black holes in galactic centers, using Sołtan's continuity equation argument [63] and assuming a mass-to-energy conversion efficiency ϵ. For a non-rotating Schwarzschild BH, ϵ is expected to be 0.054, while for a maximally rotating Kerr BH, ϵ can be as high as 0.37 [66]. The AGN demography predicted, that most normal galaxies contain supermassive black holes (BH) in their centers, which is now widely accepted (e.g. [38] and references therein). Recent determinations of the accreted mass from the optical QSO luminosity function are around $2\epsilon_{0.1}^{-1} \cdot 10^5 M_\odot Mpc^{-3}$ [13,73]. Estimates from the X–ray background spectrum, including obscured accretion power obtain even larger values: 6-9 [18] or 8-17 [17] in the above units, and values derived from the infrared band [30] or multiwavelength observations [6] are similarly high (8-9). Probably the most reliable recent determination comes from an integration of the X–ray luminosity function. Using the Ueda et al. [9] hard X–ray luminosity function including a correction for Compton–thick AGN normalized to the X–ray background, as well as an updated bolometric correction ignoring the IR dust emission, Marconi et al [5] derived $\rho_{accr} \sim 3.5\epsilon_{0.1}^{-1} \cdot 10^5 M_\odot Mpc^{-3}$.

The BH masses measured in local galaxies are tightly correlated to the galactic velocity dispersion [21,25], and less tightly to the mass and luminosity of the host galaxy bulge (however, see [44]). Using these correlations and galaxy luminosity (or velocity) functions, the total remnant black hole mass density in galactic bulges can be estimated. Scaled to the same assumption for the Hubble constant (H_0=70 km s^{-1} Mpc^{-1}), recent papers arrive at different values, mainly depending on assumptions about the intrinsic scatter in the BH–galaxy correlations: $\rho_{BH} = (2.4 \pm 0.8)$, (2.9 ± 0.5) and $(4.6^{+1.9}_{-1.4} h_{70}^2 \cdot 10^5 M_\odot Mpc^{-3}$, respectively [3,73,5]. The local dark remnant mass function is fully consistent with the above accreted mass function, if black holes accrete with an average energy conversion efficiency of $\epsilon = 0.1$ [5], which is the classically assumed value and lies between the Schwarzschild and the extreme Kerr solution. However, taking also into account the widespread evidence for a significant kinetic AGN luminosity in the form of jets and winds, it is predicted, that the average supermassive black hole should be rapidly spinning fast (see also [17,73]). Recently, using XMM-Newton, a strong relativistic Fe Kα line has been discovered in the average rest–frame

spectra of AGN–1 and AGN–2 [64], which can be best fit by a rotating Kerr solution consistent with this conjecture.

Acknowledgements I thank my colleagues in the *Chandra Deep Field South* and *XMM–Newton Lockman Hole* projects, as well as Maarten Schmidt, Takamitsu Miyaji and Niel Brandt for the excellent cooperation on studies of the X–ray background.

References

1. Alexander D.M., Aussel, H., Bauer F.E., et al., ApJ, 568, L85 (2002)
2. Alexander D.M., Bauer F.E., Brandt W.N., et al., AJ, 126, 539 (2003)
3. Aller, M. C., Richstone, D., AJ 124, 3035 (2002)
4. Appenzeller, I., Thiering, I., Zickgraf, F.-J., et al., A&A (Suppl.) 364, 443 (1998)
5. Barger A. J., Cowie L. L., Mushotzky R. F., Richards, E. A., AJ 121, 662 (2001a)
6. Barger A J, Cowie L L, Bautz M W, Brandt W N, Garmire G P, et al., AJ, **122**, 2177 (2001b)
7. Barger A.J., Cowie L.L., Capak P., et al., AJ, 126, 632 (2003)
8. Bauer F.E., Alexander D.M., Brandt W.N., et al., AJ in press, astro-ph/0408001 (2004)
9. Bower R. G., Hasinger, G., Castander, F. J. et al., MNRAS 281, 59 (1996)
10. Brandt W. N., Alexander, D. M., Hornschemeier, A. E., Garmire, G. P., Schneider, D. P., et al., AJ 122, 2810 (2001)
11. Brandt, W.N., Vignali C., Lehmer B.D., et al., this volume (2005)
12. Brandt, W. N., Hasinger, G., ARAA in press (2005)
13. Chokshi, A., Turner, E. L., MNRAS 259, 421 (1992)
14. Croom, S. M., Smith, R. J., Boyle, B. J., Shanks, T., Miller, L., et al., MNRAS 349, 1397 (2004)
15. De Luca, A., Molendi, S., A&A 419, 837
16. Duschl, W.J., Strittmatter, P.A., in Active Galactic Nuclei: from Central Engine to Host Galaxy Abstract Book, meeting held in Meudon, France, July 23-27, 2002, Eds.: S. Collin, F. Combes and I. Shlosman. To be published in ASP Conference Series, p. 76 (2002)
17. Elvis, M., Risaliti, G., & Zamorani, G., ApJ 565, L75 (2002)
18. Fabian, A. C., Iwasawa, K., MNRAS 303, 34 (1999)
19. Fadda, D., Flores, H., Hasinger, G., et al., A&A 383, 838 (2002)
20. Fan, X., Strauss, M. A., Schneider, D. P., Gunn, J. E., Lupton, R. H., et al., AJ 121, 54 (2001)
21. Ferrarese, L., Merritt, D., ApJ 539, L9 (2000)
22. Fiore F., Brusa M., Cocchia F., et al., A&A 409, 79 (2003)
23. Franceschini, A., Hasinger, G., Miyaji, T., Malquori, D., MNRAS 310, L15 (1999)
24. Franceschini A., Braito V. & Fadda D., MNRAS, 335, L51 (2002)
25. Gebhardt, K., Bender, R., Bower, G., Dressler, A., Faber S. M., et al., ApJ 539, L13 (2000)
26. Giacconi R., Rosati P., Tozzi P., et al., ApJ, 551, 624 (2001)
27. Giacconi, R., Zirm, A., Wang, J.X., et al., ApJS, 139, 369 (2002)
28. Gilli, R., Cimatti, A., Daddi, E., et al., ApJ 592, 721 (2003)
29. Gioia, I., Henry, J.P., Mullis, C.R., et al., ApJS 149, 29 (2003)
30. Haehnelt, M. G., Kauffmann, G., in *Black Holes in Binaries and Galactic Nuclei*, ed. L. Kaper, E. P. J. van den Heuvel, & P. A. Woudt, p.364 (Berlin: Springer) (2001)

31. Hasinger G., Burg R., Giacconi R., et al., A&A 275, 1 (1993)
32. Hasinger G., Burg R., Giacconi R., et al., A&A 329, 482 (1998)
33. Hasinger G., Altieri B., Arnaud M., et al., A&A 365, 45 (2001)
34. Hasinger, G., Miyaji, T., Schmidt, M., A&A submitted (2005)
35. Hornschemeier A.E., Brandt W.N., Garmire G.P., et al., ApJ 541, 49 (2000)
36. Hornschemeier A.E., Bauer F.E., Alexander D.M., et al., AJ 126, 575 (2003)
37. Kauffmann, G. & Haehnelt, M., MNRAS 311, 576 (2000)
38. Kormendy, J., Gebhardt, K., *AIP conference proceedings* 586, 363 (2001)
39. Lehmann I., Hasinger G., Schmidt M., et al., A&A 354, 35 (2000)
40. Lehmann I., Hasinger G., Schmidt M., et al., A&A 371, 833 (2001)
41. Madau, P., Pozzetti, L., Dickinson, M., ApJ 498, 106 (1998)
42. Mainieri V., Bergeron J., Rosati P., et al., A&A 393, 425 (2002)
43. Mainieri V., Rosati P., Tozzi, P., et al., A&A submitted (2004)
44. Marconi, A., Hunt, L. K. ApJ 589, L21 (2003)
45. Marconi, A., Risaliti, G., Gilli, R., Hunt, L. K., Maiolino, R., Salvati, M., MNRAS 351, 169 (2004)
46. Marshall, F. E., Boldt, E. A., Holt, S. S., et al., ApJ 235, 4 (1980)
47. Mason K. O., Carrera, F. J., Hasinger, G., et al., MNRAS 311, 456 (2000)
48. McHardy I.M., Jones, L. R., Merrifield, M. R., et al., MNRAS, 295, 641 (1998)
49. Merloni, A., MNRAS 353, 1035 (2004)
50. Miyaji, T., Hasinger G., Schmidt M., A&A 353, 25 (2000)
51. Miyaji, T., Hasinger, G., Schmidt, M., A&A 369, 49 (2001)
52. Moran, E. C., Filippenko, A. V. & Chornock, R., ApJ 579, L71 (2002)
53. Moretti, A., Campana, S., Lazzati, D., et al., ApJ 588, 696 (2003)
54. Mullis, C. R., Henry, J. P., Gioia, I. M., et al., ApJ submitted (astro-ph/0408304) (2004)
55. Mushotzky, R. F., Cowie, L. L., Barger, A. J., Arnaud, K. A., Nature 404, 459 (2000)
56. Norman, C., Ptak, A., Hornschemeier, A., et al., ApJ 607, 721 (2004)
57. Revnivtsev, M., Gilfanov, M., Sunyaev, R., et al., A&A 411, 329 (2003)
58. Rosati P., Tozzi P., Giacconi R., et al., ApJ 566, 667 (2002)
59. Salvato, M., Dissertation, Potsdam University (2002)
60. Schmidt, M., Schneider, D. P., Gunn, J. E., AJ 110, 68 (1995)
61. Schmidt, M., Hasinger, G., Gunn, J. E., et al., A&A 329, 495 (1998)
62. Schwope A., Hasinger, G., Lehmann, I., et al., AN, 321, 1 (2000)
63. Sołtan, A., MNRAS 200, 115 (1982)
64. Streblyanska, A., Hasinger, G., Finoguenov, A. et al., A&A in press (2005)
65. Szokoly G., Bergeron J., Hasinger G., et al., ApJS in press (astro-ph/0312324) (2004)
66. Thorne, K. S., ApJ 191, 507 (1974)
67. Tozzi, P., Rosati, P., Nonino, M., et al., ApJ 562, 42 (2001)
68. Ueda, Y., Akiyama, M., Ohta, K., Miyaji, T., ApJ 598, 886 (2003)
69. Vignali C., Brandt W.N., Schneider D.P., AJ 125, 433 (2003)
70. Worsley, M., Fabian, A.C., Mateos, S., et al., MNRAS 352, L28 (2004)
71. Wyithe, J.S.B., Loeb, A., ApJ 595, 614 (2003)
72. Yang, Y., Mushotzky, R. F., Barger, A. J., et al., ApJ 585, L85 (2003)
73. Yu, Q., Tremaine, S., MNRAS 335, 965 (2002)
74. Zamorani, G., et al. A&A, 346, 731 (1999)
75. Zheng W., Mikles, V. J., Mainieri, V., et al., ApJ in press, astro-ph/0406482 (2004)

GOODS Discovery of a Significant Population of Obscured AGN

C. M. Urry and E. Treister

Yale Center for Astronomy and Astrophysics, Yale University, P.O. Box 208121, New Haven CT 06520-8121, USA

Abstract. We analysed the optical and infrared properties of X-ray sources in the Great Observatories Origins Deep Survey (GOODS), a deep, multiwavelength survey covering 0.1 square degrees in two fields. The HST ACS data[1] are well explained by a unified AGN scheme that postulates roughly 3 times as many obscured as unobscured AGN, as are the spectroscopic and photometric redshift distributions once selection effects are considered. Our model predicts infrared number counts of AGN that agree well with the preliminary Spitzer data, confirming that large numbers of obscured AGN are present in the early Universe ($z > 1$).

1 Why There Might be Obscured AGN at High Redshift

Luminous Active Galactic Nuclei (AGN) have been readily found throughout the Universe, primarily in surveys at radio, optical, ultraviolet, and X-ray wavelengths. These AGN (often called quasars) are ultimately powered by gravity, as matter from the host galaxy accretes onto a central supermassive black hole. The prevalence of AGN at redshifts $z \sim 2-3$ indicates that that is the epoch of greatest black hole growth. It is also an epoch of strong star formation in young galaxies, one of several arguments that the growth of supermassive black holes must be closely tied to the formation of galaxies. Understanding the co-evolution of galaxies and black holes requires knowing the accretion history of supermassive black holes, via an accurate census of black hole demographics: how many there are, where they are, and what their masses are.

Although many thousands of AGN have been catalogued, most recently in the Sloan Digital Sky Survey (e.g., [25,2]), the demographics of supermassive black holes has proved a surprisingly elusive goal. Very few "type 2 quasars"[2] have been found (e.g., [24,28,9]). Of course, UV-excess or optical emission-line surveys would not have found most obscured AGN, nor would soft X-ray surveys such as the ROSAT All-Sky [33] or WGA [27] surveys. Instead, one needs to look

[1] Based on observations obtained with the NASA/ESA Hubble Space Telescope, which is operated by the Association of Universities for Research in Astronomy (AURA), Inc., under NASA contract NAS5-26555.

[2] "Type 2 quasars" are the luminous analogs of local Seyfert 2 galaxies, i.e., AGN lacking broad optical emission lines. According to the unification hypothesis for AGN, the central continuum and broad line region in type 2 AGN are obscured by high column densities of gas and dust ($N_H > 10^{22}$ cm^{-2}) along the line of sight.

ESO Symposia: Growing Black Holes, pp. 432–440, 2005.

at hard X-rays, where absorption is a smaller effect, or in the far-infrared, where the absorbed energy is re-radiated.

There are three good reasons to expect many supermassive black holes to be hidden behind a thick screen of gas and dust. First, local AGN conform well to the unification scenario, in which roughly 3/4 of all AGN are at least partly hidden from a direct line-of-sight [3]. Second, the 2–40 keV spectrum of the X-ray background is very hard, much harder than the typical spectrum of an unobscured AGN [22], yet high resolution X-ray imaging makes clear that the "background" is in fact summed emission from individual AGN [13]. As X-ray astronomers have understood for nearly two decades, this means most AGN are absorbed by column densities in excess of 10^{22} atoms/cm^2 [26,20,7,16]. Recent papers ([8,35,9]; see also Fabian, this volume) have argued that to explain the $\sim$ 30 keV peak in the energy density of the X-ray background requires a substantial contribution from Compton-thick AGN (with obscuring column densities $> 10^{24}$ cm^{-2}). Third, in the young Universe, where forming galaxies are often dusty and reddened, obscuration of the central AGN is even more likely. Thus, at traditional survey wavelengths, the strong line and nonthermal continuum emission by which AGN are selected and identified may be completely invisible.

Our strong reliance on optical identification has led many to argue that luminous obscured AGN, few of which have been found at high redshift, do not exist, and the obscuring material must be blown away in higher luminosity sources. While this possibility cannot be ruled out, it is certainly premature to explain the absence of obscured AGN from surveys that were remarkably insensitive to such objects.

2 Searching for Obscured AGN in GOODS

A strong motivation for the Great Observatories Origins Deep Survey (GOODS) was the discovery of obscured AGN. GOODS consists of deep imaging in the far infrared with the Spitzer Space Telescope [10] and in the optical with the Hubble Space Telescope [15] on the footprints of the two deepest Chandra fields [14,5,1]. The total area is roughly 60 times larger than the original Hubble Deep Field [34] and nearly as deep in the optical. The Great Observatories data were augmented with ground-based imaging and spectroscopy.[3] More than 85% of the GOODS X-ray sources are AGN, with luminosities $L_X > 10^{42}$ ergs/s; to avoid confusion with starburst galaxies, we limit our sample to X-ray sources above this luminosity threshold.

With extensive coverage over five decades in energy from 24 μm to 8 keV, the GOODS survey is well suited to finding a high-redshift population of obscured AGN. A complementary approach, given the relatively low surface density of AGN compared to normal galaxies, is to target higher luminosity AGN over a wider area of the sky, an approach followed by the ChaMP [17], CYDER [6], and

[3] GOODS observations are summarized at http://www.stsci.edu/science/goods/.

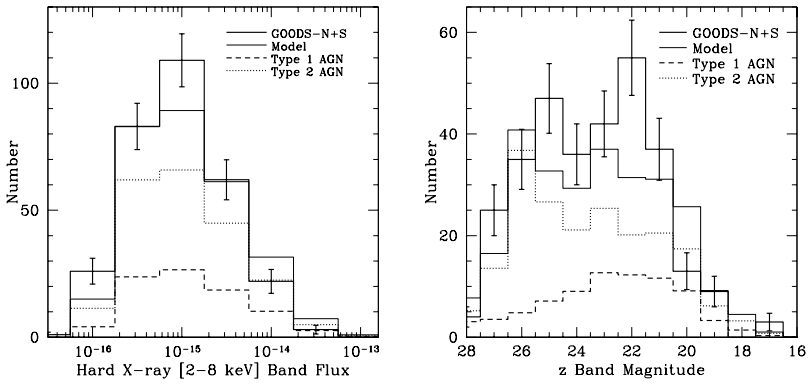

Fig. 1. X-ray fluxes and z-band magnitudes of GOODS AGN. *(Left)* Hard X-ray flux distribution for X-ray sources in the combined GOODS-North and -South fields (*heavy solid line*), compared to number counts calculated from a simple unification model (*light solid line*). Contributions from unobscured (*dashed line*) and obscured (*dotted line*) AGN are shown separately; these follow similar distributions because hard X-rays are not strongly affected by absorption. *(Right)* Distribution of observed z-band magnitudes for GOODS-North and -South X-ray sources (*heavy solid line*), compared to model distribution (*light solid line*). Obscured AGN (*dotted line*) dominate at faint magnitudes, where only the host galaxy contributes to the optical light, while bright samples consist both unobscured (*dashed line*) and obscured AGN.

HELLAS2XMM [12] surveys, among others. Here we describe the AGN detected in the X-ray and optical in the GOODS North and South fields, which represent an order of magnitude more objects than in most previous works.

Most studies of black hole demographics begin with the AGN content of a given survey, correcting where possible for selection biases to infer the underlying population. If selection effects are strong, however, one ends up making large extrapolations using little information. We therefore took a different approach: we asked, if there is a substantial population of obscured AGN, what would be seen in a deep multiwavelength survey like GOODS? This work is presented by [30]; here we briefly describe our assumptions and results.

We start with a very simple unification scheme for AGN, in which a central engine – well understood from studies of unobscured AGN – is surrounded by a dusty torus[4] that absorbs optical through soft X radiation and re-radiates the absorbed energy as thermal infrared emission. We combine well-measured spectra of unobscured AGN with plausible reddening and absorption laws, and with the dust emission models of [11] and [23], to create a grid of spectra appropriate to increasing absorbing column densities along the line of sight to the AGN. The

[4] Note that the geometry need not be a torus; we use this geometry simply to derive the distribution of absorbing column densities expected from random orientations. The resulting N_H distribution matches well the observed one, with the proviso that Compton-thick sources are missing, but so would many other geometries.

torus geometry was adjusted so that three-quarters of all AGN are obscured (i.e., have $N_H > 10^{22}$ cm^{-2}) and so the mid-plane column density is 10^{24} cm^{-2} (even the Chandra deep surveys are not sensitive to objects with higher column densities). We further assumed this geometry was independent of redshift and luminosity – the simplest assumption, and one that, frankly, we expected to prove wrong. We added an L_* host galaxy spectrum to each AGN template spectrum. Finally, we assumed the most recent, hard-X-ray-selected luminosity function and luminosity-dependent density evolution given by [9].

As shown in Figure 1, this very simple model explains very well the X-ray and optical counts in the GOODS fields. That it explains the X-ray counts is not too surprising since we start with a hard X-ray luminosity function and evolution derived from these fields, among others. For the optical, however, the agreement indicates that faint optical sources are primarily obscured AGN. Indeed, these tend to have red colors and hard X-ray spectra, as expected of obscured AGN.

These results mean that the GOODS HST data agree well with a population of obscured AGN extending from $z = 0$ to well beyond $z > 1$. Specifically, the X-ray and optical properties of GOODS AGN are fully consistent with a very simple unification picture, requiring no modification with either redshift or AGN luminosity. The implication is that some X-ray-emitting AGN are missed in the Chandra Deep Field samples, and others lack optical spectroscopic identifications. Since the best 8- or 10-m class telescopes have an effective limit at $R < 24$ mag, many obscured AGN will lack spectroscopic identification.

The redshift distribution is a critical point. The best population synthesis models for the X-ray background prior to the new Chandra and XMM deep fields [16] incorporated a high-redshift population of obscured AGN that evolves similarly to the unobscured AGN, and hence predicted a redshift distribution peaking at $z \sim 1.5$. Yet observed redshift distributions from the Chandra Deep Fields and the Lockman hole peak at much lower redshifts (see e.g., [18,4]). This has been taken as evidence of a fatal flaw in the population synthesis models.

We find the discrepancy does not imply any lack of obscured quasars at high redshift. Rather, it results from a combination of two factors: (1) the luminosity-dependent density evolution now measured for X-ray AGN, which was not used in the [16] models and which increases the fraction of AGN at lower luminosity and lower redshift, and more importantly, (2) the implicit spectroscopic limit for X-ray samples, which preferentially excludes the faint counterparts of high-redshift, obscured AGN.

The latter point is illustrated in Figure 2, which shows the redshift distribution for GOODS AGN. The upper dashed line shows the predicted redshift distribution for our unified model, which still peaks above a redshift of 1, much like the earlier population synthesis models. If we impose a spectroscopic limit of $R = 24$ mag, however, we obtain the lower dashed line, which agrees well with the observed spectroscopic redshift distribution. Note that the photometric redshifts are indeed shifted to higher redshifts compared to the spectroscopic redshifts, although they too miss the very faintest, highest redshift obscured AGN.

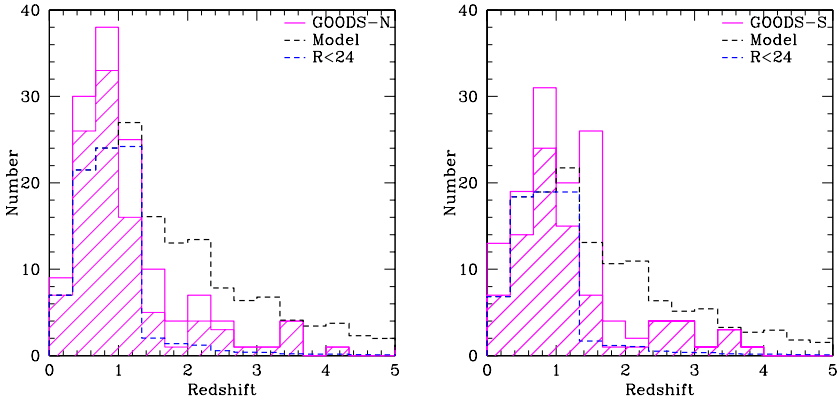

Fig. 2. Observed redshift distributions *(heavy solid line)* for AGN in the GOODS-South *(left panel)* and -North *(right panel)* fields, including both spectroscopic *(hatched area*; [4,29]) and photometric redshifts [4,21]; these are 100% complete in the GOODS-S field and 75% complete in the GOODS-N region. The predicted distribution (*upper dashed line*) peaks above a redshift of 1, similar to earlier population synthesis models and in apparent disagreement with the observed one. However, if we cut the sample at $R < 24$ mag (*lower dashed line*), as appropriate for a sample with optical spectra, the model and observed distributions agree well. The data are therefore consistent with a significant high-redshift population of obscured AGN which are missed in spectroscopic samples due to their faint optical magnitudes.

3 Spitzer Data and the Far-Infrared Properties of AGN

According to the unification scheme, dust and gas absorbs much of the luminous optical through X-ray AGN emission, and is thus heated. The absorbed energy is re-radiated as thermal emission, which should be readily visible in the far-infrared. A key element of the GOODS project is very deep imaging with the Spitzer observatory, in the IRAC bands from 3.6 to 8.4 microns and the MIPS 24-micron band. These data will provide a strong test of our unified model.

We used our simple unification model to predict the far-infrared source counts, in each Spitzer band, for the appropriate GOODS flux limits [30]. As of spring 2004, some IRAC data in the GOODS-S field were already in hand. We compared preliminary photometry of the AGN to our source count prediction. The results are shown in Figure 3 (van Duyne et al., in prep.), along with predictions for the 24-micron source counts. (The first GOODS MIPS data will be obtained in summer/fall 2004.)

Certainly these early data require closer inspection, and the model awaits a stronger test from the full multiwavelength Spitzer data set. The pending data will allow us to verify whether large numbers of obscured AGN are indeed present in the early Universe, and will also be extremely important for refining the AGN model, specifically the covering factor, dust geometry, and evolution thereof. The 24-micron images are particularly powerful, since the AGN emission

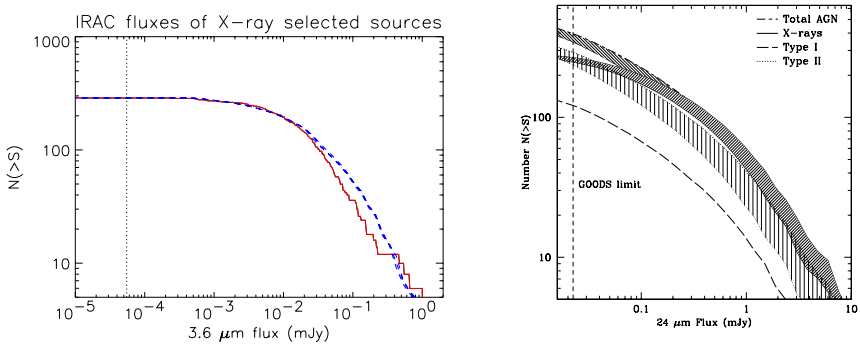

Fig. 3. Predicted Spitzer counts for the simple unified model. *(Left)* The model prediction at 3.6-μm *(dashed line)* agrees well with the preliminary Spitzer counts of GOODS-S X-ray sources *(solid histogram)*, in both normalization and shape. *(Right)* Model prediction at 24 μm for total source counts, (*upper dot-dash line*) and for AGN brighter than the X-ray flux limit of GOODS (*solid line*); the difference represents the AGN missed by Chandra. Dotted and dashed lines represent the obscured and unobscured AGN, respectively; the former dominate by the specified factor 3:1.

is most isotropic at the longest infrared wavelengths. Obscured AGN should be very bright far-infrared sources; those that are missed even by X-ray observations probably look like ultraluminous infrared galaxies.

We have looked at the spectral energy distributions of the GOODS AGN, including the available Spitzer data. Indeed, the hard X-ray sources with faint, red optical counterparts are extra-luminous in the Spitzer bands. Two example spectral energy distributions are shown in Figure 4 (van Duyne et al., in prep.). Both cases look just like a normal galaxies at optical wavelengths, but are revealed to be AGN by the luminous X-ray emission. They are clearly obscured by virtue of their faint optical magnitudes, hard X-ray spectra, and bright infrared fluxes.

4 Summary and Conclusions

The GOODS multiwavelength survey supports the idea of a significant population of obscured AGN persisting to high redshift. From a strictly observational viewpoint, we cannot rule out this population, and indeed, see every evidence for its existence. In a subsequent paper [31] we explain the apparent decline in the ratio of obscured to unobscured AGN with redshift or luminosity, which is seen in several X-ray-selected AGN samples ([19]; U03), by the same selection effects against Compton thick and/or optically faint sources.

The data are consistent with a simple unified model of a luminous AGN nucleus obscured along some lines of sight by dust and gas. Our work is not strongly

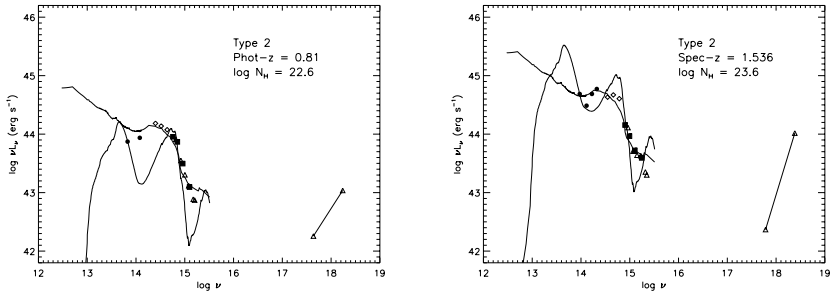

Fig. 4. Spectral energy distributions of two GOODS AGN, including HST ACS data *(squares)*, Chandra X-ray data *(triangles, straight lines)*, and Spitzer data *(filled circles)*. Also shown are the best-fit Seyfert 2 galaxy templates, both observed *(light solid line)* and model spectra *(heavy solid line)*.

sensitive to the geometry, and other configurations of dust are equally possible as long as they predict a similar distribution of absorbing column densities. We are also not sensitive to the numbers of Compton-thick AGN, a population that will be probed with future X-ray missions sensitive in the energy range 10-100 keV. In any case, we conclude that at least 3/4 of all supermassive black holes are obscured by column densities of at least $N_H \sim 10^{22}$ cm^{-2}.

The unified model implies that half the obscured AGN are not detected in X-ray fields at the Chandra Deep Field depths. They should be clearly visible in the Spitzer data, although separating heavily obscured AGN from very luminous starbursts will not be simple. Upcoming Spitzer data, along with the integral constraint from the X-ray "background" spectrum, will better constrain the geometry and other properties of the obscuring material.

Individual spectral energy distributions of the AGN will also constrain the dust geometry, and perhaps the contribution from any starburst component. Bolometric corrections in the far-infrared are likely to be significant, and affect estimates of the mass accretion rate and thus the growth rate of supermassive black holes. Note that observed spectral energy distributions never represent the actual output from the AGN engine: the luminosity of unobscured AGN is overestimated (since the optical through soft X-ray emission is not isotropic), while obscured AGN appear under-luminous relative to their intrinsic power. Bolometric corrections can be calculated from models, such as those considered here, but can not be derived empirically for any highly anisotropic source. This is critical for understanding the energetics and structures of AGN.

One strong conclusion from our work is that one should look for obscured black holes where they can be easily found, namely in the far-infrared and hard X-ray. Any substantial and widespread obscuration has important implications for the cosmic accretion history of black holes, and for the average efficiency of converting gravitational potential energy to radiation.

Acknowledgements – This work, which was supported in part by NASA grant HST-GO-09425.13-A, owes a great deal to our colleagues in the GOODS project, particularly Yale graduate student Jeff van Duyne and the co-authors of the [30] paper.

References

1. Alexander, D. M., Bauer, F. E., Brandt, W. N., Schneider, D. P., Hornschemeier, A. E., Vignali, C., Barger, A. J., Broos, P. S., Cowie, L. L., Garmire, G. P., Townsley, L. K., Bautz, M. W., Chartas, G., & Sargent, W. L. W.: AJ, 126, 539 (2003)
2. Anderson, S. F., et al.: AJ, 126, 2209 (2003)
3. Antonucci, R.: ARA&A, 31, 473 (1993)
4. Barger, A. J., Cowie, L. L., Capak, P., Alexander, D. M., Bauer, F. E., Fernandez, E., Brandt, W. N., Garmire, G. P., & Hornschemeier, A. E.: AJ, 126, 632 (2003)
5. Brandt, W. N., Alexander, D. M., Hornschemeier, A. E., Garmire, G. P., Schneider, D. P., Barger, A. J., Bauer, F. E., Broos, P. S., Cowie, L. L., Townsley, L. K., Burrows, D. N., Chartas, G., Feigelson, E. D., Griffiths, R. E., Nousek, J. A., & Sargent, W. L. W.: AJ, 122, 2810 (2001)
6. Castander, F. J., Treister, E., Maza, J., Coppi, P. S., Maccarone, T. J., Zepf, S. E., Guzmán, R., & Ruiz, M. T.: Astronomische Nachrichten, 324, 40 (2003)
7. Comastri, A., Setti, G., Zamorani, G. & Hasinger, G. 1995, A&A, 296, 1
8. Comastri, A. & the HELLAS2XMM team: Societa Astronomica Italiana Memorie Supplement, 3, 179 (2003)
9. Dawson, S., McCrady, N., Stern, D., Eckart, M. E., Spinrad, H., Liu, M. C., & Graham, J. R.:AJ, 125, 1236 (2003)
10. Dickinson, M. & Giavalisco, M.: in proceedings of the ESO/USM Workshop "The Mass of Galaxies at Low and High Redshift" (Venice, Italy, October 2001), eds. R. Bender and A. Renzini. astro-ph/0204213 (2002)
11. Elitzur, M., Nenkova, M., & Ivezic, Z.: Invited review at "The Neutral ISM in Starburst Galaxies", Marstrand, Sweden, June 2003, astro-ph/0309040 (2003)
12. Fiore, F., et al.: A&A, 409, 79 (2003)
13. Giacconi, R., Bechtold, J., Branduardi, G., Forman, W., Henry, J. P., Jones, C., Kellogg, E., van der Laan, H., Liller, W., Marshall, H., Murray, S. S., Pye, J., Schreier, E., Sargent, W. L. W., Seward, F., & Tananbaum, H.: ApJ, 234, L1 (1979)
14. Giacconi, R., Rosati, P., Tozzi, P., Nonino, M., Hasinger, G., Norman, C., Bergeron, J., Borgani, S., Gilli, R., Gilmozzi, R., & Zheng, W.: ApJ, 551, 624 (2001)
15. Giavalisco, M. et al. ApJ, 600, L93 (2004)
16. Gilli, R., Salvati, M., & Hasinger, G.: A&A, 366, 407 (2001)
17. Green, P. J., et al.: ApJS, 150, 43 (2004)
18. Hasinger, G.: in New Visions of the X-ray Universe in the XMM-Newton and Chandra Era, Ed. F. Jansen (ESTEC: ESA SP-488), XX (astro-ph/0202430) (2002)
19. Hasinger, G.: Nucl. Phys. Proc. Suppl., 132, 86 (2004)
20. Madau, P., Ghisellini, G., & Fabian, A. C.: MNRAS, 270, L17 (1994)
21. Mobasher, B. et al.: ApJ, 600, L167 (2004)
22. Mushotzky, R. F., Done, C., & Pounds, K. A. 1993, ARA&A, 31, 717 (1993)
23. Nenkova, M., Ivezić, Ž., & Elitzur, M.: ApJ, 570, L9 (2002)

24. Norman, C., Hasinger, G., Giacconi, R., Gilli, R., Kewley, L., Nonino, M., Rosati, P., Szokoly, G., Tozzi, P., Wang, J., Zheng, W., Zirm, A., Bergeron, J., Gilmozzi, R., Grogin, N., Koekemoer, A., & Schreier, E.: ApJ, 571, 218 (2002)
25. Richards, G. T., et al.: AJ, 123, 2945 (2002)
26. Setti, G., Woltjer, L.: A&A, 224L, 21 (1989)
27. Singh, K. P., Barrett, P., White, N. E., Giommi, P., & Angelini, L.: ApJ, 455, 456 (1995)
28. Stern, D., Moran, E. C., Coil, A. L., Connolly, A., Davis, M., Dawson, S., Dey, A., Eisenhardt, P., Elston, R., Graham, J. R., Harrison, F., Helfand, D. J., Holden, B., Mao, P., Rosati, P., Spinrad, H., Stanford, S. A., Tozzi, P., & Wu, K. L.: ApJ, 568, 71 (2002)
29. Szokoly, G. et al. 2004, ApJS in press, astro-ph/0312324 (2004)
30. Treister, E. et al. 2004a, ApJ in press, arXiv:astro-ph/0408099. (2004a)
31. Treister, E. et al. 2004b, ApJ submitted. (2004b)
32. Ueda, Y., Akiyama, M., Ohta, K., & Miyaji, T.: ApJ, 598, 886 (U03) (2003)
33. Voges, W. et al.: A&A, 349, 389 (1999)
34. Williams, R. E., et al.: AJ, 112, 1335 (1996)
35. Worsley, M. A., Fabian, A. C., Barcons, X., Mateos, S., Hasinger, G., & Brunner, H.: MNRAS, 352, L28 (2004)

Obscured Accreting Black Holes at High Redshift

A. Comastri[1], F. Fiore[2], C. Vignali[3], M. Brusa[4], and F. Civano[3,1]

[1] INAF–Osservatorio Astronomico di Bologna, via Ranzani 1, I–40127 Bologna, Italy
[2] INAF–Osservatorio Astronomico di Roma, via Frascati 33, I–00040 Monteporzio (RM), Italy
[3] Dipartimento di Astronomia, Università di Bologna, via Ranzani 1, I–40127 Bologna, Italy
[4] Max Planck Institut für Extraterrestrische Physik (MPE), Giessenbachstrasse 1, D–85748 Garching, Germany

Abstract. A significant fraction of the accreting black holes powering high redshift AGN are obscured by large columns of dust and gas. For this reason, luminous type 2 quasars can be efficiently discovered combining hard X–ray and near–infrared observations. We will briefly discuss the most recent results.

1 Introduction

The space density of luminous quasars in the distant Universe represents a key observational ingredient to understand the formation and evolution of supermassive black holes (SMBHs). The hard X–ray energy range (above 2 keV) is well suited for this purpose as it provides an unbiased view of the obscured accretion power which is responsible for the majority of the SMBH energy output recorded in the X–ray background (XRB) spectrum.

The capabilities of both *Chandra* and XMM–*Newton* in performing sensitive X–ray surveys have been continuously exploited in the last four years. As a result, large samples of X–ray sources spanning a wide range of fluxes (from a few 10^{-13} down to about 10^{-16} erg cm^{-2} s^{-1}) are available for reliable statistical studies on the extragalactic X–ray source population. Despite extensive campaigns of spectroscopic follow–up observations with the largest, ground–based telescopes, the X–ray source classification remains challenging. The most important reason is that the optical counterparts of many X–ray sources are too faint even for 8–10 m class telescopes (Fig. 1). The spectroscopic completeness of the deepest *Chandra* surveys (CDFS and CDFN) is of the order of 50–70 %. Deep multiband photometry is usually employed to estimate redshifts and, over restricted portions of the sky, a much higher completeness level could be achieved.

A detailed discussion on the optical identification breakdown is beyond the purposes of this paper and can be found elsewhere ([2], [18], [9]). The general picture emerging from the spectroscopic observations can be summarized as follow:

• Unobscured broad–line AGN are found up to redshift 5 and constitute the dominant population at relatively bright X–ray fluxes ($> 10^{-14}$ erg cm^{-2} s^{-1}) [3]

ESO Symposia: Growing Black Holes, pp. 441–446, 2005.

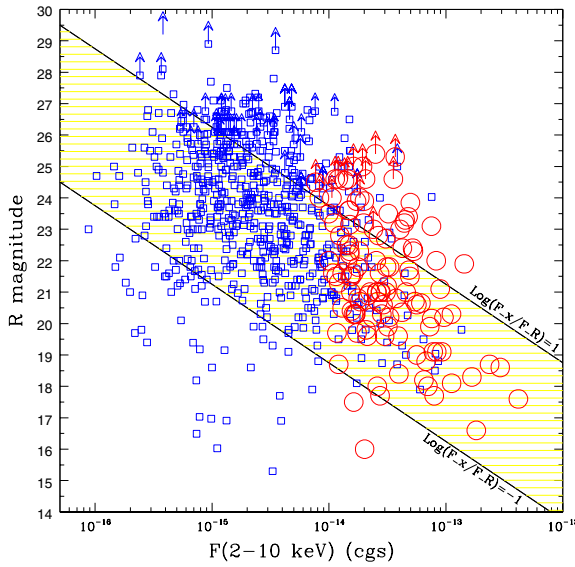

Fig. 1. The 2–10 keV flux vs. the R–band magnitude for X–ray selected sources in the Chandra (small squares) and HELLAS2XMM (large open circles)

• The space density of obscured AGN increases towards fainter fluxes. Clear signatures of X–ray and/or optical obscuration are typically detected (though some mismatch between optical and X–ray absorbing properties is present). The luminosity and redshift distribution of obscured sources is skewed toward lower values and most of them are classified as Seyfert galaxies ($L_X < 10^{44}$ erg s^{-1} and $z < 1$–1.5) rather than quasars.

• The discovery of relatively high X–ray luminosity AGN hosted in the nuclei of optically normal galaxies. Whether they are heavily absorbed Seyfert galaxies, low–luminosity AGN whose emission is diluted by the host galaxy starlight or something more exotic is still subject of debate [5].

The most important findings emerging from the identification process concern the redshift and absorption distribution of X–ray selected sources. The former is peaked at lower redshifts ($z \simeq 1$) than expected on the basis of population synthesis models for the XRB [11]. The latter seems to indicate a lack of obscured, luminous sources with respect to model predictions.

On the one hand, the results described above favour a late formation of the XRB (i.e. [17]) and call for a major revision of the AGN synthesis models which are based on the unified scheme. On the other hand, it has been suggested [19] that selection effects against the identification of obscured AGN combined with the small solid angle covered by deep surveys prevent from a reliable comparison with model predictions.

2 Large Area Surveys

A sizable number of hard X–ray surveys have been performed with both XMM–*Newton* and *Chandra* over large area (of the order of a few square degrees). The ultimate goal of these efforts is to provide a statistically robust estimate of the luminosity function and cosmological evolution of obscured accreting black holes hopefully free from the selection effects described above. Though differing in several details, the observing strategy of the various large–area surveys is designed to maximize the trade off between area and depth and thus X–ray satellite observing time (for an updated list of recent X–ray surveys see [4]). Wide–area surveys efficiently target objects in the range of fluxes around the knee of the source counts ($\log F_X = -14 \pm 1$ erg cm^{-2} s^{-1}) and thus properly sample the sources which contribute mostly to the XRB. An important benefit is that the average magnitude of the optical counterparts is relatively bright and the follow–up spectroscopic identification is within the capabilities of available telescopes. On the other hand, the large number of X–ray sources discovered in many different non–contiguous pointings makes the follow–up identification extremely time consuming.

Targets with peculiar and/or extreme properties are therefore the subject of detailed follow–up multiwavelength observations. The results of a vigorous program of spectroscopic observations with FORS@VLT [9], deep near–infrared photometry with ISAAC@VLT [14], and X–ray spectroscopy [16], strongly indicate that sources with high X–ray to optical flux ratio (high X/O) in the `HELLAS2XMM` survey [1] are obscured AGN at moderate to high redshifts. The derived X–ray luminosities and the narrow optical lines of the brightest targets allow us to classify them as type 2 quasars at z=0.7–2. A similar range of redshifts is implied using the R–K colour of the host galaxies of fainter X–ray sources [14].

Thanks to the identification of about 50% of the high X/O sources in the `HELLAS2XMM` survey, it has been possible to discover a linear correlation between the X/O ratio and 2–10 keV luminosity [9], namely: $\log L_{2-10} = log f_X/f_{opt} + 43.05$. The correlation holds for optically obscured sources and has been tested and calibrated combining the optical and X–ray data of the `HELLAS2XMM` survey with well defined subsamples of identified sources in the deep *Chandra* fields at fluxes larger than $3{\times}10^{-15}$ erg cm^{-2} s^{-1}.

Though characterized by a not–negligible dispersion (about 0.4 dex), this relation can be used to compute X–ray luminosities and then redshifts from the observed X/O ratio. The accuracy in the redshift estimate ("X–photo–z" [10]) is fairly good $\sigma(\Delta z/(1+z)) \simeq 0.2$.

3 The high–redshift Universe

The space density of high luminosity ($L_X > 10^{44}$ erg s^{-1}) obscured ($N_H > 10^{22}$) type 2 quasars among optically faint *Chandra* deep fields sources has been estimated by Padovani et al. (2004) [15] using the "X–photo–z" technique. In

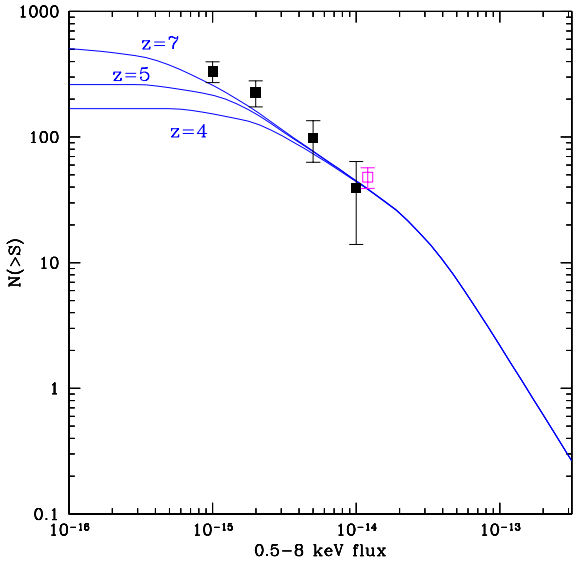

Fig. 2. The number counts of luminous [$L_X > 10^{44}$ erg s^{-1}] obscured ($N_H > 10^{22}$ cm^{-2}) quasars as estimated by Perola et al. (2004, open square), and Padovani et al. (2004, filled squares). Continuous lines represent the expected number counts from the XRB synthesis models as described in the text

order to select absorbed sources, a simple criterium based on the Hardness Ratio [HR = (H–S)/(H+S) > –0.2, where H and S is the number of counts in the 2–8 keV and 0.5–2 keV bands, respectively] is adopted. About half (31/68) of the *Chandra* sources with an hard X–ray spectrum are candidate type 2 quasars. Their number counts, computed assuming the X/O vs $L_{2-10keV}$ relation, are reported in Figure 2 along with the results obtained from the `HELLAS2XMM` survey [16].

The observed surface densities are compared with the number counts of luminous ($L_{0.5-8keV} > 10^{44}$ erg s^{-1}) obscured ($N_H > 10^{22}$ cm^{-2}) AGN predicted by XRB synthesis models [8]. The evolution of the X–ray luminosity function is parameterized by a pure luminosity law [$L(z) \propto L(z = 0) \times (1 + z)^{2.6}$] up to $z = 1.5$ and constant up to a maximum redshift z_{max}.

Model predictions are shown in Figure 2 for three different values of the maximum redshift over which the integration of the XLF is performed. At their face value the results indicate that in order to reproduce the number counts of type 2 quasars as predicted by [15], a maximum redshift as high as $z_{max} \simeq 7$ is required.

The existence of a population of very high–redshift obscured quasars hiding among the optically faint counterparts of X–ray sources has been put forward by [12]. Seven *Chandra* sources with robust detections in the X–ray band (25–

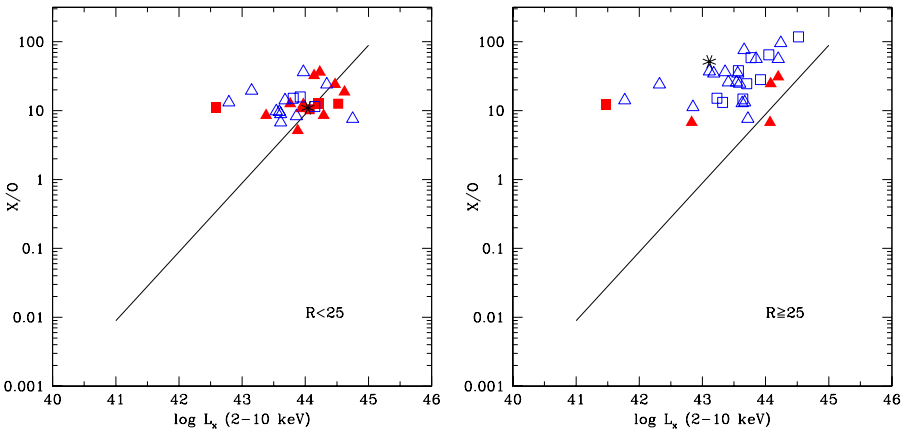

Fig. 3. The X/O ratio as a function of 2–10 keV absorption–corrected luminosity for a sample of hard X–ray selected *Chandra* sources (CDFN = squares; CDFS = triangles; spectro–z = filled symbols; photo–z = open symbols; star = redshift obtained from the iron line). *Left panel*: optically "bright" objects $R < 25$, *Right panel*: optically faint objects $R > 25$

90 counts) are not detected in deep multiband HST ACS observations. Their extreme values of the X/O ratio (EXO's) and in particular the lack of detection in the z_{850} ACS band are consistent with a redshift above 6–7 such that their Lyα emission is redshifted out of the ACS bands. However, making use of recent *Spitzer* observations in the IRAC filters (3.6–8.4 μm) and deep K$'$ data, it has been suggested [13] that their multiband photometric data are well fitted by early–type templates at redshifts 2–5, and in only one case a redshift as high as 6 is supported by SED fitting.

Given that only one spectroscopically confirmed quasar at $z > 5$ has been so far discovered in the *Chandra* deep fields [2], the possibility that even a few very high–z, presumably obscured, quasars could be hiding among high X/O and EXO's would have important consequences for the AGN evolution. However, before claiming that such a population has been indeed revealed, additional and more robust observational evidences should be provided.

The identification of type 2 quasars using the "X–photo–z" technique is based on the assumption that the X/O vs. $L_{2-10keV}$ correlation can be extrapolated beyond the magnitudes over which it has been calibrated (R< 24–25). In order to address this point, we [7] have collected redshift measurements (mainly photo–z) for all the sources in the *Chandra* deep fields with $X/O > 10$. The results are reported in Figure 3 where the sample is divided according to the optical magnitude. While relatively bright $R < 25$ sources lie, though with a substantial scatter, on the relation, optically faint objects appear to have lower luminosities than expected. Similar conclusions are reached by [3] (see their Figure 6). On the other hand, it is also important to note that at faint optical magnitudes

the probability to find by chanche a galaxy in the X–ray error box increases drammatically (i.e. up to about 0.25–0.30 for R=26 and an error circle radius of 2 arcsec, without considering source clustering). Furthermore, photo–z estimates often involve the determination of source's magnitudes in images of very different quality (e.g. space versus ground based telescopes) and, as a consequence, are affected by systematic errors.

Even if the X/O ratio appears to be an efficient selection method to search for high–z, obscured type 2 quasars [6], a reliable estimate of their number and luminosity densities must await for medium–deep, large–area hard X–ray surveys allowing to sample, with an adequate statistic, the brightest sources. For a given X/O their optical counterparts are, on average, brighter and thus within the spectroscopic capabilities of present telescopes. For extremely optically faint sources deep near–infrared photometry coupled with *Spitzer* observations would allow us to overcome the problem of chance coincidences. Significant progress are foreseen once the rich multiwavelength database of the ongoing COSMOS (2 square degrees) and ELAIS–S1 (0.5 square degrees) surveys will be exploited.

References

1. A. Baldi, S. Molendi, A. Comastri, F. Fiore, G. Matt, C. Vignali Astrophys. J. **564**, 190 (2002)
2. A.J. Barger, L.L. Cowie, P. Capak et al. Astronom. J. **126**, 632 (2003)
3. F.E. Bauer, D.M. Alexander, W.N. Brandt, D.P. Schneider, E. Treister, A.E. Hornschemeier, G.P. Garmire Astronomical J. in press, astro–ph/0408001 (2004)
4. W. N. Brandt, D.M. Alexander, F.E. Bauer, C. Vignali: In *Physics of Active Galactic Nuclei at All Scales*, eds. Alloin D., Johnson R., Lira P. (Springer-Verlag, Berlin). astro–ph/0403646 (2004)
5. M. Brusa, A. Comastri, M. Mignoli et al. A&A **409**, 65 (2003)
6. M. Brusa, A. Comastri, E. Daddi et al. A&A in press, astro–ph/0409257 (2004)
7. F. Civano, A. Comastri, M. Brusa (2005) in preparation
8. A. Comastri, G. Setti, G. Zamorani, G. Hasinger A&A **296**, 1 (1995)
9. F. Fiore, M. Brusa, F. Cocchia et al. A&A **409**, 79 (2003)
10. F. Fiore and the HELLAS2XMM team: In *Multi-wavelength AGN surveys*, Cozumel (Mexico), 8-12 December 2003, astro–ph/0406019 (2004)
11. R. Gilli, M. Salvati, G. Hasinger A&A **366**, 407 (2001)
12. A.M. Koekemoer, D.M. Alexander, F.E. Bauer, et al. Astrophy. J. **600**, L123 (2004)
13. A.M. Koekemoer (2004), these proceedings
14. M. Mignoli, L. Pozzetti, A. Comastri et al. A&A **418**, 827 (2004)
15. P. Padovani, M.G. Allen, P. Rosati, N.A. Walton A&A **424**, 545 (2004)
16. G.C. Perola, S. Puccetti, F. Fiore et al. A&A **421**, 491 (2004)
17. A.T. Steffen, A.J. Barger, P. Capak et al. Astronom. J., in press, astro–ph/0409088 (2004)
18. G.P. Szokoly, J. Bergeron, G. Hasinger et al. Astrophy. J. Supp., in press, astro–ph/0312324 (2004)
19. E. Treister, C.M. Urry, E. Chatzichristou et al. Astrophy. J., in press, astro–ph/0408099 (2004)

Local Supermassive Black Holes, Relics of Active Galactic Nuclei and the X-ray background

A. Marconi[1], G. Risaliti[1,2], R. Gilli[1], L.K. Hunt[3], R. Maiolino[1], and M. Salvati[1]

[1] INAF-Osservatorio Astrofisico di Arcetri, Largo Fermi 5, I-50125 Firenze, Italy
[2] Harvard-Smithsonian Center for Astrophysics, 60 Garden street, Cambridge, MA 02138, USA
[3] INAF-Istituto di Radioastronomia-Sez. Firenze, Largo Fermi 5, I-50125 Firenze, Italy

Abstract. We summarize a study where we test the hypothesis that local black holes (BH) are relics of AGN activity. We compare the mass function of BHs in the local universe with that expected from AGN relics, which are BHs grown entirely with mass accretion during AGN phases. The local BH mass function (BHMF) is estimated by applying the well-known correlations between BH mass, bulge luminosity and stellar velocity dispersion to galaxy luminosity and velocity functions. The density of BHs in the local universe is $\rho_{\rm BH} = 4.6^{+1.9}_{-1.4}\, h^2_{0.7} \times 10^5$ M$_\odot$ Mpc^{-3}. The relic BHMF is derived from the continuity equation with the only assumption that AGN activity is due to accretion onto massive BHs and that merging is not important. We find that the relic BHMF at $z = 0$ is generated mainly at $z < 3$. Moreover, the BH growth is anti-hierarchical in the sense that smaller BHs ($M_{\rm BH} < 10^7 M_\odot$) grow at lower redshifts ($z < 1$) with respect to more massive ones ($z \sim 1 - 3$). Unlike previous works, we find that the BHMF of AGN relics is perfectly consistent with the local BHMF indicating the local BHs were mainly grown during AGN activity. This agreement is obtained while satisfying, at the same time, the constraints imposed by the X-ray background. The comparison with the local BHMF also suggests that the merging process is not important in shaping the relic BHMF, at least at low redshifts ($z < 3$). Our analysis thus suggests the following scenario: local BHs grew during AGN phases in which accreting matter was converted into radiation with efficiencies $\varepsilon = 0.04 - 0.16$ and emitted at a fraction $\lambda = 0.1 - 1.7$ of the Eddington luminosity. The average total lifetime of these active phases ranges from $\simeq 4.5 \times 10^8$ yr for $M_{\rm BH} < 10^7 M_\odot$ to $\simeq 1.5 \times 10^8$ yr for $M_{\rm BH} > 10^9 M_\odot$.

1 Introduction

The standard paradigm for Active Galactic Nuclei is that they are powered by mass accretion onto a massive BH ($M_{\rm BH} \sim 10^6 - 10^{10}$ M$_\odot$). Combined with the observed evolution of AGN, this implies that many (if not all) nearby galaxies should host a BH in their nuclei as relic of past AGN activity. BHs are detected in ~ 40 galaxies and their mass correlates with host galaxy structural parameters like bulge luminosity/mass [8,4] and stellar velocity dispersion [4,5]. An important open question is whether local BHs are relics of AGN activity (i.e. grown entirely with mass accretion during AGN phases) or if other processes,

ESO Symposia: Growing Black Holes, pp. 447–452, 2005.

such as merging, play an important role. This can be answered by comparing the BHMF of local BHs with that expected from AGN relics [10,22]. In recent works [22,3] a discrepancy in the BHMF at high masses ($M_{\rm BH} > 10^8$ M$_\odot$) has been found: more AGN relics are expected than predicted by the local BHMF. This discrepancy can be reconciled by assuming accretion efficiencies larger than the canonically adopted value of $\varepsilon = 0.1$, i.e. $\varepsilon > 0.2$. A refinement of the analysis by [22] is also presented in [23] who find $\varepsilon > 0.1$. High efficiencies are also required from the comparison of $\rho_{\rm BH}$ derived from the X-ray Background (XRB) and from local BHs [2]. Such high efficiencies, if confirmed, would imply that most, if not all BHs, should be rapidly rotating.

In this paper we investigate the possibility that massive black holes in nearby galaxies are relics of AGN activity by comparing the local BHMF with that of AGN relics. The only assumption is that AGN activity is caused by mass accretion onto the central BH. The work is described in detail in [9] and here we focus on a few among the more critical and important issues. Similar analysis, reaching conclusions analogous to ours are presented in [12,17] and by the same authors in these proceedings.

2 The Mass Function of Local Black Holes

The mass function of local BHs can be estimated by simply convolving the existing galaxy luminosity [$\phi(L)$] or velocity functions [$\phi(\sigma)$] with the $M_{\rm BH}$-$L_{\rm bul}$ and $M_{\rm BH}$-$\sigma_\star$ relations respectively. One should apply corrections to convert from total to bulge luminosity in the first case and should take into account the intrinsic dispersion (if any) of the $M_{\rm BH}$-host galaxy relations. In Fig. 1a we verify that the $M_{\rm BH}$-$\sigma_\star$ and $M_{\rm BH}$-$L_{\rm bul}$ relations applied to the galaxy luminosity or velocity function [1,18] provide the same BHMF within the uncertainties (estimated with many Montecarlo realizations of the BHMF). Clearly, the necessary condition is that the two relations have the same intrinsic dispersion since very different BHMFs are derived when $M_{\rm BH}$-$L_{\rm bul}$ has dispersion 0.5 in $\log M_{\rm BH}$ at given $L_{\rm bul}$ and $M_{\rm BH}$-$\sigma_\star$ has 0 intrinsic dispersion. This confirms the result by [4] that all correlations $M_{\rm BH}$– host-galaxy-properties are equally good, i.e. they have similar intrinsic dispersion. In Fig. 1b we plot the estimate of the local BH mass function obtained considering galaxies from all morphological types. The density in local BHs is $\rho_{\rm BH} = 4.6(-1.4;+1.9)(h/0.7)^2 \times 10^5$ M$_\odot$ Mpc^{-3}. We have used the galaxy luminosity functions by [7,16,13] and the galaxy velocity function by [18].

Our estimate of the local BH density is a factor ~ 1.8 larger than the estimate by [22]. $\rho_{\rm BH}$ is increased by $\sim 30\%$ when taking into account an intrinsic dispersion for $M_{\rm BH}$-$L_{\rm bul}$ and $M_{\rm BH}$-$\sigma_\star$ (0.3 in $\log M_{\rm BH}$ at constant $\sigma_\star$ or $L_{\rm bul}$). $\rho_{\rm BH}$ is also increased by $\sim 50\%$ because we have used the zero points of the $M_{\rm BH}$-$L_{\rm bul}$ and $M_{\rm BH}$-$\sigma_\star$ correlations determined by [4]. These are a factor 1.5 larger than those used by [22] (see [20]) because they were determined by considering only secure BH detections, where the BH sphere of influence is resolved by the observations. Fig. 8 of [6] show that measurements obtained with data either resolving

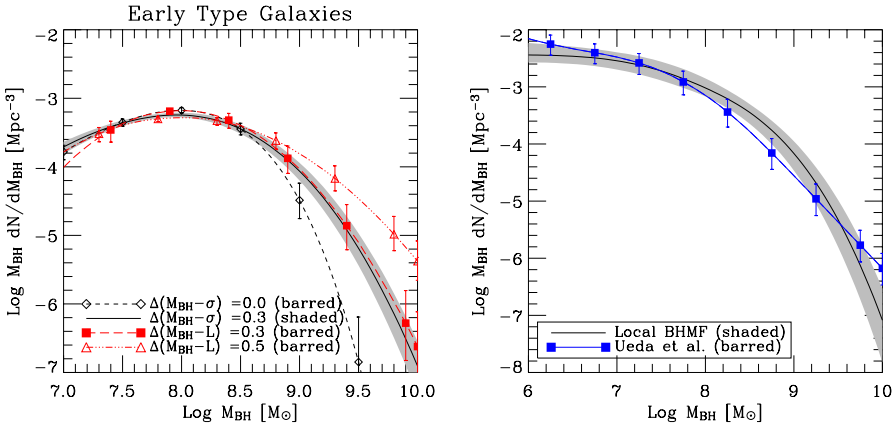

Fig. 1. (a) Local BHMF for early type galaxies based on the SDSS sample of [1]. The shaded area and error bars ("barred") indicate 1σ uncertainties. The Δ indicate the assumed intrinsic dispersions of the $M_{\rm BH}$-$\sigma_\star$ or $M_{\rm BH}$-$L_{\rm bul}$ relations. (b) Best estimate of the local BHMF (shaded area) compared with the BHMF of AGN relics obtained using the luminosity function by [21], corrected for the missing Compton-thick AGNs.

or not resolving the BH sphere of influence provide similar $M_{\rm BH}$ values, albeit with much larger errorbars in the latter case. However, from the same figure it can be evinced that on average BH measurements where the sphere of influence is not resolved are underestimated by a factor ~ 2, and this fully accounts for the larger zero points found by [4]. Apart from the larger zero points, by excluding the non-secure BH detections [4] find that $M_{\rm BH}$-$\sigma_\star$ and $M_{\rm BH}$-$L_{\rm bul}$ have the same dispersion which, as we have just shown, is independently confirmed by the requirement of obtaining the same BHMF from $M_{\rm BH}$-$\sigma_\star$ and $M_{\rm BH}$-$L_{\rm bul}$ applied to $[\phi(\sigma)]$ and $[\phi(L)]$, respectively.

3 The Mass Function of AGN Relics

The Mass Function of AGN relics is estimated with the continuity equation which relates the relic BHMF, $N(M,t)$, to the AGN luminosity function (LF), $\phi(L,t)$ [19]. The only assumption is that AGNs are powered by mass accretion onto a massive BH and that we can neglect merging of BHs. The efficiency of mass-to-energy conversion is ε and the BH is emitting at the fraction λ of the Eddington luminosity. L in the AGN LF must be the 'bolometric' luminosity. To obtain L, we derive and use bolometric corrections which do not take into account the IR radiation (reprocessed UV radiation). Thus, they are a factor $\sim 30\%$ lower than the values used by previous authors. We consider the Hard X-ray luminosity function by [21], corrected for the missing Compton-thick AGNs (factor ~ 1.6) and we apply a bolometric correction to obtain $\phi(L,t)$. Assuming that at $z = 3$ all BHs are active (this initial condition does not affect the final

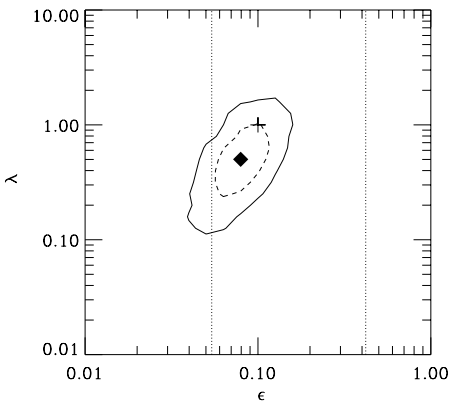

Fig. 2. Locus where ε and λ provide the best match between local and relic BHMFs. The solid and dashed lines indicate an average deviation of 1 and 0.7σ between the BHMFs. The diamond marks the ε,λ values providing the best agreement.

results), we can estimate the relic BHMF (with $\varepsilon = 0.1$ and $\lambda = 1$) and compare it with the local BHMF (Fig. 1b). The local BHMF and the relic BHMF are in good agreement within the uncertainties. Thus, it is unlikely that merging can play a major role in shaping the BHMF for $z < 3$. The [21] LF, corrected for the missing Compton-thick AGNs can also reproduce the XRB spectrum and source counts, thus satisfying the constraints imposed by the XRB. In particular, the disagreement found by [2] between the density of local massive BHs and that inferred from the X-ray background light can be reconciled noting that the average redshift of the sources making the XRB is not $\langle z \rangle \simeq 2$ but $\langle z \rangle \simeq 1$, as shown by the redshift evolution of the [21] LF. It is worth stressing the importance of the XRB constraint which effectively removes one free parameter in this analysis, i.e. the fraction of obscured AGNs. Clearly, a more refined fit of the XRB spectrum is required and is the subject of future work.

4 Accretion efficiency and $L/L_{\rm Edd}$

Accretion efficiency ε and Eddington ratio λ are the only free parameters for the relic BHMF and Fig. 2 shows the locus where they provide the best match between the relic and local BHMFs. The solid and dashed lines shows the loci where the average deviation between the BHMFs is less than 1 and 0.7σ, respectively. Outside of the solid contour, the agreement between the BHMFs is poor. The dotted lines marks the ε values for a non-rotating Schwarzschild BH and a maximally rotating Kerr BH. Acceptable values are in the range $\varepsilon = 0.04 - 0.16$ and $\lambda = 0.1 - 1.7$.

The discrepancy found by [22,3] is thus removed without requiring large accretion efficiencies because of (i) the use of the zero points of [4], (ii) the non-zero intrinsic dispersion of the $M_{\rm BH}$-$\sigma_\star$ and $M_{\rm BH}$-$L_{\rm bul}$ relations, and (iii) the smaller bolometric corrections. While (ii) and (iii) are generally accepted, (i) is more controversial because the definition of 'secure' BH mass measurement

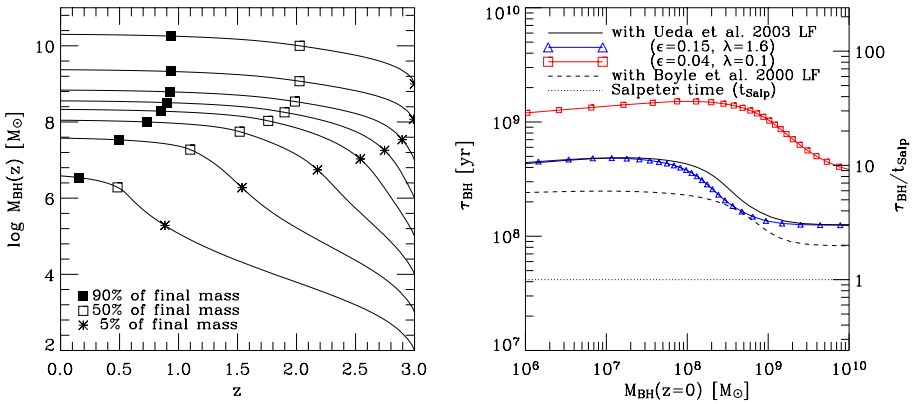

Fig. 3. (a) Average growth history of BHs. The symbols indicate the points when a BH reaches a given fraction of its final mass. (b) Average mean lifetimes of active BHs as a function of their mass at $z = 0$. The solid line corresponds the standard case ($\varepsilon = 0.1$, $\lambda = 1$).

varies from author to author. However, even using the same zero points as [22] to estimate the local BHMF we obtain $\varepsilon = 0.05 - 0.2$ and $\lambda = 0.15 - 2.5$, i.e. efficiency is still $\varepsilon < 0.2$. It is worth noticing that the average limits on $L/L_{\rm Edd}$ that we find are perfectly in agreement with the average values estimated by [14] on a large sample of SDSS quasars (see their Fig. 2).

5 Anti-hierarchical BH growth and AGN lifetimes

Fig. 3a shows the average growth history of BHs with different starting masses at $z = 3$. Symbols mark the point when a BH reaches a given fraction of its final mass. At $z < 3$, all BHs gain at least 95% of their final mass but BHs which are more massive than 10^8 $M_\odot$ grow earlier and gain 50% of their final mass by $z \sim 2$. Smaller BHs grow at lower redshifts ($z < 1$). This anti-hierarchical growth of BHs is a consequence of the redshift evolution of the [21] LF.

Fig. 3b shows the average total lifetimes of active BHs, i.e. the time required for the BH growth since $z = 3$. The solid line shows the "canonical" case with $\varepsilon = 0.1$, $\lambda = 1$. Lines with symbols show limiting cases from Fig. 2. Local high mass BHs ($M_{\rm BH} < 10^9$ $M_\odot$) have been active, on average, $\simeq 1.5 \times 10^8$ yr. On the contrary, the assembly of lower mass BHs has required active phases lasting at least three times that much ($\simeq 4.5 \times 10^8$ yr). The average lifetimes can be as large as 10^9 yr with the smaller ε and λ values compatible with local BHs ($\varepsilon = 0.04$, $\lambda = 0.1$ - see Fig. 2).

Overall, the plots in Fig. 3 indicate that smaller BHs ($M_{\rm BH} < 10^8$ $M_\odot$) find more difficulties in growing than larger ones. Indeed, this is consistent with physical models for the coevolution of BHs and galaxies. Smaller BHs form in

shallower potential wells with respect to more massive ones and are thus more subject to feedback from star formation (e.g. supernovae explosions) and from the AGN itself [15].

6 Conclusions

We have shown that the local BH mass function and that of AGN relics are in good agreement with standard accretion efficiency and $L/L_{\rm Edd}$ ratio ($\varepsilon \sim 0.1$, $\lambda \sim 1$). In particular, the local BH Mass function implies that the density in BHs is $\rho_{\rm BH} = 4.6(-1.4;+1.9)(h/0.7)^2 \times 10^5$ M$_\odot$ Mpc^{-3}, a factor 1.8 higher than estimated by [22]. Merging of BHs is either not important or it does not significantly alter the relic BHMF, at least at $z < 3$. The BH growth is anti-hierarchical, in the sense that smaller BHs ($M_{\rm BH} < 10^7$ M$_\odot$) grow at lower redshifts ($z < 1$) with respect to more massive ones ($z = 1-3$). The global picture which emerges is than that local BHs grew during AGN phases in which accreting matter was converted into radiation with $\varepsilon = 0.05-0.2$ and $L/L_{\rm bol} = 0.15-2.5$. The average total lifetime of these active phases ranges from $\simeq 4.5 \times 10^8$ yr ($M_{\rm BH} < 10^7$ M$_\odot$) to $\simeq 1.5 \times 10^8$ yr ($M_{\rm BH} > 10^9$ M$_\odot$).

References

1. M. Bernardi et al.: AJ **125**, 1849 (2003)
2. M. Elvis, G. Risaliti, G. Zamorani: ApJ **565**, L75 (2002)
3. L. Ferrarese: *Current High-Energy Emission around Black Holes*, Eds. C.-H. Lee & H.-Y. Chang (Singapore: World Scientific 2002), p. 3
4. L. Ferrarese, D. Merritt: ApJ **539**, L9 (2000)
5. K. Gebhardt et al.: ApJ **539**, L13 (2000)
6. K. Gebhardt et al.: ApJ **583**, 92 (2003)
7. C. S. Kochanek et al.: ApJ **560**, 566 (2001)
8. J. Kormendy, D. Richstone: ARA&A **33**, 581 (1995)
9. A. Marconi, G. Risaliti, R. Gilli, L. K. Hunt, R. Maiolino, M. Salvati M.: MNRAS **351**, 169 (2004)
10. A. Marconi, M. Salvati M.: *Issues in Unification of Active Galactic Nuclei*, eds. R. Maiolino, A. Marconi and N. Nagar (San Francisco: ASP 2002), p. 217
11. A. Marconi, L. K. Hunt: ApJ **589**, L21 (2003)
12. A. Merloni: MNRAS in press, astro-ph/0402495 (2004)
13. R. O. Marzke et al.: AJ **108**, 437 (1994)
14. R.J. McLure, J.S. Dunlop: MNRAS **352**, 1390 (2004)
15. N. Menci et al.: ApJ **604**, 12 (2004)
16. O. Nakamura et al.: AJ **125**, 1682 (2003)
17. F. Shankar et al.: MNRAS in press, astro-ph/0405585 (2004)
18. R. K. Sheth et al.: ApJ **594**, 225 (2003)
19. T.A. Small, R. D. Blandford: MNRAS **259**, 725 (1992)
20. S. Tremaine et al.: ApJ **574**, 740 (2002)
21. Y. Ueda et al.: ApJ **598**, 886 (2003)
22. Q. Yu, S. Tremaine: MNRAS **335**, 965 (2002)
23. Q. Yu, Y. Lu: ApJ **602**, 603 (2004)

Anti-hierarchical Growth of Supermassive Black Holes and QSO Lifetimes

A. Merloni

Max-Planck-Institut für Astrophysik, Karl-Schwarzschild-Strasse 1, D-85741, Garching, Germany

Abstract. I present a new method to unveil the history of cosmic accretion and the build-up of Supermassive Black Holes (SMBH) in the nuclei of galaxies, based on observations of the evolving radio and (hard) X-ray luminosity functions of AGN. The fundamental plane of black hole activity discovered by Merloni, Heinz & Di Matteo (2003) is used as a mass and accretion rate estimator. I adopt the local BH mass function as a boundary condition to integrate backwards in time the continuity equation for the SMBH evolution, neglecting the role of mergers. Under the most general assumption that accretion proceeds in a radiatively efficient way above a certain rate, and in a radiatively inefficient way below, the redshift evolution of the mass and accretion rate functions are calculated self-consistently. The only tunable parameters are the accretion efficiency and the critical ratio of the X-ray to Eddington luminosity at which the transition between accretion modes takes place. The evolution of the BH mass function between $z = 0$ and $z \sim 3$ shows clear signs of an anti-hierarchical behaviour: while the majority of the most massive objects ($M \gtrsim 10^9$) were already in place at $z \sim 3$, lower mass ones mainly grew at progressively lower redshift. As an example, I will discuss the consequences of these results for the lifetimes of accreting black holes.

1 Introduction

It has been known for the last ten years that the cosmological evolution of massive galaxies shows signs of 'down-sizing' [1], i.e. of a progressive decrease of the typical mass of actively star forming galaxies. Many pieces of evidence, brought forward also during this meeting (see e.g. the contributions of Bender, Kauffmann and Danese to these Proceedings), suggest that the baryonic physics of star formation processes counterbalance the hierarchical (bottom-up) growth of dark matter structures, favouring the early formation and growth of the most massive (and dense) stellar aggregates.

The ubiquity of SMBH in galactic nuclei, and their tight relation with their hosts' bulge properties [2] seem to indicate that the formation and growth of galaxies and of their resident black holes have proceeded in parallel, and probably influenced each other in the early stages of galaxy formation. As a matter of fact, the number of theoretical studies dedicated to AGN feedback in galaxy formation has flourished in the last five years (see e.g. Loeb's contribution in this proceedings, and references therein). Furthermore, a recent comprehensive study of 23 000 local AGN carried out by the Sloan Digital Sky Survey (SDSS, [3]) have demonstrated, in a direct quantitative way, that accretion onto SMBH and formation of stars are tightly coupled even in the local universe.

ESO Symposia: Growing Black Holes, pp. 453–458, 2005.

Is it possible to learn more about the formation and growth of structures by just looking at the evolution of the AGN population? The aim of the work presented here is to show to what extent this is indeed possible, and to describe a robust, self-consistent way to unveil the history of cosmic accretion and the build-up of SMBH in the nuclei of galaxies, in the form of their evolving mass function. The methodology and the main results will be discussed in the next section, while in section 3 I will expand on the consequences of these results for the issue of QSO lifetimes. Section 4 will summarize my conclusions.

2 The Evolution of the SMBH Mass Function

Under the standard assumption that black holes grow mainly by accretion [4], the cosmic evolution of the SMBH accretion rate and its associated mass density can be calculated from the luminosity function of AGN: $\phi(L_{\rm bol}, z) = dN/dL_{\rm bol}$, where $L_{\rm bol} = \epsilon_{\rm rad}\dot{M}c^2$ is the bolometric luminosity produced by a SMBH accreting at a rate of $\dot{M}$ with a radiative efficiency $\epsilon_{\rm rad}$. In practice, the accreting black hole population is always selected through observations in specific wavebands. Crucial is therefore the knowledge of two factors: the completeness of any specific AGN survey, and the bolometric correction needed in order to estimate $L_{\rm bol}$ from the observed luminosity in any specific band. On both these issues, huge progress has been made in the last few years (see e.g. [5]).

In order to progress from the study of BH mass densities to that of BH mass functions, we need to break the degeneracy between mass and accretion rate of any given observed AGN. While in most semi-analytic works this is done by assuming a constant Eddington ratio for all sources, here I will propose an alternative, physically motivated, method. In a recent paper [6] it has been shown that the hard (2-10 keV) X-ray luminosity of an accreting black holes is related to its mass and its core radio (at 5GHz) luminosity by the following relation (the "fundamental plane" of black hole activity): $\log L_{\rm R} = (0.60^{+0.11}_{-0.11}) \log L_{\rm X} + (0.78^{+0.11}_{-0.09}) \log M + 7.33^{+4.05}_{-4.07}$; which can be inverted to relate BH masses to observed nuclear radio and X-ray luminosities: $\log M \simeq g(\log L_{\rm R}, \log L_{\rm X})$. One of the consequences of this relation is that, in an ideal case, the *conditional radio/X-ray* luminosity function of active black holes, i.e. the number of sources per unit co-moving volume per unit logarithm of radio and X-ray luminosity, $\Psi_{\rm C}(L_{\rm R}, L_{\rm X})$, could be used to reconstruct the mass function of the underlying black hole population. In fact, the current lack of the exact knowledge of $\Psi_{\rm C}(L_{\rm R}, L_{\rm X})$ can be (at least partially) superseded, given the two separate radio, $\phi_{\rm R}(L_{\rm R}, z)$, and X-ray, $\phi_{\rm X}(L_{\rm X}, z)$, luminosity functions at redshift z, and an *independent* estimate of the black hole mass function, $\phi_{\rm M}(M, z)$ at the same redshift. By taking into account the fundamental plane relationship, we have that, at any z, the conditional luminosity function $\Psi_{\rm C}$ has to satisfy the following integral constraints:

$$\phi_i(L_i) d\log L_i = \int_{L_{j,\rm min}}^{\infty} \Psi_{\rm C}(L_i, L_j) d\log L_j \qquad (i,j) = ({\rm R}, {\rm X}) \tag{1}$$

$$\phi_{\rm M}(M)d\log M = \iint_{\log M<g<\log M+d\log M} \Psi_{\rm C}(L_{\rm X}, L_{\rm R})d\log L_{\rm R} d\log L_{\rm X}. \quad (2)$$

Given observational estimates of $\phi_{\rm X}$, $\phi_{\rm R}$ and $\phi_{\rm M}$, we start with an initial guess for $\Psi_{\rm C}$, and proceed via successive iterations, minimizing the differences between the projections of the conditional luminosity function onto the X-ray and radio luminosity axes and the observed luminosity functions, until a conditional LF is obtained simultaneously satisfying eqs. (1) and (2). Once such an estimate of $\Psi_{\rm C}$ is found, it is possible to derive the local distribution of the X-ray to Eddington ratio, and from this, given an appropriate bolometric correction (i.e. a specific functional form $L_{\rm X} = L_{\rm X}(M, \dot{m})$, where $\dot{m} \equiv \epsilon \dot{M} c^2 / L_{\rm Edd}$), the desired accretion rate function.

The redshift evolution of the SMBH population can then be computed integrating *backwards* the continuity equation that describes SMBH evolution driven by accretion only [7]:

$$\frac{\partial \phi_{\rm M}(M,t)}{\partial t} + \frac{\partial [\phi_{\rm M}(M,t) \cdot \langle \dot{M}(M,t) \rangle]}{\partial M} = 0, \quad (3)$$

where the mean accretion rate as a function of black hole mass and time, $\langle \dot{M} \rangle$ is calculated directly from the accretion rate distribution function at time t. Starting from $z = 0$, the local BHMF, as determined independently from the galaxy velocity dispersion distribution and the $M - \sigma$ relation, can be used as a boundary condition to integrate eq. (3) up to the redshift where hard X-rays and radio luminosity functions of AGN can be reliably estimated. The only parameters needed are the accretion efficiency ϵ, and the functional form $L_{\rm X} = L_{\rm X}(M, \dot{m})$.

Here I present the results obtained using the most recent determinations of the hard X-rays and radio LF [9,10], fixing $\epsilon = 0.1$, and assuming for the function $L_{\rm X}(\dot{m})$ a simple broken power-law expression, with $L_{\rm X} \propto \dot{m}^2$ at low accretion rates (radiatively inefficient regime) and $L_{\rm X} \propto \dot{m}^{0.8}$ at high luminosities (radiatively efficient regime, see [5,7] for details), with the transition being placed at $x_{\rm cr} = 10^{-3}$ [11].

The evolution of the black hole mass function is shown in the left panel of Figure 1. As opposed to the standard picture of hierarchical mass build up of dark matter halos in CDM cosmologies, supermassive black holes growing by accretion between $z \sim 3$ and now have a mass function which is more and more dominated by larger mass objects at higher redshift. Thus, most of the more massive black holes ($M > 10^9$) were already in place at $z \sim 3$, and as a result, the "typical" SMBH mass decreases with decreasing redshift. SMBH appear to be growing in anti-hierarchical fashion [5,12].

The right panel of Figure 1 shows instead the redshift evolution of the derived accretion rate function (expressed here as X-ray to Eddington ratio, $L_{\rm X}/L_{\rm Edd}$). While the number of sources accreting at low rates increases monotonically with decreasing redshift, the situation is different for rapidly accreting objects, that increase in number with increasing redshift. The cut-off redshift, above which the

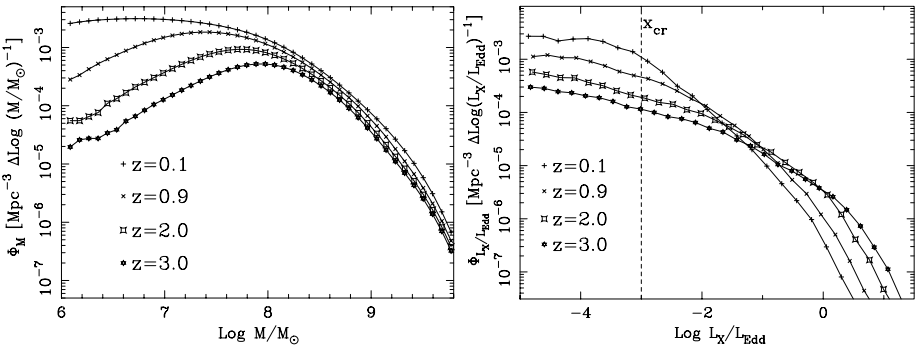

Fig. 1. Left Panel: Redshift evolution of the SMBH mass function (BHMF), from redshift 3 (lower curve) till redshift 0.1 (upper curve). Right Panel: Redshift evolution of the SMBH accretion rate function (expressed here in terms of X-ray to Eddington luminosity ratio), from redshift 3 till redshift 0.1; The vertical dashed line marks the adopted value of the critical accretion rate where a transition occurs between radiatively inefficient (below) and efficient (above) accretion.

number of sources declines again, is a function of the typical X-ray to Eddington ratio, being lower for lower accretion rate sources. Once again, it is clear that the "typical" X-ray to Eddington ratio, which can be approximately identified with the knee of the accretion rate functions of Fig.1, decreases with decreasing redshift, crossing the critical rate that separates radiatively inefficient from efficient regimes (here fixed at 10^{-3}, vertical dashed line) around $z \sim 0.5$.

3 Lifetimes of Active Black Holes

In all models that derive the properties of the SMBH population from the observed QSO evolution, a key element is represented by the typical quasar lifetime or by the almost equivalent activity duty cycle. However, the significance of these parameters is limited to the standard case in which, on the basis of an observed luminosity function in a specific waveband, one tries to derive the distribution of either BH masses or accretion rates. Usually, a constant Eddington ratio is assumed in this case, which implies that QSO are considered as on-off switches. Then, the duty cycle is simply the fraction of black holes active at any time, and the lifetime is the integral of the duty cycle over the age of the universe (see e.g. [13] and references therein).

The picture discussed here is different, in that a broad distribution of Eddington rates is not only allowed, but actually calculated for the SMBH population at every redshift. When this is the case, a more meaningful definition of activity lifetime is needed. Let us first define the mean Eddington rate for object of mass M_0 at redshift $z = 0$ $\langle \dot{m}(M_0, z) \rangle$ and then introducing the *mean accretion weighted lifetime* of a SMBH with a given mass *today*: $\tau(M_0, z) = \int_\infty^z \langle \dot{m}(M_0, z') \rangle \frac{dt}{dz'} dz'$.

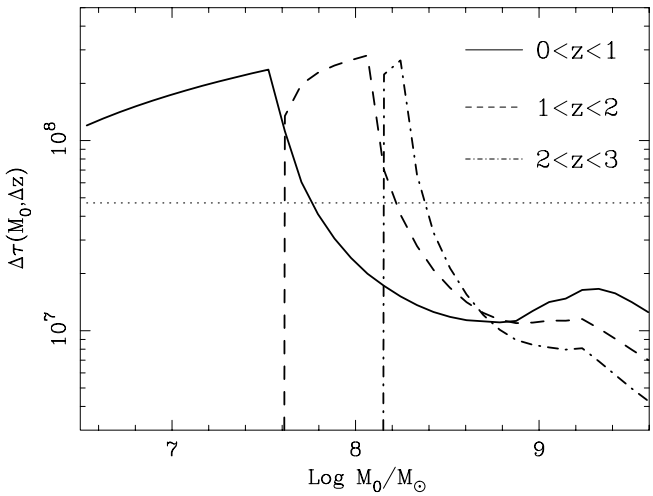

Fig. 2. Partial mean accretion weighted lifetimes (in years) of SMBH with mass today M_0, calculated for three different redshift intervals: $0 < z \leq 1$ (solid line), $1 < z \leq 2$ (dashed line) and $2 < z \leq 3$ (dot-dashed line). The horizontal dotted line is the Salpeter time for accretion efficiency of 10%.

The ratio of $\tau(M_0, z)$ to the Salpeter time, $t_{\rm S} = \epsilon Mc^2/L_{\rm Edd} = (\epsilon/0.1)4.5 \times 10^7$ yrs, gives the mean number of e-folds of mass growth for objects with mass M_0 up to redshift z. The ratio of $\tau(M_0, z)$ to the Hubble time $t_{\rm Hubble}(z) = H(z)^{-1}$, instead, is a measure of the activity duty cycle of SMBH. It is also interesting here to calculate "partial" lifetimes in a given redshift interval $\Delta z = (z_i, z_f)$:

$$\Delta\tau(M_0, \Delta z) = \int_{z_i}^{z_f} \langle \dot{m}(M_0, z') \rangle \frac{dt}{dz'} dz'. \tag{4}$$

In Figure 2, I show $\Delta\tau(M_0, \Delta z)$ for three redshift intervals: $0 < z \leq 1$; $1 < z \leq 2$ and $2 < z \leq 3$. The accretion weighted lifetime for BH of any given mass between $0 < z \leq 3$ is of course just the sum of the three. The anti-hierarchical nature of mass build-up in actively accreting AGN and QSOs is again clearly illustrated by this plot. In fact, the major growth episode of a SMBH must coincide with the period when $\Delta\tau \geq t_{\rm S}$. This happens at $z \leq 1$ for $M_0 \lesssim 10^{7.6}$, between redshift 1 and 2 for $10^{7.6} \lesssim M_0 \lesssim 10^{8.2}$, and at $2 < z \leq 3$ for $10^{8.2} \lesssim M_0 \lesssim 10^{8.4}$. Supermassive black holes with masses larger than $M_0 \sim 10^{8.5}$ today, must have experienced their major episodes of growth at redshift higher than 3. It also interesting to note that the objects that dominate the SMBH mass function today, i.e. those in the range of masses around $10^{7.5} M_\odot$, where $M_0 \phi_M(M_0, z = 0)$ peaks, mainly grew around $z \sim 1$, which is when most of the X-ray background light we see today was emitted [14].

4 Conclusion

I have presented a new method to study the growth of accreting supermassive black holes, based on the simultaneous evolution of the AGN radio and hard (2-10 keV) X-ray luminosity functions. The method is based on the locally observed trivariate correlation between black hole mass, X-ray and radio luminosity (the so-called fundamental plane of black hole activity, [6]). Thanks to this correlation, it is possible for the first time to break the degeneracy between luminosity, mass and accretion rate: QSO and AGN not only grow in mass during their evolution, but also accrete a different rates depending on their mass and age.

Qualitatively (i.e. independently on the values of the model parameters), the evolution of the black hole mass function between $z = 0$ and $z \sim 3$ shows clear signs of an *anti-hierarchical* behaviour: while the majority of the most massive objects ($M \gtrsim 10^9$) were already in place at $z \sim 3$, lower mass ones mainly grew at progressively lower redshift, so that the average black hole mass increases with increasing redshift. At the same time, the typical accretion rate of SMBH decreases with decreasing redshift. Consequently, the lifetime of an actively growing BH, measured through the partial mean accretion weighted lifetime (see section 3), is a strong function of both redshift and black hole mass.

Broadly speaking, what is presented here is the SMBH analog of the downsizing of star forming galaxies. Future more direct and detailed comparisons between SMBH mass functions, such as those shown here, and galaxy luminosity functions, both at low and high redshifts, will hold the key of our understanding of the complex interplay between formation and growth of black holes and galaxies.

References

1. L. L. Cowie, A. Songaila, E. M. Hu, J. G. Cohen: AJ **112**, 839 (1996)
2. J. Kormendy, D. Richstone: ARA&A **33**, 581 (1995); J. Magorrian, et al.: AJ **115**, 2285 (1998); L. Ferrarese, D. Merritt: ApJL **539**, L9 (2000); K. Gebhardt, et al.: ApJL **539**, L13 (2000); S. Tremaine, et al.: ApJ **574**, 740 (2002); A. Marconi, L. K. Hunt: ApJL **589**, L21 (2003)
3. T. M. Heckman, et al.: preprint astro-ph/0406218 (2004)
4. A. Soltan: MNRAS **200**, 115 (1982); Q. Yu, S. Tremaine: MNRAS **335**, 965 (2002)
5. A. Marconi, et al.: MNRAS **351**, 169 (2004)
6. A. Merloni, S. Heinz, T. Di Matteo: MNRAS **345**, 1057 (2003)
7. T. A. Small, R. D. Blandford: MNRAS **259**, 725 (1992)
8. A. Merloni: MNRAS in press. astro-ph/0402495 (2004)
9. Y. Ueda, M. Akiyama, K. Ohta, T. Miyaji: ApJ **598**, 886 (2003)
10. C. J. Willott, et al.: MNRAS **332**, 536 (2001)
11. T. Maccarone, E. Gallo, R. P. Fender: MNRAS **345**, L19 (2003)
12. G. L. Granato, et al.: ApJ **600**, 580 (2004)
13. P. Martini: in *Coevolution of Black Holes and Galaxies, from the Carnegie Observatories Centennial Symposia* ed. by L. Ho (CUP, Cambridge) p. 170 (2004)
14. G. Hasinger: AIP Conf.Proc. **666**, 227 (2003)

Growing Black Holes and Metal Enrichment in High Redshift Luminous Quasars

H. Netzer

School of Physics and Astronomy, Tel Aviv University, Tel Aviv 69978, Israel

1 BLR-size, black hole mass and accretion rates in AGN

Recent progress in reverberation mapping [5,10] enable the conversion of source luminosity and line-width into black hole (BH) mass (M) and accretion rate ($\dot{M}$; this is assumed to be proportional to L/L_{Edd}) (e.g. [8], [12] - hereafter S04). This allows the construction of the "BH mass function" of AGN which is a more physically meaningful concept compares with the usual luminosity function [3]. There are several far reaching consequences for fundamental cosmological questions like the comparison of BH growth-rate with galaxy evolution and the metal enrichment in the universe.

It has been argued that BH growth time, that can be expressed as

$$t_{grow} \simeq 4 \times 10^8 \frac{\eta}{1-\eta} \frac{L_{Edd}}{L} \; yr \,, \tag{1}$$

where η is the mass-to-radiation conversion efficiency, was high in the early universe and much lower at $z < 2$ (e.g. [7], see also Merloni in these proceedings). This leads to *anti-hierarchical* growth of supermassive black holes implying that earlier halo and galaxy mergers triggered more mass inflow into the center where the seed BH (or the two merging black holes) reside.

A complete understanding of BH evolution and reliable estimates of t_{grow} requires M and $\dot{M}$ measurements at all redshifts. This is very challenging since standard techniques that are being used to measure such masses (the "single epoch mass determination", see e.g. [8]) are based on the C iv 1548Å line profile that is very problematic and most uncertain [1]. The most reliable method is to use the combination of FWHM($H\beta$) with the optical continuum luminosity (here after the $H\beta$ method) and the Kaspi et al. [5,6] relationship for the BLR size

$$R_{BLR} \simeq 0.4 \left[\frac{\lambda L_\lambda(5100)}{10^{46} \; erg/sec} \right]^{0.6 \pm 0.1} \; pc \,, \tag{2}$$

although this entails extrapolation to very high luminosity.

2 New infrared spectroscopy of high-z AGN

Recently we have obtained good quality H and K-band spectroscopy of 29 high-z AGN (two bands around z=2.4 and z=3.4 corresponding to the redshifted

ESO Symposia: Growing Black Holes, pp. 459–462, 2005.

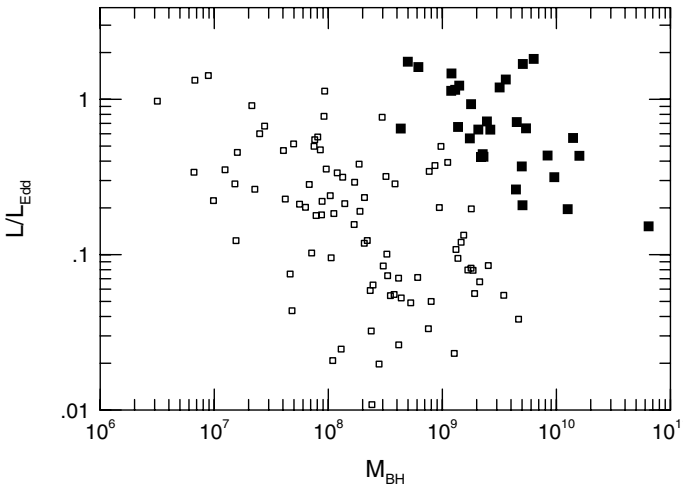

Fig. 1. New mass and accretion rates from S04 (large full symbols) and from the Boroson and Green [2] low redshift sample (small squares).

$H\beta$ line) that enables the best mass and accretion rate estimates for the most luminous sources. The results are described and discussed in two recent papers: S04 and Netzer et al. (2004). The most important findings are:

- New measurements of the most massive BHs known (the mass of the BH in several of the objects exceeds $10^{10} M_{\odot}$).
- The accretion rate of almost all sources is very high: $0.5 < L/L_{Edd} < 1.5$.
- There are several new relationships indicating that L/L_{Edd} is a major driver of important line and continuum correlations (e.g. EW($H\beta$) is correlated with L/L_{Edd})
- The BLR metalicity is strongly correlated with L/L_{Edd} and *not* correlated with the BH mass or the bolometric luminosity.

A digram showing the new mass and accretion rate measurements compared with those in a low redshift sample of luminous AGN is given in Fig. 1. Below we discuss the last point in some detail.

3 A new metalicity-accretion rate relationship

Hamann and Ferland [4] argued that the metalicity of the BLR gas in AGN as measured by the N v1240/C iv1548 line ratio, is strongly correlated with the source luminosity. Later Warner et al. [13] suggested that the BH mass, rather than the source luminosity, drives this correlation.

Our new observations supply new mass and accretion rate measurements for a large number of extremely luminous AGN. Together with about 70 more such measurements available for lower luminosity sources, there are more than 90 sources where the dependence of metalicity on M, $\dot{M}$ and L can be tested. As shown in Fig. 2, there is a strong correlation of metalicity (ala Hamann and Ferland) with L/L_{Edd}. We have tested the correlation of metalicity with M and with L and found that they are much less significant, mostly because of the presence of NLS1s, those AGN with low L yet very large L/L_{Edd}. This confirms our earlier suggestion [11] and has important cosmological implications.

4 Episodes of metal enrichment in AGN

The available new measurements of masses and accretion rates allow a direct measure of the BH growth time (eqn. 1) in hundreds of AGN. A quantitative analysis shows that the BH growth time of many high mass ($M > 10^9 M_\odot$) low accretion rate AGN, is longer than the age of the universe. In addition, all galactic nuclei BHs must spend a large part of their life in the dormant phase. Thus, we are driven to the conclusion that large mass BHs (and possibly also low mass ones) must have had episodes in their past when the growth rate was much faster than currently observed.

The combination of the conclusion about the changing mass accretion rate during the life-time of *individual* AGN, with the new metalicity vs. $/L_{EDD}$ correlation, leads to the conclusion that the BLR metalicity can change in both

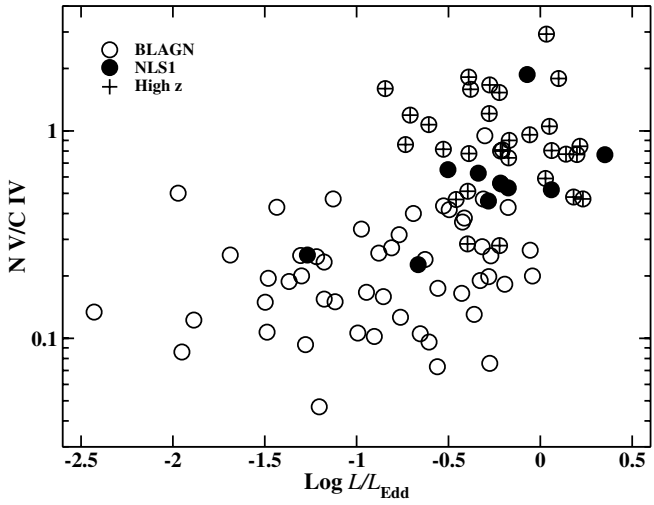

Fig. 2. The new metalicity accretion rate relationship from S04. Empty circles are broad-line AGNs with FWHM(Hβ)>1500 km s^{-1}, and empty circles with plus signs indicate $2 < z < 3.5$ quasars. NLS1s (with FWHM(Hβ)<1500 km s^{-1}) are marked with filled circles.

directions (increase as well as decrease) during the life time of an individual source. One possibility is that high accretion rate episodes are associated with enhanced star formation rate that supply mass to the vicinity of the black hole. This material becomes, for a limited time, the BLR gas. Some of this gas is then lost to the general ISM, or perhaps accreted onto the BH and the following episode brings to the center more mass that can be of higher or lower metalicity. The details of such a model must be worked out given a general scenario of merging halos and BHs that is associated by enhances mass inflow into the center.

I am most grateful to Ohad Shemmer, my student and collaborator for many years, who has work so efficiently on this project and whose Ph.D thesis contains much of the material presented here. I am also grateful to my other collaborators in the new observations, S. Croom, E. Oliva, R. Maiolino, E. Corbett and L. di Fabrizio. This research is supported by the Jack Adler Chair for Extragalactic Astronomy.

References

1. Baskin, A., and Laor, A.: astroph/0409196 (2004)
2. Boroson, T. A. & Green, R. F.: ApJS, 80, 109 (1992)
3. Corbett, E. A. et al.: MNRAS, 343, 705 (2003)
4. Hamann, F. & Ferland, G.: ApJ, 418, 11 (1993)
5. Kaspi, S., Smith, P. S., Netzer, H., Maoz, D., Jannuzi, B. T., & Giveon, U.: ApJ, 533, 631 (2000)
6. Kaspi, S., Netzer, H., Maoz, D., Shemmer, O., Brandt, W. N., Schneider, D. P.: in *Coevolution of Black Holes and Galaxies, from the Carnegie Observatories Centennial Symposia* ed. by L. Ho (CUP, Cambridge) (2004)
7. Merloni, A.: MNRAS, 353, 1035 (2004)
8. Netzer, H.: ApJL, 583, L5 (2003)
9. Netzer, H., Shemmer, O., Maiolino, R., Croom, S., & Oliva, T., & Di-Fabrizio, L.:, ApJ in press (2004)
10. Peterson, B. M. et al.: ApJ in press (2004)
11. Shemmer, O. & Netzer, H.: ApJL, 567, L19 (2002)
12. Shemmer, O., H. Netzer, R. Maiolino, E. Oliva, S. Croom, E. Corbett, and L. di Fabrizio: ApJ in press (S04) (2004)
13. Warner, C., Hamann, F., & Dietrich, M.: ApJ, 608, 136 (2004)

A New Approach to Characterizing the SEDs of AGN from Deep Multi-wavelength Observations

S. Frank[1] and P. Osmer[1]

The Ohio State University, 140 W. 18th Avenue, Columbus, Ohio 43210, USA

Abstract. We use data of the CDFN 2Ms survey and related multi-wavelength observations to investigate the nature of the intrinsic SEDs of AGN, how they vary with redshift and luminosity, and how the data are affected by obscuration and possible contributions from starbursts. We believe that shifting observational data to the emitted frame provides a direct way to visualize effects of obscuration and changes in the underlying SED from object to object.

1 Shifting from the Observed to the Emitted Frame

The 2 Ms Chandra Deep Field-North survey is the deepest X-ray observation of the universe in the 0.5-8.0 keV band. For 270 of 503 point sources in the catalogue of [1], spectroscopic redshifts could be obtained. This enables us to transform observed fluxes directly into emitted luminosities :

$$L_{em}(\nu_{em}) = L_{\nu,obs}(\nu_{obs}(1+z)) \tag{1}$$

where $L_{\nu,obs} = 4\pi d_L^2 f_{\nu,obs}(\nu_{obs})$ with z = source redshift, $f_{\nu,obs}(\nu_{obs})$ = observed flux, and $d_L = d_L(z)$ = luminosity distance.

Photometric data in the HK', z', I, R, V, B and U bands are from [2]. Fig. 1 shows a selection of SEDs constructed by this method. X-ray data are plotted as power-law with photon index Γ_{eff} and cover a 0.5-8.0 keV band shifted into the emitted frame. The redshift of each source is denoted to the right. Also plotted is the standard SED [3] for low-redshift, radio-quiet quasars. Throughout our analysis we use Ω_λ =0.73, Ω_m =0.27 and h=0.71. Plotting SEDs in the emitted frames provides a powerful tool to visualise often dramatic changes from object to object. Immediately apparent are the

- wide ranges in luminosities (up to 6 orders of magnitude)
- different wavelength/energy regimes probed in sources of different redshifts
  - the observed NIR/opt. bands shift into the UV for the emitted frame
  - the 0.5-8.0 keV observed X-ray regime transforms into a $\sim 3-50$ keV emitted interval for sources with the highest redshift of $z \sim 5.0$
- strong variations in X-ray slopes
- strong variations in optical extinction and reddening.

ESO Symposia: Growing Black Holes, pp. 463–465, 2005.

Classifying the Sources

The 2Msec Chandra exposure probes very faint X-ray sources hitherto not studied at cosmological distances. Norman et al. [5] classify 136 of them as normal starforming/starburst galaxies with little/no AGN activity. An example of such a galaxy's SED is presented in Fig. 1. The remaining AGN can be grouped by the visual appearance of their broadband SEDs into three main categories.

- Luminous, unabsorbed AGN
  - X-ray power-law slope close to the canonical $\Gamma_{eff} \sim 1.9$ of the Elvis-SED.
  - The optical/UV data show a rise or stay flat beyond 2500 Å.
  - The optical-to-X-ray flux ratio is similar to the Elvis et al. ratio.
- Red and X-ray flat AGN
  - X-ray power-law slope close to $\Gamma_{eff} \sim 1.9$.
  - The optical/UV data show a sharp decline beyond 2500 Å.
- Red and X-ray steep AGN
  - The X-ray power-law slope is much less than $\Gamma_{eff} \sim 1.9$, indicative of either an intrinsically hard spectrum or absorption.
  - The optical/UV data show a sharp decline beyond 2500 Å.

The redshift distribution of the four object types are presented in table 1. The low-z regime is dominated by galaxies, whereas sources with higher z appear to be predominantly unabsorbed AGN. Both redshift and luminosity effects can cause this schism.

2 First Results

- Transforming observed fluxes into broadband SEDs in the emitted frame allows us to study luminosity and redshift effects simultaneously.

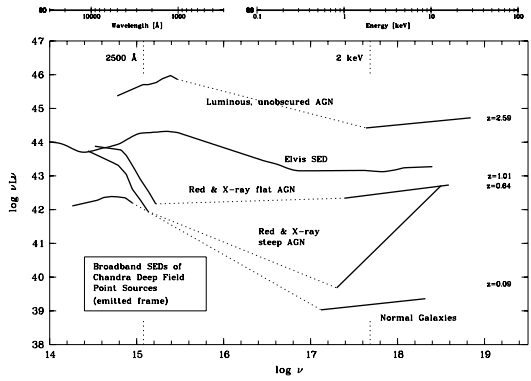

Fig. 1. Broadband SEDs of select CDF-N 2Msec sources representing the four different categories of objects. For further information see text.

Table 1. Redshift distribution of the four classes of objects. Note that by default Norman et al.(2004) only analysed sources at $z < 1.2$.

Absolute Number	$z < 1.2$	$z > 1.2$
Normal Galaxies	129	0
Unobscured AGN	14	27
Red and X-ray steep/flat AGN	47/33	8/14

- Apparent dust obscuration and reddening in the UV/optical can, but need not be, accompanied by steep X-ray spectra ($\Gamma_{eff} < 1.0$).
- As both the 2500 Å and 2keV rest-frame regions can be subject to heavy obscuration, we suggest that an optical-Xray index α_{ox} based on the (emitted) R-band and 8 keV fluxes would be a better indicator of the intrinsic source properties.
- Be aware of galaxies and starbursts at low z !
- Our approach yields new insights about the population of absorbed AGN that seem to dominate at low luminosity and redshift.

References

1. D. Alexander et al.: AJ, **126**, 539 (2003)
2. A. J. Barger et al.: AJ, **126**, 632 (2003)
3. M. Elvis et al.: ApJS, **95**, 1 (1994)
4. C. M. Gaskell et al.: ApJ, in press. astro-ph0309595 (2004)
5. C. Norman et al.: ApJ, **607**, 721 (2004)

The Growth of SMBHs in Optically-Thick Starburst Galaxies

N. Kawakatu[1], M. Umemura[2], and M. Mori[3]

[1] International School for Advanced Studies (SISSA/ISAS), Via Beirut 2-4, 34014 Trieste, Italy
[2] Center for Computational Sciences, University of Tsukuba, Ten-nodai, 1-1-1, Ibaraki 305-8577, Japan
[3] Department of Law, Senshu University, Tama-Ku, Kawasaki 214-8580, Japan

Abstract. The formation and growth of supermassive black holes (SMBHs) physically related with bulges are considered. We focus on the radiation hydrodynamic process for the growth of SMBH in the optically thick starburst galaxies. In the present scenario, it is predicted that a host luminosity-dominant "proto-QSO phase" exists as a growing BH phase before the QSO phase, and the proto-QSO phase is preceded by an optically-thick ultraluminous infrared galaxy (ULIRG) phase.

1 Introduction

The paradigm that ultraluminous infrared galaxies (ULIRGs) could evolve into QSOs was proposed by the pioneering studies [6,7]. By recent X-ray and optical observations, the evidence of active galactic nuclei (AGNs) have been detected in more than one third of ULIRGs. On the other hand, recent high-resolution observations of galactic centers have revealed that the mass ratio of the supermassive BH to the bulge is 0.002 as a median value [4]. In addition, it has been found that QSO hosts are elliptical galaxies [5]. Comprehensively judging from all these findings, it is likely that ULIRGs, QSOs, Bulges, and SMBHs are physically related to each other.

2 Coevolution of BH Growth and Bulge

Based on the radiation drag model for SMBH formation [2,8], we construct a scenario for the coevolution of SMBHs and galactic bulges. In order to treat the realistic chemical evolution of the host galaxy, we use an evolutionary spectral synthesis code 'PEGASE' [1].

In the present coevolution model, the mass accretion proportional to the bulge luminosity leads to the growth of a "massive dark object" (MDO), which is likely to form a massive dusty disk in the nucleus. However, the matter in the MDO does not promptly fall into the BH, because the BH accretion is limited by the Eddington mass accretion rate. The BH mass reaches $M_{\rm MDO}$ at a time $t_{\rm cross}$ because almost all of the MDO matter has fallen onto the central BH. The resultant mass ratio of the BH to the bulge becomes 0.001, which is just comparable to the observed ratio. Figure 1 shows the evolution of bulge luminosity

ESO Symposia: Growing Black Holes, pp. 466–467, 2005.

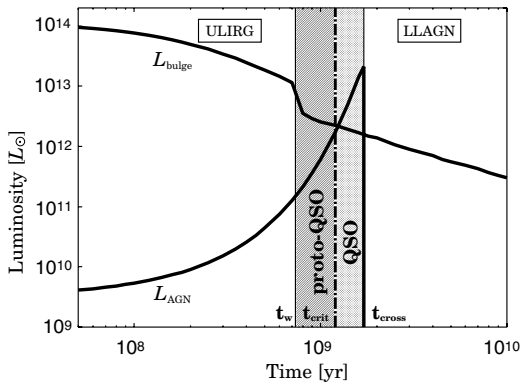

Fig. 1. AGN and bulge luminosity as a function of time. $t_{\rm crit}$ is the time when $L_{\rm bulge} = L_{\rm AGN}$. The optically-thin, bright AGN phase (*gray area*) can be divided into two phases; one is the host-dominant phase (proto-QSO), which is the dark gray area ($t_{\rm w} \leq t \leq t_{\rm crit}$) and the other is the AGN-dominant phase (QSO), which is the light gray area ($t_{\rm crit} \leq t \leq t_{\rm cross}$).

($L_{\rm bulge}$) and AGN luminosity ($L_{\rm AGN}$), assuming the Eddington luminosity. Even after the galactic wind ($t > t_{\rm w}$), $M_{\rm BH}$ continues to grow until $t_{\rm cross}$ and therefore the AGN brightens with time. After $L_{\rm AGN}$ exhibits a peak at $t_{\rm cross}$, it fades out abruptly to exhaust the fuel. The fading nucleus could be a low luminosity AGN (LLAGN).

It is found that the area of $t_{\rm w} < t < t_{\rm cross}$ can be divided into two phases with a transition time $t_{\rm crit}$ when $L_{\rm bulge} = L_{\rm AGN}$; the earlier phase is the host luminosity-dominant phase (proto-QSO phase) with massive dusty disks, whose mass is much larger than the mass of the central BH, and the later phase is the AGN luminosity-dominant phase (QSO phase). Thus, the discovery of massive disks in proto-QSOs may be strong evidence that SMBHs form by gas accretion not via BH (of stellar mass) mergers. Also, the proto-QSO phase is preceded by an optically thick phase before the galactic wind, which may correspond to ULIRGs [3]. In summary, the present model could be a physical picture of evolution of ULIRGs to QSOs.

References

1. Fioc, M., Rocca-Volmerrange, B.: A&A, **326**, 950 (1997)
2. Kawakatu, N., Umemura, M.: MNRAS, **329**, 572 (2002)
3. Kawakatu, N., Umemura, M., Mori, M.: ApJ, **583**, 85 (2003)
4. Marconi, A., & Hunt, L.K.: ApJ, **589**, L21 (2003)
5. McLure, R.J., Dunlop, J.S., & Kukula, M.J.: MNRAS, **318**, 693 (2000)
6. Norman, C., & Scoville, N.: ApJ, **332**, 124 (1988)
7. Sanders D.B., et al.: ApJ, **325**, 74 (1988)
8. Umemura, M.: ApJ, **560**, L29 (2001)

Statistical Properties of Local AGNs Inferred from the RXTE 3-20 keV All-Sky Survey

M. Revnivtsev[1,2] and S.Yu. Sazonov[1,2]

[1] Max-Planck-Institut für Astrophysik, Karl-Schwarzschild-Str. 1, D-85740 Garching bei München, Germany
[2] Space Research Institute, Russian Academy of Sciences, Profsoyuznaya 84/32, 117997 Moscow, Russia

1 Introduction

We have recently ([1]) performed an all-sky survey in the 3-20 keV band from the data accumulated during satellite slews in 1996-2002 - the RXTE slew survey (XSS). For 90% of the sky at $|b| > 10^\circ$, a flux limit for source detection of 2.5×10^{-11} erg/s/sq.cm(3-20 keV) or lower was achieved, while a combined area of 7000 sq.deg was sampled to record flux levels (for such very large-area surveys) below 10^{-11} erg/s/sq.cm. A catalog contains 294 X-ray sources. 236 of these sources were identified with a single known astronomical object. Of particular interest are 100 identified active galactic nuclei (AGNs) and 35 unidentified sources. The hard spectra of the latter suggest that many of them will probably also prove AGNs when follow-up observations are performed. Most of the detected AGNs belong to the local population (z<0.1). In addition, the hard X-ray band of the XSS (3-20 keV) as compared to most previous X-ray surveys, performed at photon energies below 10 keV, has made possible the detection of a substantial number of X-ray absorbed AGNs (mostly Seyfert 2 galaxies). These properties make the XSS sample of AGNs a valuable one for the study of the local population of AGNs. We carried out a thorough statistical analysis of the above sample in order to investigate several key properties of the local population of AGNs, in particular their distribution in intrinsic absorption column density (NH) and X-ray luminosity function ([2]). Knowledge of these characteristics provides important constraints for AGN unification models and synthesis of the cosmic X-ray background, and is further needed to understand the details of the accretion-driven growth of supermassive black holes in the nuclei of galaxies.

2 Summary

1. A well defined sample of 95 AGNs located at $|b| > 10^\circ$, detected in the 3–20 keV band by the RXTE slew survey is presented. Most of the sources belong to the local population (z<0.1). Accurate estimates of the intrinsic absorption column are presented for practically all of the sources.
2. The reconstructed NH distribution of AGNs is drastically different for low-luminosity ($\log L_x < 43.5$ erg/s) and high-luminosity ($\log L_x > 43.5$ erg/s) objects. Among the former, two thirds are X-ray absorbed ($22 < \log NH <$

ESO Symposia: Growing Black Holes, pp. 468–469, 2005.

24), whereas the corresponding fraction is less than 20% among the latter. This statistics does not take into account the population of Compton thick AGNs ($\log NH > 24$), to which our survey is not sufficiently sensitive.

3. The 3-20 keV AGN luminosity function is derived, which is the best-to-date in quality at photon energies above 2 keV for the local population. The luminosity function starts to flatten at $\log L_x \sim 43.5$ erg/s toward lower luminosities, approximately where obscured objects start to dominate the AGN population. A physical explanation for this behavior is required.
4. Comparison of the cumulative X-ray output of AGNs with $\log L_x > 41$ erg/s with the previously estimated total X-ray volume emissivity in the local Universe demonstrates that low-luminosity ($\log L_x < 41$) AGNs, non-active galaxies and clusters of galaxies together may be emitting a similar amount of X-rays to Seyfert galaxies.
5. A sample of 35 unidentified sources -AGN candidates, detected during the RXTE slew survey is presented. 12 of these have a likely ROSAT soft X-ray counterpart with a better than 1 arcmin localization, so their identification in the optical and other bands should not be difficult. The positions of the other sources are currently known with a 1 deg accuracy, and could be improved by scanning observations with X-ray telescopes.

References

1. Revnivtsev, M.; Sazonov, S.; Jahoda, K.; Gilfanov, M.: A&A, **418**, 927 (2004)
2. Sazonov, S. Yu.; Revnivtsev, M. G.: A&A, **423**, 469 (2004)

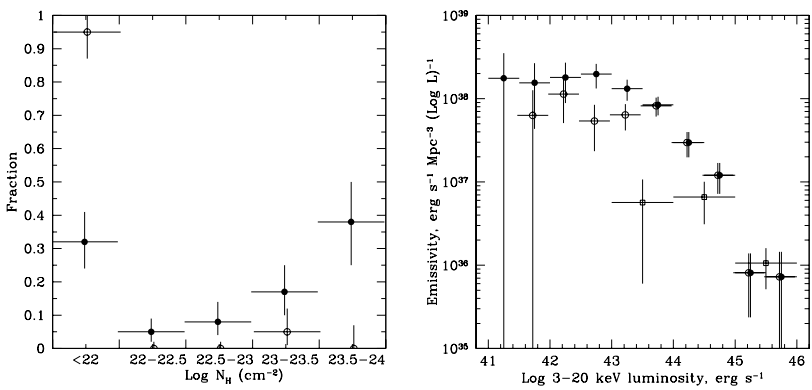

Fig. 1. *Left*: absorption column density distribution of emission-line AGNs with luminosity $\log L_x < 43.5$ erg s^{-1} (filled circles) and $\log L_x > 43.5$ erg s^{-1} (open circles). *Right*: contribution of AGNs with various luminosities to the local 3–20 keV volume emissivity of: Compton-thin non-blazar AGNs (filled circles), of unabsorbed non-blazar AGNs (open circles), and of blazars (open squares)

The Match Between Accreted and Local Mass Functions of Super-massive Black Holes

F. Shankar[1], P. Salucci[1], G.L. Granato[2,1], G. De Zotti[2,1], and L. Danese[1]

[1] SISSA/ISAS, via Beirut 2, I-34014 Trieste, Italy
[2] INAF - Osservatorio Astronomico di Padova, I-35122 Padova, Italy

Abstract. We present a new estimate of the local super-massive black hole (SMBH) mass function and show that it can be fully accounted for by the mass accreted during the luminous phases of X-ray selected active galactic nuclei (AGN) with a radiative efficiency of $\sim 10\%$. The AGN visibility times grow with SMBH relic mass and are generally in the range $\tau_{\rm vis} \geq 0.1$–$0.3\,{\rm Gyr}$.

1 Introduction

Spectroscopic and photometric studies have established that most, if not all, local galaxies with a significant spheroidal component host a central massive dark object (MDO) and that there is a well defined relationship between the MDO mass and the mass or the velocity dispersion of the host galaxy hot component. Although it is widely agreed that the MDOs are most likely quiescent SMBHs, leftovers of past nuclear activity, their evolution and growth history and their detailed relationship with AGNs is still matter of debate. We summarize here the main conclusions of a comprehensive analysis of this issue.

2 Results and Conclusions

Shankar et al. [4], following up ideas and methods presented by [2,3], have obtained new estimates of the local SMBH mass function, exploiting both photometric [1] and dynamical [5] data. The two approaches yielded fully consistent results and the mass function could be rather accurately determined in the BH mass range $10^6 \leq M_{\rm BH}/M_\odot \leq 5 \times 10^9$ where it can be well represented by:

$$\Phi(M_{\rm BH}) = \Phi_* \left(\frac{M_{\rm BH}}{M_*}\right)^{\alpha+1} \exp\left[-\left(\frac{M_{\rm BH}}{M_*}\right)^{\beta}\right], \qquad (1)$$

with $\Phi_* = 7.7(\pm 0.3) \cdot 10^{-3}\ {\rm Mpc}^{-3}\,(d\log M_{\rm BH})^{-1}$, $M_* = 6.4(\pm 1.1) \cdot 10^7\ M_\odot$, $\alpha = -1.11(\pm 0.02)$ and $\beta = 0.49(\pm 0.02)$ ($H_0 = 70\,{\rm km\,s^{-1}\,Mpc^{-1}}$). The total local SMBH mass density is $(4.2 \pm 1.1) \times 10^5 M_\odot/{\rm Mpc}^3$, about 25% of which contributed by SMBHs residing in bulges of late type galaxies.

Next [4] exploited the recent determination of the epoch dependent X-ray luminosity function of AGNs by [6], allowing for a luminosity-dependent bolometric correction, to derive the accreted SMBH mass density. For a standard mass to

ESO Symposia: Growing Black Holes, pp. 470–471, 2005.

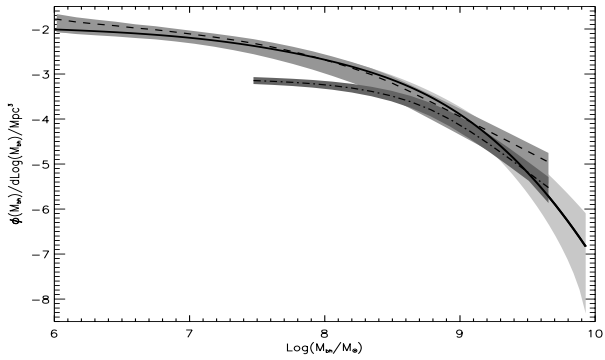

Fig. 1. Local SMBH mass function with its 1-σ uncertainty (solid line and light gray area) compared with the accreted SMBH mass function from X-ray (dashed curve and gray area) and optically (dot-dashed line and dark gray area) selected AGNs with its 1-σ uncertainty region

radiation conversion efficiency $\epsilon = 0.1$, they found $\rho_{\rm acc}^{HX} \simeq 4.1 \times 10^5 M_\odot/{\rm Mpc}^3$, in close agreement with the local SMBH mass density. Optically selected QSOs account for only $\simeq 35\%$ of the total SMBH mass density. The dominant contribution comes from Type 2 AGNs, mostly missed by optical surveys.

Further allowing for a decrease of the Eddington ratio $\lambda = L/L_{\rm Edd}$ with redshift, as suggested by observations, the accreted mass function was found to match very well the local SMBH mass function (Fig. 1). Optically selected, Type 1 AGNs account for the high mass tail of the AMF, while Type 2 AGNs take over at lower masses.

The mass-weighted duration of the luminous AGN phase is found to be $\langle \tau_{\rm lum} \rangle \simeq 0.5$–$1.5 \times 10^8$ yr. The visibility time during which the AGNs with present day BH mass $M_{\rm BH}^0$ contribute to observationally determined luminosity functions, increases with BH mass and obviously depends on the survey sensitivity; for the most sensitive X-ray surveys it ranges from $\simeq 0.1$ Gyr for $M_{\rm BH}^0 = 10^6\, M_\odot$ to $\simeq 0.3$ Gyr for $M_{\rm BH}^0 = 10^9\, M_\odot$; as for optical QSO surveys, objects with $M_{\rm BH}^0 < 3 \times 10^7\, M_\odot$ are not represented, and the visibility time of objects with $M_{\rm BH}^0 = 10^9\, M_\odot$ decreases to $\simeq 0.15$ Gyr.

References

1. R.J. McLure, J.S. Dunlop: MNRAS **331** 795 (2002)
2. P. Salucci, E. Szuszkiewicz, P. Monaco, L. Danese: MNRAS **307**, 637 (1999)
3. F. Shankar, P. Salucci, G.L. Granato, L. Danese. In: *http://www.exp-astro.phys.ethz.ch/ETH_Astro_2003/posters.html*
4. F. Shankar et al.: MNRAS accepted, astro-ph/0405585 (2004)
5. S. Tremaine et al.: ApJ **574**, 740 (2002)
6. Y. Ueda, M. Akiyama, K.Ohta, T. Miyaji: ApJ **598**, 886 (2003)

Black Hole Growth in a Cosmological Context and the Associated Cosmic Star Formation History

Y. P. Wang[1], T. Yamada[2], and Y. Taniguchi[3]

[1] Purple Mountain Observatory, Academia Sinica, China
[2] National Astronomical Observatory of Japan, Mitaka, Japan
[3] Tohoku University, Aramaki, Aoba, Sendai 980-8578, Japan

Abstract. Based on a co-evolution scenario of massive black holes (MBH) and their host spheroids, we trace the BH growth and the joint cosmic star formation history by ROSAT X-ray All sky surveys. We found: 1) the total amount of star formation associated with MBH growth is at least half of the net star formation at high redshift, which probably missed by the current UV/opt. deep surveys; 2) an upper limit of the abundance ratio of type 2 to type 1 QSOs is about 2, within the constraints of the local BH density, the Chandra hard x-ray deep surveys and the SCUBA counts; 3)the peak redshift of the massive spheroid formation in this case is around 1.5-2.

1 Modelling strategies and the results

The set of cosmological parameters $(\Omega_{\rm m}, \Omega_\Lambda) = (0.3, 0.7)$ and $\rm H_0 = 50$ km/s/Mpc is adopted throughout the calculation. The BH mass is derived from the X-ray luminosity by $\rm M_{bh} = \frac{\beta\, L_x}{0.013\,\epsilon}$, with an assumption of the Eddington ratio $\epsilon = \frac{\eta\,\dot{m}\,c^2}{\rm L_{Edd}}$. The AGN luminosity $\rm L_x$ at $0.5-2\,$KeV and $\rm M_{bh}$ are in units of 10^{40} erg s^{-1} and $\rm M_\odot$; We adopt the bolometric correction at soft x-ray $\beta = 20$ based on the mean type 1 AGN SED and assume each AGN shines for a constant time scale $\rm t_Q = 5 \times 10^8$ yrs, close to the e-folding time [3]. The "duty cycle" of AGN active phase is defined as $\rm f_{on} = t_Q/t_{Hub}(z)$, $\rm t_{Hub}(z)$ is the Hubble time. We approximate $\epsilon = 10^{\gamma\,(log L - 49)}$, $\gamma \approx 0.2$ is a scaling factor from various AGN observations.

Considering all AGNs in Miyaji et al. (2000) sample as unobscured type 1 [5], the BH mass function could be derived from the observed XLF by:

$$\frac{\mathrm{d}\,\Phi(z, M_{\rm bh})}{\mathrm{d}\,M_{\rm bh}} = \frac{0.013\,\epsilon}{\beta\, f_{\rm on}}\,\frac{\mathrm{d}\,\Phi(z, L_{\rm x})}{\mathrm{d}\,L_{\rm x}} \tag{1}$$

The abundance ratio of type 2 to type 1 AGNs is described as $\rm R_{2-1} = 4\,e^{-\frac{L_x}{L_s}} + \alpha\,(1+z)^p\,(1-e^{-\frac{L_x}{L_s}})$. $\rm L_s = 10^{44.3}$ erg s^{-1} is the e-folding luminosity. α and p are free parameters within the model constraints of local BH density and the SCUBA number counts.

The mass function of spheroids may have a similar form to the BH mass function according to a BH-bulge co-evolution scheme:

ESO Symposia: Growing Black Holes, pp. 472–474, 2005.

$$\frac{\mathrm{d}\,\Phi(z, M_{\rm sph})}{\mathrm{d}\,M_{\rm sph}} = \frac{\mathrm{d}\,\Phi(z, M_{\rm bh})}{\mathrm{d}\,M_{\rm bh}} \times \mathrm{R} \tag{2}$$

R is the BH to bulge mass ratio, a mean value of ~ 0.002 is adopted as the first approximation ([7]; [4]).

Assuming a star formation time scale $\mathrm{t_{sf}} = 5 \times 10^8$ yrs and SFR $= \frac{\mathrm{M_{sph}}}{\mathrm{t_{sf}}}$ for spheroid formation, we give similar to eq.1 the $850\,\mu m$ luminosity function at different redshift as below, with a mean value $\mathrm{L_{FIR}/L_\odot} = 3.8 \times 10^9$ SFR $(\mathrm{M_\odot\,yr^{-1}})$ and a mean color ratio $\mathrm{R_c} = \mathrm{L_{FIR}/L_{850}} \sim 5 \times 10^3$ from IRAS, ISO and SCUBA surveys [2]:

$$\frac{\mathrm{d}\,\Phi(z, L_{850})}{\mathrm{d}\,L_{850}} = f_{\widehat{\rm on}}\,\frac{\mathrm{d}\,\Phi(z, M_{\rm sph})}{\mathrm{d}\,M_{\rm sph}}\,\frac{\mathrm{d}\,M_{\rm sph}}{\mathrm{d}\,L_{850}} \tag{3}$$

where $\mathrm{f_{\widehat{on}}} = \mathrm{t_{sf}/t_{Hub}}$ reflects the fraction of galaxies with intensive star formation ongoing. $\frac{\mathrm{d\,M_{sph}}}{\mathrm{d\,L_{850}}} = \frac{\nu_{850}\ \mathrm{R_c}\ \mathrm{t_{sf}}}{3.8 \times 10^9\ L_\odot}$. The model results are shown in Fig.1.

References

1. Barger, A. J., Cowie, L. L., Bautz, M. W. et al. *AJ* **122**, 2177 (2001)
2. Chary, R., Elbaz, D. *ApJ* **556**, 562 (2001)
3. Elvis, M., et al. *ApJS* **95**, 1 (1994)
4. Merritt, D., Ferrarese, L. *MNRAS* **320**, L30 (2001)
5. Miyaji, T., Hasinger, G., Schmidt M. *A&A* **353**, 25 (2000)

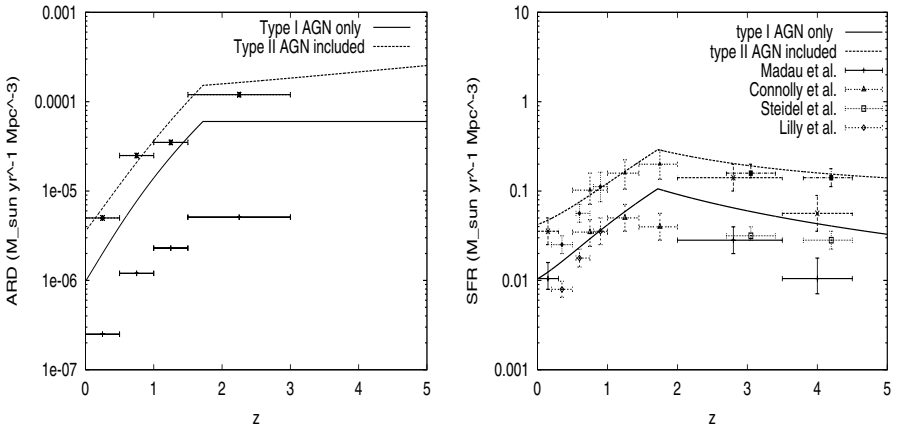

Fig. 1. (*left*) ARD vs. redshift by the model (lines). The blue asterisks represent the ARD calculated from the bolometric luminosities of 69 hard X-ray selected sources; while the red crosses from their X-ray luminosities as a low limit [1]. (*right*) Co-moving SFR in the host galaxies of different AGN samples (lines). The data are indicated in the Figure, the filled symbols are of dust correction (×4.7) [6].

6. Steidel, C. C., Adelberger, K. L., Giavalisco, M. et al. *ApJ* **519**, 1 (1999)
7. Wang, Y. P., Biermann, P. L. *A&A* **334**, 87 (1998)

Some of the LOC members and student helpers

At the Conference hall

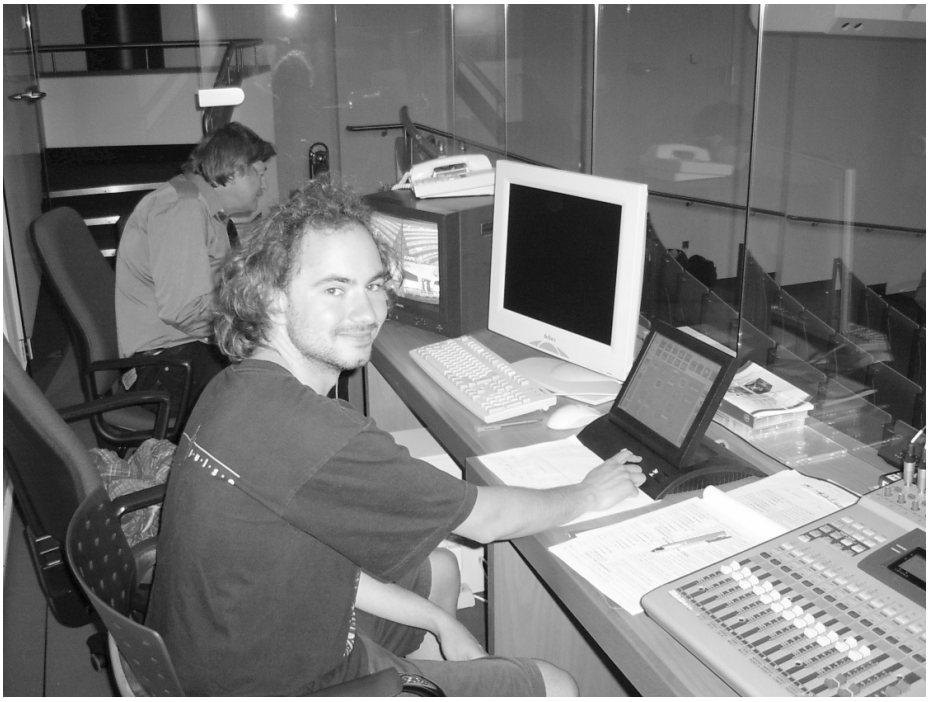

At the electronics controls

A Black Hole Manifesto

R. Blandford

KIPAC, PO Box 20450, MS29, Stanford, CA 94309, USA

Abstract. A brief overview is presented of some aspects of the study of the growth of massive black holes in active galactic nuclei. It is argued that relativistic effects described by the Kerr solution of a spinning black hole are essential and are responsible for the formation of relativistic jets. It is further asserted that when the mass accretion rate is much larger and much smaller than the Eddington rate, the accretion is adiabatic and accompanied by prodigious outflows, ultimately driven by the energy flow through the disk associated with the magnetic torque. It is conjectured that this torque is dictated by the magnetic conditions at large radius and that, typically, there is preferred radial polarity in the magnetic field that joins the disk along with freshly accreted gas at its outer boundary. The associated magnetic flux is concentrated by the inflowing gas and soon becomes dynamically dominant so that it escapes the disk, driving an MHD wind. The radial field persists all the way down to the event horizon of the black hole and supplies a large flux to the hole when the disk is thick. Consequently, rapidly spinning holes accreting rapidly or slowly should be accompanied by relativistic jets which spin down the hole. The disks associated with intermediate accretion rates should be relatively thin and spin up the hole without forming powerful jets. This model provides a qualitative interpretation of the observed cosmological evolution of AGN, whereby the black holes that form later, lose the competition with star formation and grow to smaller masses. The co-evolution of black holes and their host galaxies is briefly discussed along with the impact on the intergalactic medium.

1 Introduction

The invitation to attend a symposium on "Growing Black Holes in Garching" was irresistible. Was this a breakthrough in experimental astrophysics? Could it be an insight into the darker reaches of the military? Perhaps it was a reference to the U-Bahn extension. All this brings home the fact that the phrase "black hole", coined by John Wheeler in 1968, has become a multi-purpose metaphor and firmly established in the vernacular. It has even entered the world of commerce. For example, I am the proud owner of a gopher trap, sold under the name "The Blackhole". (Rather ominously, it is completely ineffectual.)

Now I have the distinction of being the last speaker in the meeting. I inquired as to whether or not a summary was expected or if being last had a different implication! The answer seemed to be a bit of both. I will therefore provide an idiosyncratic overview of several of the topics that have come up at this meeting and cross-reference some of the preceding contributions, in brackets. In order to organize these topics, I note that elections are very much on people's minds and I have indulged in the conceit that black holes are in need of a political manifesto

ESO Symposia: Growing Black Holes, pp. 477–490, 2005.

- a nostalgic reminder of the time when it was possible to advocate and debate policy options in a serious manner.

2 Economic Policy

2.1 Spin

Astrophysical black holes are described by the Kerr metric with one shape parameter (specific angular momentum a, or equivalently, the angular velocity $\Omega = [1-(1-a^2)^{1/2}]/2)$ and a scaling mass, m which one can set to unity for calculations. a is limited to one and Ω to a half. Numerically $m = (M/10^8\mathrm{M}_\odot)\mathrm{AU} \equiv 500(M/10^8\mathrm{M}_\odot)\mathrm{s} \equiv 2\times 10^{62}(M/10^8\mathrm{M}_\odot)\mathrm{erg}$. The spacetime around the horizon has some important properties. There is a minimum radius for stable circular orbits which shrinks from 6 to 1 as the hole is spun up from rest to its maximal value. The binding energy of this orbit increases from 0.06 to 0.42. The importance of this radius is almost certainly over-rated because of the presence of fluid, magnetic and radiative stress, together with time-dependence which can lead to a quantitatively different energy release.

2.2 Deficit Spending

Of more importance is the ergosphere, a region exterior to the horizon (radius $r_+ = 1+(1-a^2)^{1/2}$) where particles must move, with outer, equatorial radius 2. Within the ergosphere, there exist orbits with negative total energy (including rest mass) that cross the horizon. The immediate implication is that it is possible to extract mass from a spinning hole. This leads to the concept of an irreducible mass $m_0 = (r_+/2)^{1/2}$ below which the hole mass cannot shrink through classical processes and a reducible mass $1-m_0$ which is accessible in much the same way that the spin energy of a neutron star can be extracted. Up to 29 percent of the mass of a hole is available to power nonthermal processes.

There are several ways to imagine this happening in practice. One possibility is to use electromagnetic field to direct negative Poynting energy flux across the horizon. Another is to apply a magnetic torque to infalling gas just outside the horizon, so that it is dragged onto a lower angular velocity orbit spending its orbital energy in such a profligate fashion that there is a bill to be paid by the hole's gravitational mass when it crosses the horizon. There is a lot of opportunity for this to occur. If we consider the equatorial plane of the ergosphere, then we find that the proper area, spanned by a family of zero angular momentum observers, increases from zero to 18π as the hole is spun up. In a flat space it would only increase to 3π. By contrast, the hemispheric area of the horizon decreases from 8π to 4π.

Of course, all of this is predicated on general relativity being the correct theory of strong gravity. It would be wonderful to test it using observations of black holes.

2.3 Consumables

It is tempting to think that there are global "macroeconomic" principles that govern the behavior of accretion disks, large and small. If so, this would allow observers to combine observations of AGN with those of X-ray binaries to get a more complete understanding of the accretion process. Elsewhere, I have advocated one such principle – that the mode of accretion is supply-driven. Specifically, it is suggested that gas will spiral inward through the disk until it reaches a critical radius within which it can no longer radiate away the liberated energy. There is an outer radius, $r_{\rm out}$, for the disk which is roughly the square of the specific angular momentum of the supplied gas. The natural scale for the mass supply rate $\dot{m}_{\rm out}$ at this radius is the critical or Eddington rate, which in these units is $\dot{m}_E = 4\pi/\kappa$, where κ is the relevant opacity, in this case, the Thomson opacity. When $\dot{m}_{\rm out} << 1$, it appears that the liberated binding energy heats the ions which are unable to heat the electrons on the inflow timescale. The disk then becomes non-radiative, or adiabatic, within a radius $r_{\rm tr}$ which is decreasing function of $\dot{m}$. It is generally supposed that $r_{\rm tr}$ is near the horizon when $\dot{m}_{\rm out} \sim 1$ and the whole disk can radiate. Conversely, when $\dot{m}_{\rm out} >> 1$, there is no problem with radiating, but the photons cannot diffuse out of the infalling gas fast enough and the heat is advected with the gas. Typically, $r_{\rm tr}$ will increase roughly linearly with $\dot{m}_{\rm out}$ where the coefficient of proportionality will reflect detailed geometrical factors. In both the low and the high mass supply cases, the accretion rate is demand-limited.

There are two quite distinct views of what happens within $r_{\rm tr}$ when it is $>> 1$ [Abramowicz, Tanaka]. The first is that the most of the energy is carried across the horizon, with or without convection. This is the ADAF (or CDAF) viewpoint. The alternative, which Begelman and I have advocated, is that most of the energy and mass is carried off in a wind. This is the ADIOS view. The differences are not small. In typical applications, the gas densities near the black hole are different by several orders of magnitude and radiative implications enormous. The rationale for the ADIOS view is a simple piece of physics, important in the history of the subject. Gas accretes because there is a torque G which the gas interior to some radius r exerts on the exterior gas. This torque does work at a rate $G\omega$, where ω is the disk angular frequency. A simple calculation shows that, if the mass flow were conservative, as in the ADAF model, this additional outward-directed energy flux would be sufficient to unbind the infalling gas if it is unable to radiate efficiently. (If the gas can radiate, the local rate of energy dissipation is three times the rate of release of binding energy in a steady state.) Therefore, we argue, the gas itself must carry off the liberated energy in the form of a wind [King, Heinz].

When $r_{\rm tr} >> 1$, the rate of mass accretion by the hole $\dot{m}_{\rm in}$ is much less than $\dot{m}_{\rm out}$. It seems likely that when $\dot{m}_{\rm out} >> 1, \dot{m}_{\rm in} \sim \epsilon^{-1}$, where ϵ, the efficiency is ~ 0.1 so that the flow is Eddington-limited close to the hole, and at all radii less than $\sim r_{\rm tr}$. In order to see if this interpretation is viable and to be more precise about the nature of the outflow will require more detailed radiative hydrodynamical simulations than are practical at present. When $r_{\rm tr} >> 1$, the

net accretion rate will be determined by the local angular momentum transport within the disk and this is model-dependent.

3 Energy Policy

3.1 Energy Flow

If we consider the gas orbiting in a annular ring with radius r satisfying $1 << r << r_{\rm tr}$, then there will be a difference between the net flow of angular momentum (torque plus the angular momentum carried inward by the gas) entering and leaving the ring. This difference must be carried off by the outflowing gas. If the outflow is purely gas, then it will carry off roughly the specific angular momentum of the gas in the disk at its launch point. However, if, as I shall argue, magnetic field is present, then the specific angular momentum of the wind can be much larger and the mass loss correspondingly less.

The energy flow is intimately related to the angular momentum flow, with the important distinction that energy that is carried off derives from small radius, while the angular momentum resides mostly at large radius. For low mass supply rates, a reasonable conjecture is that the rate of mass accretion within $r_{\rm tr}$ rises roughly $\propto r$ so that the overall radiative efficiency with respect to the mass accreted is also high. For intermediate supply rates, when the gas can radiate down to close to the horizon and the flow is nearly conservative, we expect that the disk luminosity will be roughly $\sim \epsilon \dot{m}_{\rm out}$. However, for $\dot{m}_{\rm out} > \epsilon^{-1}$, $\dot{m}$ should again rise linearly with radius within $r_{\rm tr}$ and luminosity will exceed the Eddington value, by no more than a logarithmic factor. On this view, in all three cases mass is accreted efficiently. Black holes are green!

3.2 Magnetic Field

It is generally acknowledged that magnetic field is also responsible for the torque G [Modjaz]. The strongest argument is the existence of the magneto-rotational instability (MRI), which implies that a seed vertical field will grow in strength on a dynamical timescale, $\sim \omega^{-1}$. This is a local instability which derives from the observation that magnetic field lines that connect two orbiting rings of gas, will increase the angular momentum of the outer one and drive it further out. Now the linear instability theory only tells what cannot be. In order to understand the steady state requires extensive numerical simulations which have been carried out with increasing sophistication and resolution. They exhibit strong radial gas motions and a strong torque. The field lies mostly in the disk plane. These simulations have mostly been carried in disk models with no net magnetic field, although some have admitted a net vertical field within the disk.

There is another, interesting possibility that I would like to exhume and discuss. Suppose that there is a preferred polarity in the magnetic field that is supplied, along with the gas to the outer disk. Perhaps there is a giant molecular cloud at its Roche limit with an organized field that has been dragged into

corotation. The magnetic field will be incorporated into the inflow and have a net radial component. If we make a very simple disk model, eschewing complications like self-gravitation, and assume the height $H \propto r$, then the magnetic pressure associated with the radial component alone will vary $\propto r^{-4}$, increasing faster than the $\propto r^{-5/2}$ variation of the gas pressure in a conservative α disk model. The magnetic pressure will quickly dominate the gas pressure and flux will leak from the disk surface with a temporally- and azimuthally-averaged vertical strength $< B_z > \sim \mp H < B_r > /r$. Now, toroidal field will be generated by the differential rotation. However, it cannot build up indefinitely and there must be some dissipation to allow field lines to wander and the gas to move radially inward through the disk. This is where the MRI comes in. The vertical field, B_z is inadequate to suppress the instability and although the stress may be associated with the mean field $< B_r B_\phi > /4\pi \sim | < B_r > || < B_\phi > |/4\pi$, the dissipation is associated with the small scale field fluctuations that are constantly being regenerated by the MRI. The largest effect will be associated with magnetic loops with scale $O(H)$ and the associated kinematic viscosity will be $\sim \omega H^2$ or $\alpha \sim 1$. If we further suppose that the toroidal field builds up until $B_\phi^2/4\pi \sim P$, where P is the gas pressure, then we conclude that $| < B_r > | \sim | < B_\phi > |$. The field lines trace out a Archimedian spiral in the disk until they escape from one of its surfaces. It would be very interesting to perform numerical simulations of the MRI in accretion disks with mean radial field to test the validity of these conjectures and measure the numerical coefficients.

Nevertheless, if we adopt this model, there are several interesting consequences. The first and most immediate is that the exterior magnetic torque acting on the disk surfaces is $\mathcal{G} \sim B_z B_\phi r^2$ and therefore $\mathcal{G} \sim \partial G/\partial r$. This implies that the exterior torque is just as important as the interior torque and just as much angular momentum is extracted from the disk as flows through it, to order of magnitude. The same is true of the energy flow. Disks may therefore be associated with powerful winds. Presumably the disks are much thicker and the winds are stronger and carry away more mass when the disk gas is unable to cool radiatively. If we suppose that the mass accretion rate scales with radius as $\dot{m} \propto r^n$, then the magnetic field scaling will be $B \propto r^{n/2-5/4}$. These winds will contain toroidal magnetic field which will be increasingly important as they propagate away from the disk and will produce some collimation towards the rotation axis. Note that the pattern of signs of the toroidal component of the magnetic field is different from what would happen if the disk were threaded by a net vertical field. The observed sign will be the same on the same side of the axis and on opposite sides of the disk. This pattern may be observable. There is no reason why the flux leaving the upper and lower disk surfaces should be the same and, consequently, the two outflows could be unequal.

An additional consequence of magnetic instability near the disk surfaces is the heating of a powerful corona with temperature approaching the escape temperature. This corona is responsible for the nonthermal X-ray emission associated with accretion disks. Thermal photons are Comptonized by hot electrons in the

disk and produce the power law spectra that are commonly seen from Seyfert galaxies and quasars.

3.3 Radio-active Waste Disposal

It is of interest to ask what happens at small radius close to the central black hole [Krolik]. Again, there are differences depending upon the assumed magnetic geometry. If we continue to suppose that there is a net radial magnetic field component, similar in strength to the toroidal component, this will be advected across the horizon by the infalling gas. There must then be a corresponding magnetic field threading the horizon at high latitudes with opposite direction in the northern and southern hemispheres. The equatorial field lines derived from the disk are separated from the high latitude field lines by two conical current sheets that terminate in a Y-type neutral ring. (This contrasts with the single equatorial current sheet which must be invoked in the standard geometry.) The equatorial field lines will allow some additional energy to be extracted from the inflowing gas until it approaches the hole super-Alfvénically. This can increase the overall energy efficiency of the accretion disk while steadily spinning down the hole. (This effect is much larger when there is a net radial field than when this is absent.) The high latitude, open field lines are likely to be (electromagnetically) force-free and should extract more spin energy directly from the black hole. There should then be a very clean separation between the mildly relativistic MHD outflow on field lines attached to the disk and the ultrarelativistic outflow deriving from the black hole's event horizon.

It is possible to make a rough estimate of the ratio of the jet to disk power if we assume that all of the flux emanating from the inner edge of the disk enters and then exits the horizon and that the magnetic pressure in the disk is comparable with the gas pressure. The answer is

$$\frac{L_{\rm jet}}{L_{\rm disk}} \sim \left(\frac{\Omega}{\omega_{\rm in}}\right)^2 \left(\frac{s_{\rm in}}{\alpha\beta c}\right) \tag{1}$$

where $s_{\rm in}$ is the sound speed at the inner edge of the disk and β is the ratio of the gas to the magnetic pressure. (Detailed numerical simulations should improve this estimate.) The jet power can plausibly exceed the total disk power. The two factors which control the jet power are the disk thickness, which, in turn, is a function of the mass accretion rate, and the spin. Both of these factors depends upon the evolutionary history.

It is instructive to consider the global current flow [Sikora, Maraschi]. In the conventional magnetic geometry, the poloidal magnetic field has odd parity (like a dipole) and the poloidal current has even parity, like a quadrupole. In the possibility examined above, the opposite is true. The current is driven mostly by the unipolar inductor formed by the spinning black hole and the inner accretion disk. The EMF is given, to order of magnitude by $\mathcal{E} \sim \Omega\Phi \sim 100(B/10^4{\rm G})(M/10^8{\rm M}_\odot){\rm EV}$ (i.e. typically $10^{20}{\rm EV}$), where Φ is the magnetic

flux threading this region. The associated impedance, under electromagnetic conditions, is 100Ω and so the current is $I \sim (B/10^4\mathrm{G})(M/10^8\mathrm{M}_\odot)\mathrm{EA}$. The power carried away by the jets is roughly $\sim VI \sim 10^{45}(B/10^4\mathrm{G})^2(M/10^8\mathrm{M}_\odot)^2\mathrm{erg\,s}^{-1}$.

Now, most models of relativistic jets are, implicitly, fluid dynamical, yet their origins are commonly assumed to be electromagnetic. This requires that the electrical circuit be completed, and the electromagnetic energy either dissipated or converted into bulk kinetic energy, close to the hole (the electromagnetic energy may not be fully dissipated). The field may become quite disorganized. Mechanically, these "AC Poynting jets" behave like fluid jets with an isotropic pressure and a high internal sound speed so that they do not form strong shocks. By contrast, in the "DC Poynting flux" jet model, there is an organized magnetic field with an anisotropic stress tensor. The dissipation occurs and nonthermal emission is observed where the current flows, in particular along the jets. In other words, the jets are pinched by the toroidal magnetic field which extends outward in cylindrical radius through the sub-relativistic disk wind. Pinches are notoriously unstable but can be stabilized by the internal velocity gradient of the center of momentum frame (which moves with a speed $\boldsymbol{E} \times \boldsymbol{B}/B^2$) and the jet expansion. Some of the helical structure that is seen in observed jets may be associated with unstable modes. Depending upon the nature of the interaction with the environment, the electrical circuit will mostly complete at large distances from the hole connecting the ends of the two jets. If there is a sharp discontinuity between the expanding radio source and the circumgalactic medium, as appears to be observed sometimes in cluster radio sources, much of this will be through a sheet current flowing along this discontinuity.

Although it is possible to derive force-free solutions of jets, the observed sources are likely to contain a significant internal pressure, perhaps associated with locally-created pairs, in order to emit efficiently. There are two alternatives to diffusive shock acceleration which may not be effective under these conditions as strong shocks will not form. The first of these is electrostatic acceleration and takes place at "gaps" that open up in the plasma if there are insufficient charge carriers. This can occur especially around current sheets and reconnection sites. A turbulence cascade can also increase the need for charge carriers as the scale length of the fluctuations decreases. The second is stochastic acceleration by electromagnetic wave modes that are formed at the high frequency end of a wave turbulence spectrum. There is no problem accelerating even the X-ray synchrotron-emitting electrons, with energies up to 100TV, under these conditions.

This provides an explanation as to *how* jets and winds form. It does not explain *why* they form. One way to think about this is that accretion disks are supplied with too much angular momentum and magnetic flux and that both of these have to be removed in order for the gas to accrete. In addition, they release too much binding energy which also must be removed if the gas cannot radiate efficiently. Outflows provide the means of disposing of the surplus angular momentum, magnetic flux and energy and may carry off most of the mass.

4 Education

4.1 Grand Unified Theory

The next task is to relate these theoretical ideas to observations. The three key parameters are the hole mass m, the dimensionless mass supply rate $\dot{m}_{\rm out}/\dot{m}_{\rm E}$ and the dimensionless spin of the hole Ω. The simplest, and oldest view is that the powerful, optical quasars have high, dimensionless mass supply rates and they create powerful outflows at low latitudes driven by radiation and magnetic stress. On average, the holes spin down and radio sources – the radio-loud quasars – are only associated with younger, rapidly spinning holes. Broad absorption lines are observed from those quasars where the line of sight passes through their winds, presumably at high inclination. The outflows themselves are launched through Compton scattering and magnetic fields but, resonance lines become important in the outer parts of the flow when the gas is cooled.

Similarly, when the accretion rate is low, the disks are also thick and the holes can retain their spin for a long while. When the hole mass is large, these are the radio galaxies that evolve from FRIIs to FRIs. When the hole masses are small, these are the weak radio sources that dominate the faint counts. The situation is epitomized by Sgr A* in our Galactic center [Genzel, Eckart, Baganoff]. Here, we have a very low mass hole $\sim 3\times 10^6{\rm M}_\odot$ with a low mass accretion rate $\sim 10^{21}{\rm g\,s^{-1}}$. The bolometric luminosity, in the far infrared - sub mm region of the spectrum, is $\sim 10^{37}{\rm erg\,s^{-1}}$, suggesting a net radiative efficiency $\sim 10^{-5}c^2$ with respect to the supplied mass. However, it has recently been proposed that there are two lobes of hot, X-ray emitting gas on either side of the disk plane that require a power $\sim 10^{39}{\rm erg\,s^{-1}}$ to replenish [Morris]. Based on the scheme outlined above, I suggest that the disk is conservative down to a transition radius $r_{\rm tr}\sim 10^3m\sim 10^{15}$cm where it becomes adiabatic due to the inadequate electron-ion coupling. The disk thickens and the excess mass is blown away from all interior radii, driven by the viscous energy transport. the wind speeds range from $\sim 0.03\sim 10,000{\rm km\,s^{-1}}$ to mildly relativistic and the mass inflow rate falls with radius to $\sim 10^{17}{\rm g\,s^{-1}}$ near the hole. At these low densities the dominant emission processes are nonthermal – synchrotron and inverse Compton radiation – and the disk becomes radiatively efficient with respect to the *accreted* mass.

In between these two limiting regimes lie classical, radiative disks which are relatively thin in the vicinity of the horizon and where the influence of the magnetic coupling to the hole is minor. Here, we expect that Ω (still in units of m^{-1}) will increase at a modest rate until it reaches a large, equilibrium value, as mass is accreted from around the innermost stable circular orbit with higher specific angular momentum than the hole.

Observations of Galactic X-ray transients allow us to observe transitions between these different accretion-outflow states on vastly shorter timescales relative to the accretion timescales and seem to support this qualitative picture.

A complicating feature of these unifying models is the role of orientation. What we see depends upon where we stand. This has two major implications. Firstly, relativistic beaming of jets is a major effect. A blob moving with a

Lorentz factor of 10 is observed with a billion times more flux when approaching than when receding. In other words, the bright sources in radio catalogs are not representative. In addition, as sources are likely to be inhomogeneous, what we see can be dominated by an insignificant region in the whole source. This complicates statistical studies considerably. Secondly, many sources, especially lower power AGN, are obscured [Beckert, Urry, Comastri]. Usually, the shadow is presumed to be cast by a thick, orbiting torus. However, it has never been clear how this torus is supported and it may be more sensible to think in terms of a seriously warped, though locally quite thin, disk. An alternative possibility is that the absorption arise in a dusty wind. Hard X-ray observations are crucial as they provide the only way to see through to the relativistic region.

5 Agriculture

5.1 Hole Growth

We must next turn to the long term implications of this conjectured physical identification of modes of accretion with observed source properties. There are three relevant timescales to consider.

The first of these is the disk flow time. This is almost certainly dictated by the conditions at the outer disk radius. For illustration, take the characteristic nuclear velocity as $\sim 10^{-3}$. This implies that the orbital angular frequency is $\Omega_{\rm out} \sim 10^{-9} m^{-1}$ and the characteristic flow time $t_{\rm out} \sim \Omega_{\rm out}^{-1}(r_{\rm out}/H_{\rm out})^2\alpha^{-1}$, ignoring some serious complications like self-gravitation. This is plausibly $\sim 3M_8$Myr and comfortably more than the flowtimes in the largest observed jets and the sense of the current flow in the large scale radio source can be dictated by the net radial field at $r_{\rm out}$, as asserted above.

The second timescale is the time to change the spin of the hole. Spin up is effected by accreting orbital angular momentum. The evolution of the hole spin parameter depends upon the specific angular momentum and energy (including binding energy) crossing the horizon. As is well known, the hole spins up until it is nearly maximally rotating if we adopt the angular momentum and energy appropriate to the marginally stable orbit. This model is unrealistic, as discussed above. However, it is still generally true that the equilibrium angular velocity is likely to be quite high.

The third timescale is that to double the mass of the hole. This depends upon the mass accretion rate. We have argued above that this is "demand-limited" and that it is unlikely to be shorter than the Eddington timescale, ~ 500 Myr multiplied by the effective radiative efficiency ~ 0.1.

All three timescales are comparable for large holes which will complicate separating their influence on the observations.

5.2 Episodic Accretion

Observations of binary X-ray sources show that accretion is generically non-steady at high mass accretion rates. There are Quasi-Periodic Oscillations (QPOs)

with frequencies from Hz to kHz. Scaling up to billion solar mass holes gives timescales from months to decades. Most AGN have not been observed long enough to measure the massive black hole counterparts of QPOs although a few low mass cases have been reported. Such state transitions may have an impact on the mean mass accretion rate.

Another form of episodic accretion involves the tidal capture and disruption of stars. Recent observations of the Galactic center strongly suggest that the supply of stars to capture orbits is far greater than had been presumed. Furthermore, the discovery [Komossa] of plausible instances of this process suggests that typical AGN may accrete several percent of their mass in this fashion. However, stellar accretion is unlikely to dominate the mass supply rate [Merritt].

5.3 Cosmological Evolution and the X-ray Background

Averaging over this short term variation, we must still account for the observed, dramatic evolution of quasars. The bright quasars are found to be most prevalent when the Universe was a few Gyr old [Brandt, Fan, Netzer]. However, the fainter sources show that more numerous, lower mass holes evolve later and are most prevalent when the Universe was closer to half its present age [Hasinger]. This phenomenon, recently termed "cosmic downsizing" [Merloni], was anticipated in the "Feast or Famine" model of AGN evolution. There is much mass around at early times so that the first holes that start to grow continue to grow exponentially, in an Eddington-limited fashion, until they exhaust their gas supplies. The holes that start later, have smaller reserves of gas to call upon, as star formation will have depleted the gas supply, and reach smaller asymptotic masses.

There have been great strides in understanding the X-ray background in recent years, largely through the deep X-ray surveys [Hasinger, Fabian]. These have shown that, at energies around ~ 3 keV, the background comprises ~ 200 million resolved sources. The situation is much less clear at higher energies. Part of the problem is that we are not confident that we know the shape of the spectrum as this has not been fully measured since the days of HEAO-1. The peak of the spectrum, in $dU/d\ln E$ is around 30 keV and apparently quite sharply-peaked. This is generally associated with obscured AGN where, it is supposed, a Comptonised, power law source is processed by scattering and absorbing gas. Photo-electric absorption causes the spectrum to rise at low energy, while Compton recoil causes it to fall off at high energy. The precise emergent spectrum is quite model-dependent and a variety of shapes can be produced. However, whatever the luminosity- and angle-averaged emergent spectrum at a given redshift, it is clear from the narrowness of the peak that the source redshift distribution must be surprisingly narrow and centered on epochs much later than that of peak quasar activity. Redshift surveys of the high energy sources from Chandra do, indeed, exhibit a relatively narrow redshift distribution.

We should learn much more about this background from studies of hard X-ray variability which will limit the amount of scattering, and mid-infrared observations of the re-radiated, absorbed X-rays with the Spitzer Space Telescope

[Brandl, Koekemoer]. Swift will probably provide some more observations. However, we will have to be patient until NuSTAR is launched in 2009. This should be able to detect around 300 sources per square degree, up to 60 keV, equivalent to ten million sources over the whole sky, significantly less than the numbers seen at lower X-ray energy. On a somewhat longer timescale, EXIST will observe the whole sky up to ~ 600 keV but with lower sensitivity.

6 Social Policy

6.1 Births

An interesting puzzle is the initial mass of black holes and the manner in which they grow initially [Madau]. The general presumption has been that they are formed with $\sim 100 - 1000 M_\odot$ masses perhaps as Population III stars within rare $> 3\sigma$ peaks [Bromm]. (If they were to form at a million solar masses, for example, then we might be surprised that we do not see Gamma Ray Burst luminosities sustained for months to years.) Now, we have argued that hole growth is likely to be demand-limited and if we take this rule literally, then there may be insufficient time for holes to grow to billion solar masses in, say half a billion years. However, this law may not be relevant when the mass supply rate was so high that the trapping radius exceeded the Bondi radius, around $r_{\rm out}$. So, if the mass supply rate is $\sim 100 M_\odot\,{\rm yr}^{-1}$, then holes can grow linearly to $\sim 10^6 M_\odot$ before the accreting gas starts to be blown away.

6.2 Childhood

A detailed understanding of what actually happened to the population of black holes as the Universe expanded and galaxies formed and grew, almost certainly awaits the deeper infrared observations that will be needed to follow the star formation history of the universe and to elucidate the relationship between starburst and AGN activity. This relationship probably lies at the heart of the hole mass–bulge velocity dispersion relation.

6.3 Marriages

There has been much attention paid to the influence of black hole mergers [Loeb]. The first thing that can be said is that the extreme view – that black holes acquire most of their mass through major mergers – is quite unlikely to be true. The luminosity density of bright quasars as well as the more numerous, lower power sources responsible for the hard X-ray background is so great relative to the relict hole mass density that the holes would seem to have been assembled out of efficiently radiating gas. (This also precludes inefficient, advective flows being involved, as discussed above.) It is, however, possible, on energetic grounds, for lower mass holes to have been assembled from minor mergers. These, though, have the drawback that they tend to spin down the holes. The reason is that,

if the orbital angular momenta are randomly-directed in space, then the minor holes will plunge from larger orbital radii, with larger angular momenta when they are on retrograde, as opposed to prograde orbits. These minor mergers are among the most promising LISA sources [Phinney, Schutz, Danzmann].

A second, possible consequence of black hole mergers is that they may create a less cuspy stellar distribution in the galaxy nucleus. This can account for the measured stellar properties of massive elliptical galaxies [Bender].

It has long been recognized that asymmetric black hole mergers will impart a recoil on merged masses through the radiation of linear momentum. Recent calculations show that is nearly an order of magnitude smaller than originally estimated and, as a consequence, the black holes will not escape the nucleus [Hughes]. Recently merged holes may be significantly displaced from the center of the galaxy but this may be hard to see as such black holes may not be accreting.

7 Domestic Policy

7.1 Co-Evolution

For a long while, AGN were considered to be an unimportant and independent perturbation on the formation of galaxies. They could happen at any time without seriously impacting the initial morphology of the host galaxy and its development with time. Following the discovery of buried (or Type 2) AGN, it became clear that massive black holes were more luminous and more active than had been suspected. Extreme statements were made that the AGN luminosity density could dominate that from stars. This belief, coupled with the discovery of quasars with redshifts greater than 6 led to the suggestion that the black hole eggs precede the galactic chickens. Nowadays, the view is somewhere in between these extremes. Black holes probably play a large role in the formation and evolution of galaxies, while they do not dominate the cosmological luminosity density.

The major connection is to the bulge, most accurately through its velocity dispersion. It seems inevitable that the holes and bulges grow together [Rix, Kauffmann, Mathur, Forman, Sazonov]. The former may be assembled during gas-rich mergers of protogalaxies where some fraction of the gas falls to the bottom of the potential well. However, the response of the black hole, when supplied with copious gas, is to create a powerful, radiation-driven wind which provides a powerful feedback [Springel] on the bulge star formation rate.

8 Foreign Affairs

8.1 Clusters

Recent X-ray observations of rich clusters of galaxies have revealed that gas in the central regions starts to cool and then seems to vanish. This, too, has been seen

as a type of feedback with the freshly fueled black hole creating a radio source which can do work on the intracluster gas and heat it through viscous processes [Begelman]. There are some problems with this scheme. Firstly there may be an energetic problem in clusters like the Perseus cluster where the nominal mass cooling rate is very high and the thermal energy requirement correspondingly large, while the central hole does not appear to be very massive. Secondly, there is a worry about how the hot radio bubbles actually heat the gas. It is claimed that this is done through sound waves. However, the motions may be subsonic and not very noisy. Furthermore it is not clear what is the necessary molecular viscosity. (Hot electrons may transport efficiently a scalar like heat by virtue of their long mean free paths. However, it is much harder to see how ions can transport a vector-like momentum in the presence of a magnetic field. Instead, I suspect that the gas really does cool, non-radiatively but ends up supported by cosmic ray pressure. If so, clusters should be over-luminous ultraviolet sources.)

8.2 Intergalactic Medium

Another famous potential role of AGN is to ionize and heat the intergalactic medium [Haiman]. However, they do not appear to have been up to this task and massive, young stars are more likely to be responsible.

8.3 Cosmology

A major factor in the development of our understanding of the evolution of AGN is the advent of the standard model of cosmology. Not only has this allowed us to compute source luminosities and, in some cases, hole masses with high accuracy, but it has also allowed us to calculate comoving source densities. For our purposes, we can adopt the ΛCDM with $a \propto \sinh^{2/3} t$. The growth of structure is prescribed in this model and has been computed, adopting the microwave background fluctuation spectrum and this can be related to the formation of the first massive holes.

9 Campaign Promises

The future of the field appears to be bright. The three great observatories (Chandra, HST and Spitzer) ought to observe for several years along with their ground-based counterparts, Gemini, Keck and VLT. The short term prospects in X-ray astronomy are also good, with Swift recently launched and Astro-E2, GLAST and NuSTAR expected this decade. At radio wavelengths the improving capabilities of the VLA and VLBA should enhance our understanding of the physical properties of jets and their relationship to the central black hole while Herschel and ALMA will effectively open up the sub mm and far infrared region to large scale AGN studies. Theoretically, three dimensional MHD simulations are enhancing our understanding of the flow of gas in and away from accretion disks

and in the relativistic region around black holes. Even more challenging investigations of radiation hydrodynamics are becoming increasingly practical. I hope that these observational and theoretical developments will transform what has long been a rather qualitative and impressionistic field into one based on hard measurement.

Acknowledgments

I thank many collaborators, notably Mitch Begelman, Paolo Coppi, Max Lyutikov, Greg Madejski and Martin Rees for their advice, instruction and encouragement. I also thank the editors for their patience. Support under NASA grants NAG5 12032 and SAO TM3-4007X is gratefully acknowledged.

List of Participants

Marek Abramowicz
Chalmers University,
S-412-96 Göteborg, Sweden
marek@fy.chalmers.se

David Alexander
Institute of Astronomy,
Madingley Road, Cambridge
CB3 0HA, UK
dma@ast.cam.ac.uk

Patricia Arevalo
Max-Planck-Institut für Extraterrestrische Physik,
Giessenbachstrasse,
D-85748 Garching, Germany
parevalo@mpe.mpg.de

Bernd Aschenbach
Max-Planck-Institut für Extraterrestrische Physik,
Giessenbachstrasse,
D-85748 Garching, Germany
bra@mpe.mpg.de

David Axon
Department of Physics,
Rochester Insitute of Technology,
85 Lomb Memorial Drive,
NY 14623, USA
djasps@rit.edu

Frederick Baganoff
Center for Space Research,
Massachusetts Institute of Technology,
Cambridge, MA 02139-4307, USA
fkb@space.mit.edu

Aaron Barth
Department of Physics and Astronomy,
4129 Frederick Reines Hall,
University of California, Irvine,
CA 92697-4575, USA
barth@astro.caltech.edu

Jill Bechtold
University of Arizona,
Tucson,
AZ 85721, USA
jill@as.arizona.edu

Thomas Beckert
Max-Planck-Institut für Radioastronomie,
Auf dem Hügel 69,
53121 Bonn, Germany
tbeckert@mpifr-bonn.mpg.de

Mitchell Begelman
JILA, 440 UCB,
University of Colorado, Boulder,
CO 80309, USA
mitch@jila.colorado.edu

Ralf Bender
Max-Planck-Institut für Extraterrestrische Physik,
Giessenbachstrasse,
D-85748 Garching, Germany
bender@mpe.mpg.de

Roger Blandford
Kavli Institute for Particle Astrophysics and Cosmology,
Stanford, CA, USA
rdb@slac.stanford.edu

Hans Boehringer
Max-Planck-Institut für Extraterrestrische Physik,
Giessenbachstrasse,
D-85748 Garching, Germany
hxb@mpe.mpg.de

Thomas Boller
Max-Planck-Institut für Extraterrestrische Physik,
Giessenbachstrasse,
D-85748 Garching, Germany
bol@mpe.mpg.de

Bernhard Brandl
Sterrewacht Leiden,
P.O. Box 9513, 2300 RA Leiden,
The Netherlands
brandl@isc.astro.cornell.edu

Niel Brandt
Department of Astronomy & Astrophysics,
The Pennsylvania State University,
525 Davey Lab, University Park,
PA 16802, USA
niel@astro.psu.edu

Wolfgang Brinkmann
Max-Planck-Institut für Extraterrestrische Physik,
Giessenbachstrasse,
D-85748 Garching, Germany
wpb@mpe.mpg.de

Volker Bromm
Department of Astronomy,
University of Texas, Austin,
TX 78712, USA
vbromm@cfa.harvard.edu

Marcella Brusa
Max-Planck-Institut für Extraterrestrische Physik,
Giessenbachstrasse,
D-85748 Garching, Germany
brusa@bo.astro.it

Andreas Burkert
Universitäts-Sternwarte München,
Scheinerstrasse 1,
D-81679, Munich, Germany
andi@usm.uni-muenchen.de

Pieter Buyle
Ghent University,
Krijgslaan 281 S9,
Ghent B-9000, Belgium
Pieter.Buyle@UGent.be

Max Camenzind
Landessternwarte Königstuhl,
D-69117 Heidelberg, Germany
M.Camenzind@lsw.uni-heidelberg.de

Francisco J. Carrera
Instituto de Fisica de Cantabria (CSIC-UC),
Avenida de los Castros,
39005 Santander, Spain
carreraf@ifca.unican.es

Andrea Cattaneo
Institut d'Astrophysique de Paris,
98 bis Bd. Arago,
F-75014 Paris, France
cattaneo@iap.fr

Alfonso Cavaliere
Dip. Fisica, Universitá di Roma Tor Vergata,
Via Ricerca Scientifica 1,
I-00130 Roma, Italy
alfonso.cavaliere@roma2.infn.it

Annalisa Celotti
SISSA/ISAS,
via Beirut 2,
I-34014 Trieste, Italy
celotti@sissa.it

Catherine Cesarsky
European Southern Observatory,
K. Schwarzscild-Str. 2,
D-85748 Garching, Germany
ccesarsk@eso.org

Jens Chluba
Max-Planck-Institut für Astrophysik,
K. Schwarzschild-Str. 1,
D-85748 Garching, Germany
jchluba@mpa-garching.mpg.de

Luca Ciotti
Dipartimento di Astronomia,
Università degli Studi di Bologna,
Via Ranzani 1,
40127 Bologna, Italy
luca.ciotti@unibo.it

Michele Cirasuolo
SISSA/ISAS,
via Beirut 2,
I-34014 Trieste, Italy
ciras@sissa.it

Eugene Churazov
Max-Planck-Institut für Astrophysik,
K. Schwarzschild-Str. 1,
D-85748 Garching, Germany
churazov@mpa-garching.mpg.de

Lodovico Coccato
Dipartimento di Astronomia,
Università di Padova,
35122, Padova, Italy
coccato@pd.astro.it

Monica Colpi
Dipartimento di Fisica G. Occhialini,
Università di Milano Bicocca,
Piazza della Scienza 3,
I-20126 Milano, Italy
colpi@mib.infn.it

Andrea Comastri
INAF–Osservatorio Astronomico di Bologna,
via Ranzani 1,
I-40127 Bologna, Italy
comastri@bo.astro.it

Paolo Coppi
Department of Astronomy,
Yale University, New Haven,
CT06520-8101, USA
coppi@astro.yale.edu

Nicolas Cretton
European Southern Observatory,
K. Schwarzscild-Str. 2,
D-85748 Garching, Germany
ncretton@eso.org

Stefano Cristiani
INAF-Osservatorio Astronomico di Trieste,
via Tiepolo 11,
I-34131 Trieste, Italy
cristiani@ts.astro.it

Jorge Cuadra
Max-Planck-Institut für Astrophysik,
K. Schwarzschild-Str. 1,
D-85748 Garching, Germany
jcuadra@MPA-Garching.MPG.DE

Luigi Danese
SISSA/ISAS,
via Beirut 2,
I-34014 Trieste, Italy
danese@sissa.it

Karsten Danzmann
Institut für Atom- und Molekülphysik,
Universität Hannover,
Appelstr. 2,
30167 Hannover, Germany
danzmann@aei.mpg.de

Carlos De Breuck
European Southern Observatory,
K. Schwarzscild-Str. 2,
D-85748 Garching, Germany
cdebreuc@eso.org

Tiziana Di Matteo
Max-Planck-Institut für Astrophysik,
K. Schwarzschild-Str. 1,
D-85748 Garching, Germany
tiziana@mpa-garching.mpg.de

Wolfgang Duschl
Institut für Theoretische Astrophysik
der Universität Heidelberg,
Tiergartenstraße 15,
69121 Heidelberg, Germany
wjd@ita.uni-heidelberg.de

Andreas Eckart
I.Physikalisches Institut,
Universität zu Köln,
Zülpicher Str.77,
50937 Köln, Germany
eckart@ph1.uni-koeln.de

Torsten Ensslin
Max-Planck-Institut für Astrophysik,
K. Schwarzschild-Str. 1,
D-85748 Garching, Germany
ensslin@mpa-garching.mpg.de

Andres Escala
Departamento de Astronomía,
Universidad de Chile,
Casilla 36-D, Santiago, Chile
escala@astro.yale.edu

Stefano Ettori
INAF–Osservatorio Astronomico di
Bologna,
via Ranzani 1,
I-40127 Bologna, Italy
settori@eso.org

Andrew Fabian
Institute of Astronomy,
Madingley Road, Cambridge
CB3 0HA, UK
acf@ast.cam.ac.uk

Renato Falomo
INAF-Osservatorio Astronomico di
Padova,
Vicolo dell'Osservatorio 5,
I-35122 Padova, Italy
falomo@pd.astro.it

Xiaohui Fan
University of Arizona,
Tucson,
AZ 85721, USA
fan@as.arizona.edu

Yi Fan
Max-Planck-Institut für Extrater-
restrische Physik,
Giessenbachstrasse,
D-85748 Garching, Germany
yifan@mpe.mpg.de

Elisa Ferrero
Max-Planck-Institut für Extrater-
restrische Physik,
Giessenbachstrasse,
D-85748 Garching, Germany
ferrero@mpe.mpg.de

William Forman
Harvard-Smithsonian Center for
Astrophysics,
Cambridge,
MA 02138, USA
wrf@cfa.harvard.edu

Giovanni Fossati
Rice University,
MS 108, 6100 Main street, Houston,
TX 77005, USA
gfossati@rice.edu

Stephan Frank
The Ohio State University,
140 W. 18th Avenue, Columbus,
Ohio 43210, USA
frank@astronomy.ohio-state.edu

Wolfram Freudling
ST-ECF/European Southern Observatory,
K. Schwarzscild-Str. 2,
D-85748 Garching, Germany
wfreudli@eso.org

Poshak Gandhi
European Southern Observatory,
Casilla 19001,
Santiago 19, Chile
pgandhi@eso.org

Isabelle Gavignaud
European Southern Observatory,
K. Schwarzscild-Str. 2,
D-85748 Garching, Germany *and*
Observatoire midi-pyrenees,
Toulouse, France
igavigna@eso.org

Reinhard Genzel
Max-Planck-Institut für Extraterrestrische Physik,
Giessenbachstrasse,
D-85748 Garching, Germany
genzel@mpe.mpg.de

Ortwin Gerhard
Astronomical Institute,
University of Basel,
Venusstrasse, Basel, Switzerland
Ortwin.Gerhard@unibas.ch

Marat Gilfanov
Max-Planck-Institut für Astrophysik,
K. Schwarzschild-Str. 1,
D-85748 Garching, Germany
gilfanov@mpa-garching.mpg.de

Roberto Gilli
INAF - Osservatorio Astrofisico di Arcetri,
Largo E. Fermi 5,
50125 Firenze, Italy
gilli@arcetri.astro.it

Jose L. Gomez
Instituto de Astrofisica de Andalucia,
Apartado 3004, Granada 18080,
Spain, *and*
Institut d'Estudis Espacials de Catalunya,
Gran Capita 2-4, 08034,
Barcelona, Spain
jlgomez@iaa.es

Hans-Jakob Grimm
Harvard-Smithsonian Center for Astrophysics,
Cambridge,
MA 02138, USA
hgrimm@head.cfa.harvard.edu

Dirk Grupe
The Ohio State University,
140W. 18th Av., Columbus,
OH 43210, USA
dgrupe@astronomy.ohio-state.edu

Zoltan Haiman
Department of Astronomy,
Columbia University, New York,
NY 10027, USA
zoltan@astro.columbia.edu

Guenther Hasinger
Max-Planck-Institut für Extraterrestrische Physik,
Giessenbachstrasse,
D-85748 Garching, Germany
ghasinger@mpe.mpg.de

Sebastian Heinz
Center for Space Research, MIT,
77 Mass. Ave., Cambridge,
MA 02139, USA

heinzs@space.mit.edu

Ryan Houghton
Department of Astrophysics,
University of Oxford,
Keble Road,
OX1 3RH, UK
rcwh@astro.ox.ac.uk

Gert Huetsi
Max-Planck-Institut für Astrophysik,
K. Schwarzschild-Str. 1,
D-85748 Garching, Germany
gert@mpa-garching.mpg.de

Scott Hughes
Department of Physics and
Center for Space Research,
Massachussets Institute of Technology,
77 Massachusetts Avenue,
Cambridge, MA 02139, USA
sahughes@mit.edu

Valentin Ivanov
European Southern Observatory,
Casilla 19001,
Santiago 19, Chile
vivanov@eso.org

Agnieszka Janiuk
Copernicus Astronomical Center,
00-716 Warsaw, Poland
agnes@camk.edu.pl

Sebastian Jester
Fermilab,
MS 127, PO Box 500,
Batavia IL, 60510, USA
jester@fnal.gov

Bruno Jungwiert
Astronomical Institute,
Academy of Science of Czech Republic,
Bočnı́ II 1401,
CZ-141 31, Prague, Czech Republic
bruno@ig.cas.cz

Guinevere Kauffmann
Max-Planck-Institut für Astrophysik,
K. Schwarzschild-Str. 1,
D-85748 Garching, Germany
gamk@mpa-garching.mpg.de

Toshihiro Kawaguchi
National Astronomical Observatory of Japan,
Mitaka, Tokyo, Japan
toshihiro.kawaguchi@obspm.fr

Nozomu Kawakatsu
SISSA/ISAS,
via Beirut 2,
I-34014 Trieste, Italy
kawakatu@sissa.it

Stelios Kazantzidis
Institute for Theoretical Physics,
University of Zürich,
Winterthurerstrasse 190,
CH-8057 Zürich, Switzerland
stelios@physik.unizh.ch

Andrew King
Department of Physics and Astronomy,
University of Leicester,
Leicester LE1 7RH, UK
ark@astro.le.ac.uk

Anton Koekemoer
Space Telescope Science Institute,
3700 San Martin Drive,
Baltimore, MD 21218, USA
koekemoer@stsci.edu

Wolfram Kollatschny
Universitäts-Sternwarte,
D-37083 Göttingen, Germany
wkollat@uni-sw.gwdg.de

Stefanie Komossa
Max-Planck-Institut für Extraterrestrische Physik,
Giessenbachstrasse,
D-85748 Garching, Germany
skomossa@mpe.mpg.de

Julian Krolik
Johns Hopkins University,
Baltimore,
MD 21218, USA
jhk@ast.cam.ac.uk

Harald Kuntschner
European Southern Observatory,
K. Schwarzscild-Str. 2,
D-85748 Garching, Germany
hkuntsch@eso.org

Robert Laing
European Southern Observatory,
K. Schwarzscild-Str. 2,
D-85748 Garching, Germany
rlaing@eso.org

Bifang Liu
Yunnan Astronomical Observatory,
Chinese Academy of Sciences,
P.O.Box 110, Kunming 650011, China
bifang@mpa-garching.mpg.de

Fred Lo
NRAO,
520 Edgemont Road, Charlottesville,
VA 22903-2475, USA

Andrei Lobanov
Max-Planck-Institut für Radioastronomie,
Auf dem Hügel 69,
53121 Bonn, Germany
alobanov@mpifr-bonn.mpg.de

Abraham Loeb
Astronomy Department,
Harvard University,
Cambridge MA 02138, USA
aloeb@cfa.harvard.edu

Marco Lombardi
European Southern Observatory,
K. Schwarzscild-Str. 2,
D-85748 Garching, Germany
mlombard@eso.org

Mami Machida
Division of Theoretical Astronomy,
NAOJ, Mitaka, Tokyo,
181-8858, Japan
mami@th.nao.ac.jp

Piero Madau
Department of Astronomy and Astrophysics,
University of California,
Santa Cruz, CA 95064, USA
pmadau@ucolick.org

Asim Mahmood
Department of Astrophysics,
University of Oxford,
Keble Road, OX1 3RH, UK
mahmood@astro.ox.ac.uk

Vincenzo Mainieri
Max-Planck-Institut für Extraterrestrische Physik,
Giessenbachstrasse,
D-85748 Garching, Germany
vmainieri@mpe.mpg.de

Rowena Malbon
Department of Physics,
University of Durham,
Rochester Building, South Road,
Durham DH1 3LE, UK
r.k.malbon@dur.ac.uk

Dan Maoz
School of Physics and Astronomy,
Tel Aviv University,
Tel Aviv 69978, Israel
dani@wise.tau.ac.il

Laura Maraschi
INAF-Osservatorio Astronomico di Brera,
Via Brera 28,
Milano, Italy
maraschi@brera.mi.astro.it

Alessandro Marconi
INAF - Osservatorio Astrofisico di Arcetri,
Largo E. Fermi 5,
50125 Firenze, Italy
marconi@arcetri.astro.it

Herman Marshall
Center for Space Research, MIT,
77 Mass. Ave.,
Cambridge, MA 02139, USA
hermanm@space.mit.edu

Smita Mathur
The Ohio State University,
140W. 18th Av., Columbus,
OH 43210, USA
smita@astronomy.ohio-state.edu

Nicola Menci
INAF- Osservatorio Astronomico di Roma,
Via di Frascati 33, I-00040
Montporzio (Roma), Italy
menci@mporzio.astro.it

Andrea Merloni
Max-Planck-Institut für Astrophysik,
K. Schwarzschild-Str. 1,
D-85748 Garching, Germany
am@mpa-garching.mpg.de

David Merritt
Rochester Institute of Technology,
85 Lomb Memorial Drive,
NY 14623, USA
David.Merritt@rit.edu

Emmi Meyer-Hofmeister
Max-Planck-Institut für Astrophysik,
K. Schwarzschild-Str. 1,
D-85748 Garching, Germany
emm@mpa-garching.mpg.de

Friedrich Meyer
Max-Planck-Institut für Astrophysik,
K. Schwarzschild-Str. 1,
D-85748 Garching, Germany
frm@mpa-garching.mpg.de

Shin Mineshige
Yukawa Institute for Theoretical Physics,
Kyoto University, Kyoto
602-852, Japan
minesige@yukawa.kyoto-u.ac.jp

Takamitsu Miyaji
Department of Physics,
Carnegie Mellon University,
Pittsburgh, PA 15213, USA
miyaji@cmu.edu

Maryam Modjaz
Harvard-Smithsonian Center for Astrophysics,
60 Garden Street,
Cambridge MA 02138, USA
mmodjaz@cfa.harvard.edu

Pierluigi Monaco
Dipartimento di Astronomia,
Universita‘ di Trieste,
via Tiepolo 11,
34131 Trieste, Italy
monaco@ts.astro.it

James Moran
Harvard-Smithsonian Center for Astrophysics,
60 Garden Street,
Cambridge MA 02138, USA
moran@cfa.harvard.edu

Mark Morris
Department of Physics and Astrometry,
University of California Los Angeles,
Los Angeles, CA 90095-1562, USA
morris@astro.ucla.edu

Monika Moscibrodzka
Copernicus Astronomical Center,
00-716 Warsaw, Poland
moscibro@poczta.fm

Nelly Mouawad
I.Physikalisches Institut,
Universität zu Köln,
Zülpicher Str.77,
50937 Köln, Germany
nelly@ph1.uni-koeln.de

Kenji Nakamura
Dept. of Sci.,
Matsue National College of Tech.,
Matsue, Shimane 690-8518, Japan
nakamrkn@matsue-ct.jp

Sergei Nayakshin
Max-Planck-Institut für Astrophysik,
K. Schwarzschild-Str. 1,
D-85748 Garching, Germany
serg@mpa-garching.mpg.de

Hagai Netzer
School of Physics and Astronomy,
Tel Aviv University,
Tel Aviv 69978, Israel
netzer@wise.tau.ac.il

Alain Omont
Institut d'Astrophysique de Paris,
98 bis Bd. Arago,
F-75014 Paris, France
omont@iap.fr

Patrick Osmer
The Ohio State University,
140 W. 18th Avenue, Columbus,
OH 43210, USA
posmer@astronomy.ohio-state.edu

Paolo Padovani
European Southern Observatory,
K. Schwarzscild-Str. 2,
D-85748 Garching, Germany
Paolo.Padovani@eso.org

Thibaut Paumard
Max-Planck-Institut für Extraterrestrische Physik,
Giessenbachstrasse,
D-85748 Garching, Germany
paumard@mpe.mpg.de

Celine Peroux
European Southern Observatory,
K. Schwarzscild-Str. 2,
D-85748 Garching, Germany
cperoux@eso.org

Sterl Phinney
Theoretical AStrophysics,
California Institute of Technology,
Pasadena, CA 91125, USA
esp@tapir.caltech.edu

Delphine Porquet
Max-Planck-Institut für Extraterrestrische Physik,
Giessenbachstrasse,
D-85748 Garching, Germany
dporquet@mpe.mpg.de

Almudena Prieto
Max-Planck-Institut für Astronomy,
Königstuhl 17
D-69117 Heidelberg, Germany
prieto@mpia.de

Daniel Proga
JILA, 440 UCB,
University of Colorado, Boulder,
CO 80309, USA
proga@colorado.edu

Martin Rees
Institute of Astronomy,
Madingley Road, Cambridge
CB3 0HA, UK
mjr@ast.cam.ac.uk

Alvio Renzini
European Southern Observatory,
K. Schwarzscild-Str. 2,
D-85748 Garching, Germany
arenzini@eso.org

Mikhail Revnivtsev
Max-Planck-Institut für Astrophysik,
K. Schwarzschild-Str. 1,
D-85748 Garching, Germany
mikej@mpa-garching.mpg.de

Hans-Walter Rix
Max-Planck-Institut für Astronomy,
Königstuhl 17
D-69117 Heidelberg, Germany
rix@mpia-hd.mpg.de

Brigitte Rocca-Volmerange
Institut d'Astrophysique de Paris,
98 bis Bd. Arago
F-75014 Paris, France
rocca@iap.fr

Eduardo Rubio Herrera
Instituto de Astronomía, UNAM
Apartado Postal 70–264,
C.P. 04510 México D.F. México
eduardo@astroscu.unam.mx

Roberto Saglia
Max-Planck-Institut für Extraterrestrische Physik,
Giessenbachstrasse,
D-85748 Garching, Germany
saglia@mpe.mpg.de

Mara Salvato
Max-Planck-Institut für Extraterrestrische Physik,
Giessenbachstrasse,
D-85748 Garching, Germany
mara@mpe.mpg.de

Sergey Sazonov
Max-Planck-Institut für Astrophysik,
K. Schwarzschild-Str. 1,
D-85748 Garching, Germany
sazonov@mpa-garching.mpg.de

Hermann Ulrich Schmidt
Max-Planck-Institut für Astrophysik,
K. Schwarzschild-Str. 1,
D-85748 Garching, Germany
schmidt@mpa-garching.mpg.de

Rainer Schoedel
I.Physikalisches Institut,
Universität zu Köln,
Zülpicher Str.77,
50937 Köln, Germany
rainer@ph1.uni-koeln.de

Bernard Schutz
Max Planck Institute for Gravitational Physics
(Albert Einstein Institute),
14476 Potsdam, Germany
schutz@aei-potsdam.mpg.de

Alberto Sesana
Dipartimento di Fisica e Matematica,
Università dell'Insubria,
via Valleggio 11,
22100 Como, Italy
Alberto.Sesana@mib.infn.it

Francesco Shankar
SISSA/ISAS,
via Beirut 2,
I-34014 Trieste, Italy
shankar@sissa.it

Peter Shaver
European Southern Observatory,
K. Schwarzscild-Str. 2,
D-85748 Garching, Germany
pshaver@eso.org

Aneta Siemiginowska
Harvard-Smithsonian Center for Astrophysics,
Cambridge,
MA 02138, USA
asiemiginowska@cfa.harvard.edu

Marek Sikora
Copernicus Astronomical Center,
00-716 Warsaw, Poland
sikora@camk.edu.pl

Volker Springel
Max-Planck-Institut für Astrophysik,
K. Schwarzschild-Str. 1,
D-85748 Garching, Germany
volker@mpa-garching.mpg.de

Lukasz Stawarz
Obserwatorium Astronomiczne,
Uniwersytet Jagielloński, ul. Orla 171,
30-244, Kraków, Poland
stawarz@oa.uj.edu.pl

Ladislav Subr
Astronomical Institute,
Charles University,
Prague, Czech Republic
subr@sirrah.troja.mff.cuni.cz

Rashid Sunyaev
Max-Planck-Institut für Astrophysik,
K. Schwarzschild-Str. 1,
D-85748 Garching, Germany
sunyaev@mpa-garching.mpg.de

Linda Tacconi
Max-Planck-Institut für Extraterrestrische Physik,
Giessenbachstrasse,
D-85748 Garching, Germany
linda@mpe.mpg.de

Yasuo Tanaka
Max-Planck-Institut für Extraterrestrische Physik,
Giessenbachstrasse,
D-85748 Garching, Germany
ytanaka@mpe.mpg.de

Christian Theis
Institute für Astronomie der Univ. Wien,
Türkenschantzstr. 17,
A-1180, Vienna, Austria
theis@astro.univie.ac.at

Jens Thomas
Universitäts-Sternwarte München,
Scheinerstrasse 1,
D-81679, Munich, Germany
jthomas@usm.uni-muenchen.de

Aldo Treves
Dipartimento di Fisica e Matematica,
Università dell'Insubria,
via Valleggio 11,
22100 Como, Italy
Aldo.Treves@mib.infn.it

Joachim Truemper
Max-Planck-Institut für Extraterrestrische Physik,
Giessenbachstrasse,
D-85748 Garching, Germany
jtrumper@mpe.mpg.de

Sachiko Tsuruta
Montana State University,
Bozeman,
MT 59717, USA
tsuruta@physics.montana.edu

Tanya Urrutia
UC Davis, Department of Physics,
1 Shields Ave., Davis,
CA 95616, USA
urrutia@physics.ucdavis.edu

Meg Urry
Department of Astronomy,
Yale University, New Haven,
CT06520-8101, USA
meg.urry@yale.edu

Gijs Verdoes-Kleijn
European Southern Observatory,
K. Schwarzscild-Str. 2,
D-85748 Garching, Germany
gverdoes@eso.org

Cristian Vignali
Dipartimento di Astronomia,
Università degli Studi di Bologna,
Via Ranzani 1,
40127 Bologna, Italy
cristian.vignali@bo.astro.it

Stefan Wagner
Landessternwarte Königstuhl,
D-69117 Heidelberg, Germany
S.Wagner@lsw.uni-heidelberg.de

Jian-Min Wang
Laboratory for High Energy Astrophysics,
Institute of High Energy Physics,
Chinese Academy of Sciences,
Beijing 100039, P.R. China
wangjm@mail.ihep.ac.cn

Yiping Wang
Purple Mountain Observatory,
Academia Sinica, Nanjing,
China
ypwang@pmo.ac.cn

Michael Weidinger
European Southern Observatory,
K. Schwarzscild-Str. 2,
D-85748 Garching, Germany
mweiding@eso.org

Simon White
Max-Planck-Institut für Astrophysik,
K. Schwarzschild-Str. 1,
D-85748 Garching, Germany
swhite@mpa-garching.mpg.de

Chris Willott
Herzberg Institute of Astrophysics,
National Research Council,
5071 West Saanich Rd, Victoria,
B.C. V9E 2E7, Canada
chris.willott@nrc.ca

Margrethe Wold
European Southern Observatory,
K. Schwarzscild-Str. 2,
D-85748 Garching, Germany
mwold@eso.org

Stuart Wyithe
University of Melbourne,
Parkville Vic 3010,
Australia
swyithe@isis.ph.unimelb.edu.au

Weimin Yuan
University of Cambridge,
Institute of Astronomy, Madingley Road,
CB3 0HA, UK
wmy@ast.cam.ac.uk

Anton Zenzus
Max-Planck-Institut für Radioastronomie,
Auf dem Hügel 69,
53121 Bonn, Germany
azensus@mpifr-bonn.mpg.de

Author Index